== and ==

Proceedings of the
Seventh Europhysical Conference on
Defects in Insulating Materials Eurodim 94

Lyon 1 – University

July 5–8, 1994

Part III

Guest Editors:

M. G. Blanchin, J. Davenas, B. Moine,
C. Pédrini and M. Treilleux

19970515 150

# Radiation Effects and Defects in Solids

### AIMS AND SCOPE

*Radiation Effects and Defects in Solids* publishes experimental and theoretical papers of both a fundamental and applied nature that contribute to the understanding of either phenomena induced by the interaction of radiation with condensed matter or defects in solids introduced not only by radiation but also by other processes. Papers are categorised in three groups.

*Section A: Radiation Effects* — Suitable topics include, but are limited to, atomic collisions, radiation induced atomic and molecular processes in solids, the stopping and range of ions and radiation damage, sputtering and mixing in solids, radiation-induced transport phenomena and the role of defects and impurities introduced by radiation. Papers in ion implantation in metals and semiconductors as well as on radiation effects in insulators and superconductors, in fusion and fission devices and in space research are considered. Studies on fission tracks, isotope dating and ion beam analytic techniques are also welcome.

*Section B: Crystal Lattice Defects and Amorphous Materials* — Topics covered include atomic and electronic properties of defects, influence of defects on lattice properties and processes, the latice-defect approach to solid state reactions such as clustering, precipitation, laser annealing and the role of impurities, the defects dynamics in a non-steady state such as under particle or electromagnetic irradiation or during a rapid temperature change and problems associated with the metastable nature of amorphous materials.

*Section C: Radiation Effects and Defects in Solids Express* — This section is available separately on subscription and presents significant short notes and communications in camera-ready form from the above fields for the fastest possible publication.

Proceedings of the
Seventh Europhysical Conference on
Defects in Insulating Materials Eurodim 94

Lyon 1 – University

July 5–8, 1994

Part III

Guest Editors:

M. G. Blanchin, J. Davenas, B. Moine,
C. Pédrini and M. Treilleux

Radiation Effects and Defects in Solids   Volume 136 (1995)
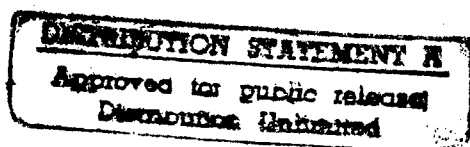
## CONTENTS – PART III

**Note on Pagination, Author Index and Table of Contents**

*The Proceedings of the EURODIM 94 Conference is being published in four volumes of Radiation Effects and Defects in Solids (Volume 134, Part I, Volume 135, Part II, Volume 136, Part III and Volume 137, Part IV). To facilitate indexing and referring to this Proceedings, the page numbers of Volume 135, Volume 136 and Volume 137 will run continuously from the end of Volume 134. An author index will appear at the end of Volume 137. A complete table of contents will appear in Volume 134, Part I and Volume 137, Part IV.*

# 8    Photorefractive and non linear materials

# 9    Radiation Defects

CONTENTS

vi                             CONTENTS

# 7 LASER MATERIALS

# ON THE TEMPERATURE DEPENDENCE OF THE RATE OF ENERGY TRANSFER BETWEEN RARE EARTH IONS IN SOLIDS

B. DI BARTOLO, G. ARMAGAN* and M. BUONCRISTIANI**

*Department of Physics, Boston College, Chestnutt Hill, MA 02167, USA; *Department of Physics, The College of William and Mary, Williamsburg, VA 23185, USA; **Department of Physics, Christopher Newport University, Newport News, VA 23606, USA*

We have conducted a number of experiments in order to ascertain the temperature dependence of the rate of energy transfer between rare earth ions in solids. The mechanism of such dependence is peculiar to each donor-acceptor pair. We report typical examples and point to some criteria that emerge from our studies.

*Key Words*: energy transfer; YAG:Er, Ho; YAG:Tm, Ho; YF$_3$:Gd, Er; rare earth ions.

The probabilities of multiphonon relaxation of rare earth ions (REI) in solids[1,2] as well as those of phonon assisted energy transfer between these systems[3] have been found to decrease according to an exponential law with the increase of the energy gap. Single energy phonon models were used by Zverev *et al.*[2] and by Yamada *et al.*[3] to fit their temperature dependent data. The latter workers studied the temperature dependence of the rate of energy transfer between REI in Y$_2$O$_3$ involving the production of 5 to 10 phonons, and found that this rate increases with temperature. We have found a different temperature dependence in energy transfer processes involving a small number of phonons.

## 1 YAG:Er, Ho

The two lowest excited states of Er and Ho in YAG are centered at $\sim$ 6,300 and $\sim$ 5,000 cm$^{-1}$, respectively. Figure 1 presents the data related to the decay of the 4I$_{13/2}$ state of Er, following pulsed excitation. These results can be summarized as follows:

1. The decay of the $^4$I$_{13/2}$ state of Er, in the presence of Ho is exponential.
2. The temperature dependence of this decay is consistent with a decrease of the Er → Ho energy transfer rate with increasing temperature.

Since the energy gap between donor and acceptor levels is bridged by creating phonons, we would expect the energy transfer process to be more probable when there are many phonons around, i.e. at high temperature. However, as we raise the temperature, we change the population distributions in the energy levels that make up the initial states of the energy transfer process ($^4$I$_{13/2}$ of Er and $^5$I$_8$ state of Ho), and increase the effective energy gap between them, reducing the energy transfer rate. The decrease of this rate at high temperature indicates that in the present case the latter mechanism (rearrangement of populations) is more relevant in determining the temperature dependence of the process than the former mechanism (phonons bridging the energy gap).

## 2 YAG:Tm, Ho

The two lowest excited states of Tm and Ho in YAG are centered at $\sim$ 5,700 and $\sim$ 5,300 cm$^{-1}$, respectively. The experimental results can be summarized as follows:
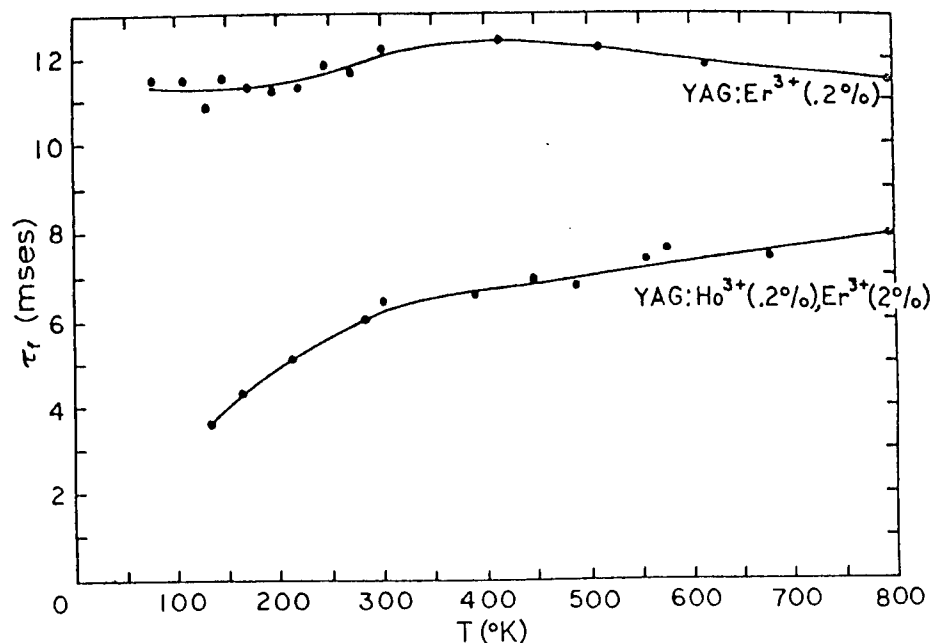
FIGURE 1    Temperature Dependence of the Er Lifetime in YAG ($^4I_{3/2}$ State).

1. The Tm ion, when excited in its $^3H_4$ state, experiences a cross-relaxation process. The cross relaxation rate is proportional to the square of the concentration of Tm ions. The decay pattern of the $^3H_4 \rightarrow {}^3H_6$ emission of $Tm^{3+}$ for various Tm concentrations is shown in Figure 2.

2. The rate of diffusion among Tm ions in their $^3H_4$ states is much slower than the cross relaxation rate.

3. The patterns of the early emissions from different spectral regions of YAG:Tm, Ho are shown in Figure 3. We see from this figure that, after about 300 $\mu$sec, the decay curves become parallel, giving evidence of thermalization among the $^3F_4$ (Tm) and $^5I_7$ (Ho) manifolds. We note here that this thermalization occurs on a time scale comparable to that of the lifetimes of the two manifolds.

## 3   $YF_3$:Gd,Er[4]

The two excited states of Gd and Er involved in the energy transfer process are centered at $\sim$ 32,000 and $\sim$ 31,400 cm$^{-1}$, respectively. The experimental results can be summarized as follows:

1. Gd $\rightarrow$ Er energy transfer takes place. The two states involved are: $^6P_{7/2}$ of $Gd^{3+}$ and $^2P_{3/2}$ of $Er^{3+}$.

2. The lifetimes of the emissions from these two states in the 20–300 K temperature region are reported in Figure 4. Comparing the lifetime of $Gd^{3+}$ in the absence of $Er^{3+}$
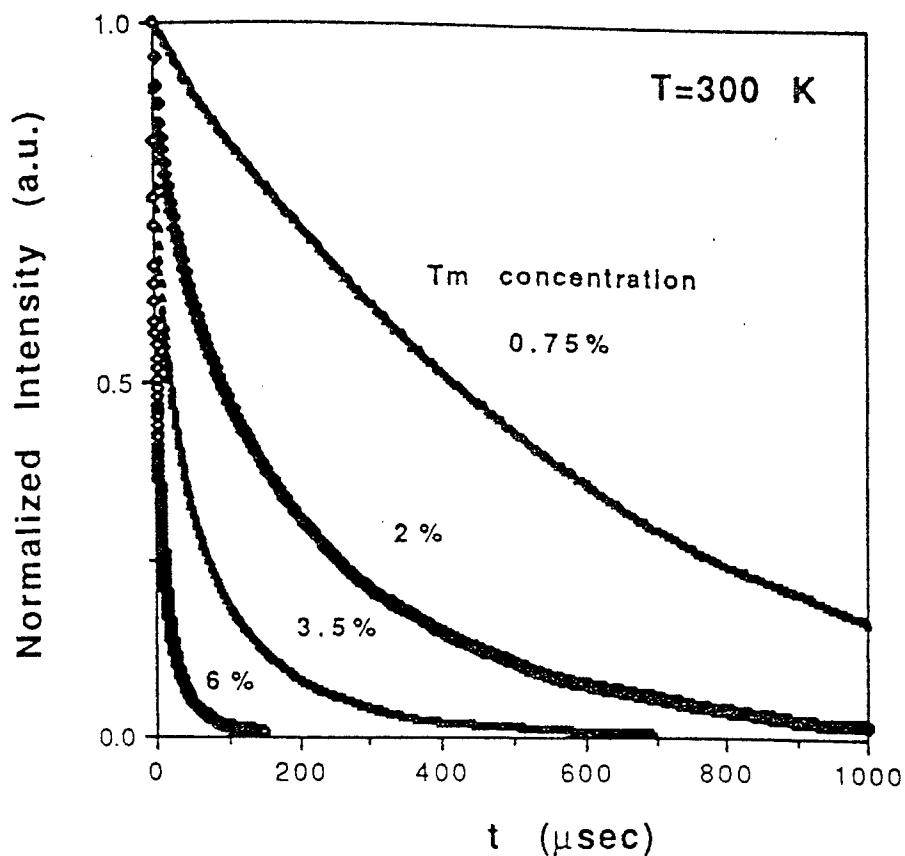
FIGURE 2   Decay Patterns of the $^3H_4 \rightarrow \, ^3H_6$ Tm Emission at 830 nm in YAG:Tm, Ho for Various Tm Concentrations at Room Temperature.

with that of the same ion in the presence of $Er^{3+}$ we see that the rate of the energy transfer process decreases with increasing temperature up to $\sim 180$ K and then increases.

This case indicates a behaviour intermediate between that of YAG:Er, Ho described above and the case considered by Yamada et al.[3] In fluorides the phonon energy cutoff is lower than in oxides; we expect then that the energy transfer process in $YF_3$ may involve the production of 2 or 3 photons.

## 4   CONCLUSIONS

Our results are consistent with the following features:
1. If the donor-acceptor energy gap can be bridged by the production of one or two phonons, then the energy transfer rate decreases with increasing temperature.
2. If the energy gap between donor and acceptor is smaller than the energy phonon cutoff, thermalization between the donor and acceptor excited states may occur.
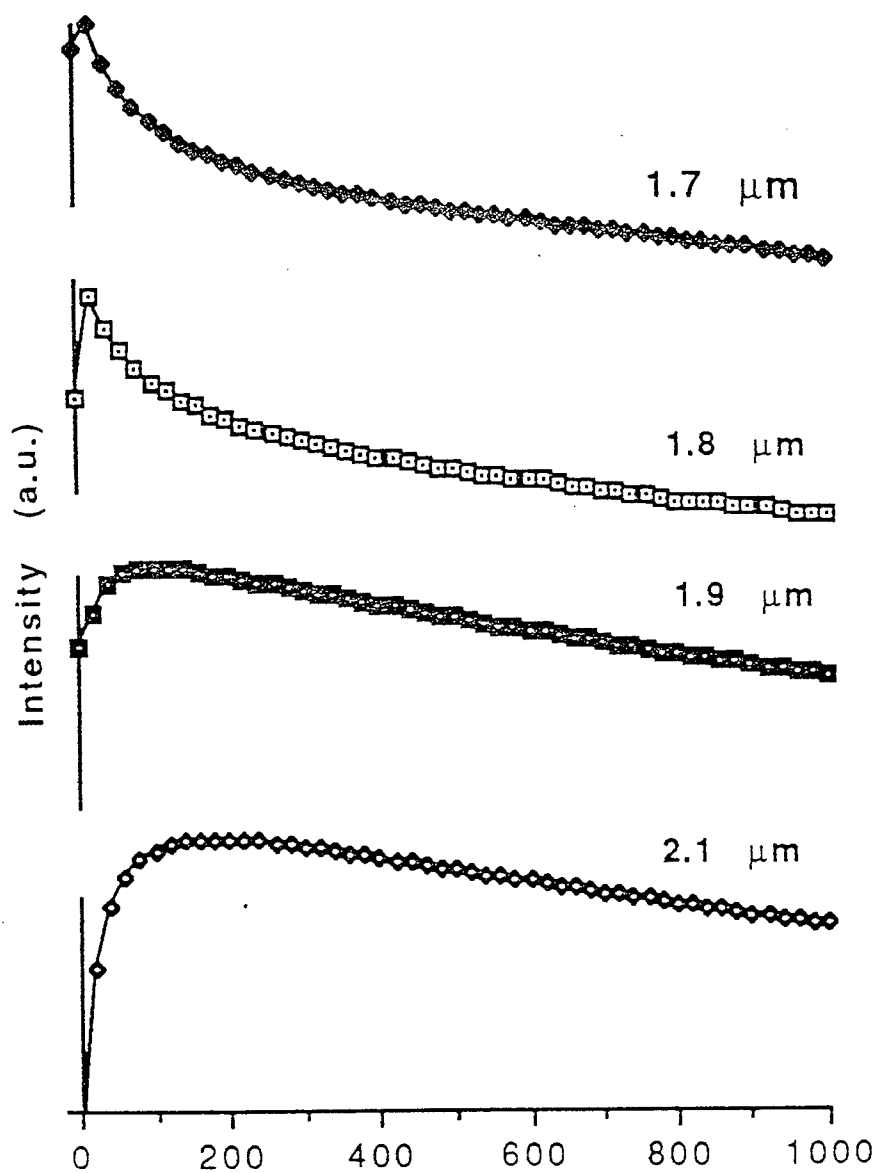
FIGURE 3   Patterns of the Early Emission from Different Spectral Regions of YAG:Tm(6%), Ho (0.5%) at Room Temperature.
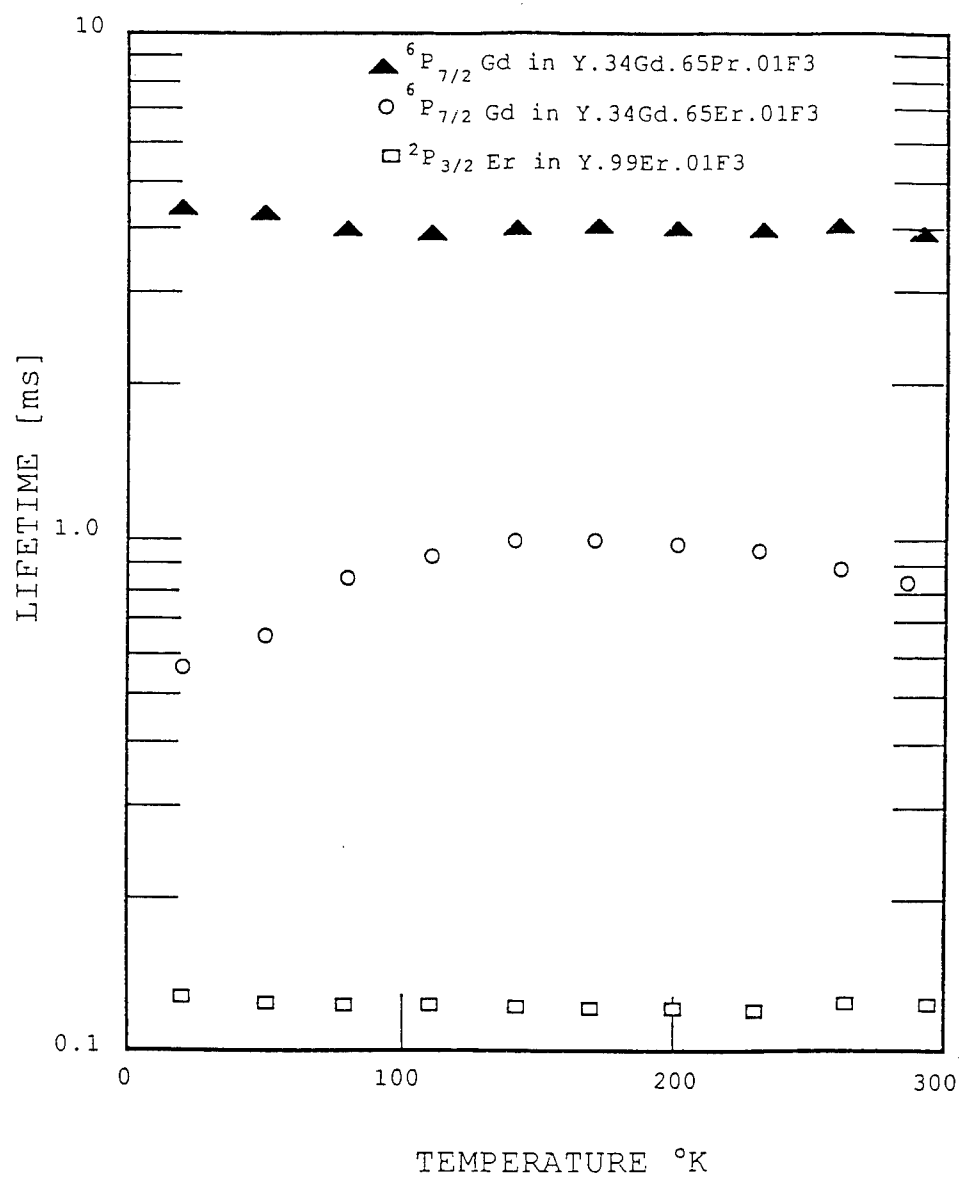
FIGURE 4   Temperature Dependence of the Lifetimes of the $^6P_{7/2}$ State of $Gd^{3+}$ and of the $^2P_{3/2}$ State of $Er^{3+}$ in Various Fluoride Samples.

(Thermalization between sharp single ion levels and pair levels of Cr ion in ruby has also been observed experimentally.)
3.  Thermalization may occur on a time scale comparable to the lifetimes of the donor and of the acceptor. In such a case it may take some time for the decay curves of the donor and of the acceptor to take exponential shapes with the same time constant.

REFERENCES

1.  M. Weber, *Phys. Rev.* **B8,** 54 (1973).
2.  G. M. Zverev, *et al., Sov. Phys. JETP* **33,** 497 (1971).
3.  N. Yamada *et al., J. Phys. Soc. Japan* **32,** 1577 (1972).
4.  J. M. Collins, B. Di Bartolo, and T. E. Peters, *Extended Abstracts of the Electrochemical Society, Vol.* **86-2,** 1046 (1986).

# PROGRESS IN ULTRAFAST COLOR CENTER LASERS

### K. MöLLMANN and W. GELLERMANN

*Physics Department, University of Utah, Salt Lake City, Utah 84112*

We report new ultrafast color center lasers operating in the near infrared spectral range. Using newly developed KCl and KBr $(F_2^+)_H$ and $(F_2^+)_{AH}$ color center systems and synchronous mode-locking we realize picosecond and subpicosecond color center laser operation for the first time in the 1.8–2.4 $\mu$m wavelength range. Using semiconductor saturable absorbers we passively mode-lock NaCl $(F_2^+)_H$ and KCl $F_A$ (Tl) color center lasers in single- and coupled-cavity configurations. This results in mode-locked laser operation in the 1.5–1.7 $\mu$m range with shortest obtained transform-limited pulses of $\sim$ 150 femtosecond duration and pulse energies as high as several nJ. As a step toward infrared spectral continuum generation we amplify these nJ-level pulse energies by a factor of $\sim 10^3$ using KCl $F_A$(Tl) amplifier crystals.

*Key words:* lasers, color center; lasers, mode-locked; lasers, solid-state; femtosecond phenomena, pulse amplification.

## 1 SYNCHRONOUSLY MODE-LOCKED COLOR CENTER LASERS

Using newly developed $(F_2^+)_H$ and $(F_2^+)_{AH}$ color center systems in KBr hosts we could achieve a significant wavelength extension of synchronously mode-locked color center lasers (CCLs) into the 1.8–2.4 $\mu$m range.[1] The tuning characteristics of these CCLs are shown in Figure 1 together with other synchronously mode-locked CCLs based on pumping with Nd:YAG lasers. Typical pulse durations of the KBr lasers are $\sim$ 1 psec, and pulses as short as $\sim$ 400 femtoseconds can be obtained at the expense of somewhat higher noise levels.

In order to improve the pulse quality of synchronously mode-locked CCLs, we applied the technique of coherent photon seeding.[2] Using an empty external cavity and feeding back coherently a very small fraction of the laser pulse intensity to a NaCl $(F_2^+)_H$ CCL crystal, timed such that it arrived shortly before the main pulse, we could generate essentially transform-limited picosecond pulses, tunable over the 1.5–1.7 $\mu$m range, with average power levels as high as 1.3 W. In addition, the pulse energy fluctuations were found to be reduced by as much as one order of magnitude.

## 2 PASSIVELY MODE-LOCKED COLOR CENTER LASERS

Using bulk and multiple quantum well semiconductors (InGaAsP) as saturable absorbers[3] we passively mode-locked the NaCl $(F_2^+)_H$ and KCl $F_A$ (Tl) CCLs. We achieved self-starting, stable, high repetition-rate, tunable laser operation in the 1.5 to 1.7 $\mu$m range.[4] We find the pulse characteristics to depend critically on pump power, output coupling, bandwidth limitation, and saturable absorption conditions. Using a resonator configuration in which both the gain material and the saturable absorber are placed in a common single cavity, we obtained under optimal conditions shortest transform-limited pulses of $\sim$ 150 femtosecond duration. Autocorrelation trace and frequency spectrum of such pulses are shown in Figure 2. To increase the relatively low pulse energy levels ($\sim$ 0.8 nJ) we removed the losses of the saturable absorber from the main cavity and placed the material instead into a weakly coupled external cavity. With this 'resonant passive mode-

K. MöLLMANN AND W. GELLERMANN
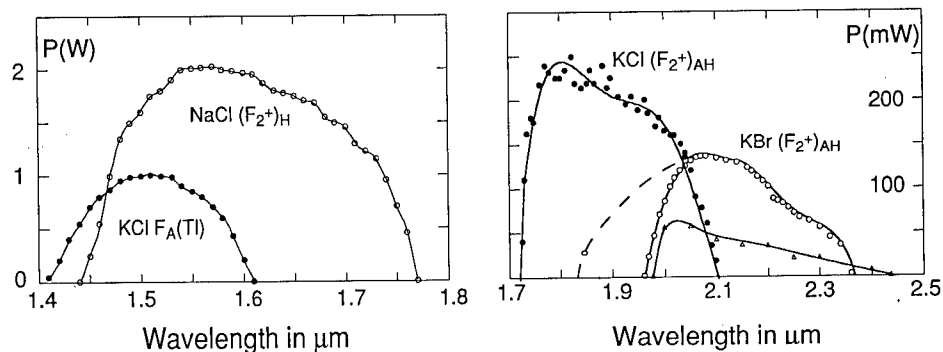


FIGURE 1   Tuning characteristics of synchronously mode-locked color center lasers.

locking' scheme we obtain a fourfold increase in pulse energy at only a modest broadening of the pulsewidths.[5]

## 3   PULSE AMPLIFICATION

We explored the possibility of using $F_A$ (Tl) centers in KCl to amplify the nJ-level pulse energies obtainable from the CCL oscillators described above. By pumping of a 1.5 cm long KCl $F_A$ (Tl) amplifier crystal with a Q-switched Nd:YAG laser we obtained pulse energies of several ten $\mu J$ in a collinear two-pass amplification scheme. These energy levels are sufficiently high to generate spectral continuum pulses in the near infrared using suitable nonlinear materials.
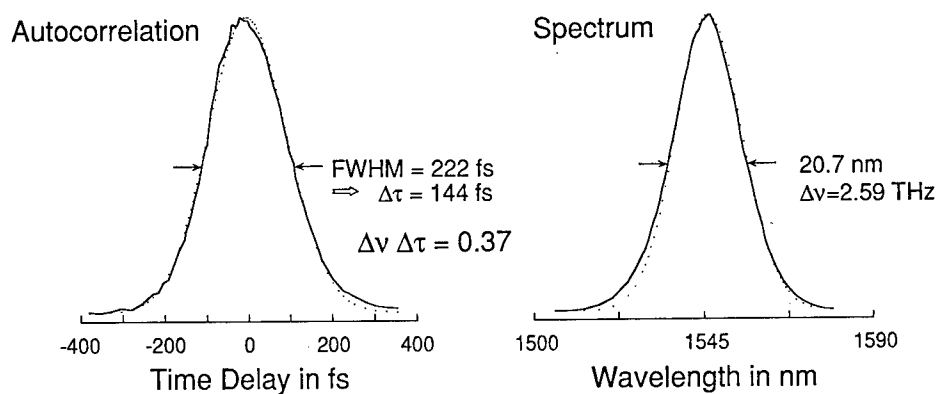


FIGURE 2   Autocorrelation and spectrum of shortest passively mode-locked KCl $F_A$ (Tl) laser pulse.

REFERENCES

1. K. Möllmann, M. Schrempel, Bing-Kun Yu, and W. Gellermann, *Opt. Lett.* **19**, 960 (1994).
2. K. Möllmann and W. Gellermann, *Opt. Lett.* **19**, 490 (1994).
3. M. N. Islam *et al.*, *IEEE J. Quantum Electron.* **25**, 2454 (1989).
4. C. E. Soccolich M. N. Islam, K. Möllmann, W. Gellermann, and K.R. German, *Appl. Phys. Lett.* **61**, 886 (1992).
5. K. Möllmann, W. Gellermann, C.E. Soccolich, and M.N. Islam, *Opt. Lett.* **18**, 42 (1993).

# THE RELEASE OF STORED ENERGY IN HEAVILY IRRADIATED NaCl. EXPLOSIVE REACTIONS.

D. VAINSHTEIN, M. VAN DEN BEMT, J. SEINEN, H. C. DATEMA
and H. W. DEN HARTOG

*Solid State Physics Laboratory, University of Groningen, Nijenborg 4, 9747 AG
Groningen, The Netherlands.*

During irradiation of NaCl with ionizing radiation at moderate temperatures (50–150°C) irregular structures of very fine Na and Cl nano-precipitates are formed. The increase of the temperature to a value between 50 and 250°C might induce explosive reactions between radiolytic Na and Cl in heavily irradiated NaCl, which are accompanied by a loss of stored energy up to 30%. The reactions produce a very fast local temperature rise of at least 800°C and are accompanied by thermal shock waves. Due to explosive reactions the crystals desintegrated into many small fragments. Experiments and theoretical calculations have been carried out to study heavily irradiated NaCl and the dynamics of the thermal shock wave.

*Key words*: explosive reactions, thermal shock wave.

## 1 INTRODUCTION

Groote and Weerkamp[1] have reported that during or after irradiation experiments some NaCl samples exploded as a result of the spontaneous back reaction between radiolytic Na and Cl. Recent experiments in which, solid samples are subjected to intense thermal radiation have demonstrated that thermal shock waves with pressures up to hundred Mbar[2,3] occur. We have used differential scanning calorimetry (DSC) and scanning electron microscopy (SEM) to perform detailed experiments on significant numbers of heavily irradiated NaCl (doped with K and KBF$_4$) and natural rock salt, which showed explosive reactions. Theoretical calculations have been carried out to simulate the propagation of dynamic thermal shock waves due to the release of stored energy in heavily irradiated rock salt.

## 2 RESULTS

Annealing experiments were combined with latent heat measurements (of melting of metallic Na) to study the decrease of the latent heat of heavily damaged NaCl due the explosive reactions. Depending upon the amount of radiation damage present in a crystal, thermal DSC-spikes associated with the explosive back reactions between radiolytic products Na and Cl, were observed between 100 and 250°C (Figure 1a). We have found that the temperature of the thermal spikes decreases with increasing amounts of metallic sodium. Very large spikes, approximately five times stronger have been observed for tightly encapsulated samples (Figure 1b). This effect is called the "fire cracker effect".

Due to the explosive reactions the crystals desintegrated into many small, irregularly shaped fragments. We have studied these small fragments by scanning electron microscopy. Some of them have rounded structures at the surface, which is indicative for local melting processes occurring during a short period after the explosive reaction. We assume that the local temperature becomes higher than melting temperature of NaCl ($\geq$ 808°C).
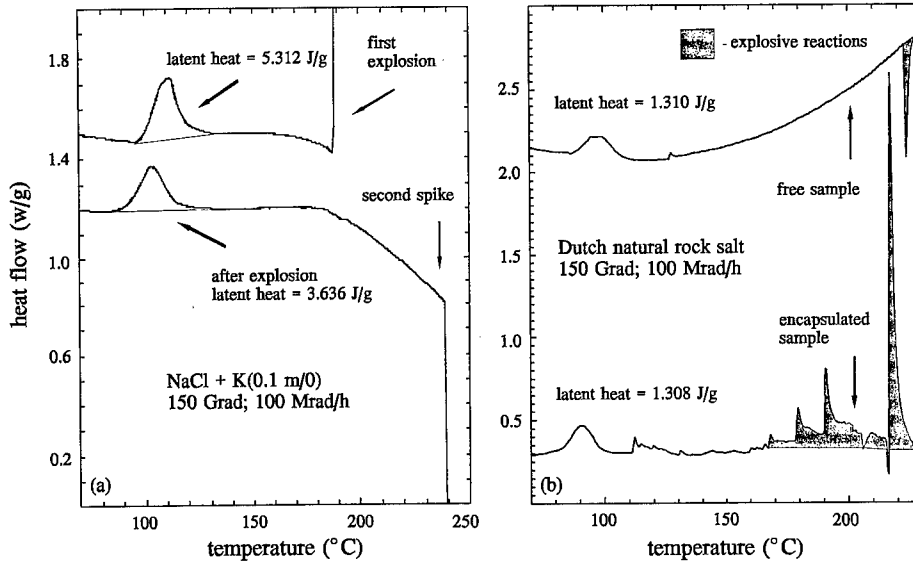
FIGURE 1   Explosive reactions in heavily irradiated NaCl; (a) the loss of latent heat associated with explosive reactions between a radiolytic products Na and Cl is about 25%; before and after explosion the sample weight is 10.32 mg, (b) the encapsulated samples show an approximately five times stronger reaction.

Theoretical calculations using the experimental results have been performed to simulate the dynamic effects due to the release of stored energy in heavily irradiated rock salt. On the basis of thermodynamics it is possible to derive equations describing the behaviour of a material in which a very rapid local a change of temperature occurs. These equations are the thermoelastic equations. For an isotropic medium they look as follows:

$$\mu\nabla^2 u_i(\vec{x},t) + (\mu + \lambda)\partial_i\partial_j u_j(\vec{x},t) - \rho\partial_t^2 u_i(\vec{x},t) - \gamma\partial_i\theta(\vec{x},t) = 0,$$

$$\nabla^2\theta(\vec{x},t) - \frac{1}{\chi}\partial_t\theta(\vec{x},t) - \eta\partial_t\partial_i u_i(\vec{x},t) = -\frac{1}{\chi}Q(\vec{x},t).$$

These equations enable us to calculate numerically the temperature, $\theta$, and the displacements, $\vec{u}$, at any position and time $(\vec{x}, t)$, and consequently the stresses. The back reaction causes a local rise of temperature of several hundreds degrees centigrade. The stresses produced by this thermal shock depend on the rate of the back reaction between Na and Cl and, if the area in which the reaction takes place spreads out, on the velocity at which it spreads out. The model calculation of the dynamics of the thermal shock wave for a spherically symmetric system has been shown in Figure 2. We believe that the local back reactions are capable to produce large stresses at remote places which may initiate more back reactions. This would explain the "fire cracker effects".

## 3   SUMMARY

The explosive reactions which are connected to a loss of latent heat are associated with back reactions between the radiolytic products Na and Cl. The heavily irradiated NaCl sample as a whole is involved in this back reaction and explodes in many small fragments.
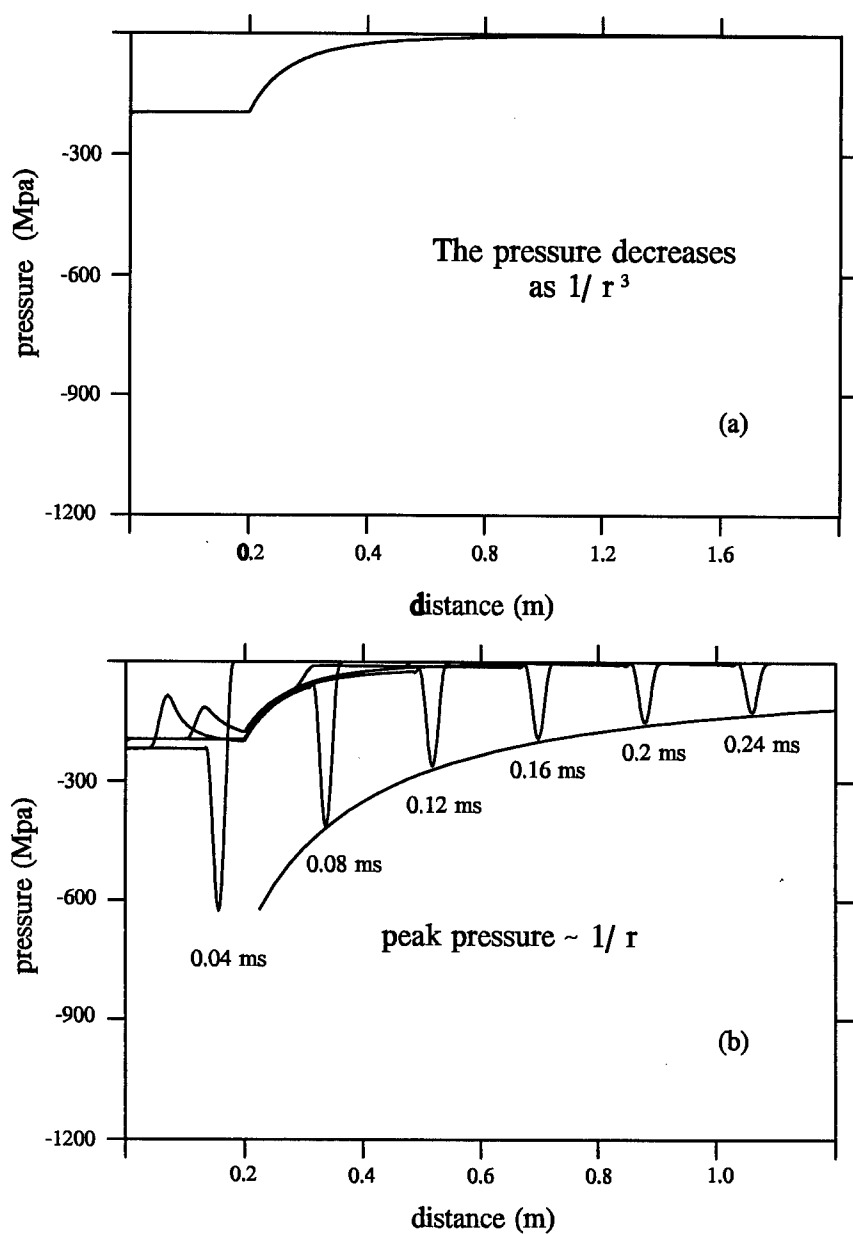
FIGURE 2   Results of model calculations of the shock wave for the spherically symmetric system; the decrease of the strength of the pressure vs distance (a) for the quasi-static stress (b) for the envelope of the peaks of the thermal shock wave.

The experimental study and theoretical calculations of rock salt has shown that for some samples a very fast temperature rise of at least 800°C as a result of local back reactions. If the region, where the spontaneous back reaction occurs, moves at the speed of sound, i.e. exactly equal to the speed of the shock wave, the magnitude of the stresses reaches a maximum value. The theoretical calculations have also shown that the strength of the shock wave decreases much slower with the distance than the quasi-static (residual) stress.

## REFERENCES

1. J. C. Groote and J. R. W. Weerkamp, *Thesis, University of Groningen* (1990).
2. R. Cauble, D. W. Phillion *et al. Phys. Rev. Lett.* **70**, 2102 (1993).
3. Th. L#ower, R. Sigel, K. Eidmann *et al. Phys. Rev. Lett.* **72**, 3186 (1994).

# ON THE MECHANISM OF CONTRAST IN THE CATHODOLUMINESCENCE IMAGING OF LASER CRYSTALS

V. LUPEI

*Institute of Atomic Physics, 76900 Bucharest, Romania*

The possibility of use of cathodoluminescence imaging in a scanning electron microscope as a method for characterization of quality of laser crystals and control of crystal growth technology is discussed. The room temperature measurements reveal a large variety of defects and non-uniformities such as striations, facets, inclusions, spiral dislocations and so on in important laser crystals such as YAG:Nd or YAG:Tm, Cr. Various mechanisms leading to differences in emission intensity such as the concentration effect and cross-relaxation or the influence of stress on the efficiency of energy transfer between the bound exciton and the rare-earth activator are discussed.

## 1 INTRODUCTION

The increasing of energetic parameter of solid state lasers (average and peak power) impose severe quality criteria upon the laser active media. Although standard sets of passive (optical, spectroscopic, etc) or active parameters for characterization exist, new methods to improve it and to add useful information for the crystal growth technology are of interest. Recently the using of room temperature imaging in a scanning microscope for studying the YAG defects was reported;[1,2] exceptionally clear images of defects such as striations, facets, inclusions, spiral dislocations and so on[2] show the potential of this method in revealing defects or structural irregularities of laser crystals. The cathodoluminescence imaging was recently[3] used for investigation of Ti-doped $YAlO_3$. The present paper discusses the features of cathodoluminescence imaging in the study of important laser systems such as YAG:Nd and YAG:Cr, Tm.

## 2 EXPERIMENTAL METHODS

Single crystals of YAG:Nd with Nd concentration up to 1.5at.% and of YAG:Cr, Tm (Cr up to 0.3at.% and Tm up to 5at.%) have been grown by Czochralski method. Samples from various parts of good quality crystals as well as from parts with technological accidents (such as interruption and restart of the growth cycle) have been selected for study. The catodoluminescence imaging was observed in a scanning electron microscope Stereoscan 100 -Cambridge Instruments, by using a standard cathodoluminescence accessory; the accleration voltage used was in the range of 20–40 kV.

## 3 EXPERIMENTAL RESULTS

The cathodoluminescence images recorded in standard conditions (about 10 sec for the registration of a picture) proved to be extremely rich in information about the crystal quality and its connection with crystal growth technological details. The images show a variety of defects, some of them difficult to observe by other methods. The growth striations in the crystals appear very clearly and their extent and spacing could be precisely
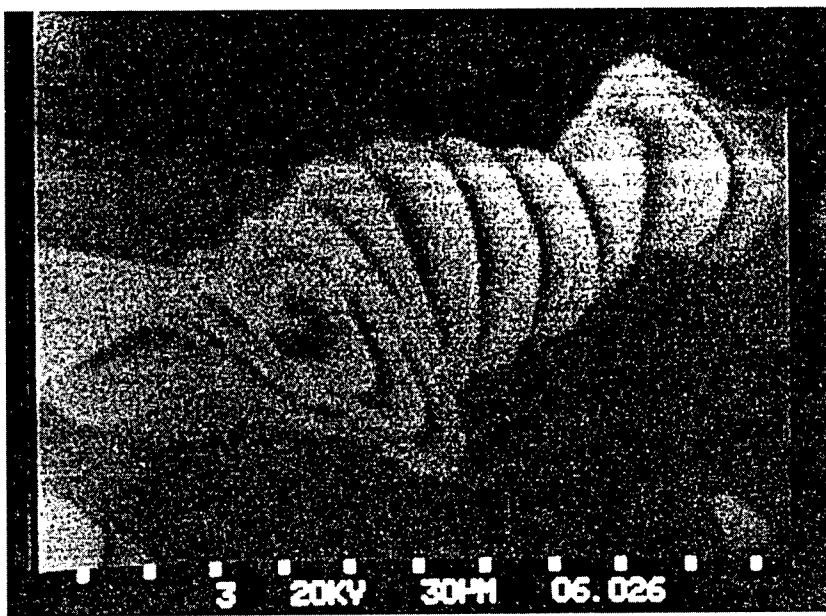
FIGURE 1    Cathodoluminescence image of a spiral dislocation in YAG:Nd.

connected with crystal growth process parameters such as the pulling speed, crystal rotation and thermal inertia of the growth set-up. The faceting shows very clearly with a lot of details about the coring of the crystal. In the regions that could be connected with technological accidents, the presence of gaseous inclusions (cavities) appear clearly, with spectacular deformation of the striations. Particularly impressive was the observation of spiral dislocations in YAG:Nd of quite large size (diameter 60–120 $\mu$m and length up to 300–400 $\mu$m) with an apparent relief much higher than the penetration of the electrons inside the crystals (Figure 1). In the case of YAG:Cr, Tm crystals an evident effect of the Cr concentration on the imaging was observed. Figure 2 shows the cathodoluminescence image of striations in the region of core for a YAG crystal containing 0.3% of Cr and 5% of Tm.

## 4    DISCUSSION

The luminescence emission of rare earths ions in crystals under X-ray and electron bombardment was the subject of intense investigation, connected with the use of these systems as X-ray phosphors, display devices with cathode-ray excitation, etc. It is generally recognized that the emission is not a direct result of the collision of incident electrons with the rare-earth ions. Due to the interaction with the lattice constituents the incident electrons are thermalized and multiplied leading to formation of electron-hole pairs. The fast capture of these electrons and holes in the vicinity of the rare-earth ions leads to the apparition of bound excitons which could recombine by transferring their excitation to the rare-earth ion. An important condition for this transfer is that the rare-earth ion should have energy levels in the proximity of the bound exciton. On the other hand, in order to have a good image it is necessary that the rare-earth emission lifetime to
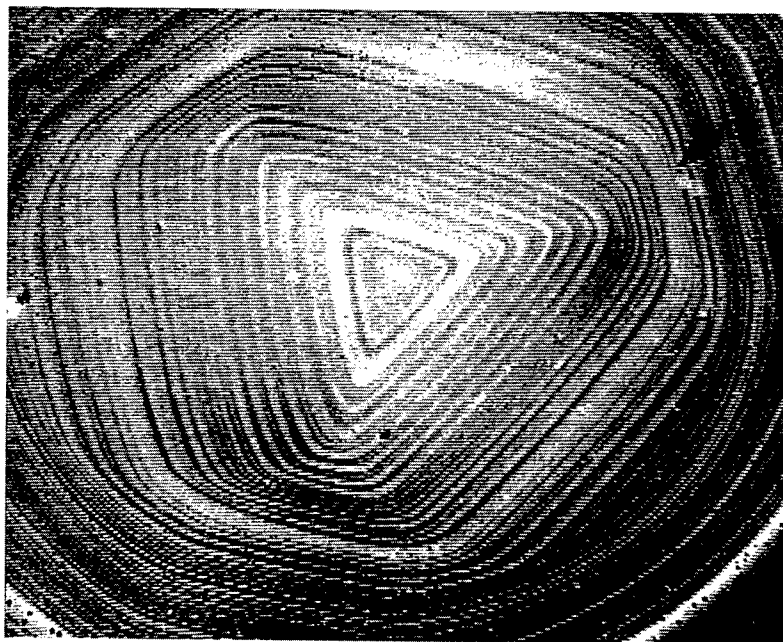
FIGURE 2   Cathodoluminescence image of striations in the region of the core in a YAG:Nd crystal.

be shorter than the dwell time of the incident electron beam. For this time of recording this means that the lifetime of the emitting state should not exceed several microseconds.

In the case of $Nd^{3+}$ a high density of electronic states from $3f^3$ and $4f^25d$ configurations lie in the forbidden gap of the crystal. The energy of the bound exciton could be transferred in these levels from which it relaxes to the $^2F_{5/2}$ level placed in the range of 38 000 $cm^{-1}$; the lifetime of this level is of the order of 3 $\mu$sec and visible emission from it to $Nd^{3+}$ levels situated in the 10 000–20 000 $cm^{-1}$ range takes place. Because of this the $Nd^{3+}$ ion is very convenient for excitation by electron bombardment of crystals. In case of Tm short lived visible emission from the uv level $^1D_2$ (whose lifetime depends strongly on the Tm concentration) to lower excited levels could take place.

A very important question which arises in this investigation is the cause of the differences in emission intensity between the various parts of the crystal. Several causes could contribute to this: (i) differences in emission intensity due to non-uniform distribution of the dopant in region of defects. It is thus known that the segregation coefficient of rare-earth ions in crystals depends on the plane of growth; thus, for instance, in the region of facetted growth of $\langle 111 \rangle$ pulled YAG:Nd crystals the concentration of Nd is larger than in the rest of the crystal; (ii) the concentration quenching of luminescence: for many rare-earth ions the quantum efficiency of emission could be dramatically reduced by the energy transfer due to cross-relaxation between the activator ions; thus as concerns the emission of these ions the more concentrated regions instead of becoming brighter behave as dark spots; (iii) the mechanical stress at the location and in the vicinity of defects could produce large variations of the energy gap of the crystal. This leads in turn to large variations of the bound excitons energies which modify the resonance conditions for energy transfer to the rare-earth ions. Taking into account the very complex situation of the doped laser crystals, a combination of these and possibly of other processes could explain

the differences in the emission intensity in vicinity of defects for the various cases. Although at the present time it is not possible to relate in a quantitative way the observed differences in emission with the specific parameters of the defects, the very rich qualitative information about the presence of various defects in the laser crystals makes this method a powerful technique of characterisation of these systems.

REFERENCES

1. Deng Peizhen, private communication (1987).
2. V. Lupei, A. Popa, I. Voicu, S. Georgescu, *Proc. Third Int. Conf. on Trends in Quantum Electronics*, Bucharest 1988, p. 155.
3. K. J. Mackey, G. M. Williams, M. J. Crosbie, A. G. Cullis, B. Cockaine, *J. Cryst. Growth* **129**, 269 (1993).

# EXCITED STATE ABSORPTION OF $Fe^{3+}$ IN GARNET CRYSTALS

V. LUPEI,* S. HARTUNG and G. HUBER

*Institute of Atomic Physics, 76900 Bucharest, Romania; Universitat Hamburg, Institut fur Laser Physik, 20355 Hanburg, Germany*

The excited state absorption (ESA) from the metastable level $^4T_1(^4G)$ of $Fe^{3+}$ in tetrahedral sites of garnets is reported. The spectra show strong lines due to spin allowed transitions to other excited spin-quartet states. It is also shown that this ESA could be strongly reduced if the metastable level could is used as donor level in the process of sensitaization of rare earths ions (such as $Tm^{3+}$) by $Fe^{3+}$.

Sensitization of rare earth emission with transition ions in laser crystals could be successfully used to improve the pump efficiency of the solid state lasers. A very important condition for the sensitizator ions is that they should not introduce any state (GSA) or excited state (ESA) absorption at the emission wavelength.

Recent work[1–6] discussed the possibility of using $Fe^{3+}$ ions as sensititzers for various rare-earth ions in garnets. Trivalent iron ($3d^5$ ground configuration) enters in these crystals both in octahedral (a) and tetrahedral (d) sites.[7]

The Taneabe-Sugano diagram for these centers are similar (however Dq/B are very different, around 2.2 for a-center and 1 for the d-center) and the ground state is a spin sextet $^6A_1$ while all the excited states are either spin quartets or spin doublets. Therefore the transitions between ground states and excited states are spin forbidden, although the spin-orbit mixing lessens this restriction allowing weak transitions especially for the d-center that also lacks inversion. The spin-orbit coupling also splits the energy levels leading to a rich density of states. The electron-phonon coupling is usually quite strong leading to broad vibronic lines in absorption. Thus the optical spectroscopy data of $Fe^{3+}$ in garnets are difficult to obtain because the absorption bands are weak and broad, excepting the $^4A_1 \rightarrow {^4T_2}$ $(^4D)$ of the d-center and the emission is given only by this center and only from the first excited state $^4T_1(^4G)$ which is less coupled to the phonons.

The $Fe^{3+}$(d) emission in garnets contains, at low temperatures, several zero-phonon lines orginating from the various spin-orbit components of $^4T_1(^4G)$ level (the lowest being at $13\,610$ cm$^{-1}$) accompanied by a phonon side band, weak and not very broad at low temperatures but strong and broad (covering all the range between $12\,100$ and $13\,500$ cm$^{-1}$) at room temperature. Fairly efficient energy transfer from the metastable level $^4T_1(^4G)$ of $Fe^{3+}$ to rare earth ions (such as $Nd^{3+}$ and especially to $Tm^{3+}$), could take place, especially at elevated temperatures; this transfer is favorized by the very good packing of the tetrahedral sites around the dodecahedral sites occupied by the rare earths activators. This suggests the using of the $Fe^{3+}$(d) centers as sensitizers for the laser emission of these rare earth ions. At the same time the long lifetime of the $Fe^{3+}$(d) emission in YAG (about 7.5 ms for the sample grown from a melt containing 1at.% Fe) could favour intense spin allowed absorption transitions from the emitting level to the upper spin quartet states.

This paper presents, to our knowledge, the first ESA measurements on $Fe^{3+}$ in garnets. The $^4T_1(^4G)$ state of $Fe^{3+}$(d) was excited by a chopped $Ar^+$ laser (which pumps the $^4T_2$ level from which the excitation relaxes fast to $^4T_1$) and the trasmission spectrum of the
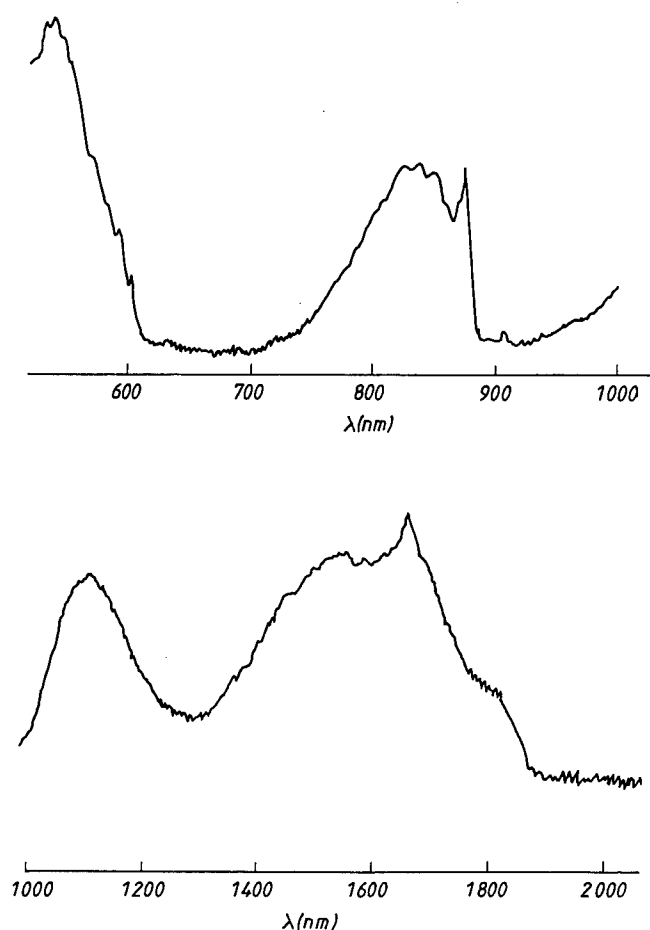
FIGURE 1   ESA of $Fe^{3+}$ tetrahedral centers in YAG, at 15 K.

radiation from a tungsten halogen lamp passing through the excited region of the sample was monitored. The absorption from the ground atate was eliminated by phase sensitive detection. The ESA spectra (Figure 1) in the 520–2000 nm show strong and broad features corresponding to transitions from $^4T_1(^4G)$ to the upper levels $^4T_2$ (G), $[^4E, ^4A_1(G)]$, $^4T_2(D)$ and $^4E(D)$. Fairly strong ESA is observed at the 1.06 microns, corresponding to $Nd^{3+}$ emission, but no evident ESA was observed in the two or three micron regions, the emission ranges of Tm, Ho, or Er lasers.

Special features, at low temperatures, shows the transition to $^4T_2(D)$: two sharp lines (one of them very weak) accompanied by a broad band with several shoulders. The large linewidths of the tansitions at low temperatures confirm the strong electron-phonon coupling; the only structured transition corresponds to levels that show structure in ground state absorption $(^4T_2(d))$ or in emission $(^4T_1(G))$. The intensities of the ESA lines of the $Fe^{3+}$ $^4T_1(G)$ level are at least one order of magnitude larger than those corresponsing to the GSA specturm.

The observed broad lines could accommodate contributions from ESA of the octahedral $Fe^{3+}$ center as well; however, the lack of emission from this center, even with excitation in the very intense charge transfer band at 260 nm shows that the quantum efficiency of the lowest excited level $^4T_{1g}(^4G)$ of this center, which should lie[7,8] in the region of 10 000 $cm^{-1}$ is very low. Thus the lifetime of the $^4T_{1g}$ emission, if it exists, would be very short, making cw ESA unlikely.

The reduction of ESA due to energy transfer from the metastable level $^4T_1(^4G)$ of the $Fe^{3+}(d)$ center was observed by co-doping the crystals with $Tm^{3+}$. Due to energy transer to the $^3H_4$ $Tm^{3+}$ level, the decay of the $Fe^{3+}(d)$ emission becomes non-exponential and its 'effective' lifetime $\tau_{2eff} = \tau_2\eta$ (where $\tau_2$ is the lifetime in the absence of the transfer and $\eta$ is the emission quantum efficiency in presence of transfer) depends on Tm concentration. This effective lifetime could be used to define a cw effective transfer rate $w = \tau_{2eff}^{-1} - \tau_2^{-1}$. By using the rate equations for the stationary regime, the intensity of light with initial value $I_{20}$ and with a wavelenght corresponding to an ESA (but not to a GSA) transition, after passing a sample of thickness $\ell$ becomes

$$I_2 = I_{20}\exp[-\frac{\frac{I_1}{I_{s1}}}{1 + \tau_2 w + \frac{I_1}{I_{s2}}} n\sigma_2\ell] \qquad (1)$$

$$I_{s1} = \frac{h\nu_1}{\tau_2\sigma_1} \qquad (2)$$

$I_1$ being the intensity of light of quantum $h\nu_1$ which excites the system to the state 2, n is the sensitizer $Fe^{3+}(d)$ concentration and $\sigma_1$ and $\sigma_2$ are the cross sections of the $I_1$ GSA and $I_2$ ESA respectively. These relations show that if the lifetime $\tau_2$ of the excited level 2 becomes very short the saturation intensity $I_{s1}$ becomes very large and thus the transmitted intensity $I_2$ is very close to the initial intensity $I_{20}$, making the observation of cw ESA unlikely.

Eq. (1) describes correctly the observed reduction of ESA with increased transfer efficiency in samples of higher Tm content. Thus, taking as model date $\tau_2 = 7.5 * 10^{-3}$s, $\sigma_1 \sim 5 * 10^{-21}$ $cm^2$, $\sigma_2 \sim 10^{-19}$ $cm^2$ (which correspond in average to $Fe^{3+}$ in garnets) the $Fe^{3+}(d)$ ESA in a sample of 0.3 cm thick is reduced by about an order of magnitude due to an energy transfer which reduce the emission efficiency of $^4T_1(^4G)$ to 0.1. The reduction increases with Fe concentration sample thickness and energy transfer efficiency.

In conclusion this study shows that strong cw ESA takes place from the metastable level $^4T_1(^4G)$ of $Fe^{3+}$ in tetrahedral sites of garnets. The ESA spectrum reflects the structure of excited spin quartet levels of this center: strong absorption is observed in the region of Nd laser emission but not at two or three microns. It was also demonstrated that if the metastable level $^4T_1(^4G)$ is used as a donor level in a sensitization process for the rare earth ions, a reduction of cw ESA (up to almost total suppression) takes place, function of energy transfer efficiency.

REFERENCES

1. L. F. Johnson, J. F. Dillion, J. P. Remeika, *Phys. Rev.* **B1**, 1935 (1970).
2. G. J. Dillon, L. F. Johnson, *Opt. Lett.* **17**, 1782 (1992).
3. M. J. Korzhik, M. G. Lifshits, Kh. S. Bagdasarov, A. M. Kevorkov, I. A. Melkonyan, M. L. Meilman *Sov. J. Quantum Electron.* **19**, 344 (1989).
4. M. V. Korzhik, M. G. Lifshits, B. I. Minkov, V. B. Pavlenko, *Sov. J. Quant. Electron.*, **22**, 24 (1992).
5. V. Lupei, G. Boulon, A. Brenier, C. Madej, M. J. Elejalde, A. Lupei, C. Tiseanu, S. Georgescu, *SPIE Proc. Int. Conf. Solid State Lasers IV*, QE/LASE'93, SPIE, vol. 1864, **68** (1993).

V. LUPEI *ET AL.*

6. V. Lupei, A. Lupei, G. Boulon, A. Brenier, C. Pedrini, M. J. Elejalde, *Phys. Rev.* **49**, 7076 (1994).
7. G. B. Scott, D. E. Lacklison, J. L. Page, *Phys. Rev.* **B10**, 971 (1974).
8. Yu. A. Voitukevish, M. V. Korzhik, V. V. Kuzmin, M. G. Lifshits, M. L. Meilman, *Opt. Spectroosc.*, 480 (1987).

# THERMAL EFFECTS ON THE QUANTUM EFFICIENCY OF 3 $\mu$m ERBIUM LASERS

Ş. GEORGESCU, V. LUPEI, T. J. GLYNN* and R. SHERLOCK*

*Institute of Atomic Physics, P. O. Box MG-6, RO-76900 Bucharest, Romania; *University College Galway , Galway, Ireland*

The temperature dependence of the main energy transfer processes involved in the building of population inversion in 3 $\mu$m Erbium lasers, mainly upconversion from $^4I_{13/2}$, $^4I_{11/2}$, and cross-relaxation from $^4I_{9/2}$, is investigated. In the temperature domain 20–100°C, which includes the usual working temperatures of solid-state lasers, the change of the quantum efficiency is mainly due to the modifications of the Stark sublevels populations involved in laser transitions. The contribution of the cross-relaxation from $^4I_{9/2}$ is estimated using new experimental data for two Erbium-doped crystals: $Er^{3+}$:YAlO$_3$ and $Er^{3+}$:YLiF$_4$.

*Key words:* Solid-state lasers; $Er^{3+}$; Energy transfer.

## 1 INTRODUCTION

In spite of the unfavourable ratio of the initial and terminal laser levels lifetimes, efficient 3 $\mu$m generation of Erbium-doped active media can be obtained due to very effective energy transfer mechanisms between $Er^{3+}$ ions. These mechanisms being generally temperature dependent, temperature changes in the active media could affect the emission properties.

The main energy transfer processes which contribute to the population inversion of 3 $\mu$m Erbium lasers (transition $^4I_{11/2} \rightarrow {}^4I_{13/2}$) are upconversion from $^4I_{13/2}$-with rate $W_1$, upconversion from $^4I_{11/2}$-with rate $W_2$, cross-relaxation from $^4S_{3/2}$, and cross-relaxation from $^4I_{9/2}$, $({}^4I_{9/2} \rightarrow {}^4I_{13/2}) + ({}^4I_{15/2} \rightarrow {}^4I_{13/2})$-with rate $W_3$.[1,2] In this paper we shall examine the influence of the temperature dependence of these mechanisms on the quantum efficiency as a function of the pump conditions, for several generation wavelengths. These considerations are exemplified on two Erbium-doped crystals: $Er^{3+}$:YAlO$_3$ and $Er^{3+}$:YLiF$_4$, using new experimental data concerning the temperature dependence of the $^4I_{9/2}$ level kinetics.

## 2 EXPERIMENTAL

The temperature dependence of the $^4I_{9/2}$ level kinetics was measured in the temperature interval 20–100°C for two samples: 45% $Er^{3+}$:YAlO$_3$ and 25% $Er^{3+}$:YLiF$_4$. The experimental apparatus used to measure the kinetics of the $^4I_{9/2}$ luminescence was presented previously.[2]

## 3 RESULTS AND DISCUSSION

The quantum efficiency of 3 $\mu$m Erbium lasers, $\eta_{ij}$, in stationary regime, between the *i*-th sublevel of $^4I_{11/2}$ and the *j*-th sublevel of $^4I_{13/2}$ depends only on two figures of merit, $p_{ij}$ and *h*. For pumping in different energy levels, the expression of $\eta_{ij}$ is:[2]
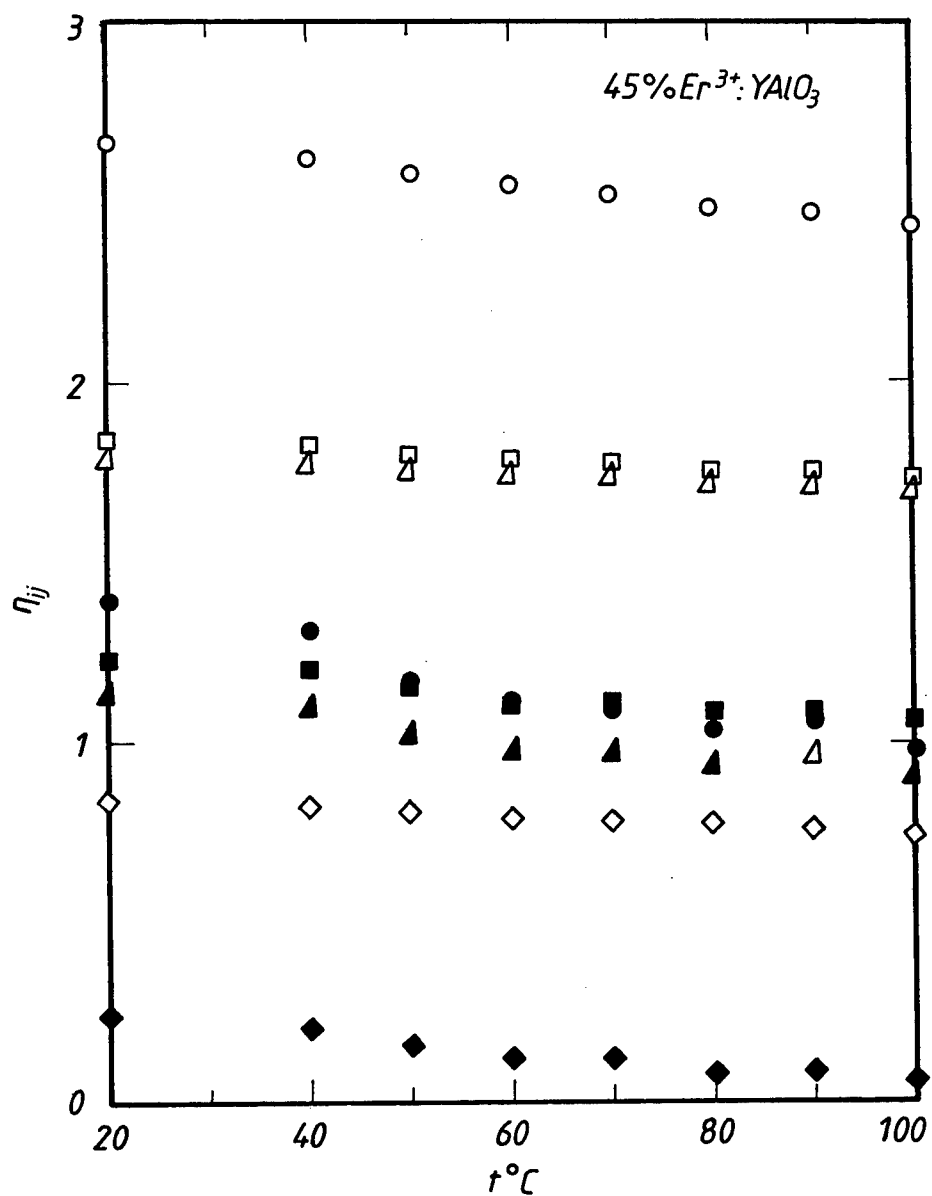
FIGURE 1    Temperature dependence of the quantum efficiency, $\eta_{ij}$, for a 45% $Er^{3+}$:$YAlO_3$ crystal (hollow symbols: transition $1 \rightarrow 7$; solid symbols: transition $1 \rightarrow 4$) for different pump conditions ($\bigcirc$, $\bullet$ in $^4S_{3/2}$; $\triangle$, $\blacktriangle$ in $^4F_{9/2}$ or $^4I_{9/2}$; $\square$, $\blacksquare$ in $^4I_{11/2}$, and $\diamond$, $\blacklozenge$ in $^4I_{13/2}$).
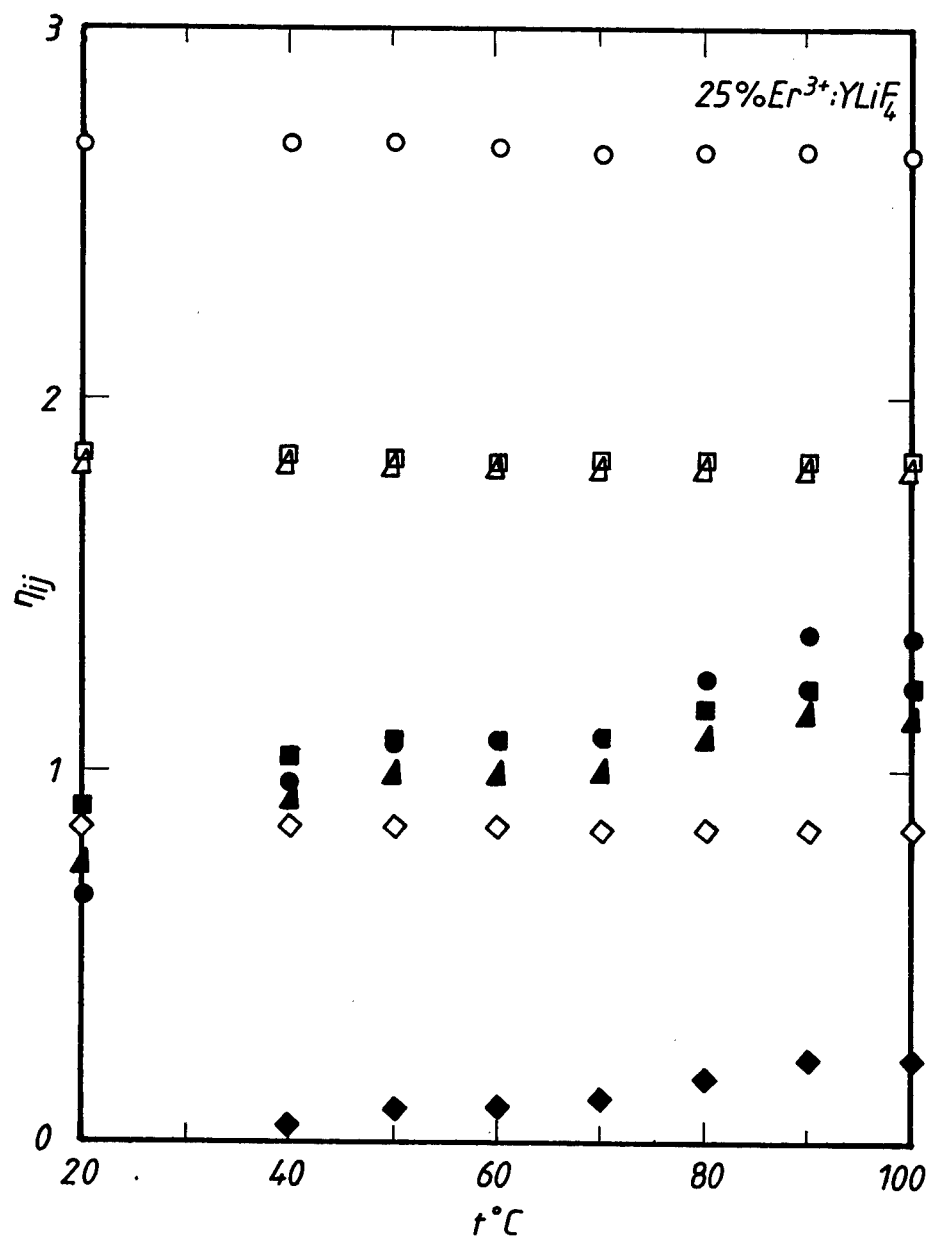
FIGURE 2    Temperature dependence of the quantum efficiency, $\eta_{ij}$, for a 25% $Er^{3+}$ $YLiF_4$ crystal (hollow symbols: transition 2 → 4; solid symbols: transition 4 → 2) for different pump conditions (○, ● in $^4S_{3/2}$; △, ▲ in $^4F_{9/2}$ or $^4I_{9/2}$; □, ■ in $^4I_{11/2}$, and ◇, ◆ in $^4I_{13/2}$).

$$n_{ij} = \frac{x(1-h) - y(1+zh)p_{ij}^2}{1 - h(1+p_{ij}^2)},\tag{1}$$

where $x = 3$, $y = z = 2$ for pump in $^4S_{3/2}$, $x = 2$, $y = 1$, $z = 3$ for pump in $^4I_{9/2}$ or $^4F_{9/2}$, $x = 2$, $y = 1$, $z = 2$ for pump in $^4I_{11/2}$, and $x = y = z = 1$ for pump in $^4I_{13/2}$. The figures of merit $p_{ij}$ and $h$ are defined by $p_{ij} = (\beta_j/\alpha_i)\sqrt{W_2/W_1}$ and $h = \tau_{30}W_3N_0/(1 + \tau_{30}W_3N_0)$. $\alpha_i$, $\beta_j$ are the Boltzmann population coefficients of the sublevels involved in the laser transition, $\tau_{30}$ is the lifetime of the $^4I_{9/2}$ level at low Erbium concentrations, and $N_0$ is the population of the ground level, $^4I_{15/2}$. Although the cross-relaxation from $^4S_{3/2}$ does not appear explicitly in Eq. (1), it plays an important role in the population building of the laser levels, any excitation reaching the $^4S_{3/2}$ level being immediately and equally redistributed to the $^4I_{9/2}$ and $^4I_{13/2}$ levels.

Due to the peculiarities of the energy level scheme of the $Er^{3+}$ ion, the lowest sublevels are involved in the upconversion processes, while in the cross-relaxation from $^4I_{9/2}$, higher sublevels of both $^4I_{9/2}$ and $^4I_{15/2}$ are required for energy conservation. Therefore, we could expect a noticeable temperature dependence for $W_3$, but a weak one for $W_1$, $W_2$, and even weaker for the ratio $W_2/W_1$. In the following, we suppose that the temperature dependence of $p_{ij}$ is given exclusively by the ratio $\beta_j/\alpha_i$.

The temperature dependence of $h$ is given by the competition between multiphonon and cross-relaxation processes. For low Erbium concentrations (no cross-relaxation), $1/\tau_{30} \approx W_{mp}$, where $W_{mp}$, the probability of the multiphonon transition

$$W_{mp} = W_0 \left[\frac{\exp(\hbar\omega/k_B)}{\exp(\hbar\omega/k_B) - 1}\right]^n,\tag{2}$$

with the number of participating phonons, $n$, given by the ratio of the energy gap to the next lower level, $E_g$ and the cutoff phonon frequency, $\hbar\omega$. For $YAlO_3$ ($E_g \approx 2200$ cm$^{-1}$, $\hbar\omega = 600$ cm$^{-1}$, $\tau_{30}$ (20°C) $= 435$ ns), results $W_0 = 1.89 \times 10^6$ s$^{-1}$, while for $YLiF_4$ ($\hbar\omega = 490$ cm$^{-1}$, $\tau_{30}$ (20°C) $= 7$ $\mu$s), $W_0 = 8.91 \times 10^4$ s$^{-1}$.

Denoting by $\tau_3(T)$ the measured values of the $^4I_{9/2}$ lifetime at temperature $T$,

$$1/\tau_3(T) = 1/\tau_{30}(T) + W_3(T)N_0 \approx W_{mp}(T) + W_3(T)N_0,\tag{3}$$

which gives for $h$:

$$h(T) \approx 1 - W_{mp}(T)\tau_3(T).\tag{4}$$

The experimental temperature dependence of $\tau_3$ for two Erbium-doped crystals, 45% $Er^{3+}$:$YAlO_3$ and 25% $Er^{3+}$:$YLiF_4$, in the temperature interval 20–100°C, are given in Tables I and II, respectively, together with the values of $W_3N_0$ (computed with Eq. (3)) and of $h$ (calculated with Eq. (4)).

A general increase of the cross-relaxation rate $W_3$ with temperature is observed. However, $h$ has a different behaviour: a weak increase for $Er^{3+}$:$YAlO_3$, but a decrease for $Er^{3+}$:$YLiF_4$. This could be explained by a stronger temperature dependence of the multiphonon transition probability for $YLiF_4$ in the considered temperature domain, due to a lower cutoff frequency.

The temperature dependence of the quantum efficiency $\eta_{ij}$, estimated with Eq. (1), was exemplified in Figure 1 for the $Er^{3+}$:$YAlO_3$ sample (transitions $1 \rightarrow 7$, $\lambda_g = 2.92$ $\mu$m, $1 \rightarrow 4$, $\lambda_g = 2.80$ $\mu$m) and in Figure 2 for the $Er^{3+}$:$YLiF_4$ sample (transitions $2 \rightarrow 4$, $\lambda_g = 2.80$ $\mu$m and $4 \rightarrow 2$, $\lambda_g = 2.66$ $\mu$m), for pump in $^4S_{3/2}$, $^4F_{9/2}$ or $^4I_{9/2}$, and $^4I_{13/2}$. Depending on the particular crystal (crystal field splitting,

Table I
Temperature dependence of $\tau_3$, $W_3N_0$, and $h$ for 45% $Er^{3+}$:$YAlO_3$.

| Temperature (°C) | $\tau_3$ (ns) | $W_3N_0$ ($10^5 s^{-1}$) | $h$ |
|---|---|---|---|
| 20 | 380 | 3.33 | 0.13 |
| 40 | 361 | 3.62 | 0.13 |
| 50 | 344 | 4.40 | 0.15 |
| 60 | 333 | 4.74 | 0.16 |
| 70 | 326 | 4.74 | 0.16 |
| 80 | 316 | 5.02 | 0.16 |
| 90 | 312 | 4.71 | 0.15 |
| 100 | 300 | 5.24 | 0.16 |

Table II
Temperature dependence of $\tau_3$, $W_3N_0$ and $h$ for 25% $Er^{3+}$:$YLiF_4$

| Temperature (°C) | $\tau_3$ ($\mu s$) | $W_3N_0$ ($10^4 s^{-1}$) | $h$ |
|---|---|---|---|
| 20 | 6.3 | 1.59 | 0.14 |
| 40 | 5.7 | 2.02 | 0.12 |
| 50 | 5.51 | 1.95 | 0.11 |
| 60 | 5.22 | 2.24 | 0.12 |
| 70 | 4.95 | 2.53 | 0.13 |
| 80 | 4.86 | 2.11 | 0.10 |
| 90 | 4.75 | 1.74 | 0.08 |
| 100 | 4.48 | 2.12 | 0.10 |

cutoff phonon frequency, etc.) and generation wavelength, the quantum efficiency could decrease (with about 30% for the $1 \rightarrow 4$ transition of Er in $YAlO_3$ for pumping in $^4S_{3/2}$), remain constant (transition $2 \rightarrow 4$ of Er in $YLiF_4$), or even increase (with up to 100%, transition $4 \rightarrow 2$ of Er in $YLiF_4$).

## 4   CONCLUSIONS

In the temperature domain 20–100°C (including working temperatures of the solid-state lasers), the main contribution to the change of quantum efficiency of 3 $\mu$m Erbium lasers is given by the figure of merit $p_{ij}$, via the population of the Stark sublevels involved in the laser transitions.

The competition between the main non-radiative processes which de-activate the $^4I_{9/2}$ level gives the temperature dependence of the figure of merit $h$. For $Er^{3+}$:$YAlO_3$, the temperature dependence of the cross-relaxation rate is stronger, leading to an increase of $h$, with negative effects on the quantum efficiency. In contrast, for $Er^{3+}$:$YLiF_4$, the multiphonon processes have a steeper temperature dependence, with positive effects on the quantum efficiency.

REFERENCES

1.  V. Lupei, S. Geogescu, and V. Florea, *IEEE J. Quantum Electron.* **29**, 426 (1993).
2.  S. Georgescu, T. J. Glynn, R. Sherlock, and V. Lupei, *Opt. Commun.* **106**, 75 (1994).
3.  L. A. Rieseberg and H. W. Moos, *Phys. Rev.* **174**, 429 (1968).

# Mn²⁺ LUMINESCENCE IN Mg-Al SPINELS

## U. R. RODRÍGUEZ-MENDOZA[1], V. D. RODRÍGUEZ[1] and A. IBARRA[2]

*[1]Dto. Física Fundamental y Experimental. Univ. de La Laguna, 38206 La Laguna-Tenerife. Spain; [2]Inst. Investigación Básica. CIEMAT, Av. Complutenese, 22. E-28040 Madrid, Spain*

Luminescence of $Mn^{2+}$ in A sites in natural and synthetic $MgAl_2O_4$ spinel has been studied. In the near perfect structure of the natural crystals the degenerate levels of the $Mn^{2+}$ are splitted due to a symmetry lower than tetrahedral. In synthetic crystals the structure of the spectra is lost as a consequence of the superposition of partial spectra related to $Mn^{2+}$ ions perturbed by the cationic disorder of the lattice. Thermal annealing modifies the spectra of natural crystals making them similar to those of the synthetic ones due to an order-disorder transition.

*Key words*: $MgAl_2O_4$, spinel, Mn, luminescence, cationic disorder.

## 1 INTRODUCTION

$MgAl_2O_4$ is the representative of a wide family of technologically important oxides with the spinel structure. In particular $MgAl_2O_4$ has received special attention in the last years due their potential use as insulator for fusion applications and as matrix for solid state lasers.

The crystalline structure of spinels with the general formula $AB_2O_4$ is a cubic close packed array of oxygen ions with A and B cations in tetrahedral and octahedral holes respectively. These materials can present some degree of disorder, that is pairs of A and B cations in interchanged positions. In $MgAl_2O_4$ the ordered structure can be found only in natural crystals. By heating, an order-disorder phase transition takes place around 900°C giving a similar crystalline structure to the synthetic one. Moreover, $MgAl_2O_4$ and $Al_2O_3$ form crystalline solution with composition $MgO \cdot X(Al_2O_3)$, with X close to 1 in natural crystals and from 1 to 5 in the synthetic ones.

The luminescence associated to intrinsic and impurities has been scarcely studied in $MgAl_2O_4$. Respect to the impurities, only octahedral $Cr^{3+}$ has been analyzed in detail due to its sensitivity to the cationic disorder.[1,2] In a previous work[3] some results were presented on the room temperature luminescence of tetrahedral $Mn^{2+}$ in natural crystal; it was found that the spectra of these ions are sensitive to the order-disorder transition. In this work the luminescence of $Mn^{2+}$ is studied in detail, considering the influence of cationic disorder, non-stoichiometry and Mn concentration.

## 2 RESULTS AND DISCUSSION

We have used natural crystals with X around 1.1 and synthetic crystals with X around 3. The approximate concentration of Mn is 400 ppm in natural crystals and 50 to 3000 ppm in synthetic ones.

In Figure 1 the excitation and emission spectra of $Mn^{2+}$ at 10 K for natural and synthetic crystals are showed, the excited and emitting levels, respectively, are indicated. The excitation of the $^4A_2(^4F)$ level in 275 nm was not included in the figure.

On the synthetic crystals, similar spectra are obtained for samples with low (50 ppm) and high (3000 ppm) concentration of Mn. These spectra do not present splitting of
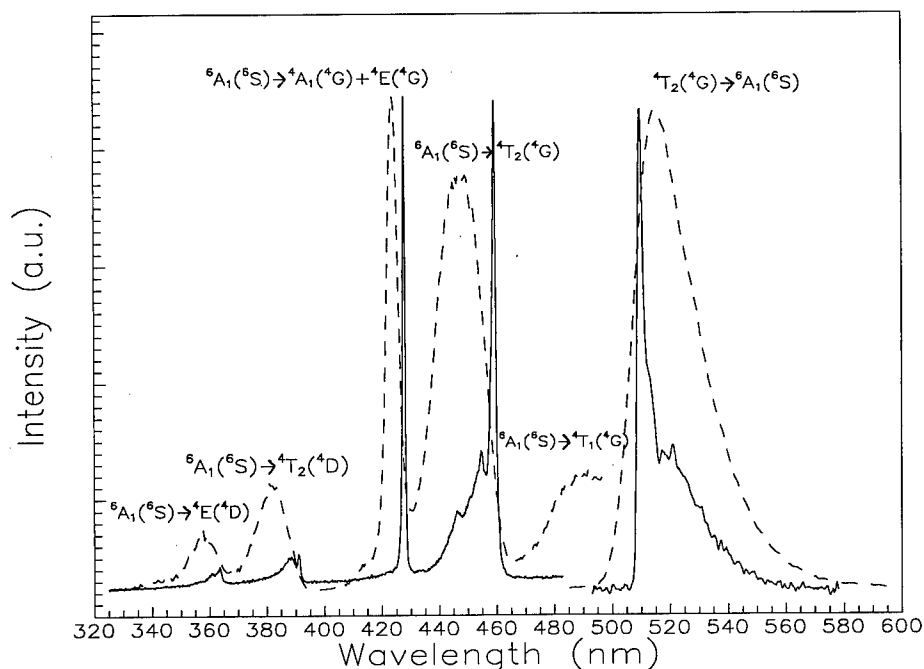
FIGURE 1   Excitation and emission spectra of natural (————) and synthetic (————) MgAl$_2$O$_4$:Mn spinels at 10 K.

degenerate levels, as it would be expected for tetrahedral sites. The crystal field parameters calculated from these bands are Dq $= 396$ cm$^{-1}$, B $= 604$ cm$^{-1}$ and C $= 3381$ cm$^{-1}$. The excitation spectrum is similar to the one presented by Palumbo and Brown (4) for synthetic MgGa$_2$O$_4$ at LNT. The lifetime of the emission does not depend on the excitation level; in the samples with high concentration of Mn it has a value of 6.0 ms at RT equal to the value obtained by Clausen and Petermann (5) in MgAl$_2$O$_4$ with 4% of Mn, and it is almost constant down to 10 K, decreasing to 5.3 ms at 675 K.

Excitation and emission spectra of the natural sample are quite different. They present splitting of degenerate levels, in particular it is clearly observed in Figure 1 the splitting of the $^4$T$_2$($^4$G) triplet in excitation. This effect clearly indicates that the symmetry is lower than tetrahedral. No stucture is observed in the $^4$E$-^4$A$_1$($^4$G) peak and its width of 65 cm$^{-1}$ is quite lower than the value 310 cm$^{-1}$ corresponding to synthetic crystals. In the natural sample spectra the $^4$T$_1$($^4$G) is not observed. These spectra are very similar to those obtained by Palumbo and Brown (4) for stoichiometric synthetic ZnAl$_2$O$_4$ spinel. The lifetime of the emission is 4.8 ms at RT, which is lower than the obtained for synthetic crystals. It changes less than 10% in the range from 10 to 675 K.

Considering the natural crystals as ordered and almost stoichiometric, the spectra of these samples would be related to Mn$^{2+}$ ions non affected by structural defects. The observed spectra of the synthetic samples can be the result of the superposition of the spectra associated to Mn$^{2+}$ ions with different perturbations. This is confirmed by site selective excitation in the nondegenerate $^4$A$_2$($^4$F) level, different emission spectra and lifetimes are obtained for excitation with different wavelength in the 275 nm peak.
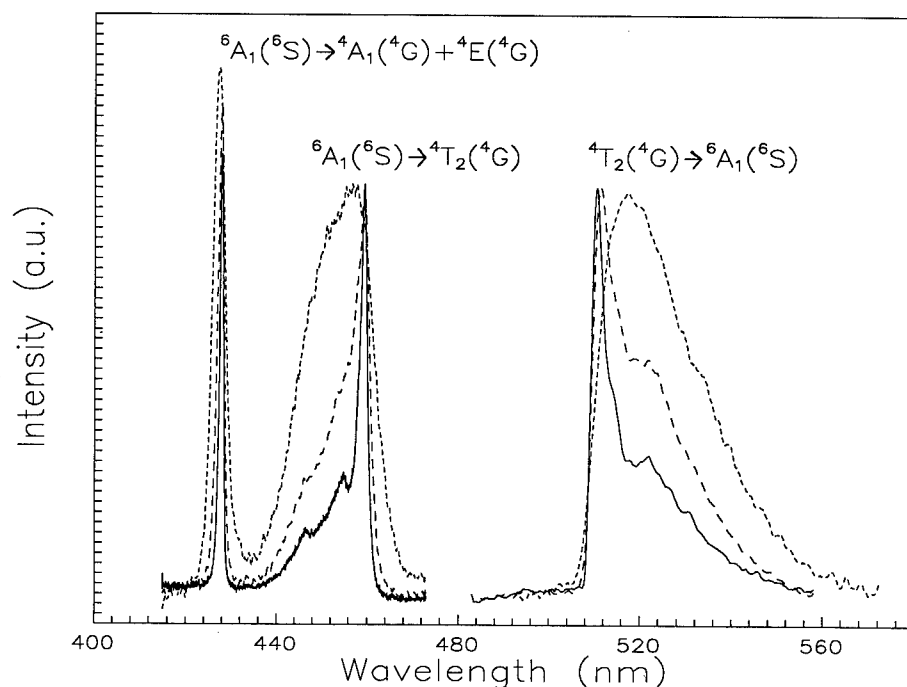
FIGURE 2   Excitation and emission spectra of natural MgAl$_2$O$_4$:Mn spinels at 10 K after annealing for 10 min to 850°C (———), 900°C (— — —) and 950°C (- - - - -).

Comparing the excitation spectra in Figure 1 it is concluded that almost all the Mn$^{2+}$ ions in the synthetic crystals are appreciably perturbed.

In order to study the effect of the order-disorder phase transition the natural crystal was annealed for 10 min. at increasing temperature with 50 K increments. The spectra recorded at 10 K are showed in Figure 2. It is found that the spectrum of the natural crystals changes tending to the spectrum of the synthetic one: the structure is lost, the width of the peaks increases and the maximum of the peaks moves to lower wavelengths in the excitation spectra and to higher wavelengths in the emission spetra.. Moreover the lifetime of the emission increased with the annealing.

In conclusion, in synthetic MgAl$_2$O$_4$ most of the Mn$^{2+}$ ions are in sites perturbed by the cationic disorder while in natural MgAl$_2$O$_4$ the Mn$^{2+}$ ions are in ideal sites, although with symmetry lower than tetrahedral.

REFERENCES

1.  W. Mikenda and A. Preisinger. *J. Lumin.* **26**. 53 (1981).
2.  W. Mikenda and A. Preisinger. *J. Lumin.* **26**, 67 (1981).

3.  J. M. G. Tijero and A. Ibarra. *J. Phys. Chem. Sol.* **54**. No. 2. 203 (1993).
4.  D. T. Palumbo and J. J. Brown, *J. Electrochem. Soc.: Sol. State Science* **117**, No. 9. 1184 (1970).
5.  R. Clausen and K. Petermann. *J. Lumin.* **40–41**, 185 (1988).

# INHOMOGENEOUS BROADENING OF THE $V^{4+}$ LUMINESCENCE IN CaYAlO$_4$

M. YAMAGA, T. YOSIDA,[1] Y. INOUE,[2] N. KODAMA[2] and B. HENDERSON[3]

*Department of Physics, Faculty of General Education, Gifu University, Gifu 501–11, Japan; [1]Nakanihon Automotive College, Sakahogi, Kamo 505, Japan; [2]Tosoh Corporation, Hayakawa, Ayase 252, Japan; [3]Department of Physics and Applied Physics, University of Strathclyde, Glasgow G4 ONG, UK*

The optical absorption spectrum of CaYAlO$_4$ single crystals codoped $V^{4+}$ and $Mg^{2+}$ comprised two intense bands at 330 nm and 430 nm and a weak band around 500 nm. Excitation with light at wavelength near 500 nm produced a broad emission band with the peak at 690 nm. The radiative center is assigned to $V^{4+}$. The peak wavelength of this emission band shifted to longer wavelength with increasing the excitation wavelength. This result indicates that inhomogeneous broadening of the $V^{4+}$ luminescence is caused by substitutional disorder on the $Ca^{2+}$ and $Y^{3+}$ sites in the host lattice.

*Key words*: transition metal ion, $V^{4+}$, optical spectra, substitutional disorder, inhomogeneous broadening.

$Ti^{3+}$:Al$_2$O$_3$ is a useful tunable solid-state laser material for the near infrared spectral region of 0.7−1.1 $\mu$m. Although the emission spectra of $V^{4+}$ doped Al$_2$O$_3$ and YAlO$_3$ are shifted into red and yellow regions, respectively, relative to $Ti^{3+}$:Al$_2$O$_3$, their laser actions have not been reported.[1] We have prepared $Ti^{3+}$ or $V^{4+}$ doped CaYAlO$_4$ with space group 14/mmm (D$_{4h}^{17}$), which is expected to shift potential laser action onto the visible region.[2]

Crystals of CaYAlO$_4$, codoped with 0.5 mol.% V$_2$O$_5$ and 0.5 mol.% MgO for charge compensation, were grown in an inert atmosphere by the Czochralski technique. $Ca^{2+}$ and $Y^{3+}$ ions in CaYAlO$_4$ are statistically distributed on their respective sublattices, while keeping the composition ratio of 1:1. Vanadium ions preferentially occupy octahedral $Al^{3+}$ sites.

Figure 1 shows that the optical absorption spectrum of the as-grown CaYAlO$_4$ crystals measured at room temperature comprises two strong bands with the peaks at 330 nm and 430 nm and a weak band with the peak at 500 nm. The two intense bands decrease on annealing the as-grown sample at 1550°C in a reducing atmosphere. These results suggest that these bands may be due to charge-transfer transitions between $O^{2-}$ and $V^{5+}$.

Figure 2 shows a broad emission band with the peak of 690 nm excited at selected wavelengths of an Ar$^+$ ion laser at room temperature. The excitation spectrum comprises two bands with peaks of 352 nm and 496 nm, features familiar from earlier studies of $V^{4+}$ in Al$_2$O$_3$ and YAlO$_3$.[1] The broad emission band is attributed to $V^{4+}$ ions, an assignment confirmed by an EPR spectrum consisting of eight hyperfine lines with the g values of $g_x = 1.84$, $g_y = 1.90$ and $g_z = 1.94$ with hyperfine parameters $A_x = 65$ G, $A_y = 45$ G and $A_z = 165$ G observed at low temperatures.

The peak wavelength of the broad emission band shifts to longer wavelengths with increasing excitation wavelengths in the 500 nm absorption band as shown in Figure 2. This excitation energy dependence of the $V^{4+}$ luminescence is similar to that reported for the $Cr^{3+}$ luminescence in glasses[3] and in gallogermanate crystals.[4] In glasses this shift is associated with inhomogeneous broadening of the band due to the inherent disorder in glasses.[3] In the case of CaYAlO$_4$ the inhomogeneous broadening of the $V^{4+}$ luminescence is caused by substitutional disorder of $Ca^{2+}$ and $Y^{3+}$ ions in the host lattice: their
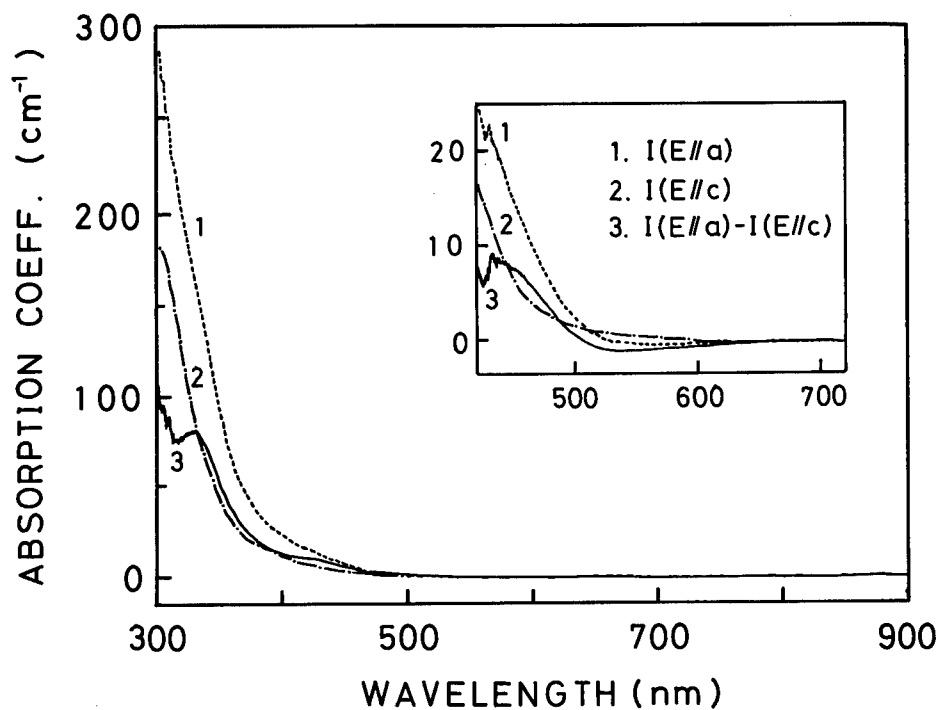
FIGURE 1   Polarization of absorption spectra of V:Mg:CaYAlO$_4$ measured at 300 K.
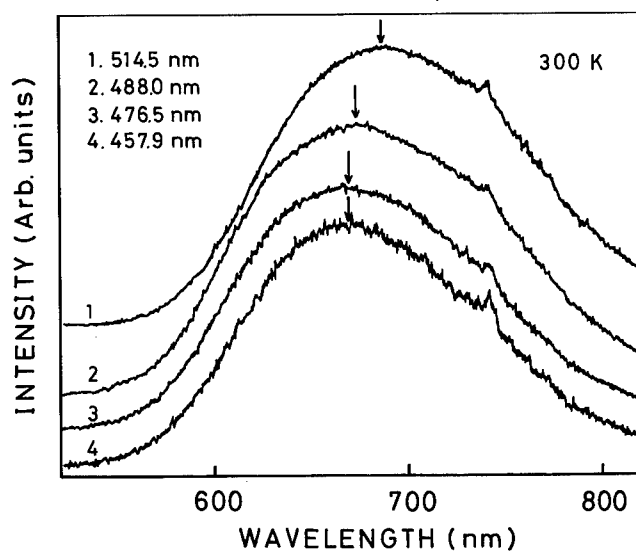


FIGURE 2   Emission spectra of V$^{4+}$ in CaYAlO$_4$ for different excitation wavelengths measured at 300 K.

differences in valency and ionic radius lead to variations in the crystal field experienced by the $V^{4+}$ ions. This type of disorder is also observed in both Sr and Ca gallogermanates.[4]

REFERENCES

1. J. P. Meyn, T. Danger, K. Petermann and G. Huber, *J. Lumin.* **55**, 55 (1993).
2. M. Yamaga, T. Yosida, Y. Naitoh and N. Kodama, *J. Phys.: Condens. Matter* **6**, 4381 (1994).
3. B. Henderson, M. Yamaga, Y. Gao and K. P. O'Donnell, *Phys. Rev.* **B46**, 652 (1992).
4. P. I. Macfarlane, T. P. J. Han, B. Henderson and A. A. Kaminskii, *Opt. Mater.* **3**, 15 (1994).

# MULTISITE STRUCTURE OF $Nd^{3+}$ IN YAG

A. LUPEI, C. TISEANU and V. LUPEI

*Institute of Atomic Physics, Bucharest, Romania*

The paper presents new results on $Nd^{3+}$ multisite structure in high-temperature grown YAG crystals, obtained by high resolution spectroscopy. The energy transfer processes involving various satellites are also analyzed. Models of crystals field perturbations leading to the spectral satellites are discussed.

## 1  INTRODUCTION

The multisite structure of $Nd^{3+}$ in YAG, due to its role in quantum efficiency, as has been discussed before,[1-5] is still a controversated problem that requires further investigation.

The YAG ($Y_3Al_5O_{12}$) structure is generally considered cubic, the space group Ia3d, with $Y^{3+}$ ions located in dodecahedral c-sites ($D_2$ local symmetry), and $Al^{3+}$ in octahedral a-sites ($C_{3i}$ symmetry) and, tetrahedral d-sites ($S_4$ symmetry), respectively. High accuracy analyses[6,7] have shown in crystals grown from the melt (high temperature—HT grown crystals) departures from the stoichiometry; i.e. part of a-sites are occupied by $Y^{3+}$ ions.

The optical spectra of trivalent RE ions in HT grown garnets present multisite structure consisting[8,9] of: (i) the prevailing N-lines corresponding to $RE^{3+}$ in non-perturbed dodecahedral c-sites; (ii) satellites assigned to nearest neighbours (n.n.) $RE^{3+}$ pairs in c-sites, M-lines; (iii) satellites present in HT crystals and assigned to c-sites perturbed by the presence of $Y^{3+}$ ions in anomalous a-sites, P-lines; (iv) weak lines assigned to $RE^{3+}$ in octahedral sites, A-lines. In YAG:$Nd^{3+}$ two P-satellites and one pair line M were previously observed in absorption. High resolution site selective excitation and the temporal behaviour of luminescence[3,5,10] confirmed this model. An alternative model, based on selective excitation of five nonequivalent sites[1,4] assumes as sources of perturbation anionic impurities such as $OH^-$. The regular appearance of the above lines and their relative intensities makes this model unlikely.

Recently,[11] based on EXAFS data, a large scale inversion model was proposed for HT garnets: about 9% of A ions and a corresponding fraction of 13.5% of B ions interchange their sites.

The present paper discusses the multisite structure of optical spectra as a test for the structural (non-stoichiometric and inversion) models of YAG.

## 2  RESULTS

Various YAG:Nd samples grown by Czochralsky or Bridgman techniques, with concentrations from 0.1 to 2.5 at% $Nd^{3+}$ have been investigated. The experimental set-ups are described elsewhere.[3,5]

### 2.1  *Transmission Spectra*

A representative transmission spectrum, at low temperatures, for the $^4I_{9/2}(1) \rightarrow {}^4F_{3/2}(1)$ $Nd^{3+}$ transition in YAG:$Nd^{3+}$ ($\sim$1 at%) is given in Figure 1. Following the notations,[9] one could observe, as the main features of the spectra, the presence of main N-line, $P_1$; $P_2$ and M satellites. The relative intensity of P/N is practically independent of $Nd^{3+}$ content C
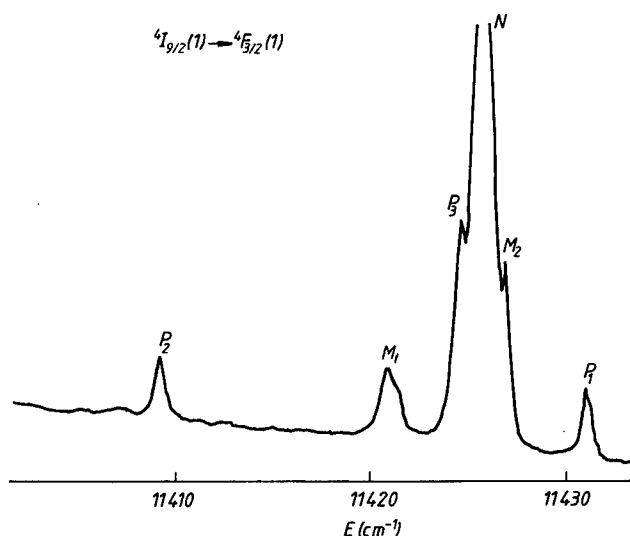
FIGURE 1    $Nd^{3+}$ transmission spectrum in $\sim 1$ at% doptted YAG for the $^4I_{9/2} \rightarrow {}^4F_{3/2}$ transition at 10 K.

and represents about 2–3%, for each of them, while that of the satellite $M_1$ increases linearly with C. Besides this structure, one should remark the presence of a small scale satellite structure close to the main line, not separated before: at least three lines are present; from concentration dependence and lifetimes results that one is of P and two of M-type. These lines are present in all the HT crystals. Additional weak absorption lines are also observed.

The satellite lines in the $^4I_{9/2}(1) \rightarrow {}^4G_{5/2}(1)$ transition, the pump level for the luminescence investigations, are less resolved, thus several sites could be simultaneously excited. A correspondence between these lines and those from $^4I_{9/2} \rightarrow {}^4F_{3/2}$ is obtained by selective excitation. No differences between Czochralsky and Bridgman samples have been noticed.

## 2.2 *Luminescence Spectra and Kinetics*

The emission spectra and the luminescence decays have also been investigated by site selective excitation in $^4G_{5/2}$ level with a pulsed dye laser (10 nsec pulse width). Since this kind of studies have been performed before[1–5,12,13], we discuss these data briefly, insisting especially on the differences from previous reports. The emission characteristics are: at a given pump wavelength the spectra contain more lines, an effect we connect mainly with pump nonselectivity, although energy transfer processes are possible; the spectra are function on temperature and at about 200 K only the main line is observed, due essentially to the temperature broadening of the pump and emission lines; all the lines observed in absorption, excepting the pair line are observed in luminescence; reabsorption in emission and absorption effects in pumping could strongly affect the relative intensities of the lines at selective pumping.
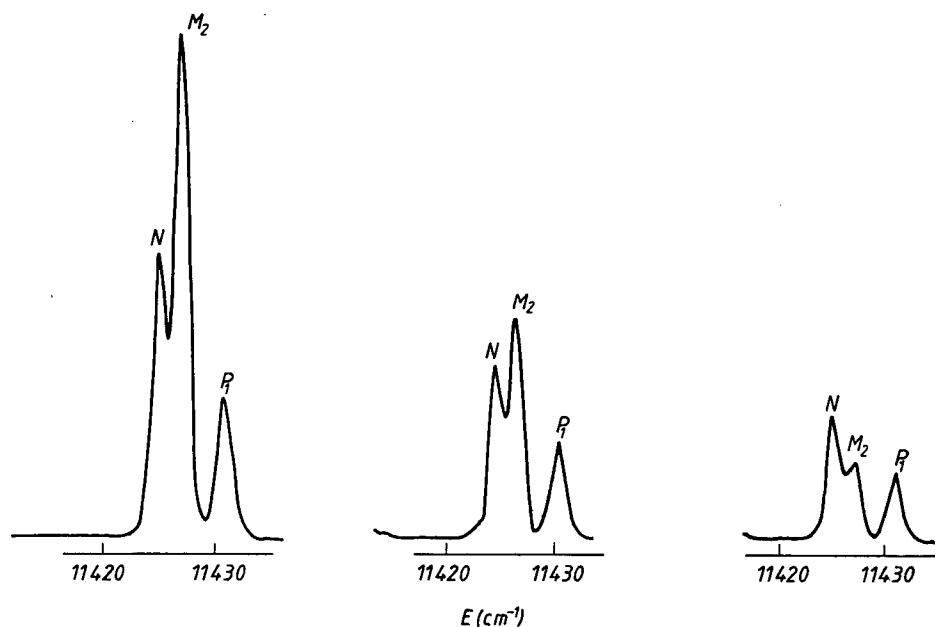
FIGURE 2 Nd$^{3+}$ time resolved spectrum in $\sim$1 at% doped YAG for the $^4I_{9/2} \rightarrow {}^4F_{3/2}$ transition at 10 K, excited with $\lambda_{ex} = 5934$ Å (M$_2$ line): a-time delay = 0; b-time delay = 100 $\mu$s; c-time delay = 200 $\mu$s.

A third P-type satellite was resolved at $-1.5$ cm$^{-1}$ from the main line N in $^4F_{3/2}$. Another satellite M$_2$ with a short lifetime has been resolved at $+1$ cm$^{-1}$ from N, in $^4F_{3/2}$. In emission, additional sites reported previously in selective excitation (sites 1 and 3[4]), but with negligible intensity in absorption, have been also observed.

The time resolved spectra suggest two types of sites: sites with strong luminescence quenching even at low Nd$^{3+}$ content (M$_1$, M$_2$) and sites with lifetimes close to that of main Nd$^{3+}$ line (P$_i$, i = 1, 3). The M$_1$ line emission is practically quenched, over all range of Nd concentration and temperature. The time resolved spectra when M$_2$ is selectively pumped is illustrated in Figure 2. The lifetime of M$_2$ is concentration dependent: $\sim$100 $\mu$sec at low concentration and $\sim$35 $\mu$sec for 2.5 at% Nd.

The luminescence kinetics of P-type satellites is similar to that of N, thus one can assume that P$_i$ and N are involved in similar energy transfer processes, a cross relaxation on intermediate levels, the acceptors being Nd in majority sites.

## 3 DISCUSSION

Our analysis has revealed a much complex multisite structure for Nd$^{3+}$ in YAG than previous reports. These Nd$^{3+}$ centers could be separated in:

(i) A prevailing Nd$^{3+}$ center (N-lines) present in all the transmission spectra. It is connected with Nd$^{3+}$ in dodecahedral nonperturbed c-sites of YAG; and presents a concentration quenching as discussed before;[2,5,10]

(ii)   Satellite lines present in all samples, with intensity dependent on C and having short lifetimes compared with $Nd^{3+}$ in normal sites. They could be associated with various Nd-Nd pairs; at least two satellites ($M_1$, $M_2$) present such behaviour. $M_1$ line has been assigned to $Nd^{3+}(c)$-$Nd^{3+}(c)$ nearest neighbour pairs[8] at 3.67 Å in YAG. It plays an important role in luminescence kinetics and efficiency as our previous data have shown.[5,10] Satellite $M_2$ (at $+1$ $cm^{-1}$ from N) with a short lifetime could be assigned to next near neighbour pairs, Nd(c) at 5.612 Å. The lowering of lifetime for pairs result from an energy transfer between the two companions by cross relaxation on intermediate levels. The transfer rate for a class of pairs can be defined as $W_i = 1/\tau_i - 1/\tau_0$ where $\tau_i$ is the lifetime for this pair ($\sim 100$ $\mu$sec for $M_2$) and $\tau_o$($\sim 260$ $\mu$sec) is the lifetime of the isolated ions. The estimated value of $W \sim 6.15 * 10^3$ $sec^{-1}$ for $M_2$ (at low concentrations) is comparable with that calculated one assuming a dipolar interaction, $W = C_{DA}/R^6$. For $R = 5.612$ Å and the transfer microparameter $C_{DA} = 1.85 * 10^{-40} cm^6 sec^{-1}$ estimated before[3] from the energy transfer to more distant Nd ions one obtains for transfer rate $W \sim 6 * 10^3$ $sec^{-1}$, in very good agreement with that estimated from lifetime. This argument supports our assignment.

(iii)   Three P-type satellites have been solved at $-16$, $-1.5$ and $+5$ $cm^{-1}$ from N. The relative intensity of $P_1$ or $P_2$ to N is of 0.02–0.03 and concentration independent. For the three P-lines, the ratio $\Sigma I(P_i)/(\Sigma I(P_i) + N)$ is about 6–9% and concentration independent. In the flux grown samples the P-type structure is absent. The P-satellites have been assigned[8,9] to $Nd^{3+}(c)$-$Y^{3+}(a)$ n.n. pairs, $Y^{3+}(a)$ being the nonstoichiometric defect of HT YAG.[6,7] Owing to low symmetry at the c-site ($D_2$), the perturbation produced by one $Y^{3+}(a)$ at the six n.n. c-sites (3.35 Å) may not be identical. Assuming that the inversion symmetry of the octahedron of c-sites around an a-site is preserved, three different distortions would be expected. From the relative intensity of P lines (.06–.09) one could estimate the concentration of $Y^{3+}$ in a-sites. Following statistical arguments, this concentration is found of about 2%, a figure as obtained by other methods.[6,7]

Therefore, the optical spectra provide arguments on the substitution of some $Al^{3+}$ ions in a-sites by $Y^{3+}$, but not for a possible exchange of $Y^{3+}$ with $Al^{3+}$ as has been assumed from the EXAFS measurements.[11] Besides, our data confirm the previous estimations of the concentration of $Y^{3+}(a)$. Our recent X-ray data show four equivalent {222} forbidden reflections in HT YAG, suggesting that only local deviations from cubic symmetry are possible and not for the entire crystal as assumed in.[11] The P-satellites are involved essentially in cross relaxation on intermediate levels, the acceptors being all the $Nd^{3+}$ ions. The loss of pump selectivity and broadening of emission with temperature and the low concentration of $P_i$ centers compared with N, could explain the apparent paradox of strong decreasing of $P_i/N$ intensity with temperature while the lifetimes are practically independent of it.

(iv)   Satellites with small intensity in absorption, but clearly detected in laser excited luminescence spectra. Besides the satellites denoted by 1 and 3 in[4] at $-19$ and respectively $-12.5$ $cm^{-1}$ from N, another satellite at $-30$ $cm^{-1}$ in emission of $^4F_{3/2}$ was observed. The last satellite is the main feature of the $Nd^{3+}$ emission at low temperatures under pumping with the second harmonic of a YAG:Nd laser (at 532 nm). This center has been tentatively assigned to $Nd^{3+}$ in octahedral sites.

REFERENCES

1.  D. P. Devor, L. G. DeShazer, *Opt. Commun.* **46**, 97 (1983).
2.  V. Lupei, A. Lupei, S. Geogescu, C. Ionescu, *Opt. Comm.* **60**, 59 (1986).
3.  A. Lupei, V. Lupei, S. Georgescu, C. Ionescu, W. M. Yen, *J. Lumin.*, **39**, 36 (1987).

4. D. P. Devor, L. G. DeShazer, R. C. Pastor, *IEEE J.Q.E.* **25**, 1863 (1989).
5. V. Lupei, A. Lupei, S. Georgescu, W. M. Yen, *J. Appl. Phys.* **66**, 3792 (1989).
6. S. Geller, G. P. Espinosa, L. D. Fullmer, P. B. Crandall, *Mat. Res. Bull.* **7**, 1219 (1972).
7. C. D. Brandle, L. R. Barns, *J. Cryst. Growth* **26**, 169 (1974).
8. Yu. K. Voronko, A. A. Sobol, *Phys. St. Sol. (a)* **27**, 657 (1975).
9. V. V. Osiko, Yu. K. Voronko, A. A. Sobol, *Crystals 10*, Springer Verlag Berlin Heidelberg, **37** (1984).
10. V. Lupei, A. Lupei, S. Georgescu, I. Ursu, *Appl. Phys. Lett.*, **59**, 905 (1991).
11. Jun Dong, Kunquan Lu, *Phys. Rev. B.* **43**, 8808 (1991).
12. R. K. Watts, W. C. Holton, *J. Appl. Phys.* **45**, 873 (1974).
13. L. D. Merkle, R. C. Powell, *Phys. Rev. B* **20**, 75 (1979).
14. J. A. Mares, Z. Khas, W. Nie, G. Boulon, *J. Phys. I* **1**, 881 (1991).

# Cr³⁺-DOPED BORATES—POTENTIAL TUNABLE LASER CRYSTALS?

G. WANG[†], H. G. GALLAGHER, T. P. J. HAN and B. HENDERSON

*Department of Physics and Applied Physics, University of Strathclyde, Glasgow, G1 1XN, Scotland*

This paper reports the top-seeded high temperature solution growth (TSSG) of large single crystals of $Cr^{3+}$-doped $YAl_3(BO_3)_4$. Optical absorption measurements at T = 300 K reveal broad bands associated with transitions from the $^4A_2$ ground state of $Cr^{3+}$ to the $^4T_2$ and $^4T_1$ excited states. The doublet R-lines and their one-phonon sideband are clearly resolved at room temperature in both absorption and luminescence spectra: the splitting of the R-lines demonstrates the effect of the even-parity trigonal distortions of their environment on the $^4A_2$ and $^2E$-levels of the $Cr^{3+}$ ions.

*Key words*: $Cr^{3+}$, $YAl_3(BO_3)_4$, TSSG, crystal growth.

## 1 INTRODUCTION

Yttrium Aluminium Borate, $YAl_3(BO_3)_4$ (YAB) belongs to a group of double borates which crystallise in a trigonal structure with space group R32.[1] YAB possesses excellent physical and chemical properties for laser applications. Furthermore, the crystal structure of YAB provides substitutional sites on which ion-ion interactions are reduced, thereby reducing luminescence quenching and enabling large concentrations of laser active ions to be substituted on either cation sublattice. In recent years, there have been a number of publications on the growth of $Nd^{3+}$ and $Er^{3+}$ doped YAB crystals and their use as gain media in single frequency lasers.[2,3] This paper reports the successful growth of large $Cr^{3+}$ doped YAB crystals and a preliminary assessment of their optical characteristics.

## 2 CRYSTAL GROWTH

YAB melts incongruently at 1280°C, therefore it is necessary to prepare crystals by growth from high temperature solution. The most important factor in this method is the choice of flux. In this work crystals of $Cr^{3+}$:YAB were grown from a $K_2Mo_3O_{10}$ flux, modified slightly by the addition of 3 wt. % $B_2O_3$.[4] Seed crystals of typical dimensions $3 \times 3 \times 6$ mm³ (grown by spontaneous nucleation) were dipped into solutions of YAB in $K_2Mo_2O_{10}$—3 wt% $B_2O_3$ saturated at around 1000°C, which were cooled at rates of $2-4$°C per day using a crystal rotation rate of 6 rpm. The resulting crystals were up to $12 \times 16 \times 22$ mm³ in size and exhibited well developed facets having the form of rhombohedral prisms characteristic of the R32 space group. They were optically clear and dark blue-green in colour.

[†] Permanent Address: Fujian Institute of Research on the Structure of Matter, Chinese Academy of Science, Fuzhou, Fujian 350002, China.

FIGURE 1    Room temperature polarised absorption spectra : a) $\sigma$-polarised (the E vector is perpendicular to the c-axis); b) $\pi$-polarised (the E vector is parallel to the c-axis). Insert shows the R-lines region in greater detail.

## 3   OPITICAL CHARACTERISATION

Optical absorption and luminescence measurements on Cr-YAB crystals have been made in the temperature range 15–300 K. Figure 1 shows the three primary absorption features characteristic to the laser-active $Cr^{3+}$ ion. Two broad brands with peaks at $\lambda = 425$ nm and 595 nm identified, respectively, with the parity-forbidden $^4A_2 \rightarrow {}^4T_1$ and $^4A_2 \rightarrow {}^4T_2$ transitions of the $3d^3$ ion.[5] Superposed on the long-wavelength edge of the $^4A_2 \rightarrow {}^4T_2$ band are two R-lines and their vibronic replicas. These sharp peaks are associated with spin- and parity-forbidden $^4A_2 \rightarrow {}^2E$ transitions. Figure 2a shows the photoluminescence spectrum, at room temperature, comprises the R-lines at $\lambda = 684$ nm ($R_1$) and 682 nm (R2) and their Stokes and anti-Stokes shifted sidebands, superposed on the vibronically-assisted $^4T_2 \rightarrow {}^4A_2$ band. Only the R-lines and their Stokes-shifted sidebands are observed in emission at low temperature, Figure 2b, strongly blue-shifted relative to their room temperature positions. These results demonstrate that, just as in $BeAl_2O_4$ (800 cm$^{-1}$) and YGG (400 cm$^{-1}$), the $^4T_2$-level is higher in energy than the $^2E$ level by some 400–600 cm$^{-1}$. In consequence, the broadband luminescence due to $^4T_2 \rightarrow {}^4A_2$ transitions occur via thermal occupancy of the $^4T_2$ level in competition with the $^2E$-level, and is observed in company with the R-lines at ambient temperature. The shifts of the R-lines with temperature, Figure 3, show that a lst-order type phase transition takes place near
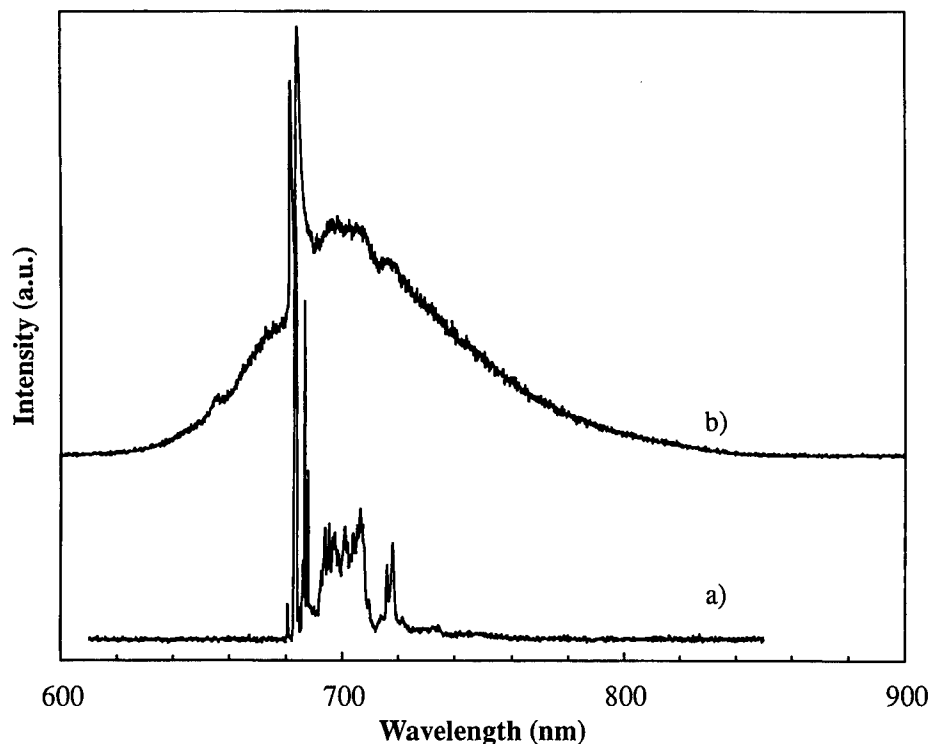
FIGURE 2    Luminescence spectra of Cr$^{3+}$:YAl$_3$(BO$_3$)$_4$ at a) 14 K and b) room temperature.

T = 185 K. However, further study is required to precisely determine the transition temperature and other properties of this transition.

Both optical absorption and luminescence spectra are polarised. The broad bands shift by some 5 nm and the peak absorbance decreases by some 10% between $\pi$- and $\sigma$-polarisation. The peak shift is caused by even-parity, T$_{2g}$, distortions of the environment along the trigonal symmetry axis of the crystal. The polarisation effects are due to odd-parity distortions of T$_{1u}$ and T$_{2u}$ symmetry. There are much larger intensity changes for the R-lines, the intensity ratio I(R$_2$)/I(R$_1$) being 1:1 in $\pi$-polarisation and 1:2 in $\sigma$-polarisation. As discussed for oxide-based crystals by Yamaga et al.,[6] such behaviour is in accord with the 3d$^3$ energy levels being coupled to odd-parity distortions of the CrO$_6^{3-}$ octahedron of T$_{2u}$ symmetry.

## 4  CONCLUSION

Large Cr$^{3+}$:YAB crystals with good optical quality have been grown from a modified K$_2$Mo$_3$O$_{10}$ flux by the TSSG method. The optical absorption and luminescence spectra decisively demonstrate that the Cr-dopant enters YAB in the trivalent form i.e. as Cr$^{3+}$. The presence of the R-lines as strong features in the room temperature luminescence spectrum shows that the optically-active impurity ions occupy the strong crystal field sites,
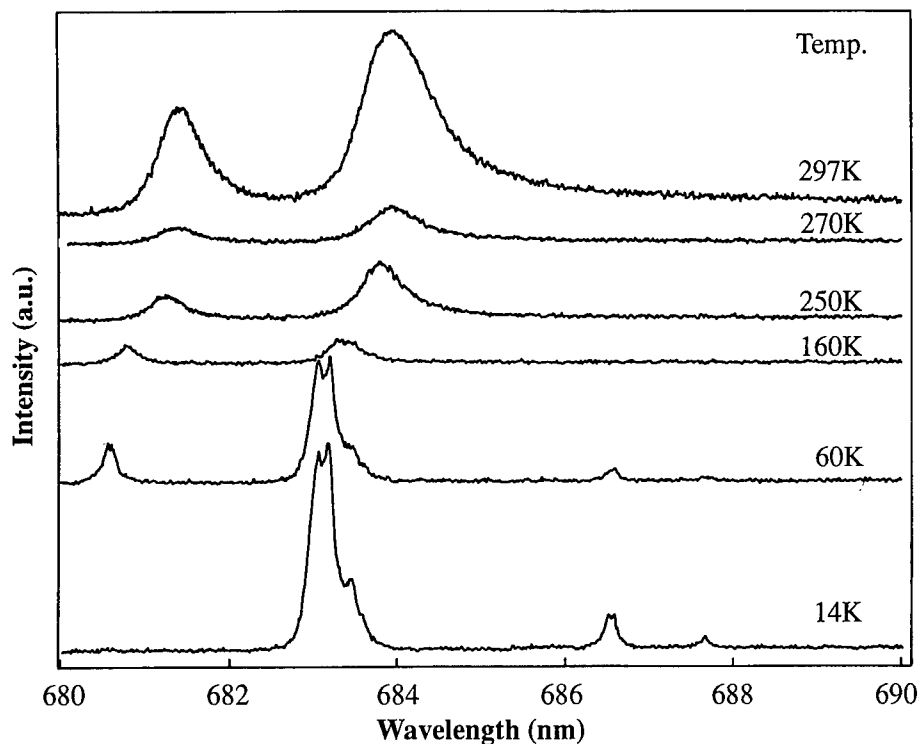
FIGURE 3   Fluorescence spectra of the R-lines as a function of increasing temperature.

more likely to eventuate at the $Al^{3+}$ sites than $Y^{3+}$. It is concluded, therefore, that the $Cr^{3+}$ ions substitute for $Al^{3+}$ ions in YAB at octahedral sites which undergo even-parity and odd-parity distortion along the trigonal axis, which lead to characteristic splittings and polarisations of the observed optical spectra.

ACKNOWLEDGEMENT

REFERENCES

1. E. L. Belokoneva, A. V. Azizov, N. I. Leonyuk, M. A. Simonov, N. V. Belov, *Zhurnar Strukturnal Khimil* **22**, 196 (1981).
2. Z. D. Luo, Y. T. Lin, A. D. Jiang, Y. C. Huang and M. W. Qui, *SPIE* vol. 1104, **132**, (1989).
3. S. F. Akhmetov, G. L. Akhmetova, V. S. Kovalenko, N. I. Leonyuk, A. V. Pashkova, *Sov. Phys. Dopkl.* 23, **107**, (1978).
4. G. Wang, H. G. Gallagher, T. P. J. Han, B. Henderson, to be submitted to *J. Cryst. Growth.*
5. B. Henderson, G. F. Imbusch, *Optical Spectroscopy of Inorganic Solids*, (Oxford University Press, 1989).
6. M. Yamaga, B. Henderson, K. P. O'Donnell, *J. Luminescence*, **46**, 397 (1990).

# Nd$^{3+}$ STRONTIUM FLUOROVANADATE (SVAP) – A PROMISING CRYSTAL FOR DIODE PUMPED LASERS AT 1.06 $\mu$m AND 1.34 $\mu$m

## M. A. SCOTT, H. G. GALLAGHER, T. P. J. HAN and B. HENDERSON

*Department of Physics and Applied Physics, University of Strathclyde, Glasgow, G1 1XN, Scotland*

The Czochralski growth of good quality, large single crystals of Nd$^{3+}$-doped Sr$_{10}$(VO$_4$)$_6$F$_2$ and their optical characterisation are reported. Optical absorption measurements show high absorption (18 cm$^{-1}$) and large linewidth (30 cm$^{-1}$) at the diode pump wavelength 810 nm. Luminescence spectra reveals near single line emission at 1.06 $\mu$m and 1.34 $\mu$m due to the $^4$F$_{3/2}$ $\rightarrow$ $^4$I$_{11/2}$, $^4$I$_{13/2}$ transitions, respectively, with the latter much more efficient than in other commonly used crystals. These excellent optical properties make Nd:SVAP an ideal prospect for diode pumped laser action at both 1.06 $\mu$m and 1.34 $\mu$m.

*Key words*: Nd$^{3+}$, apatites, crystal growth, lasers, optical characterisation.

## 1 INTRODUCTION

Fluoroapatite compounds with the chemical formula A$_{10}$(BO$_4$)$_6$F$_2$, where A = Mg, Ca, Sr etc. and B = P, As, V etc. crystallise in the space group P6$_3$/m.[1] Crystals having the apatite structure have been shown to be very efficient hosts for laser action involving the rare earth ion Nd$^{3+}$ under flashlamp pumping.[2] Nevertheless, practical laser devices have not been realised due to a combination of low thermal conductivity and difficulties in crystal growth. However, the advent of efficient and compact laser diodes as pump sources has led to a relaxation of the requirements on opto-thermal and thermal-mechanical properties and a reduction in the size of crystals used in miniature laser systems. As a result, there has been a recent resurgence of interest in apatite crystals.[3,4] In this paper, we report the crystal growth and optical characterisation of Nd$^{3+}$-doped strontium fluorovanadate, Sr$_{10}$(VO$_4$)$_6$F$_2$ (SVAP) for potential use as the gain medium for diode pumped laser action Nd-lasers.

## 2 CRYSTAL GROWTH

The Nd-SVAP charge was prepared by pre-reaction of a mixture of SrCO$_3$, V$_2$O$_5$, SrF$_2$ and Nd$_2$O$_3$ in accordance with the solid-state reaction

$$(9 - x)\text{SrCO}_3 + \frac{x}{2}\text{Nd}_2\text{O}_3 + 3\text{V}_2\text{O}_5 + (1 + y)\text{SrF}_2 \Rightarrow \text{Sr}_{10-x}\text{Nd}_x(\text{VO}_4)_6\text{F}_2 + (9 - x)\text{CO}_2 + Y\text{SrF}_2 + \frac{x}{4}\text{O}_2$$
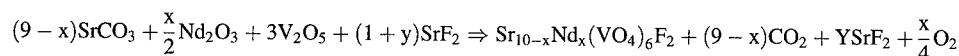
where x is chosen to give a Nd$^{3+}$ ion concentration in the crystal of 0.5–3 at% and y is in the range 1–5 mol% excess in the melt. Both a- and c-axis crystals were grown by the Czochralski technique in an iridium crucible at 1650°C. Under optimal growth conditions large single crystals measuring 60 mm × 18 mm in diameter are obtained free from light scattering defects observed in other apatites[5]. Despite careful control of both composition and oxygen stoichiometry, the as grown crystals are a marked green colour. The green colouration is due to a weak absorption background containing bands at 780 nm and 1000 nm, assigned, respectively to the $^3$A$_2$ $\rightarrow$ $^3$T$_1$, $^3$T$_2$ transitions of V$^{3+}$ ions. The V$^{3+}$
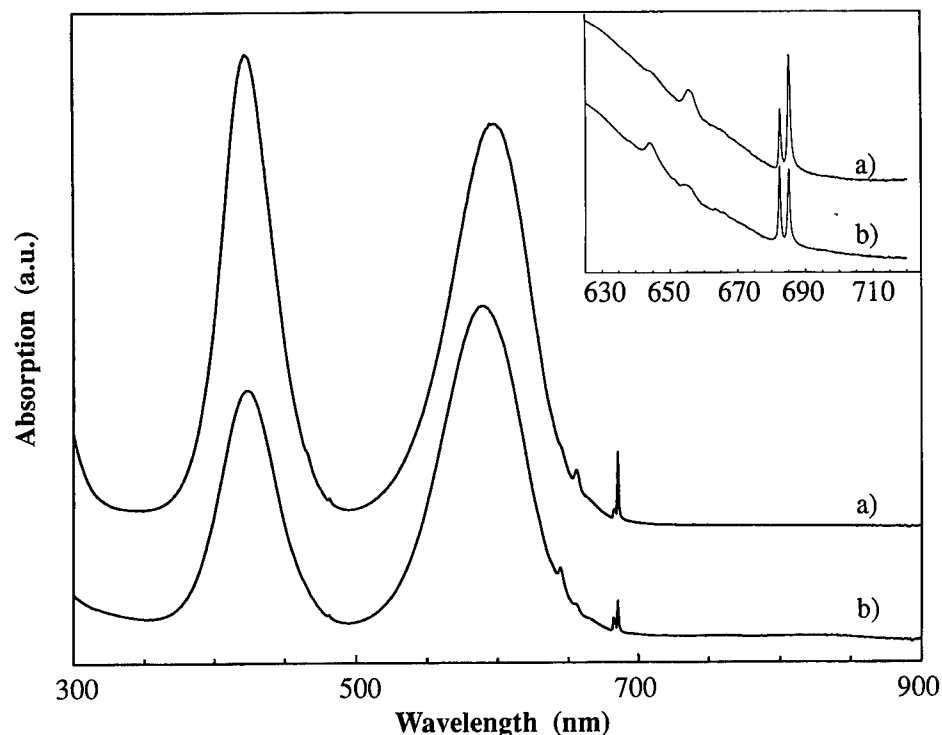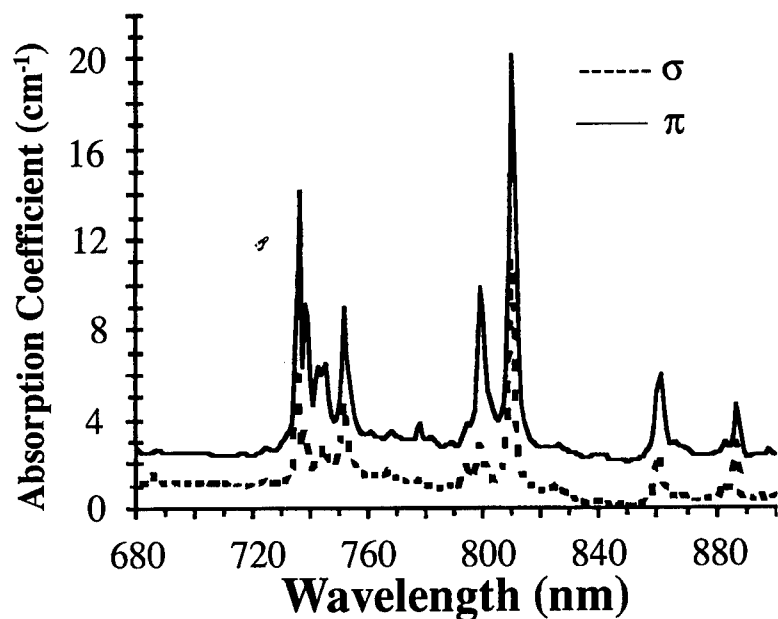
FIGURE 1    Room Temperature polarised absorption spectra of Nd:SVAP:$\sigma$-polarised (E vector perpendicular to the c-axis); $\pi$-polarised (E vector parallel to the c-axis).

ions are caused by evaporation of both $O_2$ and $F_2$ from the melt at the high temperature involved in growth, thereby promoting the reduction of $V^{5+}$ to $V^{3+}$ to compensate for the loss of anion charges. Although present in low concentrations $V^{3+}$ ions occupy tetrahedral symmetry sites where the transition probability for d-d transitions are enhanced by the absence of a centre of symmetry.[6] Post growth annealing of the crystals in a weakly oxidising atmosphere reduces the $V^{3+}$ content to negligible proportions. The crystals that then ensue are the familiar blue colour of Nd-doped ionic compounds.

## 3   OPTICAL CHARACTERISATION

Optical absorption and luminescence measurements have been made at 293 K on crystals containing 1.0 at% $Nd^{3+}$. The polarised absorption spectrum of a post growth annealed sample at room temperature is shown in Figure 1. In the near infra-red region, the absorption is partially polarised with $\pi$ (E parallel to the c-axis) stronger than $\sigma$ (E perpendicular to the c-axis) and exhibits a high absorption coefficient (18 cm$^{-1}$) and large linewidth (30 cm$^{-1}$) at the diode pump wavelength of *ca* 810 nm. The room temperature luminescence of Nd:SVAP is shown in Figure 2. Efficient, near single line fluorescence is observed for both the $^4F_{3/2} \rightarrow$ $^4I_{11/2}$ and $^4I_{13/2}$ transitions at 1.06 $\mu$m and 1.34 $\mu$m, respectively, with the latter much more efficient than the 1.34 $\mu$m emission in related apatites,[3,4] and other known hosts.[7] The fluorescence is also highly polarised, with the $\pi$ polarisation 5 times stronger for both transitions. The strong polarisation features of Nd:SVAP are derived from large odd-parity distortions at the $Sr^{2+}$ site having $C_s$
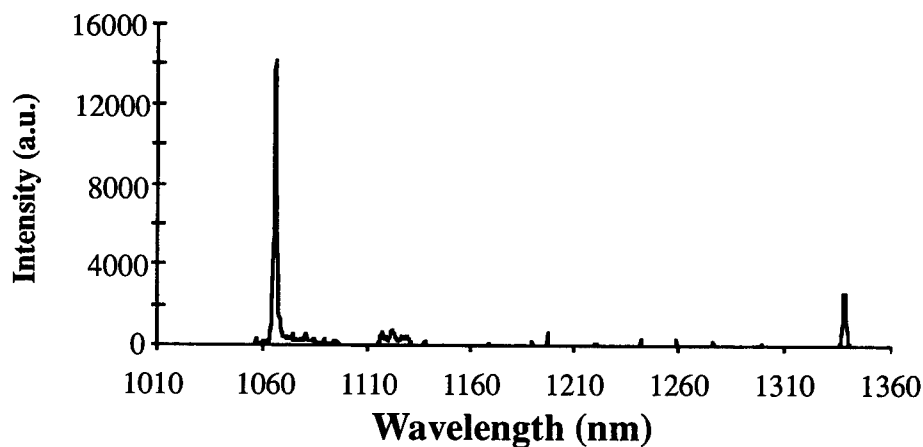
FIGURE 2  Room temperature luminescence spectrum of the $^4F_{3/2} \rightarrow {}^4I_{11/2}, {}^4I_{13/2}$ transitions of Nd:SVAP (uncorrected for spectral response of detection system).

symmetry at which the Nd$^{3+}$ ion substitutes. The polarisation characteristics of Nd:SVAP is stronger in comparison to other apatites. This is attributed to the greater distortions at the Nd$^{3+}$ site caused by substitution of the large vanadium and strontium ions in the apatite lattice. In addition the presence of large odd-parity distortions at the Nd$^{3+}$ site results in the selection of one particular transition from the $^4I$ multiplets. Consequently, the branching ratio for the 1.34 $\mu$m transition is higher than in other Nd$^{3+}$-doped laser hosts. Preliminary diode pumped experiments in an unoptimised cavity indicate a slope efficiency of the order of 40% and low lasing threshold ($ca$ 10 mW) at both 1.06 $\mu$m and 1.34 $\mu$m.

## 4   CONCLUSIONS

Excellent laser quality crystals of Nd:SVAP can be grown using the Czochralski method followed by post growth annealing in a mildly oxidising atmosphere. Odd-parity distortions on the Sr$^{2+}$ site at which the Nd$^{3+}$ ion substitutes leads to strong polarisation of the optical properties. This and the large inter-Stark crystal field splitting of the $^4F_{3/2}$ and $^4I_{11/2}$ multiplets leads to the selection of one particular crystal field transition. In consequence, the near single line fluorescence from $^4F_{3/2} \rightarrow {}^4I_{11/2}$ and $^4I_{13/2}$ transitions are very efficient, with the latter much more so than in other crystals. Furthermore, the large absorption coefficient and linewidth at 810 nm provide for efficient energy extraction from the pump beam. These excellent absorption and fluorescence properties make Nd:SVAP an ideal candidate for diode pumped lasers operating at 1.06 $\mu$m and 1.34 $\mu$m.

REFERENCES

1.  St. Naray-Szabo, $Z.\ Krist.$, ,**75**, 387, (1930).
2.  R. C. Ohlmann, K. B. Steinbruegge and R. Mazelsky, $Applied\ Optics$, **7** 905 (1968).
3.  X. X. Zhang, G. B. Loutts, M. Bass and B. H. T. Chai, $Appl.\ Phys.\ Lett.$, **64** (1), (1994).

4. X. X. Zhang, P. Hong, G. B. Loutts, J. Lefaucher, M. Bass and B. H. T. Chai, *Appl. Phys. Lett.*, **64** (24), (1994).
5. R. Mazelsky, R. H. Hopkins and W. E. Kramer, *J. Crystal Growth*, **3/4**, 260, (1968).
6. B. Henderson and G. F. Imbusch, *in Optical Spectroscopy of Inorganic Solids*, Clarendon Press, Oxford (1989).
7. A. A. Kaminskii, *in Laser Crystals* (Springer Verlag, Heidelberg, 1990).

# CHARGE COMPENSATION AND THE SPECTROSCOPY OF $Cr^{3+}$ IN $KMgF_3$

## D. R. LEE, T. P. J. HAN and B. HENDERSON

*Department of Physics and Applied Physics, University of Strathclyde, Glasgow, G 1 1XN, Scotland*

$Cr^{3+}$ ions in the cubic perovskite $KMgF_3$ enter $KMgF_3$ substitutionally for $Mg^{2+}$ ions at octahedral sites, which may or may not be distorted by the nearby presence of $Mg^{2+}$ or $K^+$ vacancies. These different $Cr^{3+}$ sites result in a number of distinguishable $Cr^{3+}$ spectra, including both R-line and broad band luminescence. The R-lines identified with $Cr^{3+}$ ions at octahedral and trigonal symmetry sites, the trigonal symmetry arising when $Cr^{3+}$ ions have nearby $K^+$ vacancies along $\langle 111 \rangle$ directions. The broad band luminescence is attributed to $Cr^{3+}$ ions in tetragonal sites created when $Cr^{3+}$ ions have a vacant $Mg^{2+}$ ion site along a $\langle 100 \rangle$ direction.

*Key words*: $Cr^{3+}$:$KMgF_3$, Photoluminescence, Charge Compensation, Perovskite.

## 1 INTRODUCTION

The energy level structure of $3d^3$ ions in ionic crystals depends upon the strength of the octahedral crystal field, Dq, which crudely distinguishes between the strong field sites (Dq $\geq$ 2.3, as in ruby) and weak field sites (Dq $\geq$ 2.3, as in $KZnF_3$). The emission from $Cr^{3+}$ in strong field sites is dominated by the $^2E \to {}^4A_2$ transition, characterised by the emission of a single R line for $Cr^{3+}$ ions in octahedral symmetry, with a radiative lifetime of several milliseconds.[1] Distortions from octahedral symmetry remove the orbital degeneracy of the $^2E$ level, and a pair of R lines is observed with lifetime reduced relative to octahedral sites.[1] In the weak field case, the lowest excited state is $^4T_2$ and $Cr^{3+}$ luminescence arises from the vibronically broadened $^4T_2 \to {}^4A_2$ transition with a radiative lifetime of between 50–100 $\mu$s. Presently $Cr^{3+}$-doped fluoride crystals are of much interest as potential tunable laser gain media.[2–5] The first $Cr^{3+}$-doped fluoride laser, which used $Cr^{3+}$:$KZnF_3$ as the gain medium, was tunable over the wavelength range 785–865 nm using luminescence on the vibronically broadened $^4T_2 \to {}^4A_2$ transition.[1]

## 2 EXPERIMENTAL RESULTS

The $KMF_3$ crystals, which were grown by Dr P. Walker at the Crystal Growth Laboratory, University of Oxford, were co-doped in the melt with $10^{19}$ ions $cm^{-3}$ of $Ni^{2+}$ and $Cr^{3+}$ for the study of exchange interactions by ESR techniques. These studies revealed $Cr^{3+}$ ions at octahedral, trigonal and tetragonal sites,[6] $Ni^{2+}$ ions in octahedral sites and low concentrations of $Ni^{2+}$-$Cr^{3+}$ pairs.[7] $KMgF_3$ is isomorphic with $KZnF_3$: the crystal field strength is slightly higher in $KMgF_3$ because of the 10–12% decrease in unit cell dimension relative to $KZnF_3$. Figure 1a shows that $Cr^{3+}$ ions substitute at octahedrally co-ordinated $Mg^{2+}$ sites. Charge compensation for the excess charge on the $Cr^{3+}$ is effected by vacancies on the $K^+$ and $Mg^{2+}$ sub-lattices. Undistorted sites for the $Cr^{3+}$ ion, Figure 1a, result when such vacancies are remote from the tripositive ion. However, when a near neighbour $Mg^{2+}$ vacancy occurs along a $\langle 001 \rangle$ direction the $Cr^{3+}$ site has tetragonal symmetry, Figure 1b. The removal of a $K^+$ ion along a $\langle 111 \rangle$ direction gives a trigonally
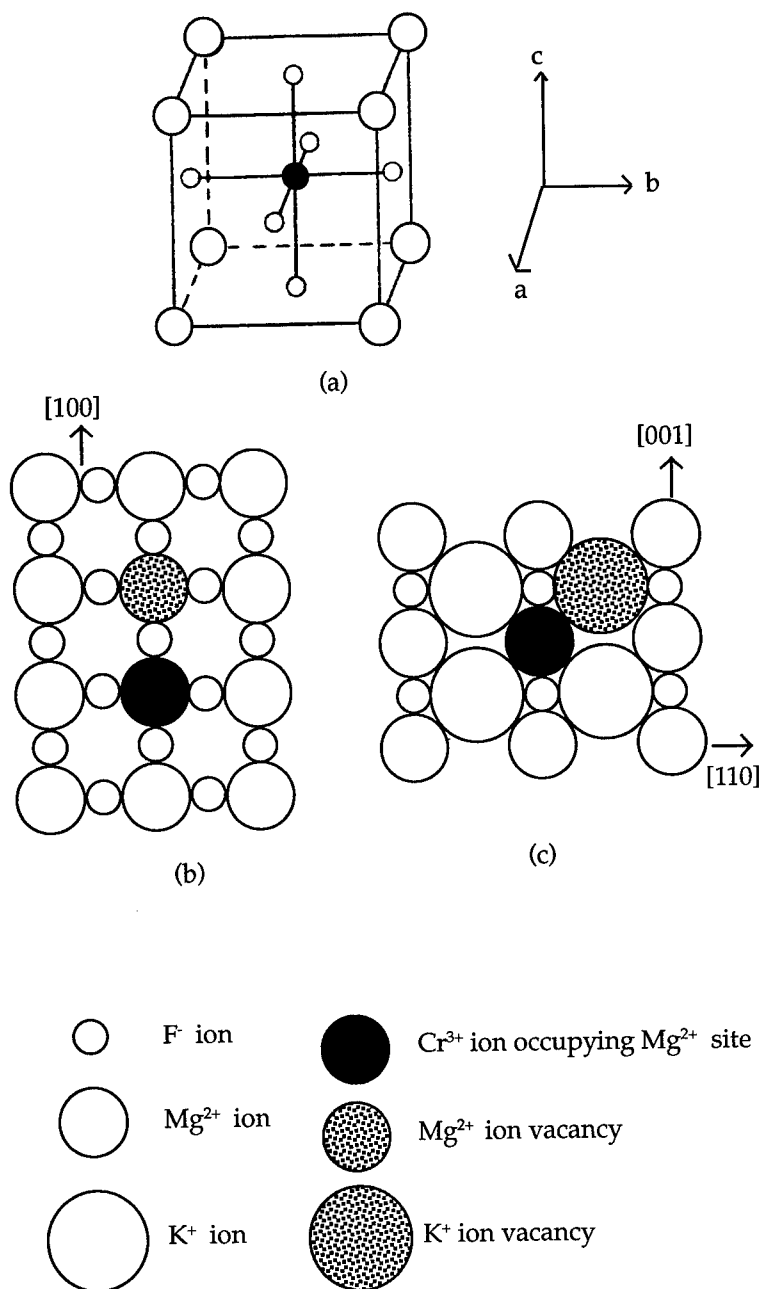
FIGURE 1   The KMgF$_3$ unit cell showing
a Cr$^{3+}$ ion substituted for a Mg$^{2+}$ ion in an octahedral arrangement of six fluorine atoms.
b A tetragonally distorted charge compensated Cr$^{3+}$ site on the (001) plane.
c A trigonally distorted charge compensated Cr$^{3+}$ site on the (110) plane.
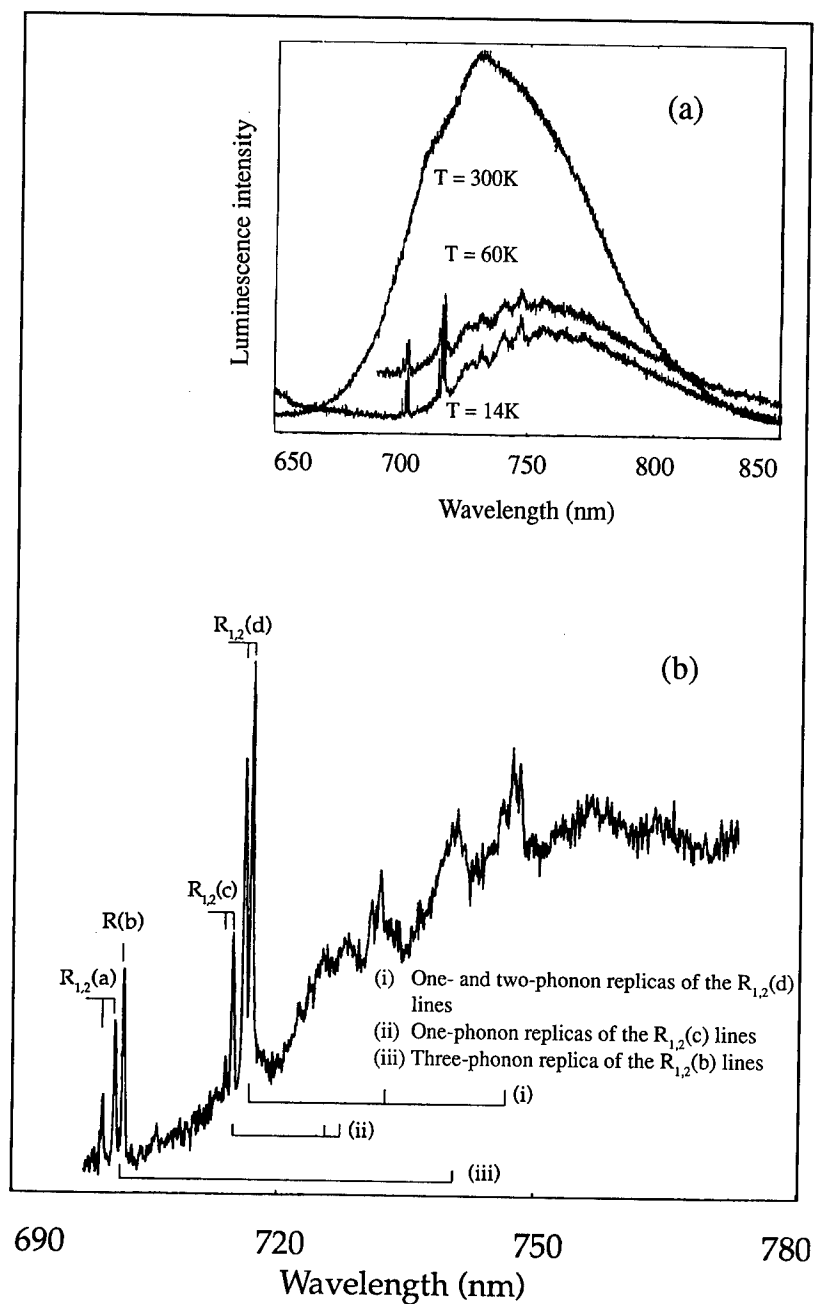
FIGURE 2 Low temperature luminescence (T = 14 K) from Cr$^{3+}$ in KMgF$_3$ showing
(a) broadband and R-line emission excited by $\lambda$ = 488 nm measured at 14 K, 60 K and 300 K.
(b) higher resolution measurements of the R-line region between 690 to 760 nm excited using the 488 nm line at T = 14 K.

symmetric site (Figure 1c). Luminescence spectra and radiative decay times of $Cr^{3+}$ ions in these different sites were measured using conventional spectroscopy. The optical absorption, fluorescence/fluorescence excitation and radiative lifetime behaviours of $Ni^{2+}$ in $KMgF_3$ are known and well understood.[8] Excitation of $Cr^{3+}$ ions was achieved using the 488 nm and 514.5 nm lines from an $Ar^+$ laser, which wavelengths were selected to avoid direct excitation of isolated $Ni^{2+}$ ions.[8]

Luminescence spectra excited at different temperatures using the 488 nm $Ar^+$ line are shown in Figure 2a: the peak positions and lifetimes of these spectra are summarised in Table I. At low temperature the R-lines and their phonon sidebands are superimposed on a broad luminescence band centred at $\lambda = 760$ nm. When excited with unpolarized radiation the 760 nm band is unpolarised, but is polarised about the four-fold crystal axis when excited with polarised laser radiation. This broadband is the only spectral feature excited using the 514.5 nm radiation. The radiative lifetime at T = 15 K is $54 \pm 15$ $\mu$s. These results suggest that the broadband is due to $Cr^{3+}$ ions in tetragonally distorted, weak field sites where $^4T_2$ lies below the $^2E$ level. This broadband luminescence becomes progressively weaker at temperatures above T = 130 K. When excited at T = 300 K using the 514.5 nm $Ar^+$ line the 760 nm band is undetectable because of strong non-radiative decay. ESR measurements on tetragonal $Cr^{3+}$ centres[6] are consistent with the lowest level of the $^4T_2$ state in tetragonal sites being below the $^2E$ level. The broadband is, therefore, assigned to $^4T_2 \rightarrow {}^4A_2$ transitions on weak field $Cr^{3+}$ sites where a $Mg^{2+}$ vacancy occupies a neighbouring cation position along a $\langle 001 \rangle$ direction.

The R-lines observed at low temperature under 488 nm excitation shown in detail in Figure 2b signal $Cr^{3+}$ occupancy of strong field sites. The R(a), R(c) and R(d) lines occur as pairs of R-lines: the R(b) line at 702.3 nm is not paired with any other line. The singlet nature of the R(b) line and long decaytime, $\tau_R = 3.0 \pm 0.5$ ms, suggest that it is associated with $Cr^{3+}$ ions in strong field sites with perfect octahedral symmetry.[1] The R(d) lines have a shorter radiative decaytime $\tau_R = 1.6 \pm 0.2$ ms and are shifted to longer wavelengths with $R_1(d)$ at 716.0 nm and $R_2(d)$ at 716.8 nm. These results suggest a slightly weaker octahedral crystal field at this $Cr^{3+}$ site, with the small splitting between the lines of 15.6 $cm^{-1}$ being caused by even parity distortions of the $CrF_6^{3-}$ octahedron. Since the splittings are of similar magnitude to values obtained for $Cr^{3+}$ ions in trigonal crystal fields[9,1] this pair of lines is assigned to $Cr^{3+}$ ions in trigonal sites, the distortion being due to a near neighbour $K^+$ ion vacancy. The positions of the R(a) and R(c) lines and their shorter lifetimes relative to R(b) and R(d), are consistent with exchange-coupled $Cr^{3+}$-$Ni^{2+}$ pairs. The radiative lifetimes of such pairs are expected to be shorter because their optical transitions are induced by the electric dipole process, the rate of energy transfer between the ions being proportional to the energy splitting between the lines.[1] Indeed weaker decay components overlapping the dominant decaytimes listed in Table I suggest that energy transfer occurs between $Cr^{3+}$ ions in different sites and close-by $Ni^{2+}$ ions. These effects are still under investigation.

Finally, the R-lines observed at low temperature when excited at 488 nm decrease in intensity with increasing temperature, especially above *ca* T = 150 K, consistent with the increasingly probable decay from the $^2E$-level by non-radiative processes. This decrease in intensity is accompanied by the appearance of a broadband peaked at $\lambda = 730$ nm, which is the dominant feature above 200 K. At T = 300 K, only vestiges of the R-lines and their sidebands are observed as shown in Figure 2a., as a consequence of the thermal population of the $^4T_2$ level at the expense of the $^2E$ level at higher temperatures. This band is unpolarised suggesting that $Cr^{3+}$ ions occupy undistorted sites. In consequence, the R-line ($^2E \rightarrow {}^4A_2$) processes decrease with increasing temperature and the $^4T_2 \rightarrow {}^4A_2$ transition becomes much more intense. These trends are very similar to those observed for $Cr^{3+}$ ions

in alexandrite and yttrium gallium garnet[10-11], where the $^4T_2 \rightarrow {}^2E$ splitting is some 800 cm$^{-1}$ and 400 cm$^{-1}$ respectively. Unfortunately, the overlapping spectra from the different Cr$^{3+}$ multisites in KMgF$_3$ makes it impossible to assess whether this broadband is due to a single octahedral centre or to a mixture of octahedral and trigonal centres.

Table I
R line and broadband luminescence data

| Label | Wavelength (nm) | Wavelength (cm$^{-1}$) | Energy separation $\delta$E (cm$^{-1}$) | Lifetime Excitation wavelength 488 nm | Lifetime Excitation wavelength 514 nm |
|---|---|---|---|---|---|
| R$_2$(a) | 700.0 | 14285.7 | 28.5 | 860 $\pm$ 80 $\mu$s | – |
| R$_1$(a) | 701.4 | 14257.2 | | | |
| R(b) | 702.3 | 14238.9 | – | 3.0 $\pm$ 0.5 ms | – |
| R$_2$(c) | 714.0 | 14005.6 | 15.7 | 690 $\pm$ 100 $\mu$s | – |
| R$_1$(c) | 714.8 | 13989.9 | | | |
| R$_2$(d) | 716.0 | 13966.5 | 15.6 | 1.6 $\pm$ 0.2 ms | – |
| R$_1$(d) | 716.8 | 13950.1 | | | |
| Broadbands 760 nm (T = 15 K) | 740 760 780 | 13,160 | – | 60 (200*) $\mu$s 60 (200*) $\mu$s 60 $\pm$ 15 $\mu$s | 54 $\pm$ 15 54 $\pm$ 15 54 $\pm$ 15 |
| 730 nm (T = 200 K) | 710 730 750 | 13,700 | – | 200 $\pm$ 20 $\mu$s 200 $\pm$ 20 $\mu$s 200 $\pm$ 20 $\mu$s | – – – |

REFERENCES

1. B. Henderson & G. F. Imbusch: *in Optical Spectroscopy of Inorganic Solids.*
2. U. Brauch and U. Durr, *Opt. Comm.*, **49**, 61 (1984).
3. S. A. Payne, L. L. Chase, H. W. Newkirk, L. K. Smith and W. F. Krupke, *IEEE J. QE* **24**, 2243 (1988).
4. J. A. Caird, S. A. Payne, P. R. Staver, A. J. Ramponi, L. L. Chase and W. F. Krupke, *ibid,* 1077.
5. S. A. Payne, L. L. Chase, L. K. Smith, W. L. Kway and H. W. Newkirk, *J. Appl. Phys.*, **66** (3) 1051 (1989).
6. J. Patel, J. J. Davis, B. C. Cavenett, H. Takeuchi and K. Morai, *J. Phys. C: Sol. St. Phys.*, **9**, 129 (1976).
7. B. Henderson and P. Benson, (unpublished data, 1973).
8. M. V. Iverson and W. A. Sibley, *J. Luminescence,* **20**, 311 (1979) and references therein.
9. R. J. Macfarlane, *J. Chem. Phys.*, **39**, 3118 (1963).
10. J. C. Walling, D. F. Heller, H. Samelson, D. J. Harter, J. A. Pete and R. C. Morris, *IEEE J. Quant. Elec. QE21, 1568 (1985).*
11. M. Yamaga, B. Henderson, K. P. ODonnell, G. Yue, *Appl. Phys.*, **B51**, 132 (1990).

# PERSPECTIVE LASER INFRARED OPTICS MATERIAL CESIUM IODIDE

## I. ANTONIV, I. GARAPYN and R. DIDYK

*Physical department, Lviv State University, 50 Dragomanova st., Lviv, 290005, Ukraine*

This paper describes some of the techniques that have been used successfully in our laboratory for the purification and preparation of a number of alkali halide crystals, particularly CsI. The methods of cesium iodide single crystals growth with a lowered amount of oxygen-containing impurities are presented. The $CO_2$-laser radiation scattering in monocrystals obtained by applying of proposed methods has been investigated. It has been concluded that scattering occurs on microinclusions, which are the products of decomposition of organic impurities presented in commercial material.

*Key words*: cesium iodide, purification, sorbent, laser resistance, scattering.

At the present time cesium halides are the object of many investigations, which are stimulated by applications of alkali halides both as laser technique optic elements and as active laser environment. Absorption of alkali halides in the middle IR-region is one of the lowest among the known materials.[1] That's why the high optical resistance is inherent for them. The last two parameters are the main parameters for IR-power optics materials and they strongly depend on nature, amount and distribution of crystal defects, caused by existence of impurities in particular. The presence of such impurities is defined by crystal growth conditions.

We propose a method which overcomes these difficulties. We present here the methods of preparing cesium halide crystals with lowered amount of oxygen-containing impurities. The nature of absorbing inhomogenities in crystals grown in different conditions is being discussed here.

The production of raw materials and sometimes even the growing of samples takes place in the presence of oxygen. As a result, the specimen produced in this way may contain a certain amount of oxygen-containing impurities. To purify samples from them we have carried out the processing of the melt in vacuum in the presence of sorbent. The scheme of relevant equipment for carrying out such a process is shown in Figure 1a.

The quartz ampoule divided into two chambers (1 and 2) isolated from each other by quartz filter-bed (3) has a lateral channel for pumping out air. The ampoule is placed into a furnace consisting of two parts (5 and 6). The electrical power supplied and the location of heating elements in the furnace provide required dependence of the temperature on the height inside the furnace (Figure 1b). The powder of CsI (4) with required experimentally determined[2] amount of sorbent for purification is placed on the bottom of the ampoule, the powder is melted and this melt is held in vacuum for several hours. Then the ampoule together with furnace is turned upside down. As a result, the filtration of the melt through the filter-bed takes place. Then the crystal in the chamber (2) is being grown.

The measure of received crystals are: 30 mm diameter, 250 grams mass.

In order to control the purification efficiency the IR-spectra of crystals grown from both purified and non-purified raw materials were measured by using "Specord -IR 75". The absorption bands peculiard for anion impurities as $NO_3^-$, $CO_3^{2-}$, $OH^-$ were absent in IR-spectra of purified CsJ crystals.

The parameters of received crystals are as follows:
- the bulk absorption coefficient at 10, 6 $\mu$m ($\beta_v$) of $10^{-5}$ cm$^{-1}$;
- resistance to $\gamma$-radiation (in comparation with crystals grown from commercial powder) increased up by two orders;
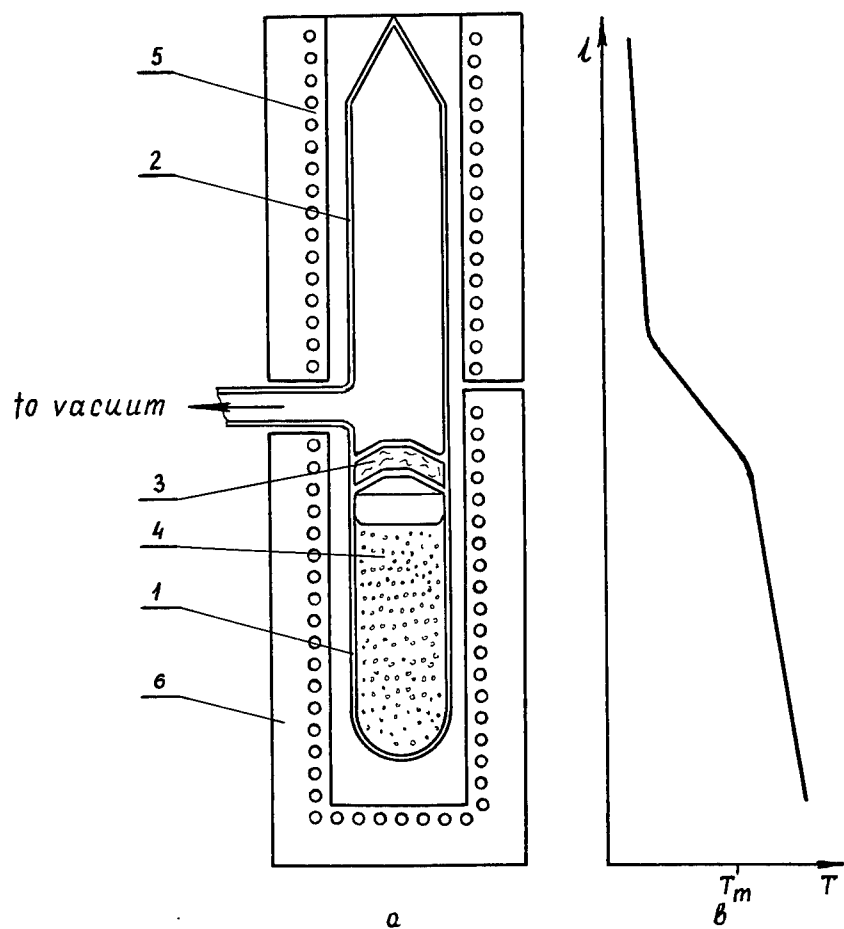
FIGURE 1   The equipment for purification and growing of samples.

- secondary electron emission coefficient of 26;
- electroconductivity of 7, $5*10^{-12}$ $Ohm^{-1}.cm^{-1}$ at 343 K;

In some cases for manufacturing IR-optic elements the structural perfect cesium iodide monocrystals with preliminary determined lattice orientation are necessary. It is difficult to achieve such aim when crystals are being grown by direct crystallization in ampoule (by Stockbarger method). For this purpose the CsI crystals were grown by pulling from melt on oriented cooled seed (by Czochralsky method) in dry inert atmosphere. The purification of melt from oxygen-containing impurities was carried out by applying sorbent too. The process goes on in isolated furnace with quartz reactor where the salt has been melt and treated by sorbent carried to the crucible with double side and then the crystal was grown.
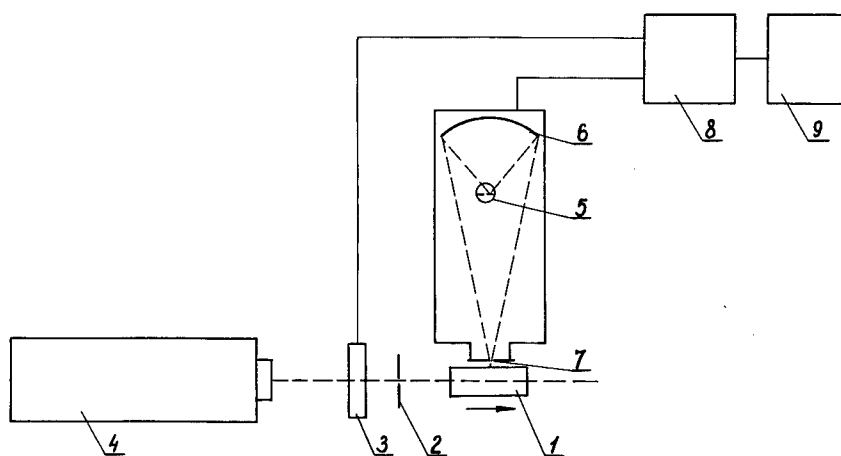
FIGURE 2   The block-scheme of installation for detecting microinclusions by using scattering of IR-radiation.

The obtained crystals with diameter 50 mm were transparent in visible region and bulk absorption coefficient (determined by laser calorimetry method) was $3*10^{-5}$ cm$^{-1}$.

The investigations of cesium iodide monocrystals resistance to IR-laser irradiation (pulsed neodimium laser, $\lambda = 1,06$ $\mu$m) showed that its laser resistance can be reduce to a high degree by extraneous microinclusions. From our point of view the decomposition of organic impurities (which were present in commercial grade) during the melting process in absence of air is one of the possible reason for appearance of such microinclusions. Carbon black is the end product of organics decomposition and it ingress into crystal.

In order to detect absorbing microinclusions the suitable installation was mounted in our laboratory. The block-scheme is shown in Figure 2. The beam by diameter 1 mm from $CO_2$-laser 4 was modulated by modulator 3 and directed through diaphragm 2 on the monocrystal 1. The section of sample was chosen by entrance slit 7 and the scattered IR-radiation from this section displayed by bolometer 5 the lightsensitive element being situated in the focal plane of sphere mirrow 6. The magnitude of bolometer signal is proportional to intensity of IR-radiation from different sections of crystal. The crystal was moving at predetermined rate in front of slit 7. The signal from bolometer after amplification by amplifier 8 was recorded on the recording apparatus.

The intensity of $CO_2$-laser irradiation scattering along A and B crystals was recorded and results are presented in Figure 3. CsI crystals were grown by Czochralski method in inert atmosphere with adding sorbent to the melt (crystals A and B). Additional but not described here method of purification from microinclusions has been used for obtaining crystal B. It should be noted that the increased means of scattering intensities at the beginning and at the end of both curves are caused by IR-radiation scattering on the end surfaces of crystal. The scattering of laser beam on microinclusions caused sharp rise of bolometer signal and appearance of peaks in the curve 1. The absence of such peaks in the curve 2 gives evidence about the absence of such scattering centers on the path of laser beam in crystal B.

The laser resistance of crystals A and B has been investigated and the results are presented in the table. Three plates with thickness 4–5 mm were cut from each of both crystals and were polished on both sides. The plates were irradiated by single impulse from
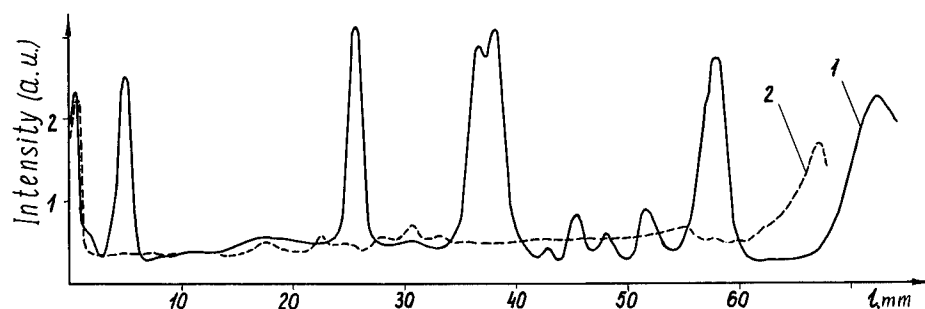
FIGURE 3   The intensity changes of $CO_2$-laser radiation scattering against length of CsI crystals grown in inert atmosphere with applying of purification from oxygen containing impurities.

TABLE I
Laser break-down energy for CsI crystals.

| Crystal | Sample specimen No. | Distance between specimen and len $\iota$ (mm) | Break-down energy (MW/cm²) | |
|---------|---------------------|-----------------------------------------------|-----------------------------|---------|
| | | | Experimental date | Average |
| | 1 | 350 | 110 | |
| A | 2 | 360 | 116 | 118 |
| | 3 | 380 | 130 | |
| | 1 | 480 | 243 | |
| B | 2 | 490 | 262 | 270 |
| | 3 | 510 | 307 | |

neodimium laser through twofocal (F = 750 **mm**) convergence len. The density of laser beam light energy ingressing on the sample has been altered by changing distance $\iota$ between a sample and a len.

It follows from the date presented in the table that laser resistance of CsI samples, which were cut from different sections of crystals may differ from one another by 25%. It is clear from the table that purification of monocrystals from microinclusions (crystal B) increased the laser resistance.

It should be noted that as the energy of laser destruction was assumed the energy of laser beam due to which the "dimness" has been created in crystal. The "dimness" was observed in microscope by scattering of visible light. The repeated investigations of $CO_2$-laser radiation scattering intensity from sample sections irradiated by impulse neodimium laser showed the "dimness" in IR-region occurrence at some lower energies.

REFERENCES

1.  N. V. Karlov, E. V. Sisakyan. *Izvestiya Akademii Nauk SSSR*, **44**, 1631 (1980).
2.  I. P. Antoniv, I. V. Garapyn and D. I. Matviichuk. *Sov. J. "Vysokochistye veschestva"*, **5**, 175 (1990).

# LASER DIODE PUMPING OF A COLOUR CENTRE LASER WITH EMISSION IN THE 1.5 $\mu$m WAVELENGTH DOMAIN

A. KONATÉ, J. L. DOUALAN and J. MARGERIE

*Laboratoire de Spectroscopie Atomique ERS 137, ISMRA, 6, Bd Maréchal Juin*
*14050 CAEN Cedex France*

We describe a colour centre laser pumped by a laser diode. The pumping is at 0.96 $\mu$m in the absorption band of the $Tl^0(1)$ centre in $KCl:Tl^+$. The laser emission is tunable around 1.5 $\mu$m with an output power of 17 mW. We have also obtained with the same device, 15 mW with $(F_2^+)_H$ centres in $NaCl:OH^-$.

*Key words:* Colour centre, Laser diode pumping, Colour centre laser, Tunable.

During the eighties, the development of semiconductor technology has provided new sources for pumping solid state lasers.[1] Rare earth ions are the materials most commonly pumped by laser diodes. For widely tunable lasers, using transition metals or colour centres, diode pumping is more difficult to use. A few years ago we introduced for the first time the laser diode pumping of a colour centre laser (CCL) (($F_2^+$)* centres in $NaF:Mg^{2+}$).[2] In the present communication, we report a laser diode pumped CCL which uses as active centre $Tl^0(1)$ in $KCl:Tl^+$.

This centre has an absorption band around 1.04 $\mu$m; it emits in a broad and homogeneous band around 1.5 $\mu$m.[3] Pumped by a Nd:YAG laser at 1.064 $\mu$m, it can deliver up to 4 W output power. It is perfectly stable at 77 K, even under intense pump radiation[4] and its emission can be tuned between 1.4 and 1.6 $\mu$m.[5]

A new laser diode emits 1 W around 0.96 $\mu$m. Its emission falls in the short wavelength wing of the absorption band of the $Tl^0(1)$ centre. The absorbed power is enough to overcome the losses in the cavity.

The sample are home grown. $KCl:Tl^+$ is coloured by radiation damage at about 77 K with a 1.6 MeV electron beam, an operation which is performed with the Van de Graaff accelerator of URA 17 of Université Paris VII.

We use a tight focusing linear optical cavity (Figure 1), with a concave input mirror and a flat output one which transmits 7% in the 1.5 $\mu$m range. The CCL input mirror is a neutral meniscus and it has 87% transmission at 0.96 $\mu$m. Therefore it does not interfere significantly in the focusing of the pump light on the sample. Between the sample and the output mirror there is a 30 mm focal length intracavity lens, tilted by $\sim$ 10° in order to correct the astigmatism induced by the crystal held at Brewster angle on a cold copper finger. The vacuum chamber is closed by the input mirror on one side and by the intracavity lens on the other.

The pumping diode is a SDL 6362 P1 from Spectra Diode Labs, it is a ten element device, delivering up to 1 W (cw) at 0.96 $\mu$m. The beam from the diode is collimated by a 6.5 mm focal length triplet, corrected by an anamorphic prism pair and focused on the sample by a 30 mm focal length doublet. The matching of the CCL waist radius and the pump beam is not good. The pumping is collinear to the CCL cavity. The waist of the laser cavity is 21 $\mu$m, while the minimum area of the pump beam is 90 $\mu$m by 10 $\mu$m.

We have obtained a stable laser emission in the 1.5 $\mu$m range with $Tl^0(1)$. The temperature of the sample is 84 K. The output power is 17 mW for 830 mW input power measured just after the focusing lens (Figure 2a). The threshold is 240 mW. We obtain a
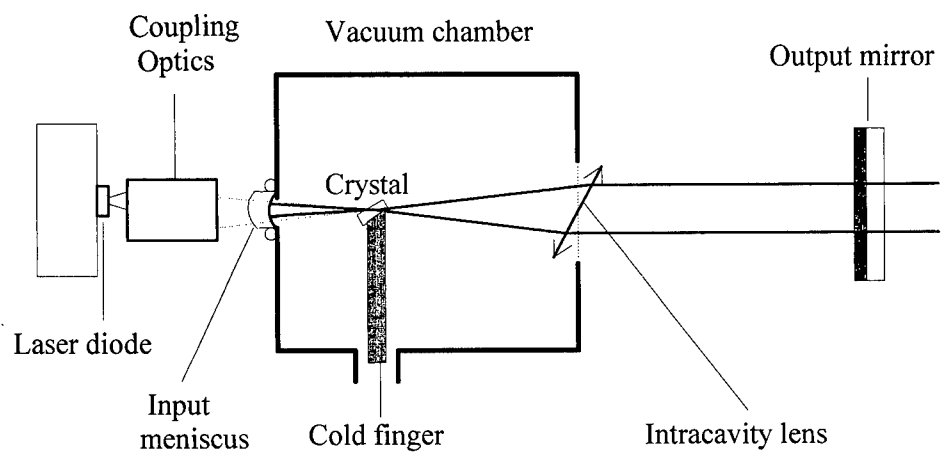
FIGURE 1    Configuration of the colour centre laser.
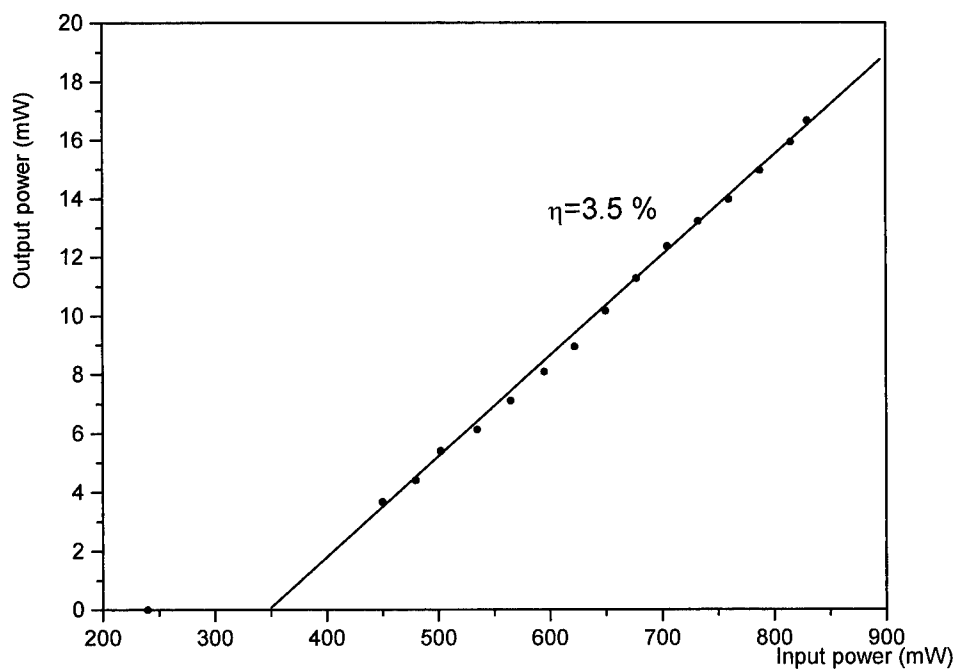


FIGURE 2(a)    Performance of the $Tl^0(1)$ laser in $KCl:Tl^+$.
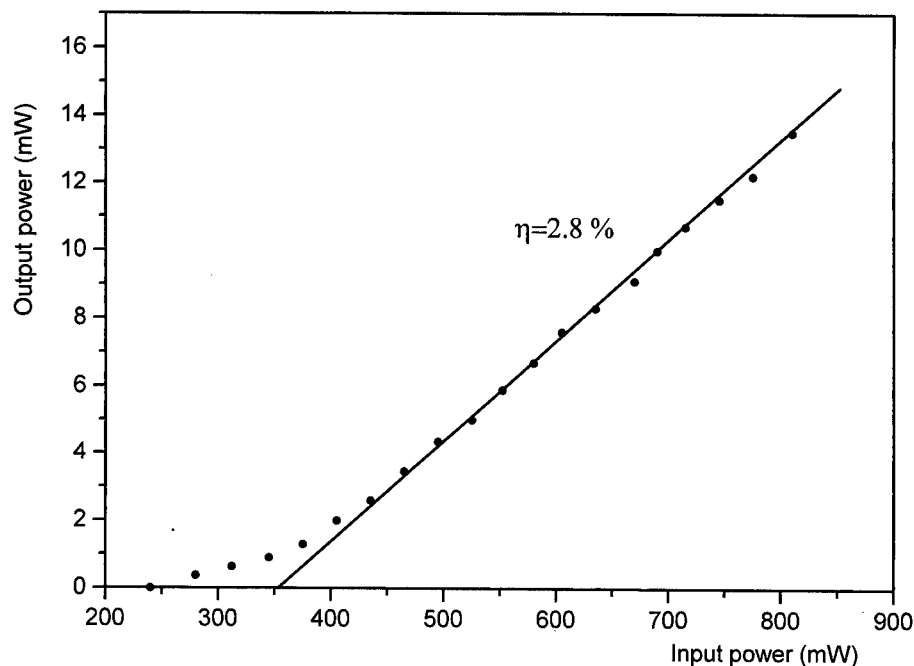
FIGURE 2(b)   Performance of the $(F_2^+)_H$ laser in NaCl:OH⁻.

slope efficiency of 3.5%, which is lower than when pumping by the 1.064 $\mu$m line of a Nd:YAG laser where we find a threshold of 70 mW. The difference can be explained by the bad matching between the pumping beam and the CCL waist. It is partly occulted by the mounting of the input mirror when entering in the cavity and moreover, only 50% of the beam reaching the crystal is absorbed. The laser emission is stable over several hours. This $Tl^0(1)$ centre is known to be stable under strong pumping by the 1.064 $\mu$m line of Nd:YAG. In our experiment the power is lower but the excitation wavelength is shorter. The stability of some colour centres depend on the pump wavelength. With $Tl^0(1)$ centre, the stability is not affected by a shorter pumping wavelength. This CCL lases on the TEM$_{00}$ mode. With a prism inserted into the cavity, between the lens and the output mirror, we can tune the laser emission between 1.485 and 1.540 $\mu$m (Figure 3). This tuning range is 35% of the $Tl^0(1)$ centre emission band width (measured at half maximum).

These results are preliminary. We hope to increase the output power and the tuning range of the laser emission. Some modifications are being made on the cavity and new experiments are in progress. Moreover the efficiency will be improved by using a laser diode emitting at a greater wavelength, such as the SDL 6362 P1 which is now available with 1 W output at 990 nm.

The current laser diode can pump some other colour centres. The most interesting one is the $(F_2^+)_H$ centre in NaCl:OH⁻.[6] With this centre we have indeed obtained laser emission around 1.55 $\mu$m in the diode pumped cavity. To overcome the orientation effect of the $(F_2^+)_H$ centres under pump power,[6] we have used the blue green light of a krypton laser,
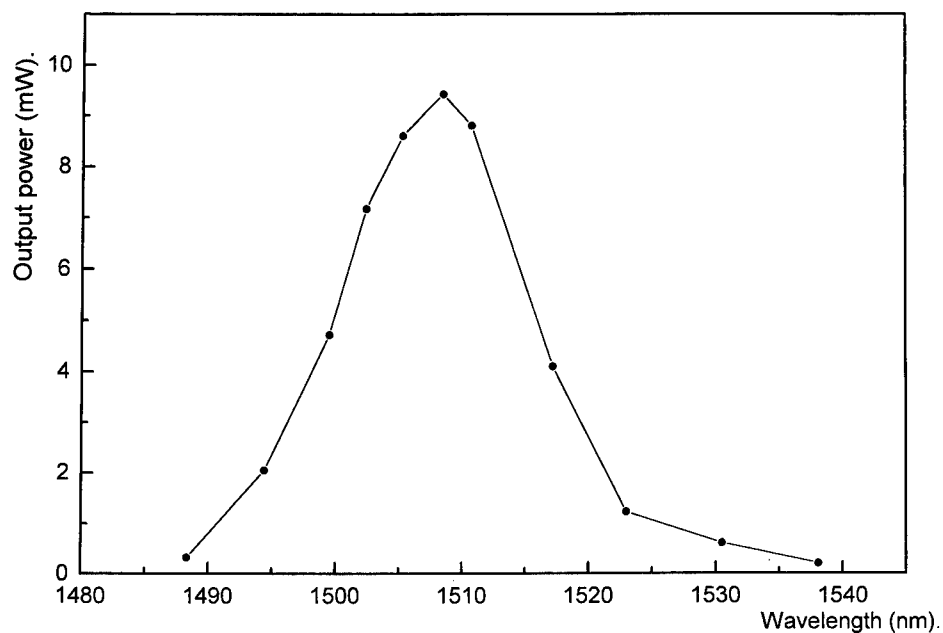
FIGURE 3    Tuning curve of the KCl:Tl$^+$colour centre laser emission for 830 mW pump power.

injected through the output mirror. This $(F_2^+)_H$ centres regeneration procedure has not been fully optimised yet. Nevertheless we have obtained 15 mW output power for 830 mW input power (Figure 2b).

REFERENCES

1.  D. W. Hughes and J. R. M. Barr, *J. of Phys. D: Appl. phys.* **25**, 563 1992.
2.  J. L. Doualan, *Opt. Comm.* **70**, 225 1989.
3.  W. Gellermann, F. Lüty and C. R. Pollock, *Opt. Comm.* **39**, 391 1981.
4.  J. L. Doualan and W. Gellermann, *Digest of Topical Meeting on Advanced Solid State Lasers* 1990, p. 94.
5.  W. Gellermann, J. Phys. *Chem. Solids* **52**, 249 1991.
6.  J. F. Pinto, E. Georgiou and C. R. Pollock, *Opt. Lett.* **11**, 519 1986.

# Ni²⁺:BaLiF₃: A PROMISING R. T. TUNABLE SOLID STATE LASER MATERIAL

M. MORTIER, J. Y. GESLAND, M. ROUSSEAU, F. AUZEL,* and D. MEICHENIN*

*Equipe de Physique de l'Etat Condensé, C.N.R.S.-U.R.A. 807 Université du Maine, Avenue Olivier Messiaen B.P.535, 72017 LE MANS cedex, France; \*France Telecom, CNET Paris B Laboratoire de Bagneux, B.P. 107, 92225 Bagneux Cedex, France*

In this paper, we present our work about the near I.R. emission broadband ($^3T_2 \rightarrow {}^3A_2$) of Ni²⁺-doped BaLiF₃ around 1.4 $\mu$m. R.T. emission spectra, absorption spectra, laser cross-section and lifetime doping ion concentration dependence are reported. High values of fluorescence lifetime and emission cross-section are evidenced.

*Key words*: absorption, emission, laser cross-section, lifetime, fluoperovskite, infrared.

## 1  INTRODUCTION

As previously mentioned,[1] we have studied the dynamical[2,3,4] and spectroscopic[5,6] properties of Ni²⁺ or Cr³⁺-doped BaLiF₃. A complete study of optical properties up to 30 000 cm⁻¹ has been done.[5,6] Single crystals of high optical quality were grown by the Czochralski technique.[7,8,9,10] X-ray investigations have shown that BaLiF₃ has the inverted perovskite structure belonging to the ($O_h^1$-Pm$\bar{3}$m) space group[7,2] with a = 3.995 Å and a density of 5.2425 g.cm⁻³. The refractive index was estimated[2] to 1.5. In the classical perovskite structure, the center of the octahedra is occupied by the divalent ion whereas in BaLiF₃, the monovalent Li⁺ is at the center. For this reason, BaLiF₃ is called inverted perovskite. This original and unique situation among the AMF₃ family of compounds confers a particular interest to the study of this host crystal. We evidenced, in Electron Paramagnetic Resonance (EPR), the substitution of Li⁺ ion by Ni²⁺ in BaLiF₃, the nickel site being cubic.[5]

## 2  CRYSTAL GROWTH

The compound BaLiF₃ melts incongruently. Its crystallisation domain extends from 0.44BaF₂ + 0.56 LiF to 0.22 BaF₂ + 0.78 LiF so that a single crystal must be grown from a non-stoechiometric melt containing BaLiF₃ with 0.3 LiF in excess.

The BaLiF₃ single crystals are pulled along a four-fold axis direction by the Czochralski technique.[7,8,9,10] Pulling runs are performed in an argon/CF₄/HF atmosphere to avoid oxygen contamination, using platinum crucibles. The melt is doped by adding nickel fluoride NiF₂. The boules are grown at a pulling rate of 1 mm/h with a crystal rotation rate of 15 rpm. Along this process, several Ø15 mm × 50 mm pale-green single crystals are obtained from melts containing respectively 0.5, 1, 2, 3, 4 and 6% of nickel fluoride.

No scattering centers are detected by examination with a 1 mW He-Ne laser. The concentration of Ni²⁺ was determined by the Inductively Coupled Plasma (ICP) analytical technique. Measurements are summarised in Table I. The mean distribution coefficient of Ni in BaLiF₃ is found to be about 0.3.

M. MORTIER *ET AL.*
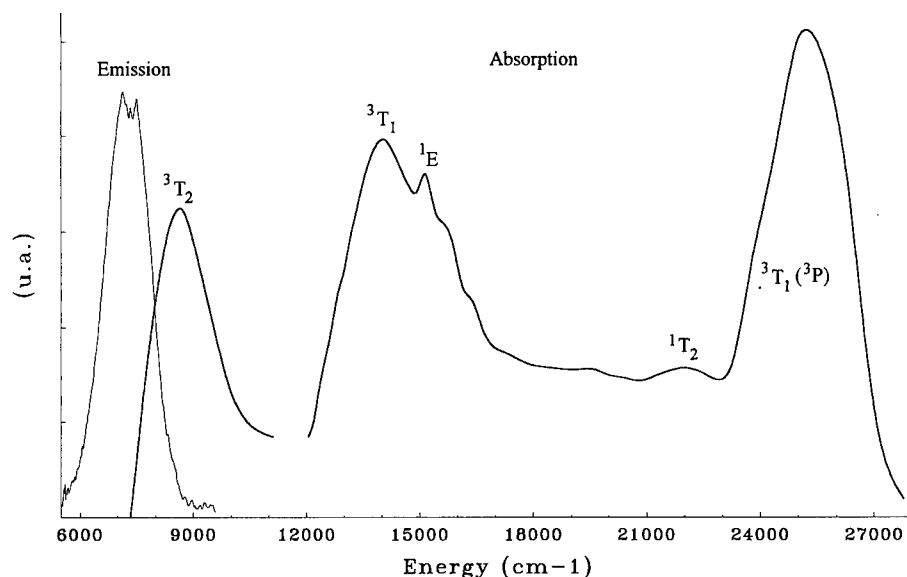


FIGURE 1    Absorption and I.R. emission spectra of $Ni^{2+}$:$BaLiF_3$ at R.T.

Table I

| melt: $BaLiF_3$+0.35 LiF | $\mu g$ Ni/g $BaLiF_3$ in crystal | nb of Ni atoms/$cm^3$ in crystal | % Li substituted in crystal | segregation coefficient |
|---|---|---|---|---|
| +0.005 $NiF_2$ | 500 | 3 $10^{19}$ | 0.2 | 0.36 |
| +0.01 $NiF_2$ | 920 | 5 $10^{19}$ | 0.3 | 0.33 |
| +0.02 $NiF_2$ | 1600 | 9 $10^{19}$ | 0.55 | 0.29 |
| +0.03 $NiF_2$ | 2700 | 15 $10^{19}$ | 0.9 | 0.33 |
| +0.04 $NiF_2$ | 3300 | 18 $10^{19}$ | 1.1 | 0.30 |
| +0.06 $NiF_2$ | 4800 | 26 $10^{19}$ | 1.65 | 0.29 |

## 3   OPTICAL MEASUREMENTS

Optical absorption measurements were recorded with a Cary 17D spectrophotometer. At R.T., the main three absorption bands correspond to the $^3T_1$ ($^3P$), $^3T_1(^3F)$, $^3T_2$ levels respectively (Figure 1). I.R. luminescence spectrum was obtained by exciting the samples with light from a 150 W Xe lamp, passed through a 0.22 m monochromator. A dry-ice cooled PbS detector from Hamamatsu, placed at the exit slit of a 0.34 m monochromator, was used to measure the emission (Figure 1). The lowest zero phonon line (ZPL), from the lowest of the four spin-orbite components, is predicted at 7510 $cm^{-1}$ with respect to the ZPL of the two visible emissions.[5,6] The purely electronic transition is a spin-allowed ($\Delta S = 0$) magnetic-dipole transition. The fluorescence spectrum appears as a broad vibronic sideband (*i.e.*, electronic transitions accompanied by the simultaneous emission of
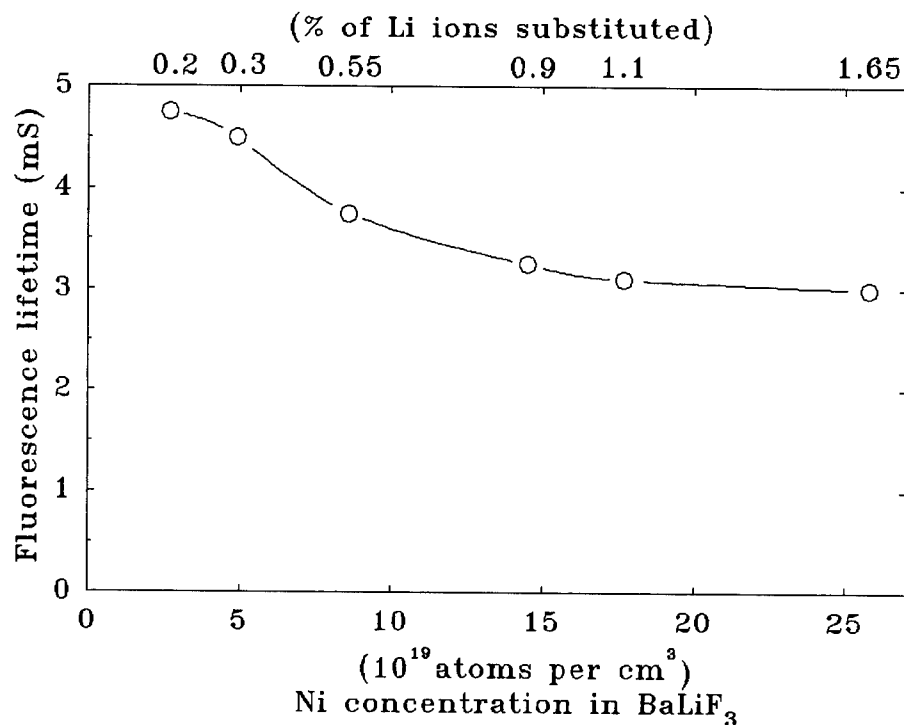
FIGURE 2    Evolution of the fluorescence lifetime versus Ni concentration on the I.R. emission at R.T. after excitation at 1.06 $\mu$m.

one or more phonons). It is generally believed that phonon-assisted transitions of localized centers in solids are predominantly electric-dipole even when the parity selection rule required zero phonon transitions to be magnetic dipole (MD). However, it has been shown[11] that the vibronic sideband of the IR emission ($^3$T$_2 \rightarrow$ $^3$A$_2$) of many fluoperovskites[12,13] is rather pure MD. As a matter of fact, this band can be estimated MD.

In a previous work,[5,6] the following parameters: Dq $= 840$ cm,$^{-1}$ B $= 937$ cm$^{-1}$ and Dq/B $= 0.9$ were estimated.

## 4    I.R. EMISSION PARAMETERS

The fluorescence lifetime versus doping ion concentration is shown in Figure 2. Lifetime measurements at R.T. were carried out with a CW 1.064 $\mu$m Nd:YAG laser chopped to deliver 35 ms excitation pulses. Time decays were recorded with a GaAs detector. For a doping level from 0.2% to 1.65% in nickel ions, a decrease from 4.75 ms to 3 ms in the 1.4 $\mu$m emission lifetime is observed. Decays are kept exponential in the range 0.2% to 0.55% Ni$^{2+}$ concentration. For higher doping levels, the decays become non exponential probably due to energy transfers implicated in self-quenching. The spectral overlap between absorption and emission justify such hypothesis. The exact mechanism is currently under investigations.
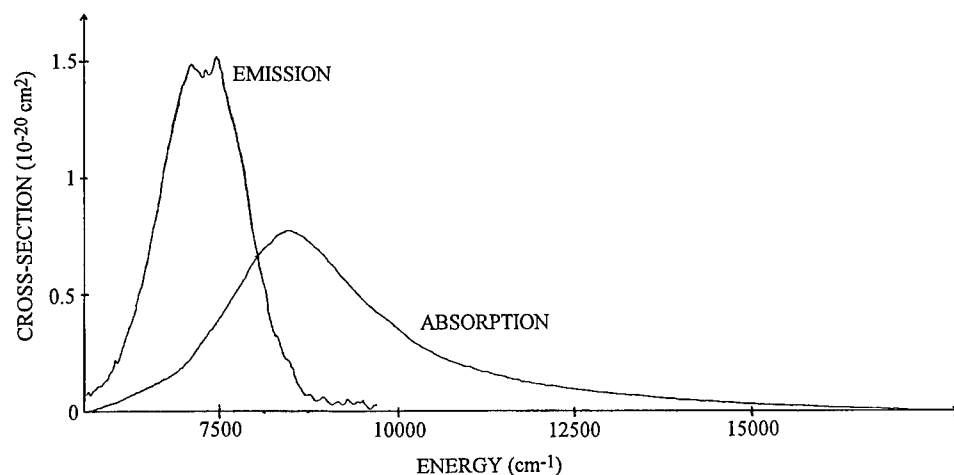
FIGURE 3   Absorption and emission spectra of $Ni^{2+}$: $BaLiF_3$ obtained at R.T. and plotted in absolute units of cross-section.


A maximum emission cross-section of $1.53 \ 10^{-20} \ cm^2$ was estimated from the normalized absorption and emission spectra (Figure 3). Calculations are based on the equivalence of the absorption and emission oscillator strengths at the intersection between both spectra.


## 5   CONCLUSION

A new infrared laser material $Ni^{2+}$:$BaLiF_3$ has been grown, the I.R. emission and absorption properties have been investigated. The 4.75 ms fluorescence lifetime and $1.53 \ 10^{-20} \ cm^2$ maximum emission cross-section are very promising for a future tunable I.R. laser.

REFERENCES

1. M. Mortier, Semaine Franco-Israelienne, Les matériaux lasers Lyon décembre 1993.
2. A. Boumriche, P. Simon, M. Rousseau, J. Y. Gesland and F. Gervais, *J. Phys.: Condens. Matter* **1**, 5613 (1989).
3. M. Mortier, J. Y. Gesland and M. Rousseau, *Solid State Com.* **89**, 369 (1994).
4. A. Boumriche, J. Y. Gesland, A. Bulou, M. Rousseau, J. L. Fourquet, B. Hennion, *Solid State Com.* **91**, 125 (1994).
5. M. Mortier, J. Y. Gesland, B. Piriou, J. Y. Buzaré and M. Rousseau, *Optical Materials.* 4 (1994) 115–120.
6. M. Mortier, *Thesis Université Paris 6* (1994).
7. R. Leckebusch, A. Neuhaus and K. Recker, *J. of Crystal Growth* **16**, 10 (1972).
8. J. Y. Gesland, *J. of Crystal Growth* **49**, 771(1980).
9. J. Y. Gesland, *Thesis Université du Maine* (1984).
10. S. L. Baldochi and J. Y. Gesland, *Mat. Res. Bull.* 891 (1992).
11. M. D. Sturge, *Solid State Com.* **9**, 899(1971).
12. J. Ferguson, H. Guggenheim, H. Kamimura and Y. Tanabe, *J. Chem. Phys* **42**, 775 (1965).
13. J. Ferguson, E. R. Krausz and H. J. Guggenheim, *Molecular Physics* **29**, 1021 (1975).

# Ag$^+$ CENTER IN ALKALINE-EARTH FLUORIDES: NEW UV SOLID STATE LASERS?

## P. BOUTINAUD, A. MONNIER and H. BILL

*Dept of Physical Chemistry, University of Geneva, Switzerland*

Oxygen-free strontium fluoride crystals containing single monovalent silver ions in a cubic site were grown. Our experiments showed that the Ag$^+$ ion remained chemically stable upon optical irradiation at 222 nm (KrCl excimer). The ion exhibits a strong UV luminescence which presents no thermal quenching up to RT. At this temperature, the emitting level time-constant is 12 $\mu$s. An explanation is proposed for the silver photostability by relating it to the large electronic bandgap of the host (11.4 ev). The 222 nm absorbing level lies below the conduction band in a way such that photoionization of Ag$^+$ is avoided, as well as other optically-induced opacity phenomena. A minimum source intensity at threshold is estimated at some 276 kW, when using a Fabry-Perot cavity. This power can normally be achieved with the excimer laser.

*Key words*: Ag$^+$, fluorides, luminescence, photostability, laser.

## 1 INTRODUCTION

SrF$_2$:Ag$^+$ crystals appear to be promising systems for the laser effect in the UV spectral range. A few arguments are developed in this direction in the following.

## 2 THE MATERIAL

Monovalent silver ions were successfully embedded in oxygen-free strontium fluoride crystals of high optical quality, grown by the Bridgman technique.[1] The main part of the as-grown crystals remains colorless and contains no colour centers. The bars cleave naturally (54.7°) very closely to the Brewster angle (55.3°), which appear convenient for future technological application.

Detailed spectroscopic investigations on the colorless samples revealed the existence of 4 Ag$^+$-related photoluminescent centers. The very preponderant one as regards concentration was shown to be the single Ag$^+$ ion substituting for a Sr$^{2+}$ cation of the lattice. It forms the non-locally compensated (Ag$^+_{Sr}$$^{2+}$)$^{\circ}$ electron-donor center and possesses cubic symmetry.[2] This center gives rise to phonon-assisted interconfigurational $4d^{10} \leftrightarrow 4d^9 5s^1$ transitions. We expect it to be laser-active. Among the 3 remaining minor centers, 2 were attributed to (Ag$^+$)$_2$ pairs with different geometries. The origin of the last center is not yet established, mainly because its concentration remains always very low in the crystals. The concentration ratio $\beta = $ (Ag$^+$ single ions/(Ag$^+$)$_2$ pairs) is sample dependent. $\beta$ can be strongly raised during the crystal growth procedure by increasing the rate of the thermal quenching: this action contributes to limitate the migration of the Ag$^+$ ions in the lattice and, concomitantly, their aggregation into pairs. The crystals obtained this way contain essentially single Ag$^+$ ions only.

## 3 OPTICAL PROPERTIES OF Ag$^+$

Upon excitation at 222 nm (transition $1\Gamma_1$ [100% spin singlet character]$\rightarrow 2\Gamma_5$ [50% s.s.c] ),[2] this center exhibits a strong UV luminescence, peaking around 315 nm
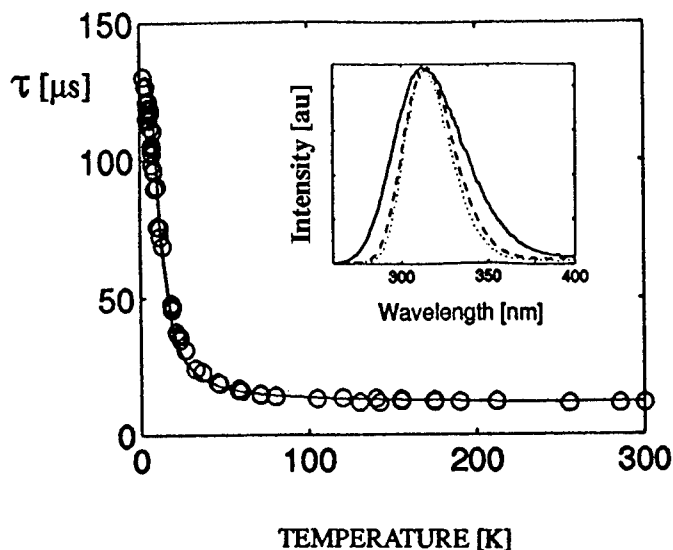
FIGURE 1  Temperature dependence of the 315 nm luminescence lifetime. o: experimental data. Solid line : parametrization of the curve within a three-levels model[3].
Insert: Normalized emission spectrum of the $(Ag^+_{Sr}{}^{2+})^\circ$ center for $\lambda_{exc} = 222$ nm. —: T = 300 K, - - -: T = 80 K and ······: T = 6 K.

(Figure 1, insert). The temperature dependence of its corresponding lifetime is displayed in Figure 1. No thermal quenching of the emission was found up to RT. At this temperature, the emitting level is $1\Gamma_5$ [2% s.s.c] and its radiative time-constant is 12 $\mu$s. The expected RT laser action involves therefore the three states $1\Gamma_1$ (ground state), $2\Gamma_5$ (absorbing state) and $1\Gamma_5$ (emitting state). This scheme is very similar to that of $Cr^{3+}$ in $Al_2O_3$.

Fluorines are well-known to be competitive lattices for laser applications because of their high chemical stability and their large electronic bandgap ($\sim 11.4$ ev for $SrF_2$). This latter property of the host insures, in our case, noticeable stability of the $Ag^+$ ions under optical pumping at 222 nm. The reason is that probably the $2\Gamma_5$ sublevel lies below the conduction band of the host, as qualitatively illustrated in Figure 2. Within this frame, direct pumping into $2\Gamma_5$ does not easily produce photoionization of the $Ag^+$ ions, followed by electron capture into some traps of the crystal (by fluorine vacancies, for instance). In this way, the so undesirable optically-induced opacity phenomenum can be avoided.

## 4   THE WORKING CONDITIONS

The last questionnable point is whether or not the $(Ag^+_{Sr}{}^{2+})^\circ$ center presents the laser effect and what are the corresponding threshold conditions. Let us consider the following experiment (currently under progress). A Fabry-Perot cavity of length L, equipped with high reflecting Al / $MgF_2$ mirrors (R1 = R2 = 0.998 = R), contains the crystal (Figure 3). If we estimate the internal losses $\gamma_i$ of this cavity at $\sim 0.05$, the total loss parameter becomes $\gamma_i = \gamma_i - Log(R) = 5.2 \ 10^{-2}$. We assume an average silver concentration in the crystal of $N_{tot} = 2.5 \ 10^{19}$ ions/cm$^3$. This corresponds to a maximum of the absorption coefficient $\alpha \sim 12$ cm$^{-1}$ at 10 K and to an oscillator strength of $\sim 10^{-3}$ in absorption.[4]

At the pumping wavelength $(\alpha_{222} = 7\ \mathrm{cm}^{-1})$, we estimate the transition cross section $\sigma_{222} = \sigma_{222}/N_{tot} = 2.7\ 10^{-19}\ \mathrm{cm}^2$. The critical population density for inversion is therefore $N_c = \gamma/d.\sigma_{222} = 9.5\ 10^{16}\ \mathrm{ions/cm}^3$. The source intensity at threshold must be
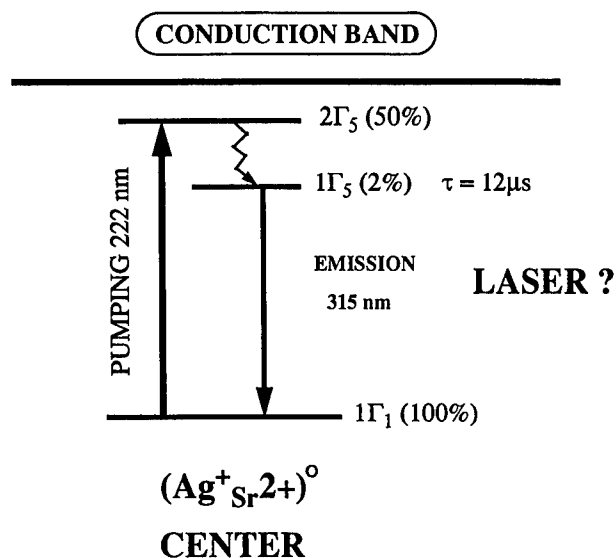


FIGURE 2   Schematic energy distribution of the 3 Ag$^+$ sublevels involved in the laser process and qualitative position of these localized levels with respect to the host conduction bands.
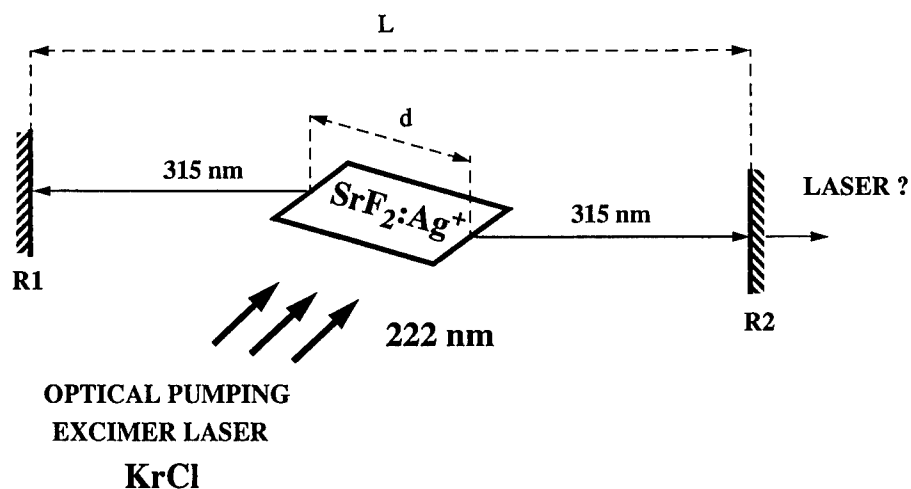


FIGURE 3   Representation of the Fabry-Perot cavity. The dimensions of the crystal plate inside this cavity are: length d = 2 cm, height = 1 cm and width = 0.5 cm, for a total volume of 1 cm$^3$. The optical pump beam of the KrCl laser is directed perpendicularly to the amplification path. Its area is 1 cm$^2$. In this geometry, 97% of the incident energy is absorbed by the crystal.

larger or equal to: $I_c = h\nu_{222}/\tau.\sigma_{222} = 2.76 \; 10^{12}$ ergs$^1$ cm$^2$ = 276 kW. This power is normally available from the excimer laser.

## 5  CONCLUSION

The strong limitation to the laser action in $SrF_2$:Ag$^+$ is the high value of $I_c$. To reduce this quantity, one should raise the value of $\tau$, i.e. decrease the value of the spin-orbit coupling constant $\lambda$ (so that the s.s.c of the emitting level $1\Gamma_5$ is diminished). One way to achieve this is to increase the crystal-field around the Ag$^+$ ions. This is for instance realized in the $CaF_2$ host, which presents the additional advantage of a larger electronic bandgap (12.2 ev) than $SrF_2$.

REFERENCES

1.  A. Monnier, P. Boutinaud and H. Bill, accepted for publication in *J. Phys. Chem. Sol.* **55**, 559 (1994).
2.  P. Boutinaud, A. Monnier and H. Bill, accepted for publication in *J. Phys. Cond. Mat.* **6**, 8931 (1994).
3.  C. Pedrini, *Phys. Stat. Sol. (b)* **87**, 273 (1978).
4.  K. Fussgaenger, W. Martienssen and H. Biltz, *Phys. Stat. Sol.* **12**, 383 (1965).

# 8 PHOTOREFRACTIVE AND NON LINEAR MATERIALS

# PHOTOREFRACTIVE CRYSTALS—THE ROLE OF DEFECTS

ECKHARD KRÄTZIG

*Universität Osnabrück, Fachbereich Physik, D-49069 Osnabrück, Federal Republic of Germany*

Defects are of crucial importance for the light-induced build-up of space charge fields in photorefractive crystals. The one-center model is explained which describes the charge transport properties of transition metal-doped $LiNbO_3$ and $LiTaO_3$ at usual cw laser intensities. One impurity center occurs in two states, e.g. Fe as $Fe^{2+}$ and $Fe^{3+}$ in $LiNbO_3$:Fe. Then we discuss the two-center model which has to be applied to other photorefractive crystals. Two interacting centers have to be taken into account, each of them occuring in two different states. Experimental observations supporting this model are presented for $BaTiO_3$ and $KNbO_3$. Furthermore, we demonstrate that the two-center model has to be used for doped $LiNbO_3$ crystals at high light intensities, too.

## 1 INTRODUCTION

Photorefractive crystals like $LiNbO_3$, $KNbO_3$ or $BaTiO_3$ offer fascinating possibilities in the fields of optical information processing, storage of holograms, laser beam manipulation or holographic interferometry.[1] Large material nonlinearities are the basis of many unique devices, among them self-pumped phase-conjugating mirrors and parametric amplifiers and oscillators. But in most cases further improvements of photorefractive properties— faster response or higher efficiency—are absolutely necessary and require detailed knowledge of the microscopic processes involved.

Photorefractive effects in these crystals are based on the transposition of a light pattern into a refractive index pattern. Under nonuniform illumination charge carriers—electrons or holes—are excited and trapped at new sites. By these means electrical space charge fields are set up which give rise to a modulation of refractive index. The trapped charge can be released and the field pattern erased by uniform illumination or by heating.

In this contribution the role of defects for photorefractive processes is examined. Defects centers are of interest, because they supply and trap charge carriers. We start with the so-called one-center model which describes the light-induced charge transport properties of transition metal-doped $LiNbO_3$ and $LiTaO_3$ at usual cw (continuous wave) laser intensities ($\leq 10^3$ $Wm^{-2}$). Then we discuss the two-center model which has to be applied to other photorefractive crystals, e.g. to ferroelectric perovskites. Experiments supporting this model are presented.

## 2 ONE-CENTER MODEL

This model allows the description of photorefractive properties of doped $LiNbO_3$ and $LiTaO_3$ at usual cw laser intensities ($\leq 10^3$ $Wm^{-2}$). The crucial influence of transition metal dopants in the crystals was discovered already very early.[2,3] Transition metal ions may occur in different valence states, making possible the generation of space charge fields. A particular role play Fe impurities which are often present in the ppm range even in undoped (nominally pure) samples. But other transition metals, e.g. Cu, Mn or Cr, cause similar effects.
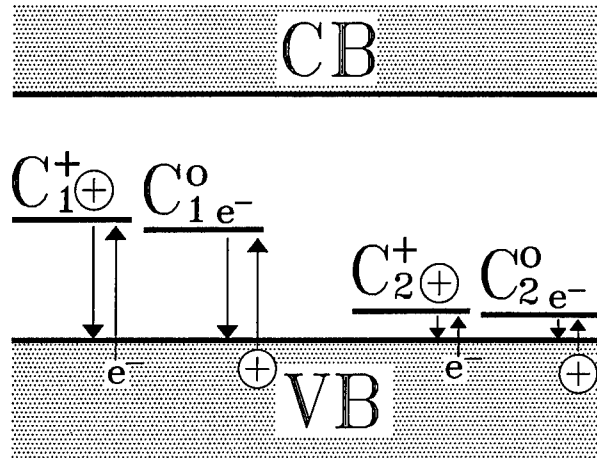
FIGURE 1   Band diagram of the two-center charge transport model (CB: conduction band, VB: valence band, $C_1$: center 1, $C_2$: center 2).

Certain valence states of transition metal ions have been identified by various methods, among them electron spin resonance, Mössbauer spectroscopy and optical absorption. In the case of Fe impurities Mössbauer spectroscopy is of special importance. Both, $Fe^{2+}$ and $Fe^{3+}$ spectra are observed,[4] thus yielding the concentration ratio $c_{Fe^{2+}}/c_{Fe^{3+}}$. These investigations also demonstrated that only $Fe^{2+}$ and $Fe^{3+}$ centers are present. The valence states of impurities in $LiNbO_3$ can be greatly influenced by suitable thermal annealing treatments.

The light-induced charge transport in doped $LiNbO_3$ is mainly determined by a photovoltaic effect[5] characteristic for pyroelectric crystals and by photoconductivity. The photovoltaic current density $\vec{J}^{pv}$ was found to depend linearly[5] on light intensity I and hence sesquilinearly[6] on the polarization (unit) vector $\vec{e}$: $j_i^{pv} = \beta_{imn}Ie_me_n^*$

For $LiNbO_3$ (point group 3m) there exist four independent nonvanishing tensor elements $\beta_{31}$, $\beta_{22}$ and $\beta_{15}$ (contracted indices). These elements are proportional to the concentration of filled traps,[7] $Fe^{2+}$ ions in the case of $LiNbO_3$:Fe. No influence of the $Fe^{3+}$ concentration or of the Li/Nb ratio is found.[8]

The photoconductivity $\sigma_{ph}$ is given by $\sigma_{ph} = Ne\mu = g\tau e\mu$, where N is the density, e the charge, $\mu$ the mobility, g the optical generation rate and $\tau$ the lifetime of excited carriers. For Fe impurity centers and electron transport one expects $g \sim Ic_{Fe^{2+}}$ and $\tau \sim 1/c_{Fe^{3+}}$, and hence $\sigma_{ph} \sim Ic_{Fe^{2+}}/c_{Fe^{3+}}$. This relation is confirmed experimentally[7,8] for light of the visible spectral region. But it should be kept in mind that these experiments were carried out at usual cw laser intensities.

Photorefractive effects may be characterized by the saturation value $\Delta n_s$ of refractive index change and the sensitivity $S = d(\Delta n)/d(It)_{|t=0}$. These quantities may be approximated by the expressions [4] $\Delta n_{so} = (1/2)n_o^3r_{13}m\beta_{31}I/\sigma_{ph}$ and $S = (1/2)n_o^3r_{13}m\beta_{31}/(\epsilon\epsilon_0)$. Here o refers to ordinary polarization, $r_{13}$ denotes the element of the electrooptic tensor, m the modulation index and $\epsilon$ the static dielectric constant.

From the above results $\beta_{31} \sim c_{Fe^{2+}}$ and $\sigma_{ph} \sim c_{Fe^{2+}}/c_{Fe^{3+}}$ we expect $S \sim c_{Fe^{2+}}$ and $\Delta n_{so} \sim c_{Fe^{3+}}$. This is again confirmed experimentally.[8] Only very strongly oxidized samples with a very small $Fe^{2+}$ concentration exhibit smaller $\Delta n_s$ values than expected[9] due to space charge field limitations by depletion of filled traps ($Fe^{2+}$ ions).
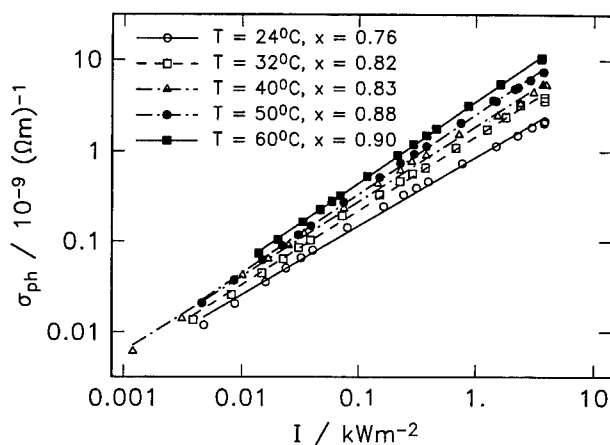
FIGURE 2   Photoconductivity $\sigma_{ph}$ of a BaTiO$_3$ sample versus light intensity I for different temperatures T. Exponents are calculated according to $\sigma_{ph} \sim I^x$.
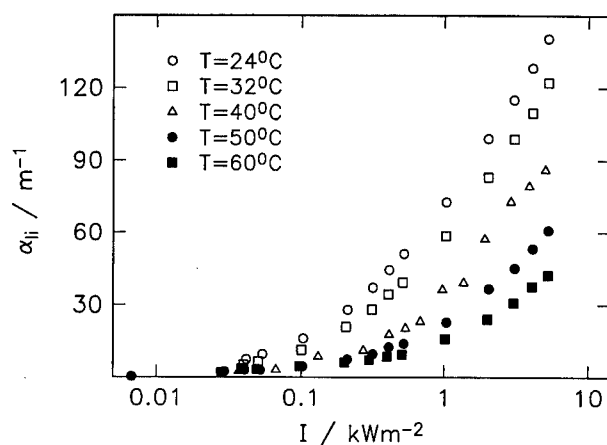


FIGURE 3   Light-induced absorption coefficient $\alpha_{li}$ of a BaTiO$_3$ sample versus light intensity I for different temperatures T.

## 3   TWO-CENTER MODEL

A very important step for the understanding of photorefractive properties of ferroelectric perovskites was the discovery of light-induced absorption in BaTiO$_3$ by Motes and Kim.[10] This increase of absorption under illumination was interpreted in terms of two kinds of centers involved,[11] each of them occuring in two different states. Holtmann[12] and later Mahgerefteh et al.[13] successfully applied this two-center model to describe the transport properties of BaTiO$_3$. Light-induced absorption was observed in KNbO$_3$, too.[14]

Because photoconductivity in ferroelectric perovskites is mostly dominated by holes in the valence band,[14,15] we assume in the following discussion of the two-center model only hole transport. With the help of Figure 1 the transport of charges may be described as

follows: We consider two different photorefractive centers $C_1$ and $C_2$. For each species $i = 1, 2$, there are hole sources and traps. We denote the concentration of sources $C_i^+$ by $N_i^+$ and the concentration of traps $C_i^0$ by $N_i^0$. The total concentration of centers of type i is $N_i = N_i^+ + N_i^0$. The first center has to be a deep-level impurity, e.g. iron, and the second one should be a more shallow trap with respect to the valence band edge. The center $C_2$ has a relatively low thermal activation energy, such that $N_2^0 \gg N_2^+$ in the dark. Upon illumination holes are generated by excitation of electrons from the valence band into $C_1^+$ centers. The holes migrate in the valence band and are trapped either by $C_1^0$ or by $C_2^0$ centers. Trapping at the latter creates $C_2^+$ centers. With increasing light intensity, more and more holes are generated and $N_2^+$ grows, too. By these means absorption processes become possible which result from optical excitations of valence band electrons to $C_2^+$ centers. This leads to light-induced absorption changes, if $C_1^+$ and $C_2^+$ have different photon absorption cross sections.

Besides the appearance of light-induced absorption the two-center model explains the nonlinear dependence of photoconductivity $\sigma_{ph}$ on light intensity.[12] The experimentally observed relationship for BaTiO$_3$ and KNbO$_3$, $\sigma_{ph} \sim I^x$ with $0.5 \leq x \leq 1$,[14,15] is confirmed by the model. Then the light-induced absorption coefficient $\alpha_{li}$ is predicted to decrease and the coefficient x to approach one with increasing temperature.[14,15] This is due to the fact that thermal excitations become more important at higher temperatures; the second center occurs essentially in the $C_2^0$ state and the transport properties are mainly determined by center $C_1$ (one-center model). These predictions are also verified experimentally as illustrated by the Figures 2 and 3 for BaTiO$_3$.[15] When a suitable set of parameters is chosen, the two-center model describes the intensity dependences of $\sigma_{ph}$ and $\alpha_{li}$ rather well. For the thermal activation energies $E_1$ and $E_2$ of the centers $C_1$ and $C_2$ the values $E_1 = 1.04$ eV and $E_2 = 0.74$ eV[15] were obtained for a BaTiO$_3$ sample and $E_2 = 0.8$ eV for a KNbO$_3$ sample.[14] At very high intensities, experimentally realized by frequency-doubled pulses of a Q-switched Nd:YAG laser, additional states with a activation energies of 0.5 eV (BaTiO$_3$) and 0.35 eV (KNbO$_3$) become involved.[16]

Recently, further experimental support for the two-center model was discovered: Activation for infrared (IR) recording[17] and dark build-up of holograms after recording.[18] When a BaTiO$_3$ crystal is illuminated homogeneously with a green light pulse, subsequent recording of a holographic grating with IR pulses is possible. After illumination with a green pulse empty shallow traps $C_2^+$ exist. Then IR recording is based on excitations of electrons from the valence band to empty shallow traps $C_2^+$. The generated holes migrate and capture electrons of deep-level impurities $C_1^0$. Thus the light pattern is transposed to a space charge pattern according to the population of deep-level impurities $C_1$. Still existing empty shallow traps $C_2^+$ are filled by electrons due to thermal excitations. The remaining grating can be read nondestructively with IR light and erased by illumination with green light.

Holograms recorded under suitable conditions in BaTiO$_3$ exhibit an unusual dark build-up.[18] The diffraction efficiency increases by some orders of magnitude after the recording beams are switched off, and then steadily decreases afterwards. The two-center model enables an explanation: Two mutually $\pi$-shifted gratings are recorded. They result from modulation of deep traps $C_1$ and shallow traps $C_2$, respectively. Both gratings largely compensate each other. In the dark, however, after switching-off illumination, the grating in the shallow traps $C_2$ relaxes faster than the grating in the deep traps $C_1$ and therefore holographic diffraction increases. Model calculations yield perfect agreement with the experimental results.

Already rather early several authors described considerable deviations from the one-center model for LiNbO$_3$ crystals, too, if high light intensities ($\gg 10^3$ Wm$^{-2}$) are

used.[19,20] A detailed investigation of $LiNbO_3$:Fe with frequency-doubled pulses of a Q-switched Nd:YAG laser demonstrates additional contributions to the charge transport properties[21] pointing to a two-center model.[22] Light-induced absorption measurements of these crystals and of samples additionally doped with Mg or Zn reveal that besides deep $Fe^{2+/3+}$ centers also $Nb_{Li}$ polarons ($Nb^{4+/5+}$ ions on $Li^+$ site) are involved.[23]

## 4  SUMMARY AND CONCLUSIONS

Defect centers are of particular interest for photorefractive processes. Usually the host crystals are transparent in the visible or near IR range. For transition metal-doped $LiNbO_3$ crystals a one-center model is sufficient to describe light-induced properties at usual cw laser intensities, e.g. in the case of $LiNbO_3$:Fe electrons are transfered from $Fe^{2+}$ to $Fe^{3+}$ ions. But for ferroelectric perovskites—which are much more attractive for many photorefractive applications—at least two interacting centers have to be taken into account, each of them occuring in two different states. Light-induced absorption and a nonlinear dependence of photoconductivity on light intensity are typical consequences of this two-center model which is now well established by many experimental observations. The two-center model also determines light-induced properties of $LiNbO_3$ crystals at high intensities. Here the second centers have been identified as $Nb_{Li}$ polarons.

REFERENCES

1. P. Günter, J. P. Huignard, *Photorefractive Materials and Their Applications I and II*, Topics in Applied Physics, Vols 61 and 62, Springer Verlag, 1989.
2. G. E. Peterson, A. M. Glass, T. J. Negran, *Appl. Phys. Lett.* **19**, 130 (1971).
3. J. J. Amodei, W. Phillips, D. L. Staebler, *Appl. Opt.* **11**, 390 (1972).
4. H. Kurz, E. Krätzig, W. Keune, H. Engelmann, U. Gonser, B. Dischler, A. Räuber, *Appl. Phys.* **12**, 355 (1977).
5. A. M. Glass, D. von der Linde, T. J. Negran, *Appl. Phys. Lett.* **25**, 233 (1974).
6. V. I. Belinicher, V. K. Malinowski, B. I. Sturman, *Sov. Phys. JETP* **46**, 362 (1977).
7. E. Krätzig, *Ferroelectrics* **21**, 635 (1978).
8. R. Sommerfeldt, B. C. Grabmaier, L. Holtmann, E. Krätzig, *Ferroelectrics* **92**, 219 (1989).
9. R. A. Rupp, R. Sommerfeldt, K. H. Ringhofer, E. Krätzig, *Appl. Phys.* **B51**, 364 (1990).
10. A. Motes, J. J. Kim, *J. Opt. Soc. Am.* **B4**, 1379 (1987).
11. G. A. Brost, R. A. Motes, J. R. Rotgé, *J. Opt. Soc. Am.* **B5**, 1879 (1988).
12. L. Holtmann, *phys. stat. sol. (a)* **113**, K89 (1989).
13. D. Mahgerefteh, J. Feinberg, *Phys. Rev. Lett.* **64**, 2195 (1990).
14. L. Holtmann, K. Buse, G. Kuper, A. Groll, H. Hesse, E. Krätzig, *Appl. Phys.* **A53**, 81 (1991).
15. L. Holtmann, M. Unland, E. Krätzig, G. Godefroy, *Appl. Phys.* **A51**, 13 (1990).
16. K. Buse, E. Krätzig, *Optical Materials* **1**, 165 (1992).
17. K. Buse, L. Holtmann, E. Krätzig, *Optics Commun.* **85**, 183 (1991).
18. K. Buse, J. Freijlich, G. Kuper, E. Krätzig, *Applied Physics* **A57**, 437 (1993).
19. Che-Tsung Chen, Dae M. Kim, D. von der Linde, *Appl. Phys. Lett.* **34**, 321 (1979).
20. P. A. Augustov, K. K. Shvarts, *Appl. Phys.* **21**, 191 (1980).
21. F. Jermann, E. Krätzig, *Applied Physics* **A55**, 114 (1992).
22. F. Jermann, J. Otten, *J. Opt. Soc. Am.* **B10**, 2085 (1993).
23. M. Simon, F. Jermann, E. Krätzig, *Optical Materials*, **3**, 243 (1994).

# HYDROGEN DEFECTS IN LiNbO₃ AND APPLICATIONS

## J. M. CABRERA

*Dpto. Físcia de Materiales C–IV, Universidad Autónoma de Madrid, Canto Blanco, Madrid E–28049, Spain*

This paper presents a brief review on the general properties of OH⁻ molecular ions in the LiNbO₃ lattice: defect production, defect characterization, microscopic model and proton transport. The central role played by this hydrogen defect in two major applications of LiNbO₃ is also discussed. One is the formation of optical waveguides by the method of proton exchange: the exchange and reverse exchange processes, the structure of exchanged layers, and relevant integrated optics devices. The other one is fixing of photorefractive volume holograms: fixing model based on proton migration, determination of material parameters and the application to a very narrow-bandwidth Bragg-reflector. By considering these subjects together, a wider perspective on the role and relevance of hydrogen in LiNbO₃ is gained.

## 1 GENERAL PROPERTIES OF OH⁻ IONS

### 1.1 *Hydrogen Doping*

Hydrogen is present in as-grown 'nominally' pure LiNbO₃ crystals in concentrations ranging from $10^{18}$ cm$^{-3}$ to $10^{19}$ cm$^{-3}$. It comes from either the starting chemical powders or the crystal growth process. Hydrogen can also be introduced into the lattice by after-growth annealing treatments in hydrogen or water vapor rich atmospheres at temperatures ranging typically from 600°C to 1000°C. Usually, water vapor atmosphere is preferred because it produces clear transparent (well oxidized) crystals. A different approach to introduce hydrogen in LiNbO₃ is the proton exchange process, discussed below, which produces a few micron thick layer with a high OH⁻ concentration ($\sim 10^{22}$ cm$^{-3}$). Protons have also been introduced in LiNbO₃ by high energy H⁺ implantation. Deuterium isotope doping has been carried out by similar procedures to those mentioned above for hydrogen. Tritium isotope has been produced in the LiNbO₃ lattice by transmutation of the $^6_3$Li nucleus via a reaction using thermal neutrons: $^6_3\text{Li} + ^1_0n \rightarrow ^3_1\text{T} + ^4_2\text{He}$.

### 1.2 *OH⁻ Microscopic Model*

A number of techniques have been used to characterize OH⁻ defects in LiNbO₃: infrared absorption, thermally or electrically assisted proton diffusion, dark conductivity, photorefractive fixing, nuclear magnetic resonance (NMR), secondary ion mass spectrometry (SIMS), ion beam methods (NRA, ERD) and others. Particularly, the infrared absorption band associated to the stretching vibration, reviewed by *Kovács and Fölválri*,[1] has proved very useful. The band is strongly polarized perpendicular to the ferroelectric c-axis, what implies that the direction of the OH⁻ bond is essentially perpendicular to that axis, i.e. lying on the oxygen plane. The band also exhibits a complex structure in congruent crystals, which is interpreted in terms of several slightly non equivalent lattice positions. By varying the Li/Nb ratio or doping of the crystals, changes in the band shape

or position have been observed. Additional changes appear in proton exchanged and proton implanted waveguides, the shift being attributed to the structural changes induced in the guiding layer by these rather aggressive processes.

The model proposed to explain the $OH^-$ infrared absorption data[2,3,4] assume that the O–H bond is directed toward one of the six nearest $O^{2-}$ ions lying on the oxygen plane perpendicular to the c-axis of the crystal. The structure of the absorption band is attributed to the three different O–O bond lengths occurring in the $LiNbO_3$ lattice. The different cation environments induce slightly different vibration frequencies for the stretching bond. Changes in the peak positions in doped crystals are attributed to the local environment in the complexes formed by the $OH^-$ molecule and the impurity.

The spectroscopy of higher vibrational states of the $OH^-$-molecule[5] closely follows the one expected from a single well Morse potential with $r_0 = 0.096$ nm. This strongly suggests a negligible contribution from hydrogen bridge bond (double well). Ion beam channeling methods in PE-guides[6] have confirmed the $r_0$ value, showing that protons lie only 0.2 Å below the oxygen plane. These experiments clearly rule out either Li or Nb substitutional positions for protons.

### 1.3 Transport Properties of Protons

By comparing $OH^-$ and $OD^-$ conductivity measurements it has been[7] found that proton/deuteron is the moving ion up to about 600°C. On the other hand, Schmidt et al.[8] have proved that protons/deuterons are the only ionic entities migrating at a temperature of 600°C, $Li^+$ contribution being negligible. Unfortunately, even when electronic and other ionic contributions can be disregarded, values of transport parameters for proton migration are considerably scattered depending on authors and methods, as reviewed by Kovács and Polgár,[9] and range from 0.9 eV to 1.8 eV for the activation energy, and 8 $cm^2/s$ to 0.01 $cm^2/s$ for the diffusion coefficient. This is partially due to the dependence of the activation energy and diffusion coefficient values on doping and stoichiometry of samples.

## 2 PROTON-EXCHANGED WAVEGUIDES

### 2.1 The Proton Exchange Process

The formation of optical waveguides by proton exchange on a $LiNbO_3$ substrate is performed by immersion in a variety of hot acid melts, in order to induce a lithium-proton exchange. The $H^+ \leftrightarrow Li^+$ exchange can range between 0.03% and 85% and gives rise to an increase of the extraordinary refractive index of about 0.12, responsible for the waveguiding, and a decrease of the ordinary index of about 0.04. Melt temperatures can range from 150°C to 470°C, and immersion times are between 5 min. and several days depending on the temperature, melt composition and substrate material used, as well as on the final desired exchange depth. An authoritative review of the subject up to 1991 has been given by Jackel.[10]

### 2.2 Structure of Exchanged Layers

The exchanged layer material can be described as $Li_{1-x}H_xNbO_3$, with $x$ indicating the fraction of lithium exchanged. It is generally considered that during the process a one-for-one exchange takes place[11] in a similar way as ion exchange in glasses. Direct proves of structural changes in the exchanged layer are provided by the finding of several phase

changes by transmission electron microscopy,[12] and the time evolution of just-exchanged layers.[11,13] Reports on rocking curve studies indicate that the exchanged layer is slightly biaxial and the biaxiality increases with the melt acidity.[14] On the other hand, a strong oxidation of $Fe^{2+}$ ions to $Fe^{3+}$ ions has been found in the exchanged layer with respect to the substrate.[15] This valence change should be a major contribution to the strong reduction of the optical damage measured in PE-guides.[16,17]

### 2.3 *Refractive Index Profiles*

Proton exchange induces characteristic index profiles on LiNbO₃ substrates with step-like forms, with $\Delta n_e \sim +0.12$, and $\Delta n_o \sim -0.04$.[18] Thus, a light beam with extraordinary polarization can be confined in the exchanged layer and the structure can guide a number of modes. As pointed out by Jackel,[10] the step-like index profile induced by proton exchange cannot be explained using any simple diffusion model. Although details of the diffusion process and of the index dependence on concentration are not yet well known, there is evidence that these processes are highly nonlinear. Several proposals to explain the index change seem not satisfactory, although a major factor to take into account is the structural change present in the exchanged layer.

### 2.4 *Reverse Exchange*

The exchange produced in a PE-LiNbO₃ substrate can be reversed by immersing the sample in a lithium rich melt. Most protons go out of the layer as monitored by the $OH^-$ infrared absorption,[19] and $Li^+$ ions are assumed to enter the lattice, giving rise to a reverse exchange. By performing a long reverse exchange on a deep PE-guide, a 1 to 4 μm thick surface layer is produced with its ordinary index greater than that of the remainder (about 5 μm thick) PE-guide. The buried PE-guide acts as barrier for ordinary polarized light, and modes with this polarization can be guided.[20] Measured losses for ordinary modes give values under 0.7 dB/cm.

### 2.5 *Relevant Devices with PE-Waveguides*

PE-guides have proved particularly efficent for SHG of blue-green light by 'quasi-phase-matching' using periodic poling inversion during the PE-process.[21] Advantage is taken of the tight confinement produced by the high index change, facilitating the efficiency of the nonlinear interaction, and of a much lower sensitivity to optical damage. Efficient operation of CW and mode-locked lasers has also been demonstrated in PE-guides on Nd-MgO-LiNbO₃ substrates,[22,23] including the integration of an electrooptic phase modulator. Q-switch laser operation has also been demonstrated on the same substrate by integrating an electrooptic directional coupler.[24]

## 3   PHOTOREFRACTIVE FIXING

### 3.1 *The Fixing Process in LiNbO₃*

An important feature of photorefractive volume holograms recorded in LiNbO₃ is the possibility of transforming them into permanent holograms by means of the *fixing* process. It consists of converting the light-erasable trapped charge pattern into a fixed (light-insensitive) matched pattern. Protons are mobile in LiNbO₃ at quite low temperatures (above 60°C), whilst trapped electrons are stable from room temperature up to about

180°C in non-reduced $LiNbO_3$. Between these two temperatures (typically $\sim 150$°C), protons can migrate without noticeable electron detrapping, driven by the space charge field created by trapped electrons. Proton migration proceeds till the space charge field is compensated. Thus, a *fixed* pattern of protonic charge, matching the initial electron/light pattern, is produced. At room temperature, the proton pattern can be further *developed* by homogeneous illumination, which removes part of the trapped electrons and leaves the protonic pattern partially uncompensated. Further illumination during reading does not at all erase the fixed-developed pattern.

## 3.2 *Material Parameters*

Some important material parameters can be determined by designing appropriate fixing experiments. One measurement of special relevance has been the determination of the absolute value of the proton concentration[25] from which the cross section for the $OH^-$ absorption has been obtained, $\sigma_{OH} = (9.4 \pm 1.6) \times 10^{-20}$ cm$^2$, which compares well with values obtained by other methods.[7] The method is based on the model developed by Carrascosa and Agulló-López,[26] and is particularly suited for the absolute measurement of very low proton concentrations, where the other methods are not applicable. The diffusion coefficient and the activation energy for proton migration have also been obtained from fixing kinetic experiments, although the temperature range where fixing models can be applied is rather limited, $120-250$°C.[27,28,29] As is the case with dark conductivity and thermally induced diffusion experiments, measured values are scattered within a wide range.

## 3.3 *Very Narrow-Bandwidth Interference Filters*

Fixing in $LiNbO_3$ has recently succeeded in producing the first commercial application of any photorefractive device: a very narrow-bandwidth interference filter. The device works as a Bragg reflector made of a photorefractive volume grating recorded, fixed and developed in a $LiNbO_3$ crystal. It has been independently reported by two groups,[30, 31] and is being commercialized by *Accuwave Corporation* (California). The device consists of a few millimeter thick $Fe:LiNbO_3$ plate on which a photorefractive grating has been previously fixed. For a typical wavelength of 514.5 nm, the following performances are achieved: a bandwidth (FWHM) under 10 pm with peak reflectivity above 50% and an angular field of view of about 6°. These performances, then, compare well with those exhibited by polarization interference filters (Lyot-Ohman and Solc filters). Additionally, the photorefractive filter can be finely tuned either thermally or electrically.[32] Protons play a central role in the fabrication process and, obviously, the success has partially been possible because of the cumulated knowledge on the $OH^-$ properties in $LiNbO_3$.

REFERENCES

1. L. Kovács, I. Földvári, in *Properties of Lithium Niobate*, EMIS Datareview Series No. 5, p. 189, RN-16018 (1989).
2. L. Kovács, V. Szalay, R. Capelletti, *Sol. St. Commun.* **52**, 1029 (1984).
3. L. Kovács, Zs. Szaller, I. Cravero, I. Földvári, C. Zaldo, *J. Phys. Chem. Solids* **51**, 417 (1990).

4. L. Kovács, M. Wöhlecke, A. Jovanovic, K. Polgár, S. Kapphan, *J. Phys. Chem. Sol.* **52**, 797 (1991).
5. A. Gröne, S. Kapphan, *Ferroelectrics* **125**, 307 (1992).
6. J. Olivares, J. M. Cabrera, F. Agulló-López, L. Rebouta, M. F. da Silva, J. C. Soares, *Proc. 6th Europ. Conf. Integr. Optics* **9–14**, Neuchotel (1993).
7. S. Klauer, M. Wöhlecke, S. Kapphan, *Phys. Rev.* **B45**, 2786 (1992).
8. N. Schmidt, K. Betzler, M. Grabs, S. Kapphan, F. Klose, *J. Appl. Phys.* **65**, 1253 (1989).
9. L. Kovács, K. Polgár, in *Properties of Lithium Niobate*, EMIS Datareview Series No. 5, p. 109, RN-16037 (1989).
10. J. L. Jackel, *Integrated Optical Circuits*, SPIE Vol. **1583**, 54 (1991).
11. G. W. Arnold, A. Carnera, G. Mazzi, P. Mazzoldi, *Mat. Res. Soc. Symp. Proc.* **101**, 453 (1988).
12. W. E. Lee, N. A. Sanford, A. H. Heuer, *J. Appl. Phys.* **59**, 2629 (1986).
13. A. Yi-Yan, J. Primot, J. Burgeat, R. Gugliemi, *Second European Conf. on Integrated Optics, Florence*, Post-Deadline Papers 17–18. October (1983).
14. V. A. Ganshin, Yu. N. Korkishko, *J. Opt. Commun.* **13**, 2 (1992).
15. J. Olivares, E. Diéguez, F. J. López, J. M. Cabrera, *Appl. Phys. Lett.* **61**(6), 624 (1992).
16. J. L. Jackel, Electronics Letters 21, 509 (1985).
17. E. Glavas, J. M. Cabrera, P. D. Townsend, *J. Phys.: Appl. Phys.* **D22**, 611 (1989).
18. J. Olivares, M. A. Díaz-García, J. M. Cabrera, *Opt. Commun.* **92**, 40 (1992).
19. J. Olivares, J. M. Cabrera, *Fib. Integ. Opt.* **12**, 277 (1993).
20. J. Olivares, J. M. Cabrera, *Appl. Phys. Lett.* **62**, 2468 (1993).
21. J. Webjörn, F. Laurell, G. Arvidsson, *J. Lightwave Techn.* **7**, 1597 (1989).
22. E. Lallier, J. P. Pocholle, M. Papuchon, C. Grezes-Besset, E. Pelletier, M. De Micheli, M. J. Li, Q. He, D. B. Ostrowsky, *Electron. Lett.* **26**(13), 927 (1990).
23. E. Lallier, J. P. Pocholle, M. Papuchon, C. Grezes-Besset, E. Pelletier, M. De Micheli, Q. He, D. B. Ostrowsky, *Electron. Lett.* **27**, 11 (1991).
24. E. Lallier, J. P. Pocholle, M. Papuchon, Q. He, M. De Micheli, D. B. Ostrowsky, *Technical Digest of GRIN'92 (Tenth Topical Meeting on Gradient-Index Optical Systems)* **T2.6**, p. 64 (1992).
25. R. Müller, L. Arizmendi, M. Carrascosa, J. M. Cabrera, *Appl. Phys. Lett.* **60**, 3212 (1992).
26. M. Carrascosa, F. Agulló-López, *J. Opt. Soc. Am.* **B7**, 2317 (1990).
27. L. Arizmendi, P. D. Townsend, M. Carrascosa, J. A. Baquedano, and J. M. Cabrera, *J. Phys.: Condens. Matter* 3, 5399 (1991).
28. R. Müller, M. Carrascosa, L. Arizmendi, J. M. Cabrera, submmitted to *J. Appl. Phys.*
29. M. Carrascosa, L. Arizmendi, *J. Appl. Phys.* **73**, 2709 (1993).
30. G. A. Rakuljic, V. Leyva, *Optics Lett.* **18**, 459 (1993).
31. R. Müller, M. T. Santos, L. Arizmendi, J. M. Cabrera, *J. Phys. D: Appl. Phys.*, **27**, 241 (1994).
32. R. Müller, J. V. Alvarez-Bravo, L. Arizmendi, J. M. Cabrera, *J. Phys. D: Appl. Phys.*, in press (1994).

# LUMINICENCE AND OPTICAL SECOND HARMONIC GENERATION BY DIPOLAR MICROREGIONS IN KTaO₃

C. FISCHER, C. AUF DER HORST, P. VOIGT, S. KAPPHAN and J. ZHAO*

*University of Osnabrück, FB Physik, 49069 Osnabrück, Germany*
*\*NW Polytechnical University, Appl. Physics, Xi'an 710072, China*

The incipient ferroelectric $KTaO_3$ being cubic down to lowest temperatures, is not expected to yield second harmonic intensity (SHG) due to the inversion symmetry of the lattice. Nevertheless a weak SHG intensity of Nd:YAG laser light is observed, which increases with decreasing temperature. This low temperature SHG is drastically enhanced in $KTaO_3$ samples which have been reduced at 1000°C in $H_2$-atmosphere. Simultaneously the luminescence intensity observed at low temperature (T = 80 K) with an emission at $\lambda_{max} = 520$ nm is increasing strongly upon reduction as well. This increase is not only due to a thin reduced surface layer, but rather uniform throughout the volume of the sample crystal. Oxidation at 1000°C in pure $O_2$-atmosphere diminishes both, the low temperature SHG- and the luminescence intensity, far below the values of the pure, 'as-grown' crystal. Sharp luminescence features reported to be at $\lambda = 687$ nm in the literature and assigned to $Ta^{3+}$ near oxygen vacancies, have not been observed in our crystals, neither in the as-grown, nor in the reduced or oxidized samples. The interpretation is based upon dipolar microregion around a defect core due to oxygen vacancy complexes, locally breaking the inversion symmetry.

*Key words*: Incipient ferroelectric, $KTaO_3$, second harmonic generation, luminescence, defect induced microregions, oxygen vacancies.

## 1  INTRODUCTION

The incipient ferroelectric $KTaO_3$ is a dielectric with a cubic perovskite structure even at low temperature. However the temperature dependence of the soft mode frequency and the inverse static dielectric constant show a behaviour as if a phase transition could be approached, but with zero-point dipolar fluctuations suppressing long-range ferroelectric order down to lowest temperatures.[1,2] Recently for the parallel case of the incipient ferroelectric $SrTiO_3$ at temperatures < 30 K new experimental evidence was presented, which led to the proposal of a coherent quantum paraelectric state.[3] On the other hand, for $KTaO_3$ there are several experimental results from SHG,[4,5] Raman-[6] and Hyper-Raman[7,8] scattering, which show that deviations from cubic symmetry do exist in microregions at low temperatures. Theoretical models have been proposed trying to explain these effects in terms of dynamic fluctuations and of defects locally breaking the inversion symmetry, thereby inducing dipolar microregions which increase with decreasing temperature proportional to the inverse of the soft mode frequency.[4]

From Raman- and fluorescence measurements exhibiting a sharp zero-phonon like emission near 687 nm, it was suggested that $Ta^{3+}$ near oxygen vacancies should be the origin of ferroelectric microregions.[9,10,11] However a comparative study[12] of crystals from different laboratories did show that there is no correlation between this luminescence at 687 nm and several other quantities like first-order Raman intensity, hyper-Rayleigh or hyper-Raman intensity etc. Moreover, some crystals did show no 687 nm intensity at all, while others vary in the amount of the sharp luminescence feature, pointing to an impurity defect source as the origin. Common for all crystals is a broadband, previously reported photoluminescence with maximum at about 520 nm under excitation with band-gap (about 3.5 eV) light.[13]

C. FISCHER *ET AL.*
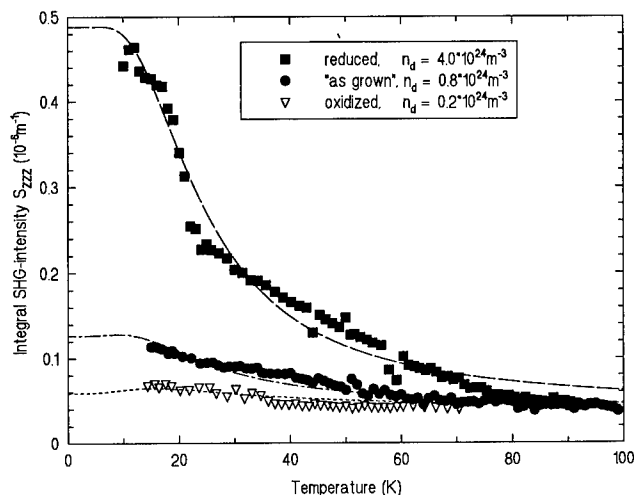


FIGURE 1  Integral SHG-Intensity $S_{zzz}$ (calibrated with respect ot $LiNbO_3$) as a function of temperature for the three $KTaO_3$ samples indicated. The lines are based on a model of Prusseit-Elffroth and Schwabl[4] for an effective dipolar off-center displacement $u_d = 0.5$ Å.

The generation of second harmonic light by an intensive laser source (Nd:YAG) is known to be a sensitive way to detect regions of broken inversion symmetry. Due to the third rank tensor characteristics and the coherence properties of the SHG-process this sensitivity extends to the discrimination of up and down dipolar regions. In applications this sensitivity to periodically antiparallel ferroelectric domains is used in the 'quasi-phase matching' method.[14,15]

Here we report about an investigation of as-grown, of oxidized and of reduced samples of nominally pure $KTaO_3$ crystals, correlating the results of SHG- and of luminescence techniques to cast new light on the properties of inversion breaking defects at low temperature.

## 2  EXPERIMENTAL TECHNIQUE

The $KTaO_3$ crystals have been grown in the crystal growth laboratory at the University of Osnabrück by H. Hesse. The very pure starting materials are $Ta_2O_5$ (Fa. Starck, Berlin, chlorine process) and $K_2CO_3$ or $KNO_3$ (Fa. Merck, optipur). The samples were cut into blocks of typically a few mm length with {100} surfaces.

The experimental setup for the SHG experiments with a Nd:YAG laser has been described in.[16] All the forward emitted, frequency-doubled intensity in a 30° cone is collected (integral SHG-intensity) and focussed by a lens to the photomultiplier. The luminescence experiments are performed with a conventional 90° excitation setup using an XBO light source (450 W), SPEX 1500 SP monochromator and RCA-C31034 GaAs-Photomultiplier. The oxidation or reduction of some of the samples was done in $O_2$- or $H_2$-atomsphere at 1000°C for several hours (up to 200 h). The reduced crystals remained clear, colorless and completely transparent as before the reduction treatment (respectively as
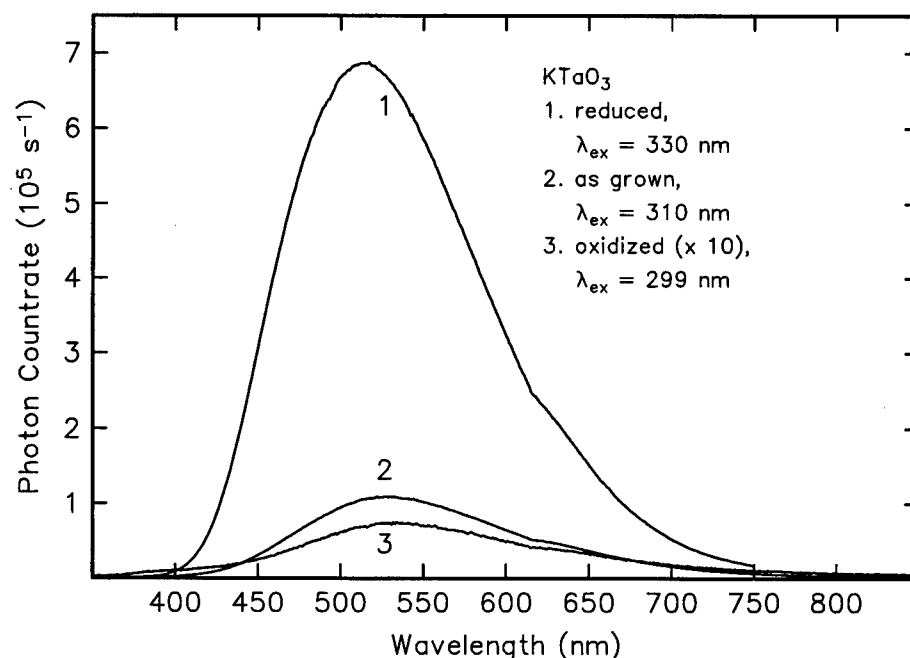
FIGURE 2 Luminescence spectra of KTaO$_3$ (same samples as in Figure 1) at T = 80 K under illumination with constant light intensity at the maxima of the excitation spectra. Values of the oxidized sample have been multiplied by a factor of ten.

grown or in the oxidized state). However the ac and dc conductivity did increase considerably (several orders of magnitude at room temperature) upon reduction.

## 3 EXPERIMENTAL RESULTS AND DISCUSSION

Figure 1 shows the increase of the SHG intensity (calibrated with respect to LiNbO$_3$) at low temperature of three samples cut from the same boule and treated as indicated. The reduced crystals show a strong increase of the low temperature SHG intensity, whereas the SHG intensity in the oxidized samples is considerably smaller compared with the as-grown crystal. This indicates an increase of concentration of inversion symmetry breaking defects upon reduction of the crystals. The values of the concentration of defects given in the insert has been gained using a theoretical model of Prusseit-Elffroth and Schwabl[4] under the assumption of an effective dipolar displacement $u_d = 0.5$Å and similar fitting parameters as described in ref.[16]

The luminescence under band edge illumination of the same samples (as in Figure 1) is shown in Figure 2. It shows that the luminescence yield is increasing upon reduction and is diminishing upon oxidation, compared to the as-grown crystal values. Absorption measurements and the excitation spectra (Figure 3) show that the band edge is slightly shifted in the reduced KTaO$_3$ crystals. To compare the luminescence yield, the samples are illuminated with the same light intensity in the respective maxima of the excitation spectra. Sharp emission features at $\lambda = 687$ nm reported in the literature[9,10,11] were not observed
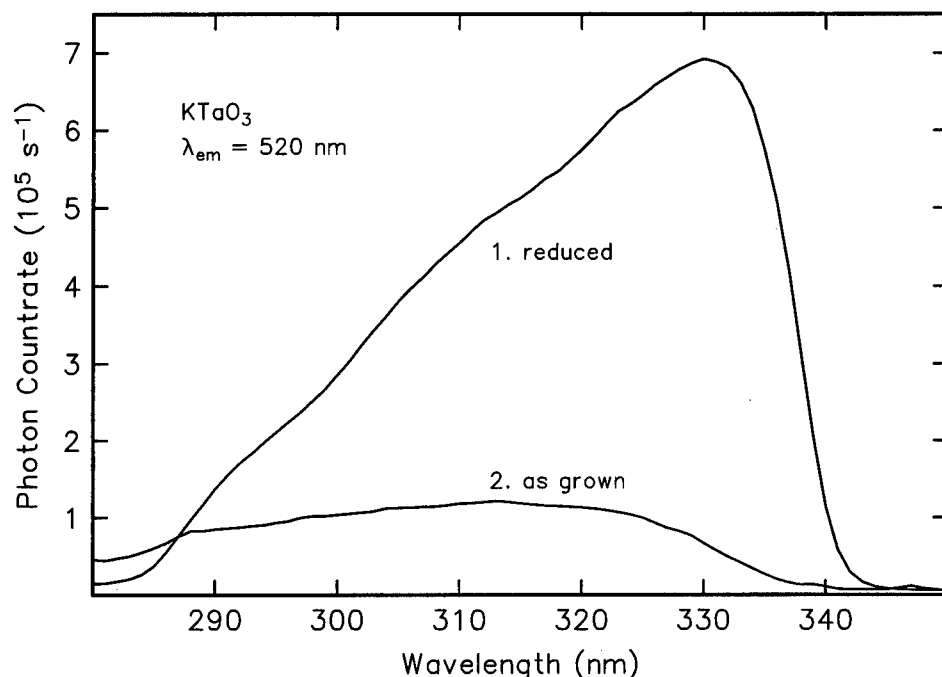
FIGURE 3   Excitation spectra of the KTaO₃ luminescence (at 520 nm) for T = 80 K: a) after reduction (2 h at 1000°C in H₂-atmosphere), b) as-grown.

in our samples in agreement with a recent comparative study.[12] Not even the highest reduced samples did show any of these sharp features near $\lambda = 687$ nm, which makes the assignment of these sharp features to $Ta^{3+}$ near oxygen vacancies as the origin of this luminescence and also of the symmetry breaking defects giving rise to microdomains even more doubtful.

To check whether the reduction of the samples was achieved homogeneously throughout the crystal or only in a thin surface layer a crystal sample was polished thinner in successive steps and the luminescence intensity was recorded under identical conditions. It turned out that samples reduced to 2 h in H₂-atmosphere at 1000°C reveal a constant luminescence intensity throughout the volume of the crystal.

A quantitative comparison of the increase in reduced samples (relative to as-grown or oxidized samples) of the luminescence yield ($\lambda_{max} = 520$ nm) and of the low temperature SHG intensity yields similar factors, supporting the assumption that both quantities are connected with the same defect centers. ESR experiments to clarify the question whether a $Ta^{3+}$ or a $Ta^{4+}$ together with oxygen vacancies or some extrinsic defects are involved, are presently under way and will be reported elsewhere.

ACKNOWLEDGEMENTS

REFERENCES

1.  C. H. Perry and T. F. McNelly, *Phys. Rev.* **154**, 456 (1967).
2.  S. H. Wemple, *Phys. Rev.* **137**, A1575 (1965).
3.  K. A. Müller, W. Berlinger, and E. Tosatti, *Z. Phys.* **B84**, 277 (1991).
4.  W. Prusseit-Elffroth and F. Schwabl, *Appl. Phys.* **A51**, 361 (1990).
5.  P. Voigt and S. Kapphan, In O. Kanert and J.-M. Spaeth, Ed., *Proceed. ICDIM, Nordkirchen 1992*, **2**, 691, World Scientific, Singapore (1993).
6.  H. Uwe, K. B. Lyons, H. L. Carter, and P. A. Fleury, *Phys. Rev.* **B33**, 6436 (1986).
7.  H. Vogt, *Ferroelectrics* **125**, 313 (1992).
8.  H. Vogt, *Phys. Rev.* **B41**, 1184 (1990).
9.  P. Grenier, G. Bernier, S. Jandl, B. Salce, and L. A. Boatner, *J. Phys.: Cond. Matter* **1**, 2515 (1989).
10. S. Jandl, P. Grenier, and L. A. Boatner, *Ferroelectrics* **107**, 73 (1990).
11. S. Jandl, M. Banville, P. Dufour, S. Coulombe, and L. A. Boatner, *Phys. Rev.* **B43**, 7555 (1991).
12. H. Vogt, *J. Phys.: Cond. Matter* **3**, 3697 (1991).
13. E. Yamaichi, K. Watanabe, and K. Ohi, *J. Phys. Soc. Jap.* **57**, 2201 (1988).
14. R. C. Miller, *Phys. Rev.* **134**, A1313 (1964).
15. G. A. Magel, M. M. Fejer, and R. L. Byer, *Appl. Phys. Lett.* **56**, 108 (1990).
16. P. Voigt and S. Kapphan, *J. Phys. Chem. Solids*, **55**, 853 (1994).

# NON-LINEAR AND FRACTAL DYNAMIC PROCESSES IN SUPERIONICS

A. E. UKSHE and N. G. BUKUN

*Institute of Chemical Physics, Chernogolovka, Moscow region 142432 Russia*

The relaxation in superionic conductor near electrode interface has been considered with computer simulation method. Specific effects have been explained in the terms of fractal nature of ion transport in the systems of conducting channels.

   Our results and also the analogy with the diffusion front in percolation theory and the fractal geometry approach allow us to propose the explanation for the described non-linear effects.

## 1 INTRODUCTION

In this work we consider relaxation in solid-state system of:

electrode | superionic conductor | electrode

Superionic conductors are the solids with a subsystem of channels wherein usually one type of ions can move. The mobility of ions in superionics approaches that in liquid electrolytes. A specific feature of our approach to the problem is that we explain certain effects that are observed in such system in the terms of fractal nature of ion transport in the system of conducting channels and formation of dynamic fractal structures adjacent the electrode where the charge accumulates.

   During investigation the relaxation properties of the system of superionic—electron conductor interface there is observed unusual and sometimes unexplainable relaxation behavior.

## 2 SLOW RELAXATION

An electrical double layer establishes at the superionic—electron conductor interface. Owing to its small thickness (on the order of the lattice constant) this double layer has a high electric capacity. Therefore, an exponential charging-discharging relaxation process should exist for this capacity. The direct measurements of the impedance of superionic heterojunction in alternating current, however, reveal additionally to the charging of the capacity of the double layer a slow relaxation process that has a square-root dependence on time. This effect was observed for electrochemical systems which are described with the following equivalent electrical circuit (Figure 1) where

$$Z_w = W/\sqrt{j\omega} \tag{1}$$

is the Warburg impedance. A hypothesis was proposed in[1] that $R_a$, $C_a$, $Z_w$ in the equivalent circuit appear due to diffusive transfer of minor charge carriers of the superionic followed by their adsorption. The diffusion equation in the case of harmonic perturbation results in (1).[1,2] And the third feature is the appearance in the equivalent circuit of a constant phase angle element (CPA)

$$C_{dl}$$

$$R_b \quad R_F$$

(1)

$$C_a \quad R_a \quad Z_W$$



$$C_{dl}$$

$$R_b \quad R_F$$

(2)
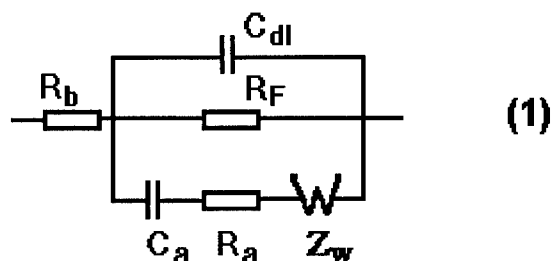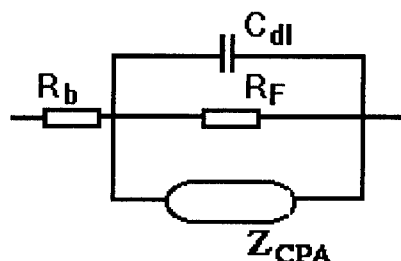
$$Z_{CPA}$$

FIGURE 1   The equivalent circuits of superionic-metal junctions with two types of relaxation
1–with the diffusion (Warburg impedance),
2–with the fractal dynamic process (CPA impedance).

$$Z_{CPA} = a(j\omega)^{-p}. \tag{2}$$

It was experimentally observed, for example, in relaxation of the interface of platinum electrode with a protonic solid electrolyte, namely, solid phosphomolybdic acid[3] and also of silver and gold electrodes with the silver-conducting electrolyte $Ag_4RbI_5$.[4,5] Figure 2 shows that the complex plane plot of the complex capacity of this systems comprise the two parts which are the arc of the quarter-circle and the straight line, this line being extrapolated intersects the same capacity of the double layer $C_{dl}$ as the arc does at $\omega \to \infty$. The deviations from this model that further turn into CPA effect appear at the frequency below certain threshold.

## 3   NONLINEAR RESPONSE

Moreover, previously,[4] we observed a nonlinear dependence of the resistance of charge transfer $R_F$ upon the integral charge transferred through interface when studying nonlinear properties of the reversible superionic junction $Ag/Ag_4RbI_5$. After the charge exceeded $2.66 \pm 0.09$ $\mu C/cm^2$ the resistance of junction increased dramatically ($R_F$ in Figure 1). This effect means that there exists a critical frequency corresponding to the integral charge transferred during a half-period changing substantially the characteristics of heterojunction.
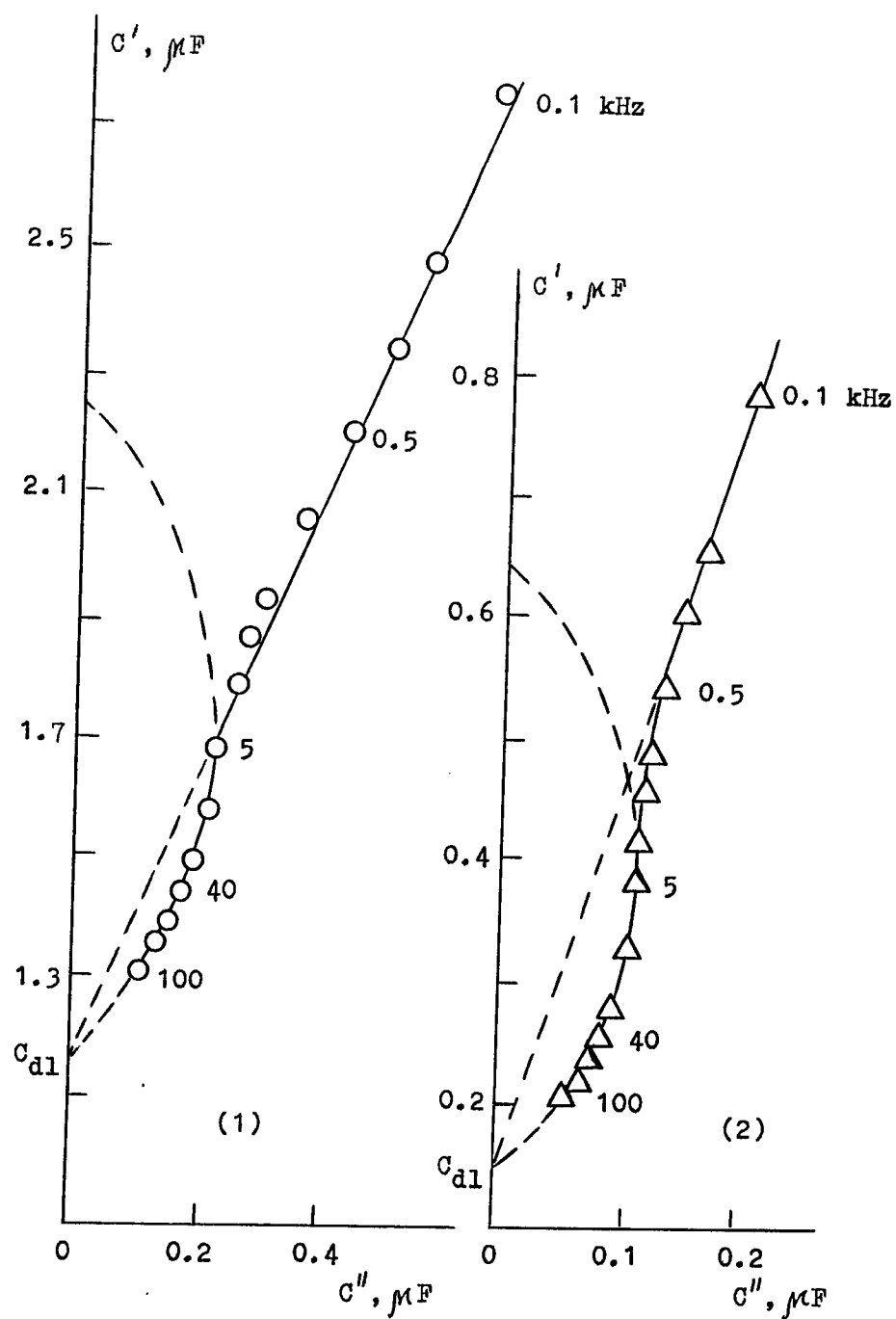
FIGURE 2   The complex plane plots of the superionic heterojunctions.
1–Ag | Ag$_4$RbI$_5$, 2–Au | Ag$_4$RbI$_5$.

A. E. UKSHE AND N. G. BUKUN
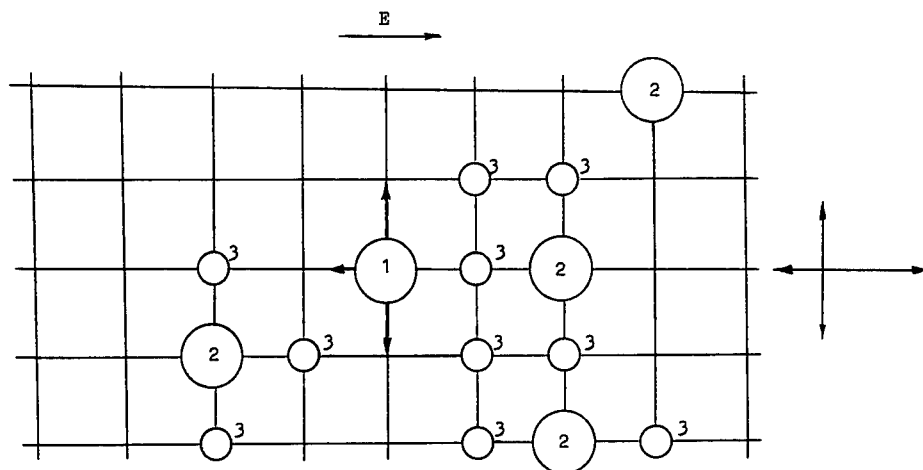


FIGURE 3   The scheme of the probabilities of ion jump in simulation.
1–the ion moving now, 2–the ions in the rest, 3–blocked sites.

Two notes are necessary in that respect. First, when they say of electrical nonlinearity, they usually mean the dependence of some parameter upon electric field or current and compare those with a characteristic value kT. In this case, similar to investigation of relaxation parameters, we encounter a change in the characteristics of the system after a substantial charge being passed through; in this case an infinitesimal current can cause nonlinear effects, provided that this current flows sufficiently long time. Secondly, the double layer has often substantial charge in equilibrium state, whereas we measure the critical charge from zero. The point is that when the current flows through the junction, an additional charge in the form of conduction ions of superionic accumulates at the interface. This charge is partially compensated with the diffusion of the minor carriers. As a result, the system relaxes slowly to a new equilibrium state.

## 4   THE MODEL OF FRACTAL DYNAMIC PROCESSES. COMPUTER SIMULATION

We can propose a model of the processes proceeding at superionic heterojunction and providing a proper description for these properties, taking into account the CPA effect resulting in the time dependence of the form

$$A = kt^{1-p}. \tag{3}$$

It was shown in[6,7] that for diffusion of particles on two- or three-dimensional lattices, the diffusion front obeys the laws of fractal geometry.

Similar methods are applicable to superionic conductors also. In superionics, the ions can move only along the lattice of ion channels formed by crystallographic sites[8] and when a site is already occupied by an ion, the path for transfer of other ions along the same channel is closed. Moreover, in[9] it is supposed that there exist preferential ion configurations that are determined by the neighboring occupied sites.
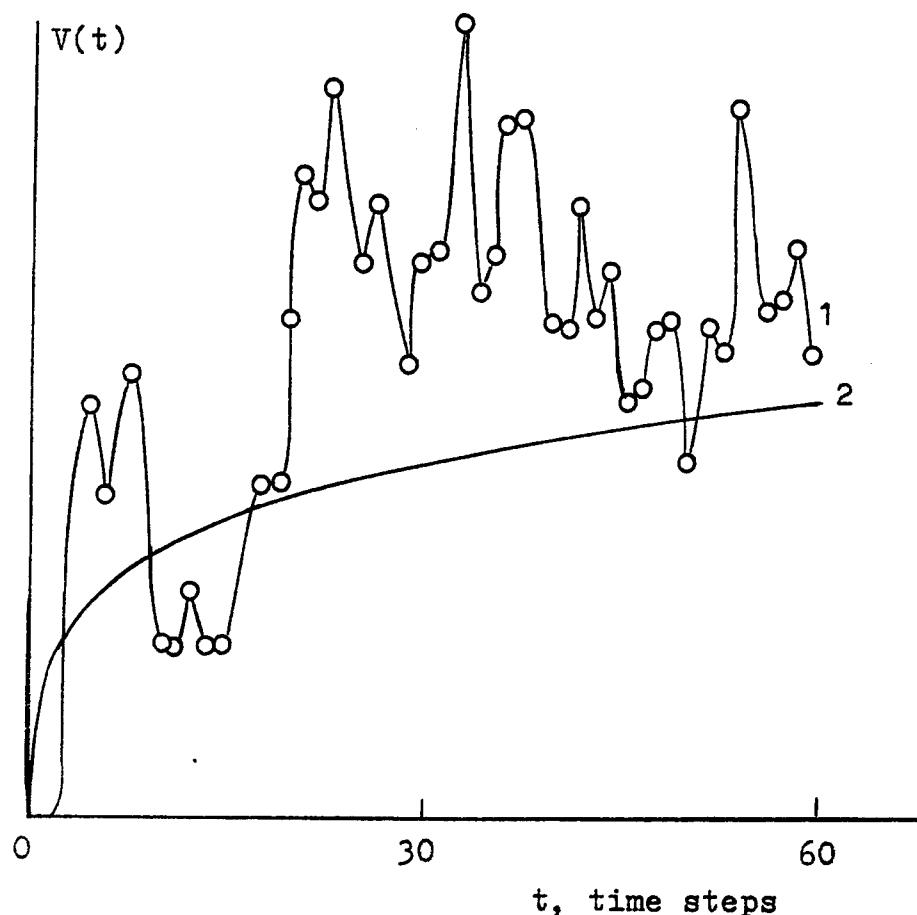
FIGURE 4   The time dependence of the potential with the direct current flowing through the junction.
Simulation at 100 × 100 lattice with semi-infinitive boundary condition.
1–calculated potentials at the begining steps of simulation;
2–curve glided by cubic splains over perfect simulation.

We performed a two-dimensional computer simulation of ion transport in superionics adjacent the heterojunction.[10,11] We employed a simple model based on the assumption that there exists a short-range order in the system of mobile ions. We assumed that there exists a lattice of channels (ion paths) with the connectivity of four and that an ion that occupies certain site blocks four neighboring sites for other ions. The external field was taken into account as a different probability of ion jump in different directions; this is presented in Figure 3. The constant field over the cell was assumed.

The time dependence of potential with the direct current flowing through the junction was calculated. This corresponds to relaxation of CPA during certain time interval (Figure 4). It was also shown that after a charge comprising 1/10 ... 1 /5 of a monolayer (this by the order of magnitude corresponds to the critical charge for the onset of charge nonlinearity)[5] a dynamic fractal structure establishes in the system of mobile ions. This

system relaxes under the effect of electric field. A strongly branched cluster of the sites occupied by the mobile ions is formed in the region adjacent the electrode. The fractal dimension of this cluster on a square lattice is 4/3. In other words, a volume charge having fractal geometry establishes in the region of the superionic junction. This effect is analogous to the formation of diffusion front.[6]

With this analogy, one can possibly extend the results obtained in[6,7] for a diffusion front to the case of electric current flowing through superionics. Thus, one might expect that for three-dimensional lattices (connectivity of 6), the dimension of the front of ion charge at heterojunction should be $\approx 0.88$.[7]

Under the effect of external field, the charge compactifies with the rate

$$d\varepsilon(t)/dt = kt^{-p},\qquad(4)$$

where $p \approx 0.8$. Therefore the frequency dependence of the capacity of heterojunction under harmonic disturbance should be

$$C(\omega) = C_0 k\Gamma(1-p)(j\omega)^{p-1},\qquad(5)$$

where $\Gamma$ is the integral gamma-function.

As a consequence the observed admittance is

$$Y(j\omega) = C_0 k(1-p)(j\omega)^p \exp(jp\pi/2).\qquad(6)$$

Such frequency dependence corresponds to CPA effect with the phase angle $\varphi = p\pi/2$. Our experimental results show that value of $p$ falls within 0.79–0.88.


## 5    THE REVERSIBLE JUNCTION

The concept of the impedance itself with the system $Ag|Ag_4RbI_5$ at the frequencies below 0.1 Hz is somewhat arbitrary because at a fixed amplitude of a signal the response becomes nonlinear. But in this case the effect of CPA was also observed. The direct current flows due to the electrochemical reaction and formation of the silver atoms. Due to the fractal structure adjacent the junction only a fraction of the ions can approach the electrode close enough and discharge. Their discharge corresponds to the critical charge of 2.66 $\mu C/cm.^2$ For further proceeding of the electrochemical reaction accompanied by deposition of silver one needs to destroy the structure of the superionic. This requires a substantial overpotential. The effect is analogous to the abrupt increase in the resistance of the junction which is observed in the case of charge nonlinearity.


## 6    CONCLUSION

Thus, the hypothesis proposed may explain, although does not provide any quantitative characteristics, some relaxation effects of the metal—superionic junctions. The interesting additional predictions can be derived from it.

The fractal structure develops due to accumulation of ion charge. Therefore, if superionic junction is disturbed without charge transfer no relaxation of CPA type should be observed. The equilibrium of heterojunction can be shifted, e.g., with an external pressure (baro-emf) or by varying the chemical composition of the environment. The experiments[12,13] showed that, indeed, in both cases no CPA is observed, and in the case of varied chemical composition, no adsorption relaxation was observed.

ACKNOWLEDGEMENT

REFERENCES

1. E. Ukshe, N. Bukun, *Elektrokhimia,* 1990, v. 26, No. 11, p. 1373–1381.
2. E. Ukshe, N. Bukun, *Solid electrolytes.* M.:'Nauka', 1977, 175 p.
3. A. Ukshe, L. Leonova, *Elektrokhimia.* 1988, v. 24, No. 2, p. 236–240.
4. A. Ukshe, N. Bukun, V. Goffman, *Fiz. Tverdogo Tela.* 1988, v.; 30, No. 10, p. 3096–3099.
5. A. Ukshe, N. Bukun, *Elektrokhimia.* 1989, v. 25, No. 2, p. 174–177.
6. B. Sapoval, M. Rosso, J. Gouyet, J. Colonna, *Solid State Ionics,* 1986, v. 18–19, p. 21–28.
7. R. Sapoval, M. Rosso, J. F. Gouyet, *The Fractal Approach to Heterogeneous Chemistry.* Edited by D. Avnir. 1989. John Wiley.
8. O. Philipenko, L. Atovmyan, V. Ponomarev, L. Alimova, L. Leonova, V. Bakaev, E. Ukshe, *Crystallographia.* 1988, v. 33, No. 1, p. 82–89.
9. M. Kompan. G. Venus, *Fiz. Tverdogo Tela.* 1990, v. 32, No. 11, p. 3214–3219.
10. A. Ukshe, *Mater. Sci. Forum.* 1991, v. 76, p. 233–236.
11. A. Ukshe, *Elektrokhimia.* 1993, v. 29, No. 1, p. 125–129.
12. A. Ukshe, E. Maklakova. *Mater. Sci. Forum.* 1991, v. 76, p. 237–240.
13. A. Ukshe, L. Leonova, *Elektrokhimia.* 1993, v. 29, No. 12, p. 1469–1473.

# MAGNETIC CIRCULAR DICHROISM AND ABSORPTION STUDY OF PHOTOCHROMISM IN Mn– DOPED Bi$_{12}$GeO$_{20}$

## F. RAMAZ,[a] A. HAMRI,[a] B. BRIAT,[a]* V. TOPA[b] and G. MITROAICA[b]

*[a]Laboratoire d'Optique Physique, ESPCI, 10 rue Vauquelin, 75231 Paris Cedex 05, France; [b]Institute of Physics and Technology of Materials, 76900 Bucharest-Magurele, Romania*

We report on the first simultaneaous investigation of the behavior of ligand field and charge transfer bands in doped Bi$_{12}$GeO$_{20}$ (BGO) under various illumination and thermal conditions. This was made possible through MCD measurements in both the near IR and the visible spectral regions. The [MnO$_4$]$^{3-}$ ion is clearly identified in the thermally bleached state. Illumination with blue light leads to the reduction of Mn$^{5+}$ while the antisite (Bi$_{Ge}$$^{3+}$ + h) defect is formed. Finally BGO is an interesting host for the popular d$^2$ ions in a tetrahedral site.

## 1  INTRODUCTION

The presence of point defects or doping ions in the crystal structure of bismuth germanate (BGO 6:1) crystals is a prerequisite for the generation and transfer of photoinduced charge carriers that are responsible for photochromic and photorefractive phenomena in these technologically important materials. Since 1990,[1–7] we have advocated the use of magnetic circular dichroism (MCD) for a microscopic characterisation of intrinsic and impurity centers in BGO and for the monitoring of light-induced charge transfer (CT) processes. Our aim in this paper is to report on the first simultaneous investigation of d-d and charge transfer bands by means of this powerful technique.[8–10] For this purpose, the spectral range of our dichrometer has been extended towards the near IR up to 1.7 $\mu$m. We recall that MCD stands for the differential absorption of left ($\sigma_+$) and right ($\sigma_-$) circularly polarised lights, presented by a sample submitted to a longitudinal magnetic field.

The case of Bi$_{12}$GeO$_{20}$:Mn happens to be particularly illustrative of the difficulties to interpret the sole optical absorption data and to provide a valuable model for the understanding of charge transfer processes. As pointed out recently,[12] complications arise for two main reasons: (i) Mn may exist in a large number of oxidation states; (ii) it may substitute for Ge(Td) or Bi (approximately Oh) or even occur at an interstitial position.[11] It is therefore not surprising that controversial assignments have been proposed for this system over the years.[11–13]

## 2  RESULTS

Prior to our experiments, the crystal was prepared in an 'initial state' by a thermal bleaching of at least 30 mn at 600°C. After quenching to room temperature in the dark, the sample was set in a liquid helium cryostat containing a superconducting magnet. MCD spectra have been taken at 4.2 K and below, and complemented by optical absorption at 80 K or 1.3 K.

---

* author to whom correspondence is to be addressed.  tel: (1) 40 79 45 83   fax: (1) 43 36 23 95

FIGURE 1   MCD spectrum in the visible spectral region at 4.2 K under 2.5 T.
a: thermally bleached sample; b: after illumination with the monochromator at 24000 cm$^{-1}$; c: after a subsequent illumination at the same wavenumber with a quartz-iodine lamp and an interference filter. For the sake of comparison, the magnitude has been reduced by a factor of 6.5 for spectrum c. The ordinate is in cm$^{-1}$.

Figure 1 shows our results in the visible spectral range. Spectrum (a) was taken on the thermally bleached crystal. We observe weak features in the red (d-d bands) as well as two broad bands (presumably CT) around 23 800 and 26 300 cm$^{-1}$. They all show a paramagnetic behaviour, as demonstrated by the temperature dependence of the signal between 4.2 K and 1.3 K. These features are all associated to the dopant since the MCD of bleached undoped crystals[6] is strictly zero in both spectral regions. Spectrum (b) was obtained after an illumination of 10 minutes with the light of the monochromator set at 24 000 cm$^{-1}$. Obviously, broad features start to develop around 17 600 and 26 000 cm$^{-1}$. A new illumination of 10 mn with a 150 W halogen lamp equiped with an interference filter at the same wavenumber leads to spectrum (c). Note that the magnitude has been divided by 6.5 (normalization at 17 600 cm$^{-1}$) for the sake of comparison. This spectrum is the same as that obtained for undoped crystals[1-6] and assigned[10] to an antisite ($Bi_{Ge}^{3+}$ + hole) defect. Furthermore, a comparison of Figures 1b and 1c indicates quite clearly that the original Mn features have essentially collapsed under illumination.

We now consider the infrared region in Figure 2. In the thermally bleached state (a), we observe a very sharp line at 8025 cm$^{-1}$ and an S-shaped MCD curve around 12 000 cm$^{-1}$. Weaker and less well defined features occur around 10 500 cm$^{-1}$. When the crystal is submited to a blue illumination at 22 000 cm$^{-1}$, all MCD bands decrease considerably. This point was further confirmed by an absorption study at 80 K under various illumination or thermal treatments. On contrary to what occurs for an undoped crystal we found that BGO:Mn is highly photochromic even at room temperature. The same situation actually also occurs for other transition metal ions.

## 3   DISCUSSION

Our near infrared MCD data demonstrate unambiguously that, in the thermally bleached state, the spectroscopic properties of BGO:Mn are dominated by $Mn^{5+}(d^2)$ at the Ge site. The crystal field description appears to be applicable since, as in vanadates and phosphates[14-16] we observe the expected sharp spin-forbidden transition $^3A_2 \rightarrow {}^1E$ (8025

FIGURE 2   MCD spectrum in the near IR (1.3 K, 1.5 T) in the bleached state (a) and after a blue illumination at 22000 cm$^{-1}$ with the quartz-iodine lamp and an interference filter. The ordinate is in optical density units.

cm$^{-1}$) and the broader features assigned to $^3T_2$ (weak, 10500 cm$^{-1}$) and $^3T_1$ (allowed, 12000 cm$^{-1}$). The S = 1 character of the ground state was probed by measuring the MCD saturation versus the magnetic field at 1.3 K. The sign for the MCD features is a very crucial test of the above assignments. Our predictions for the transitions to $^1E$ and $^3T_1$ are in agreement with our observations.

The question occurs as to the valency of Mn after illumination. As shown in Figure 2, the process is accompanied by the appearance of a broad negative MCD around 9000 cm$^{-1}$. This is the region expected for the $^4T_1 \rightarrow {}^4T_2$ transition of Mn$^{4+}$. The highest oxydation state for Mn occurs for [MnO$_4$]$^-$ (d$^0$)[17] in KIO$_4$. This ion is diamagnetic and its MCD and optical absorption are characterized by a series of sharp lines in the 17000−21000 cm$^{-1}$ region, which are not present in our data. [MnO$_4$]$^{2-}$ (d$^1$) also exists[18] in Rb$_2$SO$_4$. Its unique d-d band is found around 11000 cm$^{-1}$ while strong CT bands should occur in the visible region. In our opinion, Mn$^{2+}$ cannot be present in a large amount since we have been able to detect easily its spin-forbidden bands via MCD in the parent compound Bi$_4$Ge$_3$O$_{12}$[19] or else to monitor the amount of the isoelectronic Fe$^{3+}$ ion in undoped Bi$_{12}$GeO$_{20}$ crystals. Altogether, the most probable charge state after illumination is Mn$^{4+}$.

Although the reduction of the pentavalent ion occurs simultaneously with the formation of the (Bi$_{Ge}$$^{3+}$ + hole) defect, it is not yet firmly established whether the necessary electron proceeds via the conduction band or arises directly from the valence band. Additional photo-MCD work is needed to help in clarifying this point.

REFERENCES

1   B. Briat, C. Laulan, J.C. Launay and J. Badoz in *Technical Digest of the Topical Meeting on Photorefractive Materials, Effects and Devices*, Aussois, France 1990) p. 114.

2.  B. Briat, C. Laulan Boudy and J.C. Launay in Proceedings of the Seventh European Meeting on

Ferroelectricity, Dijon, France (1991); Ferroelectrics **125**, 467, 1992.

3.  B. Briat, J.C. Fabre and V. Topa, Proc. Inter. Conf. Defects in Insulating Materials, Nordkirchen, Germany (1992) p. 1160, Ed. O. Kanert and J.M. Spaeth, World Scientific, 1993.

4.  B. Briat, V. Topa, C. Laulan Boudy and J.C. Launay, Jour. Lumin., **53**, 534, 1992.

5.  B. Briat, *Photorefractive Materials, Effects and Devices*, Theophania, Kiev, Ukraine 1993.

6.  E. Moya, C. Zaldo, B. Briat, V. Topa and F.J. Lopez, J. Phys. Chem. sol., **54**, 809, 1993.

7.  J. Badoz, M. Billardon, A.C. Boccara and B. Briat, Symp. Faraday Soc. n°3, 27, 1970.

8.  J.M. Spaeth, J.R. Niklas and R.M. Bartran, *Structural analysis of point defects in solids*, Springer Verlag, Berlin, 1992.

9.  H.J. Reyher, U. Hellwig and O. Thieman, Phys. Rev., **B47**, 5638, 1993.

10. W. Wardzynski, H. Szymczak, M.T. Borowiec, K. Pataj. T. Lukasiewicz and J. Zmija J. Phys. Chem. Sol. **46** (1985) 1117.

11. V.V. Volkov, A.V. Egorysheva, Yu.F. Kargin and V.M. Skorikov Inorg. Mater. **29** (1993) 1364 (english translation).

12. T.V. Panchenko and N.A. Truseyeva, Ferroelectrics **115** (1991) 73.

13. J.B. Milstein, J. Ackerman, S.L. Holt and B.R. McCarvey, Inorg. Chem., **11**, 1178, 1972.

14. L.D. Merkle, A. Pinto, H.R. Verdun dan B. McIntosh, Appl. Phys. Lett. **61** (1992) 2386.

15. J.A. Capobianco, G. Cormier, R. Moncorgé, H. Manaa and M. Bettinelli, Appl. Phys. Lett., **60**, 163, 1992.

16. P.A. Cox, D.J. Robbins and P. Day, Mol. Phys., **30**, 405, 1973.

17. P. Day, L.D. DiSipio, G. Ingletto dan L. Oleari, J. Chem Soc. Dalton, 2595, 1973.

18. B. Briat, A. Hamri, F. Ramaz and C. Zaldo, this meeting (unpublished).

# R B S STUDY OF DEFECT PROFILES IN PROTON IMPLANTED LiNbO$_3$

S. OULD SALEM, B. CANUT, P. MORETTI, J. MEDDEB, S. M. M. RAMOS,
P. THEVENARD

*Département de Physique des Matériaux (U.R.A. C.N.R.S. 172), Université Claude Bernard Lyon I, F-69622 Villeurbanne Cédex, France*

Single crystals of lithium niobate were implanted at room temperature with 20 keV protons at fluences ranging from $5 \times 10^{16}$ H$^+$/cm$^2$ to $2 \times 10^{17}$ H$^+$/cm$^2$. Rutherford Backscattering Spectrometry in channeling geometry (RBS-C) performed at three beam energies ( 1, 1.5, and 2 MeV) and subsequent analysis of the energy dependence of the dechanneling cross section enabled us to show the predominant induced lattice defects are likely of a 'point' nature. Electron microscopy investigations also support this assumption.

*Key words*: Niobate lithium, Implantation, defects.

## 1 INTRODUCTION

Proton implantation in the MeV range, as for helium, has been successfully applied to waveguides fabrication in various oxides, and particularly in LiNbO$_3$ which is currently a key material for optical-device fabrication. However, little is known about the exact nature of the defects induced by light-ion (H$^+$, He$^+$) implantation which are in fact the origin of the index-barrier formation. Recently, we have shown,[1] by means of RBS-C analysis, the presence of lattice disorder induced by protons implanted in LiNbO$_3$ and that a strong correlation does exist between the latter and the fluence of the implanted ions. RBS-channeling is indeed a powerful tool to determine the depth distribution of damage, as reported for MeV-He$^+$ implantation in LiNbO$_3$.[2] However, taking into account the dechanneling effect, this technique can improve our understanding of the physical nature of defects in crystals.[3,4] Although the type and amount of defects are not directly related to backscattering yield, the analysis of the beam-energy dependence of the dechanneling cross section can be carried out to estimate the predominant type of defect in the cristal.[3,4] In this work, a numerical method is carried out to determine the dechanneling cross section and to extract the resulting defect profile[5] of proton-implanted LiNbO$_3$.

## 2 EXPERIMENT

Single crystals of LiNbO$_3$ (Y-cut) were implanted with 20 keV protons using a Balzers implantor, with three different fluences. The samples were analyzed by RBS in channeling geometry with three He$^+$ beam energies: 1, 1.5, and 2 MeV generated by a Van de Graaff accelerator. The crystals were mounted on a three axis precision goniometer with accuracy better than 0.05°. To avoid target heating or defects induced by the He$^+$ probe, the beam current was kept below 5 nA during the analysis time.

## 3 RESULTS AND DISCUSSION

Typical aligned and random spectra of an implanted sample recorded before and after
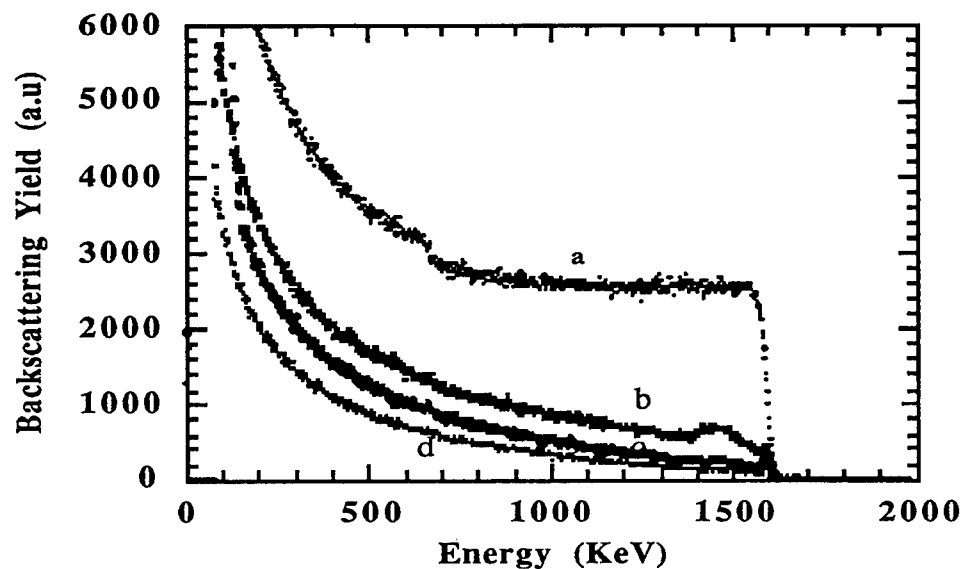
FIGURE 1    Random (a) and aligned (d) spectra of as implanted $LiNbO_3(5 \times 10^{16} \; H^+/cm^2, 20 \; keV)$. (b) and (c) aligned spectra of one and two hours annealed samples in air respectively.
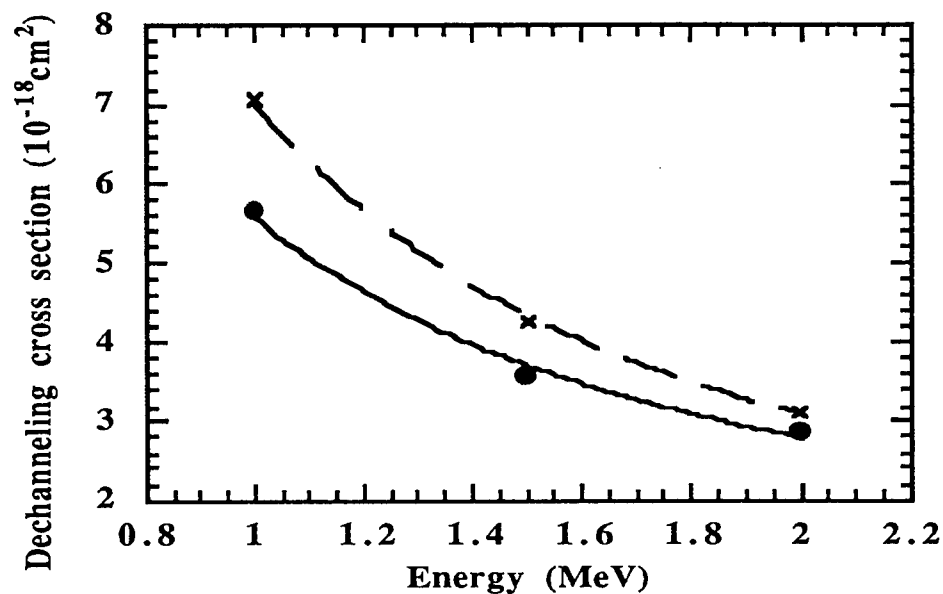


FIGURE 2    Dechanneling cross section versus analysis beam energy for implanted $LiNbO_3$ with $1 \times 10^{17} \; H^+/cm^2(x)$ and $2 \times 10^{17} \; H^+/cm^2(\bullet)$, at 20 keV.
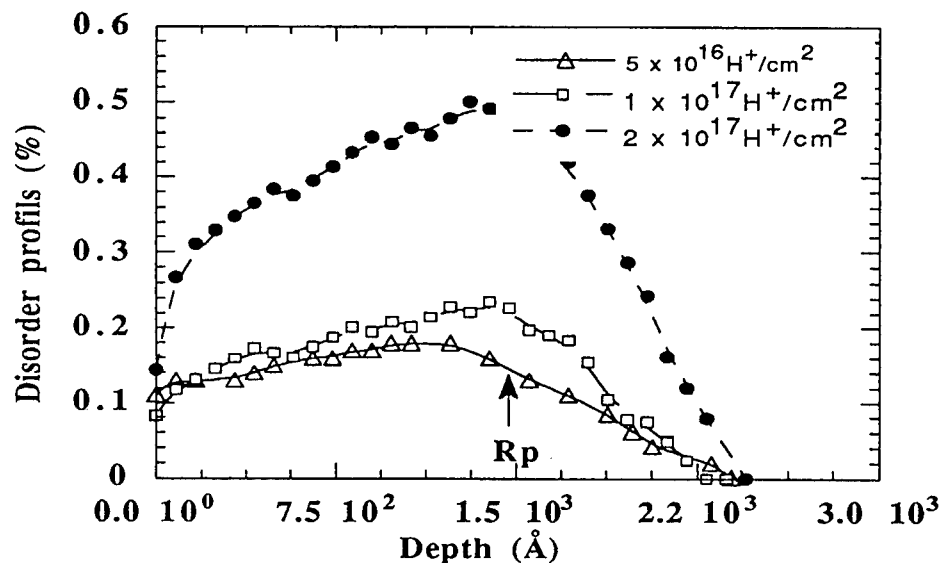
FIGURE 3    Defect profiles extracted from RBS channeling yields for implanted LiNbO$_3$ at 20 keV with fluences of 0.5, 1 and 2, $\times 10^{17}$ H$^+$/cm$^2$.

annealing at 250°C, are reported in Figure 1. One notes the hump in spectrum (b) related to the disorder created in the near surface of the sample. A decrease in damage with the annealing time is clearly seen.[1] From a procedure described elsewhere,[5] the energy dependence of the dechanneling cross section reported in Figure 2, also exhibits a decrease for the three analysed doses. According to Quéré's modél[3], we can, therefore, conclude that the dislocation defects are not predominant in H$^+$ implanted lithium niobate. In fact, Quéré demonstrated that the dechanneling cross section increases, following a root square law ($\approx$ E$^{1/2}$) if dislocations are the majority defects in the structure, while an opposite behaviour, i.e a decreasing law ($\approx$1/E), was attributed to displaced atoms generating point defects. Undoubtedly our results shown in Figure 2 are in agreement with the latter assumption. The defect profiles in H$^+$-implanted LiNbO$_3$ which have been extracted from RBS channeling yields are displayed in Figure 3. Their maximum peaking at 1500 Å is in accordance with the TRIM range value. The disorder peak corresponds exactly to the TRIM prediction, while the defect profile exhibits a broadening over the crystal surface. The plan view obtained by transmission electron microscopy and reported in Figure 4 does not show any dislocation network. In this picture, we can clearly distinguish, from the bottom to the top, successively the substrate, the 'area' damaged by proton implantation, and another thin damaged layer resulting from the ion-milling process. This result supports the energy dependence observed for the dechanneling cross section, confirming that dislocations are not the predominant defect in proton-implanted LiNbO$_3$. Therefore, the predominant induced defects are likely Nb displaced atoms or associated point defects, all the more the induced absorption band observed in implanted lithium niobate has often been interpreted in terms of point defect (F. F$^+$, Nb$_{Li}$ centers and small polarons or bipolarons).[6,7]

Area damaged by ion milling ——————▶

H$^+$ implanted zone   ——————▶

implantation interface  ——————▶

Substrat of LiNbO3    ——————▶

$\vec{C}$ ◯

0.1 μm
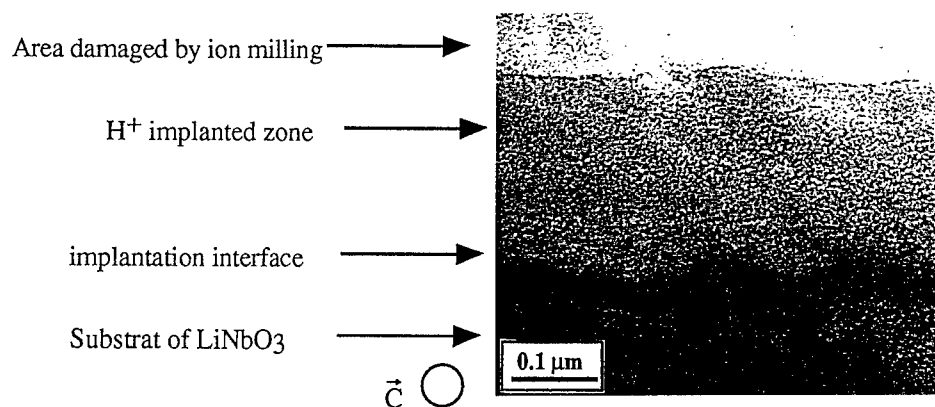
FIGURE 4   Plane view, obtained by MET in bright field near the $\vec{C}$ axis of H$^+$ implanted LiNbO$_3$ $(5 \times 10^{16}$ H$^+$/cm$^2$, at 20 keV), showing any extended defects.

## 4   CONCLUSION

Our RBS measurements, performed at various beam energies, and subsequent analysis of the dechanneling cross section enabled us to demonstrate that displaced atoms and associated defects are the predominant lattice defects in proton implanted LiNbO$_3$. Electron microscopy investigations confirm this assumption since no dislocation networks are evidenced.

REFERENCES

1.  S. Ould Salem, P. Moretti, B. Canut, K. Wirl, P. Hertel, J. Optics (Paris), Vol. 24, n°6, pp. 265–69, (1993).
2.  K. M. Barfoot and B. L. Weiss, *J. Phys. D. Appl. Phys.* **17**, L47 (1984).
3.  Y. Queré, *Ann. Phys.*, **t.5**, pp. 105–38, (1970).
4.  E. Rimini, S. U. Campisano, G. Foti, P. Baeri and S. T. Picraux, in '*Ion beam Surface Analysis*', Plenum, New-York (1976).
5.  B. Canut, L. Romana, P. Thevenard, and N. Moncoffre, *Nucl. Instr. and Meth.* **B46** (1990) 128.
6.  K. L Sweeney and L. E. Halliburton, *Appl. Phys. Lett.* **43** (4), 15 August 1983.
7.  O. F. Schirmer, O. Thiemann and M. Wöhlecke, *J. Phys. Chem. Solids* Vol. **52**, N° 1, pp. 185–210, 1991.

# XPS STUDIES OF EUROPIUM IMPLANTED LiIO$_3$

S. M. M. RAMOS,[1] C. ROSSO,[2] P. MORETTI,[1] C. GALEZ,[2] B. CANUT[1]
and P. THEVENARD[1]

[1]*Département de Physique des Matériaux (U.R.A C.N.R.S 172), Université Claude
Bernard Lyon I, 43 Bd. du 11 Novembre 1918, F-69622 Villeurbanne Cedex, France;*
[2]*Equipe de recherche sur les Matériaux pour la Ferroélectricité et l'Optique Non-linéaire,
Ecole Supérieure des Ingénieurs d'Annecy, 41 Av. de la Plaine, B.P. 806,
74016 Annecy, France*

Single crystal of lithium iodate (Z-cut samples) were implanted at room temperature with Eu$^+$ ions at 150 kev with a fluence of $5.10^{16}$ ions.cm$^{-2}$. The oxidation states of the cations have been determined by X-ray photoelectron spectroscopy (XPS). XPS spectra clearly reveal only europium in Eu$^{3+}$ along the depth profile analysis.

*Key words*: Lithium-Iodate-Europium-Implantation-XPS.

## 1 INTRODUCTION

Lithium iodate ($\alpha$-LiIO$_3$) exhibits good electro-optical and nonlinear optical effects as well as large piezoelectric coefficients which make it a potential candidate for integrated and nonlinear optical applications.[1,2] Besides we recently demonstrated that optical waveguides can be fabricated by proton implantation[3] in LiIO$_3$.The possibility to obtain high amplification and stimulated light emission in waveguiding configuration is also of the greater interest. Rare earth ion implantation could be an alternative way for doping oxides to create locally amplifying areas near to the surface of virgin substrates.

In this paper we report on the first investigation on europium implantation in LiIO$_3$. The aim is to determine the oxidation states of the lattice species and of the implant itself along the Eu distribution profile. This characterization was carried out by XPS measurements at various depths in the as-implanted samples.

## 2 EXPERIMENTAL PROCEDURE

Z-cut samples of LiIO$_3$ single crystals grown in our laboratory were implanted with europium ions of 150 keV at a fixed fluence of $5.10^{16}$ ions.cm$^{-2}$.

X-ray photoelectron spectra were recorded using a RIBER NANOSCAN 700 CX apparatus operating with radiation MgK$_\alpha$ (h$\nu$ = 1253.6 eV), a source voltage of 12 kV and an emission current of 20 mA. In order to investigate the depth profile, sequences of sputtering with a 5 keV Ar$^+$ source and acquisition runs were alternately applied. Assuming a constant sputtering rate of about 40 nm.h$^{-1}$, we have estimated the depth of the analysed area within an error of 10%. The low ion current (50 nA) and fluence (about $10^{14}$ Ar$^+$.cm$^{-2}$) used allow us to argue that both preferential sputtering effects and beam induced chemical changes have been minimized.
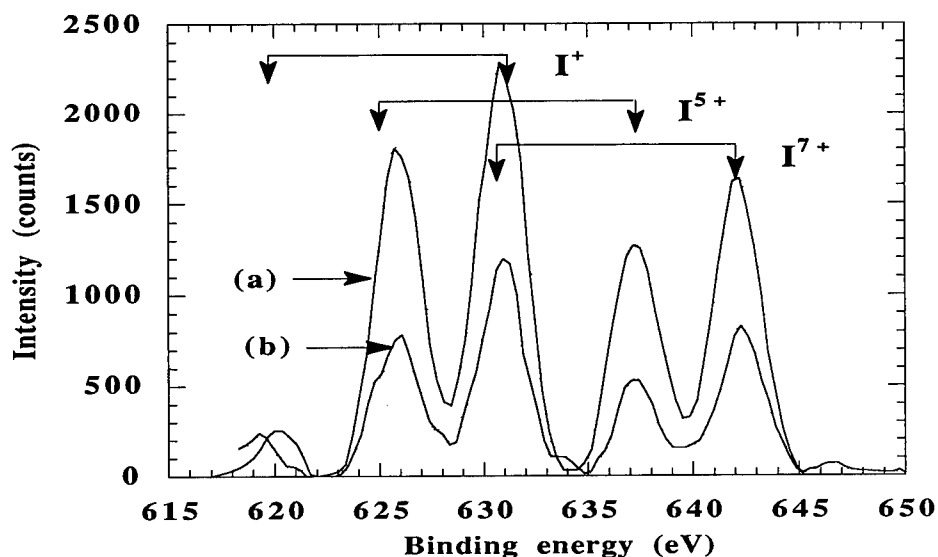
FIGURE 1   Depth analysis. Photoelectron spectra (XPS) of the I (3d) level in LiIO$_3$ (a) before any sputtering run, (b) after 5 h sputtering run. The peaks (doublets) related to the oxidation states are indicated. In both cases the spectrum is a mixture of three oxidation states.

## 3   RESULTS

XPS measurements were carried out at different depths in order to follow the evolution of the charge state of the involved species along the Eu distribution profile. Preliminary experiments were first performed in a virgin sample to separate unambigously the chemical shifts induced by the implantation itself.

   In the I (3d$_{5/2,3/2}$) spectrum of an unimplanted surface (Figure 1a and 1b), five well defined peaks are observed which could be interpreted as a mixing of three contributions, each one beeing characterized actually by a doublet. Indeed our spectrum can be fitted by three doublets peaking at the following bonding energy: 621.0–631.2 eV, 625.5–637.0 eV and 631.2–642.6 eV, which can be associated[4,5] with the 1$^+$, 5$^+$ and 7$^+$ oxidation states respectively. The relative contribution of these components to the spectrum, as determined by fitting, is respectively 7% (I$^{1+}$), 43% (I$^{5+}$) and 50% (I$^{7+}$). After a 5 h Ar$^+$ bombardement, the relative amounts of I$^{1+}$, I$^{5+}$ and I$^{7+}$ are modified becoming 17%, 38% and 45%, respectively. However, no further evolution in the spectrum was observed by sputtering sequences indicating that an equilibrium state was achieved and no more reduction occurs (Figure 1b). One must note that some difficulties arise to assign the I(3d) photoelectron lines since few XPS results are available in the literature.[4,5]

   Dealing with europium implanted LiIO$_3$, the results are significantly different. The two photoelectron spectra of the I (3d) core line given in Figure 2 have been recorded after 7 h (a) and 12 h (b) of sputtering, corresponding to a depth of about 28 nm and 48 nm, respectively. The first one corresponds to a region where the europium concentration is maximum, as expected from TRIM code calculations.[6] The second one corresponds to a
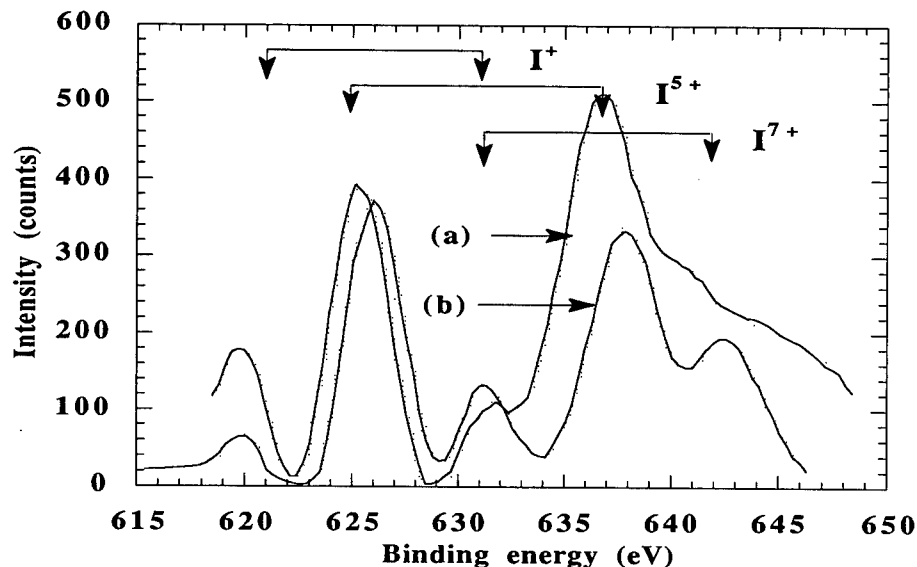
FIGURE 2   Typical photoelectron spectra of the I (3d) levels in Eu$^+$ implanted LiIO$_3$ (150 keV, 5.10$^{16}$ ions.cm$^{-2}$). After 7 h sputtering run (a): only I$^+$ and I$^{5+}$ states are present. After 12 h sputtering (b): the three characteristic oxidation states of unimplanted samples are appearing.

depth far beyond this maximum. From the top of the as-implanted surface up to a depth of 28 nm, the relative contribution of I$^{1+}$, I$^{5+}$ and I$^{7+}$ to the spectrum does not change and is of 18%, 68% and 4%, respectively. Comparatively to the virgin sample, the I$^{7+}$ contribution is drastically reduced indicating that a chemical effect is induced by the Eu implantation (Figure 2a). At a depth of 48 nm, the five characteristics peaks observed for the unimplanted sample start to be restored, with a percentage of 10% (I$^{1+}$), 61% (I$^{5+}$) and 29% (I$^{7+}$), respectively.

The XPS analysis of the Eu (3d), after a 7 h of sputtering is reported in Figure 3. Only one line with a maximum corresponding to a 1139.2 eV binding energy have been observed all along the sputtering sequences. We have already interpreted[7] this peak as beeing characteristic of 3$^+$ oxidation state. This contrasts with our results on both LiNbO$_3^7$ and SrTiO$_3^8$ implanted with europium where two oxidation states have been observed, namely Eu$^{2+}$ and Eu$^{3+}$.

## 4   CONCLUSION

XPS measurements performed in LiIO$_3$ before and after Eu implantation have shown that I signal corresponds to a mixture of three oxidation states, I$^{1+}$, I$^{5+}$ and I$^{7+}$. However in europium implanted LiIO$_3$, the iodine oxidation state I$^{7+}$ is drastically decreased, from 50% to 4%, mainly in benefit of the I$^{5+}$ state.

Morover, in the implanted layer the Eu ions are found in only one oxidation state, namely Eu.$^{3+}$ Our results suggest that it should be interesting to investigate the fluorescence of Eu$^{3+}$ in lithium iodate waveguides.$^3$
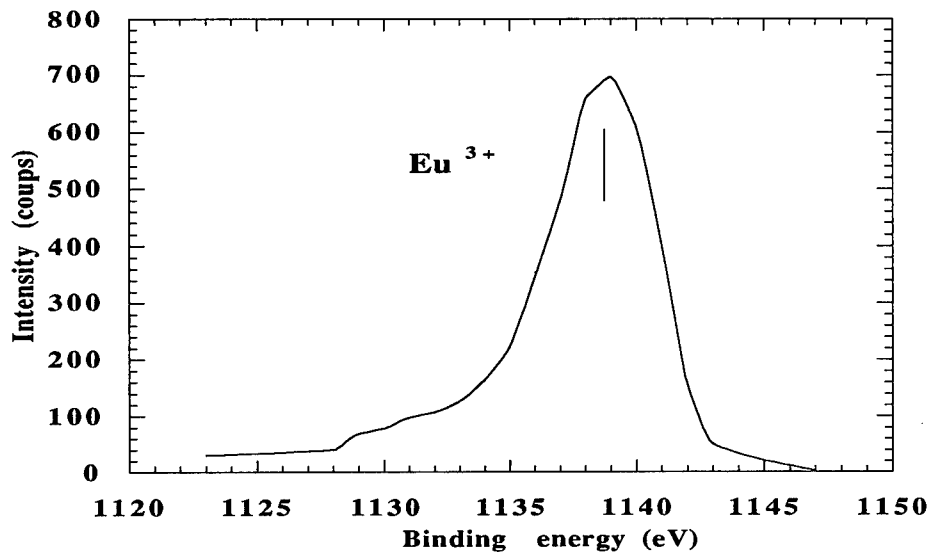
FIGURE 3   Photoelectron spectra (XPS) of the Eu (3d) level in $LiIO_3$ implanted at 150 keV with $5.10^{16}$ ions.cm$^{-2}$, showing that Eu is in only one charge state.

REFERENCES

1. T. Felikinski, J. Szewczyk, *Mat. Res. Bull.*, **16** (1981) 1505.
2. H. Buersner, A. Renn, M. Brieger, F Von Moers, A. Hese, *Appl. Phys.,* **B39** (1986) 77.
3. C. Rosso, P. Moretti, J. Mugnier, D. Barbier, Y. Teisseyre, J. Bouillot, *Phys. Stat. Sol.* **A139** (1993) K137.
4. C. S. Fadley, S. B. M. Hagstrom, M. P. Klein, D. A. Shirley, *J. Chem. Phys.* **48** (8) (1968) 3779.
5. T. Sasaki, R. S. Williams, J. S. Wong, D. A. Shirley, *J. Chem. Phys.* **71** (1) (1979) 4601.
6. J. F. Ziegler, J. P. Biersack and U. Littmark in *Stopping power and ranges of ion in mater*, vol. 1 (Pergamon, 1985).
7. P. Moretti, B. Canut, S. M. M. Ramos, R. Brenier, P. Thevenard, D. Poker, J. B. M. Da Cunha, L. Amaral, A. Vasquez, *J. Mater. Res.*, **8** (10) (1993) 2679.
8. S. M. M. Ramos, B. Canut, P. Moretti, D. Poker, P. Thevenard, *Thin Solid Films*, **259** (1995) 113.

# CHARACTERISATION OF PLANAR WAVEGUIDES FORMED BY PROTON IMPLANTATION IN LITHIUM IODATE

C. ROSSO,* P. MORETTI,** J. MUGNIER*** and J. BOUILLOT*

*\*L'Equipe de recherche sur les Matériaux pour la Férroélectricité et l'Optique Non lineaire, ESIA, 41 Av. de la Plaine, BP 806, 74016 Annecy, France; \*\*Département de Physique des Matériaux, U.R.A 172, Université Claude Bernard Lyon I, 43 Bd. du 11 Novembre 1918, 69622 Villeurbanne, France; \*\*\*Laboratoire de Physico-Chimie des Matériaux Luminescents, U.R.A 442, Université Claude Bernard Lyon I, 43 Bd. du 11 Novembre 1918, 69622 Villeurbanne, France*

Permanent optical waveguides were produced by proton implantation in lithium iodate crystals. After implantation the samples present a good optical quality. No annealing procedure is required. The index profiles have been measured by dark modes spectroscopy and the ordinary refractive index has been obtained with an inverse WKB method. Moreover, the optical barrier is relevant with a maximum index change of about 0.04. The effects of ion fluence and beam energy have been investigated on z-cut samples.

*Key words*: Waveguide—implantation—lithium—iodate—m-lines.

## 1 INTRODUCTION

In recent years, radiation damage has been investigated as a powerful means for the production of planar waveguides.[1] The light ions ($He^+$, $H^+$) used in the implantation in the MeV range can induce a damaged layer into crystalline materials at the end of the ions path, with a consequent lowering of the refractive index.[2] Thus, between the surface and this optical barrier, typically located at a few microns below, optical confinement can be obtained. The first waveguides in lithium iodate $LiIO_3$ were recently formed by proton implantation which is so far the only successful reported method.[3]

This compound was choosen, because of its wide range of applications (large piezoelectric effect, non-linear optical devices...)[4,5] and because it can be easily growth.[6,7]

In this paper, we report on the effect of ions ($H^+$) fluence and beam energy on the index profiles of $LiIO_3$ waveguides reconstructed by an inverse WKB method[8] from dark modes spectroscopy results.

## 2 EXPERIMENTAL METHOD

Lithium iodate crystals were grown by slow evaporation of an aqueous satureted solution of lithium iodate at a controlled temperature. Z-cut samples (10 mm × 10 mm × 2 mm) were mounted in the experimental chamber of 2 MeV Van de Graaff accelerator. The largest face of the samples was exposed, at room temperature, to the proton beam with an incidence angle of 10° to avoid channeling effects in $LiIO_3$. In these investigations, ion beam energy and proton dose range from 600 KeV to 1 MeV and from 1 to $4.10^{16}$ ions/cm$^2$ respectively.

The planar waveguides obtained by this technique were characterized by prism coupling method (m-lines spectroscopy) by means of a 633 nm laser beam and a glass prism with an refractive index of 2.015.
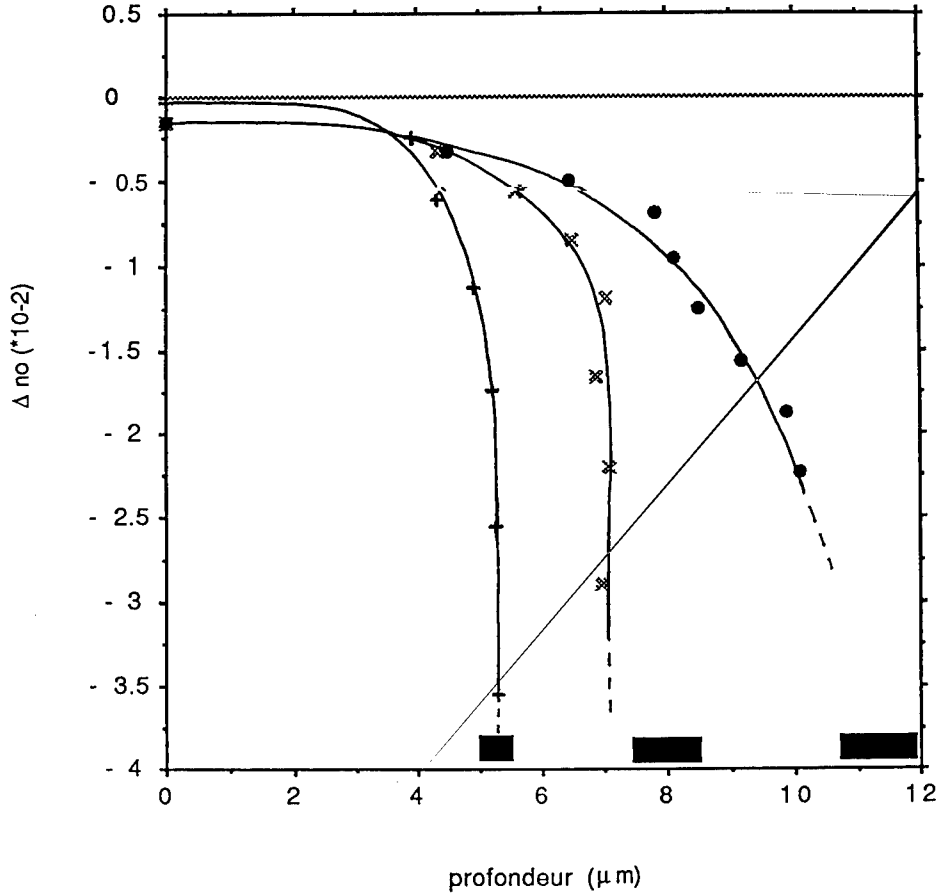
FIGURE 1   Ordinary refractive index change $n_o$ in lithium iodate waveguides. for a fluence of $4.10^{16}$ ions/cm$^2$. at various energies: 600 KeV (+), 800 KeV (×), 1 MeV (•). The related implantation area, calculated by TRIM simulation is indicated by bars on the depth scale.

## 3   RESULTS

The dark lines obtained with transverse electric (TE) propagation waves were much better defined than those obtained with transverse magnetic (TM) ones, so only the ordinary refractive index corresponding to the TE modes is given here. From this result, an inverse WKB method is used to reconstruct the refractive index profiles. The TRIM simulation program[9] is used to calculate the depth profile of implanted protons.

The values of ordinary and extraordinary refractive index in the bulk have been measured as 1.8856 and 1.7385 respectively.

One notes that no annealing process is necessary after implantation to get good planar waveguide properties on lithium iodate samples. This observation is in agreement with the fact that no difference is detected before and after implantation in the absorption spectrum measured in the range 280 to 3000 nm.
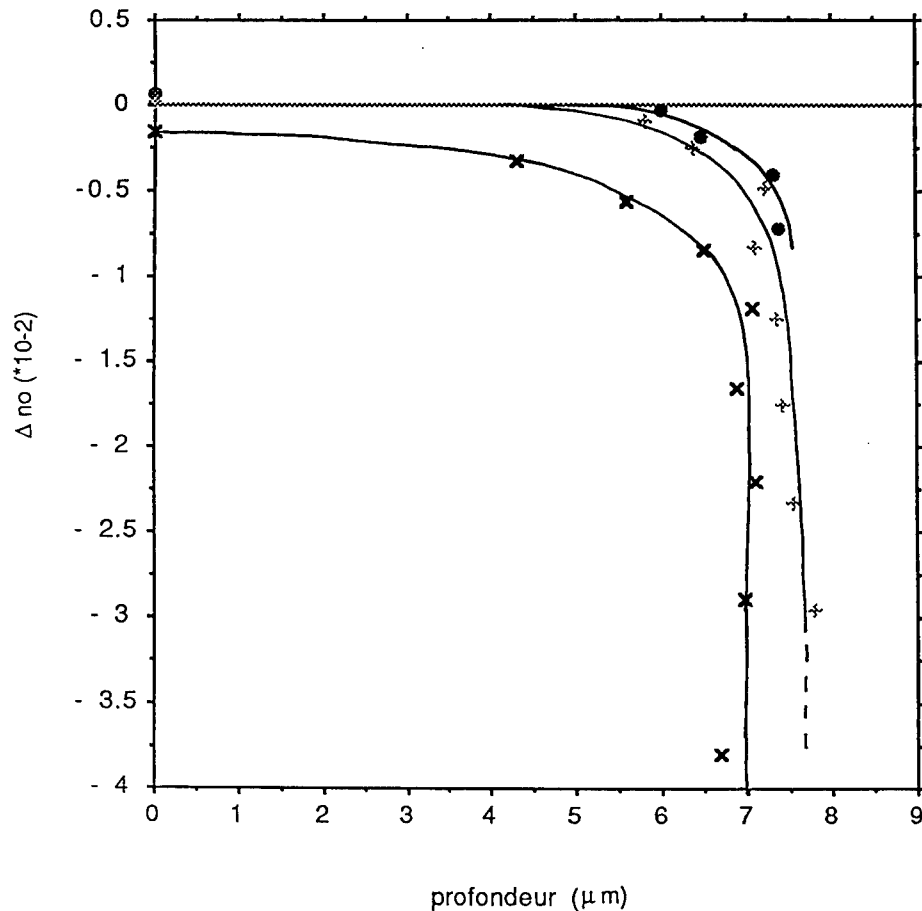
FIGURE 2  Ordinary refractive index change $n_0$ in lithium iodate waveguides. at a fixed energy (800 KeV) at various doses: 1 (●), 2 (+), $4.10^{16}$ ions/cm$^2$ (×)

Figure 1 gives the ordinary refractive index profile in waveguides obtained at implantation energies of 600 keV, 800 KeV and 1 MeV with a fluence of $4.10^{16}$ ions/cm$^2$. The related implantation area, calculated by TRIM simulation is indicated by thick bars on the depth scale. The flank position of the index barrier given by the TRIM program is in better agreement with measurement in LiIO$_3$ than for proton implanted LiNbO$_3$$^2$. The index change appears to be more abrupt for the low energy. These profiles show that the depth of refractive index barrier increases with energy.

Figure 2 shows index profiles obtained with ions fluences of 1, 2, and $4.10^{16}$ ions/cm$^2$, at 800 KeV. When the proton dose is increasing, the index barrier enlarges and becomes deeper. This phenomenon could be correlated with an increase of defects induced by nuclear collisions. The index at the surface tends to slightly decrease with ion dose and it can be related to defects created by the increasing electronic energy deposition with the fluence.

## 4   CONCLUSION

We do have elaborated planar waveguides in $LiIO_3$ by proton implantations. These implantations were performed at various beam energies and fluences and the corresponding ordinary index profiles were reconstructed. Optical properties after implantation seems to be well preserved since no absorption peak appears and no annealing procedure is required to obtain good waveguides. So lithium iodate might become a serious candidate for integrated optical applications.

REFERENCES

1.   P. D. Townsend, *Nucl. Instr. and Meth.*, **B46**, 18 (1990).
2.   P. Moretti, P. Thevenard, K. Wirl, P. Hertel, *Mat. Res. Soc. Symp. Proc.* **244**, 323 (1992).
3.   C. Rosso, P. Moretti, J. mugnier, D. barber, Y. Teisseyre, J. Bouillot, *Phys. Stat. Sol. (a)*, **139**, K137 (1993).
4.   H. Buesener, A. Renn, M. Brieger, F. von Moers and A. Hese, *Appl. Phys.* **B39**, 77 (1986).
5.   A. W. Warner and D. A. Pinnow, *J. Acoust. Soc. Amer.*, **477** (2), 791 (1969).
6.   D. S. Robertson and M. Roslington, *J. Phys. D: Appl. Phys.*, **4**, 1582 (1971).
7.   J. M. Desvignes and M. Remoissenet, *Mat. Res. Bull.*, **6**, 705 (1971)–710.
8.   J. M. White and P. F. Heidrich, *Appl. Opt.*, **15** (1), 151 (1976).
9.   J. F. Ziegler, J. P. Biersack and U. Littmark, Pergamon Press, New York, (1988).

# STRUCTURAL AND OPTICAL CHARACTERISTICS OF CRYSTALLIZED PbTiO$_3$ WAVEGUIDES PREPARED BY SOL-GEL PROCESS

C. URLACHER,* E. BERNSTEIN,* J. SERUGHETTI* and J. MUGNIER**

*Département de Physique des Matériaux (U.R.A. 172); **Laboratoire de Physico-Chimie des Matériaux Luminescents (U.R.A. 442) Université Claude Bernard, Lyon 1; 43 bld du 11 novembre 1918; 69622 Villeurbanne Cedex, France*

Crack free, transparent and crystallized sol-gel derived PbTiO$_3$ thin films were deposited on pyrex slide using the dip-coating technique. Both PbTiO$_3$ and Pb$_2$Ti$_2$O$_7$ phases were formed on monolayers whereas only pure PbTiO$_3$ perovskite was observed when depositing multilayers. Films microstructure consisted of a dense and polycrystalline layer with grain size of about 80 Å. Monolayers (about 120 nm thick) were monomode TE and TM with a refractive index around 2.01. Best optical waveguiding (over 10 mm) was achieved with monolayers when TM polarized light propagates and an optical loss of $7.5 \pm 0.8$ dB/cm was measured for the TM$_0$ mode.

*Key words*: PbTiO$_3$, Sol-Gel, Planar Waveguides.

## 1 INTRODUCTION

PbTiO$_3$ is a perovskite-type ferroelectric with a Curie temperature of 490°C and a large tetragonality (c/a = 1.06) which also presents large piezoelectric and pyroelectric effects.[1] PbTiO$_3$ thin films as planar passive waveguides have already been studied by V. E. Wood and S. L. Swartz,[2] who prepared PbTiO$_3$ films (n = 2.58 and 250 nm thick) on sapphire substrates with maximum optical waveguiding distances of about 1 mm.

The optical properties of the film strongly depend on the microstructure of the material so that several structural criteria (grain size, porosity...) must be taken into account to provide high quality transparent and crystallized waveguides.

Monolayer and multilayer films were prepared. Microstructural characterization of the films were examined by X-Ray diffraction (XRD), Transmission Electron Microscopy (TEM) and Scanning Electron Microscopy (SEM). Film quality was observed by optical microscopy examination. The 'm-lines spectroscopy' technique[3] was used to determine the refractive index and the thickness of thin films, and optical loss was finally measured.

## 2 EXPERIMENTAL

### 2.1 *Sol-Gel Processing*

The precursor materials used for preparing the lead titanate sol were lead acetate trihydrate Pb(OCOCH$_3$)$_2$, 3H$_2$O and titanium isopropoxide Ti(OCH(CH$_3$)$_2$)$_4$ (molar ratio Pb/Ti = 1). To prevent precipitation of TiO$_2$, titanium isopropoxide was first stabilized with acetylacetone.[4] The lead salt solution was prepared by dissolving lead acetate trihydrate in an acetic acid solution (concentration = 700g/l). The required amount of methanol and the stoechiometric composition of water (1 mole of water per mole of ethoxy

FIGURE 1    Microstructure of PbTiO$_3$ monolayer obtained by Transmission Electron Microscopy. A typical large grain appeared on the dense polycrystalline film.

group) were then added under strong agitation. A lead titanate yellow sol was obtained which was clear and did not gelify after a 3 month storage.

## 2.2 *Thin Films Fabrication*

The films were deposited by dip-coating onto sonically cleaned amorphous pyrex plate substrates (borosilicate glass) with a withdrawal speed of 50 mm/min. Crystallization of monolayer and multilayer films was conducted at 600°C under oxygen flow. For multilayers, the films were first heat treated at 400°C between each coating to promote organic burnout and partial densification of the film before crystallization.

## 3    RESULTS AND DISCUSSION

### 3.1 *Film Characterization*

*Microstructure* TEM investigations conducted on monolayers revealed that films consisted of a dense, uniform and polycrystalline film made up by crystallites with average grain size of about 80 Å. SEM micrograph observations confirmed the smooth and uniform aspect of the surface. However, large grains (2500 Å) formed by a set of small cyrstallites were sometimes observed as shown in Figure 1. They randomly appeared on the film and probably affected waveguiding in PbTiO$_3$ monolayers.

FIGURE 2   Optical loss of a monolayer PbTiO₃ waveguide for the $TM_0$ excited mode (632.8 nm).

*Diffraction analysis*   X-Ray Diffraction was conducted on a seven layer PbTiO₃ film annealed at 600°C. The broad amorphous peak of the pyrex substrate was superposed to crystal peaks. The resulting crystal structure of sol-gel derived thin film corresponded to the tetragonal (P4/mm) PbTiO₃ perovskite phase. Diffraction patterns were difficult to obtain for thin films, as to be expected. Monolayer crystallization was then observed by TEM diffraction. The diffraction rings of this layer corresponded to the d spacings of the tetragonal PbTiO₃ perovskite structure. However, trace of a second phase consisting of Pb₂Ti₂O₇ crystals was also detected.

### 3.2 *Optical Properties*

In the 'm-lines spectroscopy' technique, described by Ulrich and Torge[3], two propagating modes are at least required to provide a precise determination of both refractive index and thickness of single or multilayer thin films, assuming a step index waveguide structure. The incident light was polarized either parallel or perpendicular to the waveguide plane so that both 'transverse electric' (TE) and 'transverse magnetic' (TM) modes were considered as guided modes. The optical measurements were made at a wavelength of 632.8 nm.

A seven layers PbTiO₃ film was found to support three TE modes ($TE_0$, $TE_1$, $TE_2$), and three TM modes ($TM_0$, $TM_1$, $TM_2$). This film was 583 nm thick and presented different refractive indices depending on the propagating mode probably due to a preferred crystals orientation. The index of refraction varied from 2.249 for the TM polarization to 2.271 when light was TE polarized. Those values are lower than bulk single-crystal PbTiO₃(2.66)[2] because of the porosity caused by the sol-gel process. The multilayer films were opalescent so that waveguiding can not be observed.

Thinner films were monomode TE and TM. Thickness of these films was directly measured on SEM cross-section micrograph. The thickness of the monolayer was about 120 nm. Its corresponding index of refraction, determined by Ulrich and Torge equations,

was around 2.01 due to the low precision of thickness measurement method. Unlike the $TiO_2$ films,[5] the refractive indice of a monolayer waveguide is lower than that of a multilayer where the remaining pores were probably partially filled. Moreover the presence of $Pb_2Ti_2O_7$ pyrochlore phase probably reduced refractive indice of the monolayer.

Monolayer films were homogeneous, transparent and crack free. It has been observed that the $TM_0$ mode propagated with significantly less loss than the $TE_0$ mode. Indeed a maximum waveguiding distance of about 3 mm was obtained in $TE_0$ mode whereas TM polarization provided waveguiding distances of over 10 mm. The attenuation coefficient ($\alpha$) was calculated by measuring the scattered intensity at different distance all along the waveguiding, as represented in Figure 2. Optical loss values of $7.5 \pm 0.8$ dB/cm were obtained for the $TM_0$ mode. An attenuation coefficient of about 90 dB/cm could be estimated when light was TE polarized. The attenuation was believed to be primarily due to a preferred crystal orientation as observed for refractive indices measurements.

## 4  CONCLUSION

$PbTiO_3$ waveguides were prepared by the sol-gel method and their structural and optical properties have been investigated. Waveguiding distances obtained in this study on polycrystallized lead derived thin film were the best known up to date.

The difference of attenuation between the TE and TM modes probably suggested a proper orientation of the guiding $PbTiO_3$ layer although films were deposited on an amorphous substrate.

Further investigations including crystal orientation control and substrate changes are carried out to improve the optical quality of $PbTiO_3$ thin films.

REFERENCES

1. C. Chen and D. F. Ryder, *J. Am. Ceram. Soc.* **72**, [8] 1495–98 (1989).
2. S. L. Swartz, S. D. Ramamurthi, J. R. Busch and V. E. Wood, *Mat. Res. Symp. Proc.* **243**, 533–544 (1992).
3. R. Ulrich and R. Torge, *Appl. Opt.* **12**, 2901–2908 (1973).
4. M. A. Aegerter, Y. Charbouillot, N. Mohallem and L. H. De Godoy, *Ultrastructure Processing of Advanced Materials*, **53**, 613–627 (1992).
5. B. E. Yoldas, *Appl. Opt.*, **21**, 2960–2964 (1982).

# SHG PHASE MATCHING CONDITIONS FOR UNDOPED AND DOPED LITHIUM NIOBATE

U. SCHLARB,[+] A. REICHERT,[+] K. BETZLER,[+] M. WÖHLECKE,[+] B. GATHER,[*] T. VOLK[♯] and N. RUBININA[‡]

[+]*Fachbereich Physik, Universität Osnabrück, 49069 Osnabrück, Germany*[*]
*Institut für Chemie, Universität Osnabrück, 49069 Osnabrück, Germany;*
[♯]*Institute of Crystallography Russian Acad. Sci., Moscow 117333, Russia;*
[‡]*Moscow State University, Moscow, Russia*

We measured the refractive indices of undoped and Zn- or Mg-doped lithium niobate in the wavelength range 400 to 1200 nm. The results are described by a generalized Sellmeier equation which takes into account the defect structure of the material. From the generalized Sellmeier equation a simple relation between the phase matching temperature for noncritical type I second harmonic generation (SHG) and the internal critical phase matching angle is derived. Good correspondence with experimental data over a wide composition and fundamental wavelength range is observed.

*Key words*: $LiNbO_3$, refractive index, nonlinear effects.

## 1 INTRODUCTION

Lithium niobate can be fabricated with variable $Li_2O$ contents (46–50 mol%) and additional dopants. For Mg and Zn doping an abrupt change of several physical properties at a certain doping level (threshold concentration) is observed.[1,2] Since many optical applications depend on the refractive indices, a precise description of the refractive indices of $LiNbO_3$ as a function of the composition is of great importance. Here we use a Sellmeier equation with four independent variables—Li content, dopant concentration (Mg or Zn), wavelength and temperature[3]—to derive a simple relation between the phase matching temperature for noncritical type I second harmonic generation and the phase matching angle.

## 2 EXPERIMENTAL

We measured the refractive indices of undoped and doped lithium niobate by an interferometric technique[4] in a wavelength range from 400 to 1200 nm. Five samples were grown by the Czochralski technique from melts with varying Li content and were characterized by means of their Curie temperature.[5] Stoichiometric material was prepared with $K_2O$ in the melt[6] or by the vapour transport equilibration (VTE) technique.[7] The doped samples were grown from a congruent melt with up to 9 mol% XO (X = Mg, Zn). The Mg concentration in the crystals was determined applying literature data,[8] the Zn content was measured using an electron microprobe.[9]

## 3 RESULTS

The refractive indices are excellently described by our generalized Sellmeier equation which takes into account the defect structure of Li-deficient and Mg- or Zn-doped lithium niobate.

$$T_{PM} = [ (1067)^2 + 3*10^6 \cos^2\theta_{PM} ]^{1/2} - 1042$$



FIGURE 1   Phase matching temperature $T_{PM}$ for noncritical type I second harmonic generation as a function of the internal phase matching angle $\theta_{PM}$. The curve is derived from the generalized Sellmeier equation (see text). Data points represent our measurements and results reported by other authors.[13,14] Fundamental wavelength and crystal composition for each data point are listed in the inset.

The equation consists of several oscillator terms representing the contribution from the $NbO_6$-octahedron $(A_{0,i}/(\lambda_{0,i}^{-2}-\lambda^{-2}))$ and approximated contributions from the IR and far UV region $(A_{IR,i} \lambda^2 + A_{UV})$. The temperature dependence of the resonance wavelength is assumed to be proportional to the temperature dependence of the band gap $\lambda_{0,i}(T) = \lambda_{0,i} + \mu_{0,i}(f(T)-f(T_0))$, where $f(T)$ can be derived by an expression obtained by Manoogian and Woolley.[10] Since the oscillator strength is proportional to the number of oscillators per volume, we approximate the contributions from Nb antisite defects and from the dopant X (X = Mg, Zn) by $A_{Nb_{Li},i}c_{Nb_{Li}}/(\lambda_{0,i}^{-2}-\lambda^{-2})$ and $A_{X,i}c_X/(\lambda_{0,i}^{-2}-\lambda^{-2})$, respectively. For a detailed derivation the reader is referred to Schlarb and Betzler.[3] The generalized Sellmeier

equation is given by

$$n_i^2 = \frac{A_0, i + A_{\mathrm{Nb_{Li}},i} c_{\mathrm{NB_{Li}}} + A_{X,i} c_X}{(\lambda_{0,i} + \mu_{0,i} F)^{-2} - \lambda^{-2}} - A_{\mathrm{IR},i}^2 + A_{\mathrm{UV}}$$

(1)

with

$$c_{\mathrm{Nb_{Li}}} = \begin{cases} \dfrac{2}{3}(50 - c_{\mathrm{Li}}) - c_X/\alpha_X & \text{for } c_X < \alpha_X \dfrac{2}{3}(50 - c_{\mathrm{Li}}) \\ 0 & \text{for } c_X \geq \alpha_X \dfrac{2}{3}(50 - c_{\mathrm{Li}}) \end{cases}$$

$$\alpha_{\mathrm{Mg}} = 5.0; \alpha_{\mathrm{Zn}} = 6.5;$$

$$F = f(T) - f(T_0), T_0 = 24.5°\mathrm{C};$$

$$f(T) = (T + 273)^2 + 4.0238 \times 10^5 [\coth\left(\frac{261.6}{T + 273}\right) - 1].$$

$c_X$ is the dopant concentration given in mol% XO (X = Mg, Zn), $c_{\mathrm{Li}}$ denotes the initial Li content, i.e., the ratio [Li$_2$O]/([Nb$_2$O$_5$]+[Li$_2$O]) extrapolated to undoped material (measured in mol% Li$_2$O). The parameters $\alpha_{\mathrm{Mg}}$ and $\alpha_{\mathrm{Zn}}$ (which are proportional to the so-called threshold concentration) were estimated from empirical results reported by Schmidt et al.[11] and Volk et al.[2] for Mg- and Zn-doped material, respectively. The wavelength $\lambda$ is given in nm, T in °C, and $i = e$ denotes the extraordinary, $i = o$ the ordinary light polarization.

The parameters for equation (1) were calculated by a fit to our measured refractive index data for undoped and Mg- or Zn-doped lithium niobate and temperature dependent literature data.[12,7] The standard deviation was $\Delta n = 2 \times 10^{-3}$. Numerical results for the parameters are listed in Table I.

Table I
Parameters of the generalized Sellmeier equation. For the definition see Eq. (1) in the text.

| $n_o$ | | $n_e$ | |
|---|---|---|---|
| $\lambda_{0,o}$ | $= 223.219$ | $\lambda_{0,e}$ | $= 218.203$ |
| $\mu_{0,o}$ | $= 1.1082 \times 10^{-6}$ | $\mu_{0,e}$ | $= 6.4047 \times 10^{-6}$ |
| $A_{0,o}$ | $= 4.5312 \times 10^{-5}$ | $A_{0,e}$ | $= 3.9466 \times 10^{-5}$ |
| $A_{\mathrm{Nb_{Li}},o}$ | $= -7.2320 \times 10^{-8}$ | $A_{\mathrm{Nb_{Li}},e}$ | $= 11.8635 \times 10^{-7}$ |
| $A_{\mathrm{Mg},o}$ | $= -7.3548 \times 10^{-8}$ | $A_{\mathrm{Mg},e}$ | $= 7.6243 \times 10^{-8}$ |
| $A_{\mathrm{Zn},o}$ | $= 6.7963 \times 10^{-8}$ | $A_{\mathrm{Zn},e}$ | $= 1.9221 \times 10^{-7}$ |
| $A_{\mathrm{IR},o}$ | $= 3.6340 \times 10^{-8}$ | $A_{\mathrm{IR},e}$ | $= 3.0998 \times 10^{-8}$ |
| $A_{\mathrm{UV}}$ | $= 2.6613$ | $A_{\mathrm{UV}}$ | $= 2.6613$ |

The generalized Sellmeier equation allows us to derive a simple relation between the phase matching temperature $T_{\mathrm{PM}}$ for colinear noncritical type I second harmonic generation and the internal phase matching angle $\theta_{\mathrm{PM}}$ measured at room temperature.

Defining $\hat{n}_i = n_i(c_{\mathrm{Li}}, c_X, \lambda, T_0)$ and $\tilde{n}_i = n_i(c_{\mathrm{Li}}, c_X, \lambda/2, T_0)$ as the refractive indices for the fundamental ($\lambda$) and harmonic ($\lambda/2$) wavelengths at room temperature, respectively, the temperature phase matching condition $n_o(c_{\mathrm{Li}}, c_X, \lambda, T_{\mathrm{PM}}) = n_e(c_{\mathrm{Li}}, c_X, \lambda/2, T_{\mathrm{PM}})$ can be written as

$$(\tilde{n}_e^2 - \hat{n}_o^2) + F \frac{\partial(\tilde{n}_e^2 - \hat{n}_o^2)}{\partial F} |_{F=0} = 0,$$

(2)

and the parameter $F$ is approximated with coth $x \approx 1/x$ yielding

$$F \approx (T_{\mathrm{PM}} + T_s)^2 - (T_s + T_0)^2; T_s = 1042. \qquad (3)$$

The angle phase matching condition $\hat{n}_o^{-2} = \tilde{n}_o^{-2}\cos^2\theta_{\mathrm{PM}} + \hat{n}_e^{-2}\sin^2\theta_{\mathrm{PM}}$ can be written as

$$\tilde{n}_e^2 - \hat{n}_o^2 = \cos^2\theta_{\mathrm{PM}}[\hat{n}_o^2\frac{\tilde{n}_e^2}{\hat{n}_o^2} - \hat{n}_o^2] \approx \cos^2\theta_{\mathrm{PM}}[\tilde{n}_e^2 - \tilde{n}_o^2], \qquad (4)$$

where $\theta_{\mathrm{PM}}$ denotes—as already mentioned—the direction of propagation in the crystal with respect to the optical axis. A simple calculation yields

$$T_{\mathrm{PM}} = \sqrt{(T_s + T_0)^2 + \gamma(\lambda)\cos^2\theta_{\mathrm{PM}}} - T_s \qquad (5)$$

$$\text{with } \gamma(\lambda) \approx (\tilde{n}_o^2 - \hat{n}_e^2)[\frac{\partial(\tilde{n}_e^2 - \hat{n}_o^2)}{\partial F}]^{-1} \,|_{F=0, c_{\mathrm{Li}}=50, c_{\mathrm{X}}=0}$$

In the wavelength range 1000–1200 nm the parameter $\gamma(\lambda)$ varies between $2.8 \times 10^6$ and $3.2 \times 10^6$, we therefore neglect the dispersion and use $\gamma \approx 3 \times 10^6$. In Figure 1 the relation given in Eq. (5) is depicted and compared with experimental data. The results for a variety of crystal compositions and fundamental wavelengths show that the relation is a good approximation for temperatures up to at least 250°C, a maximum deviation of about 20°C is observed. Eq. (5) therefore allows to estimate the phase matching temperature by simply measuring the more easily accessible phase matching angle.

REFERENCES

1. D. A. Bryan, R. Gerson, and H. E. Tomaschke, *Appl. Phys. Lett.* **44**, 847 (1984).
2. T. R. Volk and N. M. Rubinina, *Fiz. Tverd. Tela* (Leningrad) **33**, 1192 (1991), [*Sov. Phys. Solid State* **33**, 674 (1991)].
3. U. Schlarb and K. Betzler, *Phys. Rev.* **B50** (1994), in press.
4. U. Schlarb and K. Betzler, *Ferroelectrics* **126**, 39 (1992).
5. P. F. Bordui, R. G. Norwood, D. H. Jundt, and M. M. Fejer, *J. Appl. Phys.* **71**, 875 (1992).
6. G. I. Malovichko, V. G. Grachev, E. P. Kokanyan, O. F. Schirmer, K. Betzler, B. Gather, F. Jermann, S. Klauer, U. Schlarb, and M. Wöhlecke, *Appl. Phys.* **A56**, 103 (1993).
7. D. H. Jundt, M. M. Fejer, and R. L. Byer, *IEEE J. Quantum Electron.* **26**, 135 (1990).
8. L. J. Hu, Y. H. Chang, I. N. Lin, and S. J. Yang, *J. Cryst. Growth* **114**, 191 (1991).
9. U. Schlarb, M. Wöhlecke, B. Gather, A. Reichert, K. Betzler, T. Volk, and N. Rubinina, J. Opt Mat., in print.
10. A. Manoogian and J. C. Woolley, *Can. J. Phys.* **62**, 285 (1984).
11. N. Schmidt, K. Betzler, and S. Kapphan, *Cryst. Latt. Def. and Amorph. Mat.* **15**, 103 (1987).
12. G. J. Edwards and M. Lawrence, *Opt. Quantum Electron.* **16**, 373 (1984).
13. M. V. Hobden and J. Warner, *Phys. Lett.* **22**, 243 (1966).
14. H. Y. Shen, H. Xu, Z. D. Zeng, W. X. Lin, R. F. Wu, and G. F. Xu, *Appl. Opt.* **31**, 6695 (1992).

# PHASE-CONJUGATE WAVES GENERATED BY ANISOTROPIC FOUR-WAVE MIXING IN LiNbO3 AND LiTaO3 OPTICAL WAVEGUIDES

## D. KIP and E. KRÄTZIG

*Universität Osnabrück, Fachbereich Physik, Barbarastraße 7,
49069 Osnabrück, Federal Republic of Germany Phone: +49 541/969-2660; FAX: +49
541/969-2670*

We report on anisotropic four-wave mixing in planar optical LiNbO3 and LiTaO3 waveguides fabricated by indiffusion of titanium and iron layers. The generation of phase-conjugate waves in the waveguides is demonstrated, and the experimental results are compared to numerical solutions of the corresponding system of coupled wave equations. We observe a different behaviour of the phase-conjugate wave power on pump power in LiNbO3 and LiTaO3 waveguides, respectively. While the reflectivity of the signal beam saturates in LiTaO3 for strong pump beams, there is a distinct increase in LiNbO3.

*Key Words*: LiNbO3, LiTaO3, Waveguides, Four-Wave Mixing, Phase Conjugation.

## 1 INTRODUCTION

Photorefractive crystals like LiNbO3, LiTaO3, KNbO3 or BaTiO3 are suitable media for frequency degenerate two- (TWM) and four-wave mixing (FWM) allowing for amplification and phase conjugation of coherent light beams.[1,2] Besides the widely investigated nonlocal nonlinearities owing to diffusion of carriers[3] or nearly degenerate wave mixing [4], photovoltaic currents excited by circularly polarized light[5] also permit efficient steady-state energy transfer and phase conjugation.[6]

In LiNbO3 and LiTaO3 crystals, orthogonally polarized waves can write holographic gratings via photovoltaic currents, enabling beam coupling with nearly full energy exchange and the generation of phase-conjugate waves. The pump waves are orthogonally polarized with respect to the signal and phase-conjugate waves, respectively, and thus the interaction is called frequency degenerate anisotropic wave mixing. In this letter we demonstrate anisotropic FWM in waveguides experimentally and compare our data with theoretical results.

## 2 COUPLED-WAVE EQUATIONS

Following from a phenomenological theory,[5] the polarisation-dependent photovoltaic current density is given by

$$j_k^{ph} = \beta_{klm}^s \, E_l^* \, E_m + i \, \beta_{klm}^a \, E_l^* \, E_m,\tag{1}$$

where $\beta^{s,a}$ are the real linear (symmetric) and circular (antisymmetric) components of the photovoltaic tensor and $E_{l,m}$ are the interacting light fields.

When the crystal is illuminated, the photovoltaic current causes the buildup of a periodic space-charge field $E_k$, which modulates the dielectric tensor via the electrooptic effect, $\Delta\epsilon_{ij} = -\epsilon_{ii}r_{ijk}E_k\epsilon_{jj}$, where $r_{ijk}$ are the electrooptic tensor components. The perturbation $\Delta\epsilon$ has unshifted components according to the tensor elements $\beta^s$ and
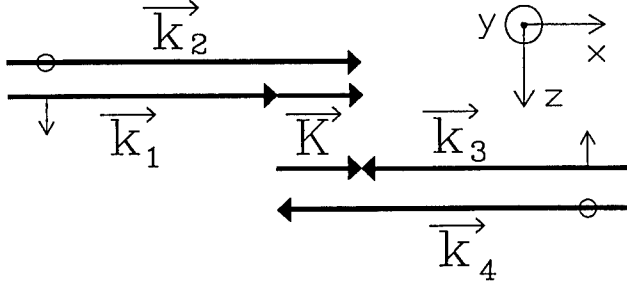
FIGURE 1    Interaction scheme of anisotropic FWM in LiNbO$_3$ waveguides $(n_0 > n_e)$ with $k_{1,3} = 2\pi n_3^*/\lambda$: TE wave vector, $k_{2,4} = 2\pi n_0^*$: TM wave vector and $K = 2\pi/\lambda$: grating vector.

components shifted by $\pi/2$ according to $\beta^a$, relative to the isophase surfaces with a phase difference of the interacting light fields $E_{l,m}$ of $2p\pi$ with $p = 0, 1, 2, \dots$ . As is well known,[3,6] in two-beam coupling the shifted grating is responsible for energy exchange between the two light beams. We investigate the interaction of an extraordinary (TE) polarized signal wave 1 propagating along the +x-axis and two ordinarily (TM) polarized counterpropagating (+x and −x) pump waves 2 and 4 in a planar y-cut waveguide (Figure 1). As has been shown in[7] in detail, in this configuration only orthogonally polarized beams travelling in the same direction can write a grating, thus reflection gratings (e.g. $\vec{k}_1 - \vec{k}_4$) can be neglected here. The waves 1 and 2 write a phase grating with wave vector $\vec{K} = \vec{k}_2 - \vec{k}_1$ and grating period $\Lambda = 2\pi/K = \lambda/(n_o^* - n_e^*)$, where $n_{o,e}^*$ are the effective refractive indices of the TM and TE modes and $\lambda$ is the vacuum light wavelength. In TWM, energy is exchanged due to the shifted part of the grating. In the case of FWM, anisotropic diffraction of wave 4 from the grating written by the waves 1 and 2 generates the extraordinarily (TE) polarized wave 3, the phase-conjugate replica of wave 1. The vector of the grating recorded by the waves 3 and 4, $\vec{K} = \vec{k}_3 - \vec{k}_4$, is identical to the initial one.

Each light wave $E$ is separated into an amplitude A and a normalized component of electric field (mode) $U$, $E(x,y) = A(x)\, U(y)$. The coupling equations for anisotropic wave mixing can be written in the form:[6]

$$\frac{dA_1}{dx} = \sqrt{h_2/h_1}/n_e^*(\gamma|A_2|^2 A_1 - \gamma^* A_2 A_4 A_3^*) - \frac{\alpha_1}{2} A_1, \tag{2}$$

$$\frac{dA_2}{dx} = \sqrt{h_1/h_2}/n_o^*(-\gamma^*|A_1|^2 A_2 - \gamma A_1 A_3 A_4^*) - \frac{\alpha_2}{2} A_2, \tag{3}$$

$$\frac{dA_3}{dx} = \sqrt{h_1/h_2}/n_e^*(-\gamma^*|A_4|^2 A_3 - \gamma^* A_4 A_2 A_1^*) - \frac{\alpha_1}{2} A_3, \tag{4}$$

$$\frac{dA_4}{dx} = \sqrt{h_1/h_2}/n_o^*(-\gamma^*|A_3|^2 A_4 - \gamma A_3 A_1 A_2^*) - \frac{\alpha_2}{2} A_4, \tag{5}$$

$$\Re(\gamma) = \frac{\omega n_o^{*2} n_e^{*2}}{2c}\chi(x)r_{232}\beta_{232}^a, \qquad \Im(\gamma) = \frac{\omega n_o^{*2} n_e^{*2}}{2c}\chi(x)r_{232}\beta_{232}^s \tag{6}$$

$$\chi(x) = \frac{1}{\sqrt{h_1 h_2}} \int U_{TE,3}(y)^* \left[\frac{U_{sc,2}(y)}{\sigma_d + \sigma_2^0 2 I(x,y)}\right] U_{TM,2}(y)\, dy. \tag{7}$$
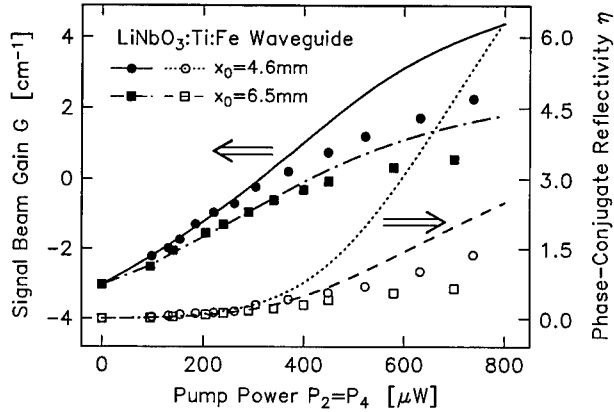
FIGURE 2  Dependence of signal wave gain (filled symbols, experimental; upper curves, theoretical) and phase-conjugate reflectivity (open symbols, experimental; lower curves, theoretical) on the input power for two different interaction lengths $x_0$.

Here $h$ is the effective thickness of the TE and TM mode, according to the normalization $\int U_i^* U_j dy = h_i \delta_{ij}, \sigma_d$ and $\sigma^0$ are dark and specific conductivity, $\alpha$ is the absorption coefficient, and $\omega$ and c are frequency and speed of light. We have assumed equal modes and absorption coefficients of the waves 1, 3, and 2, 4, respectively. The overlap of the interacting light fields with the space-charge field is expressed by the dimensionless factor $\chi$. The spatial distribution of the space-charge field, $U_{sc}$, follows from a differential equation which contains the modes $U_{TE,TM}$.[7]

## 3  FOUR-WAVE MIXING

Our $LiNbO_3$:Ti:Fe and $LiTaO_3$:Ti:Fe waveguides are prepared by successive in-diffusion of thin titanium and iron layers in y-cut samples. Because of the large content of iron the $LiNbO_3$ waveguides exhibit high dark conductivity of the order of some $10^{-11}$ $AV^{-1}m^{-1}$, considerably exceeding photoconductivity. In comparison to it, in our $LiTaO_3$ waveguides photoconductivity is dominating.

To reach a high phase-conjugate reflectivity, mode combinations with large spatial overlap $\chi$, high photovoltaic constant $\beta$ and comparatively low absorption $\alpha$ are choosen. Figure 2 shows the dependence of the signal beam gain $G = x_0^{-1}\ln(P_{1,out}/P_{1,in})$, and phase-conjugate reflectivity $\eta = P_{3,out}/P_{1,in}$(both $TE_5$ modes) as a function of pump wave power $P_2 = P_4$ (both $TM_5$ modes) for a $LiNbO_3$ waveguide and two different interaction lengths $x_0$. Here the values $\beta_{232}^a = 4.9 \cdot 10^{-13}$ $A/V^2$ and $\left|\beta_{232}^s\right| = 3.0 \cdot 10^{-13}$ $A/V^2$ obtained by measurements of two-beam coupling and diffraction efficiency are used.[7]

Because of the high absorption $(\alpha \simeq 0.3$ $mm^{-1})$ in the waveguide the outcoupled powers of the signal and the phase-conjugate beam are rather small. Nevertheless, for input powers of around 700 $\mu W$ the phase-conjugate reflectivity exceeds values of one (for $x_0 = 4.6$ mm). This value can be further enlarged by a factor of 2 when the interaction length is adjusted to an optimum value. Calculations with the same input powers and waveguide properties as above show that an interaction length of 3.0 mm promises the highest phase-conjugate reflectivities. In this experiment, however, a further reduction of

FIGURE 3   Dependence of signal wave gain (filled circles, experimental; solid curve, theoretical) and phase-conjugate reflectivity (open circles, experimental; dotted curve, theoretical) on the input power.



FIGURE 4   Temporal development of signal and phase-conjugate wave power for different input pump powers. In the first part ($t < 90$ s), pump wave (4) is off (TWM). At $t = 90$ s wave (4) is switched on, and additionally amplification owing to FWM occurs.

the interaction length was not possible because of the non-rectangular prisms.

Figure 3 shows the signal gain and reflectivity for a LiTaO$_3$:Ti:Fe waveguide. Owing to the (intensity dependent) photoconductivity, both values saturate for higher pump power because of the reduced amplitude of the space-charge field at high light intensities. The maximum reflectivity is here 9%.

The deviations between theory and experiment in Figure 2 for the LiNbO$_3$ waveguide can be explained by holographic scattering. In Figure 4 the temporal development of signal beam amplification and phase-conjugate wave power is shown for different pump wave powers. During $t = 0$ to $t = 90$ s, only signal wave (1) and pump wave (2) are switched on

(TWM), while pump wave 4 is off. At $t = 90$ s the second pump wave is switched on, and the signal wave is additionally amplified by FWM. For increasing pump power level, we observe increasing losses due to holographic scattering of light into the m-lines of the excited TM modes. This leads to a drastically reduced pump intensity. For example, for $P_{2,4} = 450$ $\mu$W, the new stationary value of the signal wave power is much lower than the value obtained by TWM. In LiTaO$_3$ waveguides, we do not observe holographic scattering, and the agreement of theory and experiment is fairly good.

In summary, we observe efficient anisotropic FWM in LiNbO$_3$:Ti:Fe and LiTaO$_3$:Ti:Fe waveguides with reflectivities of the phase-conjugate signal exceeding values of one for the former material and 9% for the last one. Comparison with the solution of the corresponding coupled wave equations shows that scattering in the LiNbO$_3$ waveguides limits the input pump power. By further reduction of undesired losses (e.g. improvement of surface quality) and optimized interaction length, still higher values for the reflectivity are expected.

## REFERENCES

1. M. Cronin-Golomb, B. Fisher, J. White and S. Yariv, *IEEE J. of Quant. Electron.* **20**, 12 (1984).
2. S. G. Odoulov and M. S. Soskin, in *Photorefractive Materials and their Applications*, Volume 62 of Topics of Applied Physics (Springer Verlag 1989).
3. D. L. Staebler and J. J. Amodei, *J. Appl. Phys.* **43**, 1042 (1972).
4. Ph. Refregier, L. Solymar, H. Rajbenbach and J. P. Huignard, *J. Appl. Phys.* **58**, 45 (1985).
5. V. I. Belinicher and B. Sturman, *Sov. Phys. Uspheki* **23**, 199 (1980).
6. A. Novikov, S. G. Odoulov, O. Oleinik and B. Sturman, *Ferroelectrics* **75**, 295 (1987).
7. D. Kip, R. Fink, T. Bartholomäus and E. Krätzig, *Opt. Commun.* **95**, 33 (1993).
8. D. Kip and E. Krätzig, *Opt. Lett.* **17**, 1563 (1992).
9. P. K. Tien, R. Ulrich and R. J. Martin, *Appl. Phys. Lett.* **14**, 291 (1969).

# PHOTOINDUCED LINEAR DICHROISM IN SILLENITE CRYSTALS AND IN DIAMOND

H.-J. REYHER, J. RUSCHKE, AND F. MERSCH

*Universität Osnabrück, Fachbereich Physik, D–49069 Osnabrück, Germany*

By illumination with linearly polarized light, a strong optical linear dichroism (LD) can be created in undoped sillenites of the type $Bi_{12}TiO_{20}$(BTO). This photoinduced LD is stable in the dark at T < 77 K and is reversible by changing the direction of the polarization appropriately. The spectra of the LD and of the magnetic circular dichroism (MCD) of the $Bi_{Ti}^{4+}$ antisite reveal some similarities; however, there is no direct evidence for attributing the LD to $Bi_{Ti}^{4+}$. The observation of the LD as a function of the direction of the polarization is shown to give information on the symmetry of the center causing the LD. Comparative studies of nitrogen containing diamond support this fact.

*Key words*: Optical linear dichroism, center alignment, $Bi_{12}TiO_{20}$, diamond.

## 1 INTRODUCTION

$Bi_{12}MO_{20}(M = Ti, Ge, Si)$ (BMO) has been investigated since a long time, mainly because of its interesting photorefractive properties,[1] which are assumed to be due to intrinsic defects.[2,3] Recently, the intrinsic $Bi_M^{4+}$ antisite has been identified by optically detected magnetic resonance (ODMR) using the MCD of absorption.[4] Extensive MCD studies of both transition metal doped and nominally pure BMO crystals were performed by Briat *et al.*,[5] pointing out the importance of a 'reference state' in which $Bi_M^{4+}$ seems not to be populated. The present work shows that there is a further strong effect, apparently related to an intrinsic defect in BMO: the photoinduced LD. This effect may be of importance in MCD studies, because the measuring light may induce an LD which then influences the MCD signal. Also, photoinduced LD may be used for writing holograms using orthogonally polarized light waves.[6] On the other hand, the study of this effect in connection with a suitable model gives important information on the underlying defect centers.

## 2 EXPERIMENTAL

Undoped, as well as Al-doped (5% in the melt) BTO samples with a typical size of $3 \times 4 \times 1$ mm were investigated. The crystals were grown at the University of Osnabrück using the top-seeded solution growth (TSSG) method. A synthetic diamond was kindly supplied to us by Drukker, The Netherlands. Also, in an undoped BGO sample, photo-LD has been found, although no further measurements were performed there. The geometrical arrangement and important definitions are shown in Figure 1. Differently cut crystals have been applied, the orientation shown being an example. Experimentally, the LD is defined as $LD = (I_{\theta=0°}^{probe} - I_{\theta=90°}^{probe})/(I_{\theta=0°}^{probe} + I_{\theta=90°}^{probe})$, where $I^{probe}$ stands for the transmitted intensity of the probe beam with its polarization axis defined by $\theta$ (see Figure 1, also for the definition of LD'). The polarization of the probe beam was modulated by a photo-elastic modulator. $\theta$ also describes the polarization of the laser beam (Ar-ion laser, 488 nm), which was used to induce the LD. All experiments have been perfomed at T < 77 K. The crystals were not thermally bleached before the measurements.[5]

## 3   RESULT AND DISCUSSION

Figure 2 shows LD and LD' of BTO:Al as function of $\theta_{laser}$ in arbitrary units (configuration as in Figure 1). Characteristic patterns are obtained which change their orientation and shape for differently cut samples, e.g., with $\vec{k}_{light}$ ∥[110]. As the crystal belongs to a cubic



$$LD \propto I^{probe}_{\theta=0°} - I^{probe}_{\theta=90°} \quad \Leftrightarrow$$

$$LD' \propto I^{probe}_{\theta=+45°} - I^{probe}_{\theta=-45°} \quad \Leftrightarrow$$

FIGURE 1   Configuration of the experimental setup and definitions of LD and LD'. The shown orientation of the crystal was used to measure the patterns of Figure 2.



LD (%)                              LD' (%)

FIGURE 2   LD and LD' as functions of the angle of the laser polarization $\theta$. The crystal was oriented as shown in Figure 1. Note the zero circle, which is unusual for polar diagrams. The calibration is in percentage of the average transmitted intensity.

FIGURE 3    The photoinduced LD as a function of the photon energy of the probe beam. The LD was divided by the photon energy to obtain the proper shape of the absorption bands. Here, a different orientation of the crystal was used, and the polarization axis of the laser was chosen to obtain a maximum signal. The laser was off during the record.

group, only reorientable defect centers of lower local symmetry allow one to understand the existence of a photoinduced LD. In a preliminary analysis we assume only one species of anisotropic centers having various orientations according to the cystal's symmetry. If $n$ is the number of centers with a certain orientation, the electric field $E_0$ of the light wave impinging on the crystal with polarization $\vec{\eta}$ is attenuated by these centers according to $\vec{E}(d) = E_0 R^{-1}(\alpha, \beta, \gamma) T\, R(\alpha, \beta, \gamma)\vec{\eta}$, where $T = n(e^{-\alpha_1 d}\, e^{-\alpha_2 d}\, e^{-\alpha_3 d})I \cdot T$ is the transmission matrix (I = identity, main absorption coefficients $\alpha_{1,2,3}$, crystal thickness $d$) and $R$ is the rotation matrix depending on the center related Eulerian angles $\alpha, \beta, \gamma$. These equations allow to calculate the relative strength of LD and LD$'$ for a given set of $\alpha_{1,2,3}$ and $\alpha, \beta, \gamma$, that is, for a certain center orientation. Next, we assume that the orienting light excites all centers with a probability related to the attenuation $R^{-1}\, T\, R$, which is a function of $\alpha_{1,2,3}$ and $\alpha, \beta, \gamma$. Subsequently, all center directions are populated statistically, what amounts to an enhanced population of those centers that absorb least efficiently. This mechanism corresponds to that found for $F_A$ centers in alkali halides and Fe in YIG:Si.[7] Since we did n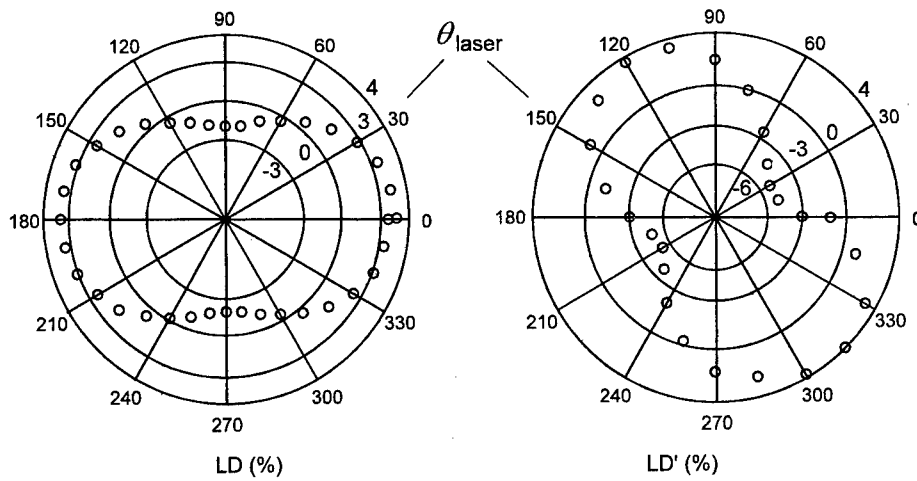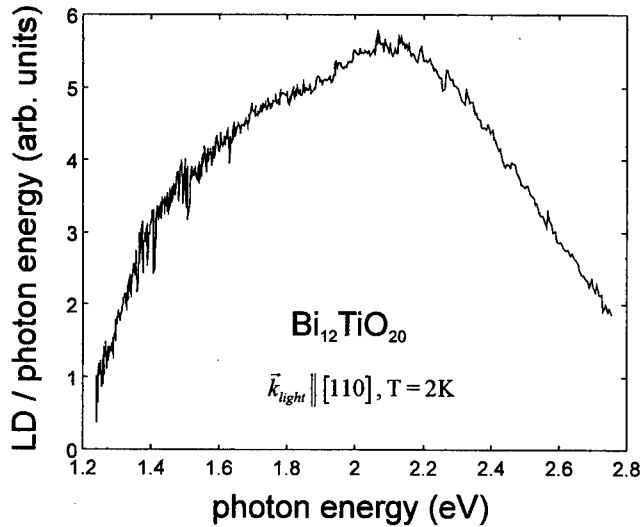ot yet complete a simulation program, we are restricted to a qualitative analysis of some simple cases, which allows one to understand patterns as shown in Figure 2. The patterns of BTO cannot be reproduced by assuming axial [111] centers ($\alpha_1 = \alpha_2 \neq \alpha_3$), but rather by orthorhombic [110] centers ($\alpha_1 \neq \alpha_2 \neq \alpha_3$). In diamond, containing N, we could also observe a photoinduced LD; there the LD patterns were compatible with axial [111] centers, as one would expect for the Pl nitrogen center.[8] The present analysis is possibly not unique; i.e., several center configurations may yield similar LD and LD$'$ patterns. Therefore, further experimental information was obtained by taking the spectrum of the photo-LD (Figure 3). The LD is observable in the same spectral range as the MCD of undoped BMO,[5] yet the spectrum is not structured enough to claim consistency between the bands of LD and MCD. Finding the same bands for LD and MCD

in undoped BMO, would give evidence that the LD stems from $Bi_M^{4+}$. This would be rather surprising since the $Bi_M^{4+}$ antisite was found to show highly isotropic ODMR signals.[4] We checked that the LD has no influence on the position or the shape of the ODMR signals of $BI_M^{4+}$. One may speculate that the observed photoinduced LD results from a diamagnetic charge state of $Bi_M$, but until now there is no evidence for this conclusion.

## ACKNOWLEDGMENT

## REFERENCES

1. P. Günther and J. -P. Huignard, eds., *Photorefractive Materials and Their Applications I* (Springer, Berlin, 1988).
2. S. L. Hou, R. B. Lauer, and R. E. Aldrich, *J. Appl. Phys.* **44**, 2652 (1973).
3. B. C. Grabmaier and R. Oberschmid, *Phys. Stat. Sol. (a)* **96**, 199 (1986).
4. H. -J. Reyher, U. Hellwig, and O. Thiemann, *Phys. Rev.* **B47**, 5638 (1993).
5. F. Ramaz, A. Hamri, B. Briat, V. Topa and G. Mitroaica, *Radiation Effects and Defects in Solids*, this meeting.
6. B. Sugg, H. Nürge, B. Faust, E. Ruza, R. Niehüser, H. -J. Reyher, and R. A. Rupp, *Optical Materials*, in press.
7. F. Lüty, in *Physics of Color Center*, W. B. Fowler, editor (Academic, New York, 1968); J. F. Dillon, Jr., E. M. Gyorgy, and J. P. Remeika, *J. Appl. Phys.* **41**, 1211 (1970).
8. J. Koppitz, O. F. Schirmer, and M. Seal, *J. Phys. C: Solid State Phys.* **19**, 1123 (1986).

# ABSORPTION SPECTRAL CHANGES WITH ULTRAVIOLET-ILLUMINATION IN GeO$_2$-SiO$_2$ GLASS FILMS PREPARED BY SPUTTERING DEPOSITION

JUNJI NISHII,[a] HIROSHI YAMANAKA,[a] HIDEO HOSONO,[b]
and HIROSHI KAWAZOE[b]

[a]*Osaka National Research Institute, AIST, 1–8–31, Midorigaoka, Ikeda, Osaka 563,
Japan;* [b]*Research Laboratory of Engineering Materials, Tokyo Institute of Technology,
Nagatsuta 4259, Midori-ku, Yokohama 227, Japan*

The absorption band peaking at 5.17 eV, which is due to neutral oxygen deficient vacancy, in rf-sputter deposited GeO$_2$-SiO$_2$ thin glass films was bleached by ultraviolet-illumination, and an intense absorption band was induced around 6.4 eV. The refractive index change calculated via Kramers-Kronig relations was of the order of $10^{-4}$, which was higher by one order of magnitude than those of bulk germanosilicate glasses prepared by VAD method. The concentration of Ge E' centers increased with the intensity of the 6.4 eV band. The oscillator strength of the 6.4 eV band, however, exceeded unity on the assumption that Ge E' centers exclusively induce this band. It was, therefore, concluded that not only Ge E' center but also other photochemically induced color centers give the 6.4 eV band, which is the origin of large refractive index change.

*Key words*: oxygen deficient vacancy, GeO$_2$-SiO$_2$ thin glass film, refractive index change.

## 1 INTRODUCTION

Oxygen deficient defects causing an absorption peak at 5 eV (5 eV band) in GeO$_2$-SiO$_2$ glasses play an essential role in the photon induced refractive index changes,[1,2] which are applicable for the formation of distributed Bragg reflectors.[3] The 5 eV band is gradually bleached by ultraviolet(uv)-illumination and a new intense absorption band is induced above 5.5 eV.[1,2] The increase in intensity of the latter is much larger than the decrease in that of the former. As a consequence, refractive index change ($\Delta$n) of the glass becomes positive via Kramers-Kronig relations. It is also generally agreed that the concentration of Ge E' centers is linearly increased with the decrease in absorptivity of 5 eV band.[1] However, no works have been reported so far the relationship between the band above 5.5 eV and Ge E' centers induced by uv-illumination, to our knowledge.

In our preceding paper,[4] it was reported that GeO$_2$-SiO$_2$ thin glass films prepared by rf-sputtering method exhibited the larger absorptivity changes around 5 eV than those of bulk glasses prepared by VAD method. In this study, we calculate the $\Delta$n by uv-illumination in GeO$_2$-SiO$_2$ thin films via Kramers-Kronig relations and discuss correlations between the major uv-induced optical band and Ge E' centers.

## 2 EXPERIMENTAL

Thin films of GeO$_2$-SiO$_2$ were prepared by the same procedures described in Ref. 4. Chemical compositions of resulting films were analyzed by XPS. UV illumination was carried out with an Hg lamp (200 W) at room temperature. X-band Electron Spin Resonance (ESR) spectra were measured at 300 K with a Brucker Model 300E applying 100 kHz field modulation. The concentration of Ge E' centers was evaluated by double numerical integration of fist-derivative spectra and comparison to a CuSO$_4$·5H$_2$O

FIGURE 1    Transmission spectra of $8GeO_2$-$92SiO_2$ thin glass film deposited on $SiO_2$ substrate. Solid line: as deposited, solid circle: annealed at 450°C for 1 h, open circle: after uv-illumination for 130 h.

reference crystal of known weight. Refractive index was measured by ellipsometry at an wavelength of 633 nm.

## 3    RESULTS

Figure 1 shows the absorption spectra of the $8GeO_2$-$92SiO_2$ thin film. A shoulder near 5 eV in as-deposited films became a distinct absorption peak centered a 5.17 eV by annealing the film at 450°C for longer than 30 min in vacuum. The 5.17 eV band was partly bleached by uv-illumination, and the increase in absortpion above 5.5 eV were recognized simultaneously. These spectral changes were saturated after uv-illumination longer than 70 h. Table I lists the saturated values of the absorptivity change $(-\Delta\alpha_\infty)$ at 5.17 eV. The film prepared by sputtering exhibited larger $-\Delta\alpha_\infty$ by an order of magnitude than bulk glasses prepared by VAD method.[2] A drastic increase in the concentration of Ge E' centers, though a trace amount of Ge E' centers ($< 10^{16}$ spins/cm$^3$) was recognized in as annealed films, was confirmed in ESR measurements. No other paramagnetic centers were observed. The ratio of $-\Delta\alpha_\infty$ to the concentration of Ge E' centers, $-\Delta\alpha_\infty$/[Ge E'], was $7.8 \times 10^{-17}$, which was close to those for bulk glasses ($6.7 \times 10^{-17}$).[2]

## 4    DISCUSSION

Figure 2 shows the difference spectrum of the $8GeO_2$-$92SiO_2$ thin film before and after uv-illumination. The absorption above 5.5 eV is due mainly to an intense uv-induced peak

FIGURE 2   UV-induced optical absorption (open circles) of 8GeO$_2$-92SiO$_2$ film. Dotted traces denote deconvoluted Gaussian components. Solid line indicates synthesized curve.

centered around 6.4 eV, which has not been assigned yet, as far as we know. Following the model by Atkins et al.,[5] the spectrum was successfully deconvoluted into four Gaussian components at 4.80, 5.17, 5.75 and 6.40 eV with the full width at half maximum (FWHM) of 1.00, 0.395, 0.300 and 0.900 eV, respectively. Russell et al.[6] suggested the change in refractive index is caused by densification of the glasses during uv-illumination. However, no change in film thickness ($< \pm 0.4\%$) was confirmed so far as our measurement by a profilometer or an ellipsometer. Then we estimated the photon induced refractive index change($\Delta$n) based on the color center model.[7,8] The $\Delta$n can be calculated by using the following equations(Kramers-Kronig relations):

$$\Delta n = C[\Delta\alpha/(1 - \lambda_0/\lambda)] \qquad (1),$$

where  $C = \{(n^2 + 2)^2/6n\} \cdot (W\lambda_0/2\pi^{3/2}E_0)$. Here,  $W = $ FWHM,  n = refractive index, $\lambda_0$ (nm) and $E_0$(eV) mean the peak positions of the uv-induced or bleached bands. Putting the values obtained by deconvolution into eq(1), the $\Delta$n was calculated as $1.1 \times 10^{-4}$ at 488 nm, which was much higher than that in the bulk glasses ($4.5 \times 10^{-5}$) irradiated by the high intensity KrF laser pules.[5]

Next interest is the structural origin of the uv-induced absorptions. We can estimate the population change for the uv-bleached band by using the following Smakula's approximation:[9]

$$\Delta N = [8.7 \times 10^{20} \, n/(n^2 + 2)^2]W \cdot \alpha/f \qquad (2)$$

Here n is the refractive index of the film, W is the FWHM of a band, $\Delta$N and $f$ are the population change and oscillator strength, respectively. When  $W = 0.395$ eV,

$\Delta\alpha = 83$ cm$^{-1}$ (see Figure 2) and $f = 0.38$,[2] the $\Delta N = 6.4 \times 10^{17}$ cm$^{-3}$, which is close to the concentration of uv-induced Ge E$'$ centers. However, the most intense absorption band at 6.4 eV(W $= 0.9$ eV, $\Delta\alpha = 175$ cm$^{-1}$) can not be attributed to only Ge E$'$ center because the calculated value of $f$ exceeds unity on the assumption that Ge E$'$ center exclusively gives the 6.4 eV band. It was suggested that a photobleachable defect (neutral oxygen mono-vacancy, i.e., Ge-Ge) is converted photochemically to a Ge E$'$ center, a Ge hole center and an electron.[2,10] Establishing the correlation between optical bands and relevant color centers is required to explain the drastic spectral changes in uv-illuminated germanosilicate glasses.

In conclusion, the intense absorption band was induced around 6.4 eV accompanying the bleach of 5.17 eV band after a prolonged uv-illumination in GeO$_2$-SiO$_2$ thin films prepared by sputtering deposition. The uv-induced refractive index change in the films was estimated to be of the order of $10^{-4}$, which was higher by one order of magnitude than those of bulk glasses. A drastic increase in concentration of Ge E$'$ centers ($10^{18}$spins/cm$^3$) was also confirmed by ESR. The uv-induced band around 6.4 eV, however, could not be attributed only due to Ge E$'$ centers because the oscillator strength exceed unity by the estimation. Photochemically induced other color centers besides Ge E$'$ might be required to explain such a large $\Delta n$ within the framework of Kramers-Kronig mechanism.

Table I

Saturated absorptivity changes of 5 eV band and the concentration of uv-induced Ge E$'$ center.

| Composition /mol% | Preparation Method | Refractive index* | $\Delta$ Absorptivity Change at 5 eV/cm$^{-1}$ | Concentration of Induced Ge E$'$ Center/spins/cm$^3$ |
|---|---|---|---|---|
| 8GeO$_2$-92SiO$_2$ | Sputtering | 1.470 | −83 | $1 \times 10^{18}$ |
| 5GeO$_2$-95SiO$_2$ | VAD | 1.464 | −2 | $2 \times 10^{16}$ |
| 10GeO$_2$-90SiO$_2$ | VAD | 1.471 | −3 | $6 \times 10^{16}$ |

*before uv-illumination

## REFERENCES

1. H. Hosono, Y. Abe, D. L. Kinser, R. A. Weeks, K. Muta and H. Kawazoe, *Phys. Rev.* **B46**, 11445(1992).
2. R. M. Atkins and V. Mizrahi, *Electron. Lett.* **28**, 1743(1992).
3. K. O. Hill, Y. Fujii, D. C. Johnson and B. S. Kawasaki, *Appl. Phys. Lett.* **32**, 647(1978).
4. J. Nishii, H. Yamanaka, H. Hosono and H. Kawazoe, *Appl. Phys. Lett.* **64**, 282(1994).
5. R. M. Atkins, V. Mizrahi and T. Erdogan, *Electron. Lett.* **29**, 385(1993).
6. P. St. Russell, D. P. Hand, Y. T. Chow and L. J. Poyntz, *Proc. SPIE* **1516**, 47(1991).
7. D. P. Hand and P. St. J. Russell, *Opt. Lett.* **15**, 102(1990).
8. J. E. Roman and K. A. Winick, *Opt. Lett.* **18**, 808(1993).
9. A. Smakula, *Z. Phys.* **59**, 603(1930).
10. R. Kashyap, G. D. Maxwell and D. L. Williams, *Appl. Phys. Lett.* **62**, 214(1993).

# ION-BEAM/CHANNELING CHARACTERIZATION OF LiNbO₃: INTERACTION BETWEEN IMPURITY SITES

L. REBOUTA,[1] M. F. DA SILVA,[2] J. C. SOARES,[3] M. T. SANTOS,[4] E. DIÉGUEZ[4] and F. AGULLÓ LÓPEZ[4]

[1]*Departamento de Física, Universidade do Minho, Largo do Paço, 4719 Braga, Portugal;* [2]*Departamento de Física, Instituto de Ciências e Engenharia Nucleares, INETI, 2685 Sacavém, Portugal;* [3]*Centro de Física Nuclear da Universidade de Lisboa, Av. Prof. Gama Pinto 2, 1699 Lisboa, Portugal;* [4]*Departamento de Materiales, C-IV, Universidad Autonoma de Madrid, Cantoblanco 28049 Madrid, Spain*

New detailed ion-beam/channeling data on the problem of the interaction between Mg and Hf sites are reported. They clearly show a gradual transfer of Hf ions from the Li to the Nb location on increasing the Mg concentration. The transfer process is complete for about 4.5% Mg concentration.

## 1 INTRODUCTION

LiNbO₃ has been extensively investigated[1] for applications to bulk and waveguide optoelectronic devices.[2] In particular, much effort has been devoted to understand its photorefractive behaviour,[3] that should play a relevant role for the implementation of optical processors and computers. One of the questions still deserving much attention is the role of certain ions, such as Mg, on the photorefractive response. In fact, remarkable inhibitions of that response have been reported.[4] Therefore, it is of primary interest to understand the interaction between impurity cation sites. To this end, Hf ions have been incorporated into LiNbO₃ crystals containing a variable amount of Mg. Hf has been selected as a probe impurity, since it has been previously ascertained[5] that it occupies the Li site in nominally pure LiNbO₃, whereas it moves to the Nb site in LiNbO₃:Mg (6% Mg concentration).

## 2 EXPERIMENTAL DETAILS

Single crystals of LiNbO₃ codoped with Hf and Mg were grown from a congruent melt ([Li]/[Nb] = 0.945) by the Czochralski method from grade I Johnson Mathey powder at the Universidad Autonoma de Madrid. The concentration of MgO in the melt for different crystals ranged from 2% to 4% in steps of 0.5% and the concentration of HfO₂ in the melt was 1% in all cases.

For RBS/channeling experiments[5,6] plates perpendicular and parallel to the c-axis were prepared. The experiments were performed with the 2 MV Van der Graaff accelerator of INETI, Sacavém. A 1.6 MeV He beam was used to measure the Nb and Hf signals, with typical currents of 1 nA, in order to keep the beam induced damage low.

## 3 RESULTS

Angular scans for Nb and Hf were measured through the $\langle 0001 \rangle$, $\langle 0\bar{4}41 \rangle$, $\langle 01\bar{1}0 \rangle$, $\langle 11\bar{2}0 \rangle$ and $\langle 02\bar{2}1 \rangle$ axes with the samples of different concentrations of Mg. From the results for
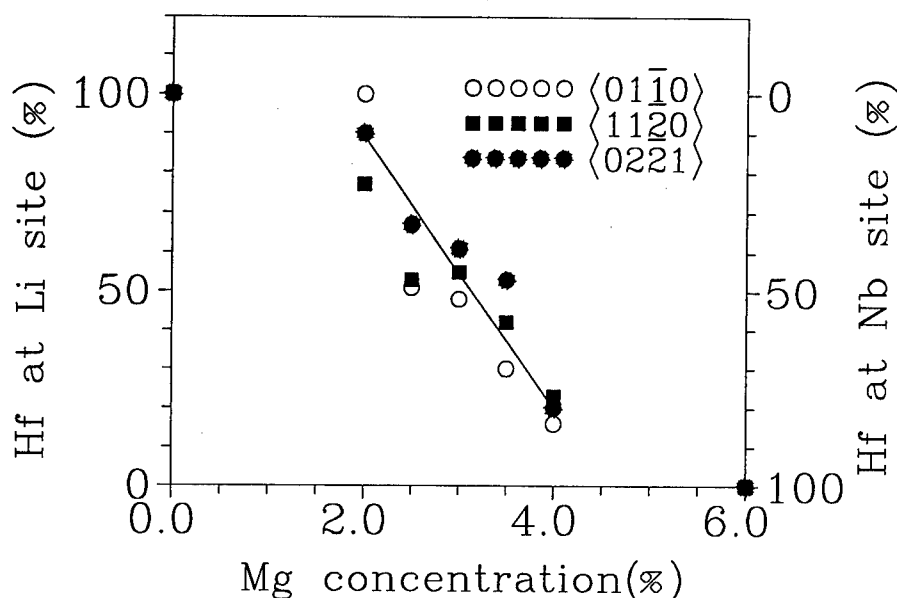
FIGURE 1   Best values for the fractions of Hf ions at Li and at Nb sites for different concentrations of Mg, obtained from the fit of the simulated angular scans through $\langle 01\bar{1}0 \rangle$, $\langle 11\bar{2}0 \rangle$ and $\langle 02\bar{2}1 \rangle$ axial directions in $LiNbO_3$:Mg, Hf crystals.

the angular scans along $\langle 0001 \rangle$ and $\langle 0\bar{4}41 \rangle$ one can exclude the occupation of a position in the vicinity of a free octahedral site leaving exclusively the Nb and Li sites as possible locations. The angular scans through the other axes for more than 2% Mg suggest the presence of two fractions of the Hf ions located at different places (Li and Nb). In the case of 4.0% of Mg the Hf dips follow the Nb dips indicating that, in this case the Hf ions are mainly at Nb site and that the fraction of Hf ions at Li site is already very small. For 6% Mg, Hf fully occupies the Nb site[5]. A Monte Carlo program, previously developed for $LiNbO_3$[5], has been used to simulate the channeling dips. The best fits to the experimental points for channels $\langle 01\bar{1}0 \rangle$, $\langle 11\bar{2}0 \rangle$ and $\langle 02\bar{2}1 \rangle$ correspond to fractions of Hf at Li and Nb sites, that are plotted in Figure 1, as a function of Mg doping. The solid line in the plot is drawn only to guide the eyes. From these fits one can conclude that Mg ions start to push Hf ions out of the Li site for concentrations above 2% and that the process becomes completed for 4.5%.

## 4   DISCUSSION

Our present data cannot unambiguously decide on specific microscopic models[7,8,9] However, a few comments may be advanced. Since a 2% Mg concentration is sufficient to start pushing the Hf (1%) ions into the Nb sites, it appears that Hf has a much lower affinity than Mg for the Li site, in comparison to the Nb site. In terms of the defect energetics, one may say that the energy of $Hf_{Li}$ and/or $Mg_{Nb}$ is higher than that for $Mg_{Li}$ and/or $Hf_{Nb}$. It is noteworthy that above 4.5% Mg concentration Hf ions fully occupy the

Nb sites in good accordance with the threshold for inhibition of the photorefractive damage.

## ACKNOWLEDGMENTS

## REFERENCES

1. Properties of Lithium Niobate, EMIS Datareviews, Series 5, INSPEC, London (1989).
2. Electrooptic and Photorefractive Materials, ed. by P. Gunter (Springer-Verlag, Berlin, 1986).
3. L. Arizmendi and F. Agulló-López, MRS Bulletin XIX, 32 (1994).
4. D. A. Bryan, R. Gesson and H. E. Tomaschke, *Appl. Phys. Lett.* **44**, 847 (1984).
5. L. Rebouta, M. F. da Silva, J. C . Soares, J. A. Sanz-Garcia, E. Diéguez and F. Agulló-López, *J. Mater. Res.* **7**, 1 (1992).
6. L. Rebouta, P. J. Smulders, D. O. Boerma, F. Agulló-López, M. F. da Silva and J. C. Soares, *Phys. Rev.* **B48**, 3600 (1993).
7. S. C. Abrahams and P. Marsh, *Acta Cryst.* **B42**, 61 (1986).
8. H. Donnerberg, S. M.Tomlinson, C. R. Catlow and O. F. Schirmer, *Phys. Rev.* **B44**, 4877 (1991).
9. N. Iyi, K. Kitamura, F. Izumi, J. K. Yamoto, T. Hayashi, H. Asomo and S. Kimura, *J. Solid State Chem.*, **101**, 340 (1992).

# MANIFESTATION OF A CONFINEMENT-TYPE LATTICE ANHARMONICITY IN THE EMISSION SPECTRA OF NIOBATE GLASS

M. GRINBERG, W. JASKÓSKI, CZ. KOEPKE, J. PLANELLES,* and M. JANOWICZ

*Instytut Fizyki, Uniwersytet Mikolaja Kopernika, Grudziadzka 5, 87–100 Toruń, Poland;
*Departament de Ciències Experimentals, Universitat Jaume I, Apartat 224, 12080
Castelló, Spain*

The observed broadening of the emission spectra of the luminescence centers with large electron-lattice coupling has been explained in terms of the ion motion confinement in the lattice. A new simple and analytically solvable model potential, instead of the harmonic potential, for the energy sheets of the excited and ground electronic manifolds has been proposed. As an example of application the emission spectrum of niobate glass has been analyzed.

*Key words*: spectroscopy, glass, Nb, electron-phonon interaction.

In the theoretical description of the emission and absorption spectra of the luminescence centers in crystals, the standard approach assumes that the excited and the ground electronics manifolds are represented by parabolic energy sheets.[1] This approach works well for the systems with a weak or medium electron-lattice coupling. However, as we have shown in our previous paper,[2] for the strong electronic-lattice coupling the harmonic forces assumption breaks down and an confinement of ions motion should be taken into account. The model potential which we proposed is:

$$V_\alpha(Q) = \frac{\alpha(\alpha - 1)}{2\sin^2 Q},$$  (1)

where Q is configuration coordinate which extends from 0 to $\pi$ (the confining region can be described also as $0 - a$, for arbitrary $a$, by simple substitution $Q' = Q\pi/a$) and $\alpha$ is dimensionless parameter, gives analytical solutions. Since the solutions fulfill recurrence relations they can be easy generated to any required order. One obtains the energies in respect to the bottom of the potential:

$$E_n = \frac{n^2}{2} + \alpha(n + \frac{1}{2}), n = 0, 1, 2..$$  (2)

and appropriate wave functions:

$$|n> = \Psi_{n,\alpha}(Q) = \sin^\alpha(Q) C_n^{(\alpha)}(\cos(Q)),$$  (3)

where $C_n^{(\alpha)}(\cos(Q))$ are Gegenbauer Polynomials.[3] Since $E_0 = \alpha/2$, one can use the energy unit: $\hbar\omega$ and obtain

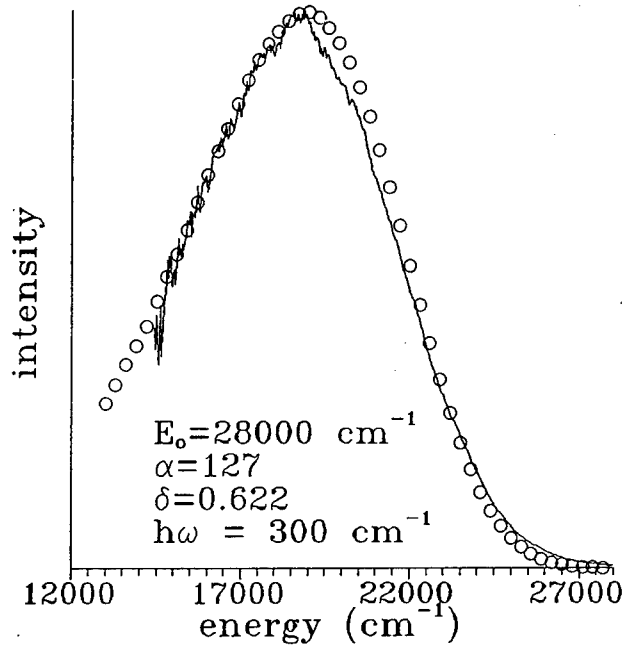$$E_{n+1} - E_n = (1 + \frac{n + \frac{1}{2}}{\alpha})\hbar\omega$$  (4)

FIGURE 1   Theoretical fit (circles) to the emission spectrum of niobate glass obtained using our model potential. Parameters of the model are listed in figure. Solid curve corresponds to the experimental lineshape.

Relation (4) shows that for $\alpha \gg 1$ and not too large values of $n$ the energies are close to those obtained for harmonic potential. Due to relation (4) we can perform calculations using generalized units, where Q changes from 0 to $\pi$ (minimunt of the potential appear for $Q = \pi/2$) and energies are given in the unit $\hbar\omega$. The electron lattice coupling is included by an offset of the ground end excited energy sheets, represented by parameter $\delta$. In this way our model is described by three independent parameters: $\alpha$, $\delta$ (both dimensionless) and $\hbar\omega$. One notices that harmonic potential is obtained when $\alpha \rightarrow \infty$. Then the radiative transition probability between the excited, $|n_e >$, and the ground, $|m_g >$, states is given by:

$$I_{nm}(\hbar\omega) = M_{eg}^2| < m_g|n_e > |^2 \delta[\hbar\omega - (\epsilon_0 + E_n^e - E_m^g)], \tag{5}$$

where $< m_g|n_e >$ is the overlap integral of the vibronic wave functions given by (3), $M_{eg}$ is electronic transition moment, independent on $n_e$ and $m_g$, $\hbar\omega$ is energy of emitted (absorbed) photon and $\epsilon_0$ is the difference between the energies of the bottoms of the excited and ground electronic manifolds. With the help of relation (5) one can calculate the emission intensity at arbitrary temperature:

$$I(\hbar\omega) = \sum_{n,m} I(\hbar\omega)_{nm} f(E_n^e, T), \tag{6}$$

where $f(E_n^e, T)$ is the Boltzman occupation factor.

Using our model potential we have reproduced the emission spectrum of niobate glass, where the six-fold coordinated molecular ions of Nb, namely $(NbO_6^{7-})$ complexes are
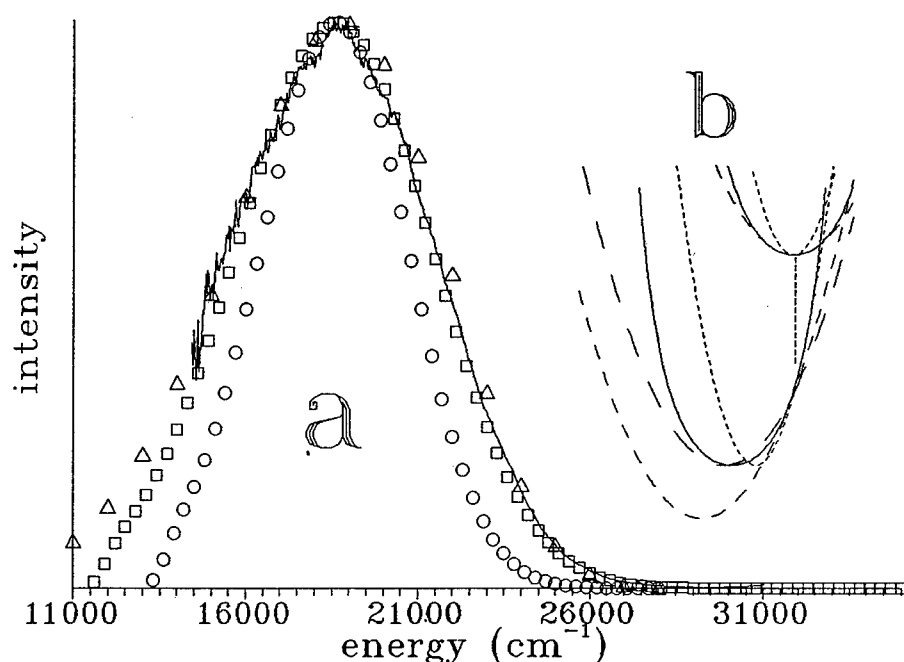
FIGURE 2   [a]Three attempts of fitting the emission spectrum of niobate glass obtained using harmonic potentials for lattice motion. Triangles, rectangles and circles correspond to (i): $\epsilon = 28\,000$ cm$^{-1}$ and $\hbar\omega = 1000$ cm$^{-1}$, (ii): $\epsilon = 35\,000$ cm$^{-1}$ and $\hbar\omega = 300$ cm$^{-1}$ and (iii): $\epsilon_0 = 28\,000$ cm$^{-1}$ and $\hbar\omega = 300$ cm$^{-1}$, respectively. b Configuration coordinate diagrams of $(NbO_6^{7-})$ resulting from fitting procedures. Solid line represents our model potential, other correspond to cases (i), (ii) and (iii) as in Figure 2.a: dotted line – (i), dashed (short) – (ii), dashed (long) – (iii). Upper curve for the cases (ii) and (iii) coincides each other due to the same value of $\hbar\omega$. Vertical arrow corresponds to the transition in the maximum of emission.

responsible for luminescence.[5] To compare the experimental data with theory we used the emission lineshape extracted from measured spectra according to procedure described in ref.[6] The results of our calculations are presented in Figure 1. It is seen that the we were able to reproduce the spectrum quite well using the values of the input model parameters; $\epsilon$, $\alpha$, $\hbar\omega$ and $\delta$ listed in the Figure 1.

It is interesting to compare the results obtained using our model confinement potential with results obtained using standard harmonic potential approach. In Figure 2 respective fits are presented. It should be pointed out, that using phonon energy $\hbar\omega = 300$ cm$^{-1}$ and energy of the zero-phonon line $\epsilon = 28\,000$ cm$^{-1}$ we cannot reproduce the shape of the spectrum (circles in Figure 2a). In the harmonic approximation the spectrum can be reproduced when the large (not realistic in this kind of materials) energy of phonon $\hbar\omega = 1000$ cm$^{-1}$ (triangles), or unacceptable energy of the zero-phonon line, $\epsilon_0 = 35\,000$ cm$^{-1}$, is assumed. In Figure 2.b the potentials used for obtaining the emission lineshapes are presented. Comparing differences between the solutions of the harmonic and our model potential (forms (2) and (3) with respective relations for the harmonic potential)[4] one can note that the absorption (emission) lineshapes, obtained in the presence of ion motion confinement, are broader then those obtained when the spatial

confinement is not taken into account. This effect is related to the increase of the inter-states energetic distance with increase of vibronic quantum number as well as to the smaller changes in the vibronic overlap integrals, in comparison to those for harmonic oscillator.

REFERENCES

1. K. Huang and A. Rhys, *Proc. Roy. Soc. London* **A204**, 406 (1950).
2. M. Grinberg, W. Jaskólski, Cz. Koepke, M. Janowicz, and, J. Planelles, *Phys. Rev. B* **50**, 6504 (1994).
3. *Handbook of Mathematical Functions*, edited by M. Abramowitz and I. A. Stegun (Dover, New York, 1965).
4. A. S. Davydov, *Mechanika Kwantowa*, edited by PWN (Warszawa, 1969).
5. Cz. Koepke, A. Lempicki and G. H. Beall, *J. Lumin.* **54**, 145 (1992), Cz. Koepke, A. Lempicki and G. H. Beall, ibid p. 151.
6. A. J. Wojtowicz, M. Kazmierczak, A. Lempicki and R. H. Bartram, *J. Opt. Soc. Amer.* **B6**, 1106 (1989).

# 9   RADIATION DEFECTS

# THE EFFECT OF THE RELAXATION OF 4d I⁻ HOLE ON THE FORMATION OF EMISSION CENTERS IN ALKALI HALIDES

A. N. BELSKY, S. KLIMOV, E. I. ZININ,* P. MARTIN,** C. PEDRINI***
and A. V. GEKTIN****

*Synchrotron Radiation Laboratory, Physics Department, Moscow State University,
117234 Moscow, Russia; *Institute of Nuclear Physics, Novosibirsk, Russia;
**Laboratoire pour l'Utilisation du Rayonnement Electromagnetique, CNRS, Batiment
209D, Centre Universitaire Paris-Sud, 91405 Orsay Cedex, France; ***Laboratoire de
Physico-Chimie des Materiaux Luminescents, University LyonI, Bat. 205, 43, boulevard
du 11 Novembre 1918, 69622 Villeurbanne Cedex, France; ****Institute for Single
Crystals, 310141 Kharkov, Ukraine*

The time-resolved luminescence spectra for KI, RbI and CsI were measured using VUV and X-ray synchrotron radiation. The emission band of fast intrinsic luminescence (FIL) was observed for all these crystals. The position of FIL band is red-shifted ($\sim$ 0.1 eV) relative to the $\sigma$-exciton band. This type of emission is showed up at the temperatures 80 to 300 K when the exciton emission was quenched and had a nonexponential decay characterised by times 0.1 and 10 ns. The FIL in CsI has the highest yield. The onset of CsI FIL excitation was shown to be at photon energies higher than 20 eV. FIL yield exponentially increases with photon energies up to the energy of 4 d iodine core level ($\sim$ 50 eV). The relaxation of 4d I⁻ hole resulting in the double ionisation of the iodine ion may play an essential role in the creation of emission centers.

*Key words*: intrinsic luminescence, energy relaxation, alkali iodide, excitation mechanism.

## 1 INTRODUCTION

Applications of optical properties of crystals often go ahead the understanding of mechanisms involved. This is the case with caesium iodide. While pure CsI for practical purposes is already supplied, you can scarcely find any convincing comments on the origin of its fast intrinsic luminescence (FIL). This might be an example of new phenomena in the relaxation of electronic excitations in crystals from which visualise through the FIL of CsI.

In this report we discuss the effects introduced by high-energy excitation in the emission of ionic crystals. Here we present the recent results of the FIL measurements of CsI, KI and RbI by the VUV and X-ray time-resolved luminescence spectroscopy. The measurements have been performed with X-ray excitation from the storage ring VEPP-3 (Novosibirsk, Russia) and with the VUV excitation at the storage ring SuperACO (Orsay, France).

## 2 EXPERIMENTAL RESULTS

The measurements using a dissector with a temporal resolution of 50 ps[1] allow for the separation of fast fluorescence components at the background of slow emission of much higher intensity. Due to this technique we were able to observe in KI and RbI (Figure 1) emission bands similar to the FIL of CsI. Their yield is much lower than in CsI (10 times in RbI and 50 times in KI). Fitting with a gaussian (solid curves in Figure 1) reveals that FIL
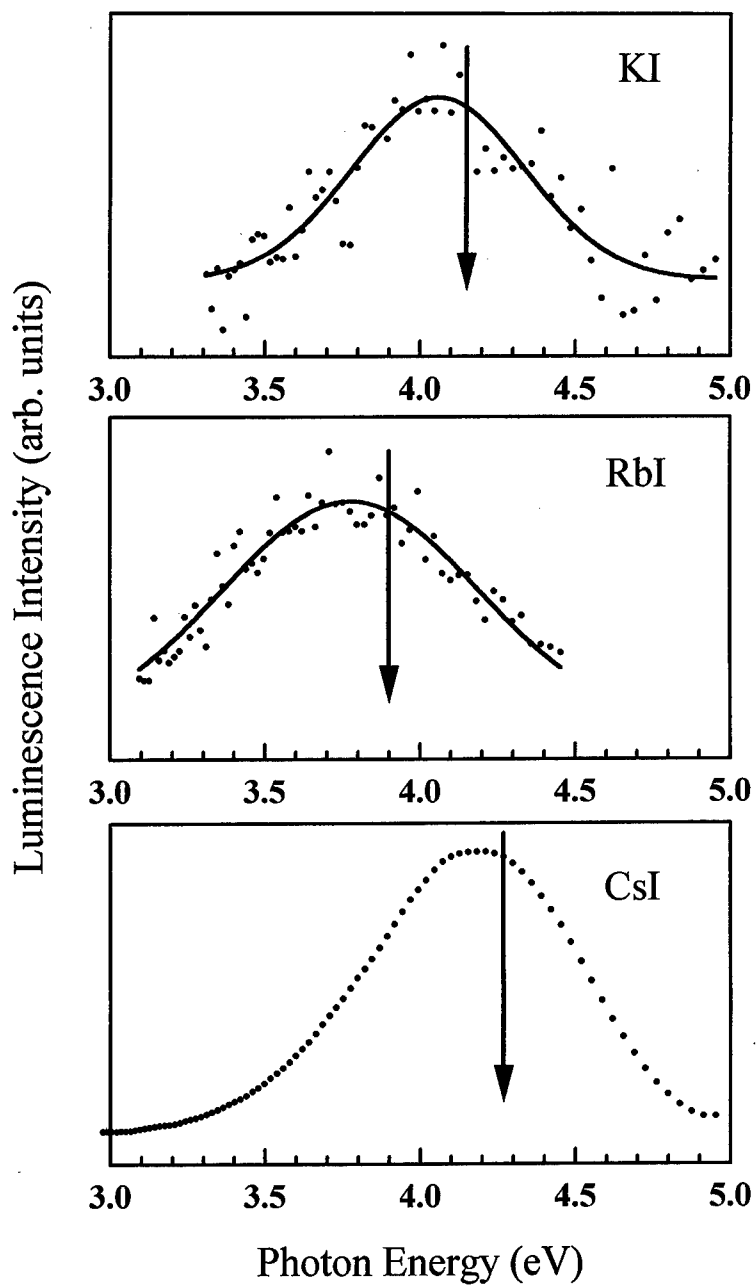
FIGURE 1  Fast component of emission spectrum of FIL of KI, RbI and CsI under X-ray excitation at temperature 300 K (dotted) and fitting with a gaussian (solid curves).
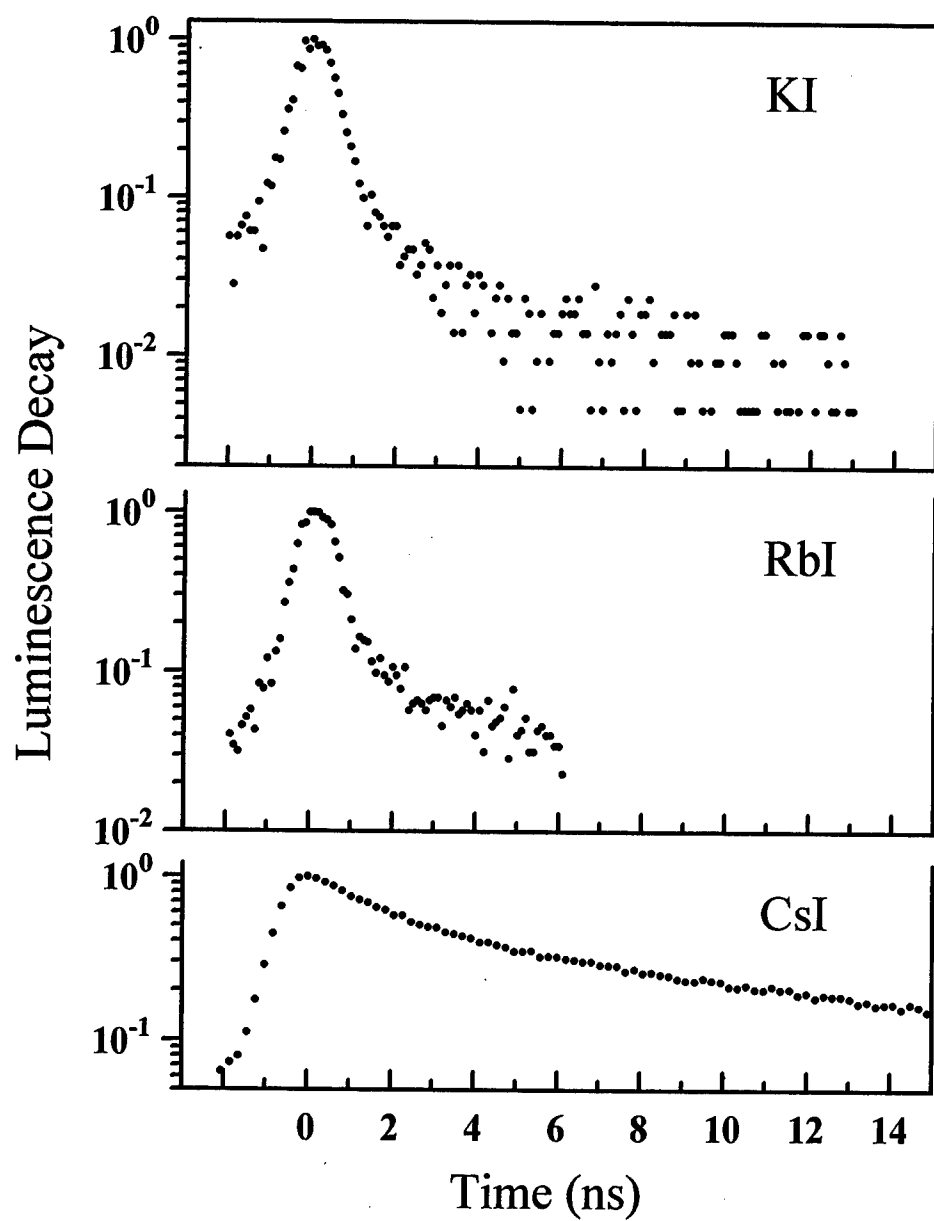
FIGURE 2   Decay curves of FIL band under X-ray excitation at 300 K.

A. N. BELSKY *ET AL.*
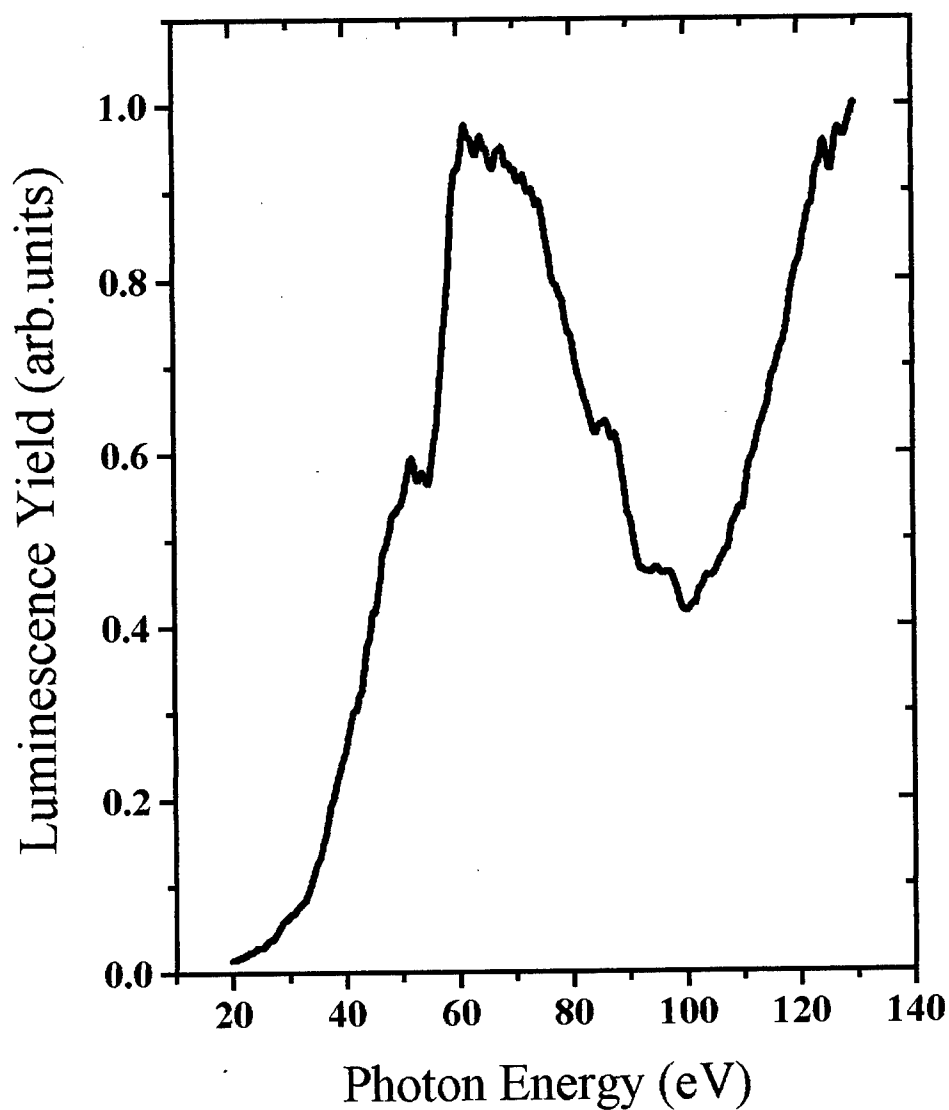


FIGURE 3    Excitation spectrum of CsI FIL at 300 K.

bands in all three crystals are shifted approximately by 0.1 eV towards lower energy relative to the maxima of s-exciton bands (see also Table I). FIL emission spectrum overlaps with the self trapped exciton emission, the intensity of the former remains substantial at temperatures higher than that of exciton quenching. We can assume that FIL can be the exciton emission in the vicinity of some lattice defect stabilizing it at elevated temperature. The emission of such excitons was observed in many crystals and its properties are well-studied:

– Decay of the emission of an exciton trapped by a defect is exponential. Temperature quenching of exciton luminescence results in the acceleration of decay kinetics, leaving it's exponential nevertheless.
– Emission of the exciton can be excited by photons starting with the region of exciton absorption, the most intensive excitation band falls in this region.

Table I
Parameters of FIL and exciton emission band in alkali iodide

| crystal | Fast Intrinsic Luminescence (FIL) at 300 K | | | | $\sigma$-exciton at 20 K |
|---|---|---|---|---|---|
| | center eV | width eV | $\tau$ fast ns | $\tau$ slow ns | center eV |
| KI | 4.06 | 0.56 | 0.1 | 2 | 4.15 |
| RbI | 3.78 | 0.82 | 0.1 | 6 | 3.84 |
| CsI | 4.17 | 0.70 | 0.8 | 12 | 4.28 |

FIL of alkhali iodides has a completely different decay kinetics (see Figure 2) and excitation spectrum (see Figure 3). Decay kinetics of FIL of KI, RbI, CsI is definitely nonexponential. At room temperature besides a 100 ps component there is another relatively slow one with $\tau$ 2...10 ns. A two-exponential fitting gives not satisfactory results. Similar profile was observed for radiation induced absorption in alkali halides.[2] Decay kinetics is characterised by a sophisticated temperature dependence. For example in CsI[3] at 90 K it can be presented by two components: an ultrafast one with $\tau$ less than 1 ns and a comparatively slow one with $\tau$ larger than 50 ns. The ultrafast component is substantially quenched at temperature higher than 90 K, meanwhile the fast component with $1 < \tau < 10$ ns shows up. Its maximal is achieved at T $\sim$ 150 K. The relative intensity of the slower component decreases with temperature leading to the decrease of the efficient decay time. Starting with 350 K, the contribution of the component with $\tau > 50$ ns is practically zero, and decay kinetics is controlled by the fast component. It is still non-exponential however.

It was found that FIL is not excited not only in the excitonic but also in the fundamental absorption range up to at least 20 eV (approximately 3 Eg).[3] It should be noted that similar results were obtained by other authors, so there are no data on the FIL excitation in the range 5 to 30 eV. At higher excitation energies, starting with soft X-rays, the yield of FIL is quite high.

It is natural to expect the threshold of CsI FIL excitation to be somewhere between 30 eV and 1 KeV. As can be seen from Figure 3 the yield of CsI FIL increases steeply starting with 20–30 eV and reaches the first maximum at 60 eV.[4] The features around 50 eV (two minima) correspond to two sharp maxima in the 4d–5p absorption of iodine.[5] In the region of 40 eV width the yield changes by two orders of magnitude, while the number of secondary excitations can't increase by more than 3–4 times. This allows to suggest that with the onset of the absorption from the 4d I core level the mechanism of FIL excitation becomes efficient. Unticorrelated behaviour of the features of the FIL excitation spectrum and iodine absorption can be due to surface losses. Similar situation is observed for the excitation of excitons at the fundamental absorption edge.

## 3   DISCUSSION

Summarising all these we can state that CsI FIL is due to the processes that are not understood completely. However, it seems to be evident that its excitation mechanism as well as the mechanism of emission center creation are different from conventional. Our knowledge at present is: (1) One electron-hole pair or an exciton can not lead to the FIL. (2) When one absorbed photon creates 4 or 5 electron-hole pairs FIL is already observed. (3) From (1) and (2) we can come to a conclusion that the FIL is the result of interaction of several electron-hole pairs at the initial stage of relaxation. (4) High FIL yield in CsI and low in KI indicates that the probability of the effects of correlated relaxation of electronic excitations with the creation of an emission center depends on the crystal and can by quite high.

Let us consider how a high energy photon create a region of interacting electronic excitation in a crystals. Absorption of a high energy quantum results in the creation of a high electron and a core hole. The mean freepath of an electron of the energy 10 to 1000 eV in a crystal is known to be less than 5 nm. So 1 KeV electron in CsI creates $E/3E_g$ electron-hole pairs, i.e. 50 pairs in the region of a radius approximately 20 nm. The relaxation of the core-hole is mainly due to a cascade of Auger processes localised in the vicinity of one ion. As a result 1 KeV hole gives birth to 10 - 40 electron-hole pairs in the region of radius less than 5 nm. This initial relaxation stage lasts for $10^{-14}$ seconds resulting in the creation of spacially non-uniform distribution of electronic excitons with regions of high local density or clusters of excitations. In such clusters of excitation interaction between electronic excitations should be quite efficient.

As core-hole relaxation is characterised by an especially compact distribution of secondary products, which can be localised on one or two adjacent ions, assuming the essential role of collective effects in the FIL emission centre creation, the absorption by a core level can result in a substantial FIL yield even at relatively low excitation energies, sufficient for the creation of a few electron-hole pairs only. As it is known relaxation of iodine 4d hole leads to double ionisation,[6] i.e. at least two electronic excitations are created at the same ion. Strong Coulomb interaction of the multiply charged ion with the adjacent ions in this case can result in a strong displacement of one of the ions, i.e. to the creation of a lattice defect. Stability of the defect will be affected both the temperature and by the specific crystal. We hope that on the basis of this model we shall be able to describe the kinetics and temperature dependence of the FIL.

REFERENCES

1.  E. I. Zinin, *Nucl. Instrum. Methods* **208** 434 (1983).
2.  Aluker E. D., Gavrilov V. V., Deitch R. G. and Chernov S. A., Fast radiation-induced processes in alkali halide crystals (Riga: Zinatne) in Russian (1987).
3.  A. N. Belsky, A. V. Gektin, V. V. Mikhailin, A. L. Rogalev, N. V. Shiran, A. N. Vasil'ev, E. I. Zinin, *Rev. Sci. Instrum.*, v. 63, N1, p. 806 (1992).
4.  A. N. Belsky, A. N. Vasil'ev, V. V. Mikhailin, A. V. Gektin, P. Martin, C. Pedrini and D. Bouttet, *Phys. Rev.* **B49** 13197 (1994).
5.  Comes F. J., Nielsen U., Schwarz W. H. E., *J. Chem. Phys.*, **58**, 2230 (1973).
6.  Nahon. L., Duffy L., Morin P., Combet-Farnoux F., Tremblay J. and Larzilliere M., *Phys. Rev.* **A41** 4879 (1990).

# SEM-ANALYSIS OF FRACTURE FEATURES FORMED IN EXCIMER-LASER INDUCED SURFACE DAMAGE OF CaF$_2$

H. JOHANSEN,* S. GOGOLL,[+] E. STENZEL,[+] M. REICHLING,[+]
and E. MATTHIAS[+]

*Max-Planck-Institut für Mikrostrukturphysik Halle, Weinberg 2, 06120 Halle, Germany; [+]Fachbereich Physik, Freie Universität Berlin, Arnimallee 14, 14195 Berlin, Germany*

The fracture damage of bulk (111)-CaF$_2$ crystals induced by pulsed irradiation in single shot mode with 248 nm laser light in air is investigated. The irradiated spots are studied with a scanning electron microscope (SEM) using different operational modes. An analysis of the fracture features yields evidence for defect induced absorption, thermal stress and shock wave generation as the main cause of damage. Fracturing is preferentially aligned along the (111)-directions resulting in a triangular shape for the tile fragments. The thickness of the fragments shows a clear dependence on incident laser fluence, what can be explained assuming an enhanced surface absorption in the CaF$_2$ crystal.

*Keywords*: Laser-induced damage, alkaline-earth halides, absorption centres, energy transfer, scanning electron microscopy.

## 1 INTRODUCTION

Laser damage of bulk crystals of CaF$_2$ can be characterized by a clear threshold behaviour[1] and the dominant damage feature is cracking along the natural cleavage planes.[2] To uncover thermomechanical details of the damage process one needs topographical information about the microscopic surface modification of the crystal and of the irradiation-induced fragments. With respect to the latter conventional SEM is especially appropriate, where a full depth of field but only a limited lateral resolution in the range of about 20 nm is required. Furthermore, to clearly interpret such phenomena as detachment of crystallites from the bulk, local melting, or the formation of droplets, it is necessary to obtain the specific contrast information of secondary electrons (SE) and backscattered electrons (BE) related to possible phase transitions in local areas of the laser irradiation.

A careful analysis of topographic damage effects by means of SEM reveals traces of the interaction process in different depths of the crystal, for example, on the surface of tiles or craters, on the subsurface below the tiles, and in form of locally detectable absorption centres in the depth. The lateral temperature variation at the periphery due to the average temperature increase in the centre of the spot entails fracture as the most significant feature. From the multitude of information revealed by an inspection of the damaged area we have choosen one topic for this contribution, namely the relationship between the fluence of single laser pulses and the resulting thickness of the detached tiles.

## 2 EXPERIMENTAL

The damage behaviour was measured in a 1-on-1 shot irradiation mode. An excimer laser provided 14 ns pulses of 248 nm light. The laser beam was guided through an aperture and
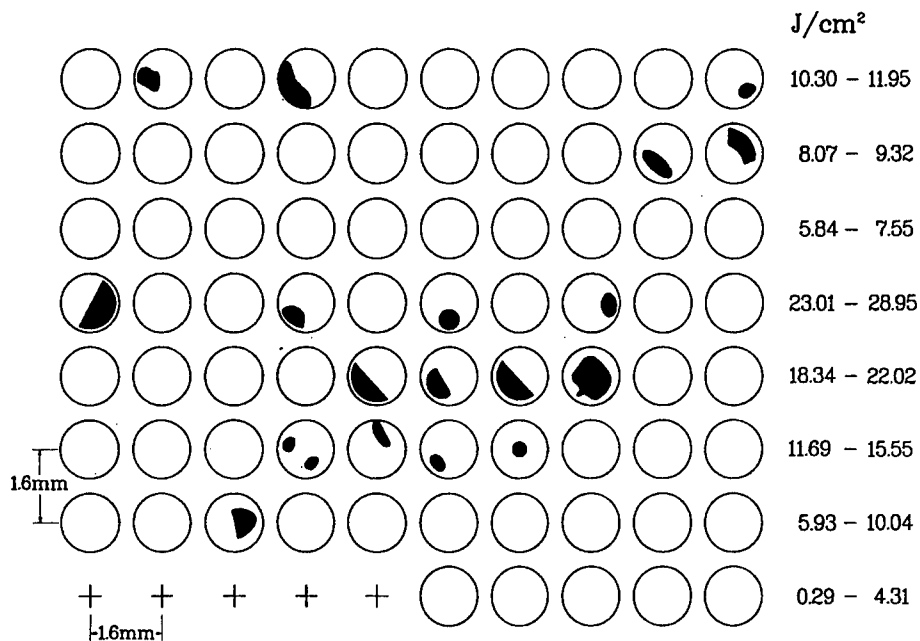
FIGURE 1(a)   Distribution of extended defect regions on the crystal surface after 1-on-1 shot irradiation with 248 nm laser light. Crosses: no damage, open circles: normal damage (tile detachment) marked regions in circles: indication for degree and morphology of massive damage in defect rich regions.

imaging optics providing a close to top-hat profile at the crystal surface. The length of the principal axes of the eleiptically shaped spot was 110 $\mu$m and 175 $\mu$m, respectively. Pulse energy was varied in the range of 0.3 to 30 mJ/pulse. In addition to the incident light the transmitted light intensity was monitored.[3] Due to the short focal length of the imaging optics the intensity on the rear face of the crystal was too low to cause backside damage.

The experiments were performed in air with an optically polished UV-grade (111) $CaF_2$ single crystal (20 $\times$ 20 $\times$ 6 mm³) purchased from Karl Korth company, Kiel.

To ensure SEM surface investigations free of charging, the crystal surface was covered with a conducting 15 nm carbon layer prior to the SEM measurements. The SEM-BE composition mode was found to be most suitable for a sensitive investigation of microcracks as low density regions, whereas potential contrast arises due to the positive charge-up of tiles using the SE mode at primary energies below 1 keV.

## 3   RESULTS AND DISCUSSION

Figure 1(a) displays a schematic survey over the damage results. As indicated by the numbers given on the right hand side, the single shot irradiation on the (111)-surface of $CaF_2$ was carried out in series with increasing intensity ordered in horizontal lines. Irradiated locations without any detectable damage are marked by crosses, the others by circles. The typical damage morphology of most of the damage spots is shown in Figure 1(b) and can be characterized by a detachment of $CaF_2$ tiles. The fluence varies
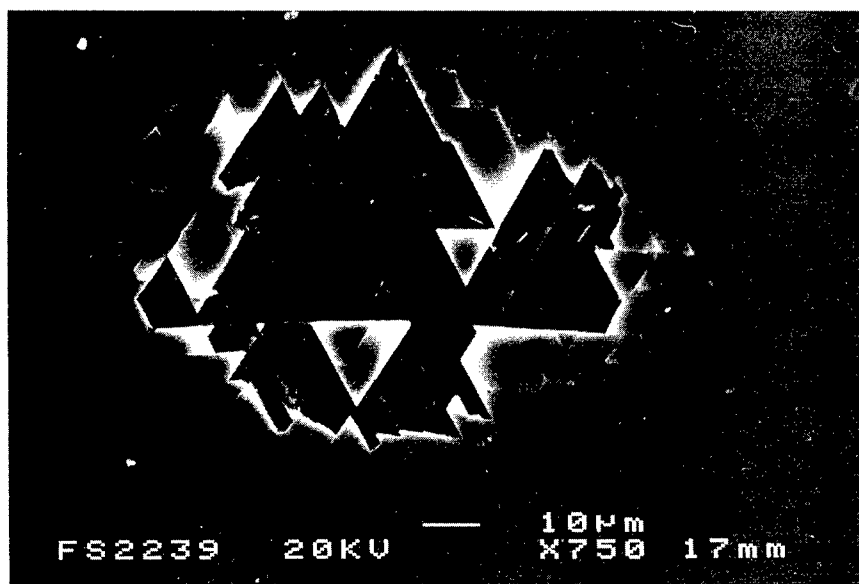
FIGURE 1(b)   SE micrograph illustrating 'normal' damage at 13.5 J/cm$^2$.

from 0.3 to 30 J/cm$^2$ in different ranges in each of these series. Although, a damage threshold can be determined (about 4 J/cm$^2$), there is no clear correlation between the extent of damage and laser fluence. Systematic SEM inspection reveals that at some irradiated spots a pronounced three-dimensional ejection of material had taken place. A typical example is shown in Figure 1(c) where a damage depth much larger than the average tile thickness is found. In Figure 1(a) those spots are represented as circles with marked regions inside, where the degree and morphology of the damage is indicated by the shading. This nonuniform distribution of severe damage characterizes the unequal quality of the original crystal and/or the influence of the polishing procedure. Local defect aggregates of unknown nature may be the source of this phenomenon. The position of the strong damage area within each spot clearly varies between different areas and does not result from inhomogeneities of the laser intensity profile. After careful inspection of the whole crystal complete series without such strong features could be found.

Investigating the damage behaviour in detail outside the strong damage regions represented in Figure 1, SEM examination reveals an onset of coherent planar damage at a pulse energy fluence of about 4J/cm$^2$. This is coincident with the observed decrease of the optical transmission.[3] Fine surface cracks having no conjunction among each other are detectable with sufficient contrast down to $\approx 2.6$ J/cm$^2$ by the SEM-BE composition mode. Fracture mostly occurs along the natural (111)-cleavage planes. Since there are four different (111)-planes intersecting the surface, rectangular patterns are expected. This is found for CaF$_2$(100). On the (111)-surface, however, the three remaining (111)-planes form tiles in the shape of equilateral triangles, trapezoids and parallelograms as found in Figure 2. Here, a local detachment of tiles vertical and parallel to the surface can be detected sensitively by the electron beam induced voltage contrast (EBIVC) for a primary

FIGURE 1(c)   SE micrograph illustrating 'massive' damage at 11.7 J/cm$^2$.

electron energy below 1 keV (see Figures 2(a) and 2(d)). This operation mode detects the positive charge built-up of partially mechanically and electrically insulated tiles forming a small chargeable capacity to ground. Furthermore, plastic deformation of a single tile near the spot centre (Figure 2(b)) and parallel sub-cracking of tiles (Figure 2(c)) are clearly discernible. Ablated tiles leave behind a substructure containing tear-off edges that are also oriented along the (111)-cleavage planes. However, no fractured surface indicates an evident topographical fine structure. This has been established for a lateral resolution of the SEM down to 1.5 nm.

Figure 3 shows the measured tile thickness as a function of laser pulse fluence. The thickness increases monotonically with the incident fluence until about 25 J/cm$^2$. To explain this we recall that cracking occurs when the temperature rise at the surface over the whole laser spot induces shear stress exceeding the tensile strength of the material.[4] Since this stress is oriented orthogonal to the surface, cracks crossing the surface at the rim of the irradiated area will fracture as seen in Figure 2(a). On the other hand, a temperature gradient into the depth can actuate fracture parallel to the (111) surface. Therefore, in combination with cross cracking near the spot periphery big tiles are formed. We assume that a threshold energy density $u_T = \alpha(t) \, F(t)$ must be deposited to cause fracture ($\alpha(z)$ is the absorption coefficient, $F(z)$ the fluence at a depth $z$). This is a criterion well established for calculating etch depths of polymeric materials and yields a tile thickness $t$ variation with fluence that can be described by the equation:[5]
$$t = d \ln \alpha_s / [(u_T / F(t)) - \alpha_b].$$

Here, $\alpha_s$ is a specific surface absorption constant, attributed to light absorption by defect centres or impurities at an average depth of $d$. Since the absorption is small in a transparent material the term $(F(z)\text{-}F(0))$ can be neglected. Further, the bulk

a) 27.6 J/cm$^2$, SE, 0.5 keV; 1 μm

b) 23.9 J/cm$^2$, SE, 7 keV; 1 μm

c) 19.5 J/cm$^2$, SE, 5 keV; 1 μm

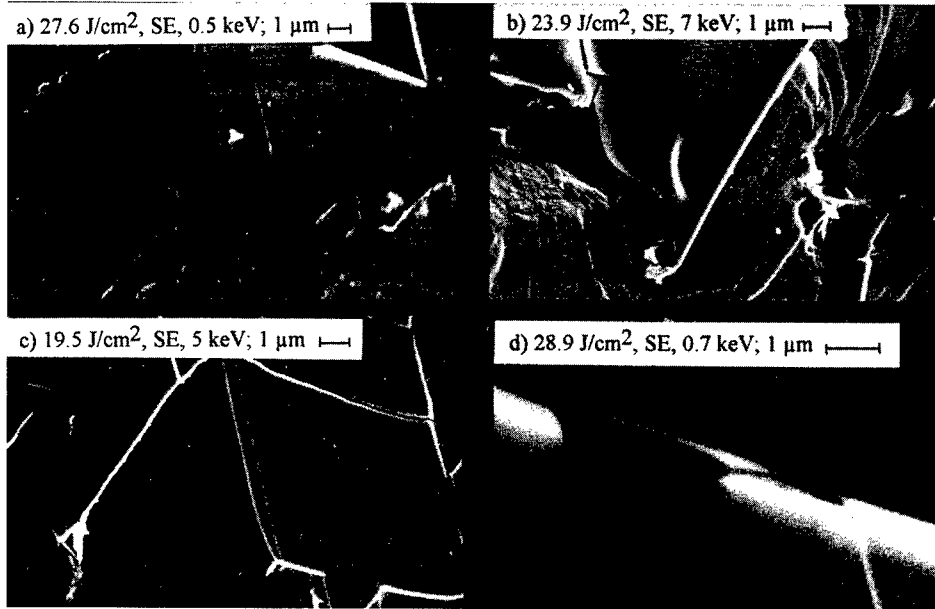d) 28.9 J/cm$^2$, SE, 0.7 keV; 1 μm

FIGURE 2    Fracture features: (a) local detachment of tiles (EBIVC), (b) surface melting near spot center (c) parallel cracking of a single tile, (d) subcracking of a small tile (EBIVC).

contribution $\alpha_b$ can be neglected motivated by the fact that damage occurs predominantly in the surface region. Thus we get a simplified expression for the tile thickness $t = d \ln \alpha_s F/u_T$.

This relation well fits the data as shown in Figure 3, yielding $d = 0.34$ μm and a threshold fluence $F_T = u_T/\alpha_s = 1.9$ J/cm$^2$. The second value is in the order of the observed threshold fluence of 4 J/cm.$^2$ A theoretical value for the threshold energy density $u_T$ can be derived from $u_T = \gamma(111)/a_{layer}$ ($\gamma$ being the surface tension) as the energy density necessary for cracking between two neighbouring CaF$_2$ layers of spacing $a_{layer} = a/\sqrt{3}$, where $a$ is the lattice constant. Inserting numbers we obtain $u_T = 1400$ J/cm$^3$ resulting in $\alpha_s = 760$/cm and a surface absorption of $\alpha_s\, d \approx 0.03$. Merely at the highest fluences above 25 J/cm$^2$ the curve does not fit the data. Presumably this indicates the onset of other damage mechanisms like dielectric breakdown.

## 4   CONCLUSIONS

Laser-induced damage of bulk CaF$_2$ like cracking parallel to and crossing the surface plane above a threshold pulse fluence has been observed. It can be described by assuming a rather homogeneous light absorption by defects in near surface regions. Damage is caused by thermal stress under nearly homogeneous absorption across the whole spot size. The tile thickness increases monotonically with incident fluence and a simple absorption model is in good agreement with the experimental data.
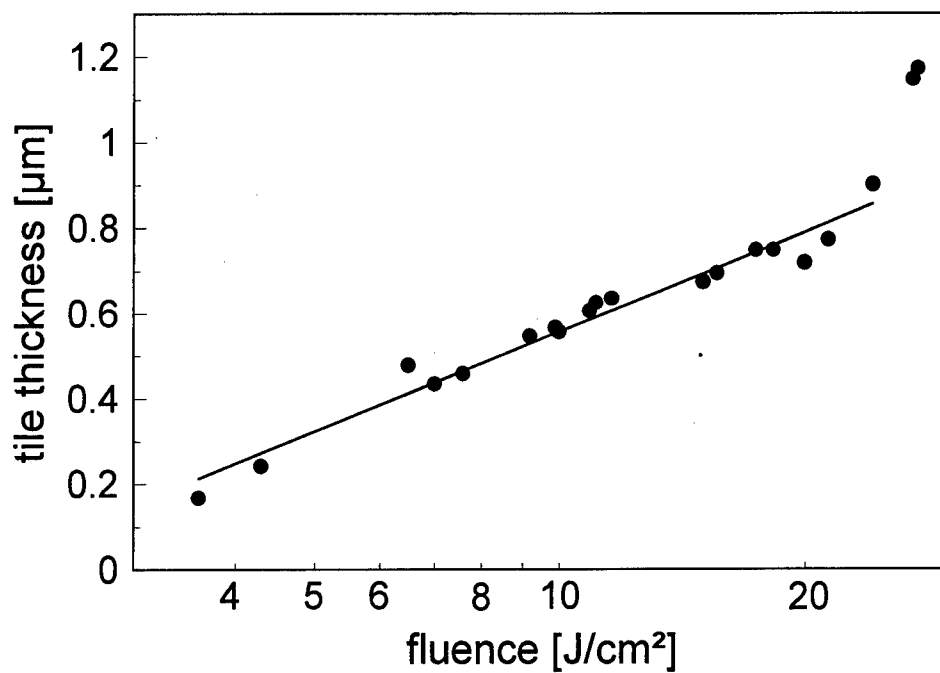
FIGURE 3    Dependence of tile thickness on laser fluence. The solid line represents a fit of the function $t = d \ln \alpha_s F / u_T$ to the data.

REFERENCES

1.  W. H. Lowdermilk and D. Milam *IEEE J. Quant. Electron.* QE–**17** 1888 (1981).
2.  M. Reichling, H. Johansen, S. Gogoll, E. Stenzel, *Nucl. Instr. Meth.* **B91**, 628 (1994).
3.  E. Matthias, S. Gogoll, E. Stenzel, and M. Reichling, *Rad. Eff. Def.* **128**, 67 (1994).
4.  R. L. Webb, L. C. Jensen, S. C. Langford, J. T. Dickinson, *J. Appl. Phys.* **74**, 2323 (1993).
5.  T. F. Deutsch and M. W. Geis *J. Appl. Phys.* **54**, 7201 (1983).

# ELECTRON SELF-TRAPPING AND PHOTOLYSIS IN PbCl₂ CRYSTALS

S. V. NISTOR*, E. GOOVAERTS and D. SCHOEMAKER

*Physics Department, University of Antwerp (U.I.A.) B-2610 Antwerpen- Wilrijk, Belgium*

Strongly anisotropic paramagnetic centers produced by X-ray or UV-irradiation of PbCl$_2$ crystals at T = 80 K have been attributed to Pb$_2^{3+}$ self-trapped electron (STEL) centers. The self-trapping of free (conduction) electrons at pure cation sites is further supported by production experiments using selective optical excitation in the fundamental absorption band. Optical bleaching experiments suggest the STEL center to be the primary defect responsible for the photolysis in PbCl$_2$, with the $g \approx 2$ centers representing hole-trapped centers.
P.A.C.S. numbers: 61.72.Ji; 63.20.Kr; 76.30.Mi; 78.50.Ec; 61.80.Ba,Cb.

*Key words*: Electron self-trapping, PbCl$_2$, photolysis.

## 1 INTRODUCTION

Exposure of lead halides to illumination in the short-wavelength side of the optical absorption (OA) spectrum induces at room temperature (RT) irreversible photochemical decomposition with formation of colloidal lead particles, accompanied by halogen desorption.[1] Below 200 K, where there is no appreciable diffusion of anion vacancies and only reversible photo-induced changes occur, it is expected that the primary defect representing the initial step in the formation of lead clusters, as trapped-electron Pb$^+$ or Pb$_2^{3+}$ centers,[2] could be observed by EPR spectroscopy.

As in the case of silver halides,[3] the primary defect involved in photolysis has eluded observation, although photoinduced paramagnetic centers with slightly anisotropic $g \approx 2$ values have been attributed[2] to such centers. However, all these interpretations are inconsistent with the theory of EPR spectra of np-centers in crystals,[4] as well as with the experimental results concerning the Pb$^+$ and Pb$_2^{3+}$ centers in alkali and alkali earth crystals.[5]

Recently, a new, strongly anisotropic paramagnetic center has been observed[6] by EPR in pure PbCl$_2$ single crystals, after UV or X-ray irradiation at T = 80 K. The EPR analysis demonstrated that the paramagnetic center represents a Pb$_2^{3+}$ molecular ion, consisting of an electron trapped at a pair of unperturbed nearest-neighbor (NN) cations along the $a$ direction of the orthorhombic ($D_{2h}^{16}$) PbCl$_2$ lattice. From its structure and production properties it has been concluded that the Pb$_2^{3+}$ center represents a self-trapped electron (STEL) center.

As will be further shown, the interpretation of production experiments by selective excitation in the fundamental optical absorption, together with earlier optical absorption and photoconductivity measurements,[7] strongly support the electron self-trapping in PbCl$_2$, a phenomenon predicted a long time ago,[8,9] but, to our knowledge, never directly observed.

Moreover, electron-hole recombination experiments induced by optical bleaching of the STEL centers suggest that the slightly anisotropic $g \approx 2$ centers, which are produced simultaneously with the STEL centers, are hole-trapped centers. The result also suggests that the STEL center is the primary center responsible for the photolysis in PbCl$_2$ as well.
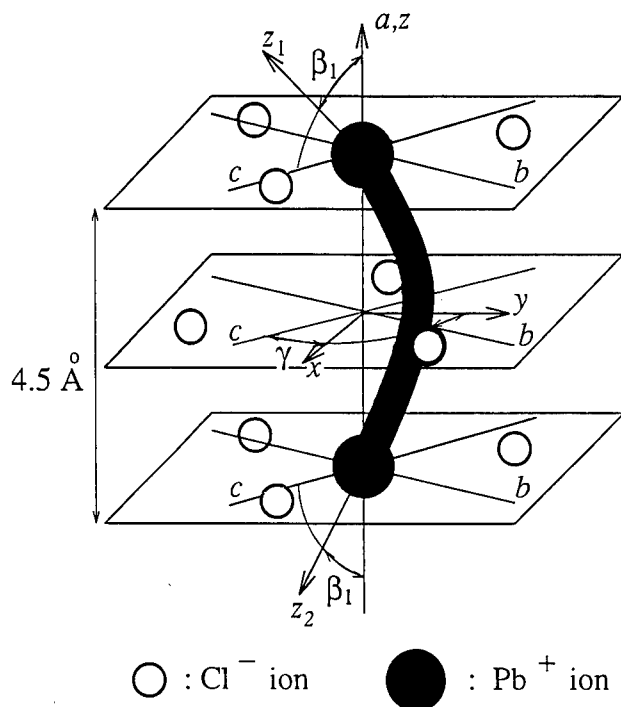
FIGURE 1   The schematic model of the $Pb_2^{3+}$ STEL center in the layered $PbCl_2$ lattice, showing the principal axes $xyz$ of the $g$-tensor and the $z_i$-axes of the axial hyperfine (hf) $A_i$-tensors. Only one of the four possible sign combinations ($\pm\gamma$ and $\pm\beta_1$) of the Euler angles is depicted. The tilting of the $z_1$-axes hf tensor axes is reflected in the bending of the $6p_1$–$6p_2$ molecular bond between the two Pb ions.

## 2   RESULTS

### 2.1 *Production and structure of the STEL center*

The STEL centers are produced[6] by UV ($\lambda < 250$ nm) or X-ray irradiation at T = 80 K of crystalline $PbCl_2$, together with the previously reported[2] A, B, and C centers at $g \approx 2$. The EPR analysis shows[6] the STEL center to consist of an electron trapped at two unperturbed cation sites, along an $a$ direction (Figure 1).

This structural model is supported by the nuclear signature due to the presence, besides the $^{even}Pb$ isotopes, of the $^{207}Pb$ isotope with nuclear spin $I = 1/2$ and natural abundance of 22%. Indeed, the EPR spectrum of the $Pb_2^{3+}$ STEL defect is fully described by the spin-Hamiltonian consisting of the Zeeman term and the hyperfine (hf) interactions with two Pb nuclei,

$$\frac{1}{g_0\mu_B}\mathcal{H} = \frac{1}{g_0}H \cdot g \cdot S + S \cdot A_1 \cdot I_1 + S \cdot A_2 \cdot I_2 \qquad (1)$$

in which $S = 1/2$ and $A_1$ and $A_2$ are related by mirror symmetry in a plane perpendicular to the internuclear axis. The second and third term occur only if the corresponding nucleus

TABLE I

The g- and hf-parameters (in mT) of the $Pb_2^{3+}$ STEL center in $PbCl_2$ at 13K. The experimental errors are ±0.001 for $g$ and ±1 for $A$. The $g$ and $A$ tensor axes are shown in Figure 1, with rotation angles $\gamma = \pm10°$ and $\beta i = \pm33°$.

| Center | $g_x$ | $g_y$ | $g_z$ | $A_x$ | $A_y$ | $A_z$ |
|--------|-------|-------|-------|-------|-------|-------|
| STEL in $PbCl_2$ | 1.549 | 1.379 | 1.718 | −85 | −85 | +109 |

is the $^{207}Pb$ isotope. The spin Hamiltonian parameters are given in Table I and the principal axes of the $g$ and $A$ tensors are defined in Figure 1.

The absence of any neighboring lattice defects (vacancies, interstitials or impurities) is supported by the symmetry properties of the center, which correspond to those of the pure lattice, as well as by its production properties, resulting in a maximum concentration after short irradiations at low temperatures where ionic movement is frozen.

## 2.2 Optically Induced Production Experiments

Additional evidence favoring the free (conduction) electron self-trapping in $PbCl_2$ is obtained from low temperature (T = 80 K) formation experiments by UV excitation in the fundamental optical absorption combined with earlier optical absorption and photo-conductivity measurements[7] (Figure 2). The optical absorption measurements show a first peak at 4.7 eV and a second, broad one, at 5 eV. According to photoconductivity and luminescence studies[7,10] the band at 4.7 eV corresponds to absorption in the localized excitonic band, where no conduction electrons are produced. Illumination in the higher energy bands (≤ 5 eV) excites electrons into the conduction band.
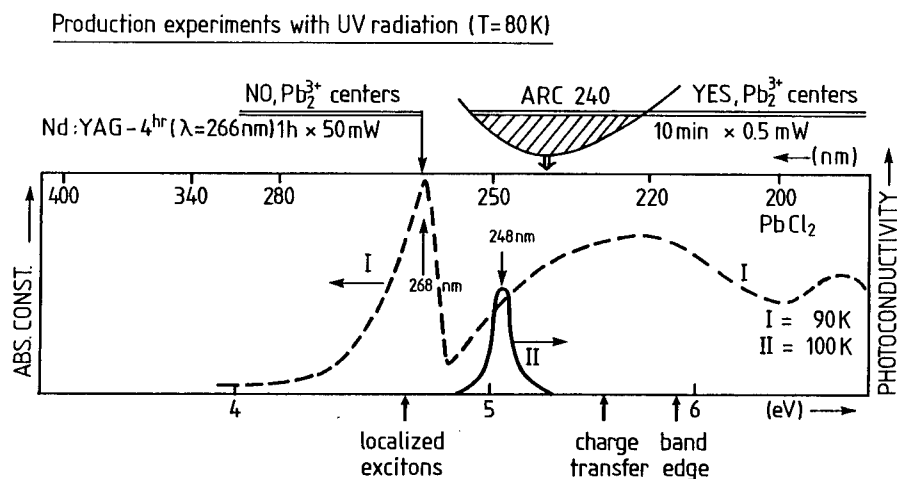


FIGURE 2  Optical absorption and photoconductivity at low temperature of crystalline $PbCl_2$. The results of production experiments of $Pb_2^{3+}$(STEL) centers by UV selective irradiation at T = 80 K are pesented in the upper part of the drawing.
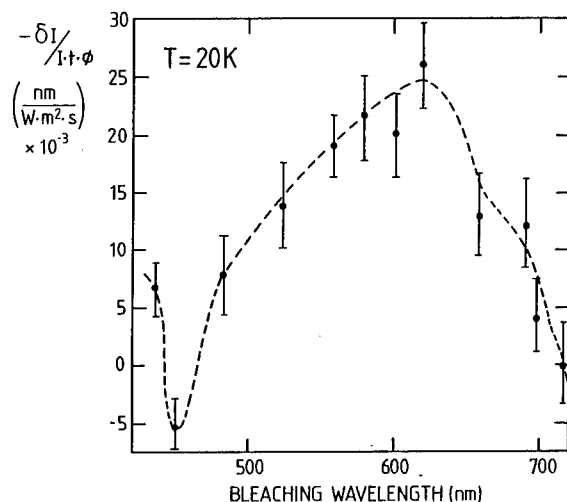
FIGURE 3  Spectral bleaching properties of $Pb_2^{3+}$ (STEL) centers in $PbCl_2$ crystals at low temperature, represented as a variation in their concentration resulting from EPR intensity changes.

In our first experiment the $PbCl_2$ crystal was illuminated with broad band UV light peaking at $\approx 5.17$ eV(240 nm), with a setup supplying a power of about 0.5 mW at the sample. EPR signals attributed to STEL centers have been clearly observed after 10 minutes of illumination. The EPR signals could be optically bleached in a few seconds by removing the ARC-240 interference filter in front of the 200 W xenon lamp and subsequently restored to the initial intensity by resetting the filter.

In a second experiment the illumination was performed with monochromatic UV-light at 4.66 eV ($\lambda = 266$ nm) obtained as the fourth harmonic of a pulsed Nd:YAG laser, supplying an average power of up to 50 mW on the sample. No EPR signals of the STEL centers could be observed even after 1 hour of illumination, although the estimated light intensity was two orders of magnitude higher than in the experiments with broadband UV-light.

The selective UV-irradiation experiments clearly demonstrate that STEL centers are produced by electron trapping, when free (conduction) electrons are available, such as by illumination at $E \geq 5$ eV.

### 2.3 *Optical Bleaching Experiments*

Optical bleaching experiments performed at $T \leq 60$ K, on $PbCl_2$ crystals X-ray irradiated at $T = 80$ K, show (Figure 3) that the STEL centers are bleached out, even at low temperatures, in a broad wavelength range (470–670)nm corresponding to the visible spectrum.

The bleaching of the STEL centers seems to be due to an optical ionization process. The observed simultaneous decrease in the intensity of the $g \approx 2$ centers suggest an electron-hole recombination process in which the $g \approx 2$ centers act as hole trapped centers. What is more important, the result strongly suggests that the STEL center is the primary defect responsible for the photolysis in $PbCl_2$ as well.

## ACKNOWLEDGMENTS

## REFERENCES

1.  J. F. Verwey, *J. Phys. Chem. Sol.* **31**, 163 (1970).
2.  J. Kerssen, W. C. De Gruijter and J. Volger, *Physica* **70**, 375 (1978) and references cited therein.
3.  J. F. Hamilton, Adv. Phys. **37**, 358 (1988).
4.  E. Goovaerts, J. Andriessen, S. V. Nistor and D. Schoemaker, *Phys. Rev.* **B24**, 29 (1981).
5.  E. Goovaerts, S. V. Nistor and D. Schoemaker, *J. Phys.:Condens. Matter* **4**, 9259 (1992) and references cited therein.
6.  S. V. Nistor, E. Goovaerts and D. Schoemaker, *Phys. Rev.* **B48**, 9575 (1993).
7.  J. F. Verwey and N. G. Westerink, *Physica* **42**, 293 (1969).
8.  L. Landau, *Physik. Z. Sowjetunion* **3**, 664 (1933).
9.  R. W. Gurney and N. F. Mott, *Proc. Phys. Soc.* **49** (extra part), 32 (1937).
10. G. Liidja and V. L. Plekhanov, *J. Luminesc.* **6**, 71 (1973) and earlier references cited therein.

# NaF FILMS: GROWTH PROPERTIES AND ELECTRON BEAM INDUCED DEFECTS

M. CREMONA,[d] A. P. SOTERO,[b] R. A. NUNES,[b] M. H. DO PINHO MAURICIO,[a]
L. C. SCAVARDA DO CARMO,[a] R. M. MONTEREALI,[c] S. MARTELLI,[c]
and F. SOMMA[d]

[a]*Dept of Physics, P.U.C./Rio, P.O. Box 38071, 22452-970, Rio de Janeiro, R. J., Brazil;*
[b]*Material Sciences and Metallurgy Dept., PUC/Rio, P.O. Box 38008, 22452-970,
Rio de Janeiro, R.J., Brazil;* [c]*ENEA, Dip. INN., C.R.E. Frascati, P.O. Box 65,
00044 Frascati (RM), Italy;* [d]*Dip. Fis. III Università di Roma, via C. Segre, 2,
00146 Roma, Italy*

Polycrystalline NaF films were grown by e-beam assisted physical evaporation on amorphous silica substrates kept, during film growth, at constant temperatures ranging from 40°C to 400°C. The structural characterization of the films was performed by X-ray diffraction and by scanning electron microscopy.

Irradiating the films with a 15 keV electron beam induced the formation of F and F-aggregate colour centres stable at room temperature. Absorption and photoemission measurements were performed and indicated a dependence of coloration on the deposition conditions.

*Key words*: NaF, thin film, colour centres, electron beam.

## 1 INTRODUCTION

Alkali halides have received very little attention as films. Nevertheless, some studies have been conducted on the growth properties and dielectric characteristics of some of these materials.[1] Recently we have analyzed the growth characteristics and the optical properties modification induced by the electron beam on LiF,[2,3] KCl, KBr and RbCl[4,5] films. The possibility to grow NaF films by Chemical Vapor Deposition (CVD) techniques was recently demonstrated.[6]

The interest in alkali halide polyclystalline films is due to applications in the area of miniaturized optical components and in several fields of basic physic. These materials are electron beam sensitive,[7] allowing the local formation of optically active point defects. Moreover the possibility to grow multilayer alkali halide films, like LiF-NaF,[8] allows to obtain new materials that cannot exist as bulk crystals. These structures permit also the study of the diffusion properties of ions of one layer into the neighboring ones.

The objective of this paper is to study the growth of NaF films on amorphous substrates as a function of their temperature during the film deposition process and to investigate the optical properties of the colour centres created by low-energy electron beams. The structural and morphological analysis of these films was carried out by X-ray diffraction and by scanning electron microscopy (SEM) techniques. Absorption and photoemission measurements were performed for the spectroscopic characterization.

## 2 EXPERIMENTAL RESULTS

NaF films were produced by electron beam assisted physical evaporation on glass substrates whose temperature $T_s$, was kept, during growth, between room temperature (RT) and 400°C. High purity powder (purity better than 99.9%) was used as starting
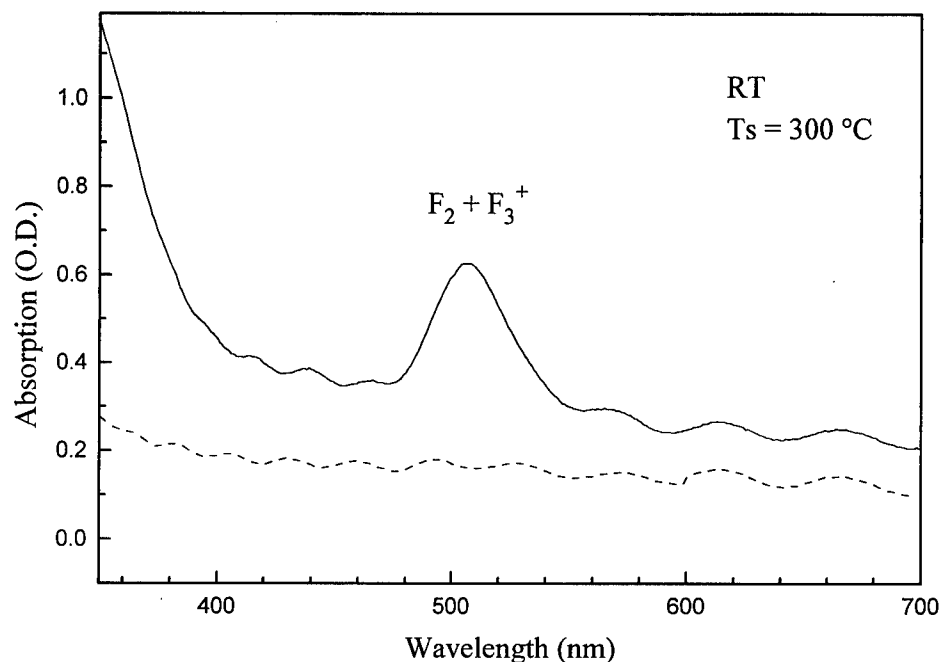
FIGURE 1   Room temperature absorption spectra of a NaF film evaporated at 300°C, dotted, and after 15 keV e-beam irradiation (dose = 125 J/cm$^2$), solid.

material. The film growth rate was 1.2 nm/s .The film thickness, $\sim$ 2.5 $\mu$m, chosen in order to avoid substrate coloration during electron beam bombardement, was controlled by a profilometer, which also showed a good surface quality.

The X-ray diffraction spectra were taken on samples grown at different Ts. We encountered three different film structural configurations by rising the Ts temperature. The pattern of the samples deposited between 40°C and 100°C show peak intensities which are close to the ones of a perfect powder sample. Rising Ts up to 300°C, the deposited NaF shows a pronounced texture with the (l00)-planes parallel to the substrate. Above 300°C a mixed configuration can be distinguished. The wrong intensity ratios, as well as the different shape of the peaks, suggest that the film is composed by layers with different preferred orientations, rather than by an isotropic crystallite distribution.

NaF films were subjected to 15 keV, 200 nA, electron beam irradiation at room temperature. In order to avoid electric charges on the surface, the samples were covered with a thin conductive layer of aluminum or carbon. The used computer controlled electron-gun arrangement was described elsewhere.[9] The beam diameter was 200 $\mu$m in order to minimize local heating of the sample. The coloured area was a 3 mm by 3 mm square. The formation of $F_2$ and $F_3^+$ centres has been evidentiated by absorption and emission measurements. A typical absorption spectrum at RT is shown in Figure 1 for a coloured sample grown at 300°C; the band at 510 nm is due to the $F_2$ (peaking at 498 nm in the bulk crystal) and $F_3^+$ centres (peaking at 520 nm)[10] unresolved bands. The waving structure observed on the spectra of the uncoloured sample (Figure 1) is a light interference pattern on the substrate-film-cover structure, and confirms the uniform thickness of the film.
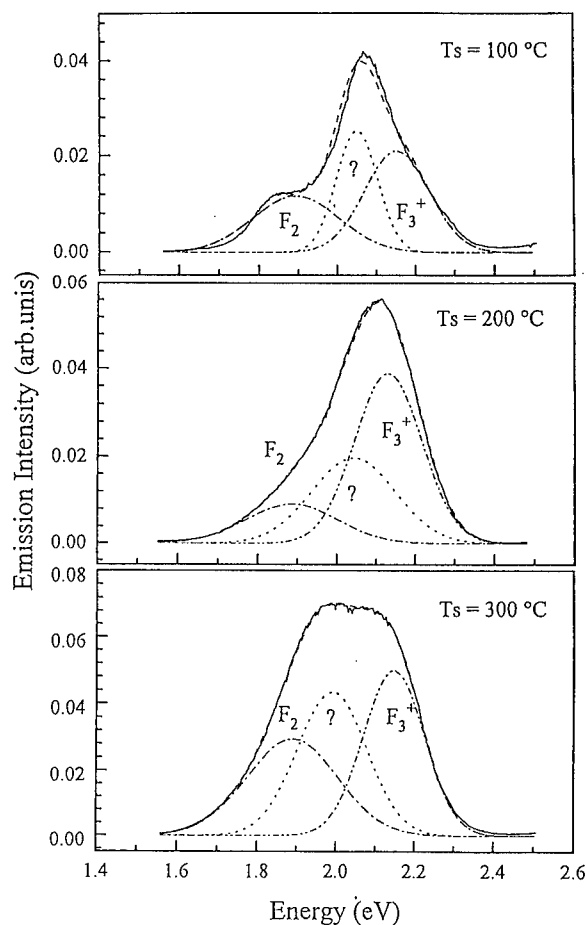
FIGURE 2    Room temperature photoemission spectra of NaF films, grown at different Ts, excited with 488 nm Ar$^+$ laser line with a power of 25 mW. Dashed lines are deconvoluted bands.

Emission measurements were made in a perpendicular geometry with appropriate light filtering. The samples were excited with the Argon laser lines and the emission was measured by a photomultiplier with S-20 response.

Figure 2 shows the RT luminescence spectra of colored films grown at 300°C, 200°C and 100°C, excited by the 488 nm Ar$^+$ laser line. They are composed of three bands, peaking at 655, 580 and 610 nm, which correspond to the $F_2$, $F_3^+$ and an unidentified centre emissions respectively. A similar unknown emission band has been previously found in LiF.[11,12] The film growth parameters influence the photoemission spectra. Indeed, decreasing the substrate temperature, the luminescence intensity is lowered and the $F_2$ emission band is less pronounced than the $F_3^+$ band. As the preferred orientation of these films is practically the same, these differences could be attributed mainly to surface structure. The morphological characterization, by SEM analysis, evidentiates three
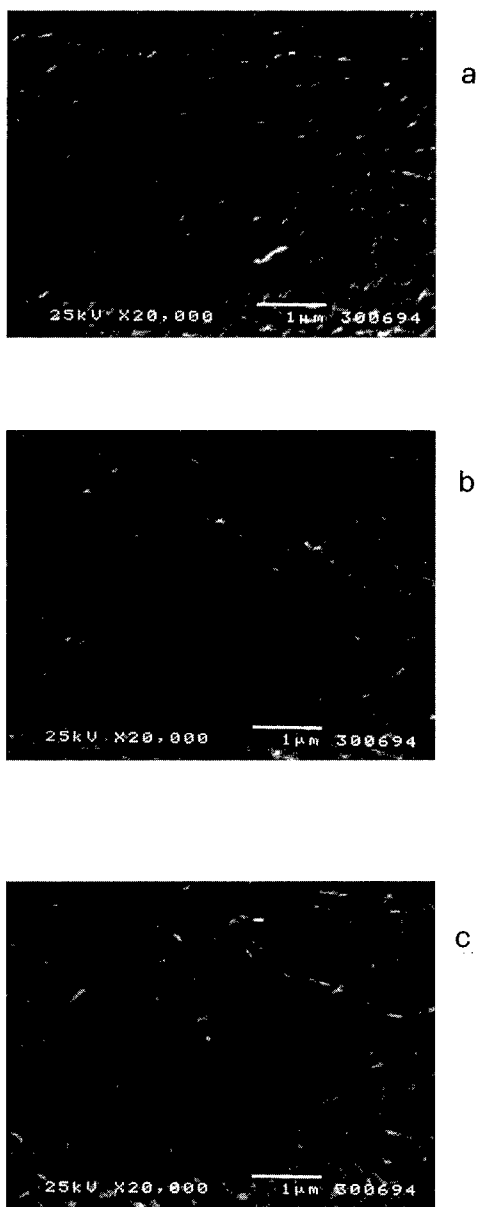
FIGURE 3   SEM pictures of NaF films at different substrate temperature, Ts = 100°C, a, Ts = 200°C, b, Ts = 300°C, c.

different structures (Figure 3). At lower temperature the film is granular with grain size ~ 200 nm; rising the temperature the grain dimension increases and the surface appears more uniform and the microcrystals more closely packed. Indeed, the higher intensity of the luminescence signal seems to be related to the film compactness, while the mechanism of the colour centres formation appears to be influenced by the grain boundary density.

# 3  CONCLUSIONS

The investigated NaF films are polycrystalline and the preferred orientation is influenced by the substrate temperature, which strongly determines surface morphology and density of the films. Low energy e-beam bombardment creates some F-aggregate centres ($F_2$, $F_3^+$) stable at RT. The luminescence spectra depend on the growth parametres. A correlation between the colour centres formation and the structural and morphological characteristics of the films has been evidentiated.

REFERENCES

1. C. Weaver, *Adv. Phys.* **42**, 83 (1962).
2. R. M. Montereali G. Baldacchini, and L. C. Scavarda do Carmo, *Thin Solid Films* **205**, 106 (1991).
3. G. Baldacchini, R. M. Montereali, L. C. Scavarda do Carmo, and S. Martelli, *Radiat. Eff. Def. in Solids* **119–121**, 713 (1991).
4. M. Ferri, A. Scacco, F. Somma, R. M. Montereali, S. Martelli, G. Petrocco and L. C. Scavarda do Carmo, *Radiat. Eff. Def. in Solids* **124**, 313 (1992).
5. F. Somma, A. Ercoli, A. Scacco, R. A. Nunes, M. Cremona, R. M. Montereali and L. C. Scavarda do Carmo *Proc. of XII Int. Conf. Def. Insulat. Mat.*, (World Scien. Publ. Co. Singapore 1993) pp. 1309 and *Radiat. Eff. Def. in Solids* **132**, 143 (1994).
6. L. J. Lingg, A. D. Berry, A. P. Purdy and K. J. Ewing, *Thin Solid Films* **209**, 9 (1992).
7. A. E. Hughes, D. Pooley, H. U. Rahman and W. A. Runciman, *Harwell Atomic Energy Res. Establishment* (1967).
8. R. A. Nunes, A. D. da Silva Sotero, L. C. Scavarda do Carmo, M. Cremona, R. M. Montereali, M. Rossi, and F. Somma, *J. Lumin.* **60–61**, 552 (1994).
9. R. A. Nunes, H. J. Kalinowski, S. Paciornik, A. M. de Souza and L. C. Scavarda do Carmo, *Nucl. Instrum. Meth.* **B32**, 222 (1988).
10. J. Nahum, *Phys. Rev.* **174**, 1000 (1968).
11. H. E. Gu, L. Qi and L. F. Wan, *Opt. Commun.* **67**, 237 (1988).
12. G. Baldacchini, M. Cremona, R. M. Montereali, L. C. Scavarda do Carmo, R. A. Nunes, S. Paciornik and F. Somma, *Opt. Commum.* **94**, 139 (1992).

# DEFECTS IN ION IMPLANTED AND ELECTRON IRRADIATED MgO AND Al$_2$O$_3$

R. S. AVERBACK,[b] P. EHRHART,[a] A. I. POPOV[c] and A. v. SAMBEEK[b]

[a]*Inst. für Festkörperforschung, Forschungszentrum Jülich, D-52425 Jülich, Germany;*
[b]*Mat. Res. Lab. Univ. of Illinois, Urbana, ILL 61801, USA;* [c]*Inst. of Solid State Phys. Univ. of Latvia, LV-1063 Riga, Latvia*

MgO and Al$_2$O$_3$ crystals have been implanted with Ne ions at temperatures between 90 K and 720 K and the damaged layers were investigated by optical absorption spectroscopy and X-ray diffraction. The damage production is discussed in terms of the number of F-centers, of the change of the lattice parameter, and of the diffuse scattering intensity close to Bragg reflections. The stability of the defects was tested in addition by subsequent subthreshold e$^-$-irradiations. No effect of an applied electric field on the defect production is observed for both oxides.

## 1 INTRODUCTION

Irradiation effects in oxides and ceramic materials are of increasing concern within a wide field of technological applications: e.g. the preparation of thin films for electronic and optical devices by ion beam modification techniques, the application of such devices in space or other radiative environments, or the use of bulk oxides as insulators or optical and HF windows in future fusion reactors. Nevertheless the basic damage processes in oxides are much less understood than in meals and alloys even for the most simple model oxides like MgO and Al$_2$O$_3$. In addition to the possibly different behaviour of the same defects within different charge states, there is a major complication for the modelling of the defect evolution in displacement cascades due to the interaction of defects on the different sublattices. These sublattices might be characterized by quite different (real or apparent) threshold energies for defect production. There is much detailed spectroscopic information on the production of F-centers (vacancies on the oxygen sublattice), however, the vacancies on the metal sublattice, V-centers, are discussed controversely and there is no information on the behaviour of the interstitial atoms. Along with the observation of radiation induced electrical degradation (RIED) there has been speculated about a strong dependence of the production rate of F-centers on small applied electric fields.[1] Similar to earlier investigations after e$^-$-irradiation,[2] we have combined optical absorption spectroscopy with X-ray diffraction techniques, that should reflect the total number of defects independent of their electronic structure, in order to get some additional insight into the defect production.

## 2 EXPERIMENTAL TECHNIQUES

The samples were [100]-oriented MgO crystals and (11$\bar{2}$0)-oriented Al$_2$O$_3$ crystals with a typical size of 15 × 5 × 0.5 mm$^3$. The ion implantations have been performed with Ne-ions of a maximum energy of 2.7 MeV at temperatures of 77 K and 250°C for MgO and at 90 K and 450°C for Al$_2$O$_3$. By varying the energy of the ions and of the angle of incidence a homogeneously implanted layer of 1.5 $\mu$m thickness was envisaged according
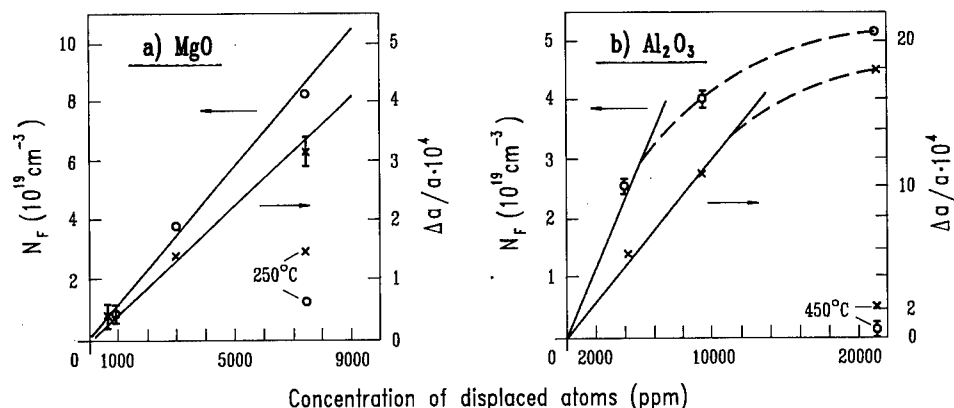
R. S. AVERBACK *ET AL.*



FIGURE 1   Dependence of the density of F-centers, $N_F$, and of the change of the lattice parameter, $\Delta a/a$ on the irradiation dose with $Ne^+$-ions. The irradiation dose is given in units of the number of displaced atoms as calculated by TRIM for MgO (a) and $Al_2O_3$ (b). The irradiation temperature was 77 K for MgO and 90 K for $Al_2O_3$, and the results of a high temperature irradiation are shown for the highest dose in addition.

to TRIM calculations, and the irradiation dose for the implanted layer will be given in terms of the total number of vacancies expected for this layer. The measurements of the optical absorption were performed at room temperature.

The change of the lattice parameter perpendicular to the surface was determined from the shift of the rocking curves with respect to the undamaged deeper layers. The intensity of the Huang diffuse scattering, $S_{HDS}$, was investigated close to different Bragg reflections using $CuK_{\alpha 1}$ radiation at a temperature of 6 K. Both $\Delta a/a$ and $S_{HDS}$ are essentially determined by the concentration, c, and the relaxation volume, $v^{rel}$ of a point defect (see e.g.[3]) and as we will consider Frenkel pairs, i.e. pairs of vacancies and interstitial atoms, this yields

$$\Delta a/a \sim c(V_i^{rel} + V_v^{rel}) \quad \text{and} \quad S_{HDS} \sim c((V_i^{rel})^2 + (V_v^{rel})^2) \tag{1}$$

The HDS is characterized by a decrease of the intensity proportional to the square of the distance q from the nearest reciprocal lattice point (i.e. $S_{HDS} \sim 1/q^2$). This scattering intensity is, however, modified if the defects interact and form larger agglomeratres: at larger values of q, i.e. $q_{crit} \geq 1/R$ (where R is the radius of the agglomerate) there is a steeper decrease like $1/q^4$ and at smaller values of q the intensity is increased proportional to the number, n, of defects within the cluster.

## 3   RESULTS AND CONCLUSIONS

### 3.1   *Dose- and Temperature Dependence of the Defect Production*

Figure 1a/b summarizes the production of F-centers and the change of the lattice parameter for MgO and $Al_2O_3$, respectively. For the 77 K irradiation of MgO we observe a linear increase of both quantities with dose whereas there is some indication of saturation for $Al_2O_3$. For the high temperature irradiations we observe a much lower density of F-centers in MgO, although there is no well-established defect annealing stage below that temperature;[2,4] however, there is a smaller decrease in $\Delta a/a$, that reflects the number of interstitial atoms. Hence, we may conclude, that at these higher temperatures a larger
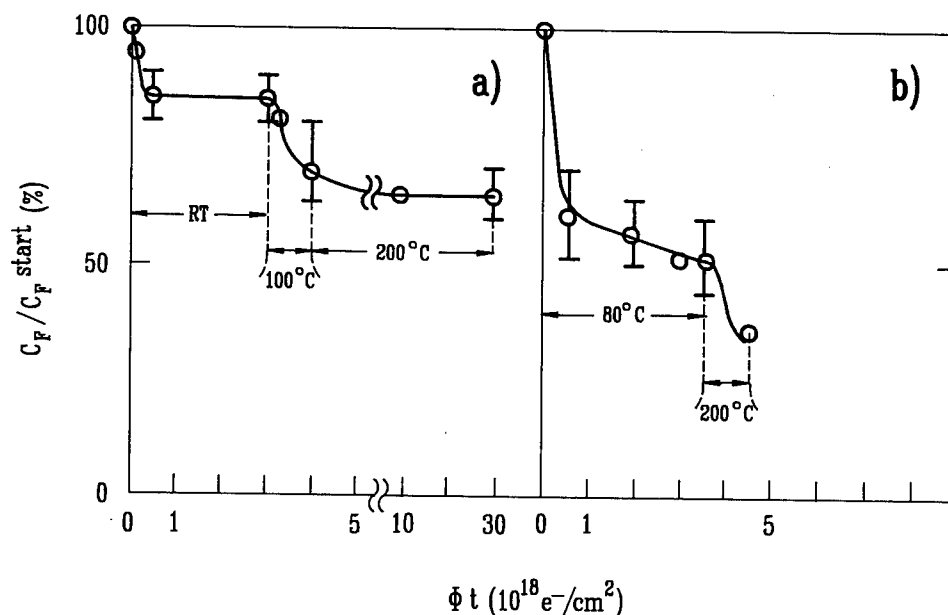
FIGURE 2 Annealing of F-centers, that have been introduced by electron irradiation at 6 K ($N_F \approx 5 \cdot 10^{17}$ cm$^{-3}$) (a) or by Ne$^+$ implantation at 77 K ($N_F \approx 10^{19}$ cm$^{-3}$) (b), during 'sub-threshold' irradiations ($E_e \leq 0.35$ MeV) at temperatures between 20°C and 200°C. The error bars represent the behaviour of samples irradiated with different doses.

percent of vacancies is contained in clusters, that are optically not detected, i.e. $c_F$ underestimates the total number of defects.

## 3.2 Stability of the Irradiation Defects

After low temperature electron irradiation a decrease of the F-center concentration was observed during a subsquent irradiation with 0.3 MeV electrons, i.e. energies below the threshold for defect production. This annealing was attributed to a ionization induced and thermally assisted annealing of close Frenkel pairs.[2] The results of such subthreshold irradiations for the Ne-irradiated samples are shown in Figure 2b and compared to some additional experiments with electron irradiated samples (Figure 2a). The annealing process is even larger for the ion irradiations and is increasing with increasing irradiation temperature. Hence, we can conclude that a large fraction of the F-centers is contained within the configuration of close Frenkel pairs or very closely correlated vacancies, that can recombine or agglomerate under subthreshold irradiation, and we may expect differences in the production rates for different irradiation particles (with different ratios of nuclear and electronic stopping) as well as for different irradiation temperatures.

## 3.3 Structure of the Defect Agglomerates

Figure 3a shows the diffuse scattering close to a (400)-reflection of low temperature Ne-implanted MgO. We observe a $q^{-2}$ decrease over a wide range of q and the indication of a steeper $q^{-4}$ decrease at the larger values of q; this yields a cluster radius $R_a \leq 4$ Å, i.e.
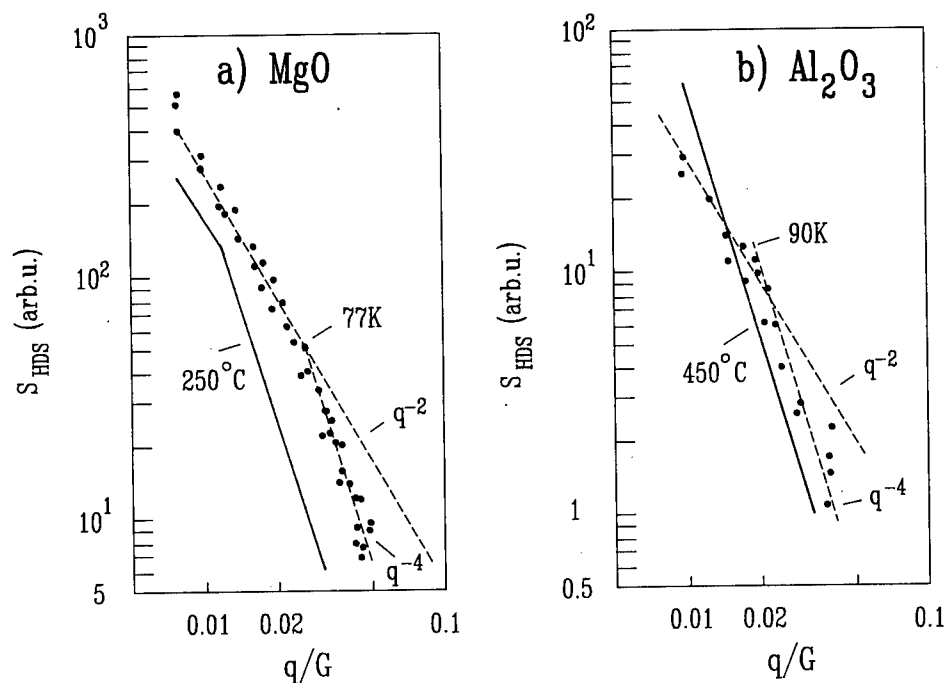
FIGURE 3   Intensity of the HDS close to a (400)-reflection of MgO (a) and close to a (22$\bar{4}$0)-reflection of Al$_2$O$_3$ (b). The distance from the Bragg reflection is given in units of the reciprocal lattice vector $G$. Data points are shown for the low temperature irradiation to the highest dose and a line shows the changes for a high temperature irradiation to the same dose.

rather small agglomerates of 10–20 atomic defects. From the details of the scattering distribution we conclude that the larger agglomerates are interstitial clusters. In addition this diffuse intensity increases faster than linearly with dose. This behaviour shows that the clusters grow during prolonged irradiation. The high temperature irradiation shows a similar intensity at small q and the begin of the $q^{-4}$ decrease indicates an increase of the cluster radius by more than a factor of 2. Figure 3b shows a very similar behaviour for low temperature implanted Al$_2$O$_3$, i.e. we observe again a defect spectrum ranging from single Frenkel pairs as evidenced by the F-center absorption up to larger defect agglomerates as indicated by the diffuse scattering.

### 3.4   *Influence of Applied Electric Fields*

Several irradiations were repeated with an electric field of $\approx$ 1300 V/cm applied during irradiation. For neither of these experiments (750 ppm at 77 K and 7500 ppm at 250°C with MgO and 20 700 ppm at 450°C for Al$_2$O$_3$) there was a significant difference to the irradiations without field in any experiment, $c_F$, $\Delta a/a$, $S_{HDS}$. Hence, we conclude there seems to be no influence of these small fields on the primary damage processes.

REFERENCES

1. E. R. Hodgson in *Defecst in Insulating Materials* (World Scientific 1993) p. 332.
2. C. Scholz and P. Ehrhart, *Mat. Res. Soc. Proc. Vol.* **279**, 427 (1993).
3. P. Ehrhart, *Mat. Res. Soc. Proc. Vol.* **41** 13 (1985).
4. B. D. Evans, *Phys. Rev.* **B9** 5222 (1979).

# EPR-STUDY OF ELECTRON-RADIATION INDUCED Ca COLLOIDS IN CaF$_2$ CRYSTALS

F. BEUNEU, C. FLOREA and P. VAJDA

*Laboratoire des Solides Irradiés, CEA-CNRS, Ecole Polytechnique, F-91128 Palaiseau*

Oriented single-crystal specimens of CaF$_2$ have been irradiated at room temperature with electrons of 0.5 and 1 MeV energies and their EPR-spectra taken in the range 4 K $\leq$ T $\leq$ 300 K. The observed spectra present numerous temperature-dependent peaks attributed to the V$_F$-center, the U-center and to Ca colloids. The defects are unstable at room temperature, the main peaks decreasing by an order of magnitude in intensity after a month. Isochronal annealing studies revealed a complex evolution of the principal peaks occurring in two stages between room temperature and 500°C. Parallel dielectric-constant measurements performed on the same specimens at room temperature exhibited analogous recovery stages of the real component of the dielectric constant, $\varepsilon'$. The results are interpreted in terms of metal-colloid formation and evolution.

*Key words*: CaF$_2$, electron irradiation, colloids, EPR, dielectric constant.

## 1 INTRODUCTION

Johnson and Chadderton described the formation of anion voids and their agglomeration into a superlattice in CaF$_2$ irradiated in a high-voltage electron microscope[1]. Cation colloids can also be formed by additive colouring, through controlled doping with Ca vapour.[2] A comprehensive review of the properties and behavior of metal colloids in ionic crystals has been given by Hughes and Jain.[3]

We shall report results obtained after irradiation of CaF$_2$ crystals near room temperature with electrons of various energies and doses, at fluences where no void ordering is observed. The introduced primary defects as well as the metal colloids were investigated by electron spin resonance and by microwave dielectric-constant measurements.

## 2 EXPERIMENTAL

Samples were cut with a tungsten wire saw from a single crystal of CaF$_2$ of 99.99 at.% metallic purity. All samples had a parallelepipedic shape with typical sizes of $5 \times 1 \times 0.2$ mm$^3$, with the main plane oriented (110) and the longest side [110], as controlled by X-rays.

Electron irradiations were performed with a Van de Graaff accelerator. The energy of the electrons was 0.5 and 1 MeV. For 0.5 MeV electrons, the range of CaF$_2$ is 800 $\mu$m,[1] much larger than the sample thickness. As the samples showed a tendency to evolved at room temperature, the EPR experiments were begun as soon as possible after the end of the irradiation. Complementary experiments consisted in (i) an X-ray irradiation at room temperature and (ii) a low temperature electron irradiation (20 K) with comparable flux.

X-band EPR experiments were performed in the 4 to 300 K temperature range. The sample could be rotated with respect to the magnetic field orientation. Dielectric constant measurements were done by introducing the same sample into a small hole drilled in a cavity with 8 resonant modes in the 7–15 GHz range. From the pertubation of these modes by the sample, the $\varepsilon'$ and $\varepsilon''$ values could be calculated.
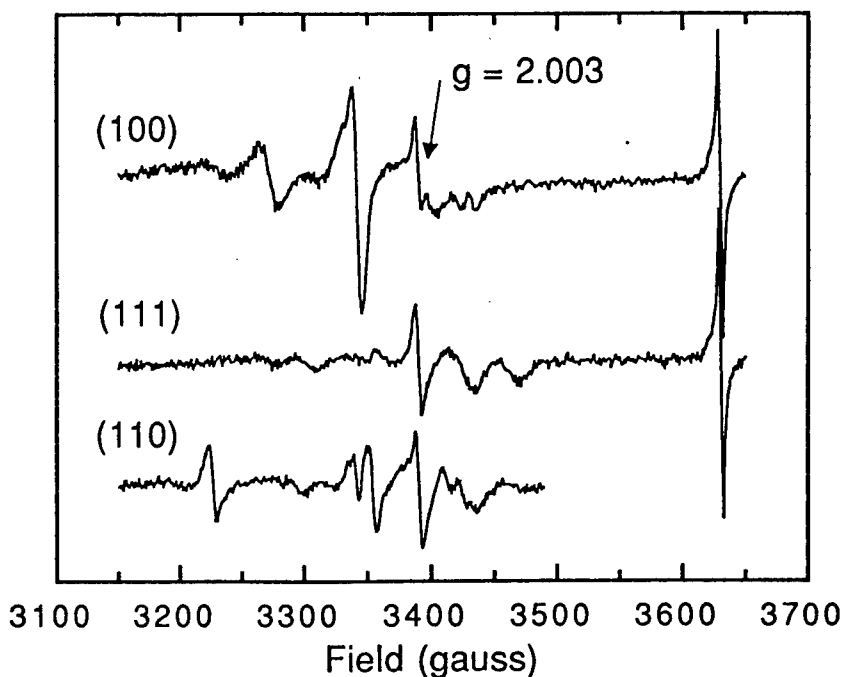
FIGURE 1    EPR spectra (at $T_m = 20$ K) of the three principal orientations of a $CaF_2$ crystal irradiated with 1 MeV electrons to a dose of 30 $C/cm^2$.

Between each cycle of measurements (EPR and dielectric constant) a thermal treatment of the sample was done: first, just waiting 24 h at room temperature; second, annealing in air from 50°C to 450°C; third, annealing under vacuum of $10^{-6}$ Torr from 500°C to 900°C.

## 3   RESULTS

Our results confirm the importance of the irradiation temperature, as reported in literature:[1,4] the sample irradiated at 20 K exhibited only slight colouring and gave an EPR signal whose hyperfine structure was consistent with an F centre, while the other samples, irradiated around room temperature, were completely black and showed the complex EPR behaviour described below.

We shall concentrate now on the room-temperature irradiated samples having received a dose of $\sim$ 30 $C/cm^2$, corresponding to $\sim$ 1 dpa. A typical EPR spectrum, taken at 20 K, is given in Figure 1, for three orientations of the magnetic field relative to the crystal. Three families of lines can be distinguished:

i)   a two-line isotropic spectrum, with 520 ± 10 gauss spacing, centred on g = 2.006, corresponding to the U centre described by,[5] i.e. an H interstitial. On Figure 1, only one line is visible around 3630 gauss.
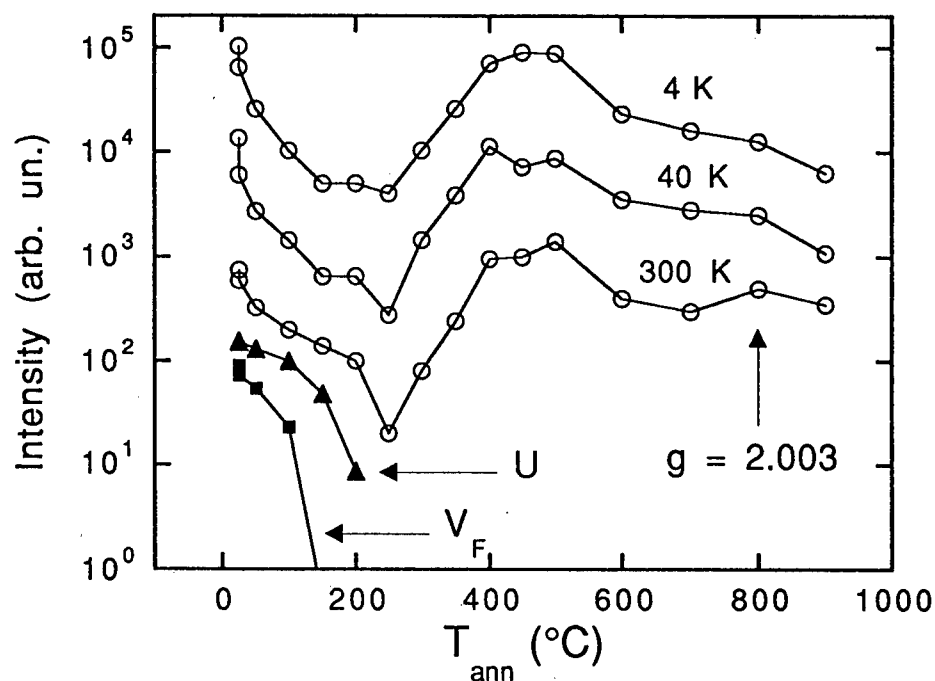
FIGURE 2   Annealing behaviour of the irradiation-induced changes. EPR-intensities of (i) colloid center
(g $= 2.003$ line) at $T_m = 4$ K, 40 K and 300 K; (ii) $V_F$ center at $T_m = 4$ K; (iii) U-center at $T_m = 40$ K. The
intensities of the three lines are in arbitrary relation to each other.

ii) a multi-line signal, very anisotropic, with a broad extent (up to 1800 gauss), attributed
   to the $V_F$ centre first described by.[6]
iii) a single, isotropic line with g $= 2.0030 \pm 0.0008$.

      All these lines follow a Curie law between 4 and 300 K, without any significant
variation of the linewidth.

      The dielectric constant measurements gave the following results: the real part $\varepsilon'$
increases from $\sim 6$ (unirradiated CaF$_2$) to 10 after irradiation, with no particular frequency
dependence in the 7–15 GHz range; the imaginary part $\varepsilon''$ is very small and thus not
measurable.

      On Figures 2 and 3 we summarize the annealing behaviour of the irradiated samples:
Figure 2 for the intensities of the 3 families of EPR lines and Figure 3 for the EPR
linewidth of the g $= 2.003$ line and for $\varepsilon'$. We note a strong intensity decrease of all
investigated lines after annealing in the region between room temperature and 250°C: the
g $= 2.003$ line in a broad structure (after the initial time-dependent drop at 25°C), the $V_F$
and the U-lines in one narrow stage each; $\varepsilon'$ exhibits its first annealing stage in this
interval. The g $= 2.003$ line recovers strikingly between 250 and 450°C, which
corresponds to the second annealing stage of $\varepsilon'$. Finally, the linewidth $\Delta H$ begins to
decrease after $T_{ann} = 400$°C.
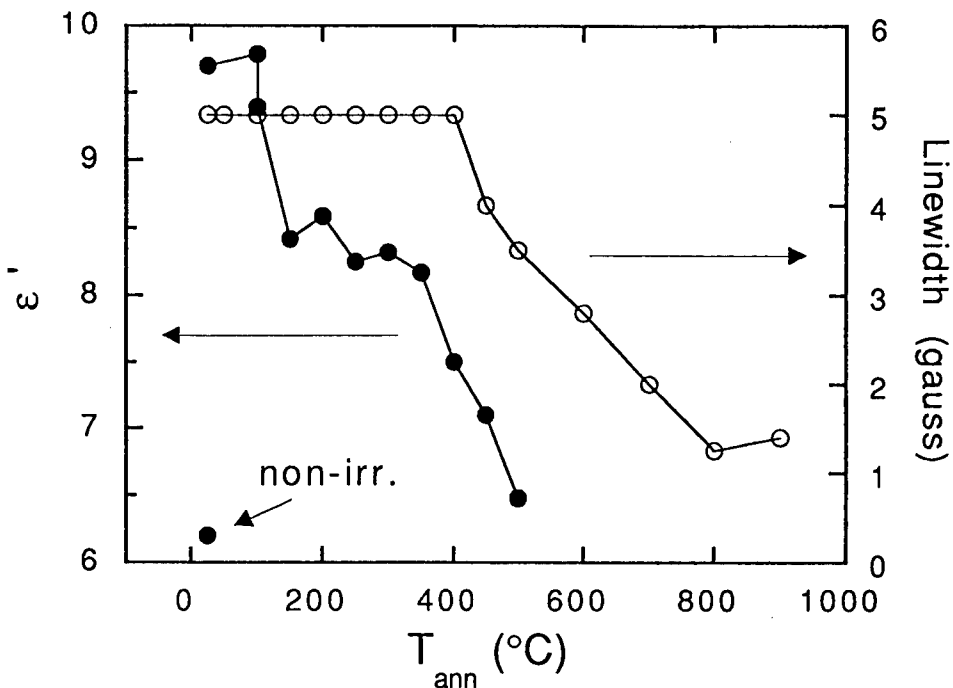
FIGURE 3    Dielectric constant $\varepsilon'$ in the X-band range, at 300 K; linewidth $\Delta H$ of the g $= 2.003$ line at 4 K.

## 4    DISCUSSION

Wurster *et al.*[4] have determined the evolution of the relative concentration of calcium clusters, $c_{rel}$, after isochronal annealing from optical absorption and phonon transmission spectroscopy. They noted a drop in $c_{rel}$ of the order of 50% between room temperature and 300°C (their first annealing point), followed by a rather steady decrease towards zero until 450°C; the cluster size is assumed to be unaffected by annealing, R $\sim$ 60 Å. At the same time, they observed a growth in the H-center (anion interstitials) and a parallel drop of the F-center concentration.

In our case (Figure 2), the colloid line (g $= 2.003$) has lost more than half of its immediate post-irradiation intensity after 24 hours at room temperature, and it drops by another factor of ten in subsequent anneals up to 250°C. It is important to note here that the annealing occurs in a broad and asymmetric stage, with a width of $\Delta T \sim 200$ K for a process centered at $\sim$ 75°C (350 K). On the other hand, the $V_F$-centers and the U-centers (Figure 2) anneal in simple narrow stages of a width $\Delta T \sim 50$ K, respectively at 120°C and 170°C. The same is true for the first recovery stage of $\varepsilon'$ (Figure 3) occurring between 100 and 150°C. It is tempting to attribute the first broad recovery stage of the g $= 2.003$ line to a complex process involving a mixture of transformation and recombination processes. The intensity increase after annealing in the region between 250 and 450–500°C, corresponding to the second recovery stage of $\varepsilon'$ (Figure 3), is another indication of the transformation of simpler defects and their contribution to the colloid line.

Further heating of the specimens leads first to a drastic reduction of the g = 2.003 line intensity (by a factor of 3 to 4) at $T_{ann}$ = 600°C, due to the dissociation of dislocation loops and the loss of their cluster trapping efficiency, then to a continuous decrease up to 900°C indicating the destruction of colloids, with probable transformation into larger units before vanishing. The latter is supported by the evolution of the linewidth, $\Delta H$, which begins to decrease after $T_{ann}$ = 400°C and continues steadily up to the highest anneals (Figure 3). This goes conform with the behaviour of metallic particles exceeding sizes of R $\sim$ 100 Å,[3] where the concept of a mean free path begins to be meaningful and surface effects are dominant. Our particle size must, however, be just at the lower limit of this behaviour, as the intensity is still following a Curie law. Finally, it is encouraging that the glow curves observed by Bangert et al.[7] in self-ion bombarded CaF$_2$ behaved rather similarly. They exhibited peaks at 180, 220 and 350°C which grew after thermal treatment at 240°C but vanished after heating to 550°C, implying the evolution and destruction of intrinsic defect clusters.

REFERENCES

1. E. Johnson, L. T. Chadderton, *Rad. Eff.* **79**, 183 (1983).
2. V. M. Orera, R. Alcala, *Phys. Status Solidi* **A38**, 621 (1976).
3. A. E. Hughes, S. C. Jain, *Adv. in Phys.* **28**, 717 (1979).
4. C. Wurster, K. Lassmann, W. Eisenmenger, *Phys. Rev. Lett.* **70**, 3451 (1993).
5. R. A. Weeks, M. Abraham, *J. Chem. Phys.* **42**, 68 (1965).
6. J. Sierro, *Phys. Rev.* **138**, A648 (1965).
7. U. Bangert, K. Thiel, K. Ahmed, P. D. Townsend, *Rad. Eff.* **64**, 153 (1982).

# DEFECT MECHANISMS IN THE THERMOLUMINESCENCE OF LiF:Mg, Cu, P

## S. MAHAJNA, D. YOSSIAN and Y. S. HOROWITZ

*Physics Department, Ben Gurion University of the Negev Beersheva, 84105 Israel*

We have studied the behaviour of the glow peaks in the thermoluminescence of LiF:Mg, Cu, P as a function of pre-irradiation annealing temperature in the range of 80°C to 170°C, and as a function of cooling rate following the 240°C/10 min. anneal used for standardization in dosimetric procedures. The intensities of the major peaks in LiF:Mg, Cu, P (as well as in LiF:Mg,Ti—the current industrial standard) seem to be determined by the dynamics of clustering of ($Mg^{2+}$-$Li_{vac}$) dipoles to dimers, trimers and a precipitate phase. The intensities of the thermal interactions, however, seem to be somewhat reduced in LiF:Mg, Cu, P compared to LiF:Mg, Ti. In addition, it seems plausible that phosphorus takes the role of titanium in LiF:Mg, Cu, P in the formation of a trapping center/recombination center spatially correlated complex.
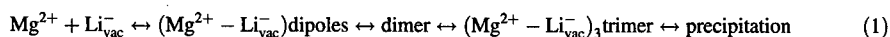
*Key words*: Lithium Fluoride, Thermoluminescence, Defects, Annealing.

## 1 INTRODUCTION

LiF:Mg, Ti is the leading material for dosimetry applications. LiF:Mg, Cu, P is a new, high sensitivity, material.[1] Their glow curves (Figure 1a, b) following various annealing procedures show obvious superficial similarities. In addition, the main TL peaks at 210°C both have anomalously high E and s values. These superficial similarities are overshadowed, however, by differences in their annealing behaviour. LiF:Mg, Ti is standardized by a 400°C anneal. LiF:Mg, Cu, P cannot be annealed above 240°C without irreversible changes in the glow curve structure.[2] The dependence on cooling rate following the 400°C anneal in LiF:Mg, Ti is believed to arise from trap conversion phenomenae.[3] Peaks 4 and 5 are based on clusters (dimers and/or trimers) of dipole trapping centers responsible for peaks 2 and 3. Clustering of pairs into dimers/trimers may also occur during glow curve readout[4] and the probability of the clustering is dependent on the microscopic spatial distribution of the dipoles.[5] Intensity correlations led Grant and Cameron[6] to suggest that peaks 2 and 3 are associated with ($Mg^{2+}$-$V_c^-$) dipoles while suggesting that peak 5 is a higher order cluster of three dipoles (trimer). More recently it has been suggested that the trimer is spatially correlated with $Ti^{+3}$ ions to form an even larger trapping-recombination complex.[7] The presence of these complicated trap conversion processes have not yet been studied to any degree in LiF:Mg, Cu, P which motivated these investigations.

## 2 RESULTS AND DISCUSSION

Reaction (1) illustrates the process of clustering. Various authors[7] have demonstrated that 250°C marks the onset of precipitation of Mg from solid solution. Taylor and Lilley[8] have illustrated that even at low temperatures substantial precipitate formation can be expected if sufficient time is allowed.

$$Mg^{2+} + Li_{vac}^- \leftrightarrow (Mg^{2+} - Li_{vac}^-)\text{dipoles} \leftrightarrow \text{dimer} \leftrightarrow (Mg^{2+} - Li_{vac}^-)_3\text{trimer} \leftrightarrow \text{precipitation} \qquad (1)$$
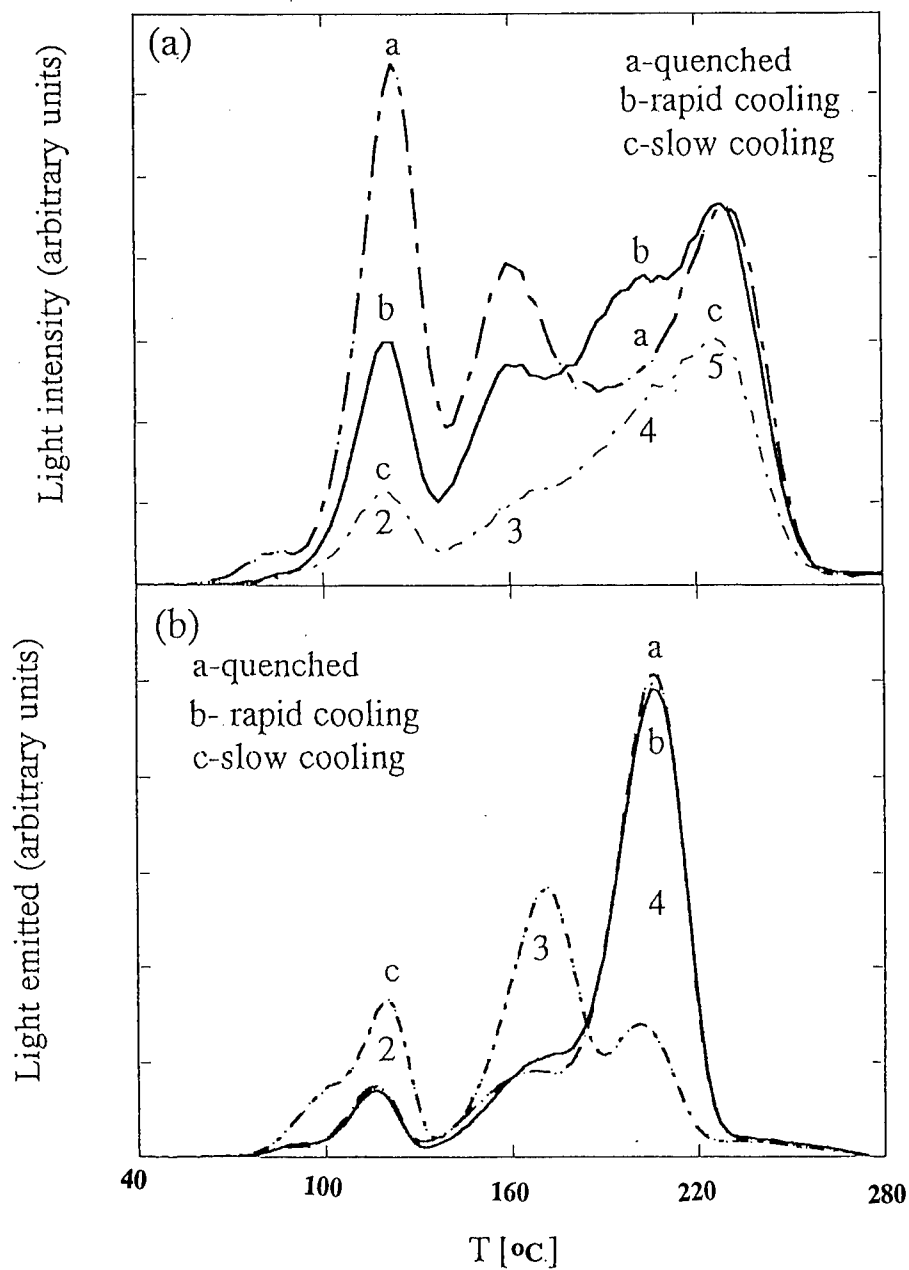
FIGURE 1    (a) Glow curves of LiF:Mg, Ti (TLD-100) showing the effect of cooling rate following the 400°C pre-irradiation anneal. (b) Glow curves of LiF:Mg, Cu, P (GR-200) showing the effect of cooling rate following the 240°C pre-irradiation anneal. (a) quenched into acetone, (b) rapid cooling rate of approximately $100°C$ $min^{-1}$, (c) slow cooling rate of approximately $1°C$ $min.^{-1}$
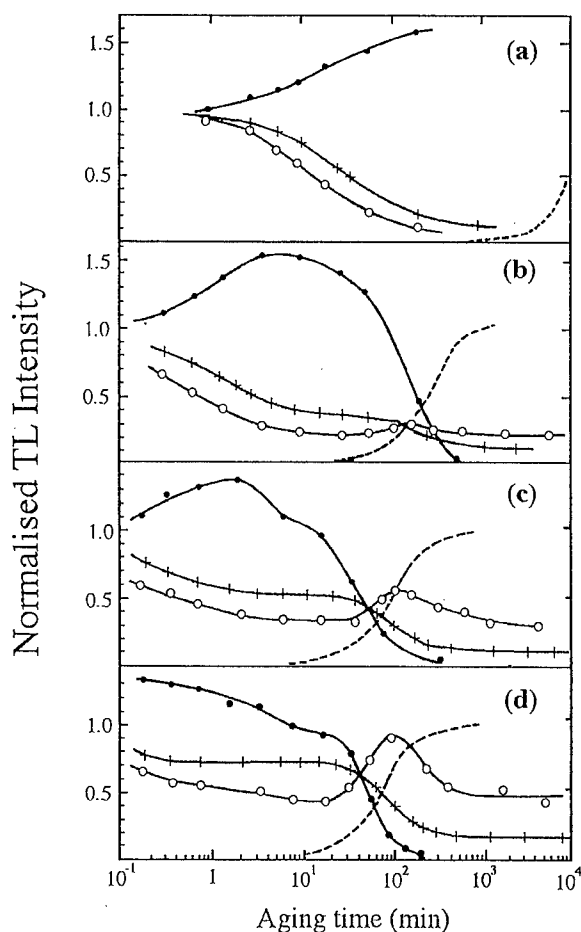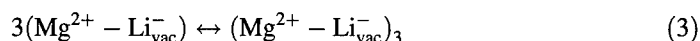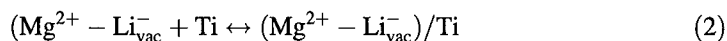
FIGURE 2   The behaviour of the intensity of peaks 2 and 5 in LiF:Mg, Ti as a function of annealing time at various pre-irradiation temperatures: (a) 80°C, (b) 130°C, (c) 150°C and (d) 170°C. ● (peak 5); ○ (peak 2); ╪ (dipole concentration); - - - - precipitate concentration. According to Taylor and Lilley (8).

Figure 2[8] illustrates the behaviour of LiF:Mg, Ti at various ageing temperatures. A close correlation exists between the decay of the dipoles and the decay of peak 2 over the initial periods of storage which breaks down at longer ageing times. This is usually cited as important evidence against the claim that peak 2 is associated with a structure based on dipoles only. On the basis of spectral emission data, McKeever[9] has suggested that peaks 2 and 5 consist of a spatially correlated electron trap based on $Mg^{2+}$ and a luminescence recombination center based on $Ti.^{3+}$ Peak 2 with a dipole based complex according to reaction (2) and peak 5 to a trimer based complex according to reaction (3).

$$(Mg^{2+} - Li_{vac}^- + Ti \leftrightarrow (Mg^{2+} - Li_{vac}^-)/Ti \qquad (2)$$

$$3(Mg^{2+} - Li_{vac}^-) \leftrightarrow (Mg^{2+} - Li_{vac}^-)_3 \qquad (3)$$
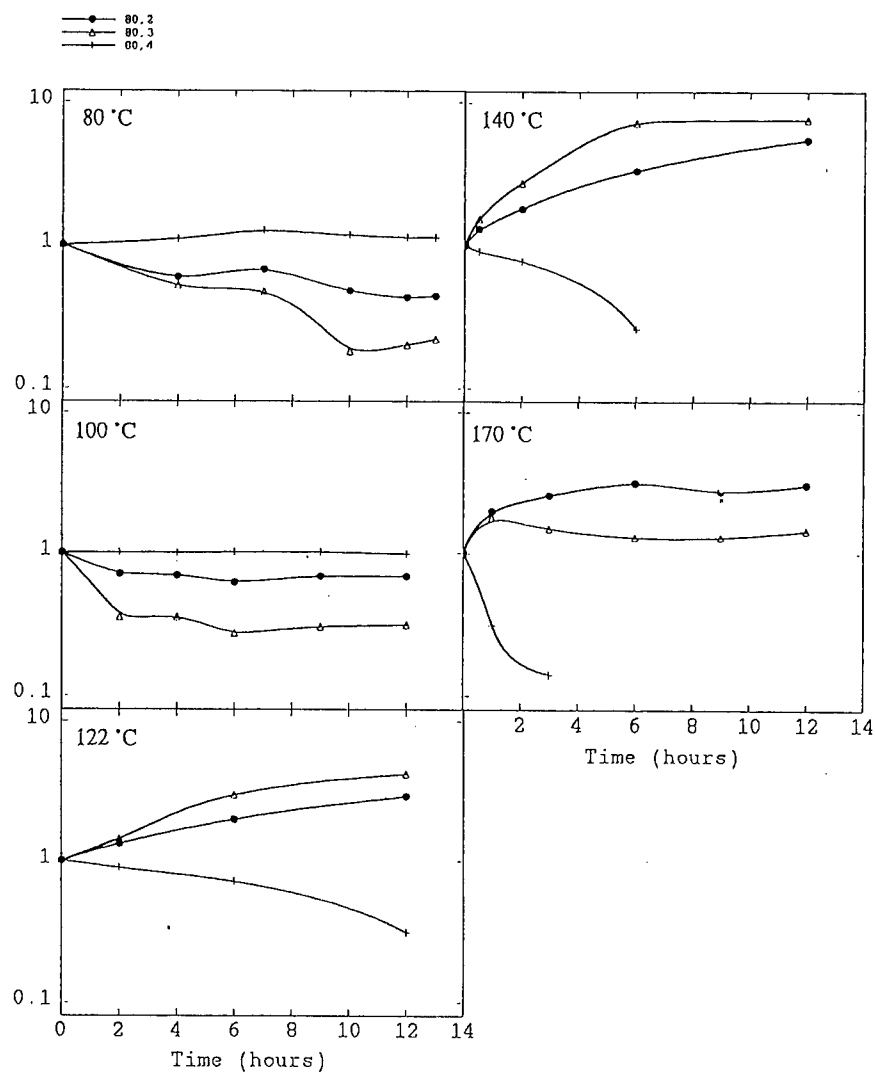
FIGURE 3   The behaviour of the intensity of peaks 2 (●), 3 (△) and 4 (|) in LiF:Mg, Cu, P as a function of duration of annealing at various temperatures (a) 80°C, (b) 100°C, (c) 122°C, (d) 140°C, (e) 170°C.

The association with Ti is indicated as the reason that the dipole concentration and peak 2 intensity data do not correlate at longer annealing times. Figure 3 shows the results of our annealing experiments for LiF:Mg, Cu, P. There are striking similarities in the behaviour of the two materials, so that it is reasonable to assume that the same defect reactions are also occurring in LiF:Mg, Cu, P with P replacing Ti as the primary entity of the

luminescent recombination center. Based on optical absorption data, McKeever et al[11] suggested that if the same Mg based defect species are dominant in LiF:Mg, Cu, P, the slightly different optical absorption observed could be due to the defect absorption being perturbed by the presence of Mg precipitate phases in LiF:Mg, Cu, P which will certainly be present even after a 240°C/10 min anneal. Phosphorus appears to play a more dominant role than Cu in the TL of LiF:Mg, Cu, P.[12] Peak 4 in LiF:Mg, Ti (which is believed to be a hole trap) appears to be absent in LiF:Mg, Cu, P. Returning to Figure 3 it is interesting to note the abrupt change in behaviour in the annealing data at 122°C and above. Peaks 2 and 3 now increase in intensity whereas peak 4 is rapidly diminished. This simply means that the trimer concentration has decreased with reaction (2) moving to the left; the concentration of dipoles has increased so that reaction (3) (with P replacing Ti) moves to the right. It is somewhat more difficult to explain the very strong increase in peaks 2 and 3 at 140°C compared to the reduced increase in intensity at 170°C, even though the reduction in peak 4 is much faster at 170°C. Reaction (1) produces a precipitate phase following trimer aggregation. The increased intensity of peaks 2 and 3 at 140°C (cf 170°C) may therefore be due to the precipitation beginning earlier at 170°C. Since precipitation is generated from the clustering of dipoles, trimers and free Mg, the onset of the precipitated phase could indeed be accompanied by a decrease in the trimer and dipole concentrations leading to a decrease in the intensity of peaks 2, 3, and 5 at 170°C. These considerations are strengthened by the cooling rate behaviour shown in Figures 1a, b. In LiF:Mg, Ti annealing at 400°C dissolves the precipitate phase and other·clusters to dipoles, free Mg and free vacancies. A rapid quench to room temperature freezes in the defect concentration as shown in curve (a) in Figure 1a., the major defect therefore is in the dipole configuration. Rapid cooling (curve (b)) decreases the intensity of peaks 2 and 3 due to the decrease in the dipole concentration and slow cooling (curve (c)) decreases the intensity of all the peaks due to the beginning of the precipitate phase which decreases the concentration of dipoles and trimers. In LiF:Mg, Cu, P the same dynamics are observed for peak 4 but peaks 2 and 3 behave in a somewhat different manner. There is no change in the intensity of peaks 2 and 3 between the quench and the rapid cool but peaks 2 and 3 are enhanced via slow cooling. This behaviour is also observed in LiF:Mg, Ti but it begins at a slower cooling rate than in LiF:Mg, Cu, P. This behaviour may be due to an increase in dipole concentration as the precipitate phase is formed from dimers and trimers. In summary it appears possible to qualitatively explain the behaviour of LiF:Mg, Cu, P in a manner similar to that of LiF:Mg, Ti. The intensities of the thermal interactions, fortunately for dosimetry purposes, seem to be somewhat reduced in LiF:Mg, Cu, P.

REFERENCES

1. Y. S. Horowitz, *Radiat. Prot. Dos.* **47**, 135 (1993).
2. A. Horowitz and Y. S. Horowitz, *Radiat. Prot. Dos.* **33**, 279 (1990).
3. S. W. S. McKeever, *Thermoluminescence of Solids*, (Cambridge University Press) (1986).
4. G. C. Taylor and E. Lilley, *J. Phys. D. Appl. Phys.* **15**, 2053 (1982).
5. B. B. Shachar and Y. S. Horowitz, *J. Phys. D. Appl. Phys.* **24**, 1649 (1991).
6. R. M. Grant and J. R. Cameron, *J. Appl. Phys.*, **37**, 3791 (1966).
7. S. W. S. McKeever and Y. S. Horowitz, *Radiat. Phys. Chem.* **36**, 35 (1990).
8. G. C. Taylor and E. Lilley, *J. Phys. D. Appl. Phys.*, **15**, 1243 (1982).
9. S. W. S. McKeever, *J. Appl. Phys.* **56**, 2883 (1984).
10. D. W. Zimmerman, C. R. Rhyner and J. R. Cameron, *Health Phys.* **12**, 525 (1966).
11. J. McKeever, D. Macintyre, S. R. Taylor, S. W. S. McKeever, A. Horowitz, and Y. S. Horowitz, *Radiat. Prot. Dos.* **47**, 123 (1993).
12. A. Horowitz and Y. S. Horowitz, *Radiat. Prot. Dos.* **33**, 267 (1990).
13. A Delgado, J. M. Gomez Ros and J. C. Portillo, *J. Phys. D. Appl. Phys.* **21** 1015 (1988).

# PHOTOINDUCED PHENOMENA IN $RbAg_4I_5$ SUPERIONIC CRYSTALS

S. BREDIKHIN,[a] N. KOVALEVA,[a] T. HATTORI[b] and M. ISHIGAME[b]

[a]*Institute of Solid State Physics, 142432, Chernogolovka, Russia;* [b]*Research Institute for Scientific Measurements, 2-1-1 Katahira, Sendai 980, Japan*

We have observed a new phenomena of photoinduced transformation of Raman scattering and photoluminescence spectra in $RbAg_4I_5$ superionic crystal. A reversible change of the fine structure in Raman spectra at low temperature and reversible change of the concentration of luninescence centers due to irradiation of sample have been studied. Both of these processes are due to the change of local concentration of mobile silver ions in irradiated region of $RbAg_4I_5$. The mechanism of interaction between nonequilibrium electrons and silver disordered ionic sublattice has been proposed. The excess concentration of electrons gives rise to diffusion flow of electrons and ions from irradiated region.

*Key words*: luminescence, Raman scattering, ambipolar diffusion.

In contrast to ordinary crystals, the electron processes in superionic conductors are complicated by the effects of disordering in one of the ion sublattices and the interaction between mobile disordered ionic and electronic subsystems. In the present work, with the aim of studying of the process of interaction between ionic and electronic subsystems, an investigation has been made of photoluminescence and Raman scattering of $RbAg_4I_5$ with high spatial resolution. The $RbAg_4I_5$ crystals obtained are rather stable and can be kept in air for a long time without noticeable changes. The samples were mounted in a helium refrigerator, with which it was possible to cool the sample to 13 K. For excitation of the photoluminescence, we have used a xenon lamp and a monochromator. By means of an optical system, the light beam was focused on an area at $150 \times 1000 \ \mu m^2$. The 4579 $A$ line of argon laser was used for Raman scattering measurements. The scattered light was analyzed by a double grating monochromator and detected by a photomultiplier.

In the previous study of the photoluminescence (PL) of the low-temperature $\gamma$-phase of $RbAg_4I_5$, it was shown that the luminescence has a center nature.[1,2] In the present work, the effect of adding of silver into $RbAg_4I_5$ on the photoluminescence is studied. Silver was deposited on one face of the sample. The photoluminescence has been measured from the opposite surface of the sample. The effect of silver dissolution into $RbAg_4I_5$ on the luminescence was investigated. Figure 1 shows the photoluminescence spectrum after the saturation of sample by silver (curve-b) and the spectrum of primary sample (curve-a). From Figure 1, it is seen that the intensities of the luminescence bands at $\lambda_{pl1} = 387$ nm and $\lambda_{pl1.1} = 397$ nm decrease while the intensities of the luminescence bands at $\lambda_{pl2} = 437$ nm and $\lambda_{pl4} = 462$ nm increase and a new band appears at $\lambda_{pl5} = 496$ nm. Assume that dissolution of the silver into the bulk would lead to the increase of the concentration of interstitial silver ions and to the decrease of the concentration of silver vacancies in the ordered $\gamma$-phase. In accordance with this, the emission bands with wave length maxima $\lambda_{pl1} = 387$ nm and $\lambda_{pl1.1} = 397$ nm may be attributed to the centers involving silver vacancies and the emission bands at $\lambda_{pl2} = 437$ nm and $\lambda_{pl4} = 462$ nm are associated with centers whose composition involves interstitial silver. The intensity of the luminescence band at $\lambda_{pl3} = 450$ nm is practically independent of the saturation by silver and of the additive coloring of $RbAg_4I_5$ in $I_2$ vapor as we will show later. The

intensity in excitation spectrum of the band at $\lambda_{pl3} = 450$ nm shows a maximum at $\lambda = 436$ nm. This result shows that this luminescence band is due to silver iodine impurity in $RbAg_4I_5$. Appearance of the band at $\lambda_{pl5} = 496$ nm at high concentrations of silver ions may be related with creation of luminescence centers whose composition involves more than one interstitial silver ion. From this investigation, it follows that the analysis of the distribution of the photoluminescence intensity along the sample length will allow us to get information of the profile of distribution of luminescence centers and of the silver cation concentration.

The effect of saturation by silver on the Raman spectrum of $RbAg_4I_5$ is studied. The typical unpolarized Raman spectrum of primary $RbAg_4I_5$ at 294 $K$ is shown in Figure 2 (curve - a). There is a broad peak at 105 cm$^{-1}$ which is due to the breathing modes of the tetrahedral iodine cage and the band around 20 cm$^{-1}$ is interpreted as the attempt
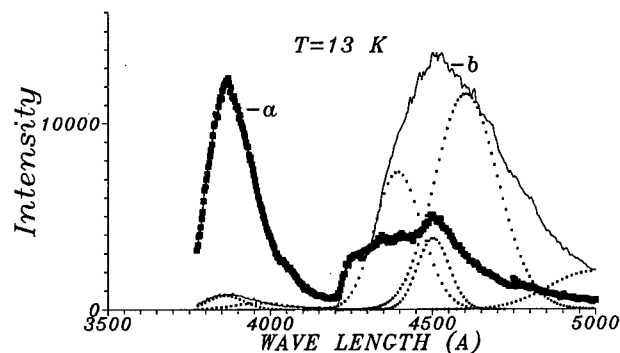


FIGURE 1    Photoluminescence spectra of primary sample (curve-a) and after saturation by silver (curve-b). The spectrum for the sample saturated by silver is fitted by six Gaussian luminescence bands (dotted curves).
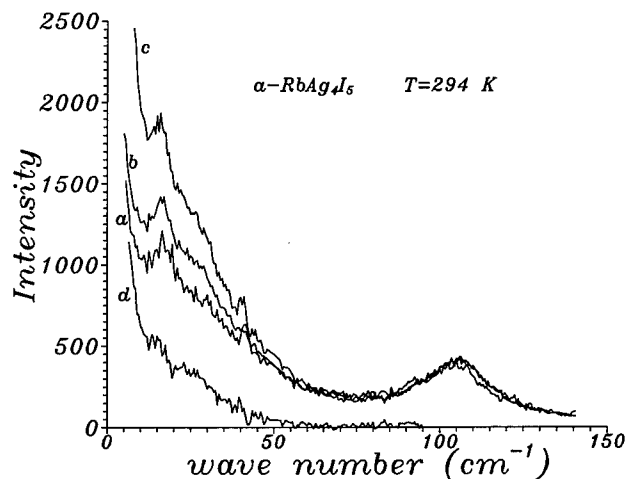


FIGURE 2    Raman spectra of $RbAg_4I_5$ at 294 $K$. a: Primary sample. b: After 42 hours from the deposition of silver contact at 294 K. c: The same sample after 54 hours from the deposition of silver contact at 294 $K$. d: Difference between Raman spectra of sample saturated by silver and of primary sample.
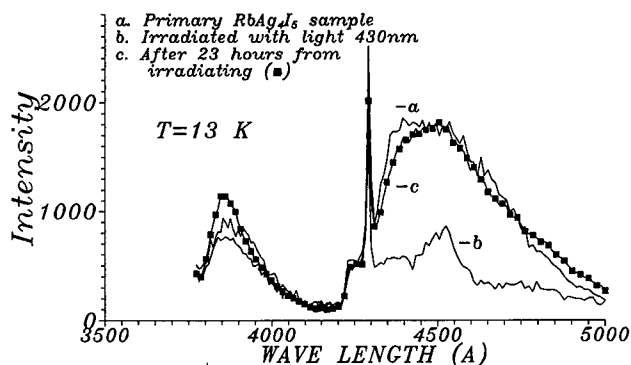
FIGURE 3   Photoinduced transformation of luminescence spectrum of $RbAg_4I_5$ by irradiation with wave length maxima 430 nm. Photoluminescence spectra of primary sample (curve-a), of irradiated one (curve-b) and after 23 hours from irradiating.
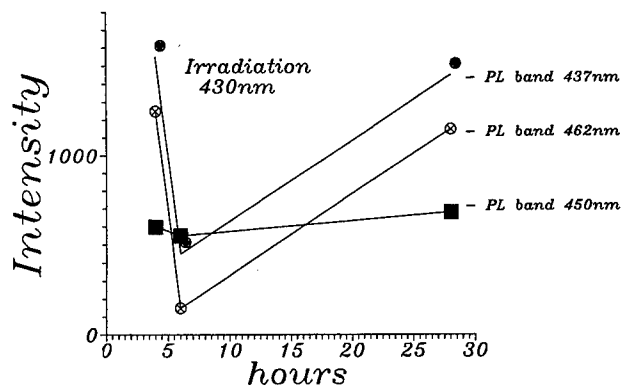


FIGURE 4   Raman spectra at 294 $K$ of primary sample (curva-a) and after irradiating of local region (curv e-b). Raman spectrum after 25 hours from irradiating (curve-c). Difference between Raman spectra of primary sample and of irradiated sample (curve-d).

vibrations of the $Ag^+$ ions. Curves b and c in Figure 2 are the Raman spectra from the opposite surface of sample after the silver dissolution (b: 42 hours after silver deposition, C: 54 hours after deposition). It is seen that dissolution of silver into the bulk leads to the increase of the intensity in the low frequency region in Raman spectra. From Figure 2, it follows that the intensity in low frequency region in Raman spectra shows the tendency to increase with increasing of the concentration of silver ions in $RbAg_4I_5$.

In the present work, we show a new phenomena of photoinduced transformation of luminescence centers in $RbAg_4I_5$. We have investigated the irradiation effect of local region on the concentration and a structure of the luminescence centers. The sample was irradiated at room temperature by using a Xenon lamp and monochromator and the energy of irradiating light ($h\nu$) is below the band gap energy ($E_g = 3.38$ $eV$) of $RbAg_4I_5$. By means of an optical system, the light beam was focused on an area of $150 \times 600$ $\mu m^2$.

After irradiation during 1 hour with wavelength maxima $\lambda = 430$ nm, photoluminescence spectrum was changed as shown in Figure. 3. In this figure, we observed the decrease of the intensity of the luminescence bands at $\lambda_{pl2} = 437$ nm and $\lambda_{pl4} = 462$ nm related to the luminescence centers involving the interstitial silver. As a time equal to 15–20 hours proceeds at 300 $K$, the intensity of these bands increase. The photoluminescence spectrum measured after 23 hours from irradiating looks like the luminescence spectrum of primary sample (Figure 3). Due to the correlation between the silver cation concentration and the intensity of the luminescence bands, it is possible to conclude that a reversible change of silver cation concentration takes place in irradiated region.

The Raman spectra at 294 $K$ of primary sample and after irradiation are shown in Figure 4. It is seen that irradiation by light with wave length 430 nm leads to decrease of intensity in low frequency region in Raman spectrum at 294 $K$. But as a time equal to 20–30 hours proceeds at 300 $K$, the intensity in low frequency region in Raman spectrum increases. From Figure 4, it is seen that the Raman spectrum measured after 25 hours from irradiating looks like that of primary crystal. This means that a reversible photoinduced transformation in Raman spectrum takes place in irradiated region of $RbAg_4I_5$.

## CONCLUSION

New phenomena of photoinduced transformation of Raman spectra and luminescence centers in irradiated region of $RbAg_4I_5$ are discovered and investigated. It is found that the irradiation of the $RbAg_4I_5$ by light having energies corresponding to the excitation of electronic centers leads to the generation of nonequilibrium electrons in the conduction band. Mobile $Ag^+$ cations, because of their high concentration in the superionic phase, should screen the electrostatic interaction between ionized centers and electrons. The excess concentration of electrons in irradiated region will give rise to diffusion flow of electrons and ions in the ambipolar diffusion regime from irradiated region. These phenomena appear as a result of strong interaction between mobile disordered ionic sublattice and electronic subsystem in $RbAg_4I_5$.

REFERENCES

1.  S. Bredikhin, T. Hattori and M. Ishigame, *Solid State Ionics* **67**, 311, (1994).
2.  S. Bredikhin, T. Hattori and M. Ishigame, *Physical Review* **B50**, 2444, (1994).

# EPR vs. TEMPERATURE OF $Fe^{3+}$ IONS PRODUCED BY RADIOLYSIS IN $CdCl_2$:Fe CRYSTALS

S. V. NISTOR,* E. GOOVAERTS and D. SCHOEMAKER

*Physics Department, University of Antwerp (U.I.A.), B-2610 Antwerpen-Wilrijk, Belgium*

$Fe^{3+}$ ions are produced by hole trapping at substitutional $Fe^{2+}$ ions in the layered $CdCl_2$ lattice, after brief X-ray irradiation at 78 K or 296 K. The resulting EPR spectra have been analysed with an improved fitting procedure, resulting in more accurate zero-field-splitting (ZFS) parameters $b_2^0$, $b_4^0$ and $b_4^3$. It is shown that the superposition model of Newman describes in a satisfactory manner the resulting ZFS parameters, predicting the lattice contraction around the $Fe^{3+}$ ion and the thermal expansion coefficient normal to the lattice layers of $CdCl_2$.

*PACS*: 76.30.Fc; 61.72.Ji; 61.80.Cb.

*Key words*: EPR, $CdCl_2$, $Fe^{3+}$, hole trapping, layered compound, superposition model, temperature dependence.

## 1 INTRODUCTION

$CdCl_2$ single crystals represent an interesting host lattice for EPR and optical studies of impurity ions in insulating crystals, due to their structure consisting of $Cd^{2+}$ cation layers sandwiched between layers of $Cl^-$ anions. The bonds inside the $Cl^-$-$Cd^{2+}$-$Cl^-$ sandwich are of ionic-covalent type and between the sandwiches are of the Van der Waals type. This results in specific properties, such as a strong temperature dependence of the crystal-field component along the $C_3$ axis, perpendicular to the plane of the layers, as revealed from EPR studies on $Mn^{2+}$ ions.[1,2]

EPR spectra attributed to $Fe^{3+}$ ions at cation sites in the rhombohedral ($D_{3d}^5$) $CdCl_2$ lattice (Figure 1) have been recently observed[3] in oxygen free $CdCl_2$:$Fe^{2+}$ single crystals after brief X-ray irradiation at 78 K or room temperature (RT). In the same paper the zero-field-splitting (ZFS) parameter $b_2^0$ has been analysed with the superposition (SP) model of Newman,[4] by considering the $Fe^{3+}$ paramagnetic ion in a substitutional cation site, sixfold co-ordinated by $Cl^-$ ligand anions. Both absolute values and temperature dependence of $b_2^0$ have been quantitatively accounted for by taking the angle between the Fe–Cl bond and the trigonal $C_3$ axis equal to the corresponding angle ($\Theta = 56.714°$) of the pure $CdCl_2$ lattice and as the Fe–Cl bond length the sum of the $Fe^{3+}$ and $Cl^-$ ionic radii.

In the present paper the EPR spectra of the $Fe^{3+}$ ion in $CdCl_2$ have been reanalysed with an improved fitting procedure resulting in more accurate values of the $b_4^0$ and $b_4^3$ parameters. Considering these new parameters it has been possible to obtain an excellent evaluation of the $b_2^0$ parameter, inside the SP model, without any *a priori* assumptions about the Fe–Cl bond parameters. Moreover, the SP model shows that a local compression of the $CdCl_2$ host lattice takes place at the impurity site, which is explained as being due to the Coulomb attraction of the $Fe^{3+}$ extrapositive charge.

## 2 EPR SPECTRA

The analysis of the resulting EPR spectra has shown[3] that the $Fe^{3+}(3d^5)$ ions are situated at

---

* On leave from the Institute of Atomic Physics (I.F.T.M.), Bucuresti, Romania.
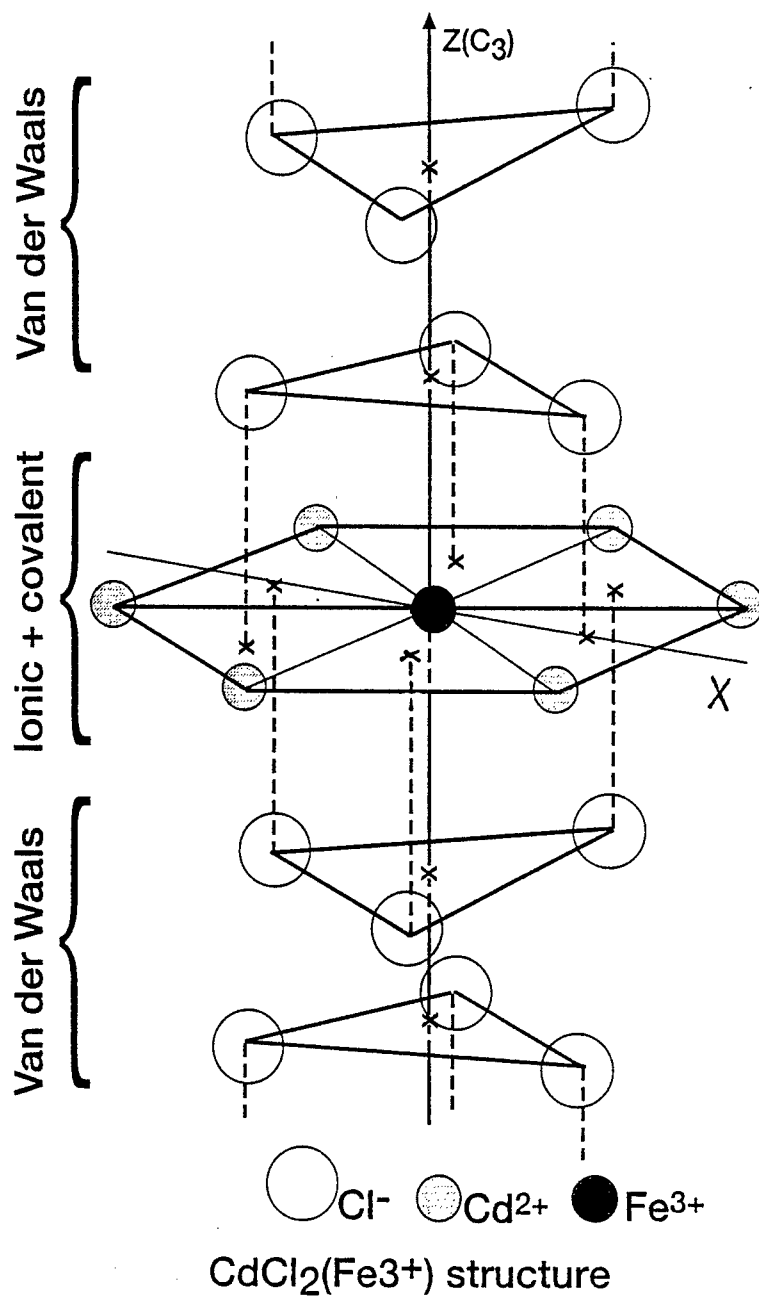
FIGURE 1   The crystalline surrounding of the substitutional $Fe^{3+}$ ion in the $CdCl_2$ lattice. Local deformations due to the impurity ion are not presented.
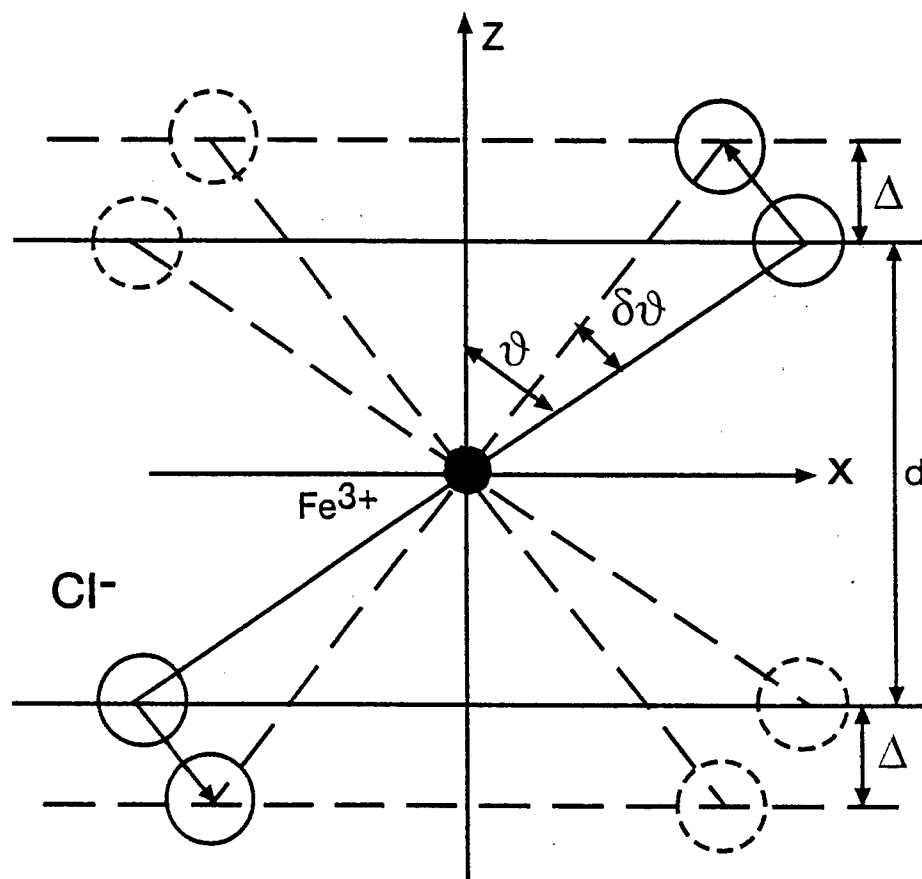
FIGURE 2  Structural model of the $Fe^{3+}$ centre in $CdCl_2$ employed in the analysis of the temperature variation of the $b_2^0$ parameter with temperature. Only the $Fe^{3+}$–$Cl^-$ bond orientation ($\Theta$ angle) is considered to change.

the six-fold co-ordinated cation sites with $D_{3d}$ symmetry of the $CdCl_2$ lattice (Figure 1). No lattice defects, such as vacancies or interstitials, seem to be present in the near neighbourhood of the $Fe^{3+}$ centre, as reflected in the trigonal symmetry of its EPR spectrum. The charge compensation of the trapped hole seems to be insured by electrons trapped at lattice sites farther away.

The strongly anisotropic EPR spectra attributed to $Fe^{3+}$ ions, visible at $T < 250$ K, are described[3] by the spin Hamiltonian with trigonal symmetry around $z(C_3)$ (usual notations[5]):

$$\mathscr{H}_S = g\mu_B \ \vec{H}\vec{S} + \frac{1}{3}b_2^0\hat{O}_2^0 + \frac{1}{60}b_4^0\hat{O}_4^0 + \frac{1}{60}b_4^3\hat{O}_4^3 \tag{1}$$

where $S = 5/2$.

In the previous analysis[3] the spin Hamiltonian parameters have been determined by a fitting procedure with the experimental transition fields for $\vec{H} \parallel \vec{c}$ ($\theta = 0°$) and $\vec{H} \perp \vec{c}$ ($\theta = 90°$), based on a full diagonalization of the spin Hamiltonian (1) in which the condition $|b_4^3| = 20\sqrt{2}b_4^0$ has been included too. The validity of the fitting procedure has been further checked by comparing the calculated $\theta$ angular dependence of the line positions for one particular plane ($\phi = 0$). This procedure resulted only in approximate absolute values for the $b_4^3$ parameter.

In the present, improved, analysis we have determined the spin Hamiltonian parameters by fitting the calculated line positions resulting from a full diagonalization of (1) with 22 to 27 experimental transition fields taken for various $0° \le \theta \le 90°$ angles and using as variables the $g$, $b_2^0$, $b_4^0$ and $b_4^3$ spin Hamiltonian parameters, as well as the unknown azimuthal angle $\phi$. Such an analysis could be however performed only for the EPR spectra recorded at temperatures $T \le 135$ K, where the full angular dependence of the $Fe^{3+}$ EPR spectrum is visible.

The results (Table I) show no essential changes in the magnitude of the $g$ and $b_2^0$ spin Hamiltonian parameters, small changes in the magnitude of the $b_4^0$ parameter and appreciable changes in the $b_4^3$ parameter. Moreover, the errors analysis has shown that the earlier[3] experimental errors were underestimated.

TABLE I

Spin Hamiltonian parameters and bond angle $\Theta$, as determined from the $b_4^3/b_4^0$ ratio, for the $Fe^{3+}$ centres in $CdCl_2$ crystals, at various temperatures. The ZFS parameters $b_2^0$, $b_4^0$ and $b_4^3$ are given in $10^{-4}$ cm$^{-1}$). The estimated errors are $\pm 0.003$ ($g$), $\pm 0.3(b_2^0)$, $\pm 0.4(b_4^0)$, $\pm 30(b_4^3)$ and $\pm 0.8$ ($\Theta$).

| Ion | T(K) | g | $b_2^0$ | $b_4^0$ | $b_4^3$ | $\Theta(^0)$ | Ref. |
|-----|------|------|---------|---------|---------|--------------|------|
| $Fe^{3+}$ | 26 | 2.008 | +815 | −13.2 | +425 | 57.1 | a |
| | 66 | 2.008 | +804 | −12.8 | +451 | 58.5 | a |
| | 135 | 2.008 | +772 | −11.8 | +423 | 57.7 | a |
| | 225 | 2.008 | +736 | −10.6 | | | b |

($^a$) Present work.
($^b$) Ref. 3.

## 3   ANALYSIS OF EPR PARAMETERS WITH THE SUPERPOSITION MODEL

### 3.1 *The ZFS Parameters*

The evaluation of the ZFS parameters for the paramagnetic ions with S-ground state is a subject of continuing controversy. Although controversy exists about the validity of this model for $3d^5$ ions, it has proved in many cases useful in determining the local environment of the impurity ion in various lattices.[4]

*Ab initio* calculations for $Mn^{2+}$ in layered structures have failed to account[6,7] for the absolute values of the most important ZFS parameter $b_2^0$.

As will be further shown, a satisfactory quantitative analysis of the ZFS parameter $b_2^0$ is obtained with the SP model.

The SP model provides the following equations for the ZFS parameters at sixfold coordinated sites with $D_{3d}$ symmetry:[4]

$$b_2^0 = 3\bar{b}_2(R_0)(R_0/R)^{t_2}(3\cos^2\Theta - 1) \tag{2}$$

$$b_4^0 = \frac{3}{4}\bar{b}_4(R_0)(R_0/R)^{t_4}(35\cos^4\Theta - 30\cos^2\Theta + 3) \tag{3}$$

$$b_4^3 = 210\bar{b}_4(R_0)(R_0/R)^{t_4} \cos \Theta \sin^3 \Theta \tag{4}$$

In this equations $\bar{b}_2(R)$ and $\bar{b}_4(R)$ are intrinsic parameters, depending on the nature of the metal-ligand bond, $R_0$ is a reference bond length, $t_2$ and $t_4$ are determined experimentally and $\Theta$ is the angle between the metal-ligand bond and the $z(C_3)$ axis.

It has been found[8] that for the $Fe^{3+}$–$Cl^-$ bond $\bar{b}_2^0 = -0.61$ $cm^{-1}$ at $R_0 = 0.219$ nm and $t_2 = 7$. To our knowledge the $\bar{b}_4(R_0)$ and $t_4$ parameters have not yet been determined for the $Fe^{3+}$–$Cl^-$ bond.

Firstly, the experimental ratio $b_4^3/b_4^0$ provides directly the value of $\Theta$ without the use of $\bar{b}_4(R_0)$ and $t_4$. As shown in Table I, in the 26 to 135 K temperature range the resulting $\Theta$ angle shows variations which are inside the estimated experimental error ($\pm$ 0.8°). (The relatively large error in determining the $b_4^3$ parameter is mainly due to the inaccuracies in determining the field transitions for orientations $\theta \neq 0°$ and $\theta \neq 90°$, as described in Reference 3. The average result ($\Theta = 57.7°$) is slightly larger than the corresponding value of the pure $CdCl_2$ lattice ($\Theta = 56.714°$), suggesting a certain local compression of the crystal lattice. This seems to be due to the smaller ionic radius of the $Fe^{3+}$ ion (r = 0.064 nm) compared to the host $Cd^{2+}$ ion (r = 0.097 nm).

In order to estimate the minimum $Fe^{3+}$–$C^-$ bond length (R distance) we use equation (2) with $b_2^0$ determined at T = 26 K. The result is R = 0.259 nm, which is smaller than the $Cd^{2+}$–$Cl^-$ distance in the $CdCl_2$ lattice (0.264 nm) and only slightly larger than the minimum bond length $R(Fe^{3+}–Cl^-) = r(Fe^{3+}) + r(Cl^-) = 0.245$ nm. The resulting local contraction of the $CdCl_2$ lattice around the $Fe^{3+}$ impurity ion can be the result of the Coulomb attraction exercised by the extra positive charge of the $Fe^{3+}$ ion. The smaller ionic radius of the $Fe^{3+}$ ion ($r = 0.064$ nm) compared to $Cd^{2+}$ ($r = 0.097$ nm) will favour this approach, but will also limit it. The existence of such a local contraction of the $CdCl_2$ lattice at the $Fe^{3+}$ site is also reflected in the larger value (about 55 times) of the $b_2^0$ parameter for the $Fe^{3+}$ ion in $CdCl_2$ compared to the corresponding value[1,2] of the isoelectronic $Mn^{2+}$ ion in the same lattice host.

### 3.2 The Temperature Variation of $b_2^0$

The strong temperature dependence of $b_2^0$ (see Figure 3 of Reference 3) can be associated with the thermal expansion of the $CdCl_2$ lattice along the $z(C_3)$ axis. Indeed, as shown by X-ray measurements[6,7] the thermal expansion coefficient perpendicular to the lattice layers $\alpha_z = 8 \cdot 10^{-5}$ $K^{-1}$ is much larger than the thermal expansion coefficients in the lattice layers $\alpha_x = \alpha_y \leq 10^{-6}$ $K^{-1}$. According to the SP model this variation can be accounted for by considering the temperature induced variations in $R$ and/or $\Theta$. Assuming that the interionic distance $R$ is less affected in this temperature range, the changes in $b_2^0$ will be due a to variation of the angle $\Theta$, i.e. to a change in the separation of the chlorine layers sandwiching the $Fe^{3+}$ ion. This hypothesis agrees with the analysis of the lattice vibrations contribution to the lattice expansion in this compound, which shows[7] the main contribution to the expansion along the $z$ axis to come from flexural waves polarised in the same direction.

Using the SP model it is possible to evaluate from the EPR data the thermal expansion coefficient $\alpha_z$. A simple geometrical analysis (Figure 2) yields the following formula:

$$\alpha_z = \frac{2R(\delta\Theta) \cos \Theta}{d(T_1 - T_2)} \tag{5}$$

where $\delta\Theta$ is the variation of the $\Theta$ angle between temperatures $T_1$ and $T_2$. A meaningful evaluation has to be done in the temperature range where the expansion coefficient is temperature independent, i.e. for $T \geq T_{Debye}$. This corresponds approximately to the

temperatures where $b_2^0$ is linear.[7] According to formula (2), $\delta\Theta = 0.3°$ for $T_1 = 225$ K and $T_2 = 66$ K. The resulting $\delta\Theta$ value is smaller than the errors in determining the $\Theta$ value from the $b_4^3/b_4^0$ ratio ($\pm 0.8°$). It is the reason why the temperature variation of $b_4^3/b_4^0$ has not been used in determining the temperature variation of $\Theta$. Substituting $\delta\Theta = 0.3°$ in (5) one obtains $(\alpha_z)_{calc} = 3 \cdot 10^{-5}$ $K^{-1}$, which is in excellent agreement with the experimental value $\alpha_z(296$ K$) = 8 \cdot 10^{-5}$ $K^{-1}$, considering all approximations involved.

## 4 CONCLUSIONS

After X-ray irradiation $CdCl_2$:$Fe^{2+}$ crystals exhibit paramagnetic centres attributed to trapped hole $Fe^{3+}$ ions at $Cd^{2+}$ sites. The ZFS parameters $b_2^0$, $b_4^0$ and $b_4^3$ are well described with the SP model. The resulting analysis shows a local compression of the $CdCl_2$ lattice at the $Fe^{3+}$ impurity site and a reduction of the $Fe^{3+}$–$Cl^-$ separation compared to the $Cd^{2+}$–$Cl^-$ separation in pure $CdCl_2$, effects which are explained by the Coulomb attraction of the extrapositive charge and the smaller ionic radius of the $Fe^{3+}$ ion.

A fair estimation of the thermal expansion coefficient perpendicular to the direction of the lattice layers is also obtained with the SP model from the variation of $b_2^0$ in the temperature range of its linear dependence, by taking into consideration an increase in the separation of the chlorine layers sandwiching the cations (intralayer expansion), without any change in the $Fe^{3+}$–$Cl^-$ bond length.

REFERENCES

1. H. G. Hoeve and D. O. Van Ostenburg, *Phys. Rev.* **167**, 245 (1968).
2. S. V. Nistor, V. Ghiordanescu and M. Voda, *Phys. Stat. Sol.* **B78**, K31 (1976).
3. S. V. Nistor, E. Goovaerts and D. Schoemaker, *J. Phys. : Condens. Matter* **6**, 2619 (1994).
4. D. J. Newman and B. Ng, *Rep. Progr. Phys.* **132**, 134 (1989).
5. A. Abragam and B. Bleaney, *'Electron Paramagnetic Resonance of Transition Ions'*, Clarendon Press, Oxford, 1970.
6. R. R. Sharma, *Phys. Rev.* **B2**, 3316 (1970); **B3**, 76 (1971).
7. V. E. Glinchuk, V. E. Goncharuk, D. L. Lyfar and S. M. Ryabchenko, *Sov. Phys. Solid State* **18**, 7 (1976).
8. R. Büscher and G. Lehman, *Z. Naturforsch.* **42a**, 67 (1987).
9. D. E. Partin and M. O'Keeffe, *J. Sol. State Chem.* **95**, 176 (1991).

# RADIATION EFFECTS IN PURE AND RE DOPED KMgF$_3$

N. V. SHIRAN, V. K. KOMAR, V. V. SHLYAKHTUROV, A. V. GEKTIN,
N. P. IVANOV, V. A. KORNIENKO, I. M. KRASOVITSKAYA
and Y.A. NESTERENKO

*Institute for Single Crystals Ukraine, Kharkov, 310001, Lenin Ave. 60*

Absorption, excitation and luminescence spectra in pure and rare-earth (RE) doped KMgF$_3$ single crystals were measured. Glow peaks corresponding to the thermal activation of colour centers formed by ionizing irradiation were registrated with the aim to study radiation damage. Thermoluminescence is intensive if the oxygen containing ions are present to crystals. The most interesting result was obtained for KMgF$_3$(Eu$_2$O$_3$) crystals: high temperature peak (390°C) is sufficiently intensive for the registration of not only ionizing but UV (with $\lambda <$ 300 nm) radiation too. The traps' nature and luminescence structure are discussed.

*Key words*: thermoluminescence, rare-earth ion, perovskite, radiation damage, oxygen, dosimetry.

## 1 INTRODUCTION

It is known that KMgF$_3$ crystals when irradiated with the ionizing radiation store energy and release it in the form of long-duration afterglow.[1] Its spectrum is in the region of 300–700 nm and consists of a number of broad superposed bands with the most well-defined maximum at 590 nm. This is connected with the presence of trace impurities (in particular Mn$^{2+}$, $\lambda_m = 590$ nm) in the crystal as well as with the luminescence of the radiation-induced F centers (270 nm) and F-aggregate colour centers (420, 465, 550 nm)[2].

## 2 RESULTS AND DISCUSSION

The KMgF$_3$ crystals were grown by Stockbarger method in the inert atmosphere. The concentration of RE dopants was from 0.01 to 1.5% in the melt.

Absorption, excitation and luminescence spectra in pure and RE doped KMgF$_3$ single crystals were measured. The absorption bands of colour centers are appeared at the X-ray radiation doses of about 10 Gy. The thermostimulated curve (TL) (heating rate 0.27 K/s at region from 20 to 500°C) (Figure 1a) consists of a number of peaks with the maxima at 80, 177, 220, 188, 380 and 402°C. It should be noted that energy store occurs also at UV irradiation (254 nm) with the energy essentially lower than the energy gap value for the crystal (Figure 1b). The comparison of the data for crystals of different purity degree showed that the store at UV irradiation the higher the more contaminated are the samples with the oxygen-containing impurities. The isochronous (20 min) annealing of the coloured with the ionizing radiation samples in the range of 100–550°C allows to compare the discolouring stages with the temperature of TL peaks (Figure 2). A full recovery of transparency is observed at 500°C.

The doping of KMgF$_3$ crystals with RE impurities showed that the majority of them presence in a threevalent state (Ce, Pr, Nd, Gd, Tb, Dy, Ho, Er, Tm, Yb, Lu). This is revealed in the spectra of absorption, excitation and luminescence typical for the said RE ions. The TL curves irrespective of the introduced impurity have the same peaks and coincide with the TL of pure crystals, but are more intensive. Unlike the above-mentioned
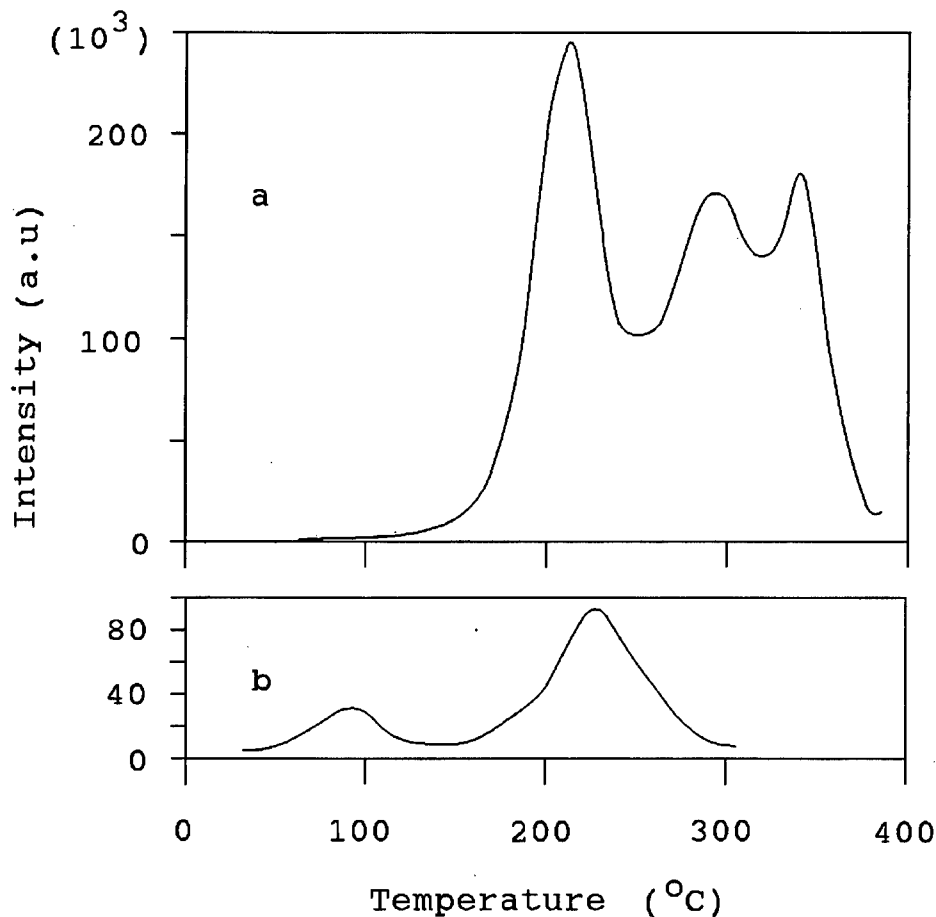
$(10^3)$



FIGURE 1   Thermoluminescence spectra of $KMgF_3$ single crystal, (a) X-irradiated $10^2$ Gy, (b) UV-irradiated, (Hg-lamp, $\lambda = 254$ nm).

RE ions europium presence in $KMgF_3$ in the form of both $Eu^{2+}$ and $Eu^{3+}$. With this the number of ions in the threevalent state makes 1–2% from the number of $Eu^{2+}$ ions.

The absorption spectra of crystals with $Eu^{2+}$ have the bands at 230 and 280 nm, the excitation takes place at 250 nm and the emission – mainly in the line with $\lambda_m = 360$ nm. Narrow luminescence bands in the region of 524–624 nm correspond to the radiation transitions in the $Eu^{3+}$ ions. With the rise of the irradiation dose the number of both $Eu^{2+}$ and $Eu^{3+}$ decreases.

The properties of the $KMgF_3$ crystal are found to depend on the form of the introduced dopant as europium fluoride or oxide. The addition of the dopant in the form of europium oxide brings a significant change to the TL curve: the main release of the stored energy occurs in the highest temperature peak 390°C (Figure 3). The intensity of the peak increases with the increase of $Eu_2O_3$ concentration in the melt and reaches saturation at 0.5%. The content of $Eu^{2+}$ when dopant added in the form of $Eu_2O_3$ is several times
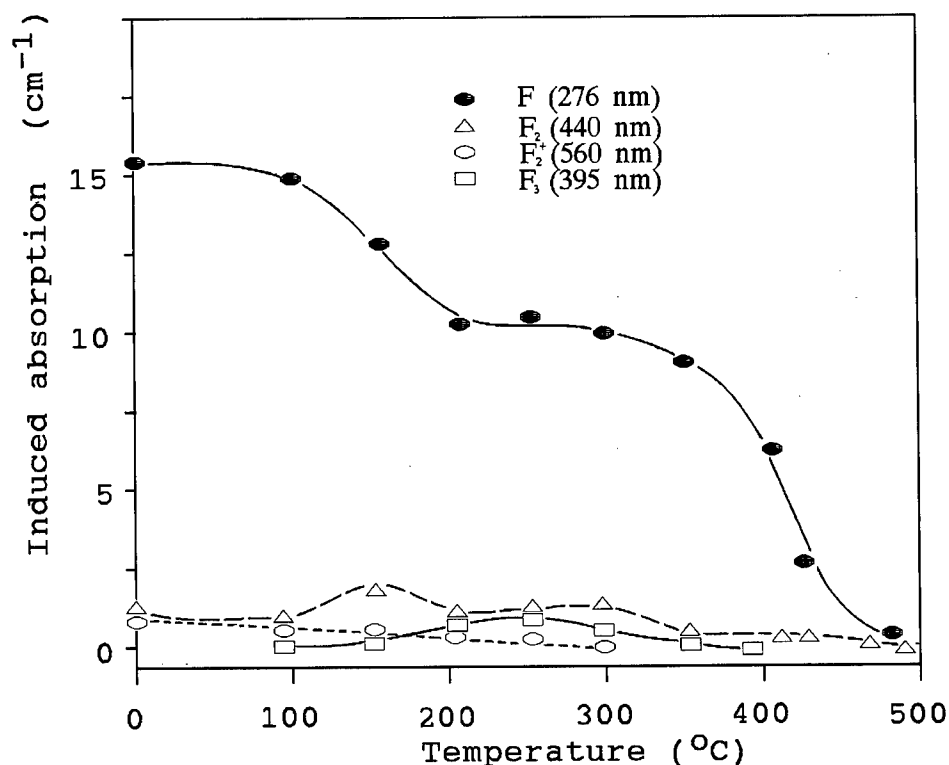
FIGURE 2   Colour centres annealing in KMgF$_3$ single crystal X-irradiated at 300 K, $D = 3.1 \ 10^2$ Gy.

higher than when doping with europium fluoride. The concentration of Eu$^{3+}$ centers increases as well but does not exceed 8% from Eu$^{2+}$ concentration.

It turned out that the energy store by KMgF$_3$ (Eu$_2$O$_3$) crystal proceeds effectively not only ionizing irradiation, but as a result of UV exposure up to the wavelengths of 300 nm which corresponds to the actinic skin sensitive region of dosimetry.

## 3   CONCLUSION

Thus, the obtained results give evidence to the fact that the observed significant afterglow in the undoped KMgF$_3$ crystals is caused by the formation of the intrinsic F- and F-aggregate colour centers as well as by the presence of oxygen-containing impurity traces. A complete discolouring of the induced colour centers is achieved by the annealing at T = 500°C for 20 min. The highest temperature trapping centers revealed in the form of a peak 390°C are most probably connected with oxygen ions. And while for the application of pure KMgF$_3$ as scintillators this impurity is harmful and must be eliminated, in the case of KMgF$_3$ (Eu) crystals' application for monitoring it is vice versa—the
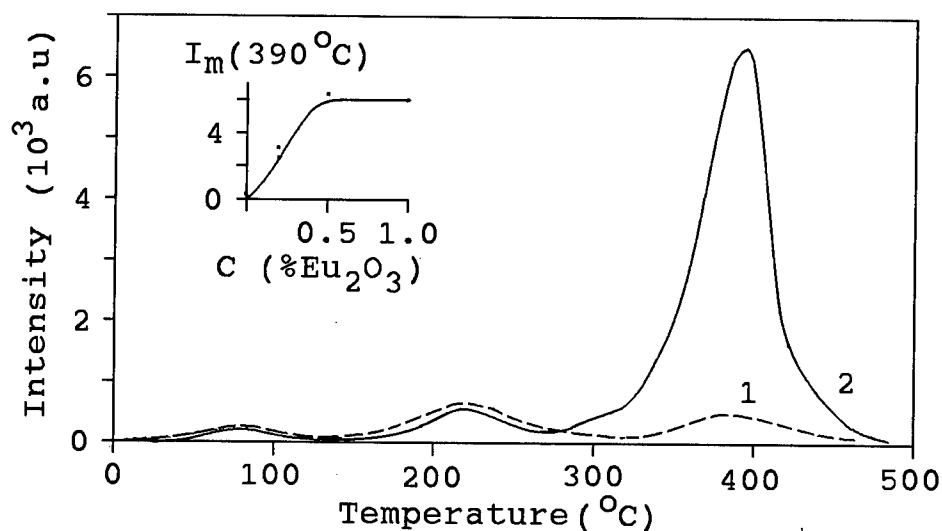
FIGURE 3    Thermoluminescence spectra of UV-irradiation $KMgF_3$ (0.5% $F_3$) (1) and $KMgF_3$ (0.5% $Eu_2O_3$) (2) single crystals. The inset shows dependence of intensity of peak $T_m = 390°C$ from the concentration of $Eu_2O_3$ in the melt.

intensive high temperature peak 390°C may be used for the determination of the stored energy according with.[3] For this purpose europium should be added to KMgF not in the form of europium flouride but oxide-$Eu_2O_3$. In this case one obtains an efficient dosimeter not only for the ionizing radiation but, which is most topical, for the UV radiation—in the part of the spectrum that affects the human organism.

REFERENCES

1.  A. E. Busulutskov, G. I. Britvich, V. I. Kochetkov *et al. Nucl. Instr. Meth.* **A322** 235 (1992).
2.  C. R. Riley, W. A. Sibley. *Phys. Rev.* **B1** 2789 (1970).
3.  C. Furetta, C. Bacci, R. Rispoli *et al. Radiat. Prot. Dosim.* **33** 107 (1990).

# SIMULATION OF THE BUILD-UP OF RADIATION DAMAGE IN NaCl:INITIAL STAGES OF COLLOID FORMATION

W. J. SOPPE and J. PRIJ

*Netherlands Energy Research Foundation ECN, P.O. Box 1, 1755 ZG Petten, The Netherlands*

In order to estimate the radiation damage that can be produced in a rock salt repository, a simulation model has been developed by which the concentrations of point defects and their aggregates can be calculated as a function of all relevant parameters. This model is based on macroscopic rate reactions and is in fact an extended version of a model derived by Jain and Lidiard. An important element in the new model is the implementation of the colloid nucleation stage. In this paper, we present model calculations of early-stage colloid formation in NaCl crystals, heated after being irradiated at a low temperature. The model calculations are compared with experimental results obtained by Inabe and coworkers. It is shown that the overall agreement between model and experiment is quite good but some details of the model—the dissociation rates of clusters containing more than two F centers – need improvement.

*Key words*: radiation damage, NaCl, colloids, nucleation, simulation, optical absorption.

## 1   INTRODUCTION

In many countries geological rock salt formation are considered as possible hosts for high-level radioactive waste (HLW) repositories. One of the aspects which need a very careful examination before such a repository can be taken into operation is the problem of radiation damage in salt.[1] It is generally known that irradiation of alkali halides can lead to a degradation of the crystal lattice through the formation of point defects (F and H centers). Further, it is known from experiments that, under certain circumstances with respect to temperature and dose, these point defects can aggregate and form alkali metal colloids and molecular halogen gas bubbles. Laboratory experiments have revealed that the concentration of these forms of radiation damage can reach values of several mole %.[2,3,4,5,6]

In 1977, Jain and Lidiard presented the first theoretical modelling of colloid formation in NaCl.[7] This model, based on kinetic rate reactions, was extended in 1979.[8] The model confirmed that, as suggested by experiments, in the process of accumulation of radiation damage the temperature and the dose rate play a major role. Van Opbroek and Den Hartog[9] have elucidated these aspects of the model.

Although some main features of colloid growth in irradiated NaCl, e.g. temperature- and dose rate dependency, are described quite well by the Jain Lidiard model, it is evident too that some other important mechanisms are treated rather rudimentary. One of these elements is the colloid nucleation stage and recent extensions of the Jain-Lidiard model by Soppe[10] were aimed towards a proper implementation of this initial growth stage. Calculations with the model of Soppe showed that, for the present designs of nuclear waste repositories in rock salt, the maximum colloid fraction in the salt near the waste containers will be less than a few mole %.[11] In this paper we will make a critical evaluation of the implementation of the colloid nucleation stage in this last model by comparison of model calculations with experimental observations on the growth of small aggregates of F centers in irradiated NaCl by Inabe and coworkers.[12]
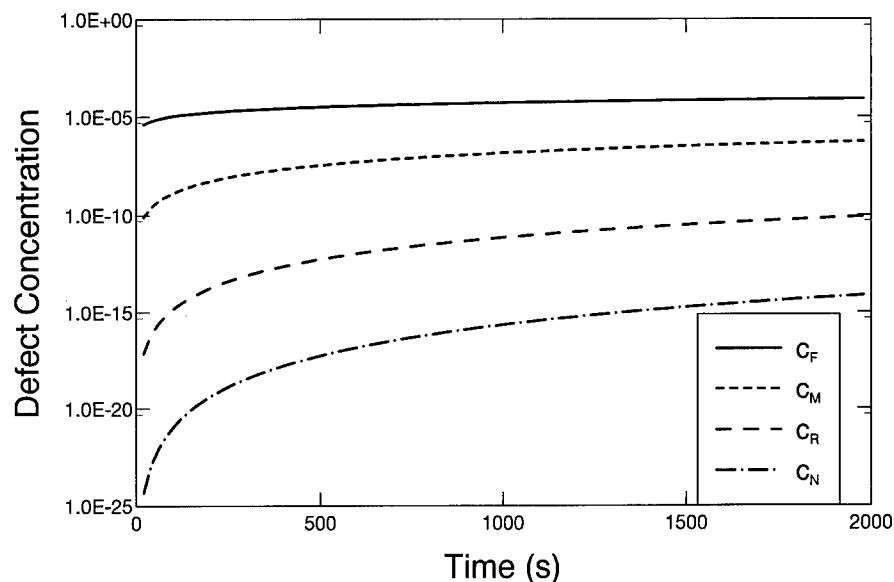
FIGURE 1    Theoretical defect concentrations during an irradiation period of 2000 s. Dose rate: 3.6 MGy/hr; temperature: 303 K.

## 2    MODEL

The model starts with the radiation induced formation of Frenkel pairs consisting of stable F centers and H centers. After the creation of a defect pair, the following reactions can be discerned.

(i)     recombination of F and H centers.
(ii)    diffusion of F centers.
(iii)   trapping of F centers and colloid growth.
(iv)   emission of F centers from small aggregates and colloids.
(v)    diffusion of H centers.
(vi)   trapping of H centers, $Cl_2$ formation, and growth of dislocation loops.
(vii)  recombination of F centers with molecular $Cl_2$.

Here, we will confine ourselves to mechanisms (iii) and (iv). Details of the other mechanisms can be found in the original paper of Soppe.[10] It is assumed that the nucleation of colloids can take place both heterogeneously and homogeneously. The homogeneous nucleation occurs by self-trapping of F centers, a process which leads to aggregation into M (= $F_2$, R (= $F_3$) and N centers.

Although there is no conclusive proof for the structure of N centers yet,[13] in this work it will be assumed that N centers consist of 4 F centers. Moreover, in the model, N centers act as colloid nuclei. From irradiation experiments, we know that the concentration of R
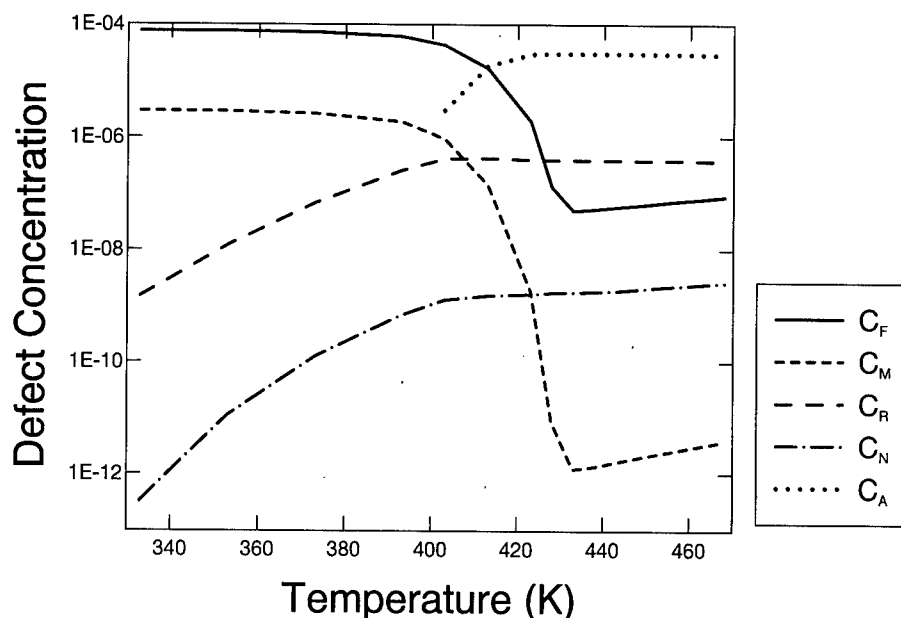
FIGURE 2   Theoretical defect concentrations during an annealing experiment. Annealing took place after irradiation (see Figure 1) at temperatures: 333 K, 353 K, 373 K, 393 K, 403 K, 413 K, 423 K, 428 K, 433 K, 438 K, 443 K, 448 K, 453 K, 458 K, 463 K, and 468 K. Duration of each annealing step was 60 s.

and N centers is always at least several orders of magnitude smaller than the M center concentration. Therefore, we impose that the formation of both R and N centers is energetically less favourable than the M center formation. The formation rate of R and N centers, $K_R$, is accordingly reduced by a temperature-dependent factor suggested by Seinen.[14]

Heterogeneous nucleation is the precipitation of F centers at sites other than N centers. The nature of these sites will remain unspecified in this paper, but it can be assumed that the concentration of these nuclei is indirectly related to the concentration of impurities and dislocation lines.[15]

The emission of F centers from colloids is a thermally activated process, governed by an activation energy of 0.3 eV.[16] If $c_F^{(e)}$ is the concentration of F centers in equilibrium with colloids, precipitation of F centers into colloids will take place as long as the F center concentration ($c_F$) is larger than $c_F^{(e)}$. This implies that, for a given dose rate, there is a temperature $T_e$ for which $c_F^{(e)}(T_e) = c_F(T_e)$ and that for temperatures larger than $T_e$, no colloid formation can take place. The linear relation between the M center concentration and the square of the F center concentration, experimentally observed[17] at temperatures below 50°C, is related to the dissociation of M centers. It can be reasoned[10] that this relation implies that the dissociation rate of M centers, $K_M^{(e)}$, is proportional to the formation rate of M centers, $K_F$. Using experimental data on $c_F$ and $c_M$ by Hodgson,[17] the ratio between $K_M^{(e)}$ and $K_F$ is determined to be approximately equal to $2 \cdot 10^{-3}$. The dissociation of R and N centers, finally, is incorporated in the net production rate of these centers: $K_R$.
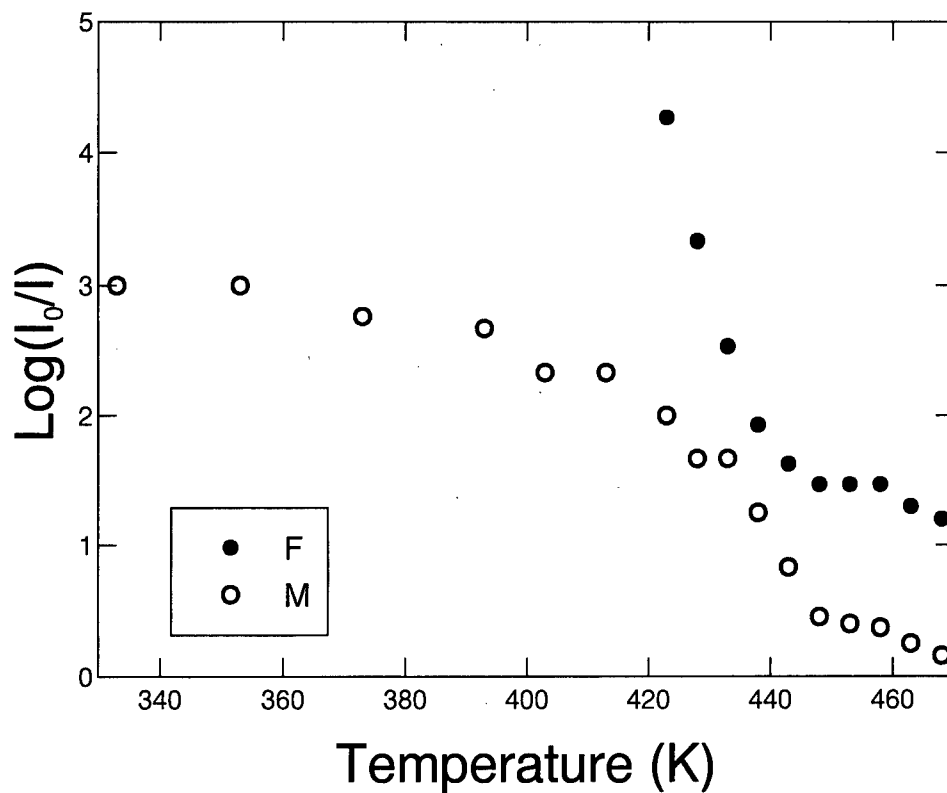
FIGURE 3    Experiment optical absorption spectra by Inabe and coworkers. (a) F and M bands.

The mechanisms, as discussed above, lead to the following rate equations:

$$\frac{dc_F}{d_t} = K + 2K_M^{(e)}c_M - 2K_F c_F c_F - K_F c_F c_M - K_F c_F c_R - K_F c_F c_N \tag{1}$$

$$+ K_H c_H c_M - 4\pi r_c C_c D_F \left( c_F - c_F^{(e)} \right)$$

$$- K_2 c_F c_H - z_F \rho_d D_F c_F - \gamma D_F c_F c_{Cl_2}$$

$$\frac{dc_M}{d_t} = K_F c_F c_F - K_H C_H C_M - K_M^{(e)} c_M - K_R c_F c_M \tag{2}$$

$$\frac{dc_R}{dt} = K_R c_F c_M - K_R c_F c_R \tag{3}$$

$$\frac{dc_N}{d_t} = K_R c_F c_R - K_F c_F c_N \tag{4}$$

$$\frac{dc_A}{dt} = K_F c_F c_N + 4\pi r_c C_c (D_F c_F - D_H c_H - D_F c_F^{(e)}) \tag{5}$$
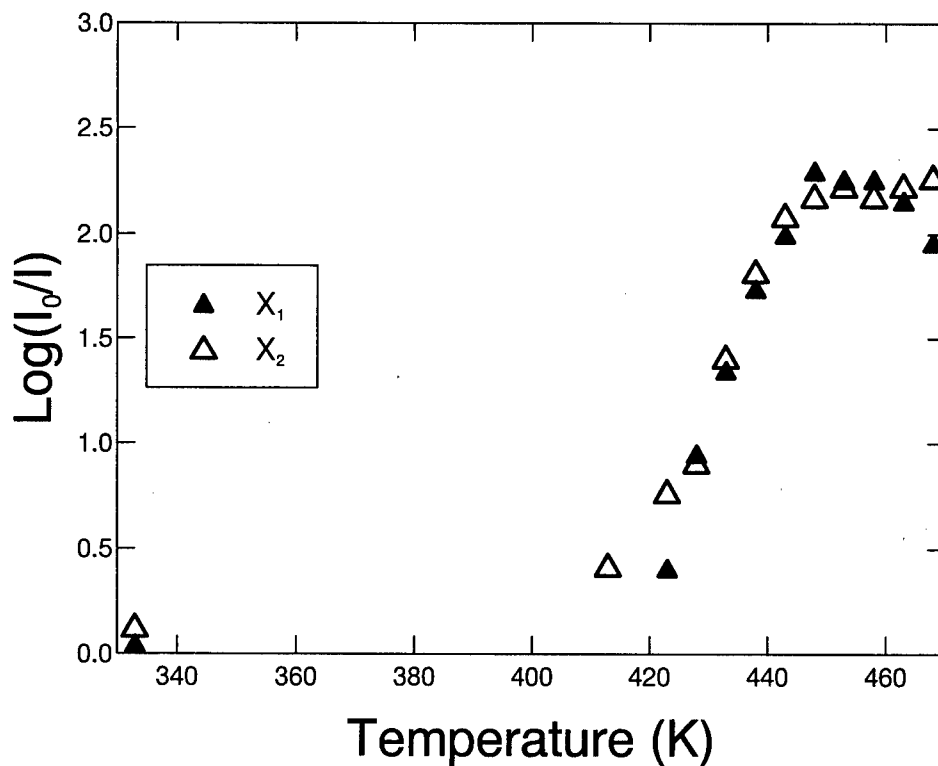
FIGURE 3    (b) $X_1$ and $X_2$ bands (colloidal bands).

Here, $K$ is the production rate of F-H pairs, $K_F$ is the reaction rate of F centers for aggregation, $K_2$ is the F-H recombination rate, $r_c$ is the mean colloid radius and $C_c$ is the number of colloids per $cm^3$.

## 3   SIMULATIONS

In order to reproduce the experimental results of Inabe and coworkers, we have used their experimental conditions as input parameters in our model. Inabe et al. used a high current electron pulse (energy 20 MeV; pulse width 1.5 $\mu s$; peak current more than 240 mA) from a linear accelerator to irradiate single-crystal NaCl samples. The radiation intensity per pulse was measured to be about 100 Gy. The frequency of the pulses was 10 Hz, so that mean dose rate was 3.6 MGy/hr. It can be shown[5] that, under these pulse conditions, the concentrations of F and H centers in first order approximation are the same as for a continuous irradiation at 3.6 MGy/hr, so latter value was used in the model calculations.
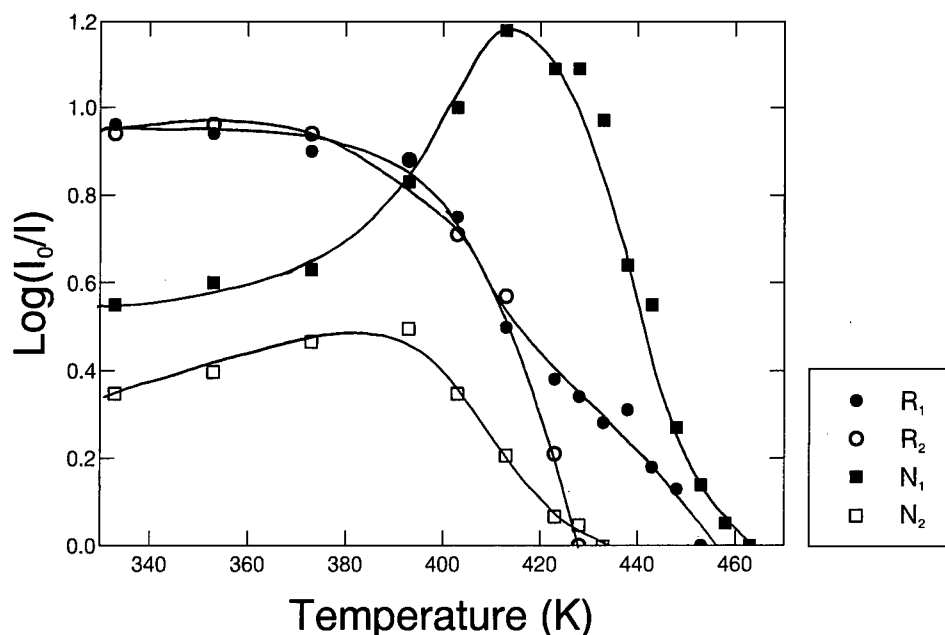
FIGURE 3   (c) R and N bands.

The duration of the irradiation was 2000 s. The experimental temperature during irradiation was not measured very accurately and was estimated to be between 30°C and 40°C. We have used a value of 30°C.

The theoretical fractions of the F centers and aggregates during irradiation are shown in Figure 1. All defect concentrations show a steady increase towards a saturation concentration. The temperature, however, is too low to reach saturation within this irradiation period. For example: the theoretical saturation fraction for the F centers is $\sqrt{(KD_H/K_2 D_F)} = 5.1 \cdot 10^{-4}$ and the actual value of the F center fraction at the end of the irradiation is $8.1 \cdot 10^{-5}$. Other defect fractions are: $c_M = 5.5 \cdot 10,^{-7}$ $c_R = 8.7 \cdot 10,^{-11}$ and $c_N = 7.9 \cdot 10^{-15}$. The concentration of the R and N centers at this stage is expected to be below the detection range of optical absorption experiments. The colloid fraction, $c_A$, at the end of the irradiation period is effectively zero.

After this irradiation period, the sample is heated in consecutive steps from 330 K up to high temperatures of about 480 K. In the laboratory experiments annealing took place at a temperature $T = T_{irr} + \Delta T$ for a period of 60 s and then the specimen was rapidly cooled to 100 K for optical absorption measurements. In the simulations we assume that changes in the defect concentrations in the measurement phase can be neglected.

During the annealing process, the F and M center fractions show a steady decrease, up to a temperature of about 430 K due to the formation of larger aggregates as R and N centers and colloids. At about 430 K, however, the colloid fraction starts to decrease again as a result of thermal dissociation. Consequently, $c_F$ and $c_M$ start to increase again for temperatures higher than 430 K. In this temperature regime, the N center concentration slightly increases too but the R center concentration decreases a little.

# 4 DISCUSSION AND CONCLUSIONS

At this stage, we will only make qualitative comparisons between experiment and theory. The translation of the results of optical absorption experiments into defect concentrations is not obvious yet for the larger aggregates (R and N centers) but in a next paper[18] we will provide more quantitative estimates of the experimental concentrations of the various defects. If we compare the experimentally observed absorption by F and M centers (see Figure 3a) with model calculations, we see that the qualitative behaviour of the theoretical results is quite well. The strong theoretical decrease of the concentrations of both defect species at about 420 K is confirmed by the experiments. However, the theoretical increase of these concentrations for temperatures above 430 K is not experimentally observed.

Inabe and coworkers observed two absorption bands, $X_1$ and $X_2$ which are attributed to (small) colloids. At the end of the irradiation period and before the annealing process, these bands are faintly present but in the first stages of annealing they disappear again until they rise steeply to significant intensities at a temperature between 420 and 440 K (See Figure 3b). For temperatures larger than 450 K, the intensities of the $X_2$ band seem to remain stable whereas the intensity of the $X_1$ band decreases again. Comparison with the model results in Figure 2 learns that the overall agreement between model and experiment is quite good but that the rise of the colloid fraction according to the model starts at a temperature of 400 K, which is lower than in the experiments.

The theoretical development of the R and N center concentration under annealing does not comply very well with the optical absorption spectra shown in Figure 3c. Firstly, the concentrations of these defects immediately after irradiation seem to be significantly larger than predicted by the model. Secondly, the absorption spectra show a continuous decrease of the R center concentration where the model predicts an increase of $c_R$ for T between 330 K and 400 K and a slight decrease for higher $T$. As mentioned above, the interpretation of the N bands in the optical absorption spectra is not beyond doubt yet. However, if we assume that the N bands are related to aggregates of four F centers, we see that as for the R centers, there is a discrepancy between model predictions and experimental results. These discrepancies are very likely due to the fact that in the model, the thermal dissociation of R and N centers is not explicitly taken into account.

A first step towards an improvement of the model would be to implement such thermal dissociation mechanisms. Further, the concentrations of the R and N centers at low temperatures seem to be too low. A correction could be accomplished through a revision of the aggregation rate parameter $K_R$.

REFERENCES

1. W. J. Soppe, H. Donker, A. García Celma and J. Prij, *J. Nucl. Mat* 1 (1994).
2. G. H. Jenks and C. D. Bopp, '*Storage and Release of Radiation Energy in Salt in Radioactive Waste Repositories*,' ORNL-TM-4449, Oak Ridge National Laboratory (1974).
3. G. H. Jenks and C. D. Bopp, '*Storage and Release of Radiation Energy in Salt and Radioactive Waste Repositories*,'ORNL-5058, Oak Ridge National Laboratory (1977).
4. J. Groote and H. R. Weerkamp, '*Radiation Damage in NaCl, small particles*,' Thesis, State University of Groningen (1990).

5.  H. Seinen, '*Radiation Damage in NaCl, The Process of Colloid Formation*,' Thesis, State University of Groningen (1994).
6.  H. Donker, W. J. Soppe and A. Garcia Celma, to be published.
7.  U. Jain and A. B. Lidiard, *Phil. Mag.* **35** 245 (1977).
8.  A. B. Lidiard, *Phil. Mag.* **A39** 647 (1979).
9.  G. van Opbroek and H.W. den Hartog, *J. Phys. Solid State Phys.*, **C18** 257 (1985).
10. W. Soppe, *J. Phys.: Condens. Matter* **5** 3519 (1993).
11. W. J. Soppe and J. Prij, *Nuclear Technology*, **107** 243 (1994).
12. K. Inabe, N. Takeuchi and S. Owaki, *Nucl. Instrum. Meth. Phys.* B 91 201 (1994).
13. E. Georgiou and C.R. Pollock, *Phys. Rev.* **B40** 6321 (1989).
14. J. Seinen, J. C. Groote, J. R. W. Weerkamp and H. W. den Hartog, *Rad. Eff. Defects Sol.* **124** 325 (1992).
15. A. E. Hughes and S. C. Jain, *Adv. Phys.* **28** *717 (1979)*.
16. A. B. Scott, W. A. Smith and M. A. Thompson, *J. Phys. Chem.* **57** 757 (1953).
17. E. R. Hodgson, A. Delgado and J. L. Alvarez Rivas, *J. Phys. Solid Phys.* **C12** 1239 (1979), *Ibid.*, **12** 4393 (1979), *Ibid.*, **14 337 (1981).**
18. W. J. Soppe and K. Inabe, in preparation.

# THEORY OF DIFFUSION-CONTROLLED DEFECT AGGREGATION UNDER IRRADIATION: A COMPARATIVE STUDY OF THREE BASIC APPROACHES

E. A. KOTOMIN,[a] V. N. KUZOVKOV,[a] M. ZAISER,[b] and W. SOPPE[c]

[a]*The University of Latvia, 19 Rainis, Riga LV 1050, Latvia;* [b]*Max Planck Institut für Metallforschung, Heisenbergstr.1, Stuttgart 70569, Germany;* [c]*Netherlands Energy Research Foundation ECN, P.O. Box 1, 1755 ZG Petten, The Netherlands*

Recent advances achieved within the framework of three basic theoretical approaches to the diffusion-controlled clustering of similar defects during irradiation are compared. These approaches (which can be identified as respectively macroscopic, mesoscopic and microscopic formalisms) have in common that they predict the existence of a critical dose rate for aggregation which increases with temperature, and a bell-shaped temperature dependency of the aggregation rate. Mesoscopic and microscopic approaches demonstrate that the elastic interaction between radiation defects plays a decisive rôle in the aggregation process. Results which are obtained via the different approaches are illustrated for NaCl crystals.

*Key words*: radiation damage, alkali halides, modelling, aggregation.

## 1  INTRODUCTION

The study of radiation-induced colour centers in alkali halides has a rather long history, spanning more than six decades by now.[1] Not long after the first observation of these colour centers, it was also discovered that one of these radiation-induced defect types (the F center) could form aggregates in the shape of alkali metal colloids.[2] It was found that this aggregate formation could be induced by either 'bleaching' lightly irradiated crystals or by performing irradiations at rather high temperatures and dose rates.[3,4] Observation of halide gas formation in irradiated crystals proved that also the H center (which is the complementary defect with respect to the F center) can be involved in accumulation processes. These aggregation processes of radiation-induced defects in alkali-halides have many interesting fundamental and applied aspects, but still some basic mechanisms are not well understood. In this paper we will deal with one of the more fundamental questions: which are the minimum conditions that have to be fulfilled in order that an aggregation of primary defects can take place?

## 2  BASIC THEORIES

A number of models have been presented for the quantitative analysis of the kinetics of defect accumulation, which differ both by physical pre-assumptions and by mathematical formalisms. The mathematical formalisms can roughly be classified into three categories: macroscopic, mesoscopic and microscopic approaches.

### 2.1  *Macroscopic Approach*

This method is based on kinetic rate equations which describe the change of the concentrations of primary defects and their aggregates as a function of time. These
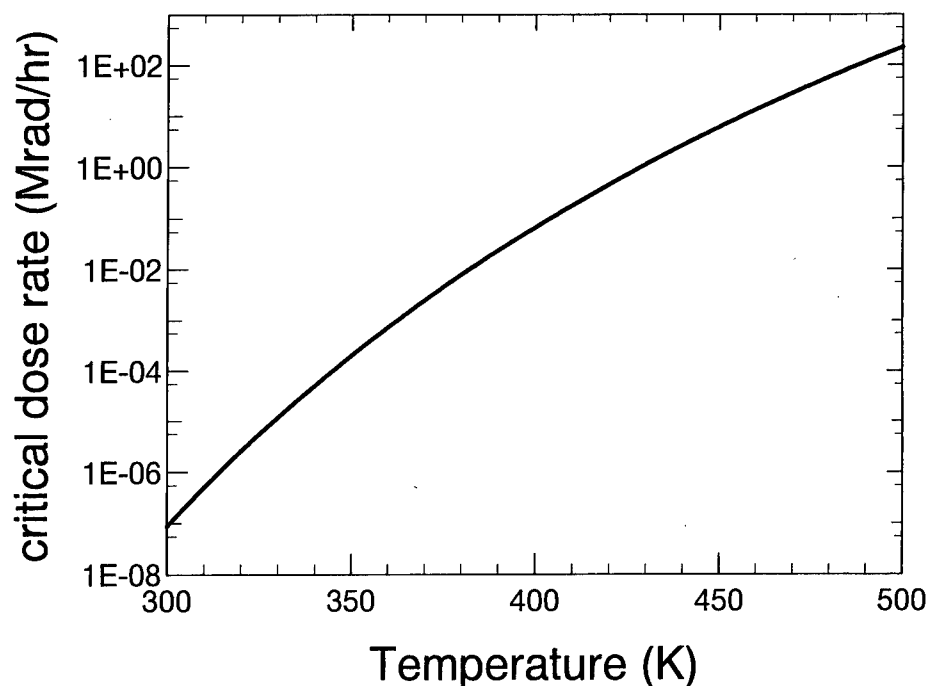
FIGURE 1   Critical dose rate as a function of the temperature according to the macroscopic approach.

macroscopic concentrations are averaged over the entire volume of the crystal and thus do not depend on the positions of the defects. The method, which is in fact based on the nucleation theory of Smoluchowski,[5] allows for the treatment of a long chain of elementary processes, including the initial stage of aggregation (transformation of single centers into dimers, trimers, etc), evaporation of single centers from colloids, defect disappearance at dislocations, etc. The principal limitation of this approach stems from its usage of phenomenological parameters (in particular: reaction rates) which are *a priori* assumed to be independent of time and concentration. Further, the approach has practical limitations since an adequate description of the most important radiolysis processes in alkali halides in terms of this approach requires usage of several parameters for which the value has not been determined very accurately yet by theory or by experiments. Nonetheless, this macroscopic approach has proven to be rather successful in describing many important features of the radiolysis processes in alkali halides and in particular in NaCl.[6,7,8,9] The main results which have been obtained by this approach are: a) the colloid formation efficiency as a function of the temperature has a bell-shape, which implies that for a given dose rate and a given total dose the fraction of colloids has a maximum at a certain temperature; b) for a given temperature, there is an optimum dose rate for colloid growth. The optimum dose rate shifts to lower values if the temperature is decreased. At their optimum dose rates, lower irradiation temperatures lead to higher colloid formation efficiencies than higher irradiation temperatures; c) reduction of the mobility of interstitials through trapping (e.g. by impurity cations) leads to an enhanced growth of colloids;
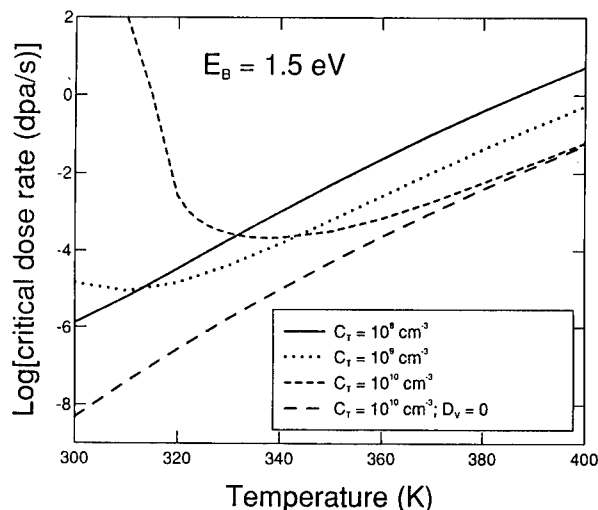
FIGURE 2   Critical dose rate as a function of the temperature according to the mesoscopic approach for various concentrations of H center traps. Elastic interaction parameters are: $\lambda_{HH} = 0.3$ eV, $\lambda_{FF} = 0.02$ eV and $\lambda_{FH} = 0.05$ eV. The long-dashed curve refers to the case in which the mobility of the vacancies (F centers) is zero.

d) there is a critical (minimum) dose rate $P_c$ for colloid growth at a certain temperature:

$$P_c = \left( \frac{z_H c_F^{(e)}}{z_H - z_F} \right)^2 4\pi r_0 D_F \tag{1}$$

Here, $r_0$ is the radius for recombination between F and H centers, $D_F$ is the diffusion coefficient of the F centers, $c_F^{(e)}$ is the concentration of F centers in thermal equililbrium with colloids, and $z_H$ and $z_F$ are bias coefficients for the drain of H and F centers to dislocations respectively. In Figure. 1, $P_c$ is shown as a function of the temperature. Note that in these calculations, a dose rate of 1 Mrad/hr is assumed to be equivalent to $1.667 \cdot 10^{-8}$ dpa/s, corresponding with a formation energy of 100 eV per F-H pair.

## 2.2 Mesoscopic Approach

In this approach towards defect accumulation and clustering, the distribution of point-defects is characterized by space-dependent concentrations of vacancies and interstitials. The recombination kinetics is treated in a mean-field procedure,[10,11,12] neglecting spatial correlations between defects and their impact on the reaction kinetics. The mesoscopic approach predicts that a non-trivial behaviour (i.e. a non-homogeneous distribution) may arise if additional interactions, such as elastic attraction between point defects,[13] or dynamic radiation-induced interactions[14] are taken into account. In the mesoscopic approach, point-defect clustering can be regarded as a phenomenon of self-organization under recombination-controlled conditions.[13] Defect aggregation under recombination-controlled conditions arises from the spatial segregation of the mixture of F and H centers into clusters of similar defects (consisting of alkali metal colloids and halide gas bubbles in the case of alkali halides) and thus requires the occurrence of net 'uphill' point defect
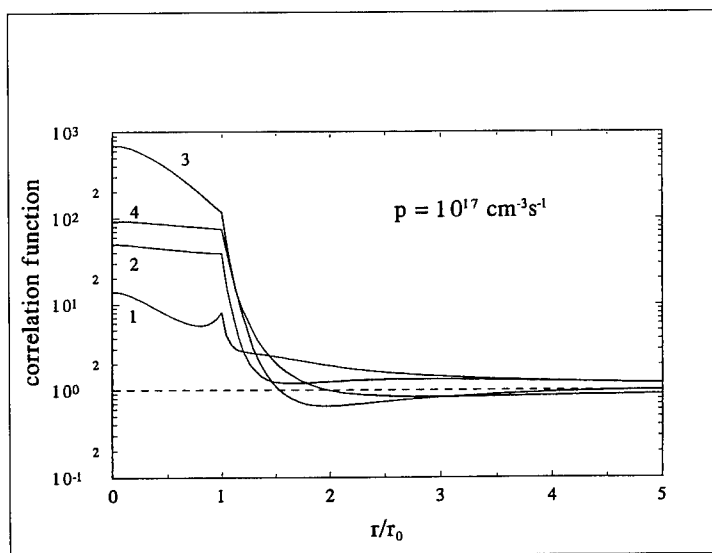
E. KOTOMIN *ET AL.*



FIGURE 3   The joint correlation functions for vacancies in NaCl at temperatures: 0°C(1), 50°C(2), 100°C(3), and 150°C(4). Only in cases (3) and (4) real aggregation occurs: the correlation function crosses the asymptotic value of X = 1 (see text). For the given dose rate (P = $10^{17}$ $cm^{-3}s^{-1}$) aggregation is most effective at 100°C.
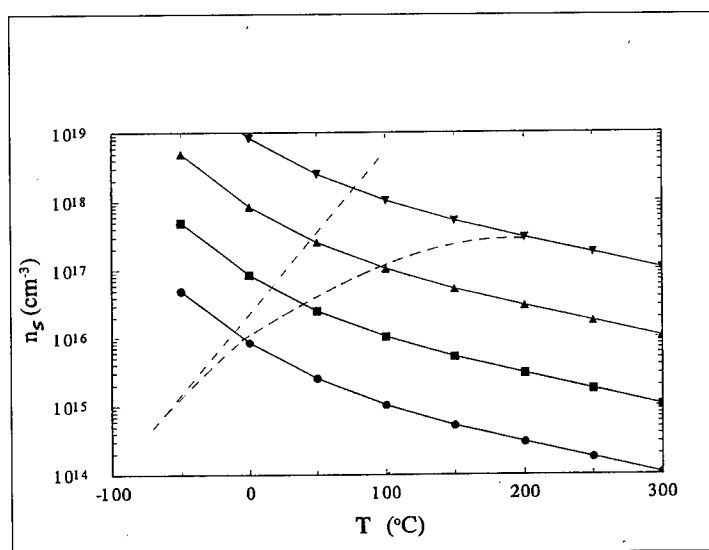


FIGURE 4   The saturation concentrations as a function of the temperature for dose rates *P*: $10^{11}$ $cm^{-3}s^{-1}$(●), $10^{13}$ $cm^{-3}s^{-1}$(■), $10^{15}$ $cm^{-3}s^{-1}$(▲), and $10^{17}$ $cm^{-3}s^{-1}$(▼). The two dashed lines indicate the region in which aggregation occurs.

fluxes. This is possible if the average drift fluxes arising from an attractive interaction between similar defects are larger than the sum of the fluxes arising from attractive interactions between dissimilar defects. Thus, spatial segregation requires *two* conditions to be fulfilled: a) there has to be an asymmetry with respect to the mean attraction between dissimilar defects and the mean attraction between similar defects; b) point-defect densities have to be rather high in order to make the drift fluxes arising from mutual interactions sufficiently large.[15]

This formalism was presented and analyzed for Frenkel defects in alkali halides by Kotomin, Zaiser and Soppe[16] with special emphasis on the rôle of the elastic interaction between similar and dissimilar defects (which is known to decay as $E = -\lambda r^{-3}$). Within the mesoscopic formalism the critical dose rate for aggregation is found to be:

Here, $r_0$ is the recombination radius, $D = D_\mathrm{H} + D_\mathrm{F}$ is the relative diffusion coefficient and $\Delta_\mathrm{el}$ is defined by the combination of the elastic interaction energies between similar and dissimilar

$$\ln(P_\mathrm{c}) \geq 2\ln\left(\frac{kT}{\Delta_\mathrm{el}}\right) + \ln(D) + \ln\left[\left(1 + \frac{D_\mathrm{F}}{D_\mathrm{H}}\right)^2 4\pi r_0\right] \tag{2}$$

defects:

$$\Delta_\mathrm{el} = \frac{4\pi}{3}\left[\lambda_\mathrm{HH} + \frac{D_\mathrm{F}}{D_\mathrm{H}}\lambda_\mathrm{FF} - \left(1 + \frac{D_\mathrm{F}}{D_\mathrm{H}}\right)\lambda_\mathrm{FH}\right] \tag{3}$$

in which $\lambda_\mathrm{FF}$, $\lambda_\mathrm{HH}$ and $\lambda_\mathrm{FH}$ stand for elastic interaction parameters for interactions between F-F, H-H and F-H pairs, respectively.

From equation (2) it can easily be deduced that if there would not be any traps for the highly mobile H centers, the critical dose rate for aggregation would be unrealistically high for a case like NaCl. If, however, H center trapping by deep traps is taken into account, the critical dose rate is reduced to more reasonable values even at rather small concentrations of traps $C_\mathrm{T}$. The presence of H center traps, with concentration $C_\mathrm{T}$, leads to a reduction of the mobility of the H centers:[17]

$$\tilde{D}_\mathrm{H}^{-1} = D_\mathrm{H}^{-1} + 4\pi C_\mathrm{T} R_\mathrm{T} v^{-1} \exp\left(\frac{E_\mathrm{B} + E_\mathrm{H}}{kT}\right) \tag{4}$$

where $E_\mathrm{H}$ is the activation energy for diffusion, $E_\mathrm{B}$ is the binding energy to the trap, $R_\mathrm{T}$ its capture radius and $v$ an attempt frequency. Recently, it was shown both theoretically and experimentally that radiation induced di-vacancies $\left(v_\mathrm{a}^+ v_\mathrm{c}^-\right)$ could form such deep $(E_\mathrm{B} \approx 1.5$ eV) traps.[18] In Figure 2 we show the critical dose rate as a function of $T$ for various trap concentrations. At high temperatures the critical dose rate decreases by one order of magnitude if $C_\mathrm{T}$ increases by one order of magnitude. The solid line is almost linear for the temperature range of this figure since the term $\ln(D)$ in eq. (2) is dominant here. Despite the effect of $C_\mathrm{T}$, there remains a discrepancy of some orders of magnitude with the macroscopial $P_\mathrm{c}$ (Figure 1).

The introduction of traps causes the aggregation also to be *limited* to a certain temperature interval. This temperature range shifts to higher temperatures if the concentration of traps is increased. The lower-temperature limit is reached when the mobility of the vacancy defects becomes significantly larger than that of the interstitials since in this case the term $\Delta_\mathrm{el}$ becomes negative due to large values of $\epsilon = D_\mathrm{F}/D_\mathrm{H}$. This limit is well observed in Figure 2 ($T_c = 310$ K for $C_\mathrm{T} = 10^{10}$ cm$^{-3}$). This trapping effect is elucidated by the long-dashed curve in Figure 2, displaying the critical dose rate for

$C_T = 10^{10}$ cm$^{-3}$ but with $D_F$ set to zero. In this particular case, the lower temperature limit does not emerge. The aggregation rate is also found to be a bell-shaped function of temperature.[16] It shifts to lower temperatures and significantly decreases in amplitude if the dose rate is decreased.

### 2.3  *Microscopic Approach*

In the microscopic approach[12,19] the defect distributions are characterized by a hierarchy of many-particle densities (or by the corresponding defect-defect correlation functions). This allows to take into account relative spatial distributions of both similar (F-F, H-H) and dissimilar (F-H) defects and thus to incorporate the influence of defect correlations on the recombination kinetics. Within this approach, it is possible to show that the very nature of the recombination process provides a tendency towards clustering of similar defects on microscopic scale. However, the aggregation process is greatly accelerated for highly mobile defects provided they interact via elastic forces.[20] It is shown that within this formalism, the critical dose rate for aggregation reads:

$$\ln(P_c) \geq \ln(D) - \frac{4\lambda_{HH}}{kTr_0{}^3} + \ln\left(\frac{3}{4\pi r_0{}^5}\right) \tag{5}$$

Comparison of mesoscopic and microscopic formalisms shows that both eqs. (2) and (5) have the same dependence on the relative diffusion coefficient, $D = D_F + D_H$, but different dependence on the elastic interaction between defects. However, in *both* cases the stronger similar defect attraction is, the lower the critical dose rate is. In the mesoscopic approach this effect is less pronounced (logarithmic vs linear dependence) and here $P_c$ is considerably higher since this approach is only able to detect those mesoscopic-size aggregates which are already well-developed.

In terms of the microscopic approach, considerable aggregation arises when the qualitative behaviour of the joint correlation function for similar defects changes from a monotonous decay with increasing distance to a non-monotonous behaviour, cf. curves 1, 2, and 3, 4 in Figure 3. Physically, this means that the aggregates start to absorb nearby similar defects due to which the concentration of these defects within a certain range is reduced below the statistical level: $X \equiv 1$. The calculated F center saturation number concentration $ns$ as a function of both dose rate and temperature are shown in Figure 4. It can easily be shown[20] that, for a weak-aggregation regime, $n_s \propto \sqrt{P/D}$. A non-trival results is that the temperature range of the defect aggregation (for a given dose rate) is limited. In Figure 4 this temperature range is the region between the two dashed lines. Another conclusion which is suggested by this figure is that the optimum temperature for aggregation decreases with decreasing dose rates.

## 3  CONCLUSIONS

We have identified 3 basic approaches for the modelling of diffusion-controlled aggregation of radiation-induced defects in alkali-halides. The approaches have in common that they predict the existence of a critical dose rate for aggregation which increases with temperature, and a bell-shaped temperature dependency of the aggregation rate.

The concept of a critical dose rate could become an important engineering factor in the design of high-level waste repositories since, if the radiation intensity in the repository could be confined below this critical dose rate, any risks in relation to radiation damage in rock salt would be eliminated.

Future investigations should be aimed towards a removal of the rather large discrepancies between the quantitative results by the three approaches.

# REFERENCES

1. R. Ottmer, *Z. Physik*, **46**, 798 (1928).
2. D. E. McLennan, *Can. J. Phys.*, **29**, 122 (1951).
3. J. H. Schulman, and W. D. Compton, *Color Centers in Solids*, (Pergamon Press, New York, 1963).
4. K. K. Shvarts and Yu. A. Ekmanis, *Dielectric Materials: Radiation-Induced Processes and Stability* (Zinatne, Riga, 1989).
5. M. Smoluchowski, *Phys. Zeit.*, **17**, 557 (1916).
6. U. Jain, and A. B. Lidiard, *Phil. Mag.*, **35** 245 (1977).
7. A. B. Lidiard, *Phil. Mag., A***39**, 647 (1979).
8. J. Seinen, J. C. Groote, J. R. W. Weerkamp, and H. W. Den Hartog, *Rad. Eff.*, **124**, 325 (1992).
9. W. J. Soppe, *J. Phys.: Cond. Matter*, **5**, 3519 (1993).
10. A. Ovchinnikov, and Y. Zeldovich, *Chem. Phys.*, **28**, 215 (1978).
11. A. Mikhalilov, *Phys. Reports*, **184**, 307 (1989).
12. V. V. Vinetsky, Yu. H. Kalnin, E.A. Kotomin, and A. A. Ovchinnikov, *Sov. Phys. Uspekh.*, **33**, 793 (1990).
13. G. Martin, *Fundamental Aspects of Radiation Damage in Metals, Vol. 2*, edited by M. T. Robinson and F. W. Young, Jr., (Gatlinburg, Tennessee, 1975) p. 1084., G. Martin, *Phil. Mag.*, **32**, 615 (1975).
14. M. Zaiser, W. Frank, and A. Seeger., *Solid State Phenomena*, **23/24**, 203 (1992).
15. E. A. Kotomin and M. Zaiser, *Appl. Phys A***57**, 117 (1993).
16. E. Kotomin, M. Zaiser and W. Soppe, *Phil. Mag* .in press (1994).
17. E. A. Kotomin, and A. B. Doktorov, *Phys. Stat. sol* (b), 114, 9 (1982).
18. V. Gektin and N. V. Shiran, *Sov. Phys. Sol. St.* **30**, 870 (1988), V. V. Gavrilov, A. V. Gektin *et al., Sov. Phys. Sol. St.* **31**, 2013 (1989).
19. V. N. Kuzovkov and E. A. Kotomin, *Rept. Prog. Phys.* **51**, 1479 (1988), E. A. Kotomin and V. N. Kuzovkov, *Rept. Prog. Phys.* **55**, 2097 (1992).
20. V. Kuzovkov and E. Kotomin, *Physica Scripta* **50**, 720 (1994).

# THERMOLUMINESCENCE OF PURE AND Eu-DOPED NaZnF$_3$

C. FURETTA, M. GRAZIANI, C. SANIPOLI, A. SCACCO

*Dipartimento di Fisica, Università La Sapienza, P. le A. Moro 2, 00185 Roma, Italy*

Thermoluminescence of pure and Eu-doped NaZnF$_3$ fluoroperovskite is studied in order to determine nature of emitting centres and possible dosimetric properties. Intrinsic and extrinsic defects, some of them due to surface oxidation processes, are related to peaks in the glow curves of the two systems.

*Key words*: TL Dosimetry, Fluoroperovskites, NaZnF$_3$:Eu.

## 1 INTRODUCTION

In the frame of a search for new thermoluminescent materials suitable for dosimetry of ionizing radiations, ternary compounds belonging to the group of fluoroperovskites were found to show attractive performances coupled to intrinsic favourable features, such as a very low hygroscopicity. In the case of KMgF$_3$, very good dosimetric behaviour was found for samples doped with efficient activators: Eu impurities originate a phosphor which exhibits high sensitivity to low radiation doses, no fading effect and practically energy independent response,[1] whereas Tl-doped samples show a surprising large range of linearity with dose which makes them proper for dosimetric application in radiation therapy.[2] The satisfactory results achieved for KMgF$_3$ suggested studies on other compounds with analogous chemical and crystalline structure to be used as hosts for the same or different activators. The lack of information on NaZnF$_3$, whose single crystals of very small size were obtained only recently,[3] prompted us to produce and dope this compound and to study its thermally stimulated luminescence in order to determine performances in dosimetry and possibly nature and properties of the point defects in the material.

## 2 PREPARATION OF MATERIALS AND EXPERIMENTAL PROCEDURE

Polycrystalline powder of NaZnF$_3$ was obtained with the following procedure: carefully dried NaF and ZnF$_2$ were mixed in the stoichiometric ratio, the mixture was heated in a graphite crucible up to the complete melting (at about 750°C) under a nitrogen atmosphere, then cooled to room temperature and finally grinded and sieved to select 100−150 $\mu$m particles. Doping was achieved by adding to the mixture suitable amounts of EuBr$_3$. Irradiations of the samples were carried out with a $\beta$ source ($^{90}$Sr, dose rate 0.027 Gy/min) after annealing for 1 hour at different temperatures. Thermoluminescence (TL) was measured by a Toledo 654 TLD reader with a heating rate of 3°C/s on samples of about 25 mg. A second reading was performed after each measurement for the IR background subtraction.
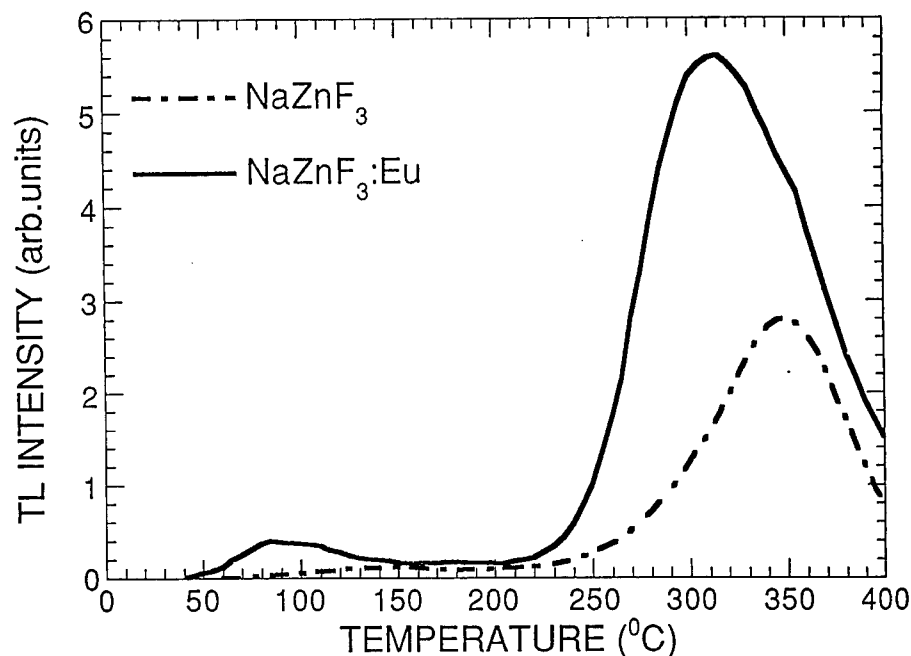
FIGURE 1   Glow curves of pure and Eu-doped (1.4 mole%) NaZnF$_3$ powders after 500°C annealing and $\beta$ irradiation (0.8 Gy).

## 3   RESULTS AND DISCUSSION

First TL measurements concerned NaZnF$_3$ samples annealed at 500°C, and supplied glow curves shown in Figure 1. Undoped NaZnF$_3$ exhibits two weak overlapping peaks at about 140°C and 190°C and a much more intense and well resolved peak at about 350°C. Eu-doped NaZnF$_3$ shows, besides those of the pure material, a further TL peak at about 90°C. The position of the high temperature TL peak is not reproducible in the various samples and ranges from 310°C to 350°C. Analogously, the peak intensity changes appreciably for different samples treated apparently in the same way and does not depend too much on the doping. When the powder is annealed at 400°C the glow curve of NaZnF$_3$:Eu is drastically changed: weak peaks between 120°C and 200°C are again observed, but the 350°C peak is almost completely suppressed and the 90°C peak becomes dominant. The dependence of the glow curve on the dopant level is displayed in Figure 2. The intensity of the low temperature peak increases almost linearly with Eu concentration, while all other peaks show much smaller variations. A careful inspection of the powder annealed at 500°C showed a thin yellowish layer on the particle surfaces, which was not found on those annealed at 400°C. As a consequence, the 350°C TL peak can be explained as the result of surface oxidation or decomposition caused by the high temperature annealing. The two peaks at 140°C and 190°C can be reasonably assigned to defects of intrinsic nature, namely F and F$_2$ centres created by the irradiation in the host material, whereas the Eu impurities are responsible for the 90°C peak. This last conclusion is not satisfactory from the point of view of the use of NaZnF$_3$:Eu as a dosimetric material, because the low
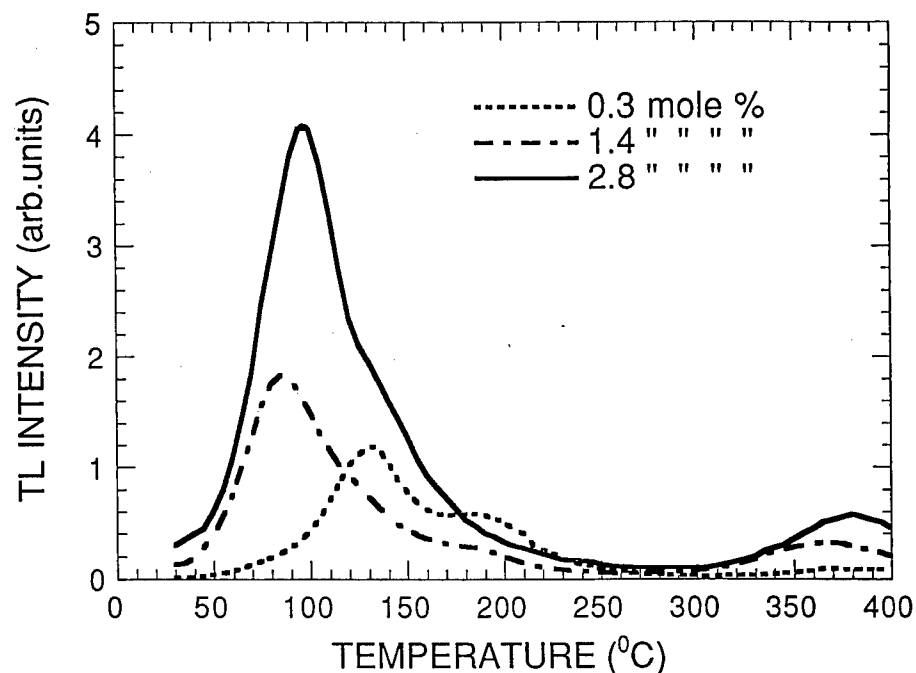
FIGURE 2    Glow curves of NaZnF$_3$ doped with different Eu concentrations after 400°C annealing and $\beta$ irradiation (1.2 Gy).

temperature peak could show fading effects. The 350°C peak, due to defects formed by oxidation at relatively high temperature, can be considered for dosimetric purposes. It is undoubtedly less sensitive to fading processes, and its intensity could be considerably increased by a systematic chemical modification of the NaZnF$_3$ powder. Studies are planned on such a peculiar behaviour of the material.

Anyway, both pure and doped systems show good linearity of the integrated TL response to the radiation dose up to 70–100 Gy, which is a very good dosimetric feature (Figure 3). In any case, Eu-doped NaZnF$_3$ shows features which are not similar to those of the other fluoroperovskite KMgF$_3$ doped with Eu impurities, where a typical dosimetric peak was found at high temperature.[1,4] This is surprising, because analogies in the chemical composition of the two systems and in the nature of dopant were expected to produce similar TL responses. Actually, the two TL peaks due to intrinsic defects in NaZnF$_3$ look quite similar to those found in KMgF$_3$.[1,5] As a consequence, the real difference is given by the TL peak caused by extrinsic centres bound to the Eu impurities, which appear to be much less stable in NaZnF$_3$ than in KMgF$_3$. In order to improve knowledge on the microscopic structure of such extrinsic centres, measurements of spectrally resolved TL are needed.

REFERENCES

1.   C. Furetta, C. Bacci, B. Rispoli, C. Sanipoli and A. Scacco, *Radiat. Prot. Dosim.* **33**, 107 (1990).
2.   A. Scacco, C. Furetta, C. Bacci, G. Ramogida and C. Sanipoli, *Nucl. Instrum. Meth., in Phis. Res.* **B91**, 223 (1994).
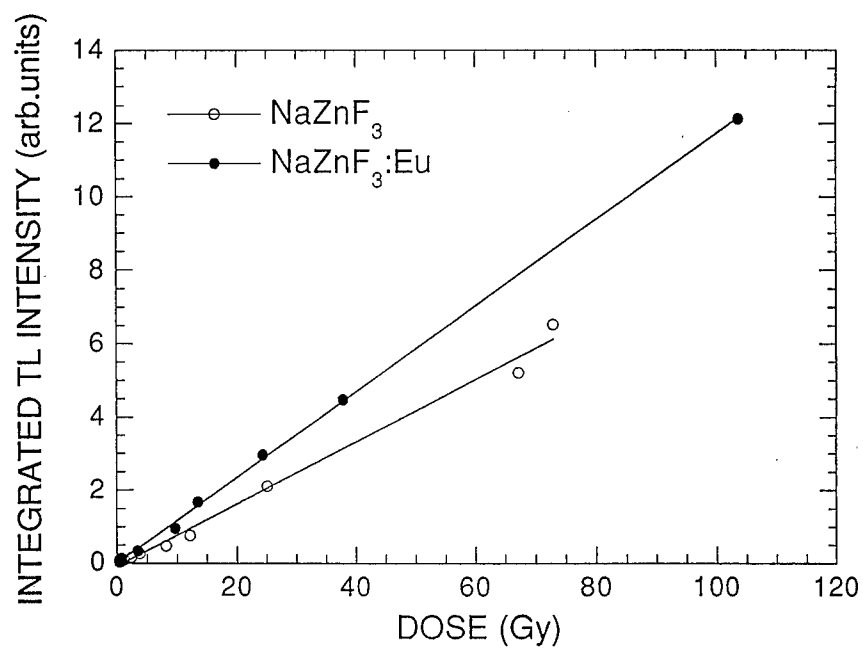
FIGURE 3    Dose dependence of integrated TL signal for pure and Eu-doped (1.4 mole%) NaZnF$_3$ annealed at 500°C.

3.   T. Wallin and J. Zeising, *Sol. St. Ionics* **39**, 273 (1990).
4.   C. Bacci, S. Fioravanti, C. Furetta, M. Missori, G. Ramogida, R. Rossetti, C. Sanipoli and A. Scacco, *Radiat. Prot. Dosim.* **47**, 277 (1993).
5.   C. Bacci, C. Furetta, G. Ramogida, C. Sanipoli and A. Scacco, *Phys. Medica* **9**, 207 (1993).

# PECULIARITIES OF A RADIATION DEFECT CREATION IN BERYLLIUM OXIDE CRYSTALS

S. V. KUDYAKOV, I. N. ANTSIGIN, S. V. GORBUNOV and A. V. KRUZHALOV

*Experimental Physics Department, Urals State Technical University,
620002 Ekaterinburg, Russia*

The radiation defect formation has been studied in beryllium oxide crystals irradiated with reactor neutrons in a wide range of fluences ($10^{15}$–$10^{20}$ cm$^{-2}$). It has been found that at high dose irradiation the saturation and reduction of anion and cation vacancies (the simplest point radiation defects) occurs in contrast to another alkaline earth oxides where only saturation takes place. A reduction of the point radiation defects under high dose irradiation has been caused not only by achieving a dynamic balance between creation and annihilation of Frenkel pairs but also by aggregation of the defects created. The mechanism of defect aggregation is discussed for the simplest aggregate defect-$P^-$-center (double cation-anion vacancy trapping an electron). A new aggregate paramagnetic centers have been registered in high-dose neutron irradiated *BeO* crystals.

## 1 INTRODUCTION

It is known that the radiation defects aren't created by an electron excitation decay in wide-gap oxides.[1] Thus the wide-gap oxides have a high stability to $X$-ray and $\gamma$-radiations influencing only an electron subsystem of crystal and recharging the native lattice defects. It was established that under neutron irradiation anion and cation Frenkel defect pairs are formed in the alkaline earth oxides.[2] The anion vacancies (one of the anion Frenkel pair components) appeared as $F^+$-centers in ESR spectra and as $F^+$-and $F$-centers in the optical absorption (OA) and luminescence spectra. The cation vacancies appeared in the ESR and OA spectra as $V^-$-and $V^o$-centers. Moreover, it is known that a cation interstitial stabilization at an anion vacancy can occur resulting in antisite defect formation.[3]

## 2 EXPERIMENTAL DETAILS

The *BeO* monocrystals grown by Czochralski-Kiropulos method were irradiated by reactor neutrons ($\Phi = 10^{15}$–$10^{20}$ cm$^{-2}$, $E_n>1$ MeV) at T = 350 K. The OA spectra in 1.5-6.0 eV range and ESR spectra were measured using a UV-5270 Beckman spectrophotometer and X-band RE-1302 ESR spectrometer, respectively. Also a thermal annealing in the 400–1000 K temperature region was used to create new aggregate centers and to study the electron and ion processes in *BeO*.

## 3 EXPERIMENTAL RESULTS AND DISCUSSION

Neutron irradiation created the radiation defects in cation and anion sublattices in beryllium oxide. In the OA spectra of neutron irradiated *BeO* crystals the bands at 6.6 and 5.4 eV connected with $F^+$- and $F$-centers, respectively, are appeared.[4] The wide OA bands at 4.0 and 2.1 eV are attributed to the $V^-$-centers.

The radiative accumulation of $F^+$-and $V^-$-centers in *BeO* has been measured over a wide range of fluences ($\Phi = 10^{16}$–$10^{20}$ cm$^{-2}$). It should be noted that at $\Phi >10^{18}$ cm$^{-2}$ the optical density in *BeO* extremely increases and measuring of OA spectra becomes

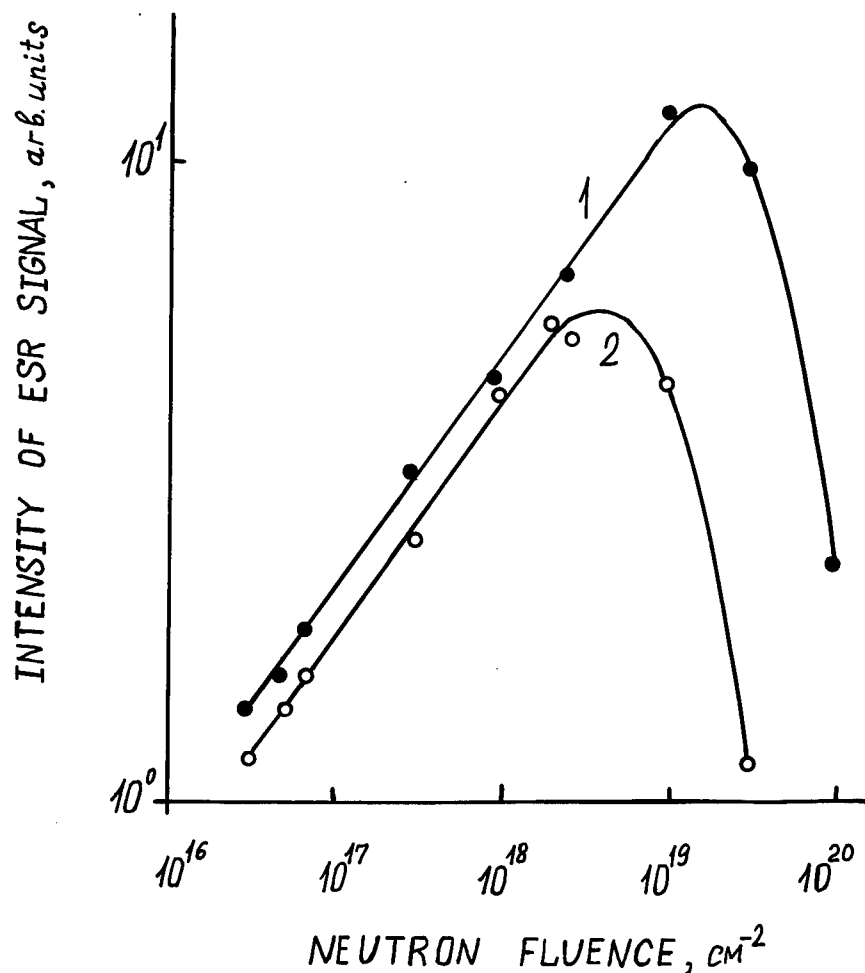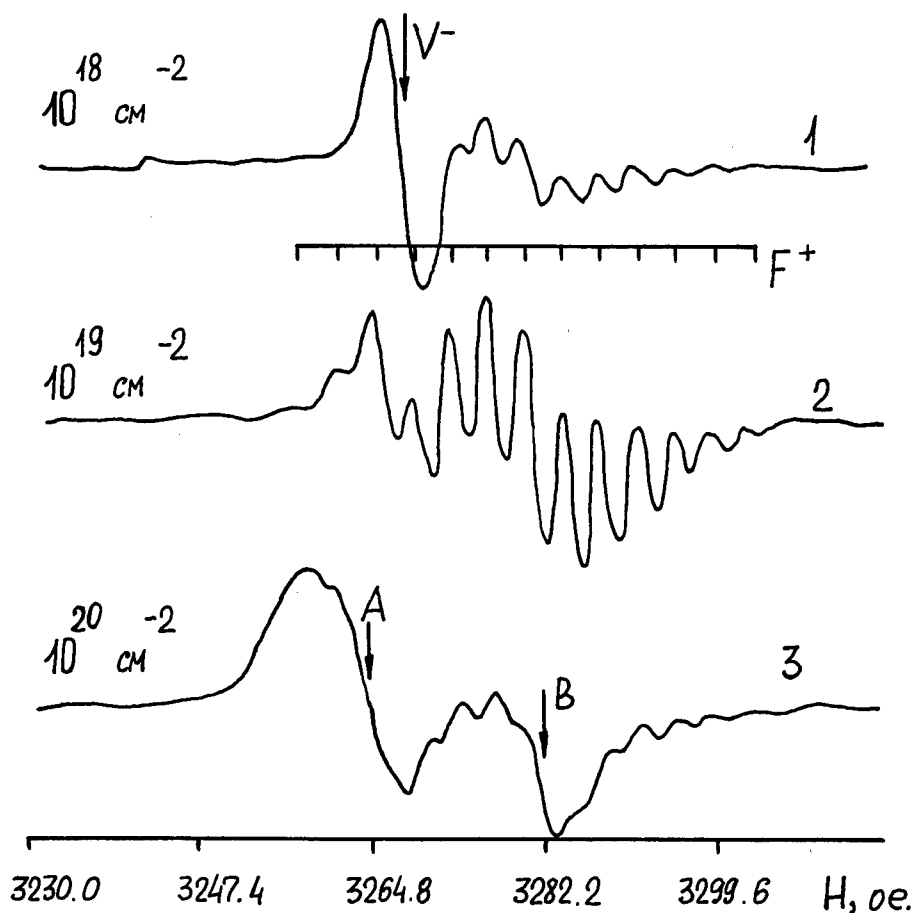FIGURE 1    Accumulation of $F^+$ -centers (1) and $V^-$ centers (2) in the neutron irradiated *BeO*.

impossible. So the data for high neutron fluences were obtained by ESR methods. As shown in Figure 1, the two typical regions on the $F^+$ -and $V^-$-center accumulation curves can be defined: 1. The ESR signal intensities of $F^+$-and $V^-$-centers increase linearly in the $\Phi = 10^{16}$–$10^{19}$ cm$^{-2}$ and $\Phi = 10^{16}$–$2.10^{18}$ cm$^{-2}$ fluence ranges, respectively. 2. Saturation and reduction of the $F^+$- and $V^-$-center accumulation curves take place at $\Phi > 10^{19}$ cm$^{-2}$ and    $\Phi > 2.10^{18}$ cm$^{-2}$, respectively, being accompanied by considerable ESR signal shape distortions (Figure 2). Besides two new ESR lines have been registered. Firstly, the $A$-line occurrence is connected with saturation and reduction of $V^-$ -center ESR signal intensity. The $A$-line $g$-factor ($g = 2.0150$) is typical of hole centers in *BeO*. Secondly, the isotropic $B$-line appears together with $F^+$-center ESR signal intensity reduction. The $B$-line $g$-factor ($g = 2.0030$) corresponds to $g$-factor region of electron centers in *BeO*.

$10^{18}$ $cm^{-2}$

$V^-$

$F^+$

1

$10^{19}$ $cm^{-2}$

2

$10^{20}$ $cm^{-2}$

A

B

3

3230.0    3247.4    3264.8    3282.2    3299.6    H, oe.

FIGURE 2   ESR spectra of *BeO* crystals irradiated with different neutron fluences.

These experimental results can be interpretted as follows. The linear sections of the $F^+$ -and $V^-$ -center accumulation curves correspond to the isolated anion and cation vacancy creation processes. The saturation and reduction are connected with the dynamic balance achievement between the Frenkel defect pair creation and their recombination processes and with neighbouring vacancy creation which interact with each other up to aggregate $F$- and $V$-type defect formation. Linear sections of cation ($10^{15}$–$2.10^{18}$ cm$^{-2}$) and anion ($10^{15}$-$10^{19}$ cm$^{-2}$) vacancy accumulation curves and also the higher accumulation velocity of $F^+$-, $F$-centers compared to $V^-$, $V^o$-centers indicate the wider mobility of cation interstitials and more difficult conditions for their stabilization by other defects or at the crystal surface. It should be noted that the direct method of vacancy component recording (as $V^0$-, $V^-$ -centers) of Frenkel cation pairs was used for the first time.

At the linear section of defect accumulation in both sublattices of neutron irradiated *BeO* we have found the beginning of a creation process of a complex defect ($P^-$ -center) consisting of both sublattice components (the anion-cation double vacancy that trapped an
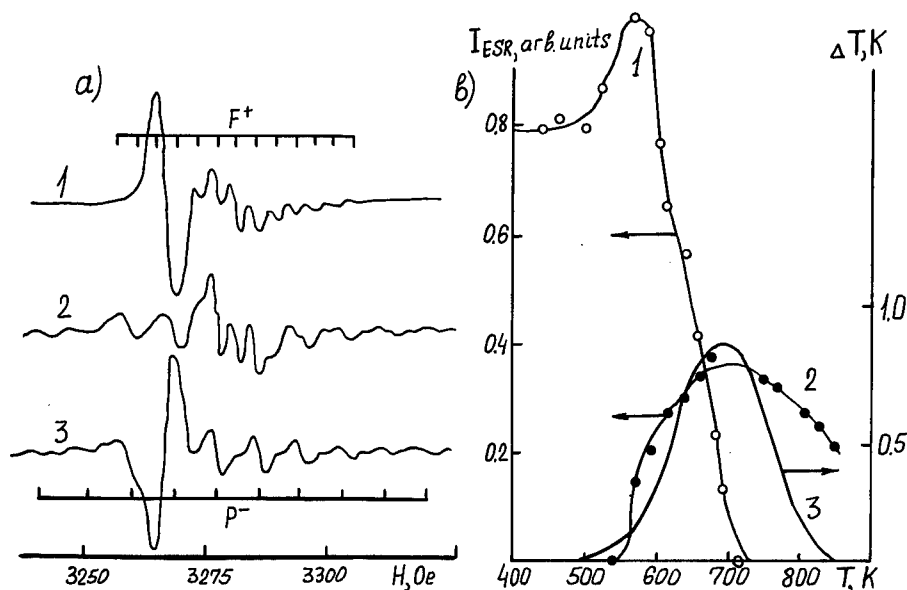
FIGURE 3  a) ESR spectra of neutron irradiated *BeO* crystals ($\Phi = 10^{18}$ cm$^{-2}$). (1)- before annealing; (2)- after annealing at 650 K; (3) = (2)-(1). The $P^-$ -center formation is shown. b) Thermal activated processes in neutron irradiated *BeO* crystals. (1)-$V^-$-center relaxation; (2)-$P^-$ center formation; (3) different thermal analysis curve.

electron)[5] (Figure 3a). However, in the ESR spectrum this double vacancy appeared as a $P^-$ center only after annealing at 700 K (temperature range of a cation interstitial mobility). As distinct from the mechanism occurring in *MgO* (a cation vacancy migration with subsequent coagulation with $F^+$-center)[2] quite another mechanism is realized here. First, the concentration reduction of $F^+$- centers is not observed in *BeO*, unlike *MgO*. Second, it is determined that the *Be* vacancy motion begins at $T > 1600$ K. The following mechanism of a $P^-$ -center formation is suggested:

1. The cation-anion double vacancies existed before the thermal annealing was done and were created under neutron irradiation. However, the absence of an ESR signal after irradiation has shown a diamagnetic state of this defect.
2. The double vacancy appearance in the wurtzite structure leads to coagulation of three or four octahedrical interstitials (the defect oriented along C axis of crystal or along the *Be-O* $_{non-axial}$ bond, respectively). This cavity could be a capacity for *Be* ions displaced from regular positions.
3. At $T > 600$ K, interstitials can leave this cavity and migrate to isolated cation vacancies ($V^-$ -centers) with subsequent annihilation of cation Frenkel pairs.
4. Vacant anion-cation double vacancy can capture an electron created from the ionic and recombination processes under thermal annealing with paramagnetic $P^-$ -center formation.

The results obtained from thermal annealing measurements have confirmed the above suggestions (Figure 3b).

It should be noted in conclusion that the saturation and reduction of anion ($\Phi > 10^{19}$ cm$^{-2}$) and cation ($\Phi > 2.10^{18}$ cm$^{-2}$) vacancies were found. The anion vacancy reduction was not observed for $MgO$, $Al_2O_3$ and others where only saturation of accumulated curve and creation of the $F_2$-type center defects occur. For oxides this feature has been observed for the first time. Also, the new paramagnetic aggregate center $C$ is formed under the thermal annealing at 700–1000 K of neutron irradiated $BeO$ crystals with $\Phi = 10^{20}$ cm$^{-2}$.[6] A $C$-center formation mechanism is connected with ionic processes because the annealing of $F$- and $F^+$ -centers caused by oxygen interstitial migration and anion Frenkel pair recombination is observed in this temperature region.

REFERENCE

1.  Ch. B. Luschik, A. Ch. Luschik. *Electron excitation decay with defect formation in solids* (Nauka, Moscow, 1989), 264.
2.  B. Henderson, J. E. Wertz, *Defects in the alkaline earth oxides with application to radiation damage and catalysis* (Taylor and Fransis, London, 1977), 159.
3.  N. Itoh, K. Tanimura, *Rad. Eff.* **98**, 268 (1986).
4.  S. V. Gorbunov, A. V. Kruzhalov, M. J. Springis. *Phys. Stat. Sol.* **B141**, 293 (1987).
5.  I. N. Antsigin, S. V. Gorbunov, A. V. Kruzhalov, B. V. Shulgin. *Hyperfine Interactions.* **60**, 881 (1990).
6.  I. N. Antsigin, S. V. Gorbunov, A. V. Kruzhalov, S. V. Kudyakov. *Zhurnal prikladnoi spectroscopii.* **56**, N3, 411 (1992).

# INTERPRETATION OF THE EXTRALARGE INHOMOGENEOUS BROADENING IN THE OPTICAL SPECTRA OF HEAVILY NEUTRON-IRRADIATED laB-TYPE DIAMOND

A. OSVET and I. SILDOS

*Institute of Physics, Estonian Acad. Sci., Riia 142, EE2400 Tartu, Estonia*

The optical properties of a neutron-irradiated laB-type natural diamond were investigated in the visible and the infrared spectral range. Concentration of the nitrogen aggregates was estimated. Spectral hole burning method was applied to investigate the relations between different spectral lines in the luminescence spectra. Extralarge inhomogeneous broadening of the 774 and 813 nm lines is explained by the high concentration of nitrogen in an aggregate form.

*Key words*: Radiation-induced defects, spectral hole burning, inhomogeneous broadening.

## 1 INTRODUCTION

A neutron-irradiated natural laB-type diamond with high concentration of nitrogen is rather a complicated system for spectroscopic studies. The luminescence spectrum of such diamond contains many zero-phonon lines, a number of which reveal photochromism.[1]

Nitrogen atoms form large aggregates[2] while neutron irradiation creates defects, interstitials and also nanometer-sized regions of disordered carbon.[3]

In this work a piece of laB-type diamond heavily irradiated with neutrons ($10^{19}$ neutrons/cm$^2$) was investigated. Both infrared and visible optical spectroscopy were applied to characterize the sample. Spectral hole burning of the zero-phonon lines was carried out to investigate the photochromic effects and the origin of spectral lines.

## 2 EXPERIMENTAL

In order to determine the contents of nitrogen, the infrared absorption spectra of the sample were measured by using an Interspectrum PFS-2000 Fourier transform spectrometer. Figure 1 shows the absorption of neutron-irradiated and untreated crystals. It has been established[4] that one-phonon absorption in perfect diamonds is strongly forbidden by the selection rules associated with the symmetry of the lattice. The intrinsic and the specimen-independent two-phonon absorption reveal themselves in the region of 1400–2800 cm$^{-1}$. The IR absorption of diamond in the one-phonon region is induced by impurities which destroy locally the center of symmetry of the diamond structure and permit an electromagnetic coupling to fundamental optical vibration frequencies. The shape and intensities of these absorption bands, mainly induced by nitrogen impurities, allows the determination of the concentration of nitrogen. We have calculated the contents of nitrogen in different aggregates, using the relations between absorption coefficients and nitrogen amount[5] and estimated the content of nitrogen in A (pairs) and B1 (large aggregates) forms to be $4 \cdot 10^{19}$ cm$^{-3}$ and $8.5 \cdot 10^{19}$ cm$^{-3}$ respectively and the concentration of B2-aggregates (platelets) to be $2 \cdot 10^{15}$ cm$^{-3}$. The 1366 cm$^{-1}$ line connected with the platelets is very sensitive to the crystal strains. According to Sobolev,[6] its peak position is correlated to the dimensions of the platelets and in our case the diameter is of the order of 200 Å.
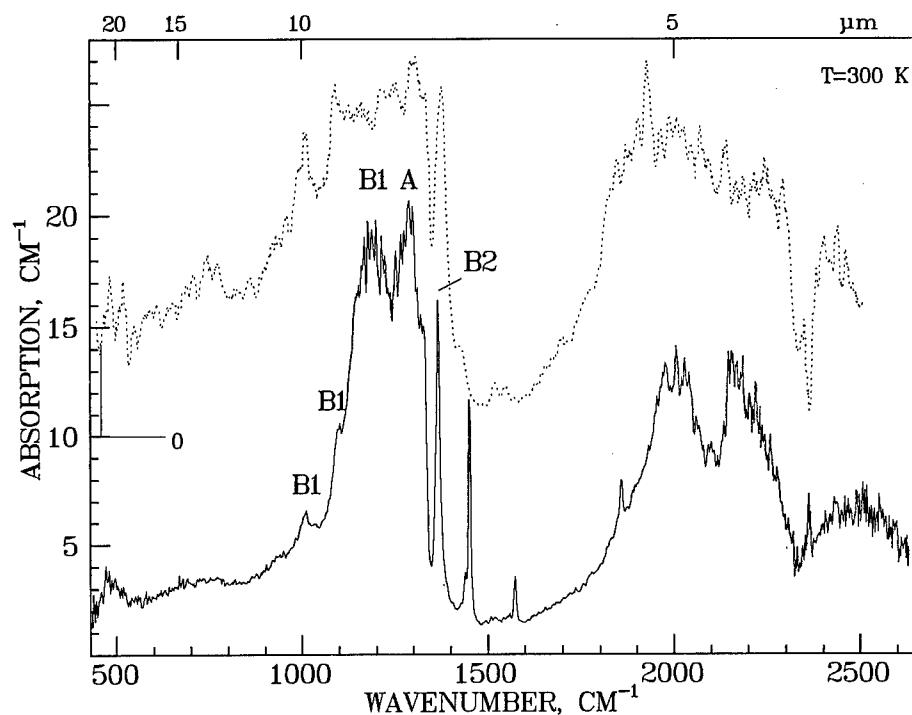
FIGURE 1   Infrared absorption spectrum of a laB-type natural diamond before (dotted line) and after (solid line) neutron irradiation. The spectra are displaced vertically.

At liquid He temperature luminescence of the sample was studied in the spectral region of 700–850 nm (excitation at 704 nm with an $Ar^+$-laser-pumped linear dye-laser). The luminescence spectrum consists of 7 lines, the most prominent ones peaking at 731, 773 and 812 nm (Figure 2). To cast light to the connection between these lines we used photochromic properties of the 731 nm line,[7] reducing its intensity by means of laser illumination. A proportional decrease of the 774 and 812 nm lines was observed (see Figure 2 curve b). We propose that these lines are originated by one and the same defect. A tentative scheme of electronic transitions is presented in the inset of Figure 2.

In[8] we investigated photochromic phenomena in several spectral lines of this sample. As it was established, the inhomogeneous broadening of the same spectral lines is exceptionally large. In the case of the 773 and 812 nm lines room-temperature persistent spectral hole burning was performed.[9] Additional investigations of these lines revealed correlation between the electronic transitions inside the 773 and 812 nm luminescence lines. Indeed, the excitation spectra detected at different positions on the contour of the 812 nm line are shifted (Figure 3A). Spectral hole burning in the 773 nm line at 773.2 nm affects the 812 nm line more than its blue-side component at 808 nm (curve b in the insert in Figure 3).
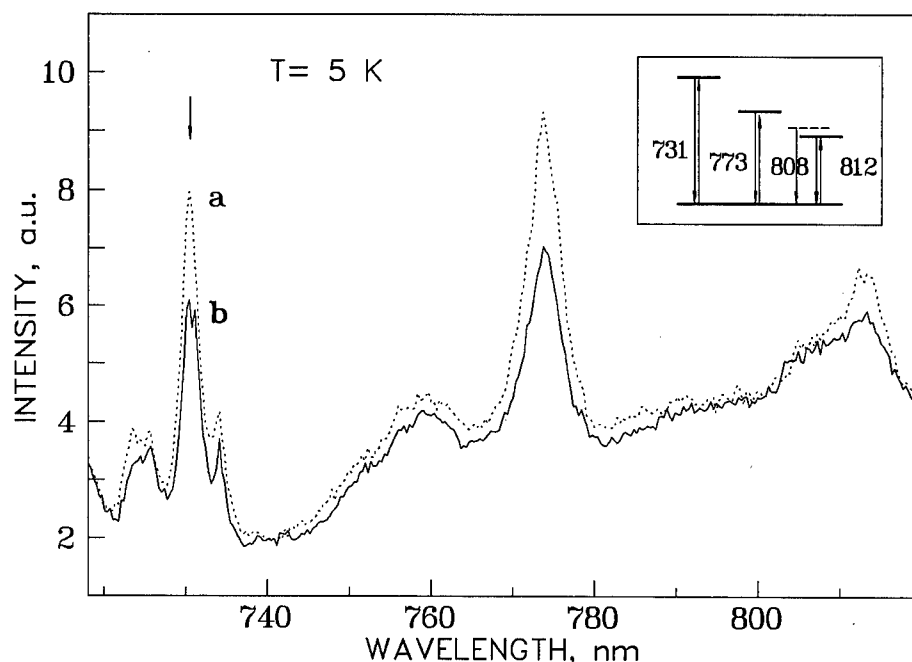
FIGURE 2   Luminescence spectrum of the neutron-irradiated sample before (dotted line) and after (solid line) laser illumination at 731 nm. Excitation of luminescence at 704 nm, 0.5 W/cm². Phototransformation was performed with cw dye laser, intensity 2 W/cm², duration 10 min.

## 3   DISCUSSION

According to Stoneham's theory[10] randomly positioned point defects and optical centres produce Lorentzian lineshapes. In case the strain field is caused by dislocations (spatially uncorrelated with optical defects), the line is gaussian-shaped. Both Lorentzian (dashed line) and Gaussian (dotted line) fittings to the 773 nm luminescence line are depicted in Figure 3B. Rather a strong gaussian component indicates strong influence of the platelets and nitrogen aggregates on the inhomogeneous broadening of this line.

REFERENCES

1. I. Sildos, U. Bogner and A. Osvet. In M. Meissner and R.O. Pohl (eds.), *Phonon Scattering in Condensed Matter VII* (Springer, Berlin 1993), p. 515.
2. J. Walker, *Rep. Prog, Phys. (GB)* **42**, 1605 (1979).
3. D. T. Morelli, T. A. Perry, J. W. Vandersande and C. Uher, *Phys. Rev.* **B48**, 3038 (1993).
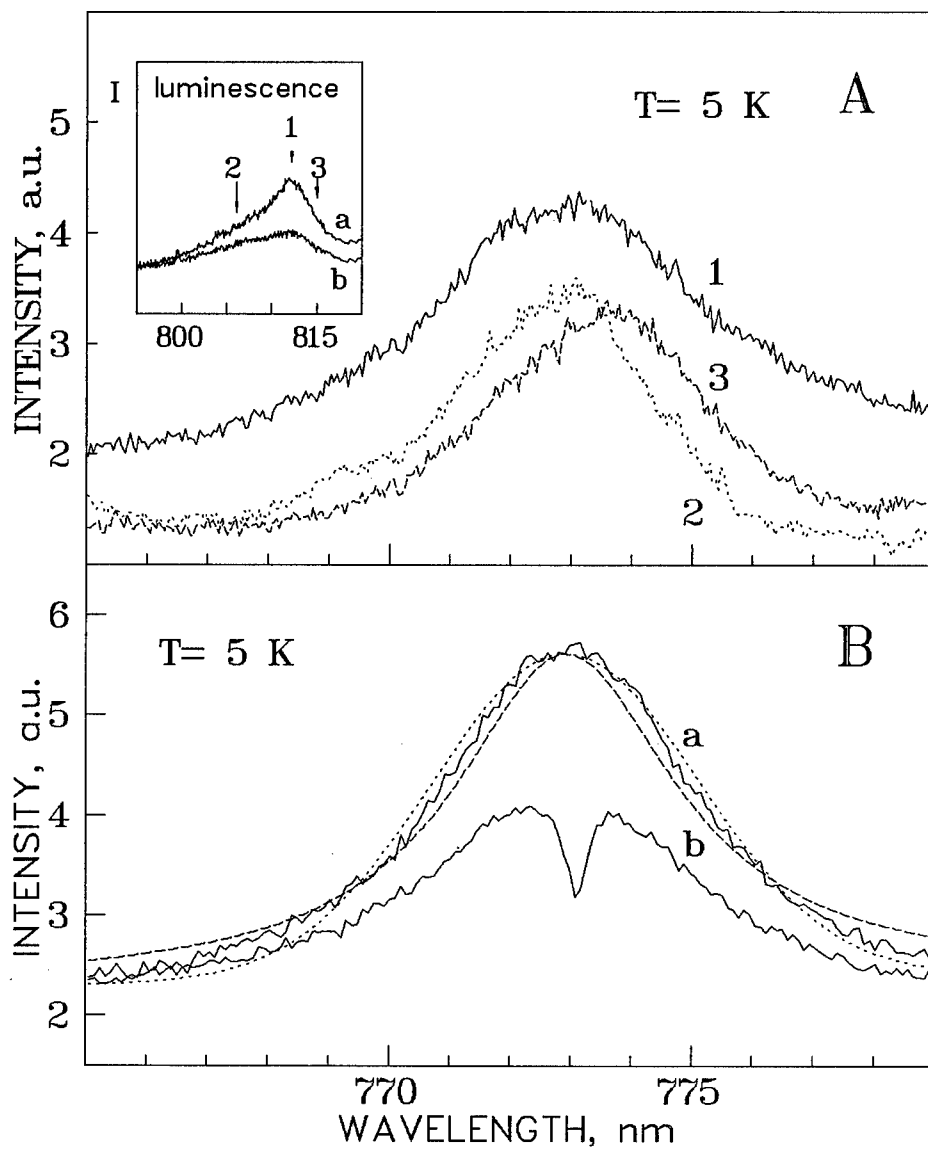
FIGURE 3   Excitation and luminescence spectra of the n-irradiated sample.
(A) Excitation profiles of 773 nm line at different detection wavelengths. The positions of detection on the inhomogeneous contour are shown in the inset with arrows 1, 2 and 3. Spectral resolution of detection was 1 nm. (B) Luminescence line before (a) and after (b) a selective laser illumination at 773.2 nm. Average intensity of the pulsed dye laser was 0.3 $W/cm^2$ duration of burning 10 min. Fittings of the line with a Guassian (dashed line) and Lorentzian (dotted line) are shown.

4. M. Lax and E. Burstein. *Phys. Rev.* **97**, 39 (1955).
5. G. S. Woods, G. C. Purser and A. T. Collins, *J. Phys. Chem. Solids* **51**, 1191 (1990).
6. E. V. Sobolev, V. I. Lisoivan and S. V. Lenskaya, *Zhurnal Strukturnoi Khimii* **9**, 1029 (1968) (in russian).
7. A. Osvet, K. Mauring and I. Sildos. In *Abstracts 6th Symposium on Unconventional Photoactive Solids*, (Leuven 1993), p. 137.
8. A. Osvet, A. Suisalu and I. Sildos. *Proc. Estonian Acad. Sci. Phys. Mat* **41**, 222 (1992).
9. R. Bauer, A. Osvet, I. Sildos and U. Bogner, J. Lumin, **56**, 57 (1993).
10. M. A. Stoneham, *Proc. Phys. Soc.* **89**, 909 (1966).

# POINT DEFECTS AND SHORT-WAVELENGTH LUMINESCENCE OF $LiB_3O_5$ SINGLE CRYSTALS

I. N. OGORODNIKOV, A. Yu. KUZNETSOV, A. V. KRUZHALOV
and V. A. MASLOV

*Experimental Physics Department, Urals State Technical University,*
*620002 Ekaterinburg, Russia*

The results of the study both on short-wavelength luminescence and point defects in the large $LiB_3O_5$ crystals grown by the advanced technique are reported. It was revealed that corpuscular or photon radiation with energy exceeding $E_g$ efficiently excites the complex broad luminescence band at 290 nm. Decay kinetics involves a principal fast component with lifetime of 4 ns and several components of millisecond range. On irradiation at 77 K, $LiB_3O_5$ crystals yield the new ESR-signals, resulted from the $B^{2+}$ electron and $O^-$ hole trapped centers which are stable at temperatures below RT. The obtained data suggest that these centers are responsible for the radiation—induced optical absorption band at 306 nm. We also investigated accumulation and thermal annealing of the point defects. The most acceptable models of defects, recombination processes with defects participation and the origin of the $LiB_3O_5$ short-wavelength luminescence are discussed.

*Key words*: Point defects; luminescence; nonlinear optical crystals.

## 1 INTRODUCTION

Lithium borate crystals $LiB_3O_5$ (space group $Pna2_1$) are reputed to be a potential material for nonlinear and integrated optics.[1] High nonlinear coefficients and radiation—optical resistance (greater than 20 J·cm$^{-2}$) are successfully combined in these crystals. To date some information about primary crystallographic, physical, chemical and optical characteristics of $LiB_3O_5$ is available, but very little is known about the properties of the point defects, about the processes of their creation, accumulation or annealing and of their interaction with electronic excitations.

$LiB_3O_5$ crystals of high optical quality grown by the advanced flux method[2] were used in the experiments. Average dimensions of the crystals were around $50 \times 40 \times 25$ mm$^3$. The main crystallographic parameters of our crystals are in a good agreement with those described in the fundamental work of König and Hoppe.[3]

## 2 POINT DEFECTS

The LBO crystals are transparent in a wide spectral region from 160 to 3500 nm and have no paramagnetic defects. The crystals were irradiated with X-ray photons and electrons (energy up to 2.5 MeV, flux up to $10^{16}$ cm$^{-2}$). The irradiation at room temperature causes no creation of defects, while electron irradiation of LBO at 77 K $E_e = 150$ keV, $\Phi = 10^{13}$ cm$^{-2}$) leads to effective formation of point defects, whose manifestations are observed through the optical, luminescent and ESR spectra.

*2.1.1. Paramagnetic centers* Near the $g$-factor of a free electron we have detected several groups of ESR lines formed by different paramagnetic centers. The quartet structure of equidistant lines with equal intensity marked by letter 'A' in Figure 1($a$) is
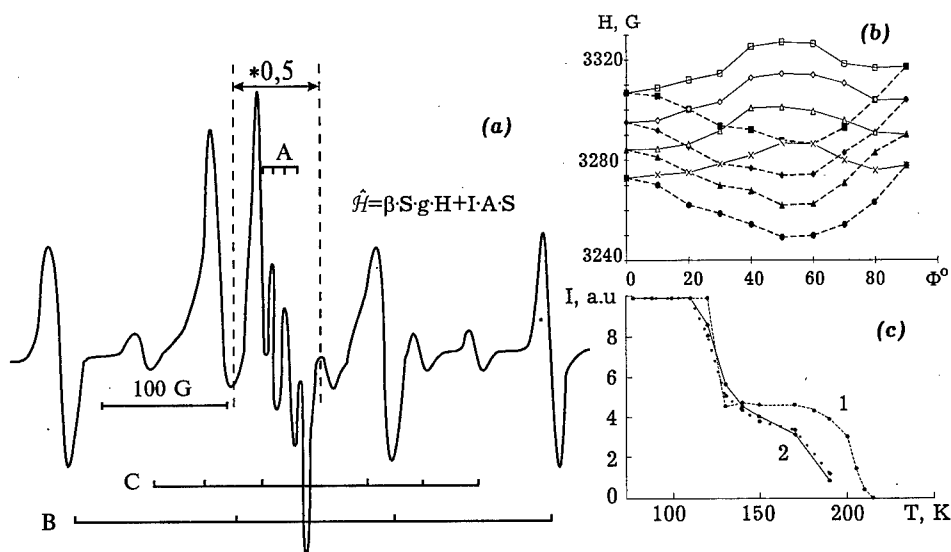
FIGURE 1  Point defects in $LiB_3O_5$ crystals.
(a) ESR-spectrum (X-band) of $LiB_3O_5$ at 77 K from $O^-$-('A'), $^{11}B^{2+}$-('B') and $^{10}B^{2+}$-('C') centers.
(b) Angle dependence of the $O^-$ lines ($\vec{H}$ $\parallel$ {010}). The related spin-Hamiltonian parameters are: $g_{xx} = 2.013$, $g_{zz} = 2.018$, $|A_{xx}| = 14.0$ G, $|A_{zz}| = 11.5$ G.
(c) ESR intensity lines of the $O^-$ (1) $B^{2+}$ (2) centers as a function of annealing temperature.

produced by super-hyperfine interaction between the non-pared spin of trapped hole center ($O^-$) with $^{11}B$ or $^7Li$ nucleus ($I = 3/2$). The angle dependence of the $O^-$ center ESR signals for orientation $\vec{H} \parallel$ {010} given in Figure 1(b) consists of two sets. Each set includes 4 curves and is produced by different $O^-$ centers. Therefore, there are two non-equivalent paramagnetic $O^-$ centers in LBO. The other group of ESR signals in Figure 1(a) consists of a four-line set (lines 'B') with equidistant lines having identical intensity and of a seven-line set (lines 'C') with equidistant lines having identical but different from the 'B'-set intensity ($|A_z| = 127$ G and 42 G, respectively). 'B' and 'C' -lines have a common center near $<g> = 2.002$ and may be assigned to the electron trapped $B^{2+}$ center. 'B' -Quartet is determined by interaction of a trapped electron with $^{11}B$ nucleus ($I = 3/2$) whereas the 'C' -septet is determined by interaction of electron with $^{10}B$ nucleus ($I = 3$).[4]

We have previously calculated the electronic structure of paramagnetic $B^{2+}$ center in $LiB_3O_5$ by an embedded cluster method which is briefly described in Ref. 5. According to our calculations the trapping of an additional electron on boron located in interstitial position seems to be the most likely model for $B^{2+}$ center.

The ESR signals of the $O^-$ and $B^{2+}$ centers, curves (1) and (2) in Figure 1(c) respectively, decrease by half in the 120–130 K temperature range. Further heating up to 180 K has no effect on the $O^-$ center. The thermal annealing of the $O^-$ and $B^{2+}$ centers occurs between 190 and 230 K ($T_a = 210$ K) and around 170–190 K ($T_a = 190$ K) respectively.

2.1.2 *Optical absorption of defects*   Figure 2(a) shows the optical absorption spectrum of $LiB_3O_5$ induced by the electron radiation at 77 K. The intense ($\Delta D = 0.9$) broad band of
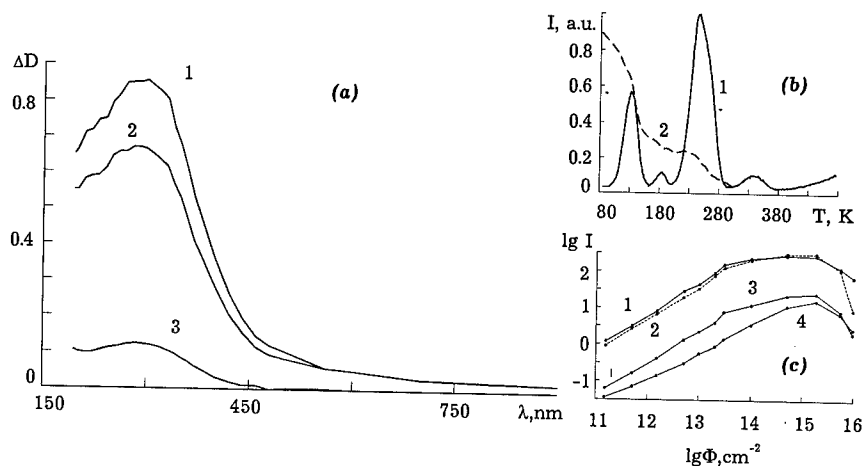
FIGURE 2   Optical properties of $LiB_3O_5$.
(a) Radiation induced optical absorption spectra of LBO at 77 K -(1), 130 -(2), 260 K -(3).
(b) Thermoluminescence (1) and thermobleaching (2) of LBO.
(c) Accumulation of defects related to TL peaks at 130 (6), 170 (8), 240 (6) and 330 K (9).

optical absorption peaks at about 306 nm, (see Figure 2(a)). The optical absorption band loses its intensity rapidly upon increasing the temperature to 130 K. Thermal annealing of the color center occurs above 260 K. However the band shape is invariant with respect to heating, (see Figure 2(a)). The thermal bleaching curve, in Figure 2(b), looks like that for the thermal annealing of the paramagnetic $O^-$ center, in Figure 1(b). Therefore, we can predict with certainty that the principal color center in LBO is related to the optical transitions in the $O^-$ center.

## 3   SHORT-WAVELENGTH LUMINESCENCE

### 3.1.1 *Luminescence spectrum*
When exciting by UV-light at 77–550 K in the transparent band the photoluminescence of LBO isn't revealed, but on exciting by electron beam or $X$-ray photons the wide band of luminescence at 290 nm is revealed, (see Figure 3(a)). The luminescence band consists of two sub-bands with the Gauss-shape at 294 and 350 nm and of a weak 'shoulder' at 250 nm. In the temperature interval of 77–240 K thermally activated increasing of luminescent intensity with activation energies equal to 10 meV (77–120 K) and 65 meV (120–240 K) occurs. There is a maximum at 240 K. A temperature quenching obeying to Mott law and having an activation energy $E_m$ of 295 meV and a frequency factor $\omega$ of $7.4 \cdot 10^4$ occurs above 240 K. Typical points in the curve (3), in Figure 3(b), (T = 130 and 240 K) correspond to the temperatures of the $B^{2+}$ and $O^-$ centers decay.

### 3.1.2 *Thermostimulated luminescence*
The TL-intensity after irradiation at room temperature was very weak (peak at 330 K), but the TL response increases on cooling. Four TL-peaks related to thermal decay of radiation defects were detected in the 80–600 K temperature region after irradiation of LBO at 77 K by electrons or $X$-ray, as seen in
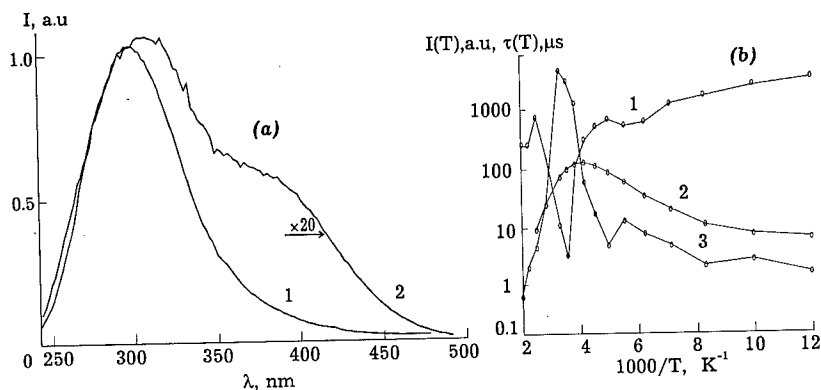
FIGURE 3   Luminescent properties of $LiB_3O_5$.
(a) Luminescence spectrum at 290 (1) and 77 K (2).
(b) Temperature dependence of luminescence (3), long-time kinetic parameters $I_0(T)((4)$ and $\tau(T)$ (5).

Figure 2(a). The spectrum of TL is like that of luminescence. The main TL-peaks are associated with the temperatures of the paramagnetic defects decay and correspond to the breaks in the curve (3), in Figure 3 (b). The activation energies of TL-peaks are close to those for annealing of paramagnetic defects, so the defects participate in the recombination processes exciting the LBO short-wavelength luminescence.

3.1.3 *Kinetics of luminescence*   We studied the kinetics of LBO luminescence in time and temperature ranges of $10^{-9}$–$10^2$ s, and 77–500 K, respectively. On exciting by a short (15 ns) electron pulse the kinetics at 294 nm contains the short exponential component with lifetime $\tau_f$ of 15 ns and several slow components in the millisecond region. Using one photon fluorimetry we have obtained a more accurate value of $\tau_f = 4 \pm 1$ ns. The long-time component of spectrum is primarily concentrated on the main band of LBO luminescence, at 294 nm, and partially located at 350 nm, while the fast component is related to the 294 and 259 nm bands.

Long-time decay kinetics may be described by an exponential law in the initial part (77–180 K) and by hyperbolic dependence in the other part (100–500 K). The breaks in the $I_0(T)$ and $\tau(T)$ curves, in Figure 3(b), deal with the typical temperatures of decay of $B^{2+}$ and $O^-$ centers. Therefore, recombination processes in LBO cause an effective channel of energy transport to luminescent centers and the latter accordingly reveals itself in the short-wavelength luminescence kinetics of $LiB_3O_5$.

3.1.4 *Accumulation of defects*   The dynamics of the defect accumulation during the irradiation by electron beam $(E = 200$ keV) at 77 K is shown in Figure 2(c). Since the intensity of respective TL peaks was used as a measure of the defect concentration, it was possible to allocate the distinctive parts in the curves of defect accumulation. In the flux region of $10^{10}$–$10^{14}$ cm$^2$ all the defects are accumulated by linear law with identical rates. At the fluxes about $10^{15}$–$10^{16}$ cm$^{-2}$ the intensities of TL peaks terminate to increase and

then begin to decrease. Large defects are created and may be visible (The so-called 'Lichtenberg's pictures'). The spectra of luminescence and of TL haven't any change in all the flux region.

## 4  CONCLUSION

At room temperature the formation of radiation induced defects in LBO is ineffective. At 77 K under electron beam or X-ray the electron trapped center $B^{2+}$ and the hole trapped center $O^-$ are accumulated. We suggested for these defects the most acceptable models: interstitial ion of a boron trapped electron ( $B^{2+}$) and a hole localized on an anion having a non-pared spin in the interaction with $^{11}B$ or $^7Li$ nucleus ($O^-$). Optical transitions in $O^-$ centers cause radiation induced absorption of LBO. No photoluminescence of defects in LBO was detected.

Thermal decay of radiation defects is accompanied by recombination processes leading to effective excitation of short-wavelength luminescence in $LiB_3O_5$. In the wide band gap oxides with low symmetry the short-wavelength luminescence with similar characteristics is usually associated with radiative annihilation of a self-trapped exciton or with a direct radiative recombination electron on deep hole trapped centers. A specific study is required to establish the origin of luminescence in $LiB_3O_5$.

REFERENCES

1. C. Chen, Y. Wu, A. Jaing, et al. J. Opt. Soc. Am. **B6**, N4. 616 (1989).
2. V. A. Maslov, L. A. Olkhovaya, V. V. Osiko, E. A. Shcherbakov, 10th Int. Conf. on Crystal Growth (Oral Presentation Abstracts). (San Diego, USA, 1992) p. 11.
3. H. König, R. Hoppe, Z. Anorg. Allg. Chem. **439**, 71 (1978).
4. I. N. Ogorodnikov, S. V. Kudyakov, A. Yu. Kuznetsov, et al. Pisma v zhurnal tekhnicheskoi fiziki (Russia) **19** N13. 77 (1993).
5. A. B. Sobolev, S. M. Erukhimovich, O. A. Keda, Zhurnal Struct. Khimii (Russia) **32**, N5. 129 (1991).

# SOME SPECIFIC FEATURES OF TL-OUTPUT STORAGE IN MgO:Fe CRYSTALS

V. S. KORTOV and A. V. MONAKHOV

*Urals State Technica*

*l University, Ekaterinburg, Russia*

Thermostimulated luminescence and ESR spectra of MgO crystals with different Fe ions concentrations, which were subjected to thermochemical treatment are studied. It has been shown that for samples with high concentration of Fe ions, depending on the time of storage, drop of the TSL maximum intensity at 400 K is due to the decrease of concentration of the emission centres (F, $Cr^{2+}$) as a result of tunnel transitions of electrons from these centres to intrinsic $Fe^{3+}$ ions.

The purpose of this paper is investigation of processes responsible for the lower intensity of thermostimulated luminescence of MgO:Fe single crystals during their long-time storage after irradiation.

TSL and ESR of MgO single crystals with Fe ions concentrations 0.02 and 0.2 wt.% were studied. The samples were submitted to thermochemical treatment (TCT) which resulted in high concentration of F-type centres. TSL curves and ESR spectra were measured after X-ray irradiation (dose $10^5$ Gy) and exposure to room temperature over time period $t_0$.

The most intensive TSL maxima of MgO:Fe single crystals subjected to the TCT are observed within the temperature range of 320–480 K (Figure 1). In MgO crystals with high concentration of Fe ions (0.2 wt.%), depending on the time of storage, TSL maximum intensity and ESR signal amplitude of $Fe^{3+}$ ions decrease, and ESR signal amplitude of intrinsic $Cr^{3+}$ ions increases (Figure 2). TSL maximum intensity decreases by 80% during five hours after irradiation. In MgO crystals with low Fe ion concentration (0.02 wt.%) TSL maximum and ESR signal intensities within the measurement error (5%) do not depend on storage time $t_0$ during a month.

The luminescence of MgO crystals may be due to the recombinations of charge carriers on intrinsic ions Fe, $Cr^{1,2}$ and F-centres:[3]

$$Fe^{2+} + e^+ \rightarrow Fe^{3+} + h\nu \tag{1}$$

$$Fe^{3+} + e^- \rightarrow Fe^{2+} + h\nu \tag{2}$$

$$Cr^{2+} + e^+ \rightarrow Cr^{3+} + h\nu \tag{3}$$

$$F + e^+ \rightarrow F^+ + h\nu \tag{4}$$

In MgO crystals with Fe concentration 0.02 wt.% luminescence at 400 K is caused by emission recombinations on $Fe^{3+}$ ions of electrons thermally delocalizing from F-type centres created by TCT.[4] Since in forbidden gap of the crystal F-type centres form energy levels of about 1.1 eV depth TSL maximum intensity in this case does not depend on storage time $t_0$ at room temperature.

According to our previous data quenching of luminescence of $Fe^{3+}$ ions in MgO crystals with Fe concentration 0.2 wt.% takes place, and, most probably $Cr^{2+}$ ions and
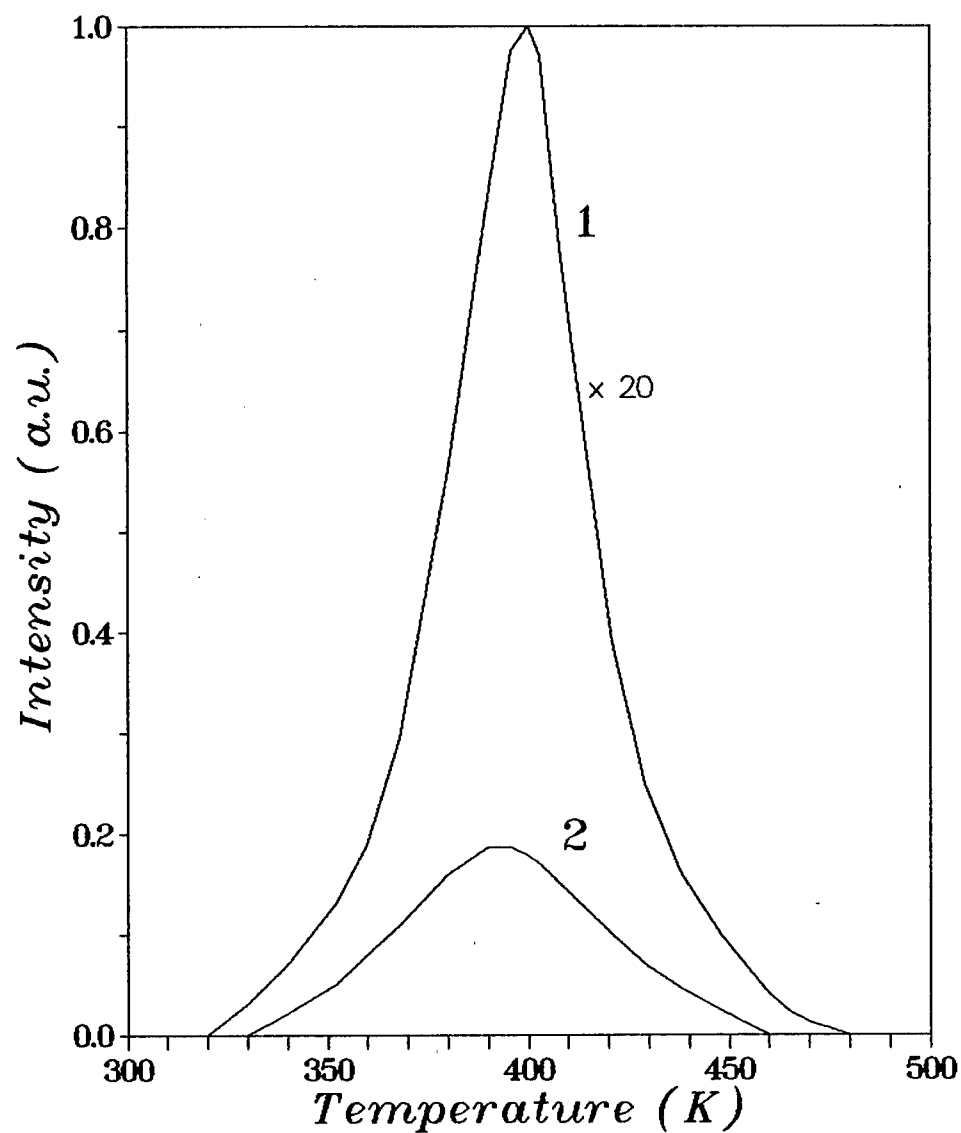
FIGURE 1    TSL maxima of MgO single crystals with Fe ions concentration 0.02 wt.% (1) and 0.2 wt.% (2).

F-centres are emission centres (reactions 3 and 4). The concentration of centres responsible for TSL at 400 K does not change significantly due to thermoionizing processes at room temperature. One can assume that in MgO crystals with high concentration of Fe (0.2 wt.%) after irradiation processes of tunnel exchange with electrons between the said centres and Fe ions takes place. As a result of tunnel transitions of electrons from F-centres
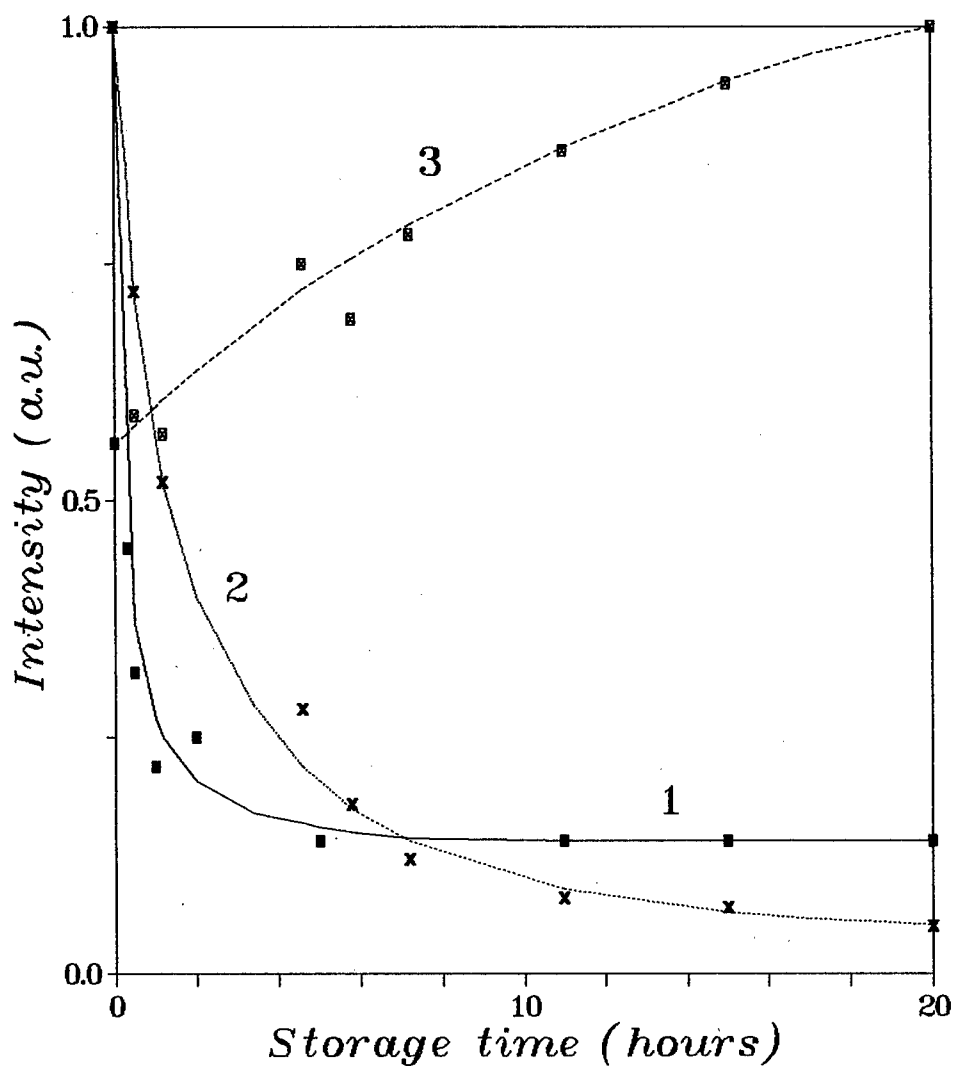
FIGURE 2   Intensity changes of the TSL maximum at 400 K (1), ESR signal of $Fe^{3+}$ ions (2) and $Cr^{3+}$ ions (3) for MgO single crystals with Fe concentration 0.2 wt.% depending on storage time $t_0$ after irradiation.

and $Cr^{2+}$ ions to neighbouring $Fe^{3+}$ ions concentrations of emission centres and $Fe^{3+}$ ions are getting lower. Here, depending on storage time $t_0$ TSL maximum intensity and ESR signal amplitude of $Fe^{3+}$ ions decrease, and ESR signal amplitude of $Cr^{3+}$ ions increases ($Cr^{2+} \rightarrow Cr^{3+}$).

Thus, for MgO single crystals with high concentration of Fe ions and F-type centres, depending on the time of storage the decrease of intensity of the TSL maximum at 400 K is

due to the processes of electron tunneling from emission centres (F, $Cr^{2+}$) responsible for the luminescence in this maximum to intrinsic $Fe^{3+}$ ions.

REFERENCE

1. W. A. Sibley, J. L. Kolopus and W. C. Mallard. *Phys. Stat. Sol.* **31,** No. 1, 233 (1969).
2. S. Clement and E. R. Hodgson. *Phys. Rev.* **B30**, No. 8, 4684 (1984).
3. G. P. Summers, T. M. Wilson, B. T. Jeffries *et al. Phys. Rev..* **B27,** No. 2, 1283 (1983).
4. V. S. Kortov, I. I. Milman, A. V. Monakhov and A. I. Slesarev *Rad. Prot. Dosim.* **47,** No. 1/4, 273 (1993).

# OPTICAL DAMAGE OF W-DOPED KTiOPO$_4$ NON LINEAR SINGLE CRYSTALS

## M. J. MARTÍN,* C. ZALDO,* F. DÍAZ,** R. SOLÉ,** D. BRAVO***
### and F. J. LÓPEZ***

*Instituto de Ciencia de Materiales de Madrid. Consejo Superior de Investigaciones Científicas. Campus Universitario de Cantoblanco C–IV. 28049 Madrid, Spain; **Laboratorio de Física Aplicada y Cristalografía. Universidad Rovira y Virgili. Tarragona, Spain; ***Departamento de Física de Materiales. Universidad Autónoma de Madrid, 28049 Madrid, Spain*

A photochromic damage has been observed in W-doped KTP single crystals. The damage consists in the growth of a broad optical absorption in the visible and near infrared. It has been determined that the excitation spectrum of this damage is mainly confined in the ultraviolet region. A complete annealing of the damage may be obtained by heating at 250°C or above. The origin of the damage has been mostly related with the presence of W$^{4+}$ ions behaving as electron donors. Ti$^{4+}$ ions trap electrons and the Ti$^{3+}$ ions formed are responsible of the optical absorption observed.

*Key words*: Defects, non-linear optical materials, EPR.

## 1 INTRODUCTION

KTiOPO$_4$ (KTP) single crystals are widely used as second harmonic generators in Nd-YAG laser systems. The irreversible optical damage threshold of the crystal is due to microscopic exfoliation at a light power density of 650 MW/cm$^2$ ($\lambda = 1060$ nm).[1] A thermally reversible darkening (often named as 'grey tracks') is also observed when KTP crystals are illuminated at lower power densities, i.e. 150 MW/cm$^2$ for $\lambda = 1060$ nm[1] and 2 MW/cm$^2$ for $\lambda = 355$ nm.[2]

The origin of the photochromism observed in undoped KTP is not well understood. Some authors have related the photochromism to the presence of impurities. In particular W-doped KTP has been found highly susceptible to this damage.[3] However in undoped crystals the origin of the effect has been ascribed to non linear absorption of sum-frequency-generated ultraviolet light.[2]

Impurities are often present in flux-grown KTP crystals. WO$_3$ rich melts are used to decrease the viscosity and volatility of the growing melts.[4] On the other hand trivalent impurities are currently added to increase the electrical resistivity of KTP.[5]

In this work we deal with the role of some impurities, namely W, Fe and Rh, in the photochromic effect observed in doped KTP crystals.

## 2 CRYSTAL GROWTH PROCEDURE AND EXPERIMENTAL TECHNIQUES

KTP crystals have been grown in our laboratories by a top seeded solution growth technique. Mixtures of 42K$_2$O:14P$_2$O$_5$:14TiO$_2$:30WO$_3$ were melted in a Pt/10%Rh crucible and cooled from 914°C to 872°C at a rate of 0.2°C/h.

The atomic absorption and electron microprobe analyses performed show that some impurities were incorporated to the crystal in the following molar concentrations: [W] = 2670 × 10$^{-6}$; [Si] = 2785 × 10$^{-6}$; [Rh] = 1900 × 10$^{-6}$; [Fe] = 318 × 10$^{-6}$ and [Co] = 197 × 10$^{-6}$. Moreover our crystals show about 10% of K deficiency.
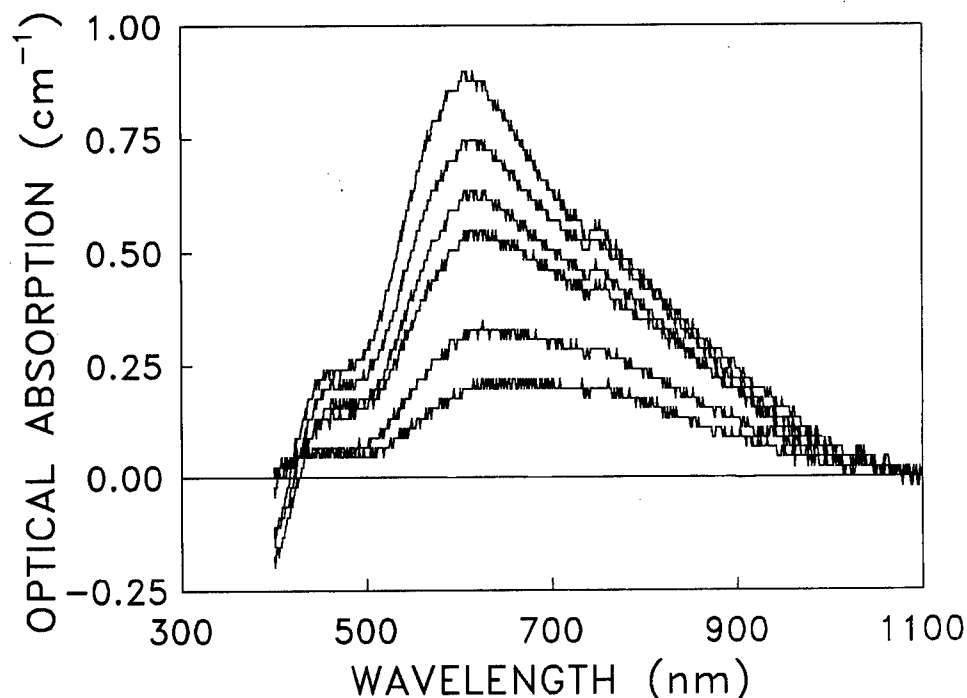
FIGURE 1   Optical absorption difference between KTP samples illuminated with 476 nm (90 mW/cm$^2$) light and thermally bleached ones. The curves with increasing intensity correspond to the following illumination times, 1 h, 2 h, 4 h, 6 h, 8 h and 11 h.

KTP crystals were illuminated at room temperature (RT) with a Coherent Ar$^+$ laser, model Innova 300, which provides visible (VIS) and ultraviolet (UV) light. Unpolarized optical absorption spectra were recorded at RT with an Hitachi spectrophotometer, model U-2000. Electron paramagnetic resonance (EPR) spectra were recorded at 90 K with a Bruker spectrometer, model ESP 300E, operating in the X-band. Thermal treatments were performed in air.

## 3   EXPERIMENTAL RESULTS AND DISCUSSION

Figure 1 shows the optical absorption difference between KTP samples illuminated with 476 nm laser light during different periods of time and samples heated in air taken as reference state. As a consequence of the illumination a broad optical absorption increase is observed in the VIS and near infrared (NIR) spectral regions. Moreover a decrease for wavelengths shorter than 417 nm is also observed.

These optical absorption changes are thermally annealed at RT although the annealing rate is much faster at higher temperatures. Figure 2a shows a normalized plot of the optical absorption evolution during isochronal heating at increasing temperatures. For this purpose the absorption was measured at the maximum of the optically induced band ($\lambda = 592$ nm).
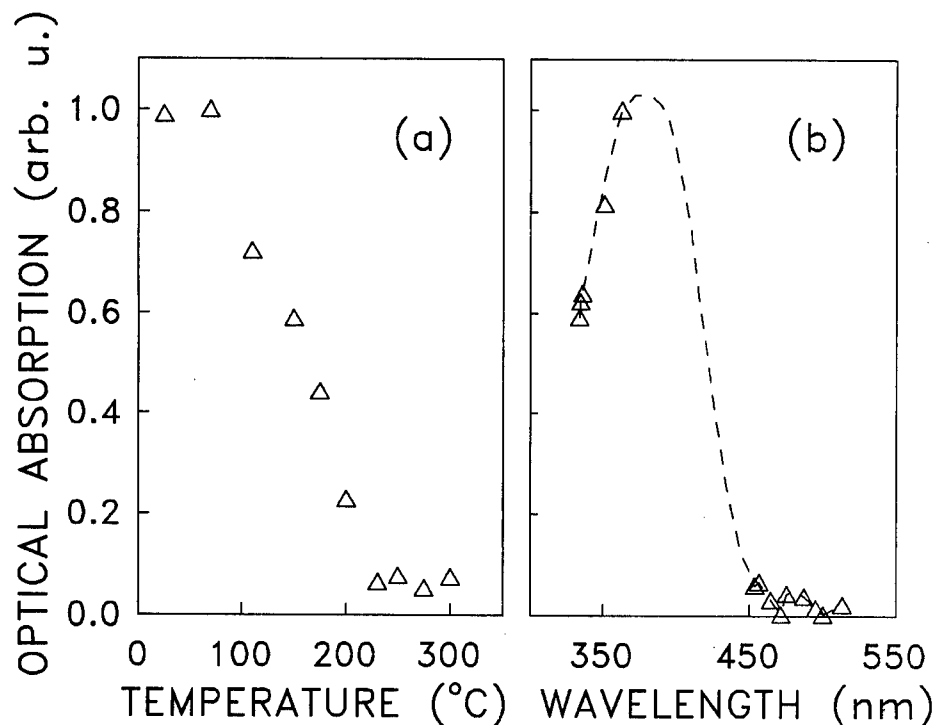
FIGURE 2   (a) Normalized thermal bleaching in air of a light-damaged sample. The sample was kept at each temperature for 30 min. The optical absorption displayed corresponds to $\lambda = 592$ nm. (b) Excitation spectrum of the photochromic damage.

In order to determine the excitation spectrum of the photochromic damage, thermally annealed samples were illuminated at several wavelengths corresponding to the emission lines of the $Ar^+$ laser. In this experiment the light power and the irradiation time were chosen in such a way that the incident number of photons was kept constant. Moreover this number of photons corresponds to the linear regime of the damage kinetics.

Figure 2b shows the excitation spectrum obtained. In agreement with previous results performed with undoped crystals in the pulsed regime,[2] the damage efficiency of UV light is larger than the efficiency observed using VIS light. Moreover the shape of the spectrum suggests that there is a maximum close to about 380 nm. The spectral distribution of the excitation spectrum is in agreement with the decrease of the optical absorption observed in figure 1 for $\lambda \leq 417$ nm.

Figure 3a shows the EPR spectrum measured at 90 K for as-grown samples. This spectrum is due to $Fe^{3+}$ (Ref. 6), $Rh^{2+}$ (Ref. 7) and $W^{5+}$ (Ref. 7) centres. The EPR spectrum of $W^{5+}$ is characterized by a central line and a weak hyperfine (HF) doublet with 130 G of splitting. The HF splitting is related to the 14% natural abundant $^{183}W$ isotope which has nuclear spin $I = 1/2$. A similar but weaker EPR spectrum is observed at lower magnetic field. The analysis of these spectra gives evidence that tungsten enters in the two Ti-sites of the lattice though the tungsten concentration of each site is different.

Figure 3b shows the EPR spectrum observed after illumination at RT with 476 nm light. The illumination induces the appearance of new signals as well as the increase of the $W^{5+}$
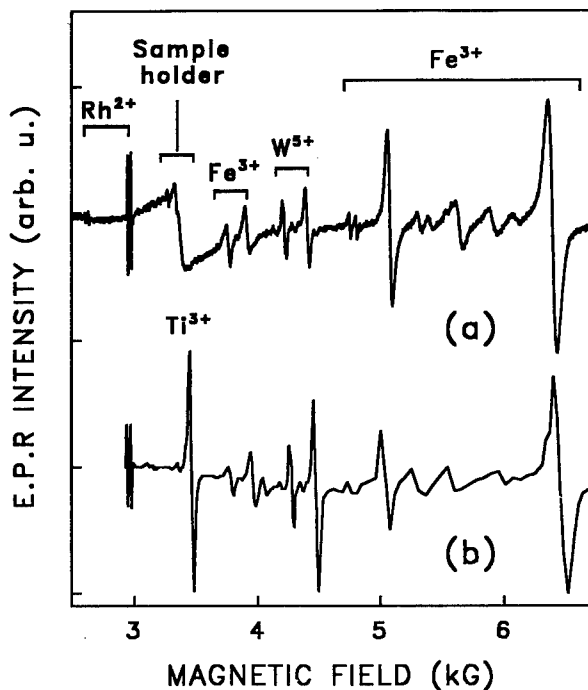
FIGURE 3   Electron paramagnetic resonance spectra of KTP measured at 90 K with the magnetic field parallel to the b-axis of the crystal. (a) As-grown sample. (b) Sample illuminated for 7 h with $\lambda = 476$ nm light.

EPR line peaking at high magnetic field. The light-induced EPR line near 3300 G with an effective g-value of 1.958 is ascribed to $Ti^{3+}$ ions. The intensity of the EPR spectrum related to $Fe^{3+}$ does not change upon illumination.

Heating the samples at 300°C leaves the $Fe^{3+}$ EPR spectrum unchanged whereas the EPR spectrum associated to $Ti^{3+}$ in optically damaged KTP samples disappears. Furthermore, the intensity of the EPR spectra associated to $W^{5+}$ and $Rh^{2+}$ initially decrease with increasing temperatures up to 200°C where a minimum intensity is reached. By heating above 200°C a recovery of both spectra has been observed. The EPR spectrum of $W^{5+}$ recovers to 40% of the intensity observed in damaged samples, while the EPR spectrum associated to $Rh^{2+}$ reaches 100% of its initial intensity.

The experimental results described above show that the EPR spectrum of $Ti^{3+}$ is the only one which behaves in parallel to the intensity changes observed in the optical absorption. Therefore the light induced optical absorption shown in Figure 1 must be related to the presence of $Ti^{3+}$ centres. In a previous work[8] we have shown that the optical absorption arising from the overlapping of $^2T_2 \rightarrow {}^2E$ transition of $Ti^{3+}$ for the two crystallographic sites of this ion, gives rise to an optical absorption band peaking at 585 nm (0.37 eV of halfwidth). This contribution is likely responsible of the main maximum observed in Figure 1. Moreover other minor absorptions contribute at 451 nm (0.23 eV of halfwidth) and 721 nm (0.38 eV of halfwidth). The origin of these contributions remains uncertain.

The experimental results obtained indicate that electrons are trapped in the constitutional $Ti^{4+}$ producing $Ti^{3+}$ centres. The origin of these electrons must be related with the impurities present in the crystal. In particular a considerable increase of the EPR spectrum associated to $W^{5+}$ is induced by illumination.

Tungsten is expected to enter in the KTP lattice mainly as $W^{6+}$ since $WO_3$ was used to enrich the melt. Besides the presence of a fraction as $W^{5+}$ has been disclosed by the EPR experiments. $W^{5+}$ appears also after thermal reduction, what requires that $W^{6+}$ ions act as electron trap. We suggest that in addition there is a partial incorporation of tungsten in the 4+ oxidation state ($W^{4+}$). This would be a photoexcitable electron donor responsible of the increase of $W^{5+}$ and $Ti^{3+}$ EPR signals upon illumination.

The presence of $W^{4+}$ ions is quite likely because the electric charge of $W^{4+}$ matches that of the substituted ion ($Ti^{4+}$), thus not charge compensation is required. Furthermore the ionic radii of $W^{4+}$ and $Ti^{4+}$ are both 0.68 Å.

In conclusion we have suggested that the valence change of W ions incorporated to KTP single crystals is the origin of the photochromic effect observed. $W^{4+}$ ions would be the electron donors while $Ti^{4+}$ ions are the electron traps. $Ti^{3+}$ ions formed by illumination are the main responsible of the optical absorption increase observed.

## REFERENCES

1. T. A. Driscoll, H. J. Hoffman, R. E. Stone, P. E. Perkins, *J. Opt. Soc. Am.* **B3**, 683 (1986).
2. R. Blachman, P. F. Bordui and M. M. Fejer. *Appl. Phys. Lett.* **64**, 1318 (1994).
3. G. M. Loiacono, D. N. Loiacono, T. McGee and M. Babb, *J. Appl. Phys.* **72**, 2705 (1992).
4. K. Iliev, P. Peshev, V. Nikolov and I. Koseva. *J. Cryst. Growth* **100**, 225 (1990).
5. P. A. Morris, A. Ferreti, J. D. Bierlein and G. M. Loiacono. *J. Cryst. Growth* **109**, 367 (1986).
6. J. M. Gaite, J. F. Stenger, Y. Dusausoy, G. Marnier and H. Rager, *J. Phys. Cond. Matter.* **3**, 7877 (1991).
7. D. Bravo, M. J. Martín, R. Solé, J. Gavaldá, C. Zaldo and F. J. López. *Phys. Rev.* **B50**, 16224 (1994).
8. M. J. Martín, D. Bravo, R. Solé, F. Díaz, F. J. López and C. Zaldo, *J. Appl. Phys.* **76**, 7510 (1994).

# LOW TEMPERATURE PHOTOSTIMULATED LUMINESCENCE OF KBr—In CRYSTAL AFTER UV IRRADIATION

## L. E. TRINKLER and M. F. TRINKLER

*Institute of Solid State Physics, University of Latvia, Kengaraga str. 8, Riga, Latvia*

It has been found that the photostimulated luminescence (PSL) of KBr-In crystal after UV irradiation at 80 K is characterized with a complex stimulation spectrum, including 2.0, 1.8, 1.6 and 0.6 eV bands. It is proposed that the PSL is due to the optically stimulated recombination of the close defect pairs created after the decay of both lattice and near-impurity excitons. The same recombination centers are produced during the photoionization in the C absorption band.

*Key words*: alkali halide crystals, radiation defects, exciton, photostimulated luminescence.

## 1  INTRODUCTION

The photostimulated luminescence (PSL) in KBr-In crystals after UV irradiation at room temperature (RT) is a well known phenomenon[1,2] characterized by a creation spectrum, including the exciton and the C band and a stimulation spectrum coinsiding with the F absorption band. The PSL after the exciton irradiation is explained mainly by the creation of the close $F\text{-}In^{++}$ pairs as a result of the lattice exciton decay near $In^{++}$ ions and their recombination under stimulation irradiation followed by the indium luminescence. Hereafter we shall mention this process as the **exciton mechanism of PSL storage**. Some other electron centers can contribute to the process,[3] but it will not be discussed here. Under the C irradiation the non-correlated $F\text{-}In^{++}$ pairs are produced as a result of the $In^+$ ionization and electron trapping by the anion vacancy.

The PSL in KBr-In after UV irradiation at low temperatures (80 K), studied by us, has some interesting peculiarities.

In order to explain them it is useful to turn to the similar observation of the KI-Tl crystal.[4] The creation spectrum of this crystal at low temperatures (10–80 K) besides the C band has a shortwave band, which surely can be ascribed to the D and not to the exciton absorption band. The polarization properties of the PSL enabled to propose the low temperature **D mechanism of PSL storage**. In terms of this model the irradiation of the crystal in the D absorption band excites the halide ion near $Tl^+$, its relaxation is followed by the electron transfer either to the $Tl^+$, or the $K^+$ ions, perturbed by the close indium impurity. The close $Tl^0 - V_k$, $K^0_{(Tl)} - V_k$ pairs are formed. The stimulation spectrum has 2 bands at 80 K, and 4 bands at 10 K, none of which coinsides with the F absorption band. The IR stimulation in $Tl^0$ and $K^0_{(In)}$ bands rises the recombination of the close pairs, finishing with the indium luminescence. The concepts of the exciton mechanism and D mechanism of PSL storage will be used in discussion of the KBr-In low temperature PSL.

## 2  EXPERIMENTAL

The $In^+$ concentration in the KBr-In crystal was estimated as $5 \cdot 10^{17}$ cm$^{-3}$. The UV irradiation channel was provided with the deuterium lamp and the MDR-2 mono-chromator, the IR channel—with the halogen lamp and the SPM-2 monochromator or the
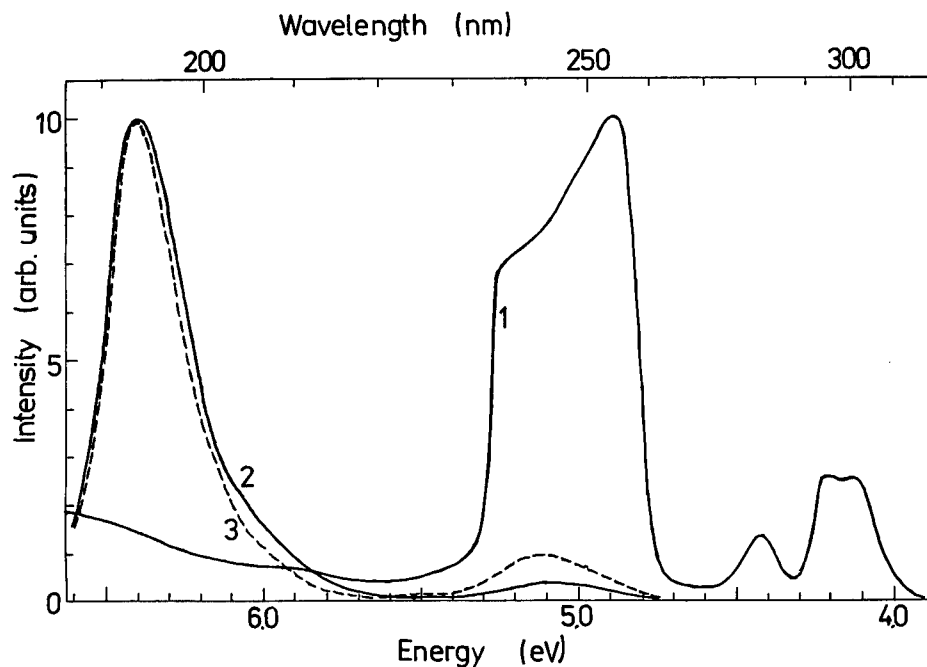
FIGURE 1    Excitation spectrum of $In^+$ luminescence (1) and PSL creation spectra, corresponding to 0.6 eV (2) and 1.9 eV (3) stimulation in KBr-In crystal at 80 K.

set of the appropriate glass filters. The indium luminescence was selected by the glass filters (300–500 nm). All the spectra are given after the necessary corrections.


## 3   RESULTS

The KBr-In low temperature creation spectrum is showed on Figure 1. Compared with that at RT it has differences: the C band (5.1 eV) has become much smaller and the short wavelength band has shifted to the larger energies (6.4 eV), coinsinding with one of the D bands in the $In^+$ luminescence excitation spectrum.

The main changes caused by the temperature decrease are observed in the stimulation spectrum—Figure 2: the analysis of its shape enables to divide it into 4 bands peaking at 2.0, 1.8, 1.6 and 0.6 eV.

All the stimulation bands appear after KBr-In crystal irradiation in both 6.4 and 5.1 eV creation bands, but with the different relative intensities. The stimulation spectrum measured at 170 K is presented with 2 bands peaking at 2.0 and 1.6 eV. Optical bleaching of the high energy part of the stimulation spectrum rises the intensity of the low energy part—something like 'pumping' between the stimulation bands takes place.


## 4   DISCUSSION

Analysing the PSL process in KBr-In crystal after UV irradiation it seems that both mentioned types of the PSL storage mechanisms coexist at 80 K.
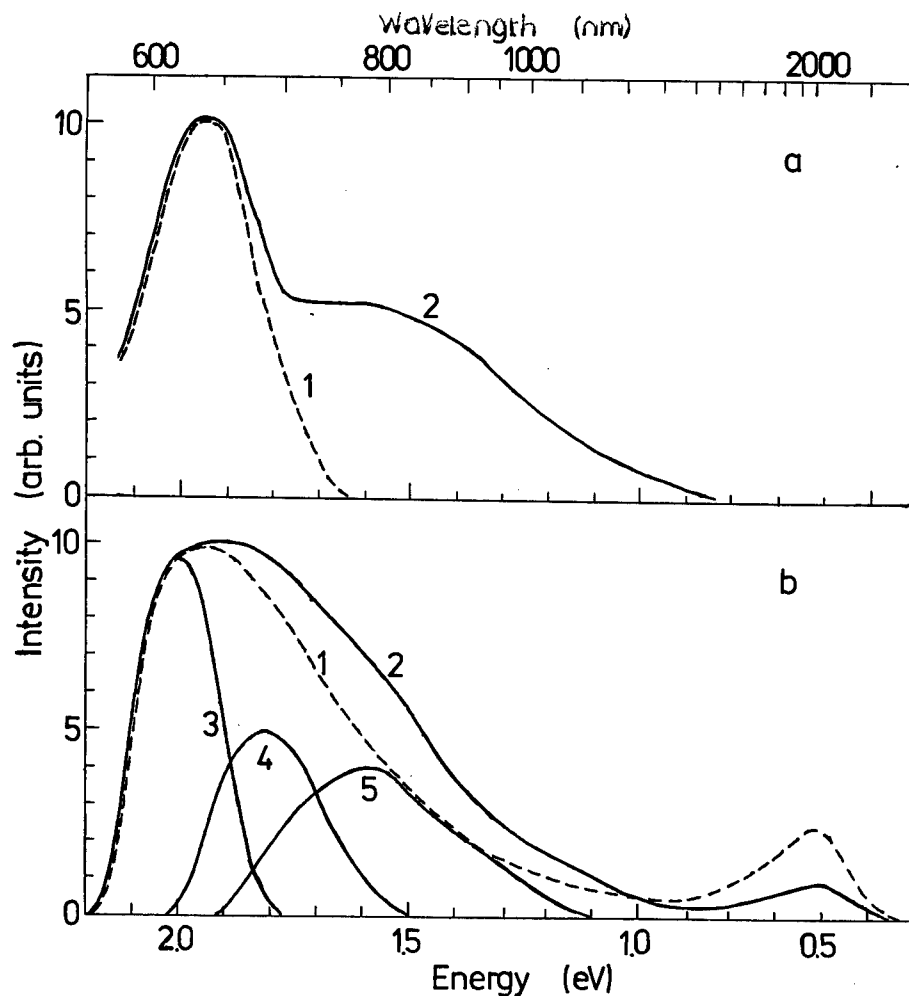
FIGURE 2(a)   PSL stimulation spectrum of KBr-In crystal created at 6.3 eV at RT(1) and 170 K (2).
(b)   PSL stimulation spectrum of KBr-In crystal created at 6.3 eV (1) and 5.1 eV (2) at 80 K; (3), (4), (5)—the result of the curve (1) decomposition.

The 6.4 eV creation band is situated in the same time in the exciton and the D absorption bands region, so the irradiation in this band can create both lattice and near-impurity excitons, each of them producing its own characteristic defects.

The exciton mechanism of the PSL storage implying the creation and recombination of the F-In$^{++}$ pairs is proved by the presence of the F band (2.0 eV) in the stimulation spectrum. The other stimulation bands cannot be explained in terms of this model, but are quite reasonable if we apply the D-mechanism of PSL storage. Electron centers In$^0$ and K$^0_{(In)}$ and hole centers V$_k$ and In$^{++}$ are the most probable defects created after the decay of the near-impurity exciton. The following close defect pairs could be responsible for the PSL: In$^0$-V$_k$,   K$^0_{(In)}$-V$_k$,   K$^0_{(In)}$-In$^{++}$. The possibility of Na$^0$ center, having absorption band in IR region is not excluded.[5]

As it follows from the similarity of the stimulation spectra, all the above mentioned defects appear under the C irradiation as a result of the indium ionization. In this case the $F$, $In^0$, $K^0_{(In)}$ electron centers can be formed by the trapping of the released electrons. The hole centers include $In^{++}$ and, besides, the $V_k$ centers. The appearence of the $V_k$ centers under the C irradiation in alkali halide crystals was proved by EPR studies.[6] So, in this case the $F$-$In^{++}$, $In^0$-$In^{++}$, $In^0$-$V_k$, $K^0_{(In)}$-$V_k$ and $F$-$V_k$ pairs are possible.

The following interpretation of the stimulation bands seems to be reasonable: the 2.0 eV band is ascribed to the F center, the 1.8 eV band—to $In^0$ center, the 1.6 eV Band-to $V_k$ center (its position fits the $V_k$ absorption band)[7] and the 0.6 eV band—to the $K^0_{(In)}$ center. The $In^{++}$ center doesn't reveal itself in the stimulation spectrum.

The increase of the temperature destroys first the $K^0_{(In)}$ and $In^0$ centers, so at 170 K the stimulation spectrum is presented with the F and $V_k$ bands. At higher temperatures $V_k$ centers are destroyed and only the F band presents the stimulation at RT. The 'pumping' effect can be explained by the retrapping of the electron released from some electron center by the $K^+$ ion near-impurity.


## 5   CONCLUSIONS

The complex sructure of the stimulation spectrum of KBr-In crystal found at low temperatures enables to suggest that the PSL storage is due to the close defect pairs created after the decay of both lattice and near-impurity excitons. The same defects are produced during the photoinization under the C-irradiation.

REFERENCES

1. A. Kanins, I. Plavina, A. I. Popov and A. Tale, *J. Phys. Condens. Matter* **3**, 1265 (1991).
2. P. F. Bratslavets, A. Kanins, I. Plavina, A. I. Popov, B. I. Rapoport and A. Tale, *phys. stat. sol. (b)* **170**, 395 (1992).
3. I. Plavina and A. I. Popov, *Radiation Effects and defects in Solids* **128**, p. 27 (1994).
4. M. F. Trinkler and L. E. Trinkler, *Opt. Spectrosc. (USSR)* **63**(2), 180 (1987).
5. I. Schneider, *Sol. State Commun.* **25**, 1027 (1978).
6. A. G. Badalyan, P. G. Baranov, P. A. Zhitnikov, *Solid State Physics (USSR)* **19**, N12, 3575 (1977).
7. M. N. Kabler, In: *Point defects in solids.* New York, Plenum Press, 1972, pp. 327–380.

# PECULIARITIES OF INTERSTITIALS IN A SIMPLE CUBIC CsCl CRYSTAL

A. LUSHCHIK,[1,2] K. IBRAGIMOV,[1,2] I. KUDRJAVTSEVA,[1,2] and L. PUNG[1]

[1]*Department of Physics, Tartu University, Tahe 4, EE2400 Tartu, Estonia;*
[2]*Institute of Physics, Estonian Acad. Sci., Riia 142, EE2400 Tartu, Estonia*

The processes of the thermal annealing of $V_K$ centres (160–190 K) and anion interstitials (I and II centres) have been studied in a CsCl crystal by means of luminescent and EPR methods. The thermal annealing of I centres in a CsCl crystal takes place in a narrow region of 16–20 K, in contrast to the multistage annealing of I centres in KCl. The tunnel recharge of a primary F, H pair leads to the formation of an $\alpha$ centre and a localized (not crowdion-type) split I interstitial.

*Key words*: luminescence, radiational defects, interstitial, CsCl.

The processes of radiational creation and thermal annealing of anion interstitials have been studied in detail in face-centred cubic alkali halides (AH). In comparison with *fcc* AH, the low-temperature motion of self-trapped holes ($V_K$ centres) and H interstitials as well as the processes of creation and annealing of F, H and $\alpha$, I pairs of Frenkel defects have some peculiarities in a simple cubic CsBr crystal.[1] The aim of the present study is to discuss the peculiarities of $V_K$ centres and anion interstitials in a sc CsCl crystal. Single crystals of CsCl and CsCl:Tl were grown by the modified Stockbarger method from a salt preliminarily refined by manyfold recrystallization from the melt.[2]

A CsCl:Tl crystal was investigated by EPR method at 77 K. $Tl^+$ impurity ions (50 ppm) serve as effective electron traps in the case of the irradiation of a crystal. A typical EPR spectrum consisting of seven absorption lines was detected in CsCl:Tl X-irradiated at 77 K, which was ascribed to $Cl_2^-$ molecules situated at two anion sites and oriented along $\langle 100 \rangle$ directions. Figure 1(b) presents the pulse annealing curve of the EPR signal of $V_K$ centres in CsCl:Tl. The EPR signal was recorded at 77 K after a 2 min exposure at each temperature. The annealing of $V_K$ centres occurs at 160–190 K and it is accompanied by a partial decrease of the optical absorption of $Tl^0$ centres (4.5 eV) and the intensive peaks of thermally stimulated luminescence (TSL) at 160 and 185 K. The TSL peak at 315 K corresponds to the ionization of $Tl^0$ centres. These TSL peaks were also detected after the irradiation of CsCl:Tl by photons of $h\nu \geq E_g = 8.4$ eV which form separated electrons and holes on band-to-band transitions (see Figure 1(b)). Weak TSL peaks at 210, 245 and 260 K were also observed in a CsCl crystal irradiated at 80 K. The intensities of the peaks at 210, 245 and 260 K increase with the increase of the concentration of $Rb^+$, $Br^-$ and $K^+$ impurity ions, respectively.

TSL peaks at 17, 19, 24, 30, 39, 50, 68, 110, 160, 185, 210, 220, 245 and 260 K were detected in a CsCl crystal irradiated by VUV-radiation at 5 K. Weak peaks at 50, 68, 210, 220, 245 and 260 K are connected with various impurity ions. These peaks are especially intensive after the irradiation of the crystal by photons with the energies outside the region of intrinsic absorption. Of special interest are the TSL peaks connected with the annealing of I centres (17 and 19 K) and H centres (24, 30 and 39 K). The creation spectra of these peaks spread over the region of intrinsic absorption, $h\nu \geq 7.8$ eV. A narrow peak at 17 K corresponds to the annealing of F, I, $V_K$ triplets.[2,3] At 17 K mobile I centres recombine with spatially more close F centres. A typical 2.85 eV emission of self-trapped excitons (STE) arises on the subsequent recombination of the released electrons with $V_K$ centres. The TSL peak at 19 K corresponds to the annealing of $\alpha$, I pairs.[2,3] Mobile I centres partly
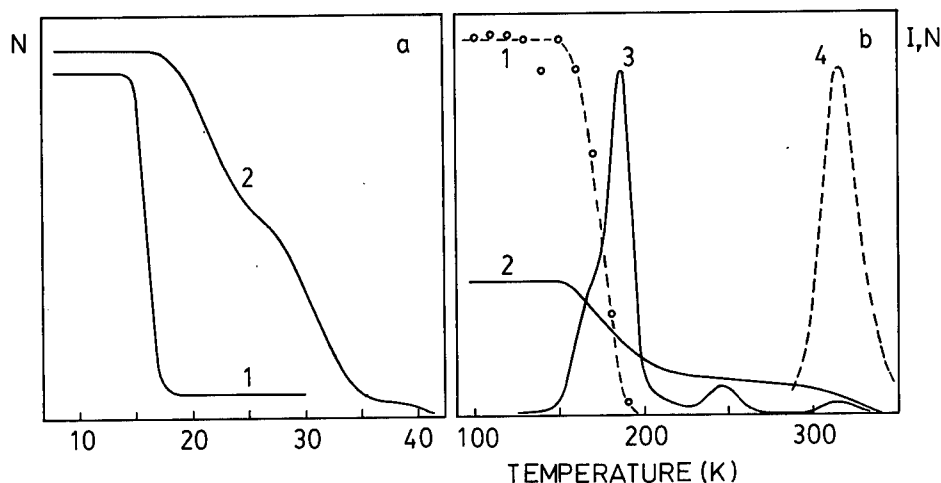
FIGURE 1    (a) The thermal annealing of $\alpha$ centres in CsCl (1) and KCl (2) crystals irradiated at 5 K by photons in the region of exciton absorption bands (8.1 and 7.75 eV, respectively).
(b) The thermal annealing of the EPR signal of $V_K$ centres (1), optical absorption of $Tl^0$ centers (2) and thermally stimulated luminescence (3, 4) in a CsCl:Tl crystal irradiated at 80 K by X-rays (1, 2) or the 10.2 eV photons (3, 4). The emission was registrated in the region of 2.5–3.2 eV (3) and 3.6 eV (4). The heating rate was 0.15 K/s.

recombine non-radiatively with anion vacancies and partly with F centres. The emission of STE is dominant in TSL peaks at 17 and 19 K not only in pure CsCl, but also in doped CsCl crystals.

Figure l(a) shows the thermal annealing of $\alpha$ centres in CsCl and KCl crystals irradiated by photons in the region of exciton absorption bands (8.1 and 7.75 eV, respectively). The intensity of the $\alpha$-luminescence (3.2 eV in CsCl and 2.7 eV in KCl) stimulated in the maximum of the $\alpha$ absorption band (6.8 and 6.95 eV, respectively) is taken as the measure of the number of anion vacancies ($\alpha$ centres). In a KCl crystal the annealing of $\alpha$ centres occurs at 12–40 K in several stages, corresponding to various numbers of jumps of the I interstitial necessary for its recombinations with anion vacancies.[4] In contrast with KCl, the annealing of $\alpha$, I pairs takes place in a *sc* CsCl crystal in a narrow temperature region of 18–20 K. A special consideration is needed to explain such behaviour of interstitials in CsCl.

Stable F, H pairs of Frenkel defects arise on the non-radiative decay of excitons generated by VUV-radiation in a KCl crystal at 5 K. A partial tunnel recharge of F, H pairs leads to the creation of $\alpha$, I pairs. A mobile crowdion-type I interstitial is formed at the tunnel recharge of F, H pairs in a KCl crystal with H centres oriented along $\langle 110 \rangle$ closely packed anion rows.[4] Such an I crowdion may be displaced by several interanion distances even at 5 K and only then localize at a tetrahedral interstitial lattice site.[4]

The annealing of H centres in CsCl occurs in three stages at 23, 30 and 39 K, i.e. at lower temperatures than in KCl. It is necessary to pass through a 'cation diaphragm' formed by four $Cs^+$ ions in case of H centre motion along $\langle 100 \rangle$ anion rows. The size of this diaphragm is not large enough for a chlorine ion, while a chlorine atom can pass it through. Probably that is the reason why an additional low-temperature displacement is impossible in the case of the I interstitial formed after the tunnel recharge of a primary F, H pair (created on the decay of STE) in a *sc* CsCl crystal. In contrast to KCl, no $\alpha$, I pairs
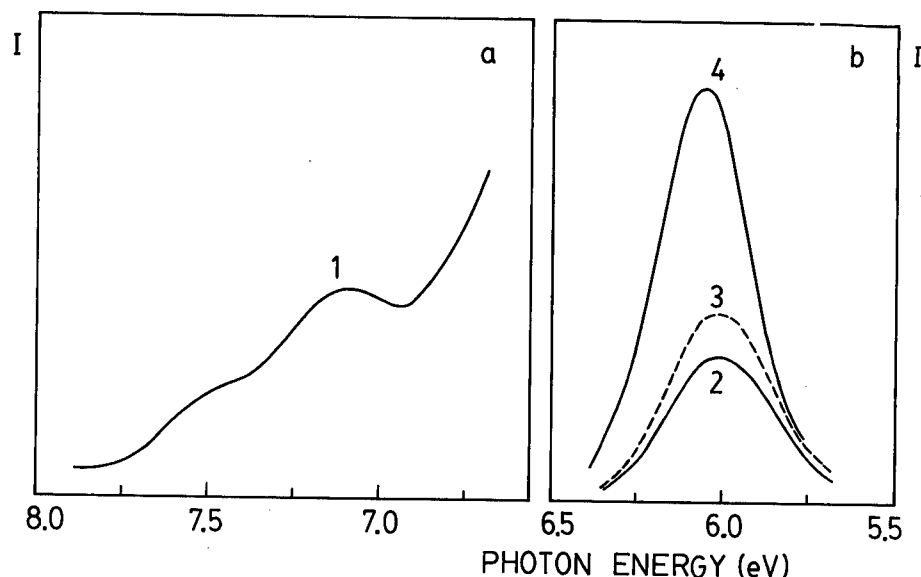
FIGURE 2   The emission spectra of a CsC1 crystal measured at 8 (1, 2) and 80 K (3, 4) on the crystal excitation by a 5 keV steady electron beam (1–3) or single nanosecond pulses of a 300 keV electron beam (4). The crystal was preliminarily irradiated by an electron beam at 8 (2) and 80 K (3, 4).

with various interdefect distances can be formed in CsCl due to the motion of a crowdion-type interstitial halogen ion in the direction off the anion vacancy. According to theoretical estimates[5] 'the split I interstitial', which is not oriented along closely packed anion rows, is energetically profitable in a sc CsCl crystal.

The spectrum of F, H pair creation by VUV-radiation at 5 K has been measured for a CsCl crystal.[3] The efficiency of F, H pair formation is high in a wide region of intrinsic absorption (7.8–10 eV), including the regions of selective generation of exitons with n = 1 and of separated electrons and holes. On the other hand, the efficiency of $\alpha$, I pair formation is high on the non-radiative decay of excitons with n = 1, being at least by an order of magnitude lower on the non-radiative recombination of electrons with relaxed $V_K$ centres.[3]

A weak emission with the maximum at 7.1 eV (see Figure 2(a)) above the background of intraband luminescence has been detected by using a double VUV-monochromator in the spectrum of steady cathodoluminescence of CsCl at 8 K.[3] We suppose that this band is probably connected with the luminescence of metastable one-halide STE. The moment of the transformation of one-halide STE into two-halide one is the most favourable for the formation of an F, H pair with a large interdefect distance. A stable $\alpha$, I pair arises after the tunnel recharge of this F, H pair.

The irradiation of a CsCl crystal at 8 K by a 5 keV electron beam leads to the creation of defects responsible for the intensive emission band with the maximum at 6.05 eV and the half-width of 0.3 eV (see Figure 2). The 6.05 eV emission has a duration less than 2 ns at 80 K. The heating of the crystal from 80 to 160 K leads to the quenching of this emission. The 6.05 eV emission can be excited by photons of $h\nu \geq 14$ eV. We suppose that this emission is caused by radiative transitions (probably crossluminescence) with the participation of anion or cation interstitials. The nature of these interstitials is not clear yet.

REFERENCES

1. Ch. Lushchik, A. Lushchik and E. Vasil'chenko, *Defects in Insulating Crystals* ed. V. M. Tuchkevich and K. K. Swarts (Zinatne, Riga; Springer Verlag, Berlin, 1981) p. 324.
2. K. I. Ibragimov, A. Ch. Lushchik, Ch. B. Lushchik, A. G. Frorip and N. A. Yaanson, *Sov. Phys. Solid State* **34** 1690 (1992).
3. A. Lushchik, E. Feldbach, A. Frorip, K. Ibragimov, I. Kuusmann and Ch. Lushchik, *J. Phys.: Condens Matter* **6** 2357 (1994).
4. A. Ch. Lushchik and A. G. Frorip, *Phys. Status Solidi* **B161** 525 (1990).
5. D. K. Rowell and M. J. L. Sangster, *J. Phys. C: Solid State Phys.* **14** 2909 (1981).

# RADIATION PROCESSES ON THE SURFACE OF IRRADIATED CORUNDUM MONOCRYSTALS

V. V. HARUTUNYAN,[a] A. K. BABAYAN,[a] V. A. GEVORKYAN[a]
and V. N. MAKHOV[b]

[a]*Yerevan Physics Institute, Alikhanian Brs.2, Yerevan, Armenia;* [b]*P. N. Lebedev Physical Institute, 117234, Moscow, Russia*

The reflectivity of corundum ($\alpha$-$Al_2O_3$) was measured by a spectral-kinetical set up, using the synchrotron radiation (SR).

It is shown, that as a result of irradiation, in the surface layers the stoichiometry is disturbed due to the elastic interaction with crystal lattice. The radiation-stimulated oxygen desorption occurs and restored Al fills vacancy pores and dislocation loops on the surface of irradiated corundum, thereby increasing the reflectivity in the energy range of E > 25 eV.

The peculiarities of the electron energetic structure of the surface of $\alpha$-$Al_2O_3$ containing structural defects and absorption complexes are investigated mainly by the methods of electron and X-ray spectroscopy.

In the present paper, the surface destruction of $\alpha$-$Al_2O_3$ has been studied according to the reflection factors in the VUV.

The relative reflectivity of corundum crystals was measured in the energy range from 5 to 30 eV by a spectral-kinetical set up using the synchrotron radiation of C-60 accelerator. Spectral resolution of monochromator was from 0.5 to 1 nm.[1]

The nominally pure stoichiometric $\alpha$-$Al_2O_3$ were grown by the horizontal-oriented crystallization method (HOC) and Verneil's method, in which the concentration of uncontrolled impurity ions of iron group was from $10^{-4}$ to $10^{-3}$ mass %. The optical axis $C_3$ was parallel to the large side of the samples. The crystals were irradiated by 50 Mev electrons and 2 MeV neutrons.

The reflection (absorption) bands of 6.1; 5.4, 6.3–6.4, 7, 8; 6.2 eV up to the fundamental absorption edge can be found in the experimental reflection spectra, measured with different orientations of SR electric vector $\vec{E}$ to $C_3$, see Figure 1 (a, b) and Figure 2(a, b). The interpretation of the observed optical absorption (OA) bands is given in Ref.[2–4] and attributed to F- and $F^+$-centres respectively, and in Ref.[5] where the band 6.2 eV is attributed to $F^{2+}$-centre for unirradiated crystals. Ions of iron group and corundum's own structure defects cause the appearance of closely located absorption bands, and as a result of these the OA bands of 6–6.5 and 7–8 eV are observed in the spectra.[4,6]

After irradiation, anion (F-, $F^+$-centres), cation (V-centres) and interstitial ions are formed. Besides, at irradiation there occurs an inelastic interaction, which changes the charge states of pre-irradiation structure defects.

In the R(E) spectra one can observe intensive long-wave peaks at 8.9 and 9.1 eV. The exciton maxima shift by ±0.2 eV after irradiation. The exciton nature of this maximum ($\Gamma$ – exciton) is confirmed by the photoconductivity measurements.[7]

In the R(E) of unirradiated crystals one can observe a non-elementary wide maximum in the region of 12–25 eV. The group of bands in the reflection spectra of HOC crystals (Figure 1) is observed more clearly than in Verneil's ones (Figure 2). It is connected with the 'impure' surface of Verneil crystals, i.e. the uncontrolled impurity ions of iron group and growth defects lead to stoichiometry disturbance in the anion and cation sublattice.
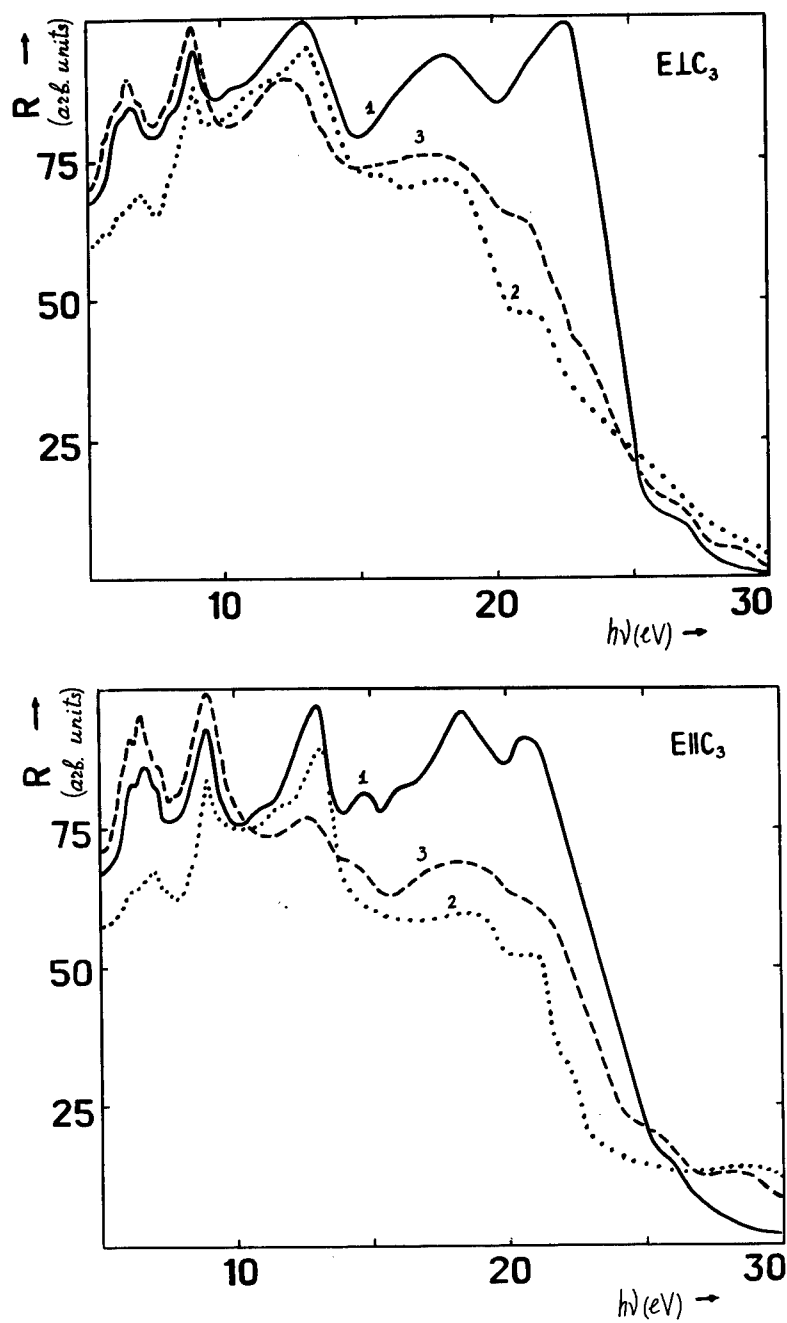
FIGURE 1  Reflection spectra of HOC corundum monocrystals
  a. $\vec{E} \perp C_3$
  b. $\vec{E} \parallel C_3$
    curves: 1 – unirradiated crystal
      2 – neutron-irradiated with dose $1 \times 10^{18}$ n/cm.$^2$
      3 – neutron-irradiated with dose $1 \times 10^{17}$ n/cm$^2$ and annealed at 500°C.
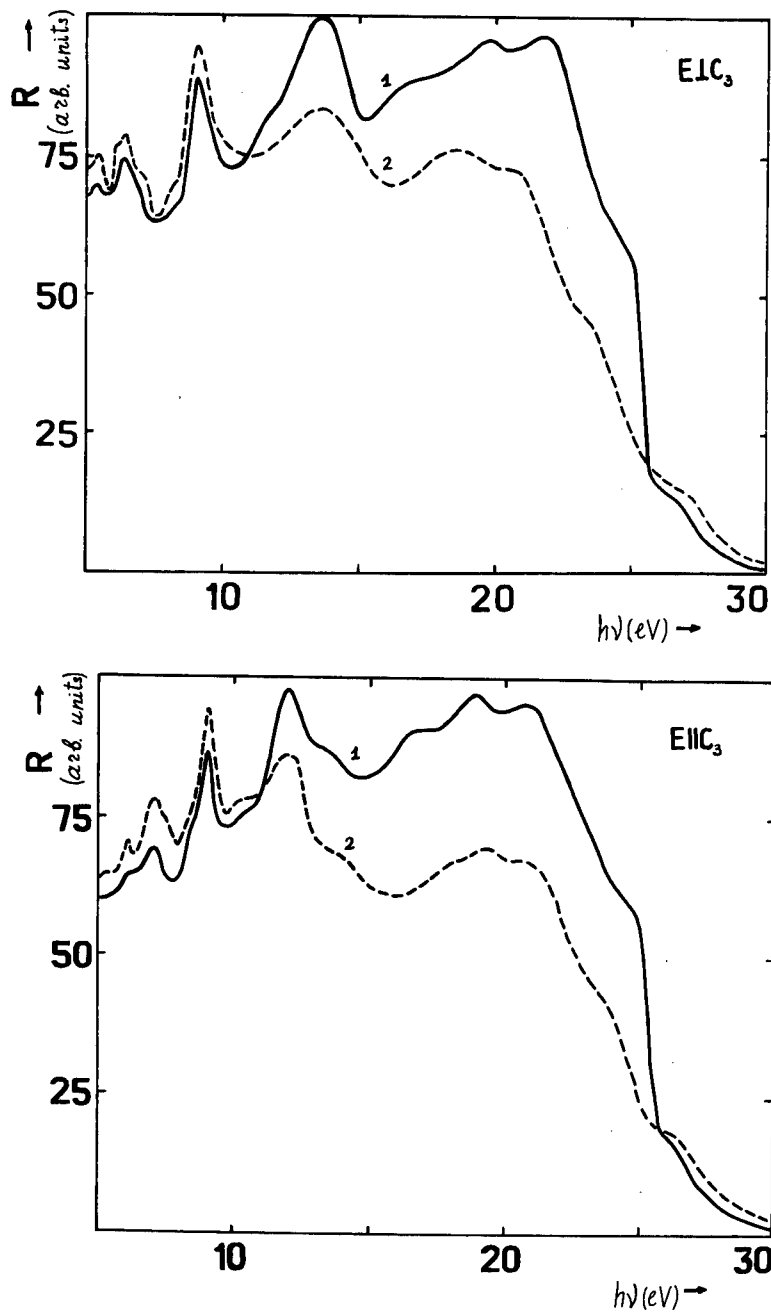
FIGURE 2    Reflection spectra of Verneil corundum monocrystals

   a. $\vec{E} \perp C_3$

   b. $\vec{E} \parallel C_3$

         curves : 1 – unirradiated crystal

                     2 – electron-irradiated with dose $3 \times 10^{17}$ e/cm$^2$.

The group of maxima in the reflection spectra is due to the allowed transitions from the high symmetry points of Brillouin zone, formed by 2p orbitals of $O^{2-}$ and 3s states of $Al^{3+}$.

It is clear from the reflection spectra, that after neutron (Figure 1) and electron (Figure 2) irradiation there occurs a strong stoichiometric disturbance of the near-surface and surface layers of corundum. It is especially observed in the region from 15 to 25 eV. On Figure 1 (curve 2, 3) it is shown the influence of different doses of neutron-irradiation on the surface condition of the crystals. Near-surface structure disorder due to enhancement of vacancies and interstitial ions concentration takes place as a result of irradiation. Oxygen is desorbed leaving the surface rich in elemental Al, i.e. the process of radiation-stimulated desorption occurs, which is due to ionization of the main cation levels accompanied by Auger cascades. As a result of oxygen desorption the metalic Al particles fills the vacant micropores which are space-localized dislocation loops.

The neutron-irradiated crystals were annealed at 500°C (Figure 1, curve 3). The oxygen is desorbed at annealing and metalic aluminum forms a dislocation gathering with nonhomogeneous distribution on the crystal surface. In neutron-irradiated corundum, besides the colour centres of vacancy type (F, $F^+$, V), [$Al_iF$]-type complex colour centres are formed.

Starting from 25 eV one can see an increase of reflectivity of irradiated crystals which is due to the decoration of the radiation damages on the surface of $\alpha$-$Al_2O_3$.

REFERENCES

1.  Yu. M. Alexandrov, V. N. Kolobanov, V. N. Makhov, T. I. Sureichikova, M. A. Yakimenko, *Zh. Prikl. Spektr.* (Russia) **36**, 941 (1982).
2.  K. H. Lee and J. H. Crawford, *Phys. Rev.* **B15**, 4065 (1977).
3.  K. H. Lee and J. H. Crawford, *Phys. Rev.* **B19**, 3217 (1979).
4.  V. V. Harutunyan, A. N. Belsky, V. A. Gevorkyan, N. E. Grigorian, G. N. Eritsian, *Nucl. Instrum. Meth.* **A308**, 197 (1991).
5.  V. V. Arutunyan, G. N. Eritsyan, R. K. Ezoyan, V. A. Gevorkyan, *Phys. Stat. Sol.* **B149**, K 77 (1988).
6.  S. V. Choi, R. H. Bastram, R. T. Cox, *J. Phys. Sol.* **34**, 1079 (1973).
7.  E. R. Ilmas and A. I. Kuznetsov, *Fiz. Tverd. Tela* (Russia) **14**, 1464 (1972).

# INFLUENCE OF THE CRYSTALLOGRAPHIC ORIENTATION OF THE SURFACE ON DAMAGE AND CHEMICAL EFFECTS IN ION-IMPLANTED MgO

L. GEA,* P. THEVENARD, R. BRENIER, B. CANUT, S. M. M RAMOS
and M. BERANGER

*Departement de Physique des Materiaux-Universite Claude Bernard-LYON I 43, Bd du 11
Novembre 1918–69622 Villeurbanne Cedex*

The influence of the crystallographic orientation of the surface on ion implantation damage was studied in MgO single crystals. For this purpose, rare gas ions (150 keV-argon) or reactive ions (150 keV-niobium) were implanted at room temperature in (100) and (110) MgO surfaces at a fluence of $5.10^{16}$ ions.cm$^{-2}$. With the mean of Rutherford Backscattering Spectroscopy in channeling geometry (RBS-C), it is shown that the damage depends on the crystallographic orientation of the MgO surface. The (100) irradiated surfaces exhibit a localized damage as predicted by TRIM code calculations while in (100) MgO, the defects extend in depth. Chemical effects are also dependent on the crystallographic orientations of the implanted surfaces: the substitutional fraction of the implanted niobium determined by RBS-C and the niobium binding energy estimated by XPS analysis are different in the (110) and (100) MgO irradiated surfaces.

*Key words*: Implantation, MgO, Single Crystal, Orientation, Irradiation Creep.

## 1 INTRODUCTION

MgO is an ionic crystal with the NaCl structure. It exhibits a peculiar behaviour when it is submitted to an implantation beam: on the contrary to most of the oxides, it does not amorphize, even for the highest fluences (up to a few $10^{17}$ ions.cm$^{-2}$). Implantation effects have been widely studied in MgO. However, the influence of the crystallographic orientation of the surface has never been shown. In this paper, we will emphasize the consequences of 150 keV implantation of inert argon ions and then reactive niobium ions in (100) and (110) MgO single crystals. In particular, we will study damage and chemical effects (formation of chemical bonds between the implanted species and atoms of the matrix).

## 2 EXPERIMENTAL PROCEDURE

150 keV argon and niobium ions were implanted with a fluence of $5.10^{16}$ ions.cm$^{-2}$ in (100) and (110) single crystals of optical grade MgO from Oak Ridge National Laboratory. The specimens were thick enough (0,5 mm) so that no bending of the samples could be permitted during the irradiation. Irradiations were performed at room temperature with the mean of a 200 keV Balzers implantor. The fluence rate was about $10^{12}$ ions.cm$^{-2}$.s$^{-1}$. An angle of 7° was kept between the normal to the sample surface and the beam direction in order to avoid parasiting channeling effects. The RBS (Rutherford Backscattering Spectroscopy) in random and channeling geometry and the XPS (X-Ray PhotoSpectroscopy) techniques were used to characterize the damage and location of ions, and the

---

* Present address, Solid State Division, Oak Ridge National Laboratory, P.O. BOX 2008, Oak Ridge, TN 37831-MS6056 (U.S.A.)
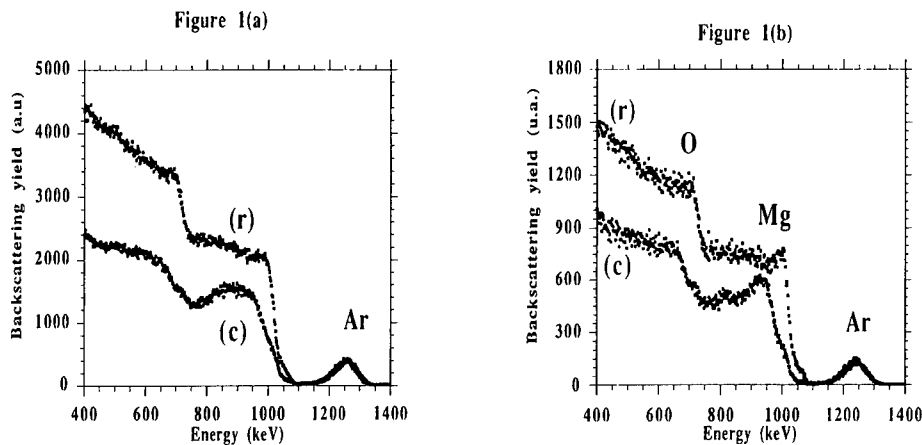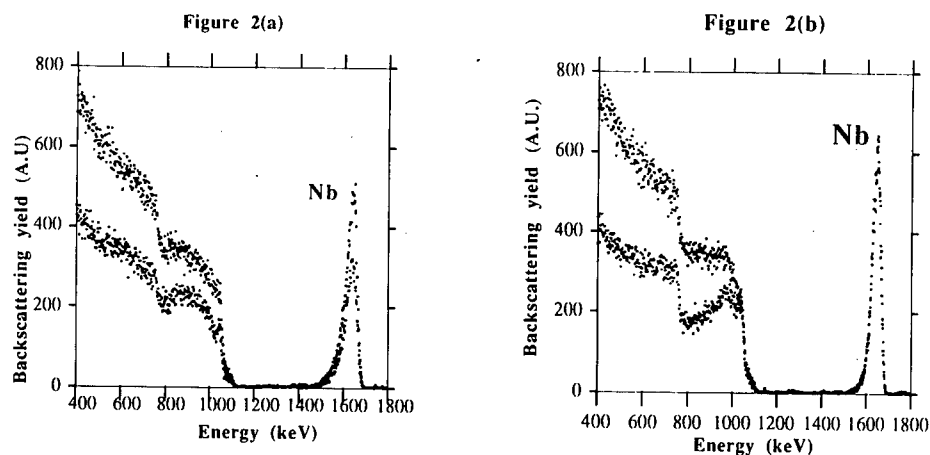
Figure 1(a)

Figure 1(b)



FIGURE 1   RBS spectra of Ar implanted MgO samples (room temperature, fluence $5.10^{16}$ $Nb.cm^{-2}$) in
channeling (c) and random (r) geometry
(a) MgO with a (100) surface
(b) MgO with a (110) surface.

residual charge state of the implanted species respectively. RBS analysis was performed
using a 2 MeV $^4He^+$ beam generated by a Van de Graaff accelerator, with a beam current
around 10 nA. The samples were mounted on a three-axis gonniometer head, offering an
angle resolution better than 0,05°. A 15 keV resolution surface barrier detector was set at
an angle of 150° with respect to the incident beam. In these experiments, the cross section
of the beam impinging the sample never exceeded 1 $mm^2$. X-Ray PhotoSpectroscopy
(XPS) was performed using a Riber Spectrometer, model CX700, and $AlK_\alpha$ radiation. The
depth profile analysis was obtained by using successive bombardments of 5 keV argon
ions.

## 3   RESULTS

### 3.1 *Ar Implanted Specimens*

In this particular range of energy (150 keV), damage and ions distributions peak at about
the same depth and one may expect significant interactions between defects (Frenkel pairs
and dislocations) and implanted species. However, as argon ions are inert and their radius
is relatively small (1.54 Å) we will neglect these interactions in a first approximation.

   **Figure 1(a)** shows the RBS spectra of (100) MgO implanted with $5.10^{16}$ $Ar.cm^{-2}$. At
the depth of 100 nm (corresponding to an He energy of 950 keV), the dechanneling rate
XMg (channeled yield / random yield of the Mg signals) equals 70%. The implanted layer
is very damaged without being amorphous. The damage extends in depth, far beyond the
expected value of 100 nm obtained with the TRIM theoretical calculations.[2] For the (110)
MgO sample (**Figure 1(b)**), the damage is characterized by a peak (XMg = 90%) at the
depth of 100 nm, in agreement with the theoretical predictions.

   In both cases, the distributions of the argon atoms have a mean projected range of
96 nm, in agreement with the theoretical value. A negligible distortion of the argon profile
is visible in (100) MgO. As a matter of fact, the use of *argon* atoms has allowed us to
minimize interactions between defects and implanted species and *to study the effect of the*

Figure 2(a)

Figure 2(b)



FIGURE 2   RBS sprectra of Nb implanted MgO samples (room temperature, fluence $5.10^{16}$ Nb.cm$^{-2}$) in channeling (c) and random (r) geometry
(a) MgO with a (100) surface
(b) MgO with a (110) surface.

*crystallographic orientation of the surface on damage only.* However, it has to be noted that with heavier gas atoms such as Kr and Xe,[2,3] one observes a more important dissymetry of the distributions. This effect is probably related to non negligible elastic interactions between the implanted atoms and the defects (size effect).

### 3.2 Nb Implanted Specimens: Chemical Effects

Damage, when implantation is performed with reactive ions ($5.10^{16}$Nb.cm$^{-2}$, 150 keV) is similar to that obtained with the argon ions: it is localized for the (110) orientation (XMg = 71%) and thus in agreement with theoretical calculations, while it is extended in depth for the (100) orientation (XMg = 53%)

The distribution of the niobium atoms is outstanding. For the (110) orientation, the distribution is perfectly symmetric and thus is in agreement with the theoretical TRIM distribution. However, for the (100) orientation, the Nb distribution extends in depth as for the damage.

This effect seems to have significant consequences. First, it affects the local concentration of the implants. The effect is particularly visible at the maximum of the projected range (56 nm) where one can calculate a Nb concentration of 20% for the (110) orientation versus 15% for the (100) orientation. On the second hand, it affects the location of the Nb atoms in the matrix. The comparison of the channeled and random yield for the Nb signals gives further indication as to the location of the Nb ions in the MgO matrix. The percentage of substitution of the Nb ions is taken as $\alpha$Nb = (1-XNb) / (1-XMg) with XNb = area (Nb)c / area (Nb)r. In our case, $\alpha$Nb $\approx$100% for the (100) orientation: the majority of the Nb ions substitute for Mg atoms and then occupies an octahedral site of oxygen atoms. This environment is similar to that of a Nb atom in Nb2O5 compounds and this indicates that the chemical effects are important (high oxidation state of Nb). For (110) MgO, the percentage of substitution is negligible.

These results are confirmed by XPS measurements. By performing successive abrasion and analysis, the oxidation state of the implanted Nb ions was studied as a function of depth. For the (100) orientation, the oxidation state of the niobium is high (like in Nb2O5 and NbO2 oxides) and constant with depth.[4] In the (110) orientation, it varies with depth (thus with local concentration). At the maximum of the distribution, Nb bonds are of the type found in NbO oxide. The different chemical states of niobium atoms have been identified in agreement with the results from litterature.[5]

## 4   DISCUSSION

The different results are summarized as follows:

|      | (100) | (110) | |
| --- | --- | --- | --- |
| Ar | damage | extended in depth | localized |
| Nb | damage ions | extended in depth diffusion tail in depth | localized gaussian |

The striking difference in the implantation behaviour of the (100) and (110) MgO oriented surfaces exists with Ar as well as with Nb: no chemical effect can be invoked. Furthermore, it cannot be explained by the primary defect creation because the number of displacements is the same in both cases. As a matter of fact, in order to understand the results described above, the processes of implantation damage have to be reviewed in detail. Point defects are created by the nuclear collisions of the impinging ions and then aggregate into dislocation loops. Dislocation loops grow by the absorption of the point defects that are continuously created by the irradiation. When the dislocation density is large enough, dislocations interact and a dislocation network builds up. However, defects induce a volume change in the implanted layer. The constraints of the substrate to hold the lateral dimensions constant produce a compressive in-plane stress[6] in the implanted region which can be partially relaxed by plastic flow.[2] For materials that remain crystalline, relaxation of stress occurs via the absorption of interstitials to the dislocations that are parallel to the surface (if they exist). In MgO, the plastic flow involves dislocations known to lie on {110} planes. Therefore, dislocation loops are differently oriented with respect to the stress, in the (100) implanted surface and in the (110) one. As a matter of fact, in the (110) oriented surfaces, interstitial loops can easily grow in {110} planes, thus permitting the relaxation of the implantation stress. For the (100) surfaces, such a process is not allowed. However, interstitials are likely to move out of the implanted zone to regions where the stress is less important (ie towards the surface or towards the inside of the material) via favourable paths along the [001] direction. This mechanism is in agreement with the experimental data: damage extends in depth for the (100) MgO only. For both Ar and Nb implantations, the extension of the damage profile is then correlated with the dechanneling yield. Furthermore, the distortion of the implantation profiles suggest that the implanted atoms contribute to the relaxation via a similar mechanism (they either migrate to dislocation loops inside the implanted layer or diffuse out of the implanted layer depending on the crystallographic orientation of the surface).

One may then understand the chemical effects of implantation. In (110) MgO, the local environment is not favourable to the chemistry of Nb which necessitates a specific environment of compensation charge vacancies[8]. For (100) MgO, the depletion in interstitials of the implanted layer favours such an environment. Furthermore, the easy

migration of the Nb atoms (as for the interstitials) also favours chemistry; diffusion is probably associated to the presence of favourable migration paths along[001] : these could be dislocations perpendicular to the surface already existing in the virgin sample or further developped by the irradiation.


## 5  CONCLUSION

It has been shown in this paper that the crystallographic orientation of the MgO surface plays an important role on damage and chemical effects. Damage is extended in depth for (100) MgO while it is localized for the (110) MgO orientation. This effect is believed to be due to the relaxation of the implantation stresses that occur via the migration of the interstitials that are continuously produced by the irradiation (irradiation creep). The difference between the two orientations probably lies in the availability of sinks to capture the interstitial For (110) MgO, interstitital loops parallel to the surface are known to play such a role. In (100) MgO, as no such sinks are available, interstitials will move out of the implanted layer, to regions where the stress is less important, probably via dislocations perpendicular to the surface. Chemical effects, more important in (100) MgO, are favoured by such a mechanism.

REFERENCES

1. J. F. Ziegler, J. P. Biersack, U. Littmark, '*The Stopping and Range of Ions in Solids*' Pergamon, New York (1980).
2. R. Brenier, B. Canut, L. Gea, S. Ramos, P. Thevenard, *Nucl. Inst. Meth. Phys. Res.* **B80/81** (1993) 1210.
3. L. Gea, J-L. Loubet, R. Brenier, P. Thevenard, to be published.
4. S. M. M. Ramos, B. Canut, L. Gea, L. Romana, J. LeBrusq, P. Thevenard, M. Brunel, *Nucl. Inst. Meth. Phys. Res.* **B59/60** (1991) 1201.
5. C. Durand, Thesis, Universite Claude Bernard, Lyon, France (1985).
6. G. B. Krefft, *J. Vac. Sci. Technol.* **14** (1977) 533.
7. C. A. Volkert, A, Polman, *MRS Symp. Proc.* **235** (1992) 3.
8. L. Gea, C. R. A. Catlow, S. M. M. Ramos, B. Canut, P. Thevenard, *Nucl. Inst. Meth. Phys. Res.* **B65** (1992) 282.

# ESR STUDY OF THE INSULATOR-CONDUCTOR TRANSITION IN POLYIMIDE KAPTON INDUCED BY SWIFT HEAVY ION IRRADIATIONS

J.-P. SALVETAT,* A. BERTHAULT, F. BRISARD,* J-M. COSTANTINI,*
J. DAVENAS**

*CEA, *Service PTN, BP 12, 91680 Bruyères-le-Châtel, France; **Université Lyon I, UA CNRS 172, Département de Physique des matériaux 43 Bd du 11 Novembre, 69622 Villeurbanne Cedex, France*

Kapton-H thin films have been irradiated with heavy ions in the MeV/u range, in the electronic stopping power (*Se*) regime. Effective ion track radii are extrapolated from spin density measurements and are consistent with simulations of the radial distribution of the energy density deposited by secondary electrons. This yields an apparent quadratic dependence of the data versus *Se*. We postulate that the paramagnetic defects are dangling bonds on aromatic condensed structures, and that conductivity appears by overlap of these structures. The final product is a highly amorphous carbonaceous substance with a conductivity ($10^4 \ \Omega^{-1}.m^{-1}$) and a spin density ($5 \times 10^{19} \ g^{-1}$) near that of ion implanted or pyrolysed Kapton.

*Key words*: ESR, Kapton conductivity, ion bombardment, secondary electrons, ion track.

## 1 INTRODUCTION

Many studies have shown that an insulator-conductor transition can be induced by energetic ion irradiations in polymers.[1] It has been proved that the main mechanism is a carbonization induced by the electronic excitations.[1,2] However, the conduction in such carbonaceous substances is not completely understood because of the lack of microstructural informations.

This work focuses on the effect of irradiation with swift heavy ions of energy around a few MeV/nucleon in the electronic stopping power regime on polyimide Kapton films. Film thicknesses being lower than the ion projected range, no end-of-range effects occur like in ion implantation.

## 2 EXPERIMENTAL

Ion beams of 50 MeV $^{63}$Cu, 50 MeV $^{32}$S, 30 MeV $^{18}$F, and 30 MeV $^{12}$C were delivered by the 7 MV Van de Graaff Tandem accelerator at CEA Bruyères-le-Châtel. 7.5 and 12.5 $\mu$m thick polyimide Kapton-H films (Dupont de Nemours) were irradiated under high vacuum at room temperature (RT). Beam currents never exceeded 30 nA/cm$^2$, to prevent any heating of the targets during irradiation. An electrostatic scan allowed a good homogeneity of the irradiated surface, around 1 cm$^2$. Fluences were measured by counting the backscattered ions on a 100 nm gold layer deposited under vacuum on an aluminium mask, or directly on the Kapton films. This insured an accuracy of about 20%.

Most Electron Spin Resonance (ESR) experiments were done with a Varian E-line spectrometer at RT. Spin densities have been measured in a double cavity, where the outgased irradiated sample and a reference (Strong Pitch Varian) were placed. Low microwave power has been used to avoid saturation. Both sample and Strong Pitch signals were numerically fitted by a linear combination of elementary shapes (lorentzian and
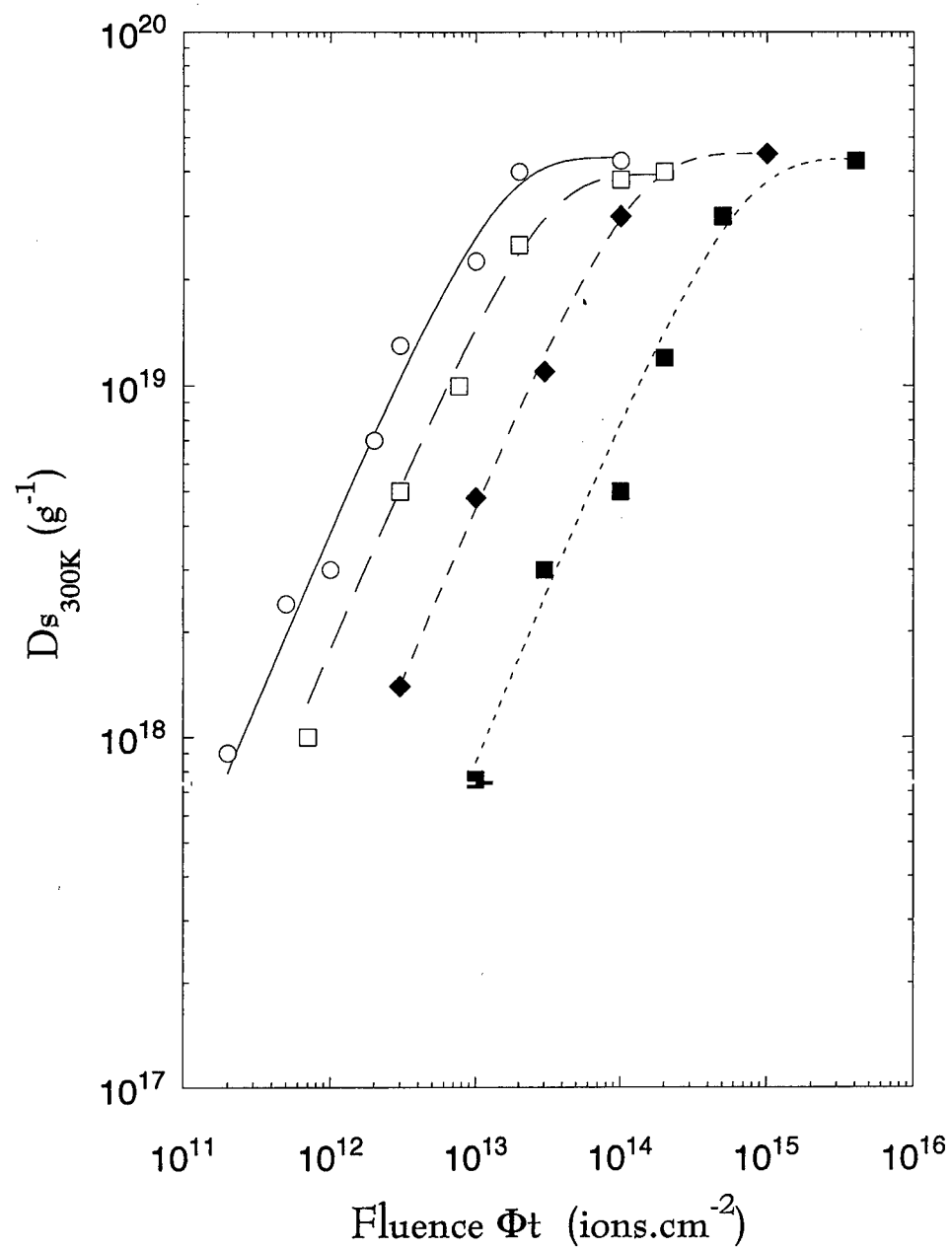
FIGURE 1   room temperature spin density versus ion fluence; 50 MeV $^{63}$Cu(○), 50 MeV $^{32}$S(□), 30 MeV $^{18}$F(◆), 30 MeV $^{12}$C (■) irradiations.

Table I

Mean electronic ($Se$) and nuclear ($Sn$) stopping powers, mean projected ranges (Rp), and effective track radii ($R_{eff}$) in Kapton-H (density $\rho = 1.43$ g.cm$^{-3}$)

| ion | $Se$(MeV.$\mu$m$^{-1}$) | $Sn$(MeV.$\mu$m$^{-1}$) | Rp($\mu$m) | $R_{eff}$(nm) |
|---|---|---|---|---|
| 50 MeV Cu | 4.92 | $4 \times 10^{-2}$ | 12.9 | 1.7 |
| 50 MeV S | 3.26 | $7 \times 10^{-3}$ | 17.4 | 1.2 |
| 30 MeV F | 1.56 | $2 \times 10^{-3}$ | 20.2 | 0.58 |
| 30 MeV C | 0.61 | $4 \times 10^{-4}$ | 39.5 | 0.25 |

gaussian). We preferred this to the direct double integration. Low temperature ESR measurements have also been done on a Brucker X-band spectrometer down to 4.2 K.

D.c. resistivity measurements were performed at RT both in transverse and longitudinal modes, with two or four gold electrodes directly evaporated on the samples.

Electrical and spin resonance measurements have been performed on self supported regions, where the damage is mainly due to the electronic stopping power $Se = (-dE/dx)_e$, which is nearly constant in the samples, and much higher than the nuclear stopping power $Sn = (-dE/dx)_n$ (see Table I).

## 3 RESULTS AND DISCUSSION

First of all, it is to be noted that the spin levels are doublets with a susceptibility following a Curie law versus temperature. Therefore, we are sure to measure a real number of paramagnetic localized defects. Figure 1 shows the dependence of the RT spin density (Ds) versus fluence ($\Phi$t) for the different ions. In the first stages of irradiation, a linear increase of the spin density is clearly seen, then a saturation (D$_\infty$ = 5 $\times$ 10$^{19}$ g$^{-1}$) appears at higher fluences.

Figure 2 shows that all the spin density and conductivity data can be fitted by a universal curve showing an apparent $Se^2$ dependence. Low fluence conductivity data have already been published.[3] A first striking point is the lagging of the conductivity data with respect to spin density data, as was already seen in similar studies.[4] The other important point is that neither fluence nor absorbed dose $\phi$t $\times$ $(Se/\rho)$ are good scaling parameters: heavy ions are more efficient in producing defects than light ions. Besides, it is known from previous work that energetic electrons (2.5 MeV) are much less efficient than ions in inducing a high conductivity.[3]

To explain these results we will use the ion track model as is usually done with swift heavy ions.[5,6] The latter model states that damage is concentrated around the ion path in a cylindrical shell of effective radius $R_{eff}$. The spin density after $\Phi$t random impacts is Ds = D$_\infty$[1 - exp($-\pi$R$_{eff}^2\Phi$t)], by postulating that the spin density saturation corresponds to the full overlap of ion tracks.[5] Thus, $R_{eff}$ can be deduced by least-squares fits of the data of figure 1. The track radii so obtained are displayed in table I, with the mean stopping powers and projected ranges, as calculated with the *TRIM-90* code.[7]

Simulations of the radial distribution of energy density ($D_E$) deposited by the secondary electrons have been done with a computer code based on the Katz-Kobetich model.[8] The percentage of the total energy deposited corresponding to the secondary electrons was set to 65%.[5] $D_E$, normalized against $Se$, is plotted versus radius in Figure 3. Within a good approximation, the track radii are found to correspond to the *same* minimum $D_E$ value around 0.15 eV/Å$^3$ (0.15 keV/nm$^3$) . Below this energy density threshold, it seems that
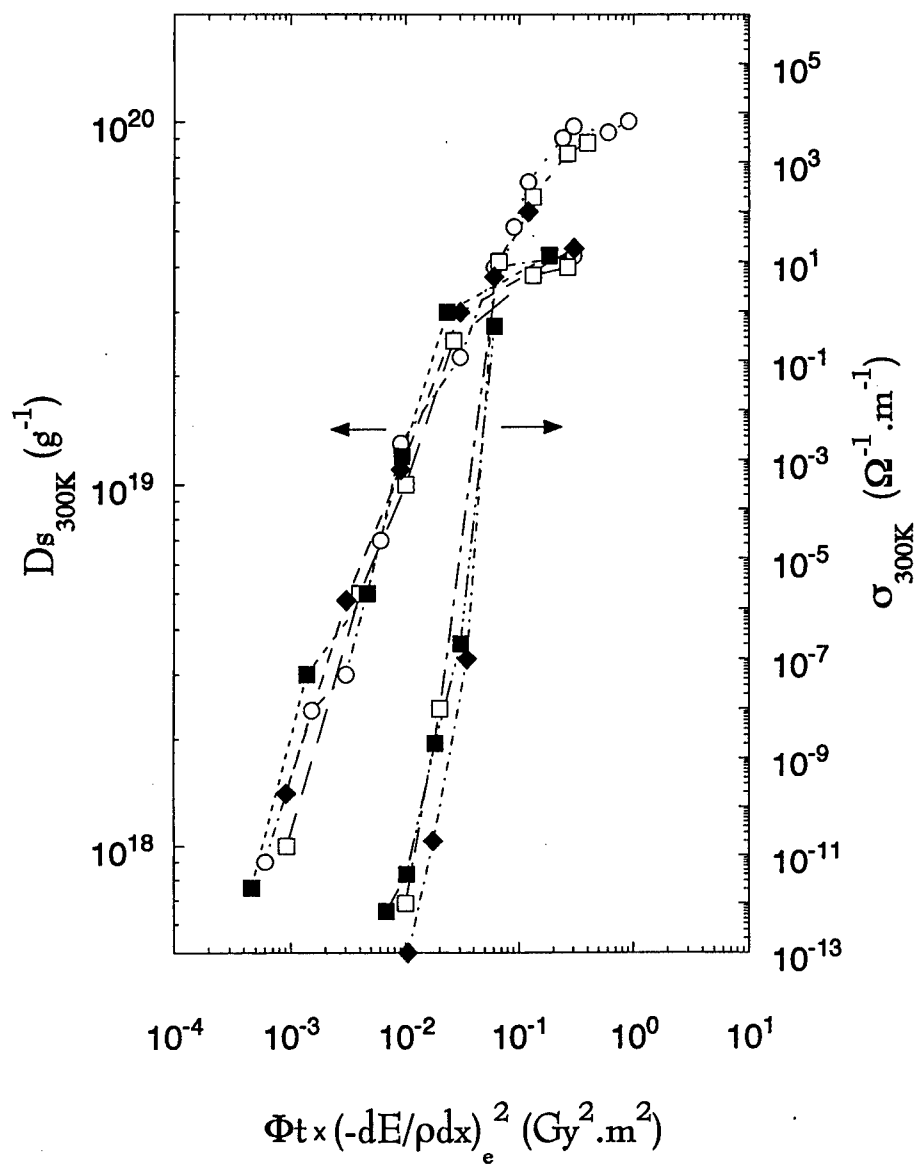
FIGURE 2    room temperature spin density and conductivity versus fluence times the square of electronic energy loss: 50 MeV $^{63}$Cu($\bigcirc$), 50 MeV $^{32}$S($\square$), 30 MeV $^{18}$F($\blacklozenge$), 30 MeV $^{12}$C ($\blacksquare$) irradiations.

the radiolytic process induced by the secondary electrons is no longer efficient to create defects.

In case of cylindrical ion tracks, the apparent quadratic dependence versus *Se* comes from an apparent linear dependence of $R_{eff}$ versus *Se*. This implies that at any stage of the
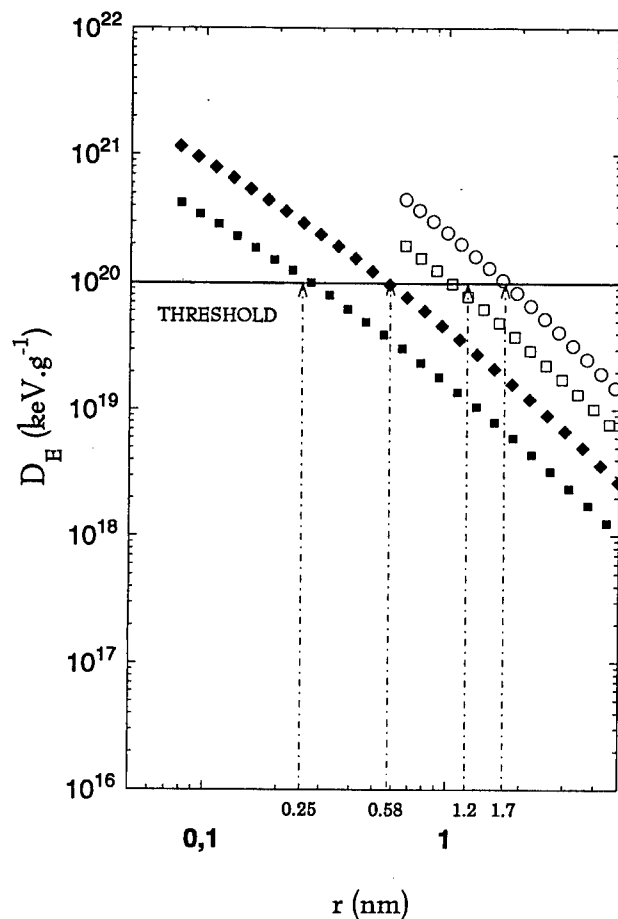
FIGURE 3   simulations of the radial distribution of the energy density deposited by the secondary electrons generated on the passage of ions through Kapton films: 50 MeV $^{63}$Cu($\bigcirc$), 50 MeV $^{32}$S($\square$), 30 MeV $^{18}$F($\blacklozenge$), 30 MeV $^{12}$C ($\blacksquare$) ions.

irradiations, the spin density remains constant and equal to $D_\infty$ in each ion track. Moreover, Figure 1 shows that $D_\infty$ is the same for all ions, and near the maximum spin density obtained in pyrolysed Kapton.[9]

## 4   CONCLUSIONS

We have studied the insulator-conductor transition in polyimide Kapton induced by the dense electronic excitations produced by swift heavy ion irradiations, in the electronic stopping power regime.

Effective track radii have been deduced from the spin density data versus fluence. These radii correspond to the same energy density threshold around 0.15 eV/$\text{Å}^3$ (0.15 keV/nm$^3$) deposited by the secondary electrons around the ion path. An apparent quadratic scaling

versus stopping power is found for spin density data. This is interpreted by a constant spin density in each track, equal to the saturation value, which is the same for all ions. This value is near the maximum spin density in pyrolysed Kapton.

## REFERENCES

1. T. Venkatesan, L. Calcagno, B. S. Elman and G. Foti, in: *Ion Beam Modification of Insulators*, P. Mazzoldi and G. W. Arnolds (Eds.) (Elsevier, Amsterdam, 1987), chap. 8, p. 301.
2. J. Davenas, G. Boiteux and M. Fallavier, *Nucl. Instr. and Meth.* **B39**, 796 (1989).
3. J. M. Costantini, J. L. Flament, V. Mori, L. Sinopoli, J. Trochon, J. L. Uzureau, L. Zuppiroli, L. Forro, J. Ardonceau and D. Lesueur, *Radiat. Eff. and Defects in Solids*, **115**, 83 (1990).
4. B. Wasserman, M. S. Dresselhaus, G. Braunstein, G. E. Wnek and G. Roth, *J. Electron. Mater.*, **14**, 157 (1985).
5. A. Perez and P. Thévenard, in: *Ion Beam Modification of Insulators*, P. Mazzoldi and G.W. Arnolds (Eds.) (Elsevier, Amsterdam, 1987), chap. 4, p. 156.
6. F. H. Ruddy, J. Bartko and K. F. Schoch, Jr., *J. Mater.Res.*, **3** (6), 1253 (1988).
7. J. P. Biersack and L. G. Haggmark, *Nucl. Instr. and Meth.*, **174**, 257 (1980).
8. E. J. Kobetich and R. Katz, *Phys. Rev.*, **170**, 391 (1968).
9. S. D. Bruck, *Polymer*, **6**, 319 (1965).

# THE EXFOLIATION OF LiF IMPLANTED WITH ALKALI IONS AT LOW TEMPERATURE

J. DAVENAS and B. V. THIEN,

*Université Cl. Bernard Lyon 1-UA CNRS 172; Département de Physique des Matériaux, 43 Bd du 11 Novembre, 69622 Villeurbanne Cedex, France*

The implantation of alkali ions in LiF at liquid nitrogen temperature leads to the formation of a continuous metallic layer according to an insulator-metal transition. Due to the precipitation of the implanted ions, this metastable phase relaxes near room temperature giving rise to the formation of a granular layer. The depth distribution of the implanted ions determined by Rutherford Backscattering Spectrometry (RBS) shows the appearance of alkali ions at the crystal surface upon exposure to the air. Such a profile is explained by the crystal exfoliation resulting from an explosive reaction of the implanted layer, which has the properties of the bulk alkali metal. Scanning electron microscopy (SEM) indicates that the thickness of the detached crystal platelets corresponds to the penetration depth of the incident ions, so that the analysing beam detects in fact the implanted ions at the surface in the exfoliated regions.

*Key words*: alkali halides, ion implantation, exfoliation, RBS, SEM.

## 1 INTRODUCTION

LiF crystals implanted at room temperature with alkali ions display a characteristic coloration, which depends on the implanted specie; braun for $Li^+$, pink for $Na^+$ and blue for $K^+$. We have shown in the past[1] that the plasma resonance of metallic nanoparticles, resulting from the precipitation of the implanted ions, is at the origin of this coloration. The absorption spectrum exhibits an extrinsic colloidal band, which is fully revealed by thermal annealings. The absorption spectrum of LiF crystals implanted at liquid nitrogen temperature does not show any colloidal band as long as the diffusion of implanted species is blocked. A characteristic metallic absorption, growing from the visible to the infrared, is however observed at high irradiation fluences due to the formation of a continuous metallic thin film. The formation of this conducting phase has been interpreted in the past in the framework of a percolation mechanism,[2] which accounts for the observed fluence threshold. The transition near room temperature of this continuous metallic layer to a granular one is shown by the evolution of the optical spectrum and by the resistivity enhancement.

However this model does not provide a satisfactory explanation for several experimental observations:

- The intensity of the colloidal band increases linearly with the ion fluence and is independent of the implantation temperature up to the percolation fluence threshold. Crystals implanted at low temperature are partially bleached after annealings, with a corresponding drop of the colloidal band magnitude, above the fluence threshold.
- The RBS spectrum shows for these last crystals a distribution of implanted ions extending to the surface. As the ion fluence increases, a surface peak can in particular be resolved. An oxygen contamination at the surface is noticed in correlation with the development of this peak.

Since implanted crystals are generally exposed to the air before the RBS analysis, we have undertaken new investigations in a single chamber to avoid air oxidation. We show

that the RBS "surface peak" is in fact an artefact due to the crystal exfoliation and confirmation is provided by the SEM observation of a crystal cross section.

## 2 EXPERIMENTAL PROCEDURE

We have performed the ion implantation and RBS analysis in a single chamber using the ion beams provided by a Van de Graaff electrostatic accelerator. LiF crystals were mounted on the sample holder of a cryostat cooled at liquid nitrogen temperature during the experiment duration ($\approx$ 24 h) in a vacuum of the order of $10^{-8}$ Torr. The beam of alkali ions is produced by thermoionic emission of a solid pearl, heated by a tungsten filament at the high voltage terminal of the VDG accelerator, for the 500 keV ion implantation. The accelerator is then opened and a RF gas source mounted at the terminal to enable the production of the 2 MeV He$^+$ beam for the RBS analysis. The irradiation chamber is placed in the cell of a spectrophotometer modified to perform in-situ optical measurements in the UV-visible and near infrared. A JEOL JSM 35 scanning electron microscope has been used to observe LiF crystal cross-sections.

## 3 RESULTS AND DISCUSSION

Figure 1 shows the RBS spectra of a LiF crystal implanted with $6 \times 10^{16}$ K$^+$/cm$^2$ at liquid nitrogen temperature (1), when the sample is warmed up to room temperature (2) and after being exposed to the oxygen of the air (3). A nearly gaussian distribution of the implanted potassium ions is observed on the high energy side of the backscattering spectrum. The depth profile calculated from the RBS spectrum provides a maximum of the potassium concentration at 4500 Å in accordance with the TRIM[3] calculation of the ion ranges and a significantly broader distribution than the longitudinal straggling. A small oxgyen peak is detected on the fluorine contribution, which is probably due to the condensation of the residual H$_2$0 vapour at the sample surface. Few modifications are noticeable on the room temperature RBS spectrum, apart a broadening of the implanted species distribution probably due to diffusion and loss of the H$_2$0 contamination layer. A surface peak of potassium ions is detected after introduction of the air in the irradiation chamber. Oxygen traces are shown at the same time on the fluorine contribution to the RBS spectrum. These effects are magnified for higher fluences of implanted ions.[4] As a first conclusion, evidence is provided that the potassium does not diffuse to the crystal surface when the sample is warmed up, but appears at the surface after contact of the implanted LiF crystal to the air. It must however be recalled that the depth scale is provided in RBS by the He$^+$ backscattering energy. A chemical element is in particular detected at the surface when there is no energy losses of the probing particle due to the crossing of matter before and after scattering. This implies that RBS is not sensitive to surface topography modifications.

A direct eye observation shows the discoloration of the crystal when introducing the air in the irradiation chamber, as indicated by the evolution of the optical spectrum followed in situ. Such a bleached crystal has been cleaved in the irradiated zone and observed by scanning electron microscopy. Figure 2a shows the heavily damaged surface of the crystal. Extended crystalline platelets have been removed by the violent reaction of the implanted crystal to the air. We have observed the crystal cross section in order to estimate how the RBS spectrum is perturbed by this irregular surface. The thickness of the partially detached crystal foils measured from Figure 2b corresponds to the penetration depth of the implanted ions: 4600 Å. Since the size of the analysing spot is larger than the irregularities dimensions the RBS spectrum is the sum of He$^+$ particles backscattered in exfolied
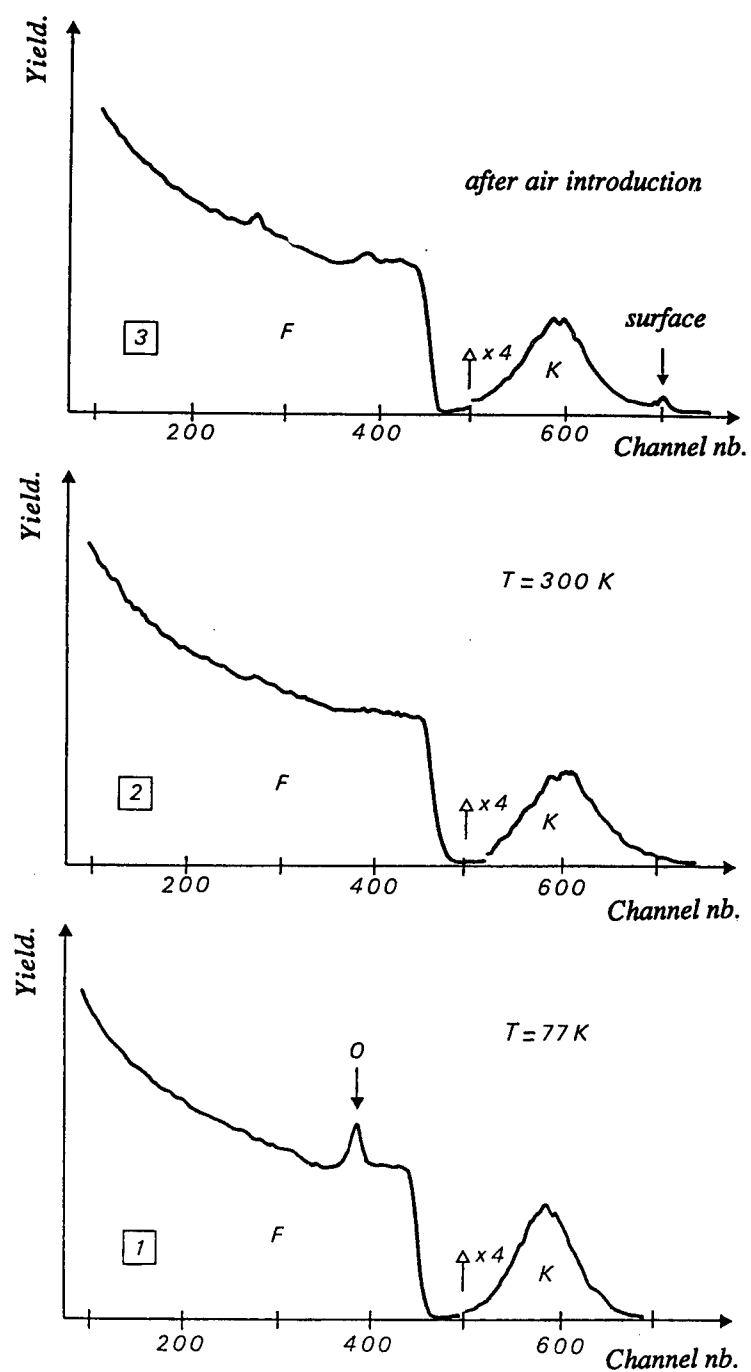
FIGURE 1    RBS analysis performed with 2 MeV He$^+$ -spectra of a LiF crystal implanted with 6 × 10$^{16}$ K$^+$/cm$^2$ at 500 keV: (1) LNT, (2) RT in vacuum, (3) after air introduction.

J. DAVENAS AND B. V. THIEN
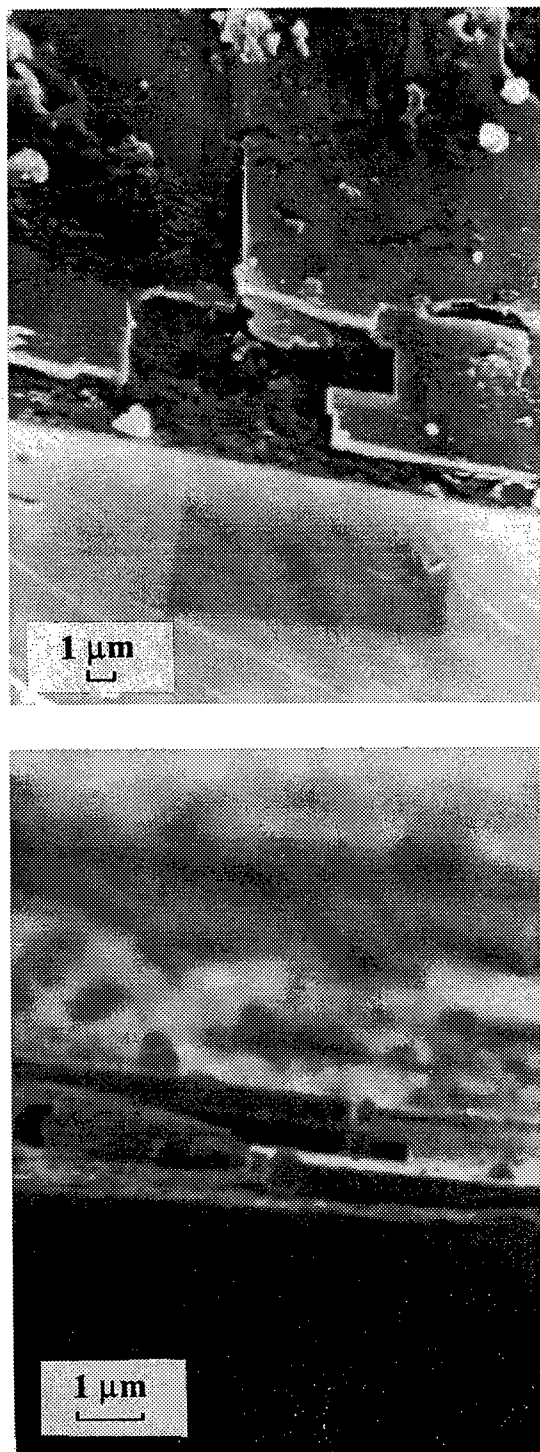


FIGURE 2    SEM micrograph of the cross section of a freshly cleaved LiF crystal: (2a) observation with a 40° inclination showing the exfolied surface; (2b) the cross section, thickness of the crystalline lamellas: 4600 Å.
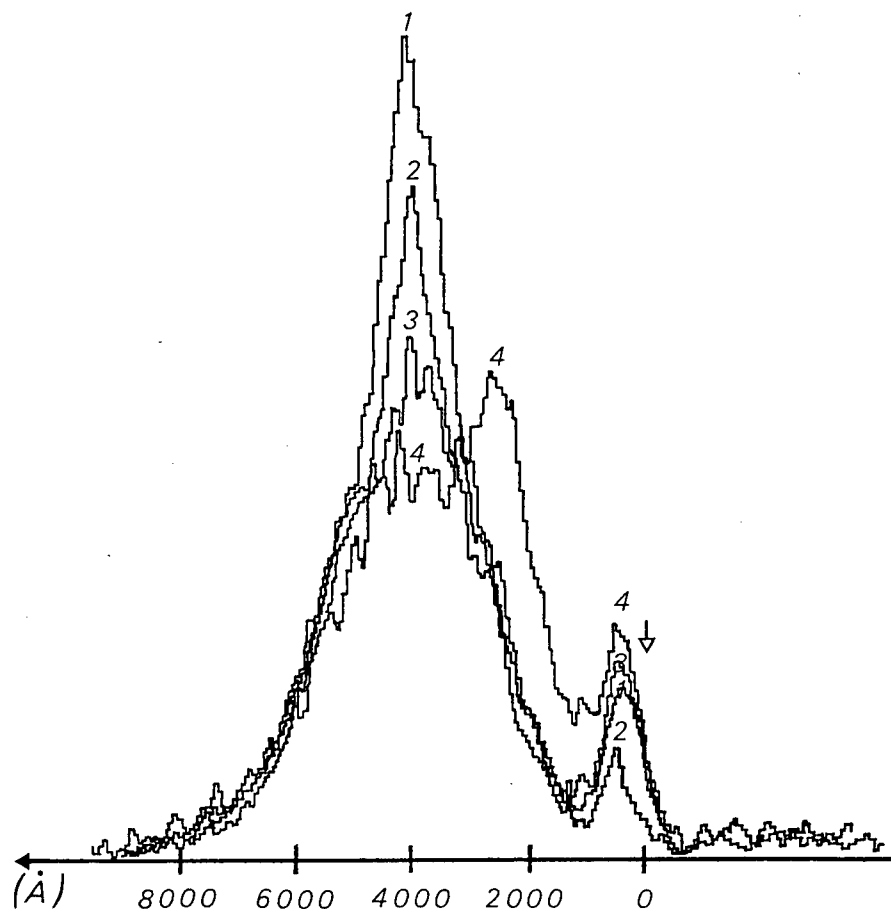
FIGURE 3   RBS profile of potassium in a LiF crystal implanted with $10^{17}$ $K^+/cm^2$ at LNT: (1) warmed up to RT, after air exposure, (2) thermally annealed for 1 h. at 250°C, (3) at 300°C, (4) at 350°C.

regions, where potassium is detected at the surface, and in less degraded regions, where potassium is probed at a normal depth.

To check the influence of the mechanical stresses induced in the burried layer, rare gases have been implanted with identical beam conditions. No exfoliation resulted. A complementary consideration supporting the oxidation mechanism is the correlation between the appearance of oxygen and potassium surface peaks. In particular oxidized potassium will not precipate upon annealing, which would explain the weakness of the colloidal band at high implantation fluences, in spite of the potassium content conservation. The combination of RBS and SEM studies leads to the conclusion that optical bleaching and surface contribution of the implanted metal are due to the crystal exfoliation induced by the air oxidation.

The implanted crystals remain brittle after implantation. In particular, the RBS profile of potassium shows (Figure 3) an increase of the surface peak indicating that the exfoliation process goes on upon thermal annealings.

At last, the difference of reactivity of the potassium must be emphasized in relation with the dispersion of the metal: the oxidation of the extended metallic metallic film is violent whereas potassium nanoparticles are not oxidized. It is however probable that the damage induced in the LiF matrix is not the same for these distinct implantation temperatures and can influence the oxygen diffusion.

## 3   CONCLUSION

The exfoliation of LiF crystals implanted with alkali ions has been evidenced by scanning electron microscopy. A coherent interpretation of optical bleaching and RBS profile could be provided, showing the explosive reaction of the burried film of alkali metal upon oxidation.

REFERENCES

1.  J. Davenas, A. Pérez, P. Thévenard, C. Dupuy, *Phys. Stat. Sol.* **A19**, 679 (1973).
2.  J. Davenas, C. Dupuy, *Surf. Science*, **106**, 327 (1981).
3.  J. P. Biersack, *Nucl. Inst. and Methods*, **182**, 199 (1981).
4.  J. Davenas, J. P. Dupin, B. Vu Thien, C. Dupuy, *J. de Phys., sup.* n° 7, 41, 385 (1980).

# EUROPIUM DIFFUSION IN Y- AND Z-CUT LiNbO₃ PRE-IRRADIATED BY GEV URANIUM IONS

S. M. M. RAMOS, R. BRENIER, B. CANUT, G. FUCHS, A. MEFTAH,* P. MORETTI,
S. OULD SALEM, P. THEVENARD, M. TOULEMONDE,* M. TREILLEUX

*Université Claude Bernard LYON I, Département de Physique des Matériaux
(URA CNRS 172) 69622 VILLEURBANNE Cédex—France; *Centre Interdisciplinaire de
Recherche avec les Ions Lourds (G.A.N.I.L.) Boulevard A. Becquerel—14040 CAEN
Cédex—France*

Single crystals of LiNbO₃ with y- and z-cut orientations were irradiated at GANIL with 3.37 MeV/amu ²³⁸U ions at a fluence ranging from $1.0 \times 10^{11}$ to $4.0 \times 10^{11}$ ions.cm⁻². The damage resulting from these irradiations at high electronic stopping powers (> 10 KeV/nm) consists mainly of amorphous tracks. After irradiation the samples were implanted with europium ions of 70 keV energy at a fixed fluence of $5 \times 10^{16}$ ions. Subsequent annealings in air, in the range 700–1100°C, were applied to investigate the influence of the pre-irradiation damage on the thermal evolution of Eu implanted LiNbO₃ crystals. Rutherford Backscattering Spectrometry (RBS) results clearly show that the existence of the amorphous tracks enhances the europium diffusion. An anisotropy effect has been observed in the diffusion process.

*Key words*: Lithium, niobate, europium, diffusion, irradiation and enhancement.

## 1 INTRODUCTION

In the last few years, several works have been devoted to investigate the optimal conditions for the incorporation of the rare-earth ions into the substitutional sites of LiNbO₃ matrix.[1–6] However, if some positif results have been obtained by Buchal *et al.*[3–4] for erbium and neodymium diffusion in LiNbO₃, the same has not been observed for europium.[6]

On the other hand, it is well stablised in the literature[7–8] that the diffusion of both metallic and noble gas ions in the oxides depends highly on the defects present in these materials.

As recently, B. Canut *et al.*[9,10] have shown that the LiNbO₃ can be highly damaged by GeV ion irradiations, we investigate, in this work, the influence of this damage in the thermal evolution of Eu implanted LiNbO₃ (y- and z-cut).

## 2 EXPERIMENTAL PROCEDURE

Single crystals of LiNbO₃ (y- and z-cut orientations) were irradiated at GANIL with 3.37 MeV/amu ²³⁸U at a fluence ranging from $1.0 \times 10^{11}$ to $4.0 \times 10^{11}$ ions.cm⁻². These samples were post-implanted at room temperature with Eu⁺ ions of 70 keV at a fixed fluence of $5 \times 10^{16}$ ions.cm⁻².

Annealing treatments were carried out in air at a temperature range 700–1100°C for 2 h. In order to follow the thermal evolution of Eu implanted in pre-irradiated LiNbO₃, Rutherford backscattering spectrometry (RBS) in channeling geometry was performed using a 2 MeV ⁴He⁺ beam generated by a Van de Graaff accelerator.

S. M. M. RAMOS *ET AL.*
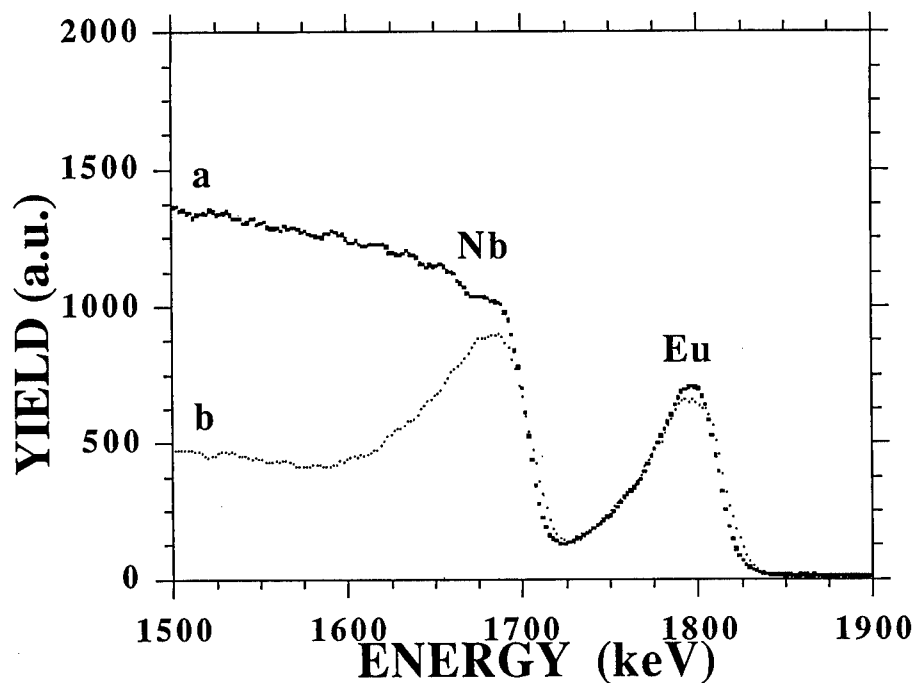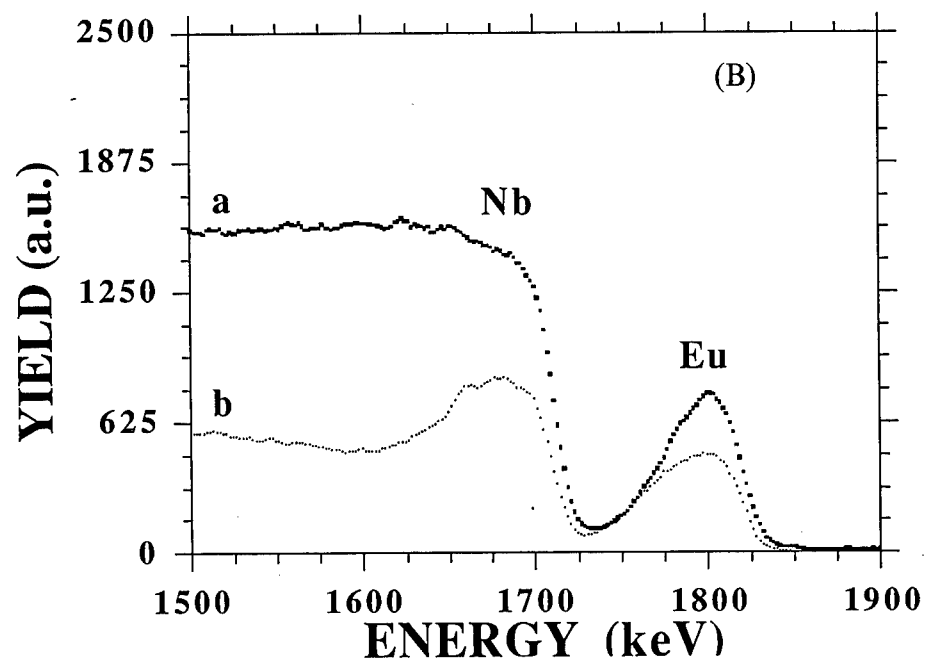


FIGURE 1A



FIGURE 1(B)

FIGURE 1   RBS spectra for the two crystallographic orientations of  (y-cut (A) and z-cut (B)). These samples were pre-irradiated with $10^{11}U^+.cm^{-2}$ at 201 MeV, implanted with  $5 \times 10^{16}$ $Eu^+.cm^{-2}$ at 70 keV and annealed at 900°C for 2h. (a) and (b) random and channeled spectra respectively.

## 3   RESULTS AND DISCUSSION

The damage induced in $LiNbO_3$ by Gev uranium ions irradiation has been investigated by Canut et al.[10] and discussed elsewhere. In the present work we start our experiments with the damaged samples.

Figure 1 shows a typical spectra in random (a) and in channeling (b) geometries obtained for a pre-irradiated sample ($10^{11}U^+.cm^{-2}$ at an energy of 201 MeV) implanted and annealed at 900°C for 2h. Two crystallographic orientations are investigated (y-cut in Figure 1A and z-cut in Figure 1B) and three mean features can be put forward from a comparison between these figures:

- The recrystallization of the amorphous layer, induced by Eu implantation, is more efficient in the samples of z-cut orientation.
- In both cases, a significant amount of Eu is transported by diffusion into the bulk showing that a diffusion process can be enhanced by the amorphous tracks presence. In the previous studies we have shown that the diffusion process of europium in virgin $LiNbO_3$ requires more drastic annealing conditions (T > 1000°C for 6 h) to become significant.[11]
- No Eu on substitutional sites was observed for $LiNbO_3$ of y-cut orientation. However, a substitutional fraction of 45% was determined for the samples with z-orientation, suggesting that the diffusion mechanism is not exactly the same for these two orientations.
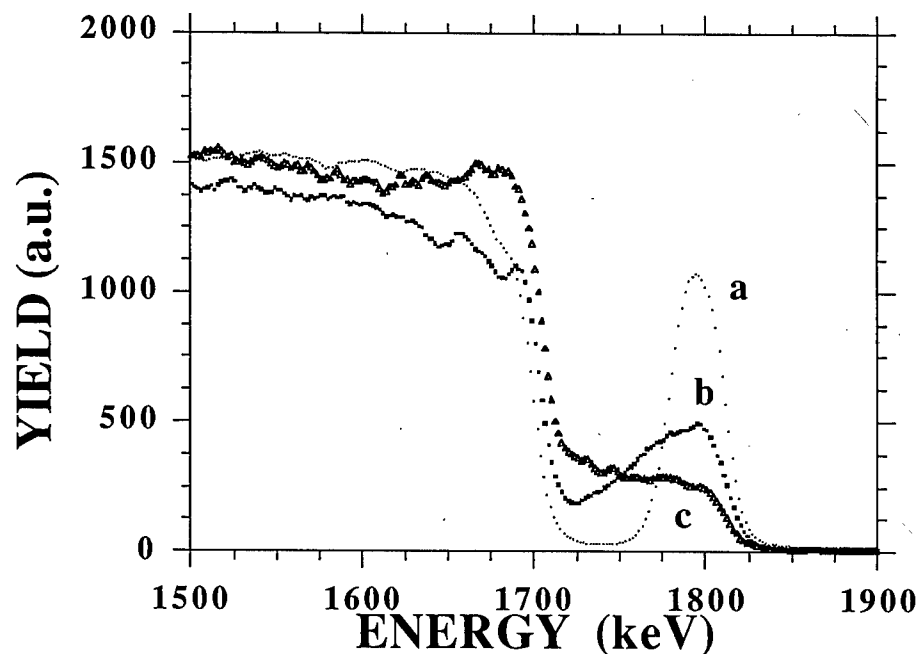


FIGURE 2   Random RBS spectra for the same sample as Figure 1. (a) spectrum for $LiNbO_3$ (y-cut) as-implanted. (b) and (c) spectra of annealed samples with y- and z-orientation, respectively. Annealing] temperature : 1100°C.

The annealing at 1100°C for 2 h confirms the Eu diffusion, as displayed in Figure 2, and more it evidences an anisotropy effect in this process. Figure 2a shows the Eu distribution in the as-implanted y-LiNbO$_3$. Before annealing this distribution is the same for y- and z-cut orintations. Figure 2 (b and c) clearly shows that the Eu-diffusion is faster along the hexagonal axis (z-orientation) of LiNbO$_3$.

From the RBS spectra the europium concentration profiles can be determined and consequently a diffusion coefficient has been estimated to be about $2.9 \times 10^{-15} \text{cm}^2 . \text{s}^{-1}$ and $9.3 \times 10^{-15} \text{cm}^2 . \text{s}^{-1}$, for the samples with y- and z-orientations annealed at 1100°C.

These results are in good agreement with was observed by Buchal *et al.*[3] for Er diffusion in LiNbO$_3$. In the refered article two crystallographic orientations (x- and z-cut) were also investigated, and a preferential diffusion in z-cut was observed.


## 4  CONCLUSION

In the present work we show that:

The Eu diffusion can be enhanced by the amorphous tracks presence. A diffusion length has been estimated as about 65 nm and 120 nm for the samples with y- and z-cut orientations respectively. These values are several times higher than the projected range (Rp = 21 nm) of the implanted particles.

The Eu diffusion is faster in the z-orientation and in this case the diffusion is followed by a significant substitution fraction of these ions in the regular sites.

In summary, our results suggest that the diffusion mechanisms can be correlated with the tracks recrystallization which seems depend on the crystallographic orientation of the samples.

REFERENCES

1. E. Lallier, J. P. Pochole, M. Papuchon, C. Grezes-Besset, E. Pelletier, M. De Micheli, M. J. Li, Q. He and D. B. Ostrowsky, *Electron. Lett.* **25** (1989) 14.
2. R. Brinkmann, W. Sohler and H. Sushe, *Electron. Lett.* **27** (1991) 415.
3. Ch. Buchal and S. Mohr, *J. Mater. Res.*, **6** (1) (1991) 134.
4. M. Fleuster, Ch. Buchal, E. Snoekes and A. Polman, *J. Appl. Phys.*, **75** (1) (1994) 173.
5. D. M. Gill, S. Judy, L. Mc Caughan and & J. C. Wright, *Appl. Phys. Lett.*, **60**(2) (1992) 1067.
6. P. Moretti, B. Canut, S. M. M. Ramos, R. Brenier, P. Thevenard, D. Poker, J. B. M. Da Cunha, L. Amaral and A. Vasquez, *J. Mater. Res.* **8** (10 (1993) 2679.
7. C. Monty and A. Atkinson *Cryst. Latt. Def. and Amorph. Mat*, **18** (1989) 97.
8. A. Atkinson and R. I. Tailor, *Phil. Mag. a* **395** (1979) 581.
9. B. Canut, R. Brenier, A. Meftah, P. Moretti, S. Ould Salem, S. M. M. Ramos, P. Thevenard and M. Toulemonde, to be published in *Nucl. Instr. and Meth.*
10. B. Canut, R. Brenier, A. Meftah, P. Moretti, S. Ould Salem, M. Pitaval S. M. M. Ramos, P. Thevenard and M. Toulemonde, to be published.
11. S. M. M. Ramos private communication.

# OPTICAL STUDY OF DEFECTS IN RbI AND KI BOMBARDED WITH HIGH ENERGY ARGON IONS AT TEMPERATURES BETWEEN 20 K AND 300 K

M. A. PARISELLE,[1] E. HOURDEQUIN,[1,2] J. D. COMINS,[3] E. BALANZAT,[4]
S. LEFRANT[1] and B. RAMSTEIN[5]

[1]*Laboratoire de Physique Cristalline, Institut des Matériaux, 44072 Nantes cedex 03 France;* [2]*Laboratoire de Physique Nucléaire, Faculté des Sciences, 44072 Nantes cedex 03 France;* [3]*Department of Physics, University of the Witwatersrand, Johannesburg, Wits 2050, South Africa;* [4]*CIRIL, rue C. Bloch, BP 5133, 14040 Caen, France;* [5]*Ecole Navale, Lanvéoc Poulmic, 29240 Brest-Naval, France*

RbI and KI crystals have been bombarded with high energy argon ions at temperatures between 20 K and 300 K followed by an *in situ* measurement of the optical absorption. The defect inventory at each temperature has been studied. The efficiency of F centre production in its broad features follows that observed using X-irradiation; the rate is low at 20 K and rises to a maximum at 200 K followed by a decrease at 300 K. The 20 K results for RbI also show the relatively small presence of H centres and di-interstitial halogen aggregates but also significant concentrations of $\alpha$-centres and the complementary I-centres. The results are discussed in the light of the excitonic mechanism and the current ideas concerning the deposition and dissipation of energy in the ion tracks. Micro-Raman spectroscopy has been used to study the concentration profile of halogen aggregates along the ion tracks in samples bombarded at 300 K.

## 1 INTRODUCTION

In principle, a sensitive test of the possibility of altered defect production processes under the extreme conditions of high energy ion bombardment can be made with type I alkali halides such as KI and RbI in which defect production by the excitonic mechanism is very inefficient at low temperatures ($\geq$ 20 K). By making use of the facilities available in the ISOC chamber at GANIL, samples of KI and RbI grown in our laboratory were bombarded with 6.7 MeV/A argon ions at different temperatures between 20 and 300 K, then studied *in situ* after irradiation using a specially adapted optical absorption spectrophotometer over the range 190 to 1200 nm. In a further study, samples bombarded at 300 K with 13.6 MeV/A argon ions were examined exterior to the sample chamber using a Raman microscope facility to evaluate of the concentration profile of defects along the ion tracks. Sets of experiments were performed on RbI and KI; we shall concentrate on the former.

## 2 EXPERIMENTAL RESULTS

Figure 1 shows the absorption spectra of RbI produced by bombardment with argon ions at 20 and 100 K respectively. Defect production rates are conventionally reported in terms of F centres; in this regard the broad patterns observed in X-irradiated RbI (and KI) are preserved. F-centre production is low at 20 K, increases considerably at 100 K, has a maximum rate at 200 K and is significantly reduced at 300 K. However, in assessing the defect inventory produced at 20 K it should be emphasised that the F centres or their complements (H centres and their aggregates) are not the dominant defect form. There is a substantial concentration of $\alpha$ centres as evidenced by the prominent $\alpha$-band at 5.21 eV.
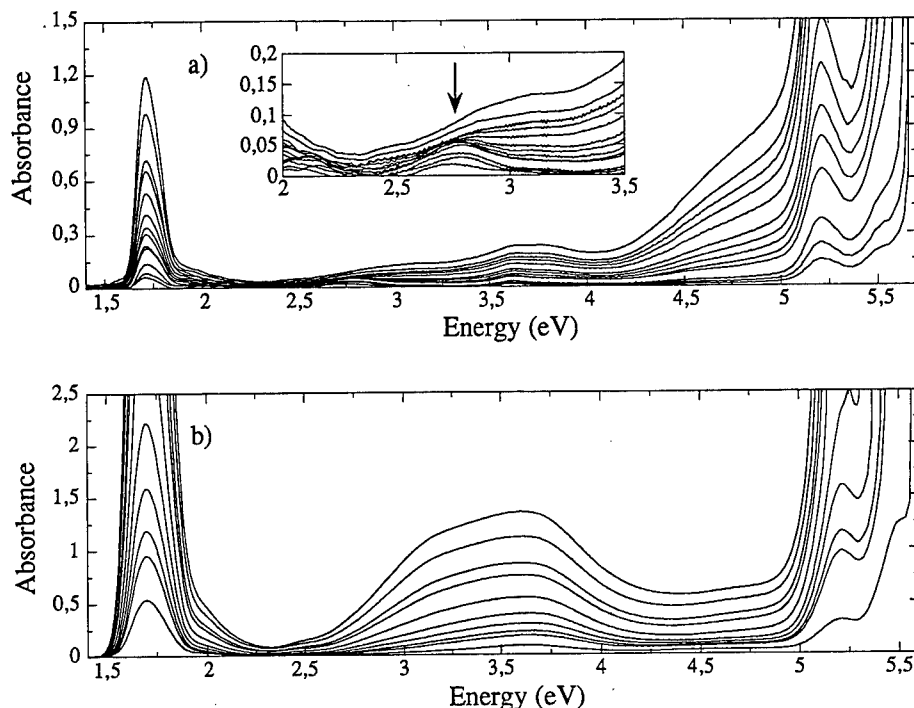
FIGURE 1　The results for samples of RbI bombarded with 6.7 MeV/A argon ions. Optical absorption spectra are made *in situ* at the irradiation temperature. (a) Growth of defects at 20 K. Fluences are from $5.10^{10}$ to $5.10^{12}$ ions/cm$^2$. The arrow in the insert shows the position of the H band. (b) Growth of defects at 100 K. Fluences are from $5.10^{10}$ to $3.10^{12}$ ions/cm$^2$.

Furthermore we suggest that the relatively strong and broad absorption near 4.6 eV is associated with I centres. The responsible defects have a substantial annealing stage between 20 and 35 K consistent with the properties of such centres in alkali halides.[1] In concert with the production of F-centres there is an initial growth of a band 2.8 eV which saturates and leads to a broader and complex V band profile ranging from 2.5 to about 4.2 eV. The 2.8 eV band is identified as being due to the H centre.[2] The identification is supported by the present result H$^2$ $\alpha$ V before saturation of the H band (as found in KBr regarding the H and H$'$ bands[1]). Hence, according to our result, the V band is comprised of di-interstitial halogen. Annealing of the crystal results in complex modifications of the V band profile, suggesting re-organisation of the basic di-interstitial constituents. Annealing to 100 K shows that the profile while being reminiscent of that formed directly at 100 K, does nonetheless show a more structured shape. Unlike the situation in X-rayed KCl and KBr where annealing of samples irradiated at 5 to 77 K show similar concentrations of defects to crystals irradiated to the same dose at 77 K,[3,4] this is not the case for RbI (or KI). The anion vacancy concentration is still biased towards $\alpha$ centres and there is a significant residual absorption near 4.6 eV. Further annealing shows decreases in the $\alpha$ band, 4.6 eV band, V band and F band above about 150 K. This is likely to result from the onset of the mobility of the $\alpha$-centre.

　　The 100 K bombardment shows rather efficient F-centre formation together with a substantial V band profile, the relative contribution of $\alpha$-centres to the total anion vacancy
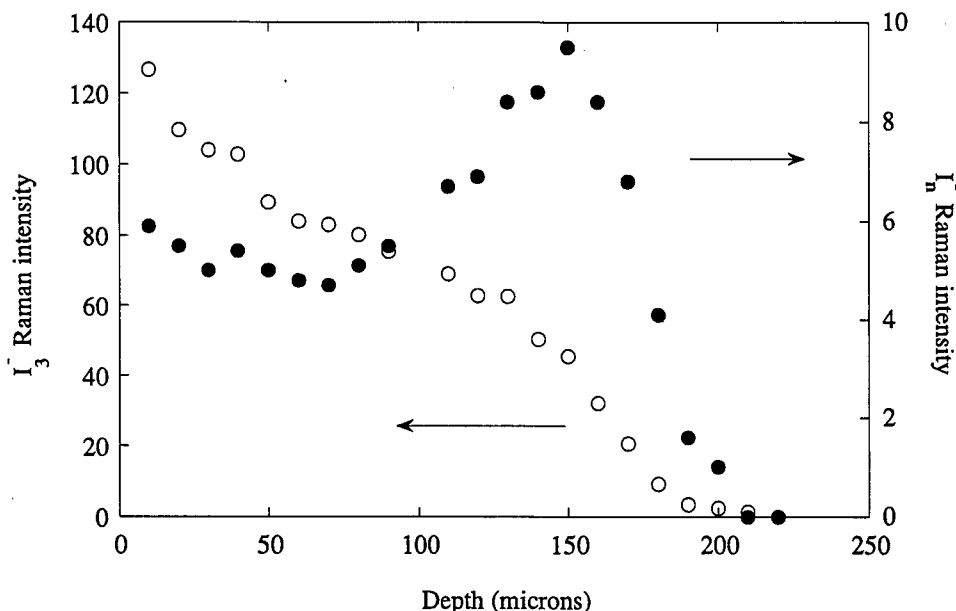
FIGURE 2    Results of the micro-Raman study on RbI bombarded at 300 K to a fluence of $2.10^{13}$ ions/cm$^2$.
Depth profile of the $I_3^-$ centres (empty circles). Depth profile of the ($I_n^-$) centres (full circles). Excitation
wavelength 514.5 nm. Measurements made at 77 K.

concentration is non-negligible, but much less than at 20 K; the I band is not obviously
evident, nor the H band.

Figure 2 shows the micro-Raman results on RbI ion-bombarded to a fluence of $2*10^{13}$
ions/cm$^2$ at 300 K. The defects created are $I_3^-$ (Raman band at 113 cm$^{-1}$) and ($I_n^-$) (Raman
band at 173 cm$^{-1}$) similar to those formed by X-rays at this temperature.[5,6] The depth
profiles show a dominance of the smaller clusters in the region of relatively lower
excitation density but in the region of highest density (the Bragg peak) the ($I_n^-$) clusters are
formed more efficiently.

## 3   DISCUSSION

In evaluating the mechanisms of energy deposition by high energy ions, numerous
complex factors need be considered. These include the processes of energy exchange
between the incoming ion and the alkali halide, the formation of excitons, their radial
movement from the core of the ion track, the creation of $\delta$-rays, the possibility of a thermal
spike, its radial extent and time scales in relation to the characteristic time of defect
creation and finally the role, if any, of direct collisional damage.

Perhaps the most striking feature, considering the above extreme conditions generally
assumed for ion bombardment is the similarity of the results on nominally pure RbI and KI
over an extended range of temperature to those observed with X-rays in pure alkali halides
(there is a relative paucity of information on low temperature X-irradiations of RbI and KI;
we have such experiments currently in progress). Although there are differences in detail,

such as the detailed shapes of the V band profiles for example, the fact that we identify H and I-centres whose low thermal stability is known, a defect production rate which is at least consistent with the predictions of the excitonic mechanism for type I alkali halides (although at 20 K the rate is by no means negligible owing to the $\alpha$-I contribution) indicates that whatever the detailed nature of the complex interactions discussed above, the residual defects and their creation processes appear surprisingly little affected (we note that in impure KI and in the mixed crystal $K_{0,8}Rb_{0,2}I$ more significant differences are observed).

Any successful interpretation must incorporate time scales of the above proposed effects which are consistent with the formation of the measured defects in an otherwise relatively unaffected lattice in which the bulk crystal temperature is relevant to defect formation.

The micro-Raman results demonstrate the favouring of more complex interstitial halogen clusters ($I_n^-$) over the simple di-interstitial form $I_3^-$ in the region of highest excitation density (the Bragg peak). This, we believe, is a convincing demonstration of the basic concepts of interstitial halogen cluster development. Further experiments are in progress to check whether the maximum ($I_n^-$) intensity corresponds accurately to the maximum of the nuclear damage peak.

REFERENCES

1. N. Itoh, *Cryst. Latt. Def.* **3**, 115 ( 1972).
2. H. N. Hersh, *J. Chem. Phys.* **31**, 909 (1959).
3. A. Behr, H. Peisl and W. Waidelich, *Phys. Stat. Solidi* **21**, K9 (1967).
4. J. D. Comins, *Phys. Stat. Solidi* **33**, 445 (1969).
5. S. Lefrant and E. Rzepka, *J. Physique Coll.* **41**, C6–476 (1980).
6. A. M. T. Allen and J. D. Comins, *J. Phys. Condens. Matter* **4**, 2701 (1992).

# SELF-TRAPPED EXCITON LUMINESCENCE UNDER DENSE ELECTRONIC EXCITATIONS: ION-INDUCED TRANSIENT THERMAL EFFECTS

L. PROTIN, E. BALANZAT, S. BOUFFARD, A. CASSIMI, E. DOORYHEE,
J.L. DOUALAN*, C. DUFOUR, J.P. GRANDIN, J. MARGERIE*, E. PAUMIER,
M. TOULEMONDE

*CIRIL, CNRS/CEA BP 5133, 14040 Caen Cedex, France; *ERS 137, CNRS/ISMRa,
14050 Caen Cedex, France*

We have measured the low temperature luminescence of the self-trapped excitons, STE, in NaCl submitted to very dense electronic excitations induced by swift heavy ions. We have compared the features of the excitonic luminescence excited by X-ray and by high energy ion irradiations. The luminescence yield results from a competition between radiative (temperature independent) and non-radiative (temperature dependent) recombinations. For swift heavy ion irradiations, the high density of the deposited energy is supposed to induce a very significant transient temperature increase in the vicinity of the ion path. In this paper we have studied the influence of a thermal spike on the STE luminescence yield. Using numerical computations based on equilibrium thermodynamics, we predict the local increase of the temperature as a function of time t, and of the distance r, from the ion path. At every (r, t) we calculate the temperature induced decrease of the STE non-radiative recombination lifetimes, and we deduce the corresponding changes in the STE luminescence yields. It appears that the numerical predictions of the luminescence yield are very sensitive to the radial extent of the energy deposition, and consequently of the STE concentration. The role of the different parameters and the hypotheses of the calculations are discussed.

*Key words*: Alkali-halides, Self-trapped excitons, Luminescence, Ion irradiation, Thermalspike.

## 1 INTRODUCTION

In the energy range of a few MeV per atomic mass unit (MeV/amu), the stopping of ions in solids is governed by the electronic stopping power $(dE/dx)_e$. For heavy ions, extremely high $(dE/dx)_e$ are reached: a few tens of keV/nm. This huge amount of energy is deposited close to the ion path. New damage processes are induced by this high electronic energy deposition. The most explicit consequence of these new processes is the damage, above a $(dE/dx)_e$ threshold, of materials which are completely insensitive to the ionising component of low $(dE/dx)_e$ particles like electrons or X/γ-rays (radiolysis resistant materials). The experimental results on high $(dE/dx)_e$ damage of radiolysis resistant materials have been recently reviewed.[1,2]

Different models have been proposed for explaining the high $(dE/dx)_e$ damage. The Coulomb explosion[3,4] and the thermal spike[5] have been applied for metallic, semiconductor and insulating targets. For insulators, exciton-exciton interactions have also been considered.[6] In this case, the classical excitonic mechanism of damage is supposed to be modified due to self-trapped exciton (STE)-exciton interactions and/or to STE-STE interactions.

In this work we shall consider the possibility that, in an alkali-halide a thermal spike interferes with the classical excitonic process. Among the radiolysis sensitive materials, the alkali-halides are the materials where the excitonic processes have been the most studied and understood, at least under electron or photon irradiations.[7-9] The radiation generated carriers are efficiently trapped forming the STE. On the one hand, the STE may undergo a
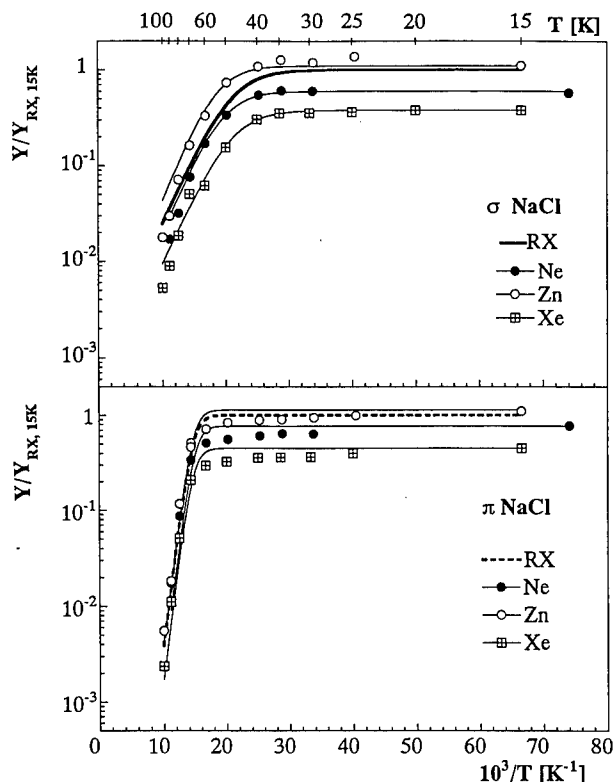
FIGURE 1   Experimental results on the quenching of the STE luminescence in NaCl.[10] The luminescence yields Y are normalised to the X-ray yield at 15 K. See text for the ion irradiation parameters.

dissociative recombination creating a stable $F + H$ Frenkel pair which is possibly converted into an $\alpha + I$ pair. On the other hand, the STE may undergo a radiative recombination giving two luminescence bands $\sigma$ and $\pi$, in most cases.

In a previous work[10] we have studied the STE luminescence at low temperatures $(12 - 100 \text{ K})$ in NaCl and KBr submitted to different swift heavy ion beams. The electronic stopping power was varied from 0.9 keV/nm to 12.5 keV/nm using Ne, Zn, and Xe ions at energies of respectively 12.8, 11.3, and 7.2 MeV/amu. The luminescence induced by X-ray irradiations and by high energy ion irradiations was compared under the same experimental conditions. Increasing the electronic stopping power does not change the spectral features of the STE luminescence in the low fluence regime: it does not appear any new band and the relative amplitude of the $\sigma$ and $\pi$ bands strictly remains constant.[10] Figure 1 shows that the thermal quenching of the luminescence of NaCl is unaffected by $(dE/dx)_e$. Moreover, the yields at 12 K of the ion excited luminescence are close to the yield of the X-ray excited luminescence; the yield for Xe irradiation is just slightly lower. The same observations are valid for KBr.

In this paper we first present the estimate of the thermal spike for a 10 keV/nm irradiation ($\approx$ the Xe case). Further on, we evaluate the effect of the transient temperature increase on the STE luminescence yields. We finally discuss the role of the different parameters and the different hypotheses of the calculations.
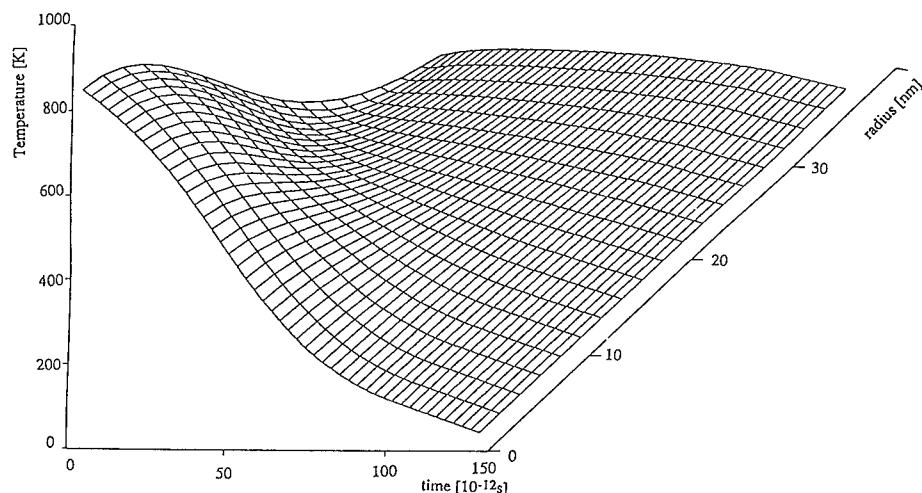
FIGURE 2   Transient local increase of the temperature after a 10 keV/nm ion impact. $\beta = 20$ nm; R = 1. No melting occurs since T < 1073 K: the value of L is consequently irrelevant.

## 2   TRANSIENT TEMPERATURE INCREASE

The transient temperature increase is calculated using the formulation of the thermal spike model proposed by C. Dufour et al..[11,12] We use a simplified form where the heat equation is explicitly solved for the lattice only; an approximate solution is given for the energy deposition on the lattice.[13] We assume that the energy stored in the electronic system is transferred to the atom system providing an exponential dependence in time, characterised by a time constant $\tau$, and a Gaussian dependence in space, characterised by a mean radius $\beta$. Consequently, the rate of the energy density deposition A (r, t) [J nm$^{-3}$ s$^{-1}$] is given by:

$$A(r, t) = R(dE/dx)_e(1/\pi\beta^2) \exp - (r^2/\beta^2)(1/\tau) \exp - (t/\tau) \tag{1}$$

and

$$\int_{t=0}^{\infty} \int_{r=0}^{\infty} A(r, t) 2\pi \, r dr \, dt = R(dE/dx)_e$$

R is a coefficient $\leq 1$, which takes into account the fact that all the energy deposited by the projectile cannot by transferred to the lattice as heat. Part of the energy must be first stored in STE, and later on released onto the lattice by the non-radiative recombinations or lost out during radiative recombinations.

The transient temperature increase is obtained by numerically solving the following heat equation:

$$Cs(T)\left(\frac{\partial T}{\partial t}\right) = \frac{1}{r}\frac{\partial}{\partial r}\left(r \, K(T)\frac{\partial T}{\partial r}\right) + A(r, t) \tag{2}$$

where T is the temperature, Cs the heat capacity, K the thermal conductivity. Cs and K are the measured temperature dependent equilibrium values. The phase changes, melting or

L. PROTIN *ET AL.*
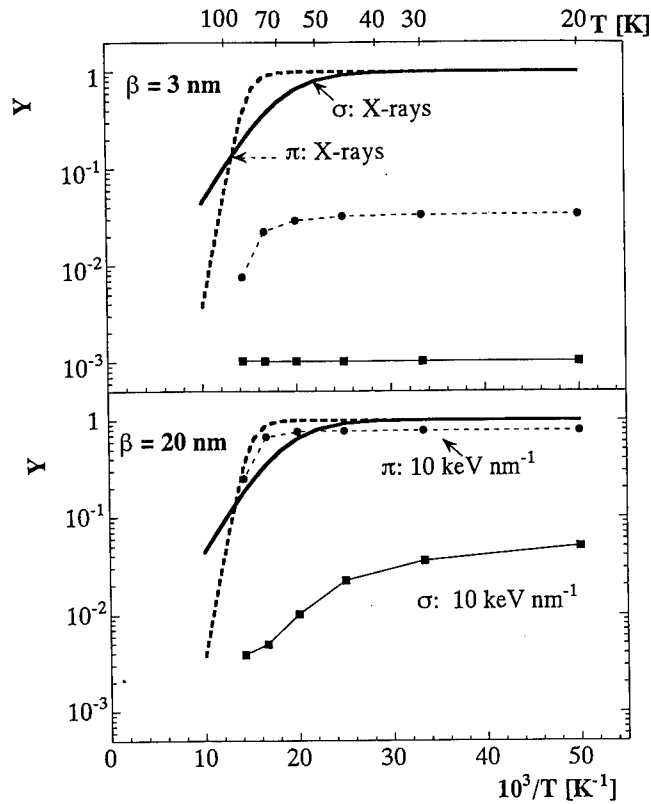


FIGURE 3   Numerical predictions for the quenching of the ion induced STE luminescence for two values of $\beta$; $R = 1$; thermodynamical equilibrium conditions. The results with no thermal spike effect (X-rays), are also reported: the dashed and solid thick curves.

vaporisation, can be taken into account by introducing the corresponding latent heats. Figure 2 shows one example of the predicted space-time evolution of the temperature $T(r, t)$.

## 3   LUMINESCENCE YIELD

The calculation of the $\sigma$ and $\pi$ luminescence yields $Y_\sigma$, $Y_\pi$ is identical. The STE recombination rate $\nu(r, t)$ is the sum of a constant radiative term ($\nu_{r,\pi} = 3.3\ 10^3\ s^{-1}$ and $\nu_{r,\sigma} = 3.3\ 10^8\ s^{-1}$) and a non-radiative term $\nu_{nr}$ which depends on the temperature.

$$\nu(r, t) = \nu_r + \nu_{nr} = \nu_r + \nu_0 \exp(-E_0/kT(r, t)) \tag{3}$$

The STE population $N_{STE}(r, t)$ and the number of emitted photons $Y$ are given by the following differential equations:

$$dN_{STE}(r, t)/dt = -\nu(r, t)N_{STE}(r, t) \quad dY(r, t)/dt = \nu_r\ N_{STE}(r, t) \tag{4}$$

Table I.

Calculated luminescence yields for different parameters of the thermal calculation: R, $\beta$ and phase transitions. $L = L_{eq}$ is for thermodynamical equilibrium latent heats; $L = 0$ when the phase transitions are suppressed. In some cases the sample does not reach the equilibrium melting temperature, the value of L is irrelevant. Left $Y_L$ values are when the best fit to the X-ray data of figure 1 is obtained; $\nu_0$, $\sigma = 3 \ 10^{11} \ s^{-1}$, $E_{0,\sigma} = 32$ meV; $\nu_0$, $\pi = 1 \ 10^{11} \ s^{-1}$, $E_{0,\sigma} = 100$ meV. For the right $Y_L$ values, we have a still acceptable fit with minimum values for $\nu_0$: $\nu_{0,\sigma} = 5 \ 10^{10} \ s^{-1}$, $E_{0,\sigma} = 24$ meV, and $\nu_{0,\pi} = 1 \ 10^{10} \ s^{-1}$, $E_{0,\sigma} = 86$ meV. Bold indicate a rough experiments-numerical predictions agreement.

| Calculation parameters | | | Luminescence yield for a sample initially at 20 K | | | |
|---|---|---|---|---|---|---|
| R | $\beta$ [nm] | L | $Y_\sigma$ | $Y_\pi$ | $Y_\sigma$ | $Y_\pi$ |
| 1 | 3 | $L_{eq}$ | $10^{-3}$ | $3.3 \ 10^{-2}$ | $3.2 \ 10^{-2}$ | 0.68 |
| 1 | 3 | $L = 0$ | $1.9 \ 10^{-3}$ | $4.1 \ 10^{-2}$ | $6.0 \ 10^{-2}$ | 0.74 |
| 1 | 10 | $L_{eq}$ | $2.1 \ 10^{-3}$ | 0.37 | $9.9 \ 10^{-2}$ | 0.83 |
| 1 | 10 | $L = 0$ | $3.8 \ 10^{-3}$ | 0.41 | 0.11 | 0.87 |
| 1 | 20 | no fusion | $5.2 \ 10^{-2}$ | 0.78 | **0.29** | **0.95** |
| 0.5 | 3 | $L_{eq}$ | $1.9 \ 10^{-2}$ | 0.18 | 0.14 | 0.84 |
| 0.5 | 3 | $L = 0$ | $2.6 \ 10^{-2}$ | 0.24 | 0.16 | 0.87 |
| 0.5 | 10 | $L_{eq}$ | $3.5 \ 10^{-2}$ | 0.71 | **0.36** | **0.92** |
| 0.5 | 10 | $L = 0$ | $3.9 \ 10^{-2}$ | 0.73 | **0.39** | **0.9** |
| 0.5 | 20 | no fusion | **0.275** | **0.95** | **0.63** | **0.98** |
| Quenching parameters | | | best fit: ($\nu_0$, $E_0$) | | minimum $\nu_0$ | |

with

$$N_{STE}(r, 0) = (1/\pi\beta^2) \exp(-r^2/\beta^2); \quad \int_{r=0}^{\infty} N_{STE}(r, 0) 2\pi r \ dr = 1 \tag{5}$$

$$N_{STE,\pi}(r, 0) = N_{STE,\sigma}(r, 0) \quad \forall (dE/dx)_e \tag{6}$$

Hence, we have supposed that the initial STE distribution around the ion path (equation 5) is identical to the radial distribution of the energy deposition at $t = 0$ (equation 1); the STE do not migrate during all the time considered. The STE initial number is normalised to one (equation 5). Moreover we consider that $(dE/dx)_e$ does not modify the relative population of the $\pi$ and $\sigma$ STE states (equation 6). Integration of equation 4 gives the luminescence yield Y which can be compared with the experimental results:

$$Y = \int_{r=0}^{\infty} N_{STE}(r, 0) \ 2\pi r \ \nu_r \int_{t=10^{-12}}^{\infty} \exp\left[ -\int_{10^{-12}}^{t'} \nu_{STE}(r, t'')dt'' \right] dt' \ dr \tag{7}$$

We consider that the STE are created $10^{-12}$ s after the ion impact.[14]

For X-ray irradiation the STE recombination rate $\nu$ is not space-time dependent, since there is no thermal spike. Thus equation 7 reduces to the classical formula $Y = \nu_r/\nu$. At the lowest temperatures $\nu \doteq \nu_r$ (equation 3) and $Y = 1$, which is consistent with the normalization done in equation 5 and in Figure 1.

## 4   RESULTS

Several parameters of the calculations are difficult to estimate *a priori*. The most important one is $\beta$. The energy deposited onto the electronic system is, to some extent, spread out

radially away from the ion path by the energetic primary and secondary electrons. The ejection time of the electrons corresponds to the interaction time of the projectile with the target atoms, i.e. around $10^{-17}$ s, the ballistic part of the electronic cascade created by the high energy electrons lasts $10^{-15}$ s. In the time scale of the electronic cascade the energy is still confined around the ion trajectory, since half of the energy is deposited over a few nm: $\approx 2.5$ nm for a 7 MeV/amu irradiation of NaC1.[15] The fate of the excited electrons from t $\approx 10^{-15}$ s, to the self-trapping (t $= 10^{-12}$ s) is poorly understood. In our formulation, this time period is described by equation 1 were $\tau$ represents an electron-phonon time constant, fixed at $10^{-13}$ s. The minimal value for $\beta$ might be the radius of the initial ballistic expansion, *i.e.* $\approx 2.5$ nm, $\beta = 20$ nm is chosen as an upper limit.

It is conceivable that the coefficient R in equation 1 must be very close to one. Only a small fraction of the deposited energy is supposed to be stored in the form of STE. Again, we shall consider R $= 1$ and R $= 0.5$ as extreme values.

The other questionable hypothesis is the use of equilibrium thermodynamics. The most palpable effect of a non-equilibrium situation is a change in the melting temperature (super heating). We shall consider either the equilibrium latent heats or (L $= 0$).

The last degree of freedom concerns the values $\nu_0$ and $E_0$ of equation 3; $\nu_0$ and $E_0$ are obtained by fitting equation 3 to the X-rays experimental data of figure 1. We shall consider two different couples $(\nu_0, E_0)$: the first gives the best fit to the data of Figure 1, for the second couple, $\nu_0$ is fixed to the minimum value which allows an acceptable fit of the Figure 1 data when $E_0$ is adjusted. In fact, during the thermal spike $T(r, t) \gg E_0$ and consequently $\nu_{nr} \approx \nu_0$. Therefore, the value of $\nu_0$ greatly influence the thermal spike effect on the STE luminescence yield.

Figure 3 presents the numerical results for luminescence yield for two $\beta$ values and different substrate temperatures. The $\sigma$ luminescence is much more affected than the $\pi$ luminescence. Experiments (Figure 1) and predictions differ by orders of magnitude. Table I presents the results for the 20 K luminescence yields when changing widely the calculation parameters. A better agreement of the predicted Y with the experimental values is obtained for the lowest value of $\nu_0$, for large values of $\beta$ and for small values of R: a rough agreement between numerical predictions and experiments is only obtained by pushing forward the parameters to what could be considered as extreme values.

## 5   CONCLUSION

Thermal spike calculations carried out with 'classical' parameters over estimate the effect of the transient temperature increase on the non-radiative recombinations of the self-trapped excitons and consequently the predicted decrease of the luminescence yield is too large. However the radial localisation of the self-trapped excitons and the radial expansion of the excited electrons are poorly defined. The relevance of the thermal spike model cannot definitely be proved by this procedure.

REFERENCES

1.  E. Balanzat, Radiat. *Eff. and Defects in Solids* **126** (1993) 97.
2.  A. Dunlop and D. Lesueur, *Radiation Eff. and Defects in Solids* **126** (1993) 123.
3.  R. Fleisher, P. B. Price and R.M. Walker—*Nuclear tracks in solids—Principles and Applications—* University of California Press, Berkeley (1975).
4.  D. Lesueur and A. Dunlop, *Radiation Eff. and Defects in Solids* **126** (1993) 163.
5.  F. Seitz and J. S. Koelher, *Solid State Physics* **2** (1956), Ed by F. Seitz and D. Turnbull.

6.  N. Itoh, *Radiation Eff. and Defects in Solids* **110** (1989) 19.
7.  *Defect Processes Induced by Electronic Excitations in Insulators*, Ed. N. Itoh, (World Scientific, Singapore, 1989).
8.  N. Itoh and K. Tanimura, *J. Phys. Chem. Solids* **51** (1990) 717.
9.  R. T. Wiliams and K. S. Song, *J. Phys. Chem. Solids* **51** (1990) 679.
10. E. Balanzat, S. Bouffard, A. Cassimi, E. Doorhyee, L. Protin, J. P. Grandin, J. L. Doualan and J. Margerie, *Nucl. Instr. and methods* **B91** (1994) 134.
11. C. Dufour, B. Lesellier De Chezelles, V. Delignon, M. Toulemonde and E. Paumier, *Modifications induced by irradiation in glasses*, P. Mazzoldi Ed., Elsevier, (1992) 61.
12. Z. G. Wang, Ch. Dufour, E. Paumier and M. Toulemonde *J. Phys.: Condensed Matter* (1994) in press.
13. M. Toulemonde, C. Dufour and E. Paumier, *Phys. Rev.* **B46** (1992) 14362.
14. K. S. Song and R. T. Williams, Self-Trapped excitons, *Springer Series in Solid-State physics* **105**, (1993) 209.
15. M. P. R. Waligorski, R. N. Hamm and R. Katz, *Nucl. Tracks Radiat. Meas.* **11** (1986) 309.

# RAMAN AND OPTICAL ABSORPTION STUDIES OF THE ANNEALING OF γ-IRRADIATED KI AND KI (Sr)

J. D. COMINS,[*+] A. M. T. ALLEN,[*] E. RZEPKA[+] and S. LEFRANT[+]

[*]*Department of Physics, University of the Witwatersrand, Johannesburg, Wits 2050, South Africa;* [+]*Laboratoire de Physique Cristalline, Institute des Matériaux de Nantes, 2 rue de la Houssinière, 44072 Nantes Cedex 03, France*

Crystals of KI (pure) and KI (Sr) have been γ-irradiated at room temperature to doses between 250 and 1000 Mrad, then subjected to a variety of annealing routines. The annealing behaviour, the shape of the V-bands and their evolution, and the formation of potassium colloids depends on the presence of impurities and dislocation structures. Insights are provided by the alteration in the lattice mode structure of large $(I_2)_n$ aggregates for KI (pure) irradiated to 1000 Mrad.

The results are examined with regard to previous considerations of the annealing of alkali halides.

*Key words*: Colour centres, Irradiation damage, Annealing.

## 1 INTRODUCTION

The dominant halogen aggregates formed by prolonged irradiation of KI crystals near 300 K are large $(I_2)_n$ clusters. The resulting V-band profile and 180–189 cm$^{-1}$ Raman doublet have been previously studied.[1-4] The present annealing studies provide new information regarding the role of divalent impurities, dislocation structures, the morphology of the halogen clusters and the formation of colloids.

## 2 EXPERIMENTAL PROCEDURES

KI (pure) and KI (0.01 mol% Sr) crystals were γ-irradiated to 250 Mrad for the isochronal, isothermal and step annealing experiments to determine the kinetics, order of reaction and to monitor the evolution of the defects using optical absorption and Raman spectroscopies. KI (pure) crystals were also γ-irradiated to 1000 Mrad to examine their annealing behaviour.

## 3 RESULTS

For the 250 Mrad irradiations the V-band profile for KI (Sr) was relatively unstructured while that for KI (pure) had more structure. The F:V band peak absorption ratio also differed for the two crystals.

Figures 1 and 2 show the isochronal annealing results for the various defects and the 180 cm$^{-1}$ Raman feature for the different crystals. The KI (Sr) annealing processes are relatively simple, have an activation energy of 1.4 eV, are of first order, and do not involve potassium colloid formation. The 180 cm$^{-1}$ Raman feature due to the $(I_2)_n$ aggregates decayed concurrently. The annealing process in KI (pure) is more complex. The V-band decay occurs in two stages (I and II), the first of which correlates with the decay of the $(I_2)_n$ aggregates measured by Raman spectroscopy. F-band decay starts during stage I and potassium colloid formation also occurs, but accounts for only a fraction of the F-centres
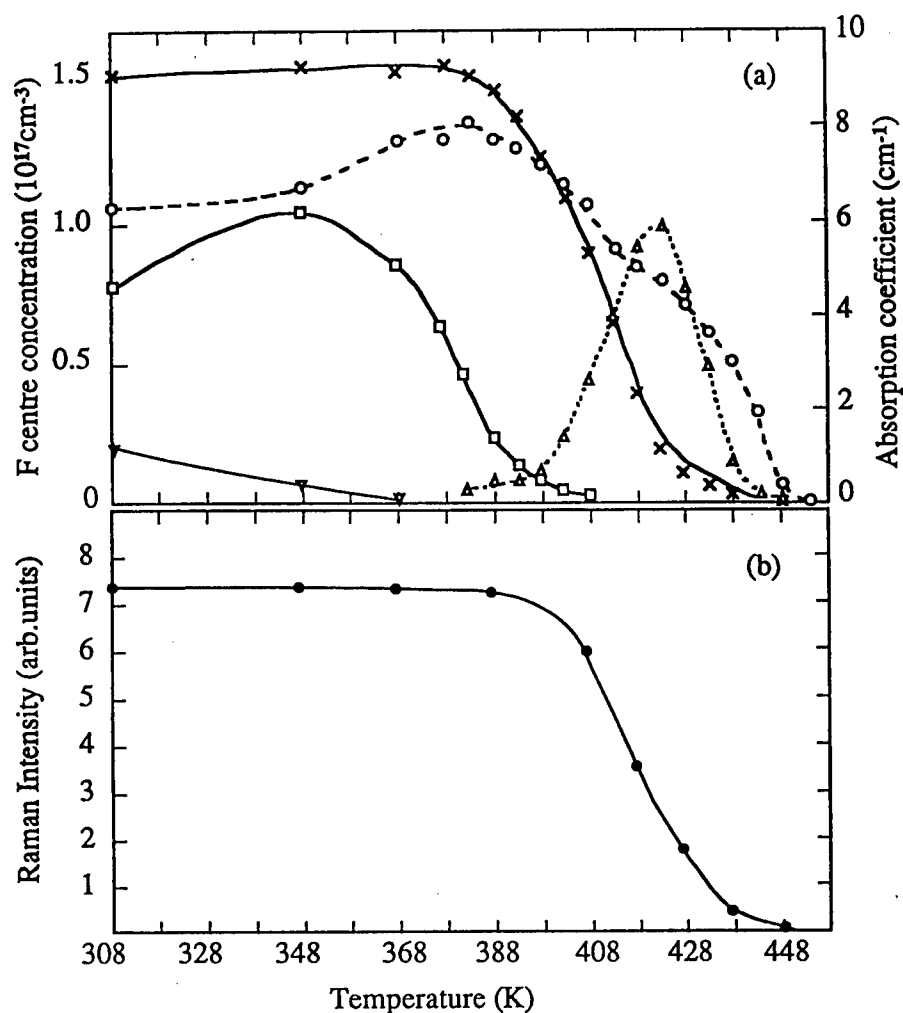
FIGURE 1(a)　Results of isochronal annealing experiments on KI (pure), $\gamma$-irradiated at 295 K to 250 Mrad. Crosses: F- centre concentration; open circles: V-band absorption coefficient; open squares: $F_2$-band absorption coefficient; inverted open triangles: $F_3$-band absorption coefficient; open triangles: potassium colloid band absorption coefficient. Spectra measured at 80 K. (b) Isochronal annealing of $(I_2)_n$ clusters measured by the intensity of the 180 cm$^{-1}$ Raman band for KI (pure) treated as for (a). Excitation wavelength 488 nm. Spectra measured at 80 K.

which are annealed. The activation energy spectrum from a Primak analysis shows two peaks at 1.76 eV (for F-centre and stage I V-band decay) and 1.86 eV (for stage II V-band and colloid decay).

In Figures 3a and b we present the Raman spectra for KI (pure), $\gamma$-irradiated to a dose of 1000 Mrad. Besides the intense 180–189 cm$^{-1}$ signature of $(I_2)_n$ clusters, there is the lattice mode structure of crystalline iodide;[4] peaks are observed at 54, 75, 85, 213, 239 and 265 cm$^{-1}$. Figure 3b shows the effect of annealing to 410 K, close to the midpoint of the
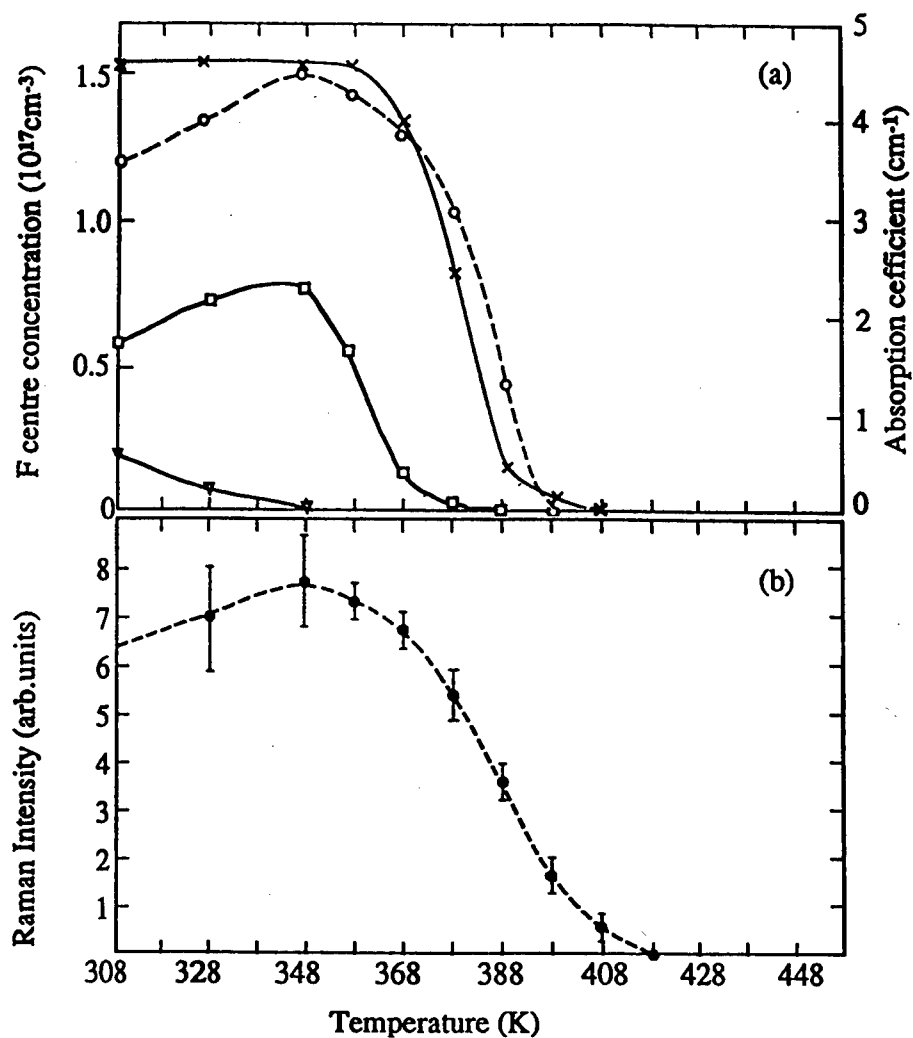
FIGURE 2(a) Results of isochronal annealing experiments on KI (Sr). Treatments and symbols as in Figure. 1(a). (b) Isochronal annealing of $(I_2)_n$ clusters measured by the intensity of the 180 cm$^{-1}$ Raman band for KI (Sr) treated as in (a). Excitation wavelength 488 nm. Spectra measured at 80 K.

180 cm$^{-1}$ Raman band decay shown in Figure 1b. There is a substantial decrease in the 180–189 cm$^{-1}$ doublet and the spectrum of lattice modes is greatly altered.

## 4 DISCUSSION

The simple nature of the annealing process in KI (Sr) with a single activation of 1.4 eV and first order kinetics indicates a relatively uniform nature of the responsible $(I_2)_n$ clusters.
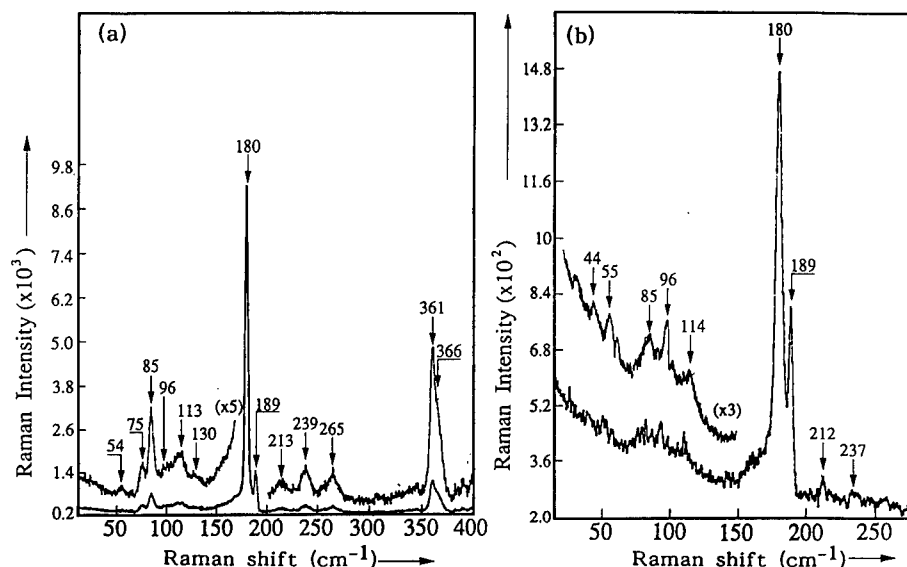
FIGURE 3(a)   Raman spectrum of KI (pure) $\gamma$-irradiated at room temperature to 1000 Mrad. Measurement temperature 78 K, excitation wavelength 488 nm, resolution 4 cm$^{-1}$. Iodine lattice modes at 54, 75, 85, 213, 239 and 265 cm$^{-1}$. (b) Raman spectrum after annealing to 410 K.

The lower temperature of the annealing in KI (Sr) as compared with KI (pure) indicates that the stabilisation mechanism of the $(I_2)_n$ is different; this is compatible with nucleation and growth of the clusters at I-V dipoles or their aggregates.[5] The structured shape of the V-band in KI (pure), the range of activation energies in two stages of annealing and the different F:V absorption ratio suggests structural and morphological differences in the responsible $(I_2)_n$ clusters. If, for example, the absorption is concerned largely with the peripheral regions of a cluster, the detailed geometry could have a marked effect. The formation of colloids is considered to result from the presence of dislocation structures in the crystal.

The stage I annealing processes in KI (pure) are further elucidated by the alteration of the lattice modes as seen in the 1000 Mrad irradiated specimen (Figures 3a and b); in addition a large reduction in the 180–189 cm$^{-1}$ Raman doublet occurs. This clearly shows that the iodine crystallites formed by self-organisation of the $(I_2)_n$ clusters at high irradiation doses are being destroyed. Residual small iodine clusters which have a larger surface to volume ratio could have significant optical absorption from their peripheral regions, but very weak Raman signals. In stage II, these residual V-centres mutually annihilate with the colloids formed from F-centres in stage I with a higher activation energy in the range 1.8 to 1.9 eV. The results re-interpret the previous studies of annealing in irradiated alkali halides.[7-9]

REEFERENCES

1.   S. Lefrant and E. Rzepka, *J. Phys. C* **12**, L573 (1979).
2.   E. Rzepka, M. Bernard, S. Lefrant and J. D. Comins, *Cryst. Lett. Def. and Amorph. Mat.* **17**, 113 (1987).

3.   A. M. T. Allen and J. D. Comins, *J. Phys. Condens. Matter* **4**, 2701 (1992).
4.   E. Rzepka, J. L. Doualon and L. Taurel, *J. Phys.* **C16**, 4769 (1983).
5.   J. D. Comins and B. O. Carragher, *Phys. Rev.* **B24**, 283 (1981).
6.   B. V. Shanabrook and J. S. Lannin, *Solid State Commun.* **38**, 49 (1981).
7.   A. B. Lidlard, *Comments Solid State Phys.* **8**, 73 (1978).
8.   A. E. Hughes, *Comments Solid State Phys.* **8**, 83 (1978).
9.   C. R. A. Catlow, K. M. Diller and L. W. Hobbs, *Phil. Mag.* **A42**, 123 (1980).

# A COMPARATIVE STUDY OF GLOW CURVES IN PHOTO-TRANSFERRED AND PRE-DOSE SENSITIZED THERMOLUMINESCENCE (PTTL AND TL) IN LiF:Mg, Ti

T. M. PITERS,* E. M. YOSHIMURA, C. M. SUNTA,** E. OKUNO, N. K. UMISEDO
and M. P. DIAZ***

*Instituto de Física-Universidade de S. Paulo; Caixa Postal 66318, CEP 05389-970
S. Paulo, Brasil; *Centro de Investigación en Física- Universidad de Sonora; Apdo.
Postal 5-088, 83190 Hermosillo, Sonora, México; **Atomic Energy Regulatory Board,
V. S. Bhavan; Anushaktinagar, Bombay-400094, India; ***Instituto Astronômico e
Geofisico; Caixa Postal 9638, CEP 04301-904, S. Paulo, Brasil*

The glow curves of pre-dosed LiF:Mg,Ti samples irradiated with gamma rays and UV light are investigated by means of glow curve de-convolution. The results are discussed in terms of a partly interactive trap system proposed earlier. Our results show that thermoluminescence (TL) of the samples irradiated with UV light is supralinear with pre-dose and suggest that TL in these samples is mainly due to interactive traps. The glow curve of the gamma irradiated samples consists of two parts due to interactive and non interactive traps with slightly different trapping parameters. The TL contribution of the non interactive traps is approximately constant while the contribution of the interactive traps is sublinear with pre-dose.

*Key words*: thermoluminescence, photo-transfer, sensitization, supralinearity, LiF(Mg, Ti), PTTL., TL.

## 1  INTRODUCTION

Recent models about the dose response of thermoluminescent materials[1–4] have explained supralinearity in LiF:Mg,Ti, assuming a competitive capture of released charge carriers into deep traps during heating. The thermoluminescence process during heating is shown schematically in Figure 1. During irradiation, deep and active traps are filled and luminescent centers are created. So, with increasing dose the number of available deep traps decreases while the number of luminescent centers increases causing an increase of the thermoluminescence (TL) signal greater than linear (supralinearity). To account for the observed linear dose response of LiF:Mg,Ti in the low dose range it is assumed that only a part of the active traps interacts with the deep traps (Partly Interactive Trap System (PITS)). In the theory of Mische and McKeever[1] the non interactive traps are thought to be paired with the luminescent centers.

Recently the PITS model has also been used to explain the pre-dose sensitization effect.[4,5] Sensitization is obtained when pre-dosed samples are heated in such way that the active traps are emptied and the deep traps are left intact. Now, if a small test dose is given to the samples, the active traps are filled again. During the readout (measurement of TL during heating) the probability of the capture of released charge by deep traps will be much less than in the case of virgin (i.e. not pre-dosed) samples because the number of available deep traps is much less. This causes an enhancement of the TL signal compared to the virgin samples.

If pre-dosed LiF:Mg,Ti samples are irradiated with UV light instead of ionizing radiation, a photo transference of charge carriers from deep to active traps takes place. The situation during the readout is expected to be similar to that of the samples irradiated with a

Conduction band
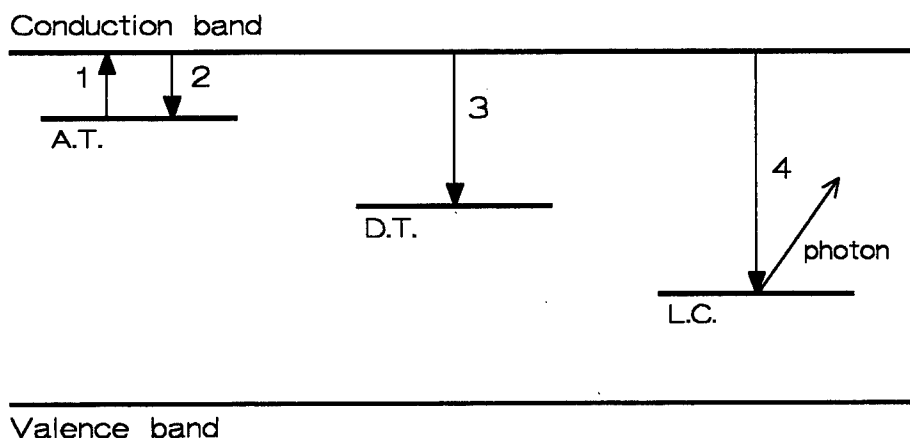


FIGURE 1   Energy level diagram in solids with active trap (AT), deep trap (DT) and luminescent center (LC). Transition 1 is the release of charge carriers during heating. They can be recaptured (transition 2) or captured by deep traps (transition 3) or by luminescent centers producing a photon (transition 4).

small test gamma dose. A comparative study of not sensitized TL, pre-dose sensitized TL and photo- transferred TL (PTTL) provides a possibility to verify these ideas.

## 2   MATERIALS AND METHODS

The samples used were LiF:Mg,Ti (Harshaw TLD-100 ribbons). They were submitted to a standard anneal of 400°C for one hour and 100°C for two hours followed by a quick cool to room temperature (see Table (I)). Then they were pre-dosed with a $^{60}$Co source (doses between 0 Gy and 1 kGy). Peaks 2, 3, 4 and 5 were cleaned by a heating until 350°C at a heating rate of 1°C/s. After this they received a low UV dose (at a distance of 4 cm from a 4W UV mineral lamp for 30 s) or a gamma test dose (100 mGy of a $^{60}$Co source). The TL was monitored by a photon-counting system at a heating rate of 1°C/s. The TL signal as a function of temperature (glow curve) was de-convoluted assuming first order kinetics (Randall Wilkins model).

## 3   RESULTS AND DISCUSSION

Figure 2 shows the glow curves of the samples after the treatments of Table (I). Figure 2A shows the TL glow curve of a virgin sample (treatment A of Table (I)). The parameters of the de-convoluted peaks 2, 3, 4 and 5 are shown in Table (II) column (a). Figures 2B and 2C correspond to the TL and PTTL glow curves of pre-dosed (100 Gy) samples (treatments B and C in Table (I)). The shape of the PTTL glow curves is similar for all the pre-doses while for the TL glow curves the shape shows a strong pre-dose dependence (i.e. peak 2, 3 and 5 become sensitized and peak 4 not). Also we observed that for high pre-doses (> 500 Gy) the TL and PTTL glow curves are similar.

The solid curves in Figures 2B and 2C are the results of simultaneous fittings of 5 glow curves of samples with different pre-doses (3 Gy, 50 Gy, 100 Gy, 500 Gy and 1000 Gy). During the fitting, the activation energies $E$ and frequency factors $s$ of each peak were
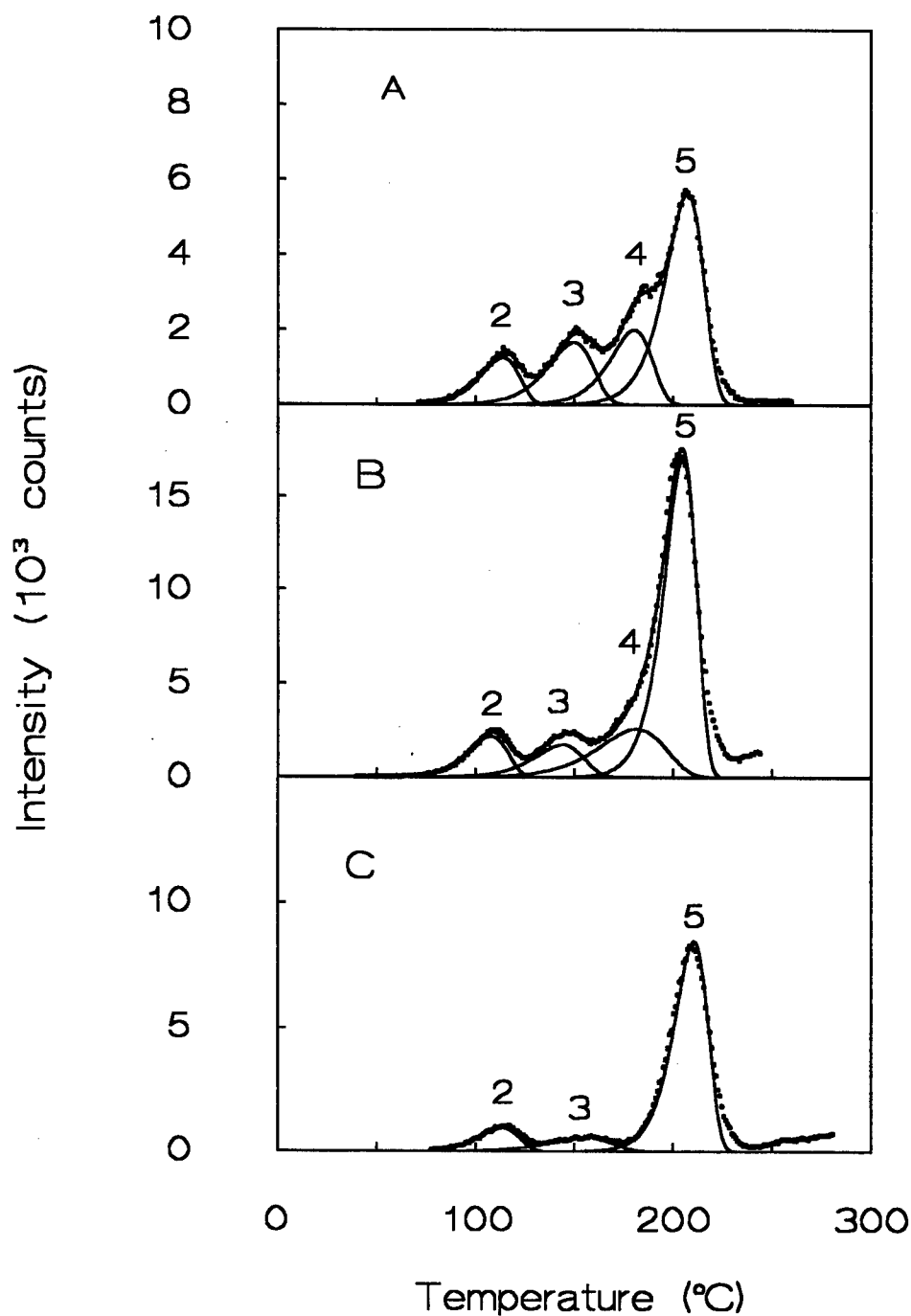
FIGURE 2   TL glow curve of LiF:Mg,Ti(TLD-100) for (A) virgin sample irradiated with a gamma test dose of 100 mGy (treatment A in Table I), (B) pre dosed (100 Gy) sample after irradiation with a 100 mGy gamma test dose (treatment B in Table I), and (C) pre-dosed (100 Gy) sample after UV irradiation (treatment C in Table I). The points are experimental results and the solid lines are the glow peaks according to first order kinetics obtained by a fit of (A): one glow curve, (B) and (C): five glow curves simultaneously.
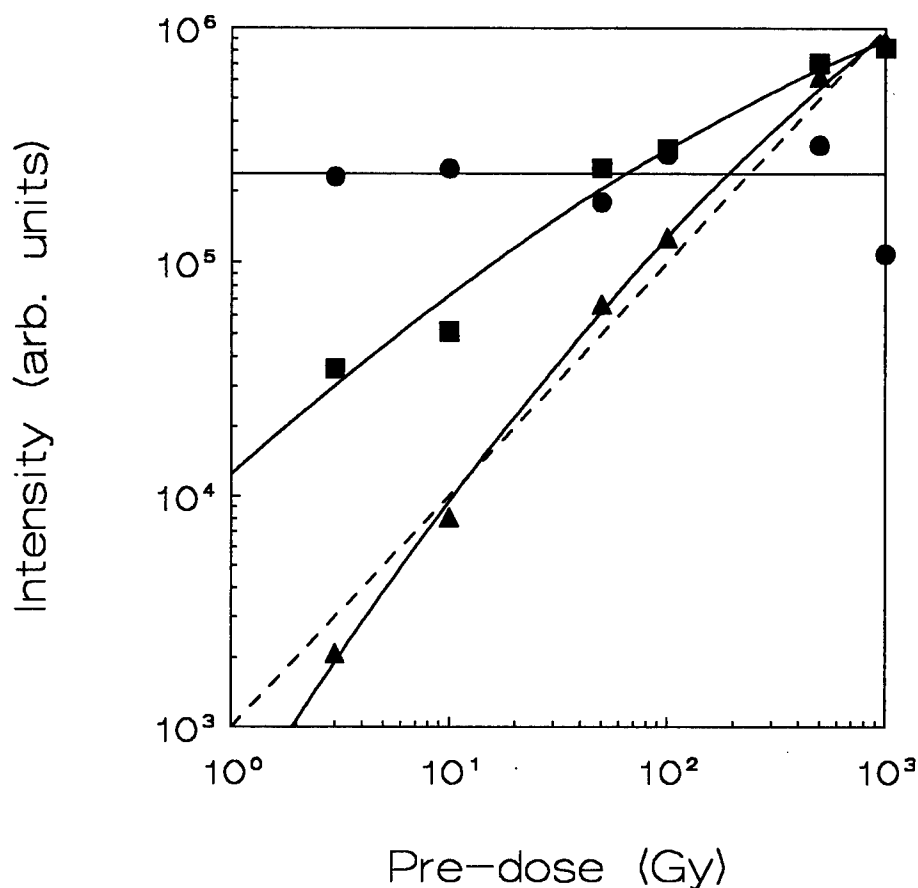
FIGURE 3    Contributions of interactive (■) and non interactive (●) traps to the total TL signal as function of pre-dose. The PTTL intensity as function of pre-dose is mainly due to the interactive traps (▲). The dashed line corresponds to a linear behavior.

adjusted but kept equal for all five glow curves. The glow curves were allowed to shift in temperature to account for different thermal contact.

Table I
Characteristics of the experimental steps applied on different samples. Step 1: The initial annealing procedure. Step 2: The sensitization irradiation dose (pre-dose). Step 3: The maximum temperature of the first heating to clean peaks 2 to 5. Step 4: The test dose. Step 5: The measurement of thermoluminescence.

| | step 1 | step 2 | step 3 | step 4 | step 5 |
|---|---|---|---|---|---|
| A | 1h 400°C + 2h 100°C | 0 Gy | 350°C | 100 mGy | TL |
| B | 1h 400°C + 2h 100°C | 3-1000 Gy | 350°C | 100 mGy | TL |
| C | 1h 400°C + 2h 100°C | 3-1000 Gy | 350°C | UV | PTTL |

The TL glow curves of the pre-dosed samples (Figure 2B) were fitted with four peaks (see Table (II) column (b)), but despite of tedious fitting we could get no satisfactory result

($\chi_r^2 = 1.69$, which is far out of the 99% confidence interval $0 < \chi_r^2 < 1.28$). The PTTL glow curves (Figure 2c) were fitted with 3 peaks (see Table (II) column (c)) with a good result ($\chi_r^2 = 0.82$). However, the values of the parameters $E$ and $s$ differ significantly from those of the virgin sample (Table (II) column (a)).

Table II

Fitting parameters $E$ (eV) and $s$ (s$^{-1}$) of LiF:Mg,Ti (TLD-100) after treatments A, B and C of Table (I). The parameters are obtained by (a): fitting of a single glow curve, (b) and (c): simultaneous fitting of 5 glow curves with 5 different pre-doses, (d) simultaneous fitting of the same 5 glow curves as in (b), adding to them the 3 peaks of column (c), whose peak parameters and relative intensities are kept constant.

| peak | (a) gamma (A) | | (b) gamma (B) | | (c) UV (C) | | (d) gamma (B) | |
|---|---|---|---|---|---|---|---|---|
| | E | ln(s) | E | ln(s) | E | ln(s) | E | ln(s) |
| 2 | 1.32 | 37.3 | 1.25 | 35.9 | 1.27 | 35.7 | 1.31 | 37.0 |
| 3 | 1.34 | 34.5 | 1.20 | 30.8 | 1.02 | 24.9 | 1.37 | 35.3 |
| 4 | 1.70 | 41.1 | 1.04 | 23.7 | – | – | 1.67 | 40.4 |
| 5 | 2.06 | 47.5 | 2.43 | 56.9 | 2.36 | 54.5 | 2.16 | 50.0 |

These observations can be explained in terms of a PITS if it is assumed that during UV irradiation only interactive traps (spatially disconnected from luminescent centers) are filled and during gamma irradiation interactive as well as non interactive traps (spatially connected to luminescent centers) are filled. It is expected that the trapping parameters of non interactive and interactive traps differ slightly because of a different lattice configuration around the trap. This explains why the peak parameters are different for the PTTL glow curves (mainly interactive traps) and TL glow curves of virgin samples (mainly non interactive traps). At high pre-doses one expects that deep traps are filled and that the contribution of the interactive traps to the glow curve becomes dominant, giving rise to a similar shape for the TL and PTTL glow curves. It also explains why it is not possible to fit the TL glow curves of low and high sensitized samples simultaneously with only four peaks. To verify these ideas we have fitted again the TL glow curves including the interactive traps obtained from the fitting of the PTTL glow curves (Table (II), column (c)). The relative concentrations of the interactive traps are kept equal to those obtained by fitting the PTTL glow curves. A $\chi_r^2$ of 1.04, which is well within the 99% confidence interval, was obtained using this procedure. The peak parameters associated to the non interactive traps obtained in this fit are shown in column (d) of Table (II). From Table (II) it is seen that the values of these non interactive peak parameters are very close to those of the virgin sample (column (a)) which are supposed to be due mainly to non interactive traps.

In Figure 3 the contributions of the interactive and non interactive traps to the total TL and PTTL signal (sum of peaks 2, 3, 4 and 5) are shown as function of the pre-dose. It is seen that the contribution of the non interactive traps in the TL signal is almost constant as expected from a PITS. The contribution of the interactive traps increases sub-linearly with pre-dose for the TL signal and supralinearly-sublinearly for the PTTL signal.

REFERENCES

1. E. F. Mische and S. W. S. McKeever, *Radiat. Prot. Dosim.* **29**, 159 (1989).
2. S. W. S. McKeever, *Radiat. Prot. Dosim.* **33**, 83 (1990).
3. Y. S. Horowitz, *Radiat. Prot. Dosim.* **33**, 75 (1990).
4. C. M. Sunta, E. M. Yoshimura, and E. Okuno, *J. Phys. D: Appl. Phys.* **27**, 852–860 (1994).
5. C. M. Sunta, E, Okuno, J. F. Lima and E. M. Yoshimura, *J. Phys. D: Appl. Phys.* **27**, 2636–2643 (1994).

# LATENT TRACK FORMATION IN LiNbO₃ SINGLE CRYSTALS IRRADIATED BY GeV URANIUM IONS

B. CANUT,[1] R. BRENIER,[1] A. MEFTAH,[2] P. MORETTI,[1] S. OULD SALEM,[1]
M. PITAVAL,[1] S. M. M. RAMOS,[1] P. THEVENARD[1] and M. TOULEMONDE[2]

[1]*Département de Physique des Matériaux (URA CNRS 172), Université Claude Bernard
LYON I, 69622 VILLEURBANNE Cédex, France;* [2]*Centre Interdisciplinaire de
Recherches avec les Ions Lourds, GANIL, Bd. A. Becquerel, 14040 CAEN Cédex, France*

Single crystals of LiNbO₃ (Y-cut orientation) have been irradiated at GANIL with ²³⁸U ions using three different energies: 0.84, 2.01 and 2.73 MeV/a. All the irradiations were performed at room temperature, up to a fluence of $4 \times 10^{11}$ ions.cm⁻². The lattice disorder resulting from the high electronic stopping power (between 28 and 40 keV/nm) has been characterized by Rutherford backscattering spectrometry in channeling geometry (RBS-C), in conjunction with high resolution transmission electron microscopy (HRTEM). According to RBS-C analysis, the damage cross-section $\sigma_d$ depends on the electronic stopping power of the incident ions and a velocity effect is observed. HRTEM observations show a damage morphology consisting mainly of cylindric amorphous zones (latent tracks) having a mean core radius of about 2 nm.

*Key words*: Lithium, Niobate, Irradiation, Uranium, Disorder, Track.

## 1 INTRODUCTION

It has been proved for many years that radiolysis resistant insulators can be damaged by collective electronic excitations resulting from heavy ions irradiations in the GeV range.[1,3] In a recent study,[4] Canut *et al.* reported that ¹⁵⁵Gd ions of a few MeV/a energy induce extended defects in monocristalline LiNbO₃. The aim of this paper is to confirm such an effect by means of ²³⁸U irradiations in the same range of energy. Complementary analysis techniques have been used, in order to get informations about the relative disorder and the damage morphology of the irradiated samples.

## 2 EXPERIMENTAL PROCEDURE

Single crystals of LiNbO₃ (Y-cut orientation) have been irradiated at GANIL with ²³⁸U ions using three different energies: 0.84, 2.01 and 2.73 MeV/a. The corresponding electronic stopping powers $(\frac{dE}{dx})e$ were of 28.1, 37.2 and 39.6 keV/nm respectively. All the irradiations were performed at room temperature, with fluences extending from $10^{11}$ to $4 \times 10^{11}$ ions.cm⁻². The lattice disorder has been characterized by Rutherford back-scattering spectrometry in channeling geometry (RBS-C), using a 2 MeV ⁴He⁺ beam generated by a Van de Graaff accelerator. High resolution transmission electron microscopy (HRTEM) was performed using a TOP CON 002B equipment, operating at 200 kV and offering a resolution of 0.18 nm.

## 3 RESULTS

As an example, Figure 1 displays the RBS-C spectra (curves a, b and c) recorded on a sample irradiated at increasing fluences with ²³⁸U ions of 2.01 MeV/a energy. For
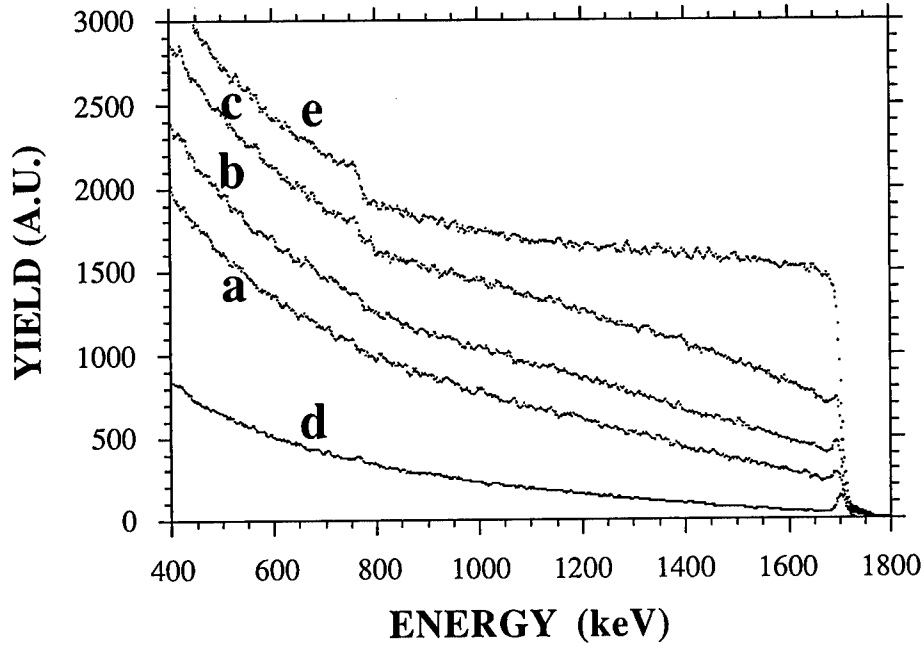
**FIGURE 1**    RBS spectra for LiNbO$_3$ irradiated with $^{238}$U ions of 2.01 MeV/a incident energy. (a) $10^{11}$ ions.cm$^{-2}$ (aligned), (b) $2 \times 10^{11}$ ions.cm$^{-2}$ (aligned), (c) $4 \times 10^{11}$ ions.cm$^{-2}$ (aligned), (d) virgin sample (random) and (e) virgin sample (aligned). Analysis conditions : 2 MeV $^4$He$^+$ ions; detection angle = 150°.

comparison, the aligned (curve d) and random (curve e) spectra corresponding to a pristine crystal are also presented. The fluence-dependent increase of the backscattering yield in channeling conditions is related to extended defects induced by the irradiations. Such an effect, already observed after Gd bombardment,[4] is necessarily imputable to the high electronic energy losses of the incident ions. As a matter of fact, the nuclear processes may be regarded here as negligible in damage creation $((\frac{dE}{dx})_n \approx 10^{-3}.(\frac{dE}{dx})_e$ at the sample surface). For each incident energy the relative disorder $\alpha$, deduced from RBS-C data, has been plotted versus the irradiation fluence $\Phi_t$ in Figure 2. The experimental points have been fitted satisfactorily by a Poisson's law (dashed lines) resulting from a direct impact model:[5]

$$\alpha = 1 - \exp(-\sigma_d.\Phi_t)$$

where $\sigma_d$ is the damage cross section. The respective $\sigma_d$ values for 0.84, 2.01 and 2.73 Me V/a energies are the following : (i) $1.30 \times 10^{-12}$ cm$^{-2}$, (ii) $1.40 \times 10^{-12}$ cm$^{-2}$ and (iii) $1.24 \times 10^{-12}$ cm$^{-2}$. These damage cross sections are nearly two times higher than the ones measured previously by using $^{155}$Gd ions irradiations. This is evidently due to the higher $(\frac{dE}{dx})_e$ values associated to $^{238}$U bombardments. However, the present results show that the highest damage cross section does not correspond to the highest electronic stopping power. According to Meftah *et al.*,[6] at a given $(\frac{dE}{dx})_e$, $\sigma_d$ increases conversely with the ion velocity. For this reason, the highest efficiency for disorder creation results from the best compromise between a high electronic stopping power and a low velocity of the incident ions.
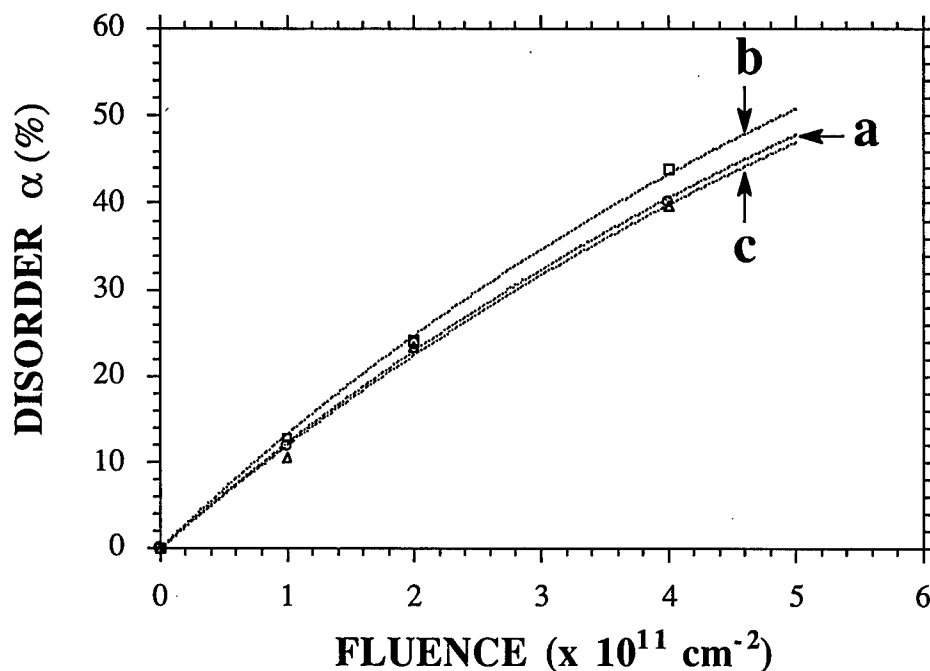
FIGURE 2 Fluence dependence of the relative disorder $\alpha$ in irradiated LiNbO$_3$. (a) 0.84 MeV/a, (b) 2.01 MeV/a and (c) 2.73 MeV/a. The dashed lines correspond to the best fits of the experimental data, by using a Poisson's law (see text).

On the basis of similar studies performed on magnetic insulators,[7] it was expected that the disorder in irradiated LiNbO$_3$ should consist mainly of amorphous tracks surrounding each incident particle trajectory. This assumption has been confirmed by HRTEM observations. The micrograph presented in Figure 3 corresponds to a typical plane view of a bombarded LiNbO$_3$ surface (irradiation conditions:10$^{11}$ U ions.cm$^{-2}$ of 2.01 MeV/a energy). In this example, the track radius has been found to be about r = 2 nm. Surprisingly, this value is three times lower than the one deduced from damage cross section measurements ($\sigma_d = \pi.r^2$). Such a discrepancy may be explained by assuming the presence of two components in the track:

(i) A core region of low diameter. This first component is amorphous and responsible to the major part of the contrast in microscopic observations.

(ii) A surrounding crown region of higher diameter. This second component would consist of highly stressed LiNbO$_3$ and would contribute, with a comparable efficiency than an amorphous zone, to the observed dechanneling effects.

REFERENCES

1. M. Toulemonde, G. Fuchs. N. Nguyen, F. Studer and D. Groult. *Phys. Rev.,* **B35** (1987) 6560.
2. F. Studer, D. Groult, N. Nguyen and M. Toulemonde. *Nucl. Instr. and Meth.,* **B19/20** (1987) 856.
3. B. Canut, S. M. M. Ramos, P. Thevenard, N. Moncoffre, A. Benyagoub, G. Marest, A. Meftah, M. Toulemonde and F. Studer. *Nucl. Instr. and Meth.,* **B80/81** (1993) 1114.
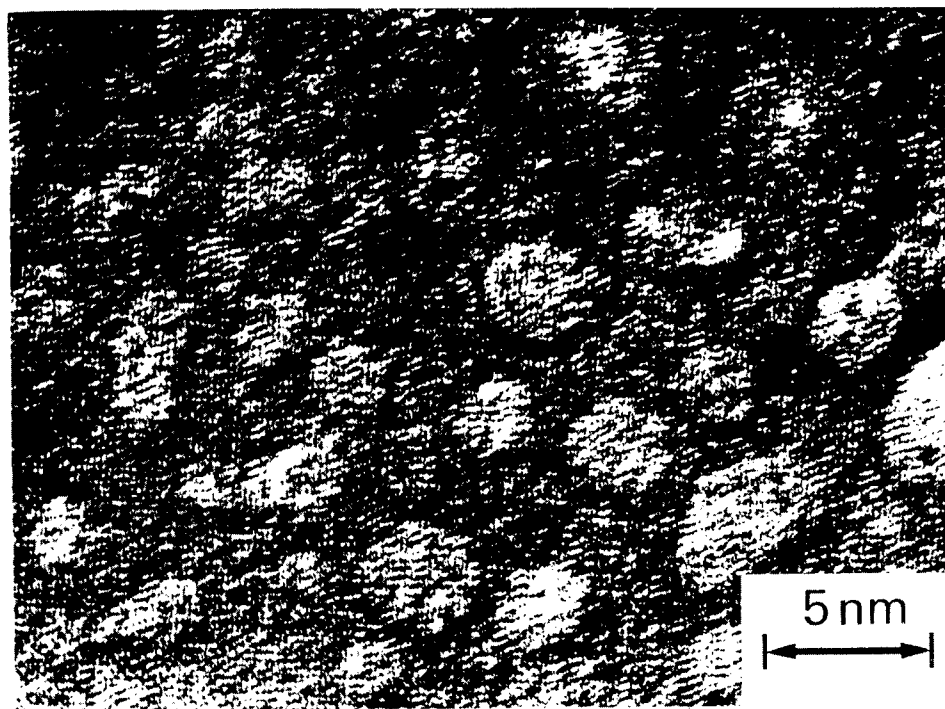
FIGURE 3   Dark field HRTEM micrograph of LiNbO$_3$ irradiated with $^{238}$U ions of 2.01 MeV/a energy. Fluence : $\Phi_t = 10^{11}$ ions.cm$^{-2}$.

4.  B. Canut, R. Brenier, A. Meftah, P. Moretti, S. Ould Salem, S. M. M. Ramos P. Thevenard and M. Toulemonde. *Nucl. Instr. and Meth.,* **B91** (1994) 312.
5.  J. F. Gibbons. *Proc. IEEE,* **60** (1972) 1062.
6.  A. Meftah, F. Brisard, J. M. Costantini, M. Hage-Ali, J. P. Stoquert, F. Studer and M. Toulemonde. *Phys. Rev.* **B48**, 2 (1993) 920.
7.  F. Studer. C. Houpert, H. Pascard, R. Spohr, J. Vetter J. Yun Fan and M. Toulemonde *Radiat. Eff. Def. Sol.,* **116** (1991) 59.

# MODIFICATION OF MAGNESIUM PHOSPHATE GLASS BY H$^+$ IRRADIATION:FORMATION OF OH-BOND AND PHOSPHORUS-COLLOID

## N. MATSUNAMI, K. KAWAMURA* and H. HOSONO*.

*Energy Engineering and Science, School of Engineering, Nagoya University, Furo-cho, Chikusa-ku, Nagoya 464-01, Japan; *Research Laboratory of Engineering Materials, Tokyo Institute of Technology, Nagatuta, Midori-ku, Yokohama 226, Japan*

MgO·P$_2$O$_5$ glasses were irradiated with 120 keV H$^+$ ions at room temperature to a dose of $10^{16} \sim 10^{18}$/cm$^2$. Optical absorption above 2 eV was found to increase by the ion irradiation and this is ascribed to phosphorus colloid formation. FTIR measurements showed that the absorption intensity near 3200 cm$^{-1}$ due to PO-H bond decreased at low ion dose ($<10^{17}$/cm$^2$) and increased at higher dose. This is ascribed to combination of PO-H bond breaking by ion irradiation and PO-H bond formation due to chemical interaction of H$^+$ ions with the substrate. Molecular water formation which was also found at a high dose and P colloid formation can be explained by reduction of P$_2$O$_5$ component with H$^+$ ions.

*Key words*: H$^+$ irradiation, MgO·P$_2$O$_5$ glass, P colloid, OH bond.

## 1 INTRODUCTION

Energetic ion irradiation has been known as interesting and attractive method to modify the properties of insulating oxide glasses. The modifications are based on the ion-induced rearrangements of substrate bonds and chemical interactions of ions with substrates. At present, such researches have been concentrated on especially SiO$_2$ and silicate glasses.[1-3] Although phosphate glasses have some unique applications such as biomaterials and protonic conduction,[4] few works have been reported on ion irradiation effects on phosphate glasses.[5,6] The previous paper[5] reports on P colloids formation in BaO·P$_2$O$_5$ glasses by D$^+$ ion irradiation, and a speculation of OD bond formation.

The present paper reports on OH bond breaking and OH bond formation by H$^+$ ion irradiation in MgO·P$_2$O$_5$ glasses. The OH bond breaking is discussed on the basis of the electronic energy deposition by ions. The OH bond formation may be understood in terms of Gibbs free energy, as described in the previous paper.[5] The Gibbs free energy of formation of 2MgO and (2/5)P$_2$O$_5$ are –1200 and –600 kJ/mol[7], respectively, suggesting the H$^+$ ion irradiation induced preferential reduction of P$_2$O$_5$. Effects of H$^+$ ion irradiation are considered from the relation between P colloid and OH bond formations.

## 2 EXPERIMENTAL

Samples of MgO·P$_2$O$_5$ glasses were prepared as follows. The mixture of water and reagent grade MgO and H$_3$PO$_4$ (85%) in a silica beaker was stirred well and heated to about 200°C. The resulting dried products were melted for 1 hr in a Pt crucible at $\sim$ 1450°C.

Then the melts were poured on a carbon plate and annealed around the glass transformation temperature of 550°C.

The glass substrates were irradiated in a vacuum of $\sim 10^{-6}$ mbar at room temperature and at normal incidence, using a 200 kV ion accelerator, as described previously.[5] The
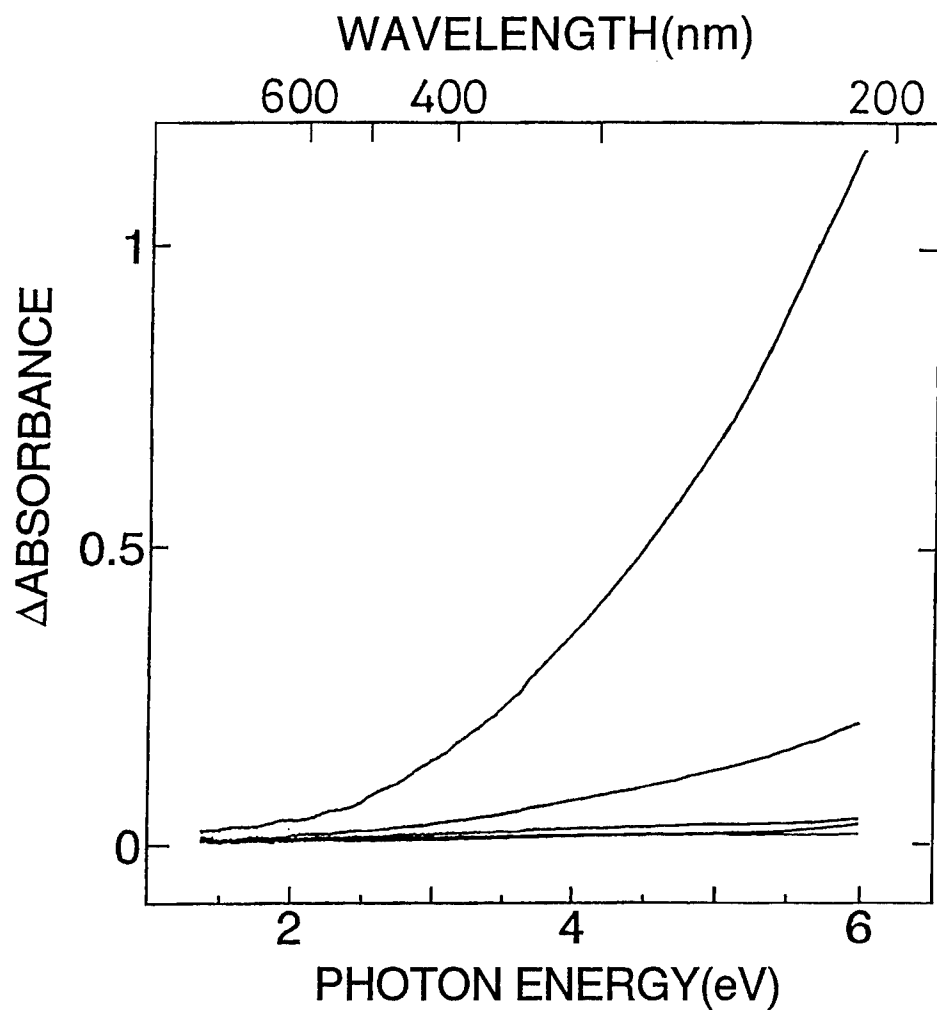
FIGURE 1   Optical absorption spectra of MgO·P$_2$O$_5$ glasses induced by irradiation with 120 keV H$^+$ to doses of 1 × 10$^{16}$, 3 × 10$^{16}$, 1 × 10$^{17}$, 3 × 10$^{17}$ and 1× 10$^{18}$/cm$^2$, from the bottom to top curves. Here the optical absorption of unirradiated sample was subtracted.

beam size was 5 mm in diameter and the beam current was ∼ 3 $\mu$A. The temperature rise during irradiation was < 50°C.

Optical absorption was measured using a conventional dual-beam spectrometer. FTIR(Fourier transform infra-red spectroscopy) measurements were performed using a Perkin Elmer model 1615 spectrometer.

## 3   RESULTS AND DISCUSSION

Figure 1 shows the optical absorption of MgO·P$_2$O$_5$ glasses irradiated with 120 keV H$^+$. The optical absorption from 2 to 6 eV increased as increasing ion dose and this is ascribed
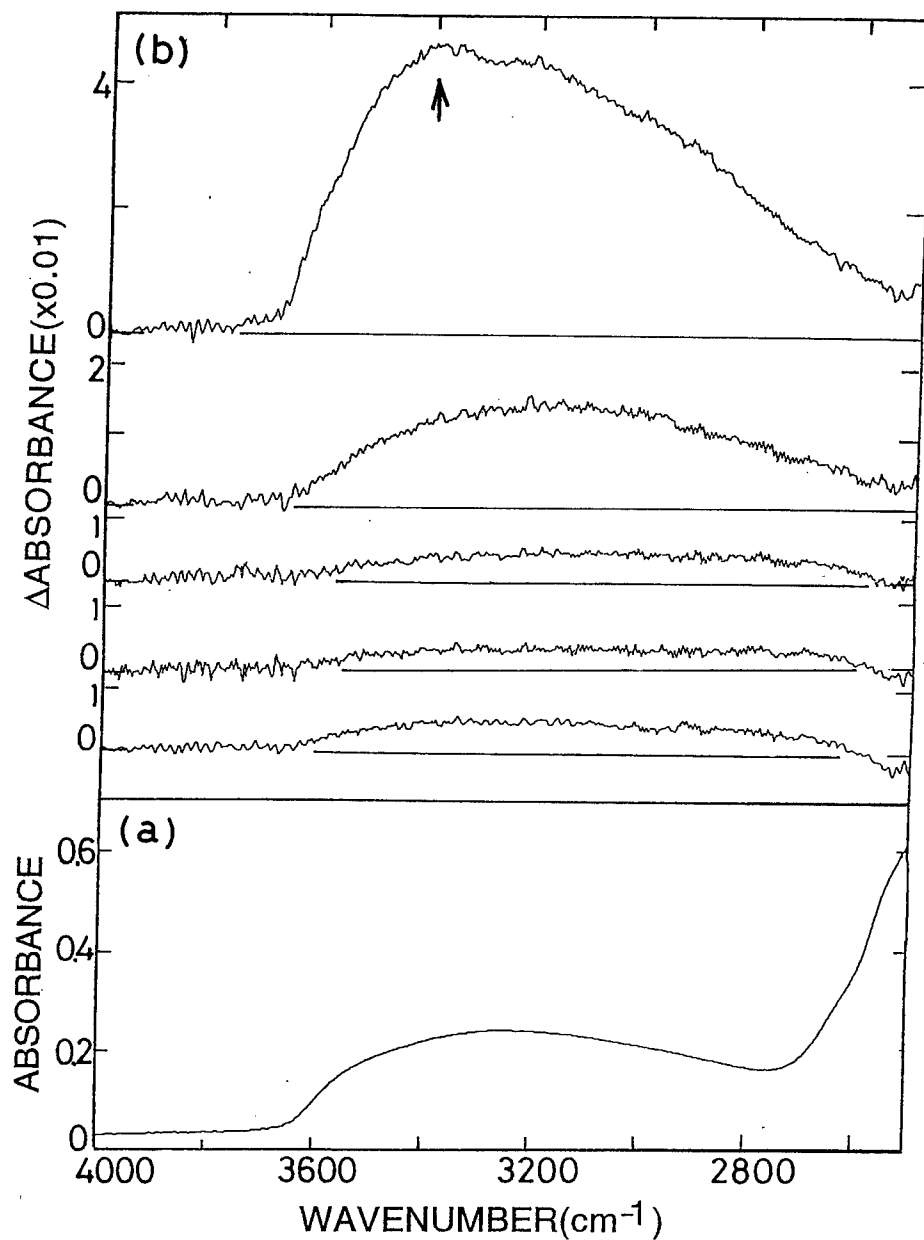
FIGURE 2   (a) FTIR spectrum of unirradiated $MgO \cdot P_2O_5$ glass. Intensive band appearing below $\sim 2700$ cm$^{-1}$ is due to overtones of fundamental vibration of P-O network. (b) FTIR spectra of $MgO \cdot P_2O_5$ glasses irradiated with 120 keV H⁺ to doses of $1 \times 10^{16}$, $3 \times 10^{16}$, $1 \times 10^{17}$, $3 \times 10^{17}$ and $1 \times 10^{18}$/cm$^2$, from the bottom to top curves. Each spectrum was obtained by subtracting the spectrum of unirradiated sample from that of irradiated one. An arrow on the top near 3400 cm$^{-1}$ denotes a band assigned to molecular water.
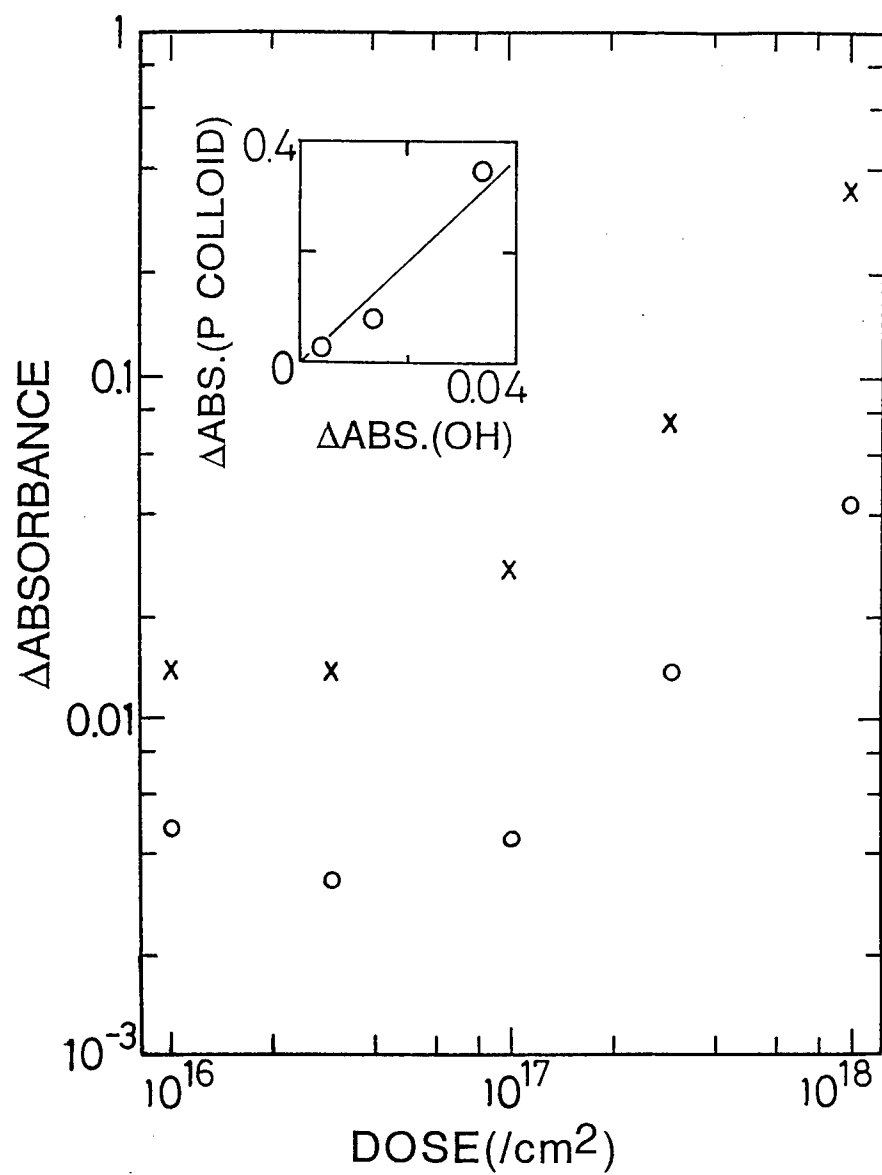
FIGURE 3   $H^+$ ion dose dependence of optical absorbance at 4 eV (x) due to P colloids in Figure 1 and FTIR absorbance at 3200 $cm^{-1}$(o) due to OH bonds in Figure 2(b). The relation between these two absorbances for dose > $10^{17}$/$cm^2$ is shown in the inset.

to P colloid formation, as in $D^+$ ion irradiated $BaO \cdot P_2O_5$ glasses,[5] referring to the results for $P^+$ ion irradiated $SiO_2$ glasses.[8]

FTIR spectrum for unirradiated sample is shown in Figure 2(a). The peak around $3200 \text{ cm}^{-1}$ originates from PO-H incorporating into the substrate structure.[9] Using the absorption cross section ($5 \times 10^4 \text{ cm}^2/\text{mol}$) in ref.[9] and sample thickness of 0.4 mm, the concentration of OH bonds was estimated as $6 \times 10^{19}/\text{cm}^3$. Figure 2(b) shows the change in FTIR spectra by $H^+$ ion irradiation. It is seen that the absorption due to PO-H bond near $3200 \text{ cm}^{-1}$ decreases below $10^{17}/\text{cm}^2$ and then increases at higher doses. At a dose of $10^{18}/\text{cm}^2$, a new peak around $3400 \text{ cm}^{-1}$ appears, which is tentatively ascribed to molecular water ($H_2O$).[10]

Figure 3 shows the $H^+$ ion dose dependence of optical absorbance at 4 eV in Figure 1 and FTIR absorbance at $3200 \text{ cm}^{-1}$, which represent numbers of P atoms in P colloids and OH bonds induced by $H^+$ ion irradiation, respectively. For doses $> 10^{17}/\text{cm}^2$, both numbers increase with nearly the same rate as the ion dose, as shown in the inset of Figure 3, indicating the close relation between P colloid and P-OH bond formations. Furthermore, absorption near $3200 \text{ cm}^{-1}$ was found to decrease for 120 keV $He^+$ ion irradiation, confirming the significant contribution of irradiated $H^+$ ion to OH bond formation. The fraction of irradiated $H^+$ contributing to OH bond formation is estimated as $\sim 50\%$. Here it is assumed that irradiated hydrogens distribute within the projected range, considering the observations that the depth profile of D becomes broad at $10^{18}/\text{cm}^2$ and tends to be uniform within the irradiated region, as shown in Table I, where TRIM[11] and NRA results are summarized. In conclusion, the $H^+$ ion irradiation effects at high doses can be ascribed to the reduction of $PO_4$ tetrahedron to neutral P state such as P colloid, resulting in P-OH and $H_2O$ formations.

Table I

Projected range (Rp), FWHM (full width at half maximum) of the range profiles, and electronic and nuclear energy depositions calculated with TRIM for 120 keV $H^+$, 120 keV $He^+$ and 100 keV $D^+$ in $MgO \cdot P_2O_5$ glass (density = 2.42 $g/cm^3$). The results of range profiles of $D^+$ obtained with $D(^3He, {}^4He)p$ nuclear reaction analysis are also included. Here $E(^3He) = 1, 1.5$ MeV, detection angle of 160° and normal incidence are employed.

| Ion | $H^+$ | $He^+$ | $D^+$ | |
|---|---|---|---|---|
| E(keV) | 120 | 120 | 100 | |
| TRIM | | | | |
|   Rp ($\mu$m) | 1.1 | 0.74 | 1.1 | |
|   FWHM ($\mu$m) | 0.15 | 0.22 | 0.19 | |
|   Energy deposition | | | | |
|   Electronic (keV) | 119 | 111 | 98 | |
|   Nuclear (keV) | 1 | 9 | 2 | |
| NRA | | | | |
|   Dose ($10^{17}/\text{cm}^2$) | | | 1 | 10 |
|   D retention($10^{17}/\text{cm}^2$) | | | 0.89 | 8.4 |
|   Rp ($\mu$m) | | | 1.2 | 0.92 |
|   FWHM($\mu$m) | | | 0.38 | 0.81 |
|   Maximum of $N_D/N_p^{1)}$ | | | 0.14 | 0.63 |

1) $N_D$ and $N_p$ denote densities of D and P, respectively.

It is also noticed that the maximum density of D or H in $MgO \cdot P_2O_5$ glasses is comparable with P density and no saturation was observed in this study. This makes a contrast with the low saturation value of H(D), namely, 5–10% of Si in $SiO_2$ glasses.[12] Since the Gibbs free energy of formation of $SiO_2$ is –850 KJ/mol[7], the reduction of $SiO_2$ is much harder than that of $P_2O_5$ and the incorporation of H into $SiO_2$ network is limited to a certain low value.

At low ion doses, the rates of decrease in P-OH bonds are $7 \times 10^{-4}$ and $4 \times 10^{-4}$ per $10^{16}/cm^2$ for 120 keV $H^+$ and $He^+$, respectively. Referring to Table I, the nuclear energy deposition $\Delta En$ by $He^+$ is larger by an order of magnitude than $\Delta En$ by $H^+$, and the electronic energy deposition $\Delta Ee$ are similar for both ions. Thus the electronic energy deposition is responsible for the OH bond breaking.

## 4    SUMMARY

By $H^+$ ion irradiation in $MgO \cdot P_2O_5$ glass, OH bonds break up due to the electronic energy deposition by ions at low dose ($< 10^{17}/cm^2$). At higher doses, the reduction of $PO_4$ tetrahedron to neutral P (or P colloid) overcomes OH bond breaking due to interaction of irradiated $H^+$ with substrate and this results in P-OH and $H_2O$ formations. The maximum concentration of D(H) in $MgO \cdot P_2O_5$ glass is considerably large, in contrast to low saturation value of 5–10% in $SiO_2$ glass.

REFERENCES

1.  G. W. Arnold and P. Mazzoldi (eds.), *Ion Beam Modification of Insulators* (Elsevier, 1987) p. 195.
2.  P. Mazzoldi (eds.), *Modifications Induced by Irradiation in Glasses* (North-Holland, 1992).
3.  R. A. Weeks, *Mater. Sci. and Technol.* **Vol. 9** (VCH Verlagsgesellschaft; Weinheim, Germany, 1991) chap. 6.
4.  Y. Abe and H. Hosono, *Inorganic Phosphate Materials*, ed. by T. Kanazawa (Elsevier, NY, 1989) chap. 10.
5.  N. Matsunami and H. Hosono, *Nucl. Instrum. & Meth.* **B91**, 525 (1994).
6.  N. Matsunami and H. Hosono, *Nucl. Instrum & Meth.* **B80/81**, 1233 (1993).
7.  R. C. Weast and M. J. Astle, *CRC Handbook of Chemistry and Physics* 63ed. (1982).
8.  H. Hosono, Y. Suzuki, Y. Abe, K. Oyoshi and S. Tanaka, *J. Non-Cryst. Solids* **142**, 287 (1992).
9.  H. Hosono, T. Kamae and Y. Abe, *J. Amer. Ceram. Soc.* **72**, 294 (1989).
10. F. M. Ernsberger, *J. Amer. Ceram. Soc.* **60**, 91 (1977).
11. J. F. Ziegler, J. P. Biersack and U. Littmark, *The Stopping and Ranges of Ions in Solids* (Pergamon Press, 1985).
12. G. W. Arnold, *Nucl. Instrum. & Meth.* **B32**, 268 (1988).

# Notes for Contributors

## EQUATIONS AND FORMULAE (CHEMICAL)

Ring formulae, and other complex chemical matter, are extremely difficult to typeset. Please therefore, supply reproducible artwork for equations containing such chemistry. Long reaction sequences should be designated as "Schemes" and treated like figures: i.e. keep artwork separate from the text, indicate in the margin an appropriate position, and supply a separate list of scheme captions. Where necessary, individual chemical formulae can be identified with bold arabic numbers. Chemical equations referred to in the text should be indicated with arabic numbers set over to the right in parentheses.

*Marking*: Where chemistry is straightforward and can be set (e.g. single-line formulae), please help the typesetter by distinguishing between e.g., double bonds and equal signs, and single bonds and hyphens, where there is ambiguity. The printer finds it difficult to identify which symbols should be set in roman (upright), italic, or bold type, especially where the paper contains both mathematics and chemistry. Therefore, please help the printer as much as possible by adding marginal notes in pencil.

## TABLES

Number tables consecutively with roman numerals, and give each a clear descriptive caption at the top. Avoid the use of vertical rules in tables.

## UNITS

Metric units are preferred. Acceptable abbreviations of units are given in the *Style Manual* of the American Institute of Physics and similar publications.

## REFERENCES AND NOTES

References and notes are indicated in the text by consecutive superior arabic numbers. The full list should be collected and typed at the end of the paper in numerical order. Listed references should be complete in all details but excluding article titles in journals. Authors' initials should precede their names: journal title abbreviations should conform to *Physical Abstracts*. Examples:

1. A. B. Smith and C. D. Jones, *J. Appl. Phys.* **34**, 296 (1965).
2. R. B. Brown, *Molecular Spectroscopy* (Gordon and Breach, New York, 1970), 3rd ed., Chap. 6, pp. 95, 106.

## TEXT HEADINGS

Set first-level headings in the text over to the left, type all in capitals (upper-case); begin the text on the following line. Second-level headings should be typed in small (lower-case) letters with all main words capitalized. Underline the heading and start the text on the next line. For third-level headings, only the first letter should be a capital. Underline, then run on the text after three typewriter spaces.

FIRST LEVEL HEADING

Second-Level Text Headings

Third-level headings. With text run on.

## PROOFS

Authors will receive proofs (including figures) by airmail for correction, which must be returned to the printer within 48 hours of receipt. Please ensure that a full postal address is given on the first page of the manuscript, so the proofs are not delayed in the post. Author's alterations in excess of 10% of the original composition will be charged to authors.

## REPRINTS

The senior author of each paper will receive 25 complimentary reprints. Additional reprints may be ordered by completing the appropriate form sent with proofs.

## PAGE CHARGES

There are no page charges to individuals or to institutions.

## A FINAL NOTE

Typescripts which do not conform to the required standards of preparation for submission outlined here will be returned to authors for correction before review.

# SCIENCE SPECTRA

THE INTERNATIONAL MAGAZINE OF CONTEMPORARY SCIENTIFIC THOUGHT
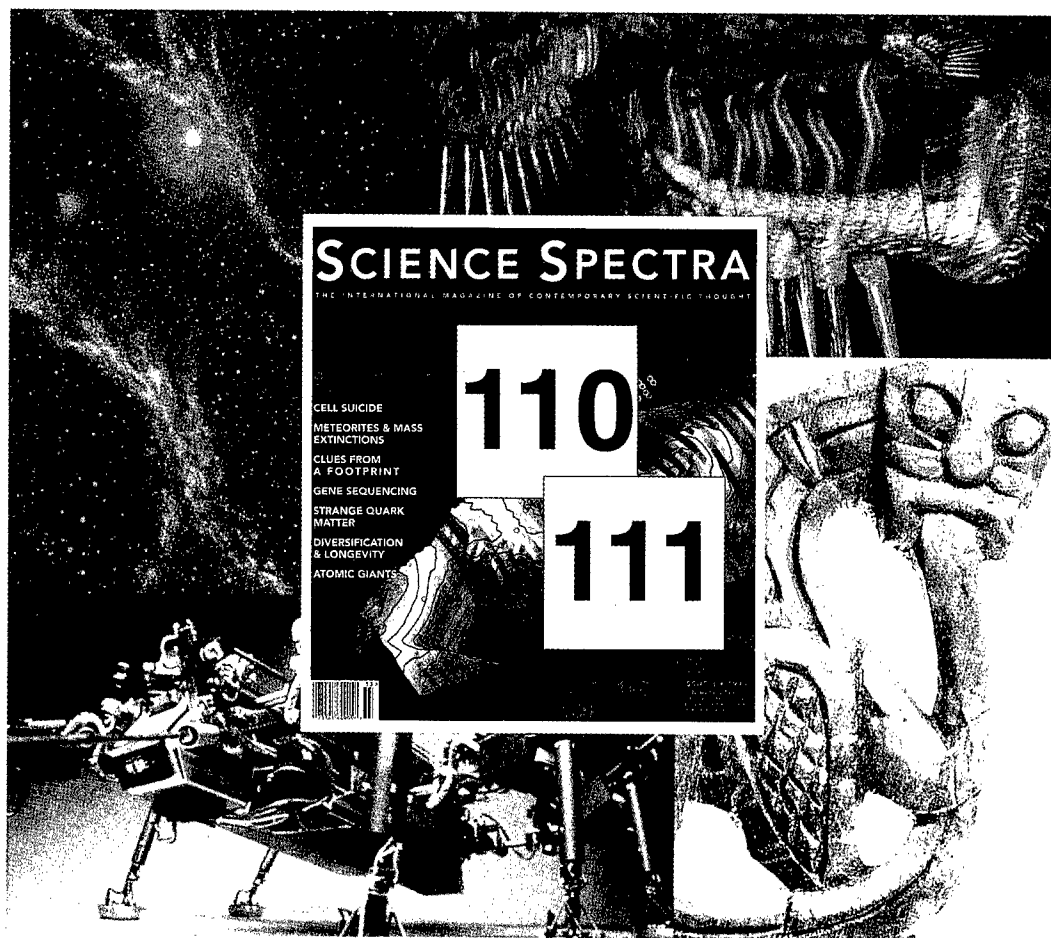


FROM CELLS TO SUPERNOVAS, FROM NUCLEAR CHEMISTRY TO ARTIFICIAL INTELLIGENCE, FROM ANCIENT HISTORY TO FUTURE THOUGHT...

*Science Spectra* is a magazine for scientists, by scientists, that takes you on a journey to the frontiers of research and contemporary scientific thought. With a team of editors who are leading scientists in their fields, and backed by the international science publishing house Gordon and Breach, *Science Spectra* is a cross-disciplinary magazine that brings you the full spectrum of today's science.

**Subscribe now at US$32/£20/SFr48/Aus.$34 for four issues (15% off cover price), or at US$49/£32/SFr73/Aus.$52 for eight issues (35% off cover price).** Your check or money order should be directed and made payable to: